



# LUND UNIVERSITY

## Atomic Electrons as Sensitive Probes of Nuclear Properties and Astrophysical Plasma Environments

### A Computational Approach

Papoulia, Asimina

2021

*Document Version:*

Publisher's PDF, also known as Version of record

[Link to publication](#)

*Citation for published version (APA):*

Papoulia, A. (2021). *Atomic Electrons as Sensitive Probes of Nuclear Properties and Astrophysical Plasma Environments: A Computational Approach*. [Doctoral Thesis (compilation), Lund University]. Lund University.

*Total number of authors:*

1

*Creative Commons License:*

Unspecified

#### General rights

Unless other specific re-use rights are stated the following general rights apply:

Copyright and moral rights for the publications made accessible in the public portal are retained by the authors and/or other copyright owners and it is a condition of accessing publications that users recognise and abide by the legal requirements associated with these rights.

- Users may download and print one copy of any publication from the public portal for the purpose of private study or research.
- You may not further distribute the material or use it for any profit-making activity or commercial gain
- You may freely distribute the URL identifying the publication in the public portal

Read more about Creative commons licenses: <https://creativecommons.org/licenses/>

#### Take down policy

If you believe that this document breaches copyright please contact us providing details, and we will remove access to the work immediately and investigate your claim.

LUND UNIVERSITY

PO Box 117  
221 00 Lund  
+46 46-222 00 00

# Atomic Electrons as Sensitive Probes of Nuclear Properties and Astrophysical Plasma Environments

ASIMINA PAPOULIA

FACULTY OF SCIENCE | DEPARTMENT OF PHYSICS | LUND UNIVERSITY 2021



Atomic Electrons as Sensitive Probes of Nuclear Properties and  
Astrophysical Plasma Environments





# Atomic Electrons as Sensitive Probes of Nuclear Properties and Astrophysical Plasma Environments A Computational Approach

by Asimina Papoulia



**LUND**  
UNIVERSITY



**MALMÖ**  
UNIVERSITY

Thesis for the degree of Doctor of Philosophy  
Thesis advisors: Prof. Tomas Brage, Prof. Per Jönsson, and  
Assoc. Prof. Jörgen Ekman  
Faculty opponent: Prof. Patrick Palmeri

To be presented, with the permission of the Faculty of Science of Lund University, for public criticism  
in the Rydberg lecture hall (Rydbergsalen) at the Department of Physics, Sölvegatan 14A, Lund, on  
Friday, the 7th of May 2021 at 13:15.

Organization <b>LUND UNIVERSITY</b> Department of Physics Box 118 SE-221 00 LUND Sweden		Document name <b>DOCTORAL THESIS</b>
		Date of disputation 2021-05-07
		Sponsoring organization
Author(s) Asimina Papoulia		
Title and subtitle Atomic Electrons as Sensitive Probes of Nuclear Properties and Astrophysical Plasma Environments - A Computational Approach		
Abstract <p>This thesis deals with the relativistic modeling of atoms and ions. To interpret the stellar spectra and gain more insight from astrophysical observations, the underlying processes that generate the spectra need to be well understood and described. Examples of such processes are the interactions of atomic electrons with internal and external electromagnetic fields and with the nucleus.</p> <p>By exploring different computational methodologies, Paper I analyzes how the transition probabilities, of transitions involving high Rydberg states, depend on the gauge and the orbital set that is used in the calculations. Papers II and III contain large homogeneous data sets of parameters related to atomic radiative processes, namely transition energies, transition probabilities, weighted oscillator strengths, and lifetimes of excited states, for carbon and aluminium systems. These parameters are essential in astrophysical applications, e.g., in abundance and plasma analyses of stars. In addition, Paper IV presents extended data of Landé g-factors, used to characterize the response of spectral lines to a given value of an external magnetic field.</p> <p>The description of effects arising from the interplay between atomic electrons and nuclei, such as hyperfine structure splittings and isotope shifts, requires that the nuclear structure properties giving rise to these effects are well determined. This is, however, not always the case; as we move away from the valley of stability, data of nuclear structure observables are scarce. High-resolution measurements of hyperfine structures and isotope shifts, combined with first-principles atomic structure calculations, are commonly used to probe the structures of nuclei, including short-lived and radioactive systems. In Papers V and VI, measurements of the hyperfine structure in neutral tin were combined with atomic structure calculations to extract the electric quadrupole moments of tin isotopes. Paper VII presents a novel method that combines experimental isotope shifts and calculations of atomic parameters to probe details of nuclear charge density distributions, other than charge radii.</p>		
Key words computational atomic structure, relativistic atomic theory, transition probabilities, abundance analysis, Landé g-factors, hyperfine structure, nuclear quadrupole moments, isotope shift, field shift, nuclear deformation		
Classification system and/or index terms (if any)		
Supplementary bibliographical information		Language English
ISSN and key title		ISBN 978-91-7895-801-6 (print) 978-91-7895-802-3 (pdf)
Recipient's notes		Number of pages 235
		Price Security classification

I, the undersigned, being the copyright owner of the abstract of the above-mentioned dissertation, hereby grant to all reference sources the permission to publish and disseminate the abstract of the above-mentioned dissertation.

Signature



Date 2021-03-25

# Atomic Electrons as Sensitive Probes of Nuclear Properties and Astrophysical Plasma Environments

## A Computational Approach

by Asimina Papoulia



**LUND**  
UNIVERSITY



**MALMÖ**  
UNIVERSITY

A doctoral thesis at a university in Sweden takes either the form of a single, cohesive research study (monograph) or a summary of research papers (compilation thesis), which the doctoral student has written alone or together with one or several other author(s).

In the latter case the thesis consists of two parts. An introductory text puts the research work into context and summarizes the main points of the papers. Then, the research publications themselves are reproduced, together with a description of the individual contributions of the authors. The research papers may either have been already published or are manuscripts at various stages (in press, submitted, or in draft).

**Cover illustration front:** Equations that describe atomic structure properties computed in the papers that are included in the thesis.

**Funding information:** The thesis work was financially supported by the Swedish Research Council (VR) under contract 2015–04842.

© Asimina Papoulia 2021

Faculty of Science, Department of Physics

ISBN: 978-91-7895-801-6 (print)

ISBN: 978-91-7895-802-3 (pdf)

Printed in Sweden by Media-Tryck, Lund University, Lund 2021



Media-Tryck is a Nordic Swan Ecolabel certified provider of printed material. Read more about our environmental work at [www.mediatryck.lu.se](http://www.mediatryck.lu.se)

**MADE IN SWEDEN** 

*Dedicated to  
my parents*



# Contents

List of publications . . . . .	iii
Acknowledgements . . . . .	v
Popular summary . . . . .	vii
Populärvetenskaplig sammanfattning på svenska . . . . .	ix
<b>Atomic Electrons as Sensitive Probes of Nuclear Properties and Astrophysical Plasma Environments - A Computational Approach</b>	<b>I</b>
<b>1 Introduction and Motivation</b>	<b>3</b>
<b>2 Relativistic Atomic Structure</b>	<b>9</b>
2.1 Relativistic Many-Electron Hamiltonians . . . . .	10
2.1.1 The Dirac-Coulomb Hamiltonian . . . . .	10
2.1.2 Breit interaction . . . . .	11
2.2 Relativistic Wave Functions . . . . .	13
2.2.1 One-electron Dirac orbitals . . . . .	14
2.2.2 Configuration state functions . . . . .	17
2.2.3 Atomic state functions . . . . .	18
2.3 Multiconfiguration Dirac-Hartree-Fock . . . . .	19
2.3.1 Energy matrix elements . . . . .	20
2.3.2 The MCDHF equations . . . . .	22
2.3.3 Self-consistent field procedure . . . . .	23
2.3.4 Relativistic configuration interaction . . . . .	25
2.4 Computation of Atomic Properties . . . . .	25
2.5 General Computational Methodology . . . . .	26
<b>3 Spectrum Calculations of Transition Properties Involving Rydberg Series</b>	<b>29</b>
3.1 Transition Properties . . . . .	32
3.2 C I-IV . . . . .	35
3.2.1 Results and discussion . . . . .	36
3.3 Al I-II . . . . .	38
3.3.1 Computations . . . . .	40
3.3.2 Results . . . . .	41
3.3.3 Beyond Paper III . . . . .	42

3.4	Landé g-factors . . . . .	43
<b>4</b>	<b>Hyperfine Structure - Extracting Nuclear Quadrupole Moments of Tin Isotopes</b>	<b>45</b>
4.1	Hyperfine Structure . . . . .	48
4.2	Computing the Electronic Factors $A_{el}$ and $B_{el}$ . . . . .	51
4.2.1	The SrD-MR-MCDHF and RCI calculations . . . . .	52
<b>5</b>	<b>Probing Nuclear Properties in Heavy Atoms via Isotope Shifts</b>	<b>57</b>
5.1	Isotope Shift . . . . .	60
5.1.1	Mass shift . . . . .	61
5.1.2	Field shift . . . . .	62
5.2	Realistic Nuclear Charge Distributions . . . . .	65
5.3	Simultaneous Extraction of $\delta\langle r^2 \rangle$ and $\delta\langle r^4 \rangle$ . . . . .	68
5.4	Errors in the Extraction of $\delta\langle r^2 \rangle$ and $\delta\langle r^4 \rangle$ . . . . .	69
5.4.1	Systematical errors . . . . .	69
5.4.2	Statistical errors . . . . .	69
<b>6</b>	<b>Outlook</b>	<b>71</b>
	<b>Appendices</b>	<b>73</b>
	<b>Appendix A Non-relativistic Electric Dipole Transition Operators</b>	<b>75</b>
	<b>Appendix B Non-relativistic Mass Shift</b>	<b>77</b>
	<b>References</b>	<b>79</b>
	<b>Scientific Publications</b>	<b>93</b>
	Author contributions . . . . .	93
	Paper I: Coulomb (Velocity) Gauge Recommended in Multiconfiguration Calculations of Transition Data Involving Rydberg Series . . . . .	97
	Paper II: Extended theoretical transition data in C I-IV . . . . .	115
	Paper III: Extended transition rates and lifetimes in Al I and Al II from systematic multiconfiguration calculations . . . . .	137
	Paper IV: Multiconfiguration Dirac-Hartree-Fock calculations of Landé g-factors for ions of astrophysical interest: B II, C I-IV, Al I-II, Si I-IV, P II, S II, Cl III, Ar IV, Ca I, Ti II, Zr III and Sn II . . . . .	155
	Paper V: Structural trends in atomic nuclei from laser spectroscopy of tin . . . . .	169
	Paper VI: <i>Ab initio</i> electronic factors of the $A$ and $B$ hyperfine structure constants for the $5s^25p6s\ 1,3P_1^o$ states in Sn I . . . . .	181
	Paper VII: Effect of realistic nuclear charge distributions on isotope shifts and progress towards the extraction of higher-order nuclear radial moments . . . . .	199



# List of publications

This thesis is based on the following publications, referred to by their Roman numerals:

- I **Coulomb (Velocity) Gauge Recommended in Multiconfiguration Calculations of Transition Data Involving Rydberg Series**  
A. Papoulia, J. Ekman, G. Gaigalas, M. Godefroid, S. Gustafsson, H. Hartman, W. Li, L. Radžiūtė, P. Rynkun, S. Schiffmann, K. Wang, and P. Jönsson  
*Atoms*, 2019, 7(4), 106
- II **Extended theoretical transition data in C I-IV**  
W. Li, A. Amarsi, A. Papoulia, J. Ekman, and P. Jönsson  
*Monthly Notices of the Royal Astronomical Society*, 2021, 502(3), 3780
- III **Extended transition rates and lifetimes in Al I and Al II from systematic multiconfiguration calculations**  
A. Papoulia, J. Ekman, and P. Jönsson  
*Astronomy & Astrophysics*, 2019, 621, A16
- IV **Multiconfiguration Dirac-Hartree-Fock calculations of Landé g-factors for ions of astrophysical interest: B II, C I-IV, Al I-II, Si I-IV, P II, S II, Cl III, Ar IV, Ca I, Ti II, Zr III and Sn II**  
W. Li, P. Rynkun, L. Radžiūtė, G. Gaigalas, B. Atalay, A. Papoulia, K. Wang, H. Hartman, J. Ekman, T. Brage, C. Y. Chen, and P. Jönsson  
*Astronomy & Astrophysics*, 2020, 639, A25
- V **Structural trends in atomic nuclei from laser spectroscopy of tin**  
D. T. Yordanov, L. V. Rodriguez, D. L. Balabanski, J. Bieroń, M. L. Bissell, K. Blaum, B. Cheal, J. Ekman, G. Gaigalas, R. F. Garcia Ruiz, G. Georgiev, W. Gins, M. R. Godefroid, C. Gorges, Z. Harman, H. Heylen, P. Jönsson, A. Kanellakopoulos, S. Kaufmann, C. H. Keitel, V. Lagaki, S. Lechner, B. Maaß, S. Malbrunot-Ettenauer, W. Nazarewicz, R. Neugart, G. Neyens, W. Nörtershäuser, N. S. Oreshkina, A. Papoulia, P. Pyykkö, P.-G. Reinhard, S. Sailer, R. Sánchez, S. Schiffmann, S. Schmidt, L. Wehner, C. Wraith, L. Xie, Z. Xu, and X. Yang  
*Communications Physics*, 2020, 3(1), 107

VI **Ab initio electronic factors of the  $A$  and  $B$  hyperfine structure constants for the  $5s^25p6s\ ^1,^3P_1^o$  states in Sn I**

A. Papoulia, S. Schiffmann, J. Bieroń, G. Gaigalas, M. Godefroid, Z. Harman, P. Jönsson, N. S. Oreshkina, P. Pyykkö, and I. I. Tupitsyn  
*Physical Review A*, 2021, 103(2), 022815

VII **Effect of realistic nuclear charge distributions on isotope shifts and progress towards the extraction of higher-order nuclear radial moments**

A. Papoulia, B. G. Carlsson, and J. Ekman  
*Physical Review A*, 2016, 94(4), 042502

All papers are reproduced with permission of their respective publishers.

## Acknowledgements

I would like to express my most sincere gratitude to my supervisors, Per Jönsson, Jörgen Ekman, and Tomas Brage, for their constant guidance and support during these past four and a half years. Thank you for giving me the opportunity to work with you, in the first place, and for all our discussions, the time you spent answering my questions, and your invaluable feedback. You have made me feel inspired and motivated, and I can most certainly say that this has been an exciting journey!

I would also like to thank Henrik Hartman, for all the discussions that we had, on astrophysical topics and beyond, the fun times at the conferences in Shanghai and Brussels, and for showing me the way to the coffee machine my first day at work at Malmö University. First things first! I am especially grateful to Mats Persson for his warm welcome to the MTM Department at Malmö University and for always being happy to help me with all kinds of matters. I am also thankful to Katja Frid for her thoughtfulness and immediate assistance in the most critical times. I wish the circumstances were different this past one year and had the opportunity to spend more time with you in person. It has always been a pleasure discussing with you. In addition, I thank all the PhD students that I shared the office with; I am grateful for all the interesting discussions that we had and viewpoints that we shared.

I further wish to thank the members of the LUMCAS group and the broader CompAS community for making me enjoy every single meeting and conference and reminding me that physics is, above all, fun. In particular, I am thankful to Michel Godefroid for the crucial help and perpetual guidance that he provided during the collaborations of Paper v and, especially, Paper vi. Your careful investigations and comments, as well as your kindness, have continuously inspired me during my PhD studies. I would also like to thank Henrik Jönsson and Brian Thorsbro for the nice figures of spectra that made my introduction more interesting and for their insights on astrophysics, reminding me why all this computational power is worth spending.

I wish to thank my colleagues at the division of Mathematical Physics at Lund University, and in particular, Katarina Lindqvist for creating a nice atmosphere and for always being helpful, even during the busiest times. I also want to thank Sara Kheradsoud, Bahareh Goldozian, Josef Josefi, Gunnar Eriksson, and all the PhD students I have met at the division over the years. Special thanks go to Cecilia Jarlskog for the interesting stories and advice that she had been sharing with me.

I would also like to express my deep appreciation to Olga Paizi, who has been in this entire journey with me, guiding me to explore my inner shelf and helping me to grow.

Coming that far –being sleepless two days in a row and having a few hours left before

printing this thesis– would not have been possible without the support and encouragement of my friends. Thank you Marina for never getting tired of listening to me, for never getting tired of me being tired, and thank you for simply being you. Thank you Lorena for being the most genuine person I know and always speaking your mind to me, for your support, and for being in my life. Thank you Zizi for being the amazing person that you are and for continuously inspiring me, Virginia for always being there for me and for mutually creating the best year of our lives in Sweden, which is probably one of the reasons that I am still here, and Chryssa for your continuous encouragement. I would also like to thank all these friends that have made Sweden feel home to me.

I am far beyond grateful, Katerina. You have supported me like no other, believed in me from day one, and firmly been by my side –even during the most challenging times. Thank you!

I am most thankful to my mom and dad for supporting me at every step and direction I took in life. It is thanks to their sacrifices that I could get this far and complete this work. Thank you for encouraging me to get out of my comfort zone and to do what truly makes me happy in life.

## Popular summary

To correctly describe the laws that govern the physical world, we have to study the structure of matter and the interactions between the fundamental constituents of the universe. The basic building block for all regular matter in the universe is the atom, which is made up of electrons orbiting the atomic nucleus. The atom is a quantal many-body system, characterized by the discrete, and distinctive for each element, energy levels of the electrons. Interactions of the electrons with internal and external electromagnetic fields give rise to atomic transitions, through absorption, or emission, of photons with certain energies, causing the total energy of the system to change. Since the allowed energy levels are unique to an element, so are the energies corresponding to transitions between those levels.

Our knowledge on the formation and evolution of the universe, in principle, comes from the electromagnetic radiation that is emitted from stars through atomic transitions. The emitted electromagnetic radiation is, commonly, displayed as an energy spectrum, which contains lines of different energies and intensities. The positions of the spectral lines reveal the elements a specific star consists of, and from their intensities the elemental abundances can be deduced. For the interpretation of the observed spectra, reference atomic data are, however, needed. Laboratory measurements are usually costly and time-consuming, and as a result, the produced experimental data are not always sufficient. It is, therefore, necessary to develop –and continuously improve the already existing– quantum mechanical models that describe the atomic structure and underlying processes that generate the observed spectra. Computations can, then, be performed to predict atomic parameters, such as energies and probabilities of atomic transitions. Such examples are the computations that were performed in Papers I-III for several carbon and aluminium ions. Atomic parameters used to characterize the response of spectral lines to a given value of an external magnetic field were additionally generated in Paper IV.

Although the atomic nucleus is  $\sim 10^4$  times smaller than the size of the atom, its finite mass and extended charge density distribution have a measurable effect on the atomic spectra. For a particular element, the spectral lines from different isotopes display a small shift in energy, known as the isotope shift. In systems containing a nucleus with a non-zero total spin, the nuclear electromagnetic moments, further, interact with the electromagnetic field generated by the electrons at the region of the nucleus. This interaction results in splittings of the atomic energy levels, known as the hyperfine structure, and in consequence, transitions between these levels emerge in the spectra as different lines. The atomic electrons are, therefore, sensitive probes of the properties of the nucleus they are bound to. In Papers V-VII, we show how the modeling of isotope shifts and hyperfine structures can be combined with experimen-

tal data to extract information about the specifics of the charge density distributions and the electromagnetic moments of nuclei. Nuclear-model independent information are used to benchmark nuclear structure calculations based on different effective interactions. An understanding of the structure and dynamics of atomic nuclei is fundamental to our overall picture of the universe, as nucleosynthesis is inseparably connected with stellar and galactic evolution.

## Populärvetenskaplig sammanfattning på svenska

För att beskriva lagarna som styr den fysiska världen, behöver vi studera materiens struktur och hur dess olika delar växelverkar. Den grundläggande byggstenen för all känd materia i universum är atomen, vilken består av elektroner som rör sig runt en atomkärna. Atomen är ett kvantiserat mångkropparsystem, vars struktur karakteriseras av de diskreta och för ämnet unika energinivåer. Växelverkan mellan elektroner och interna- och externa elektromagnetiska fält leder till energiövergångar genom absorption eller emission av fotoner med väldefinierade energier. Dessa övergångar medför att elektronerna hoppar från ett tillstånd till ett annat, varvid atomens energinivå ändras. Eftersom energinivåerna är unika för ämnet, så blir på motsvarande sätt energierna för övergångarna mellan dessa nivåer unika.

Vår kunskap om universums skapelse och utveckling kommer i huvudsak från ljuset som sänds ut från atomerna i stjärnorna. Ljuset uppdelas i ett energispektrum, med spektrallinjer med olika energier och intensiteter. Spektrallinjernas energier, eller positioner, avslöjar vilka ämnen som bygger upp stjärnorna, och från linjernas intensitet kan förekomsten av de olika ämnena bestämmas. För att tolka observerade spektra behövs atomär referensdata. Dessa data kan bestämmas via laboratoriemätningar, men dessa är ofta dyra och tidskrävande. Data från experiment täcker inte heller behoven fullt ut. Det är därför nödvändigt att utveckla och förbättra kvantmekaniska modeller och teorier, vilka beskriver atomens energinivåer och övergångarna mellan nivåerna. Baserat på dessa modeller kan sedan beräkningar utföras, vilka ger de tillåtna energinivåerna och sannolikheterna för energiövergångar. Exempel på sådana beräkningar presenteras i Artiklarna I-III för ett antal joner i kol och aluminium. Atomär data som karakteriserar hur atomer påverkas av externa magnetiska fält beskrivs i Artikel IV.

Även om atomkärnan är ungefär  $10^4$  gånger mindre än atomen, så har dess massa och utsträckta laddningsfördelning en mätbar effekt på atomens energispektrum. För ett givet ämne uppvisar spektrallinjerna från olika isotoper ett litet energiskift, känt som isotopskiftet. I atomer med kärnor med ett totalt rörelsemängdsmoment skilt från noll växelverkar kärnans elektromagnetiska moment med det elektromagnetiska fältet genererat av elektronerna. Denna växelverkan leder till en experimentellt mätbar uppsplättning av energinivåerna, känd som hyperfinstruktur. Atomens elektroner är alltså känsliga prober, vilka känner av egenskaperna hos kärnan. I Artiklarna V-VII visar vi hur modellering av isotopskift och hyperfinstruktur kan kombineras med experimentell data, för att bestämma kärnornas laddningsfördelningar och elektromagnetiska moment. Sådan modellberoende information kan sedan användas för att validera kärnstrukturberäkningar baserade på olika effektiva krafter mellan nukleonerna i kär-

nan. Tillsammans är en ökad förståelse för kärnornas struktur och dynamik viktig för vår övergripande bild av universum, då kärnsyntes är tätt knuten till stjärn- och galaxutveckling.



**Atomic Electrons as Sensitive  
Probes of Nuclear Properties and  
Astrophysical Plasma Environments  
- A Computational Approach**



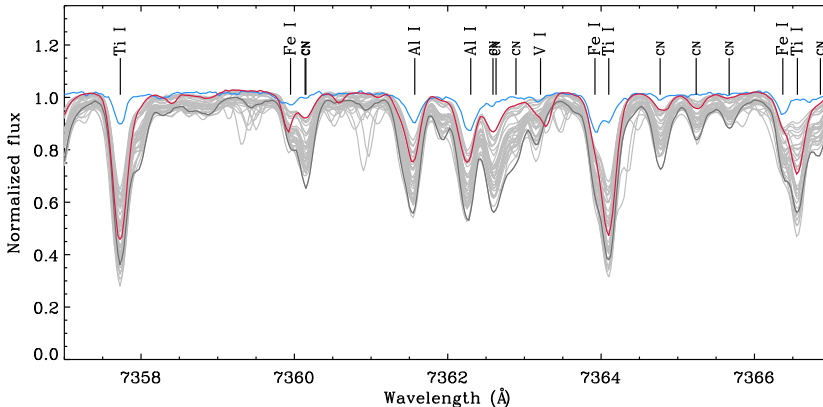
# Chapter 1

## Introduction and Motivation

Physics investigates the basic principles and laws that govern the physical world we live in. Through astrophysical observations, a continuous effort is put to unveil the mysteries of our universe. To understand how the universe, its galaxies and solar systems were formed and evolved, we need to closely study their constituents; celestial objects including our Sun and other stars. Stars are hot spheres of plasma that are powered by nuclear fusion in their cores, where various elements are formed. Stellar evolution studies are, thereby, inseparable with nucleosynthesis and chemical evolution [1].

The main source of information about stars is the “light” they emit. When the emitted electromagnetic radiation is displayed according to the energy/wavelength, the result is an energy spectrum. Hot opaque objects, such as the photospheres of stars, resembling a black-body, emit electromagnetic radiation at all wavelengths, which results in continuum spectra. As soon as the electromagnetic radiation is observed through the stars’ cooler atmospheres, some of the light is, however, absorbed, giving rise to so-called absorption spectra (see, e.g., Fig. 1.1). Conversely, if one examines the incoming light from a low-density gas cloud, such as a nebula, only the emitted wavelengths are observed, producing an emission spectrum. Absorption and emission spectra consist of lines of different energies and intensities. The positions of the observed lines depend on the elements an astronomical object consists of and, from their shapes, the elemental abundances can be deduced [2, Ch. 16]. Correct deduction of elemental abundances and chemical evolution modeling are essential for putting together a complete picture of the stellar and galactic evolution [3–5].

The elemental abundances are, however, not observed, but interpreted. To extract more useful information from astrophysical observations, the underlying processes that generate the spectra need to be well understood and described. Examples of such



**Figure 1.1:** Sample of spectra in the optical region that are used for abundance analysis. The blue spectrum corresponds to the Sun, the red and dark gray spectra are the standard benchmark giants Arcturus and  $\mu$ Leo, while the lighter gray spectra represent about 50 other giants [6]. For a more thorough description of the spectra, see: <http://www.astro.lu.se/~henrikj/posters.shtml>.

processes are the interactions of the electromagnetic radiation with different atomic systems, causing them to transition from one energy state to another. In many cases, the descriptions of atomic structures and interactions are only available through quantum mechanical calculations that need to be benchmarked against precision experiments. Reliable atomic data can, then, be generated and may be used to identify the observed spectral lines [7, 8] and to deduce elemental abundances. Papers I-III, included in this thesis, are examples of atomic structure calculations of *transition rates*, *weighted oscillator strengths*, as well as *lifetimes* of excited states. The *transition rates* and *weighted oscillator strengths*, respectively, determine the anticipated intensities of emission and absorption lines, for a certain amount of a particular species and under certain plasma conditions (pressure, temperature, density, and so on). They are, thus, essential in astrophysical applications, e.g., in abundance and plasma analyses of stars.

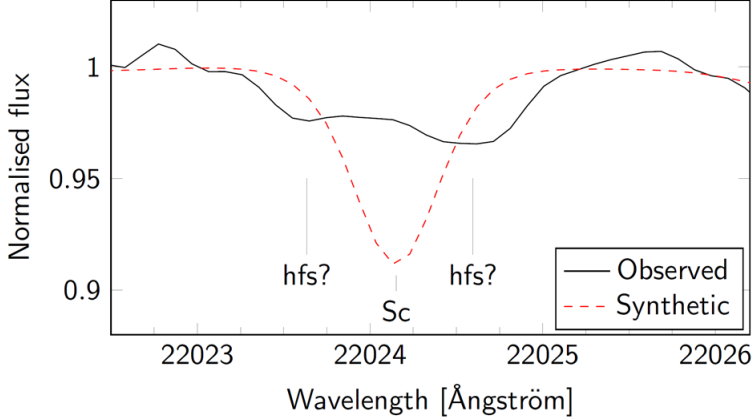
The universe is abundant in sources of magnetic fields, such as planets and stars. Magnetic fields play a key role in some of the most important astrophysical phenomena, such as stellar flares, X-ray emission, and starspots, which are observed at the surface layers of stars, including our Sun [9–12]. Cosmic magnetism is studied, e.g., through the detection of polarized light, exhibiting the effects stemming from the presence of magnetic fields. Quantifying the polarization of light as a function of the wavelength, known as spectropolarimetry, is the most powerful tool for identifying the magnetic fields in astrophysical objects [13]. An important parameter in the interpretation of spectropolarimetric observations is the *Landé g-factor*, describing the splitting of the

atomic energy levels for a given value of the magnetic field. Paper IV reports on calculations of *Landé g-factors* in several atoms and ions of astrophysical interest. The *Landé g-factors* are also interesting from a purely theoretical viewpoint, as they provide valuable information about the coupling conditions in atomic systems, and they can be used to identify and label the atomic states [14, 15].

The presence of different isotopes of the same element in astronomical objects gives rise to splittings of the atomic spectral lines, which are referred to as *isotope shifts*. When these splittings are resolved in the observed spectra, *isotope shift* data can be used to derive the isotopic abundances (see, e.g., [16]). Observed stellar isotopic abundances may reveal admixtures, which are very different from the ones observed in our solar system and are referred to as isotope anomalies [17, 18]. Such anomalies are powerful tools for gaining more insight into the mechanisms that occur during nucleosynthesis [19, 20]. *Isotope shift* data are crucial even when the isotopic splittings are not resolved. In the latter case, they appear in the spectra as line broadenings, altering the shapes of the line profiles, as well as the total line intensities. To correctly interpret the observed spectra and perform abundance analyses, it is necessary that the modeling of the line profiles accounts for the predicted *isotope shifts* [21].

In species with non-zero nuclear spin, i.e., odd number of nucleons, the non-central electromagnetic interactions between the nuclei and the electron clouds in atoms cause further splittings of the fine-structure energy levels, which are known as the *hyperfine structure*. High-resolution spectra often reveal the different components of the atomic spectral lines that correspond to the transitions between the *hyperfine structure* levels. Yet, when these lines are not resolved, they represent an additional broadening mechanism. Correct interpretation of the observed spectral lines requires that both *isotope shifts* and *hyperfine structure* splittings are taken into account in the calculations of the synthetic spectra [22, 23]. Figure 1.2 shows an example of a synthetic spectrum, where the *hyperfine structure* has been omitted, thus hampering the interpretation of the observed spectrum. It should be noted that as the hyperfine interaction breaks the  $J$  symmetry of the atom, it may open forbidden ( $J = 0 \rightarrow J = 0$ ) transitions, known as hyperfine-induced transitions. Such transitions are important for plasma diagnostics, such as the determination of densities and isotopic ratios in low-density plasmas [24, 25].

The *isotope shifts* arise from the isotope specific properties of atomic nuclei. The finite nuclear masses give rise to recoil energies, which reflect the mass shift contributions to the total *isotope shifts*, whereas the extended and unique nuclear charge density distributions induce dissimilar central fields felt by the electrons that represent the field shift contributions. Both these contributions to the observed *isotope shifts* can be factorized into electronic and nuclear parts. The nuclear parts are written in terms of the nuclear masses and the radial moments of the nuclear charge density distribu-



**Figure 1.2:** Line of neutral scandium at 22024.15 Å. The black line is observed spectrum from Arcturus, and the red line is a synthetic spectrum using data for the scandium line that do not include hyperfine structure. For more details see [26].

tions, for the mass and field shift effects, respectively. On the other side, the *hyperfine structures* emerge from the interactions between the electrons' magnetic and inhomogeneous electric fields and the electromagnetic moments of the nucleus. The lowest non-trivial nuclear magnetic and electric multipoles are the magnetic dipole and electric quadrupole moments. To the lowest orders, the hyperfine splittings can, thus, be described by (1) the interaction of the nuclear magnetic dipole moment with the magnetic field generated by the electrons at the site of the nucleus and (2) the interaction of the electric quadrupole moment with the electric field gradient at the nucleus. All in all, the quantum mechanical calculations of *isotope shifts* and *hyperfine structures* must rely on the information on the relevant nuclear structure parameters.

The *isotope shifts* and *hyperfine structures* can, alternatively, be evaluated using high-precision experimental techniques, such as laser spectroscopy [27] and dielectronic recombination [28]. The measurements of the *isotope shifts* and *hyperfine structures* can further be combined with first-principles (*ab initio*) calculations of the electronic parts of these interactions to deduce nuclear properties, such as spins, multipole moments, and charge radii. As of today, this combined effort from theory and experiment has made available nuclear structure properties for isotope sequences, spanning the entire periodic table [29]. The observed trends are used to benchmark the nuclear structure calculations, which are key to understanding the nucleosynthesis mechanisms. In Papers v and vi, the *hyperfine structure* measurements that were performed in neutral tin using collinear laser spectroscopy [30] were combined with atomic structure calculations to extract the electric quadrupole moments of odd-mass tin isotopes. Paper vii

presents a novel method that combines experimental *isotope shifts* and calculations of the electronic mass and field shift parameters to probe details of nuclear charge density distributions beyond the –typically extracted– charge radii.

This thesis aims at complementing Papers I-VII by giving an insight on the computations of the aforementioned atomic parameters, while addressing the greatest challenges. During the past decades, various computational methods have been developed for the description of the atom and its structure (see, e.g., [31–33]). The results of the papers included in this thesis were produced using the latest versions of the General Relativistic Atomic Structure Package (GRASP) [32, 34], which implements the multiconfiguration Dirac-Hartree-Fock (MCDHF) approach [35]; a fully relativistic variational method. Chapter 2 provides the theoretical background of fully relativistic atomic structure calculations, focusing on the principles of the MCDHF approach, and thereafter, Chapters 3, 4, and 5 summarize the works that were performed in Papers I-IV, Papers V-VI, and Paper VII, respectively. Chapter 6 contains a brief outlook of the thesis.





## Chapter 2

# Relativistic Atomic Structure<sup>1</sup>

The relativistic atomic structure theory is fully discussed in a number of previous works, including the book on atomic structure by Johnson [37], which uses the framework of perturbation theory to illustrate the fundamental concepts of the relativistic treatment of atoms. The book by Grant [35] describes in great detail the relativistic modeling of atoms and molecules using a variational approach, and in particular, the multiconfiguration Dirac-Hartree-Fock (MCDHF) method, which is the method of our choice. A very readable description of the relativistic atomic theory can also be found in the publication by Dyall *et al.* [38], which reports on the MCDHF method and its implementation into the GRASP code. Finally, both non-relativistic and relativistic multiconfiguration methods are discussed in the recent review article by Froese Fischer *et al.* [39]. With this chapter, we aim at providing the reader with the basic principles of the relativistic multiconfiguration method as it applies to the most-up-to-date versions of GRASP [32, 34].

As a starting point, in Sec. 2.1, the relativistic many-electron Hamiltonians, which are at the heart of the variational and configuration interaction problems, are presented. By introducing the concept of the central field approximation, in Sec. 2.2, we show how the approximate wave functions of fine-structure states, known as atomic state functions, can be obtained as expansions over antisymmetrized basis functions, which are coupled products of one-electron Dirac orbitals. Thereafter, Sec. 2.3 describes the variational and configuration interaction methods that are implemented to determine, from an energetic point of view, the “best” atomic state functions. Besides the energies of atomic levels, the resulting atomic state functions are also used to compute other measurable quantities. The matrix elements of tensor operators associated with these observables are evaluated according to Sec. 2.4. The chapter concludes with an

---

<sup>1</sup>This chapter is based on a similar chapter from the licentiate thesis of Papoulia A. [36].

account of the general computational methodology that is followed in the multiconfiguration calculations for generating the atomic state expansions (see Sec. 2.5).

## 2.1 Relativistic Many-Electron Hamiltonians

For complex atomic systems with  $N > 1$  electrons, the Hamiltonian can be expressed in terms of a sum over  $N$  one-particle operators  $h_i$  and  $N(N-1)/2$  two-particle operators  $h_{ij}$ ,

$$\mathcal{H} = \sum_{i=1}^N h_i + \sum_{i<j}^N h_{ij}, \quad (2.1)$$

where the restriction  $i < j$  on the sum of the second part ensures that particles do not interact with themselves, and that there is also no occurrence of terms involving the same pair of particles, such as  $h_{12}$  and  $h_{21}$ .

### 2.1.1 The Dirac-Coulomb Hamiltonian

A common first approach to the relativistic treatment is to apply a Dirac-Coulomb approximation in which the one-electron operator in Eq. (2.1) has the general form

$$h_i = T_i + V_{\text{nuc}}(r_i), \quad (2.2)$$

where  $T_i$  is the kinetic energy of the electron  $i$  and  $V_{\text{nuc}}(r_i)$  is the potential energy arising from the Coulomb interaction of this electron with the atomic nucleus, with  $r_i$  being the distance between the electron and the nucleus.

The potential  $V_{\text{nuc}}(r_i)$  accounts for an extended nuclear charge density distribution, instead of the one from a point-like nucleus. An extended charge distribution can be obtained by an approximate model, such as the Fermi distribution [40], which is used in the latest versions of GRASP. The nuclear charge distribution models are central to Paper VII and will be discussed more thoroughly in Ch. 5.

According to Dirac's theory, the kinetic energy in Eq. (2.2) is given by

$$T_i^{\text{D}} = c \boldsymbol{\alpha}_i \cdot \mathbf{p}_i + (\beta_i - 1)c^2. \quad (2.3)$$

This expression is shifted so that the zero-energy corresponds to the electron ionization limit (to coincide with non-relativistic conventions). The constant  $c$  denotes the speed

of light in atomic units<sup>2</sup>,  $\mathbf{p} \equiv -i\nabla$  is the electron momentum operator, where  $i$  denotes the imaginary unit and  $\nabla$  is the gradient, or else nabla, operator, and  $\boldsymbol{\alpha}$  and  $\beta$  are the  $4 \times 4$  Dirac matrices:

$$\boldsymbol{\alpha} = \begin{pmatrix} 0 & \boldsymbol{\sigma} \\ \boldsymbol{\sigma} & 0 \end{pmatrix}, \quad \beta = \begin{pmatrix} I & 0 \\ 0 & -I \end{pmatrix}, \quad (2.4)$$

where  $I$  is the unit  $2 \times 2$  matrix, and  $\boldsymbol{\sigma} = (\sigma_x, \sigma_y, \sigma_z)$  is defined by the Pauli spin-matrices:

$$\sigma_x = \begin{pmatrix} 0 & 1 \\ 1 & 0 \end{pmatrix}, \quad \sigma_y = \begin{pmatrix} 0 & -i \\ i & 0 \end{pmatrix}, \quad \sigma_z = \begin{pmatrix} 1 & 0 \\ 0 & -1 \end{pmatrix}. \quad (2.5)$$

In the relativistic treatment of the atom, the one-particle Dirac operator is, then, given by

$$h_i^{\text{D}} = T_i^{\text{D}} + V_{\text{nuc}}(r_i). \quad (2.6)$$

The two-particle operator in Eq. (2.1) can, to a first approximation, be represented by the potential energy  $V(i, j)$  that emerges from the Coulomb interaction between two electrons  $i$  and  $j$ , that is

$$h_{ij}^{\text{C}} = V(i, j) = \frac{1}{r_{ij}}, \quad (2.7)$$

where  $r_{ij} = |\mathbf{r}_i - \mathbf{r}_j|$  is the inter-electronic distance. Inserting (2.6) and (2.7) in Eq. (2.1) results in, what is known as, the Dirac-Coulomb Hamiltonian

$$\mathcal{H}^{\text{DC}} = \sum_{i=1}^N [c \boldsymbol{\alpha}_i \cdot \mathbf{p}_i + (\beta_i - 1)c^2 + V_{\text{nuc}}(r_i)] + \sum_{i < j}^N \frac{1}{r_{ij}}. \quad (2.8)$$

The Dirac-Coulomb Hamiltonian is the one used in the self-consistent field (SCF) calculations. The SCF procedure will be discussed later in Sec 2.3.3.

### 2.1.2 Breit interaction

In relativistic atomic structure, the two-electron interaction is essentially much more complex than the instantaneous Coulomb interaction given by Eq. (2.7), making the

---

<sup>2</sup>The atomic units are defined by requiring that the Planck's constant  $\hbar$ , and the electron's rest mass  $m_e$  and charge  $e$ , all have the value 1. The speed of light in the vacuum is given by  $c = 1/\alpha$ , where  $\alpha \approx 1/137$  is the fine-structure constant.

Dirac-Coulomb Hamiltonian (2.8) only a first approximation. For precision calculations, further corrections suggested by quantum electrodynamics (QED) [41] must be taken into account [42].

The leading correction to the Coulomb interaction is given by the so-called transverse Breit operator, describing the magnetic interactions and retardation effects. The latter effects emerge from the finite speed of the exchanged virtual photons between a pair of electrons [43]. The frequency-dependent Breit operator, correct to first-order, is expressed as

$$\mathcal{H}^{\text{B}}(\omega) = -\sum_{i<j}^N \left[ \frac{\boldsymbol{\alpha}_i \cdot \boldsymbol{\alpha}_j \cos(\omega_{ij} r_{ij}/c)}{r_{ij}} + (\boldsymbol{\alpha}_i \cdot \nabla_i)(\boldsymbol{\alpha}_j \cdot \nabla_j) \frac{\cos(\omega_{ij} r_{ij}/c) - 1}{\omega_{ij}^2 r_{ij}/c^2} \right], \quad (2.9)$$

where  $\omega_{ij} = |\epsilon_i - \epsilon_j|/c$  is the angular frequency of the exchanged virtual photon, related to the differences between the one-particle energies of the electrons  $i$  and  $j$  and  $\nabla$  is the gradient operator involved in the differentiation of  $r_{ij} = |\mathbf{r}_i - \mathbf{r}_j|$ .

In the low frequency approximation, where  $\omega_{ij} \rightarrow 0$ , the Breit interaction reduces to

$$\mathcal{H}^{\text{B}} = -\sum_{i<j}^N \frac{1}{2r_{ij}} \left[ (\boldsymbol{\alpha}_i \cdot \boldsymbol{\alpha}_j) + \frac{(\boldsymbol{\alpha}_i \cdot \mathbf{r}_{ij})(\boldsymbol{\alpha}_j \cdot \mathbf{r}_{ij})}{r_{ij}^2} \right], \quad (2.10)$$

where the first term on the right-hand side is referred to as the magnetic (Gaunt) operator and the second term is the retardation correction.

Accounting for the Breit interaction by adding either the operator (2.9) or the operator (2.10) to the Hamiltonian (2.8), results in the Dirac-Coulomb-Breit Hamiltonian

$$\mathcal{H}^{\text{DCB}} = \mathcal{H}^{\text{DC}} + \mathcal{H}^{\text{B}}(\omega) \simeq \mathcal{H}^{\text{DC}} + \mathcal{H}^{\text{B}}. \quad (2.11)$$

The Breit corrections to the Dirac-Coulomb Hamiltonian are accounted for in the relativistic configuration interaction (RCI) calculations that follow the SCF procedure. Additional significant QED contributions, such as the self-energy (SE) and vacuum polarization (VP), can also be included in the RCI calculations. This yields the final Hamiltonian

$$\mathcal{H}^{\text{DCB+QED}} = \mathcal{H}^{\text{DCB}} + \mathcal{H}^{\text{SE}} + \mathcal{H}^{\text{VP}}. \quad (2.12)$$

## 2.2 Relativistic Wave Functions

In studies of atomic structure, the fundamental problem is the calculation of the wave functions that describe the quantum states of interest. Once the wave functions have been determined, a number of atomic properties can be computed (see Sec. 2.4). The Hamiltonian operators (2.8) and (2.12) have both a discrete and a continuous spectrum. In this thesis, we shall limit ourselves to the wave functions that belong to the discrete spectrum, which represent bound states. Wave functions representing bound states are assumed to be normalized.

A stationary state of an  $N$ -electron system is described by a wave function  $\Psi(\mathbf{r}_1, \dots, \mathbf{r}_N)$ , where  $\mathbf{r}_i$  represents the space coordinates of the electron  $i$ . To determine the wave function, we need to solve the wave equation for the Hamiltonian  $\mathcal{H}$  of choice, which, in mathematical terms, is an eigenvalue problem

$$\mathcal{H}\Psi(\mathbf{r}_1, \dots, \mathbf{r}_N) = E\Psi(\mathbf{r}_1, \dots, \mathbf{r}_N). \quad (2.13)$$

Solutions to (2.13), thus, exist only for certain values of  $E$ , representing the total energy of the system. Due to the two-particle term (2.7) that enters the Dirac-Coulomb Hamiltonian (2.8), the eigenvalue problem cannot be solved exactly, and the atomic structure calculations are based upon an approximation, in which the original wave function is replaced by products of one-electron orbitals.

In the context of the central field approximation, the potential arising from the Coulomb interaction between the electrons is replaced by a central average potential due to the nucleus and the other electrons, i.e.,

$$V_{\text{av}}(r_i) = V_{\text{nuc}}(r_i) + u(r_i). \quad (2.14)$$

The Dirac-Coulomb Hamiltonian of Eq. (2.8) can, then, be expressed as

$$\mathcal{H}^{\text{DC}} \approx \mathcal{H}_0 = \sum_{i=1}^N h_i^{\text{D}}, \quad (2.15)$$

where

$$h_i^{\text{D}} = c \boldsymbol{\alpha}_i \cdot \mathbf{p}_i + (\beta_i - 1)c^2 + V_{\text{av}}(r_i) \quad (2.16)$$

is the modified Dirac Hamiltonian operator representing the energy of an electron  $i$  moving in the spherically symmetric scalar potential of (2.14).

The eigenvalue problem is approximated by

$$\mathcal{H}_0\Psi_0(\mathbf{r}_1, \dots, \mathbf{r}_N) = E_0\Psi_0(\mathbf{r}_1, \dots, \mathbf{r}_N), \quad (2.17)$$

and since the approximate Hamiltonian  $\mathcal{H}_0$  is separable, the eigenvalues and eigenfunctions can, respectively, be written as

$$E_0 = \langle \Psi_0 | \mathcal{H}_0 | \Psi_0 \rangle = \sum_{i=1}^N \epsilon_i \quad (2.18)$$

and

$$\Psi_0(\mathbf{r}_1, \dots, \mathbf{r}_N) = \prod_{i=1}^N \phi_i(\mathbf{r}_i), \quad (2.19)$$

where  $\phi_i(\mathbf{r}_i)$  are the one-electron wave functions and  $\epsilon_i$  are the corresponding one-electron energies.

### 2.2.1 One-electron Dirac orbitals

The central field orbitals  $\phi(\mathbf{r})$  satisfy the single-particle Dirac equation

$$h^D \phi(\mathbf{r}) = \epsilon \phi(\mathbf{r}). \quad (2.20)$$

The Hamiltonian  $h^D$  commutes with the parity  $\pi$  and total angular momentum  $\mathbf{j} = \mathbf{l} + \mathbf{s}$ , where  $\mathbf{l}$  is the orbital angular momentum and  $\mathbf{s} = \frac{1}{2}\boldsymbol{\sigma}$  is the electron's spin, in units  $\hbar = 1$ . One must, thus, seek Dirac orbital solutions  $\phi_{nlsjm}(\mathbf{r}_i)$  that are simultaneous eigenfunctions of these operators, so that

$$\begin{aligned} \pi \phi_{nlsjm} &= (-1)^l \phi_{nlsjm}, \\ \mathbf{j}^2 \phi_{nlsjm} &= j(j+1) \phi_{nlsjm}, \\ j_z \phi_{nlsjm} &= m \phi_{nlsjm}, \quad m = -j, -j+1, \dots, j. \end{aligned} \quad (2.21)$$

Dirac orbitals determined in a central field form an orthonormal set. Additionally, the Dirac equation (2.20) allows the separation of the radial coordinates from the angular and spin coordinates, and the Dirac orbitals take the general form

$$\phi_{nlsjm}(\mathbf{r}) = \frac{1}{r} \begin{pmatrix} P_{nlj}(r) \Omega_{lsjm}(\theta, \varphi) \\ i Q_{nlj}(r) \Omega_{\tilde{l}sjm}(\theta, \varphi) \end{pmatrix}, \quad (2.22)$$

where  $P_{nlj}(r)$  and  $Q_{nlj}(r)$  are, respectively, the large and small components of the radial function and  $\Omega_{lsjm}(\theta, \varphi)$  are the two-component spin-angular functions, known as spherical spinors. The spherical spinors  $\Omega_{lsjm}(\theta, \varphi)$  are constructed from the coupling of the spherical harmonics  $Y_{lm_l}(\theta, \varphi)$  with the spinors  $\chi_{\frac{1}{2}, m_s}$ , that is

$$\Omega_{lsjm}(\theta, \varphi) = \sum_{m_l, m_s} \langle l, \frac{1}{2}; m_l, m_s | j, m \rangle Y_{l, m_l}(\theta, \varphi) \chi_{\frac{1}{2}, m_s}, \quad (2.23)$$

where  $\langle l, \frac{1}{2}; m_l, m_s | j, m \rangle$  is a Clebsch-Gordan (CG) coefficient and

$$\chi_{\frac{1}{2}, \frac{1}{2}} = \begin{pmatrix} 1 \\ 0 \end{pmatrix}, \quad \chi_{\frac{1}{2}, -\frac{1}{2}} = \begin{pmatrix} 0 \\ 1 \end{pmatrix}. \quad (2.24)$$

The spherical spinors satisfy the orthonormality conditions, just as the spherical harmonics do.

From the coupling of the angular momentum and spin, it follows that  $j = l \pm s$  with  $s = \frac{1}{2}$  and, for a given value of  $j$ , the  $l$  quantum number can take two possible values, i.e.,  $l = j \pm \frac{1}{2}$ . In Eq. (2.22), the spherical spinors of the large and small radial components are obtained by, respectively, choosing  $l$  and  $\tilde{l}$ , which are associated to each other with the relation

$$\tilde{l} = \begin{cases} l + 1 & \text{for } j = l + \frac{1}{2} \\ l - 1 & \text{for } j = l - \frac{1}{2}. \end{cases} \quad (2.25)$$

In this manner, the pair of two-component spinors will have opposite parity. This is a consequence of the fact that the relativistic parity operator is given by  $\pi = \beta \pi_0$ , where  $\pi_0$  is the ordinary parity operator with  $\pi_0^2 = 1$ . Besides the parity  $\pi$ , the spherical spinors are eigenfunctions of  $\mathbf{l}^2$  and  $\mathbf{s}^2$ , as well as the total angular momentum  $\mathbf{j}^2$  and  $j_z$ , so that

$$\begin{aligned} \mathbf{l}^2 \Omega_{lsjm} &= l(l+1) \Omega_{lsjm}, \\ \mathbf{s}^2 \Omega_{lsjm} &= \frac{1}{2} \left( \frac{1}{2} + 1 \right) \Omega_{lsjm}, \\ \mathbf{j}^2 \Omega_{lsjm} &= j(j+1) \Omega_{lsjm}, \\ j_z \Omega_{lsjm} &= m \Omega_{lsjm}. \end{aligned} \quad (2.26)$$

The quantum numbers  $n$ ,  $j$ , and  $m$  are not sufficient to uniquely describe an atomic state, and the modified Dirac Hamiltonian of Eq. (2.16) does not commute with  $\mathbf{l}$  and  $\mathbf{s}$ . Since the Hamiltonian (2.16) commutes with  $\mathbf{j}^2$ ,  $\mathbf{l}^2$  and  $\mathbf{s}^2$ , it also commutes with  $\mathbf{s} \cdot \mathbf{l}$ , and it is convenient to introduce the additional quantum number  $\kappa$  as the eigenvalue of the operator  $\mathcal{K} = -(1 + \mathbf{j}^2 - \mathbf{l}^2 - \mathbf{s}^2) = -1 - \boldsymbol{\sigma} \cdot \mathbf{l}$ , so that

$$\mathcal{K} \Omega_{lsjm} = \kappa \Omega_{lsjm}, \quad (2.27)$$

where

$$\kappa = \begin{cases} -(l+1) & \text{for } j = l + \frac{1}{2} \\ l & \text{for } j = l - \frac{1}{2}. \end{cases} \quad (2.28)$$

In doing so, we can rewrite the Dirac orbitals of Eq. (2.22) as

$$\phi_{n\kappa m}(\mathbf{r}) = \frac{1}{r} \begin{pmatrix} P_{n\kappa}(r)\Omega_{\kappa m}(\theta, \varphi) \\ iQ_{n\kappa}(r)\Omega_{-\kappa m}(\theta, \varphi) \end{pmatrix}. \quad (2.29)$$

Each quantum state is now uniquely described by the quantum numbers  $n, \kappa, m$ .

The spherical spinors are linearly independent, and after inserting the Dirac orbitals of Eq. (2.29) in the wave equation (2.20), we get

$$\begin{aligned} (V_{\text{av}}(r) - E)P_{n\kappa}(r) - c \left( \frac{d}{dr} - \frac{\kappa}{r} \right) Q_{n\kappa}(r) &= 0 \\ c \left( \frac{d}{dr} + \frac{\kappa}{r} \right) P_{n\kappa}(r) + (V_{\text{av}}(r) - 2c^2 - E)Q_{n\kappa}(r) &= 0. \end{aligned} \quad (2.30)$$

These equations are solved for each electron  $i$ , in the common average potential,  $V_{\text{av}}$ , produced by the nucleus and the remaining  $N - 1$  electrons. The radial functions  $\{P_{n\kappa}(r), Q_{n\kappa}(r)\}$  are defined on a grid

$$r_i = A(e^{B(i-1)} - 1), \quad i = 1, \dots, i_{\text{max}}, \quad (2.31)$$

where  $A$  represents the first non-zero grid point,  $B$  is a constant, and the  $i_{\text{max}}$  is chosen to properly capture the full extent of the large and small components of the continuous radial function<sup>3</sup>.

For bound states, the radial orbitals must be square integrable and must also satisfy the orthonormality condition, i.e,

$$\int_0^\infty [P_{n\kappa}(r)P_{n'\kappa}(r) + Q_{n\kappa}(r)Q_{n'\kappa}(r)]dr = \delta_{nn'}. \quad (2.32)$$

Further, the radial amplitudes should vanish at the endpoints, that is  $r \rightarrow 0$  and  $r \rightarrow \infty$ . Near the origin, the radial functions can be expanded in power series of the form

$$P_{n\kappa}(r) = r^s(p_0 + p_1r + \dots), \quad Q_{n\kappa}(r) = r^s(q_0 + q_1r + \dots), \quad (2.33)$$

---

<sup>3</sup>In the standard version, GRASP2018, a default value for  $i_{\text{max}}$  is 590 grid points, and the first non-zero grid point has a  $Z$ -dependence according to  $A = 2^{-6}/Z$ .



where  $p_i$ ,  $q_i$ , and the index  $s > -1/2$  are constants that depend on the nuclear potential model and the Dirac orbital, and they are determined by solving the set of equations (2.30). For large  $r$ , the radial functions reduce asymptotically to zero. By convention, the first oscillation of the large component  $P_{n\kappa}(r)$  is chosen to be positive. The number of nodes in  $P_{n\kappa}(r)$  is given by  $n-l-1$ , just as in the non-relativistic case, while the number of nodes in the small component  $Q_{n\kappa}(r)$  is given by  $n-l-1$  for  $\kappa < 0$  and  $n-l$  for  $\kappa > 0$ . Node counting is essential in SCF methods, such as the MCDHF approach (see Sec. 2.3), ensuring that the desired physical states are found.

At this point, it should be noted that multiconfiguration methods do not assume a  $V_{av}$ , but rather assume the forms of the one-electron orbitals and, then, use the “full” Hamiltonian to solve the eigenvalue problem (2.13). In the MCDHF approach, the forms of the (Dirac) orbitals result from solving Eqs. (2.30) as described above.

### 2.2.2 Configuration state functions

The Hamiltonian  $\mathcal{H}_0$  of (2.15) is invariant with respect to permutations of the electron coordinates  $\mathbf{r}_i$ , and thus, any permutation in the product function of (2.19) also leads to an eigenfunction. According to the Pauli exclusion principle, only wave functions that are antisymmetric describe physical atomic states and such wave functions can be represented by what is known as a Slater determinant

$$\Phi(\mathbf{r}_1, \dots, \mathbf{r}_N) = \frac{1}{\sqrt{N!}} \begin{vmatrix} \phi_{\alpha_1}(\mathbf{r}_1) & \phi_{\alpha_1}(\mathbf{r}_2) & \dots & \phi_{\alpha_1}(\mathbf{r}_N) \\ \phi_{\alpha_2}(\mathbf{r}_1) & \phi_{\alpha_2}(\mathbf{r}_2) & \dots & \phi_{\alpha_2}(\mathbf{r}_N) \\ \dots & \dots & \dots & \dots \\ \phi_{\alpha_N}(\mathbf{r}_1) & \phi_{\alpha_N}(\mathbf{r}_2) & \dots & \phi_{\alpha_N}(\mathbf{r}_N) \end{vmatrix}, \quad (2.34)$$

which, in a more compact manner, can be written as

$$\Phi(\mathbf{r}_1, \dots, \mathbf{r}_N) = \frac{1}{\sqrt{N!}} \sum_{\mathcal{P}} (-1)^p \mathcal{P} \prod_{i=1}^N \phi_{\alpha_i}(\mathbf{r}_i), \quad (2.35)$$

where  $\mathcal{P}$  is an operator that permutes the coordinates of the electrons, with the sum  $\mathcal{P}$  being over all possible  $N!$  permutations,  $p$  is the parity of the permutation, and  $\alpha_i = n_i \kappa_i m_i$  is the quantum label that uniquely describes a Dirac orbital.

The relativistic  $N$ -electron Dirac-Coulomb Hamiltonian, which also includes the electron-electron Coulomb interaction, commutes with the total angular momentum operator  $\mathbf{J} = \mathbf{j}_1 + \mathbf{j}_2 + \dots + \mathbf{j}_N$ . Hence, we seek many-electron solutions to

the eigenvalue problem (2.13) that are eigenfunctions of  $\mathbf{J}^2$  and  $J_z$ , with  $J$  and  $M$  being good quantum numbers together with the parity  $P$ , so that

$$\begin{aligned}\Pi\Phi &= P\Phi, \quad P = (-1)^{l_1+\dots+l_N}, \\ \mathbf{J}^2\Phi &= J(J+1)\Phi, \\ J_z\Phi &= M\Phi, \quad M = -J, -J+1, \dots, J.\end{aligned}\tag{2.36}$$

The approximate wave functions (2.35) in the form of Slater determinants are usually not eigenfunctions of  $\mathbf{J}^2$ . However, by taking linear combinations of Slater determinants belonging to the same configuration<sup>4</sup>, we can obtain wave functions with the desired  $J$ -symmetry. These functions are better approximations to the exact wave functions than the Slater determinants themselves. Each such solution defines a configuration state function (CSF), denoted

$$\Phi(\gamma P J M) \equiv |\gamma P J M\rangle,\tag{2.37}$$

where  $\gamma$  represents the configuration, the angular momentum coupling tree, and other quantum numbers that are necessary to entirely describe the CSF. We require that the CSFs form an orthonormal set, so that

$$\langle \gamma_\mu P_\mu J_\mu M_\mu | \gamma_\nu P_\nu J_\nu M_\nu \rangle = \delta_{\mu\nu}.\tag{2.38}$$

Alternatively, a CSF can be constructed from products of Dirac orbitals using a recursive method in terms of coefficients of fractional parentage (CFPs) and explicit antisymmetrization. In GRASP, the latter approach is applied, which is described in detail in the review article by Fischer *et al.* [39] and the book by Grant [35, Ch. 6].

### 2.2.3 Atomic state functions

The single CSF approach does not capture effects that arise from the correlated motion of the electrons. To include electron correlation [44] (for more details see Sec. 2.5), we must look for a better approximation to the exact wave functions. For a certain parity  $P$ , there is an infinite number of CSFs coupled to the same total angular momenta  $J$  and  $M$ . Each set of CSFs with the same  $P$ ,  $J$ , and  $M$  quantum numbers form a basis for a function space of approximate wave functions, which are known as atomic state functions (ASFs). An ASF,  $\Psi(\Gamma P J M)$ , is then written as a linear combination

---

<sup>4</sup>That is determinants with the same set of  $n_i \kappa_i$  quantum numbers, but with different  $m_i$  quantum numbers.

of CSFs,  $\Phi(\gamma_\mu P J M)$ , i.e.,

$$\Psi(\Gamma P J M) \equiv |\Gamma P J M\rangle = \sum_{\mu=1}^{N_{\text{CSFs}}} c_{\gamma_\mu J} \Phi(\gamma_\mu P J M), \quad (2.39)$$

where  $c_{\gamma_\mu J} = \langle \gamma_\mu P J | \Gamma P J \rangle$  (suppressing now the quantum number  $M$  for brevity) are the mixing coefficients of the expansion. As follows from the orthonormality of the CSFs (see Eq. (2.38)) and the normalization property of the total wave functions, the mixing coefficients must satisfy the condition

$$\sum_{\mu=1}^{N_{\text{CSFs}}} c_{\gamma_\mu J}^2 = 1. \quad (2.40)$$

The label  $\Gamma$  of the ASF is, normally, the same as the label  $\gamma_\mu$  of the dominating CSFs after transformation from  $jj$ - to  $LSJ$ -coupling according to the prescription of Gaigalas *et al.* [45].

In atomic structure calculations, it is likely that we are interested in more than one atomic state, represented by multiconfiguration functions according to Eq. (2.39). When performing multiconfiguration calculations that target multiple atomic states  $|\Gamma^i P J^i\rangle$ ,  $i = 1, \dots, N_{\text{ASFs}}$  at the same time, the different ASFs are chosen to be orthonormal, so that

$$(\mathbf{c}_{\Gamma^i J^i})^\dagger \mathbf{c}_{\Gamma^j J^j} = \delta_{ij}, \quad (2.41)$$

where the column vector

$$\mathbf{c}_{\Gamma J} = \{c_{\gamma_\mu J}, \mu = 1, \dots, N_{\text{CSFs}}\} \quad (2.42)$$

contains the mixing coefficients that determine an atomic state.

## 2.3 Multiconfiguration Dirac-Hartree-Fock

In the previous section, it was shown that the wave function of an atomic state can be approximated by a superposition of CSFs  $\Phi(\gamma_\mu P J)$ , according to Eq. (2.39). The CSFs are, however, constructed based on the assumption that the one-electron Dirac orbitals  $\phi_{n\kappa m}$ , with radial parts  $\{P_{n\kappa}(r), Q_{n\kappa}(r)\}$ , arise from a general central field approximation. To determine the radial orbitals and mixing coefficients that yield the “best” approximation—in terms of energy—to the exact wave functions, the MCDHF method is employed. In the MCDHF method, the large and small components of the radial functions are obtained by solving a set of integro-differential equations that result from applying the variational principle [46, 47] on the energy functional of one,

or more, ASFs, with additional terms ensuring the orthonormality of the orbitals. The MCDHF equations are presented after a brief introduction to the calculation of the matrix elements that are needed for the construction of the energy functional.

### 2.3.1 Energy matrix elements

Approximate eigenenergies of the atom at hand are obtained as diagonal expectation values of the approximate Dirac-Coulomb Hamiltonian, i.e.,

$$E_{\Gamma J} = \langle \Gamma P J | \mathcal{H}^{\text{DC}} | \Gamma P J \rangle = (\mathbf{c}_{\Gamma J})^\dagger \mathbf{H} \mathbf{c}_{\Gamma J}, \quad (2.43)$$

where  $\mathbf{H}$  is the Hamiltonian matrix with elements

$$H_{\mu\nu} = \langle \gamma_\mu P J | \mathcal{H}^{\text{DC}} | \gamma_\nu P J \rangle. \quad (2.44)$$

The matrix elements  $H_{\mu\nu}$  are expressed as sums of products of spin-angular coefficients and radial integrals, i.e.,

$$H_{\mu\nu} = \sum_{ab} t_{ab}^{\mu\nu} I(a, b) + \sum_{abcd;k} v_{abcd;k}^{\mu\nu} R^k(ab, cd), \quad (2.45)$$

where, for instance,  $a$  represents the Dirac orbital in the subshell  $n_a \kappa_a$  occupied in the  $\mu$ :th CSF.

In Eq. (2.45), the one-particle contributions of the operator (2.6) give rise to the spin-angular coefficients  $t_{ab}^{\mu\nu}$  and the radial integrals  $I(a, b)$  given by

$$\begin{aligned} I(a, b) = & \delta_{\kappa_a \kappa_b} \int_0^\infty [P_{n_a \kappa_a}(r) V_{\text{nuc}}(r) P_{n_b \kappa_b}(r) \\ & - c P_{n_a \kappa_a}(r) \left( \frac{d}{dr} - \frac{\kappa}{r} \right) Q_{n_b \kappa_b}(r) \\ & + c Q_{n_a \kappa_a}(r) \left( \frac{d}{dr} + \frac{\kappa}{r} \right) P_{n_b \kappa_b}(r) \\ & + Q_{n_a \kappa_a}(r) (V_{\text{nuc}}(r) - 2c^2) Q_{n_b \kappa_b}(r)] dr, \end{aligned} \quad (2.46)$$

where the condition  $\kappa_a = \kappa_b = \kappa$  follows from the orthogonality property of the spherical spinors. In the special case of diagonal matrix elements,  $t_{aa}^{\mu\mu}$  is given by the occupation number  $w_a^\mu$  of the orbital  $a$  in the  $\mu$ :th CSF. The two-particle contributions of the operator (2.7) are evaluated by first expanding the Coulomb potential in

terms of Legendre polynomials, so that

$$\frac{1}{r_{ij}} = \sum_{k=0}^{\infty} \frac{r_{<}^k}{r_{>}^{k+1}} P_k(\cos \omega), \quad (2.47)$$

where  $\omega$  is the angle between the position vectors  $\mathbf{r}_i$  and  $\mathbf{r}_j$ ,  $r_{<} \equiv \min(r_i, r_j)$ , and  $r_{>} \equiv \max(r_i, r_j)$ . In the coupled tensorial form, the above equation takes the form

$$\frac{1}{r_{ij}} = \sum_{k=0}^{\infty} \frac{r_{<}^k}{r_{>}^{k+1}} (\mathbf{C}^{(k)}(\theta_i, \phi_i) \cdot \mathbf{C}^{(k)}(\theta_j, \phi_j)), \quad (2.48)$$

where the  $\mathbf{C}^{(k)}(\theta_i, \phi_i)$  are renormalized spherical harmonics of rank  $k$ . Eq. (2.48), finally, yields the spin-angular coefficients  $v_{abcd;k}^{\mu\nu}$  and the relativistic Slater integrals  $R^k(ab, cd)$ , which are given by

$$R^k(ab, cd) = \int_0^{\infty} [P_{n_a \kappa_a}(r) P_{n_c \kappa_c}(r) + Q_{n_a \kappa_a}(r) Q_{n_c \kappa_c}(r)] \frac{1}{r} Y^k(bd; r) dr, \quad (2.49)$$

with the relativistic Hartree  $Y^k$ -functions defined by

$$Y^k(ab; r) = r \int_0^{\infty} \frac{r_{<}^k}{r_{>}^{k+1}} [P_{n_a \kappa_a}(s) P_{n_b \kappa_b}(s) + Q_{n_a \kappa_a}(s) Q_{n_b \kappa_b}(s)] ds, \quad (2.50)$$

where  $r_{<} (r_{>})$  denotes the smaller (larger) of  $r$  and  $s$ . By introducing the  $Y$ -functions, Hartree showed in [48] that the double radial integrals of the two-body Coulomb interaction could be evaluated through a pair of one-dimensional integrals given by Eqs. (2.49) and (2.50).

In GRASP, the evaluation of the spin-angular coefficients  $t_{ab}^{\mu\nu}$  and  $v_{abcd;k}^{\mu\nu}$ , needed for constructing the Hamiltonian matrix elements  $H_{\mu\nu}$ , relies on the latest angular-momentum methods developed by Gaigalas *et al.* [49, 50]. These methods use algebraic expressions for matrix elements adapted for spin-angular integrations in  $jj$ -coupling, involving the calculation of reduced CFPs and completely reduced matrix elements of double tensors.

### 2.3.2 The MCDHF equations

In the publications included in this thesis, the wave functions of the targeted atomic states were simultaneously determined using the extended optimal level (EOL) scheme [p. 401; 35, 38]. The EOL energy functional is expressed in terms of the statistical weight of each targeted state  $|\Gamma^i J^i\rangle$ , i.e.,

$$\mathcal{F}(\{c\}, \{P\}, \{Q\}) = \frac{\sum_{i=1}^{N_{\text{ASF}}} (2J^i + 1) E_{\Gamma^i J^i}}{\sum_{i=1}^{N_{\text{ASF}}} (2J^i + 1)} + \sum_{ab} \delta_{\kappa_a \kappa_b} \lambda_{ab} C_{ab}, \quad (2.51)$$

where the orthonormality of the radial orbitals is ensured by introducing the Lagrange multipliers  $\lambda_{ab}$  for each orthonormality constraint

$$C_{ab} \equiv \int_0^\infty [P_{n_a \kappa_a}(r) P_{n_b \kappa_b}(r) + Q_{n_a \kappa_a}(r) Q_{n_b \kappa_b}(r)] dr - \delta_{n_a n_b} = 0. \quad (2.52)$$

The energy functional (2.51) is optimized by requiring that it remains stationary with respect to variations in both the mixing coefficients,  $c_{\gamma_\mu J}$ , and the radial parts of the Dirac orbitals,  $\{P_{n\kappa}(r), Q_{n\kappa}(r)\}$ .

For a specific set of radial functions  $\{P_{n\kappa}(r), Q_{n\kappa}(r)\}$ , initial estimates are provided by, either one-electron orbitals resulting from the Thomas-Fermi statistical theory of the atom [51, § 7.8], or, simply, screened hydrogenic orbitals with an effective nuclear charge

$$Z_{\text{eff}} = Z - \sigma(n\kappa), \quad (2.53)$$

where  $\sigma$  is a screening constant that depends on the Dirac orbital [52, p. 39]. Using the initial estimates of the radial functions, the optimal values of the mixing coefficients  $\mathbf{c}_{\Gamma J} = \{c_{\gamma_\mu J}, \mu = 1, \dots, N_{\text{CSF}}\}$  are obtained as solutions to the RCI problem

$$\mathbf{H} \mathbf{c}_{\Gamma J} = E_{\Gamma J} \mathbf{c}_{\Gamma J}. \quad (2.54)$$

Given a set of mixing coefficients  $c_{\gamma_\mu J}$ , the stationary condition with respect to coupled variations in the radial orbitals, i.e.,  $\{\delta P_{n\kappa}(r), \delta Q_{n\kappa}(r)\}$ , leads to a set of coupled integro-differential equations similar to (2.30)

$$w_a \begin{bmatrix} V(a; r) & -c \left[ \frac{d}{dr} - \frac{\kappa_a}{r} \right] \\ c \left[ \frac{d}{dr} + \frac{\kappa_a}{r} \right] & V(a; r) - 2c^2 \end{bmatrix} \begin{bmatrix} P_{n_a \kappa_a}(r) \\ Q_{n_a \kappa_a}(r) \end{bmatrix} = \sum_b \epsilon_{ab} \delta_{\kappa_a \kappa_b} \begin{bmatrix} P_{n_b \kappa_b}(r) \\ Q_{n_b \kappa_b}(r) \end{bmatrix}, \quad (2.55)$$

which are known as the MCDHF equations. In Eq. (2.55),  $w_a$  is the generalized occupation number of the orbital  $a$  and  $\epsilon_{ab}$  are energy parameters related to the Lagrange multipliers. To incorporate the correct qualitative features of the exact wave functions, the radial orbitals must satisfy the boundary conditions discussed in Sec. 2.2.1. Subject to these conditions, the MCDHF equations are solved for each subshell  $n_a \kappa_a$ , on the logarithmic grid given by (2.31), using a finite difference method.

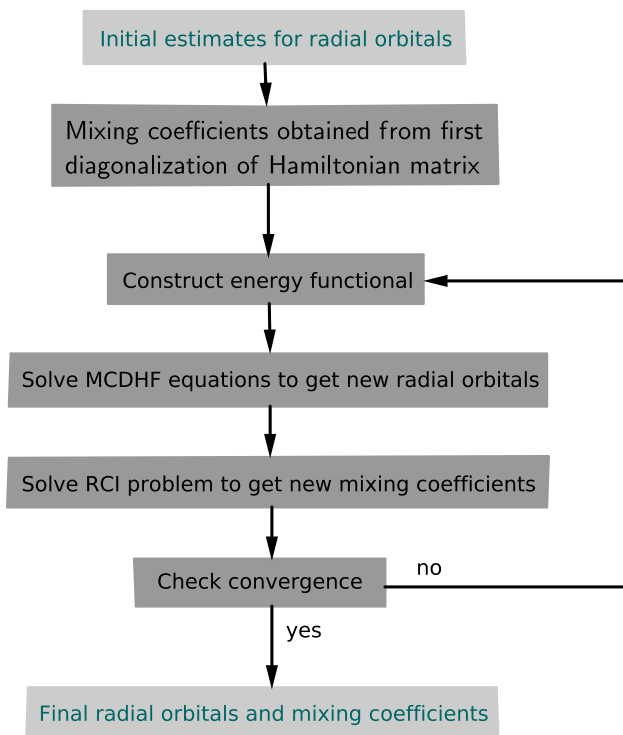
The average and central field MCDHF potential  $V(a; r)$  is built from the nuclear, direct, and exchange contributions, i.e.,

$$V(a; r) = V_{\text{nuc}}(r) + Y(a; r) + \bar{X}(a; r). \quad (2.56)$$

Variations of the Slater integrals of the type  $R^k(ab; ab)$ , weighted with the angular coefficients and the state averaged mixing coefficients, contribute to the direct potential  $Y(a; r)$ . On the other hand, variations of the other  $R^k(ab; cd)$  integrals, where  $a \neq c$  and  $b \neq d$ , and the off-diagonal  $I(a, b)$  integrals, both weighted with the angular coefficients and the state averaged mixing coefficients, contribute to the non-local exchange potential  $\bar{X}(a; r)$ . The expressions for the direct and exchange potentials, involving both diagonal and off-diagonal contributions are rather lengthy, and thus not provided here. Instead, the interested reader is referred to Dyall *et al.* [38], or the book by Grant [35, p. 400].

### 2.3.3 Self-consistent field procedure

Since the direct and exchange potentials depend on the radial orbitals, the RCI problem of Eq. (2.54) and MCDHF equations given by (2.55) are simultaneously solved through an iterative non-linear process, which is referred to as the self-consistent field (SCF) procedure. This procedure –as its name reveals– is continued until self-consistency is reached, with respect to the radial orbitals, mixing coefficients, and energies, based on specified convergence criteria. The SCF procedure can be summarized in the following steps (see also Fig. 2.1):



**Figure 2.1:** The algorithm to solve the MCDHF equations based on the SCF scheme. The first and last instants, respectively, correspond to the required input and the output of the SCF calculations.

1. Given initial estimates for the radial orbitals, the energy matrix elements are evaluated. The mixing coefficients are obtained by a first diagonalization of the Hamiltonian matrix.
2. The energy functional (2.51) is constructed and the stationary condition is applied; first, with respect to variations in the radial orbitals (step 3) and then with respect to variations in the mixing coefficients (step 4).
3. The diagonal and off-diagonal Lagrange multipliers are estimated. The MCDHF equations (2.55) are solved by using the direct and exchange contributions to the potential (2.56) from the previously resulted radial orbitals. An improved estimate for the radial orbitals is obtained.
4. The RCI problem (2.54) is solved after utilizing the new set of radial orbitals. An improved estimate for the mixing coefficients is obtained. The total energies



of the targeted states are determined.

5. The convergence of the radial orbitals, mixing coefficients, and energies is examined. If the convergence criteria are met, the SCF calculations are completed, yielding the final orbital basis and mixing coefficients. If not, the process is repeated from step 2.

### 2.3.4 Relativistic configuration interaction

The MCDHF method is employed to generate the orbital basis. Given this basis, the final wave functions of the targeted states are determined in subsequent RCI calculations, based on the Dirac-Coulomb-Breit and QED Hamiltonian of Eq. (2.12). In the RCI calculations, the CSFs are fixed and only the mixing coefficients,  $c_{\Gamma J}$ , are evaluated by diagonalizing the Hamiltonian matrix. The eigenvalues of the Hamiltonian matrix represent the total energies of the targeted states.

## 2.4 Computation of Atomic Properties

Once the wave functions have been determined from MCDHF and RCI calculations, measurable properties can be obtained by evaluating the expectation values, or, in the case of transition properties, the amplitudes, of one- or two-electron operators. One-electron operators describe the electric and magnetic multipole transitions (see Ch. 3), the hyperfine structure interactions (see Ch. 4), and the normal mass shift and field shift effects (see Ch. 5). On the other hand, the specific mass shift interaction is an example of a two-electron operator (see Ch. 5).

According to the Wigner-Eckart theorem [51, §11.4], the matrix elements of a one-electron spherical tensor operator  $O_q^{(k)}$ , of rank  $k$ , can be written as

$$\langle \Gamma P J M | O_q^{(k)} | \Gamma' P' J' M' \rangle = (-1)^{J-M} \begin{pmatrix} J & k & J' \\ -M & q & M' \end{pmatrix} \langle \Gamma P J || \mathbf{O}^{(k)} || \Gamma' P' J' \rangle, \quad (2.57)$$

where the entire dependence on the magnetic quantum numbers is contained in the  $3j$ -symbol and the phase factor. The physical nature of the operator is, thus, entirely contained in the reduced matrix element  $\langle \Gamma P J || \mathbf{O}^{(k)} || \Gamma' P' J' \rangle$ .

After inserting the multiconfiguration expansions of Eq. (2.39), the reduced matrix elements are given by

$$\langle \Gamma P J || \mathbf{O}^{(k)} || \Gamma' P' J' \rangle = \sum_{\mu, \nu} c_{\gamma_{\mu} J} c_{\gamma'_{\nu} J'} \langle \gamma_{\mu} P J || \mathbf{O}^{(k)} || \gamma'_{\nu} P' J' \rangle. \quad (2.58)$$

The reduced matrix elements between CSFs, in the right hand side of of (2.58), are, in turn, written as

$$\langle \gamma_{\mu} P J || \mathbf{O}^{(k)} || \gamma'_{\nu} P' J' \rangle = \sum_{a, b} d_{ab; k}^{\mu\nu} \langle a || \mathbf{o}^{(k)} || b \rangle, \quad (2.59)$$

where  $d_{ab; k}^{\mu\nu}$  are the spin-angular coefficients, containing all the information about the configurations and the angular couplings [49, 50], and  $\langle a || \mathbf{o}^{(k)} || b \rangle$  are the one-electron reduced matrix elements between two Dirac orbitals  $a$  and  $b$ . The latter are written as products of radial integrals and matrix elements involving the spherical spinors of the two Dirac orbitals.

The matrix elements of a two-electron operator,  $G$ , between CSFs can be expressed as

$$\langle \gamma_{\mu} P J M | G | \gamma'_{\nu} P' J' M' \rangle = \sum_{abcd; k} \xi_{abcd; k}^{\mu\nu} W^k(ab, cd), \quad (2.60)$$

where  $\xi_{abcd; k}^{\mu\nu}$  are the spin-angular coefficients containing information about the structure and couplings of the CSFs and  $W^k(ab, cd)$  are the effective interaction strengths, which can be written in terms of double radial integrals and factors involving matrix elements between the spherical spinors of the active orbitals.

The one-electron reduced matrix elements of Eq. (2.59) and the effective interaction strengths of Eq. (2.60) depend only on the nature of the interaction operator and the Dirac orbitals. The shapes of the Dirac orbitals are determined by the effective fields in which the electrons move, which are established by the included CSFs in the expansions of Eq. (2.39). They might, thus, vary based on the specifics of the computational approach that is followed.

## 2.5 General Computational Methodology

The accuracy of multiconfiguration calculations relies on the expansions of the ASFs in Eq. (2.39), which need to be truncated so that the CSFs effectively capture electron correlation [44]. To generate lists of CSFs that systematically account for the electron correlation effects and build accurate wave functions, multiconfiguration calculations often follow a well-defined optimization scheme, known as the SD-MR approach [39,

52, §4.2.2]. In this section, we describe the general methodology of atomic structure calculations that are based on this approach. The details, which depend on the shell structure of the atomic system at hand and the number of targeted states, will be discussed within the next chapters.

In the SD-MR approach, the starting point is to define a multi-reference (MR) set. The MR set contains the configurations of the targeted atomic states, which can be merged with important, e.g., closely degenerate, configurations [39]. Applying the rules for coupling angular momenta, the configurations in the MR produce a set of CSFs that account for the leading electron correlation effects and the major part of the ASFs. These effects describe what is known as static correlation, which contributes to the long-range rearrangement of the electron charge distribution. By performing an MCDHF calculation with a CSF expansion built from the MR configurations, a first approximation of the wave functions of the targeted states is acquired. The orbitals of the states that we optimize on are considered as occupied and are, thus, required to have the node structure of hydrogenic orbitals, which is determined by the principal quantum number,  $n$ , and azimuthal,  $l$ , quantum numbers, as discussed in Sec. 2.2.1. They are referred to as spectroscopic, while the orbitals that make up the rest of the MR configurations are part of the correlation orbitals. The resulting radial orbitals from this initial MCDHF calculation are kept frozen in all subsequent calculations.

The initial approximation of the wave functions is improved by also accounting for dynamic correlation effects, which are related to the cusp condition<sup>5</sup> [53]. To do so, the atomic state expansions are enlarged with CSFs that interact, i.e., have non-zero matrix elements, with the ones generated by the MR configurations. Due to the one- and two-body operators in the Hamiltonian, such CSFs are built from configurations that are formed by allowing single (S) and double (D) substitutions of electrons from the MR orbitals to an active set (AS) of correlation orbitals. The AS is systematically increased by introducing, at each step, a “layer” of correlation orbitals, consisting of at most one orbital per angular symmetry [54, 55]. The correlation orbital layers in the AS are optimized in successive MCDHF calculations by keeping the previously generated orbitals frozen. Based on the nature of the SD substitutions, the CSFs are classified into: CSFs that capture valence-valence (VV), core-valence (CV), and core-core (CC) correlation effects [39, 52, §4.2.2]. The radial orbital basis is obtained by performing MCDHF calculations, where all, or some, of the classes of CSFs are considered. After the orbital basis is generated, additional electron correlation effects, even beyond the SD-MR model, can be accounted for in the final RCI calculations.

The classes of CSFs that are selected to build the wave functions depend on the computed atomic properties. When computing transition parameters, the outer parts of

---

<sup>5</sup>The cusp condition arises from the singularity of the inter-electronic Coulomb interaction  $1/r_{ij}$  near points of coalescence where  $r_{ij} = 0$ .

the wave functions must be well approximated, and CSFs that capture VV and CV electron correlation effects are the most critical [56]. On the other side, the computations of properties arising from electron-nucleus interactions, such as isotope shifts or hyperfine structures, require that the parts of the wave functions close to the origin are ably described, making core-correlation effects important [57, 58]. Even so, the inclusion of one, or more, classes of CSFs does not ensure that the correlation orbitals will be properly localized to effectively capture the relevant correlation effects.

In the MCDHF calculations, the correlation orbitals are obtained by applying the variational principle on the weighted energy functional of the targeted states. As a result, the orbitals of the first correlation layers mainly overlap with the spectroscopic orbitals accounting for the effects that minimize the energy the most, and the wave functions are optimized so that they, primarily, give accurate total energies [59, 60]. Taking as an example the “conventional” set of computations in beryllium-like carbon presented in Paper 1, the MCDHF calculations were performed with CSF expansions built from SD-MR substitutions from all spectroscopic orbitals with the restriction that only one substitution was allowed from the  $1s^2$  core. In this way, the CSFs capture VV and CV correlation effects. Since the  $1snl$  pair-correlation effects are comparatively important, correcting for the cusp condition, the orbitals of the first correlation layers were spatially localized between the  $1s$  orbital and the  $2s$  and  $2p$  orbitals. Consequently, there were not enough correlation orbitals localized farther from the  $1s^2$  core to ably describe the outer parts of the wave functions representing highly-excited states. To obtain orbitals localized in regions of space, which might describe effects that do not lower the energy much, but are important for other properties, the energetically dominant effects must first be saturated. This eventually leads to very large orbital sets and CSF lists, which are often limited by the available computational resources, and therefore, alternative computational strategies must be explored.

## Chapter 3

# Spectrum Calculations of Transition Properties Involving Rydberg Series

During the past few decades, technology has rapidly been progressing, and the high-resolution instruments that are now used in astronomical spectroscopy have raised the demands on atomic transition data [61]. The new generation of telescopes and astronomical spectrographs have been designed for the infrared wavelength region [62–64], and reference data from the higher parts of atomic spectra must also be made available [65]. Due to the limited resources and the numerous possible transitions, laboratory measurements are not capable of supplying astrophysicists with complete sets of data relevant to radiative processes. Therefore, the interpretation of the observed starlight largely relies on theoretical results, whose accuracy steadily improves with the increasing computing power and the continuous advances in computational methods [7, 8, 66].

In line with the most recent astrophysical needs, Papers I and II report on extended transition data, namely wavelengths, transition rates, weighted oscillator strengths, and lifetimes, for the systems of neutral and singly-, doubly-, and triply-ionized carbon (C I-IV). In particular, we note that the considered levels in each of the C I and C III ions amount to a hundred, or more. Paper III provides a large amount of data, of the same aforementioned transition parameters, for the systems of neutral and singly-ionized aluminium (Al I-II). In addition, Paper IV presents extended data of Landé  $g$ -factors for several atoms and ions, including C I-IV and Al I-II.

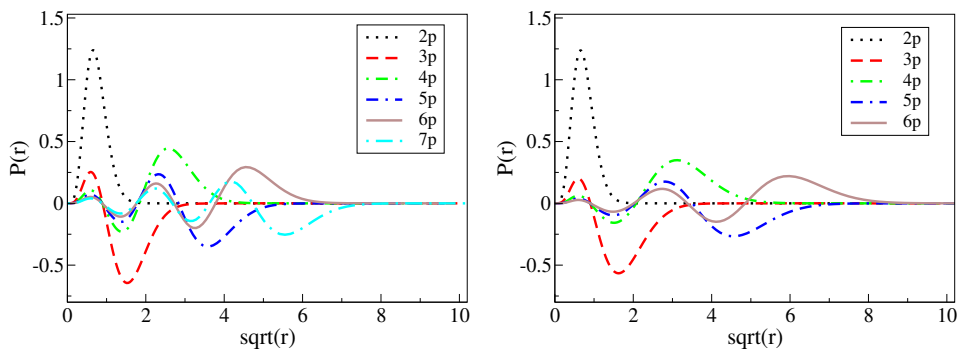
Performing large-scale spectrum calculations, where numerous atomic states are concurrently targeted, is most certainly not trivial. To build wave functions that produce not just accurate energy levels, but also reliable transition data for all considered states,

special attention must be paid to the optimization scheme of the orbital basis. For instance, the shapes of the generated correlation orbitals must be such that they account for the  $LS$ -term dependencies [67], i.e., the dependencies on the coupling of the CSFs to form different terms from the same configuration [52, p. 55]. At the same time, the spectra of C I-IV and Al I-II involve states that are part of Rydberg series, bringing additional challenges to the computations (see, e.g., [68]). A Rydberg series is defined as the set of the configuration states that are formed by exciting the outermost electron of the ground state configuration to orbitals of increasing principal quantum number  $n$ , but same  $l$  symmetry (see also [69, p. 85]). In magnesium-like ions, as for instance Al II, where the ground state configuration is  $[\text{Ne}]3s^2$ —using  $[\text{Ne}]$  to indicate the 10-electron neon core—, a Rydberg series can be represented as

$$[\text{Ne}]3snl \ 2^{S+1}L, \quad n > 3. \quad (3.1)$$

It is common that doubly-excited states, referred to as perturbers, enter the Rydberg series and strongly interact with them (the closer the perturber and a Rydberg state come in energy, the stronger is the interaction between them). For instance in Al II, members of the  $3snf \ ^3F$  series (omitting now the neon core for brevity) are strongly-mixed with the  $3p3d \ ^3F$  perturber, meaning that the ASFs of the Rydberg states include the CSF representing the perturber, with the latter having a large expansion coefficient. To correctly predict the positions of strongly-mixed states, the wave functions must be highly correlated, which translates to a very large orbital basis and, most likely, millions of CSFs. Moreover, states that are part of Rydberg series encompass valence orbitals of increasing principal quantum number  $n$ . Accordingly, spectrum calculations involving Rydberg series have to describe states with electron distributions localized in different regions of space, extending far away from the atomic core (see also Fig. 3.1). Since the overlap between Rydberg states can be minor, finding an optimal orbital basis that describes all Rydberg states equally well is not straightforward and different computational strategies must be explored.

As, in general, with the studies of atomic structure, the difficulties associated with Rydberg series, which are related to electron correlation, are more prominent in neutral and near-neutral systems. It is, however, seen that computations in more heavily-charged systems may also be undermined by an improper choice of optimization strategy for the radial orbital basis used to construct the wave functions. Paper I reports on spectrum calculations of transition data, focusing on the C IV and C III ions. Different computational strategies for optimizing the orbital basis were investigated in this work, and the quality of the respective results was, ultimately, assessed. It was observed that, for transitions involving low-lying states, and as long as enough correlation orbitals have been generated, the transition data are accurately computed independently of the specifics of the orbital optimization strategy. Yet, the transition data related to transitions involving high Rydberg states are subject to disproportion-



**Figure 3.1:** The spectroscopic  $np$  orbitals, comprising the  $3snp\ ^1,3P^o$  and  $3s^2np\ ^2P^o$  Rydberg series in each of the calculated spectra of Al II (left) and Al I (right), are displayed as a function of  $\sqrt{r}$ . The 2p orbital is part of the core, whereas the orbitals with  $n > 2$  belong to the valence shell, occupying different regions in space, as eventually do the total electron distributions of the Rydberg states.

ately large theoretical uncertainties when the chosen optimization strategy results in correlation orbitals that are contracted in comparison to the outer Rydberg orbitals.

In Paper I, it was further shown that, when the generated correlation orbitals are properly localized to effectively describe the outer parts of the wave functions representing the high Rydberg states, reliable transition data can be obtained for all targeted states. This is achieved by performing MCDHF calculations based on CSF expansions, which are, most often, constructed by imposing restrictions on the allowed electron substitutions from inner subshells. (For further details, the reader is referred to the paper.) The high-quality transition data in C IV and C III, which were included in Paper II to facilitate the analysis of astrophysical spectra, resulted from the orbital optimization schemes suggested in Paper I. Drawing on the detailed investigations of Paper I, specialized orbital optimization strategies were applied in Paper II to further produce accurate transition data for the more complex systems of C II and C I.

By paying special attention to the orbital optimization strategies, updated transition data were also computed for the systems of Al I-II, which are contained in Paper III. Although the computed transition properties are, on average, of high quality, the transitions involving high Rydberg states were found to be problematic. Additional computations have now been performed in Al II (manuscript in preparation), and the results have demonstrated that the overall accuracy of the transition data can be improved by choosing a more appropriate strategy for constructing the radial orbital basis. It appears that the improvement in accuracy is impressive for transitions that involve high Rydberg states (see also Sec. 3.3.3).

In Sec. 3.1, we describe how the various atomic transition properties are theoretically evaluated and introduce the quantity that was used in Papers I-III to estimate the theoretical uncertainties. Subsequently, in Sec. 3.2, we focus on the computations that were performed in the carbon ions and discuss the accuracy of the energies and transition data contained in Paper II. Sec. 3.3 is dedicated to the computations that were carried out in Al I and Al II. Within this section, the orbital optimization strategies that were applied in Paper III are described and motivated. The most significant results and conclusions, which emphasize the computational challenges in these two systems, are then summarized. Some engaging results based on the newly applied computational schemes in Al II, which lead to an overall reduction of the theoretical uncertainties of the computed transition data, are also presented. Sec. 3.4 discusses the accuracy of the Landé  $g$ -factors that were computed in Paper IV.

### 3.1 Transition Properties

As a result of the interactions of the atomic electrons with the electromagnetic field, transitions between a lower state  $|\Gamma P J M\rangle$  and an upper state  $|\Gamma' P' J' M'\rangle$  are observed through emission, or absorption, of a photon with energy  $h\nu = E_{\Gamma' J'} - E_{\Gamma J}$  and wavelength  $\lambda = c/\nu$ . Following the early works in Refs. [70, 71], as well as Ch. 8 in Grant's book [35], the relativistic expression providing the rate, or probability,  $A^{(k)}$  for a spontaneous emission, from an upper state  $|\Gamma' P' J' M'\rangle$  to any of the  $2J + 1$  states  $|\Gamma P J M\rangle$  of lower energy, gives

$$A^{(k)}(\Gamma' P' J', \Gamma P J) = \frac{2\omega}{c} \frac{1}{(2k + 1)(2J' + 1)} |\langle \Gamma P J | \mathbf{T}^{(k)} | \Gamma' P' J' \rangle|^2, \quad (3.2)$$

where  $\omega$  is the angular frequency of the transition and  $\mathbf{T}^{(k)} = \sum_{i=1}^N \mathbf{t}^{(k)}(i)$  is the multipole transition operator of rank  $k$ , with the sum running over the number  $N$  of electrons. The transition rate does not depend on the arbitrary choice of the orientation of the coordinate system, and it is, therefore, independent of the projection quantum number  $M'$ .

The one-particle interaction operator,  $\mathbf{T}^{(k)}$ , can be separated into individual operators for multipole transitions of electric ( $E_k$ ) and magnetic ( $M_k$ ) type. The electromagnetic scalar and vector potentials defining the operator  $\mathbf{T}^{(k)}$  are expressed in terms of composite spherical tensor operators. Their analytical expressions are, e.g., given in Eqs. (8.1.5) and (8.1.10) of Ref. [35].



Instead of giving the rate, the strength of a transition is often expressed in terms of the weighted oscillator strength  $gf^{(k)}$ , which is defined as

$$gf^{(k)}(\Gamma P J, \Gamma' P' J') = \frac{1}{\omega} \frac{1}{(2k+1)} |\langle \Gamma' P' J' || \mathbf{T}^{(k)} || \Gamma P J \rangle|^2, \quad (3.3)$$

and is directly proportional to the intensity of a spectral line. The weighted oscillator strengths are most commonly used in the analyses of astrophysical spectra consisting of absorption lines.

According to Sec. 2.4, the reduced matrix elements of the transition operator, which are parts of Eqs. (3.2) and (3.3), are subsequently written in terms of one-electron reduced matrix elements between two Dirac orbitals  $a$  and  $b$ , so that

$$\langle a || \mathbf{t}^{(k)} || b \rangle = \langle j_a || \mathbf{C}^{(k)} || j_b \rangle \mathbf{M}_{a,b}(\omega; G^{(k)}), \quad (3.4)$$

where  $\mathbf{C}^{(k)}$  is the renormalized spherical harmonic of rank  $k$  and  $\mathbf{M}_{a,b}(\omega; G^{(k)})$  is the radial transition integral, which corresponds to either an electric  $Ek$ , or a magnetic  $Mk$ , multipole amplitude. The magnetic multipoles are independent of the gauge parameter,  $G^{(k)}$ , whereas the electric multipoles are expressed as

$$\mathbf{M}_{a,b}(\omega; G^{(k)}) = \mathbf{M}_{a,b}^e(\omega; 0) + G^{(k)} \mathbf{M}_{a,b}^l(\omega), \quad (3.5)$$

where  $\mathbf{M}_{a,b}^l(\omega)$  represents the longitudinal part of the electric interaction. The analytical expressions of the  $Ek$  and  $Mk$  transition integrals can be found in [35, p. 439-40].

By setting  $G^{(k)} = 0$  in Eq. (3.5), the computations are performed in what is known as the Coulomb gauge, while, for  $G^{(k)} = \sqrt{2}$ , the  $Ek$  transition integrals are computed in the so-called Babushkin gauge. In non-relativistic calculations, the Coulomb and Babushkin gauges, respectively, correspond to the velocity and length forms (see also Appx. A). The latter naming is often adopted in relativistic calculations, as is the case with Papers II and III.

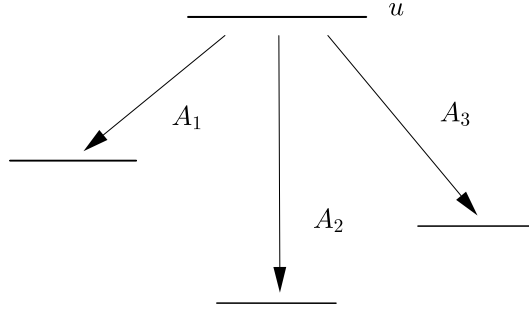
The two gauges are equivalent for hydrogenic wave functions based on an infinitely heavy point nucleus, that is for exact solutions. As long as approximate many-electron wave functions are used, the two gauges result in different values [71]. Taking the non-relativistic limit (see Appx. A), it is seen that, in the computations of transition integrals corresponding to the Coulomb gauge, the emphasis is given to the inner parts of the radial orbitals, whereas in the transition integrals corresponding to the Babushkin gauge, the weight is put on the ‘‘tail’’ of the radial orbitals. Producing transition data, for many-electron systems, that are weakly sensitive to the choice of

gauge, hence, requires that the wave functions are accurately represented in regions of space both near and far from the nucleus.

The lifetime  $\tau_{\Gamma'P'J'}$  of any of the excited states  $|\Gamma'P'J'M'\rangle$  is given in terms of a sum over transition rates for all the possible decay channels, so that

$$\tau_{\Gamma'P'J'} = \frac{1}{\sum_{k,\Gamma PJ} A^{(k)}(\Gamma'P'J', \Gamma PJ)}. \quad (3.6)$$

Figure 3.2 shows three possible decay channels of an upper state  $u \equiv |\Gamma'P'J'M'\rangle$ , each with rates  $A_1$ ,  $A_2$ , and  $A_3$ . The lifetime of this state is given by  $\tau_u = 1/(A_1 + A_2 + A_3)$ . Although single line properties, such as transition rates and weighted oscillator strengths, are generally hard to measure, measurements of the lifetimes of excited states are easier to perform. If the lifetime measurements are precise enough, they can be used to benchmark the theoretical predictions and to guide the labelling of the energy levels.



**Figure 3.2:** An example of an upper state  $u$  having three possible decay channels. The corresponding transition rates for each channel are  $A_1$ ,  $A_2$  and  $A_3$ .

Another quantity that is easier to obtain experimentally is the branching fraction  $Q$ , which represents the relative intensity of lines originating from the same upper state  $u \equiv |\Gamma'P'J'\rangle$  and is expressed as

$$Q^{(k)}(\Gamma'P'J', \Gamma PJ) = \tau_{\Gamma'J'} \sum_k A^{(k)}(\Gamma'P'J', \Gamma PJ). \quad (3.7)$$

According to Eq. (3.7), in the example of Fig. 3.2, the branching fraction of “transition 1”, in particular, is given by  $Q_1 = A_1/(A_1 + A_2 + A_3)$ . It follows that  $A_1 = Q_1/\tau_u$ , and correspondingly  $A_2 = Q_2/\tau_u$ , and so forth. Thus, by combining

measurements of branching fractions with reference data of lifetimes, transition rates and weighted oscillator strengths can be derived (see, e.g., [72]).

Electric dipole (E1) transitions, typically, dominate over magnetic and higher electric multipole transitions, yielding the largest rates, and thus having the largest contributions to the lifetimes of the excited atomic states. In Papers I-III, solely E1 transition rates have been computed, from which the lifetimes were deduced.

As previously mentioned, the matrix elements of the E1 transition operator can be evaluated in both Babushkin and Coulomb gauges. The agreement between the computed values in the two different gauges can be used to indicate the accuracy of the computed transition parameters [73]. Accordingly, in Papers I-III, the uncertainties of the computed transition data, such as transition rates  $A$ , were estimated using the quantity (see also [74]):

$$dT = \frac{|A_B - A_C|}{\max(A_B, A_C)}. \quad (3.8)$$

Although the uncertainties  $dT$  should, generally, be used in a statistical manner for a group of transitions with similar properties (as done in Papers II and III), individual  $dT$  values can point out problematic transitions, which could further be analyzed. Such analysis was, for example, conducted in Paper I, which eventually allowed the computational strategies to improve.

### 3.2 C I-IV

Carbon is the fourth-most abundant element in the universe (after hydrogen, helium, and oxygen) [75], and it plays a critical role in understanding the mechanisms of nucleosynthesis and in stellar and galactic chemical evolution modeling [76, 77]. In particular, carbon-rich stars and white dwarfs call for more insight from observations to improve constraints on stellar and galactic evolution models [77, 78]. To effectively analyze the obtained high-resolution spectra within large spectroscopic surveys (see, e.g., [79–82]), up-to-date reference atomic (together with molecular) data should be available. Owing to its high abundance, carbon has a significant impact on the opacity in the atmospheres and interiors of stars. The opacity is a parameter necessary to understand and model stellar atmospheres and radiation transport [5, 83]. Calculating the opacities and modeling stellar atmospheres requires accurate information on very large numbers of atomic transitions.

To address the astrophysical demands, the MCDHF-RCI calculations of transition properties that were performed in Papers I and II targeted the 100, 69, 114, and 53 lowest energy levels, in C I-IV, respectively. In turn, these energy levels resulted in

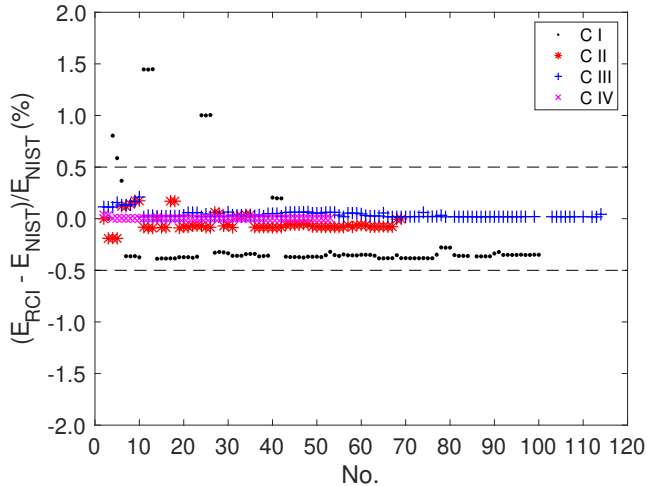
1553, 806, 1805, and 386 possible E1 transitions, in each of the carbon ions. The computational schemes are described in detail in the papers. A summary is also given in Table 1 of Paper II, including the configurations of the targeted states, MR spaces, active sets of orbitals, and numbers of generated CSFs in the final RCI calculations. In the following, we discuss the theoretical uncertainties of the computed data and compare their accuracy among the different carbon ions.

### 3.2.1 Results and discussion

The computed excitation energies,  $E_{\text{RCI}}$ , were benchmarked against the critically evaluated energies,  $E_{\text{NIST}}$ , suggested by the National Institute of Standards and Technology (NIST) Atomic Spectra Database [84]. Figure 3.3 displays the relative differences between the computed energies and the NIST recommended values for all four carbon ions. As seen, in the majority of the cases, the relative discrepancies,  $(E_{\text{RCI}} - E_{\text{NIST}})/E_{\text{NIST}}$ , are of the order of 0.35%, 0.08%, 0.03%, and 0.003%, for C I-IV, respectively. In a few instances, however, the relative discrepancies appear to be greater than 1.0%. These correspond to states in C I that belong to the  $2s2p^3$  configuration and which are, in general, strongly-mixed. More particularly, we note that the  $2s2p^3 \ ^3P^o$  states, represented by No = 24–26 in the figure, are more than 50%-mixed with other  $^3P^o$  states. When taking into account the outliers, the average discrepancies between the computed and the NIST recommended energies are, ultimately, found to be 0.41%, 0.081%, 0.041%, and 0.0044%, for C I-IV, respectively.

The quality of the produced transition data was, primarily, assessed based on extensive comparisons with results from both previous calculations and available measurements. In addition, the theoretical uncertainties of the computed transition rates and lifetimes were evaluated based on the agreement between the reduced matrix elements of the transition operator, respectively, evaluated in the Babushkin and Coulomb gauges, or else the quantity  $dT$  (see Eq. (3.8)).

The weak transitions usually do not have a noticeable impact on the modeling of stellar atmospheres. For this reason, the discussion on the theoretical uncertainties  $dT$  of the computed transition data is restricted to transitions with rates  $A > 10^2 \text{ s}^{-1}$ , in C I and C II, and  $A > 10^0 \text{ s}^{-1}$ , in C III and C IV. The scatter plots of the estimated  $dT$  values, for all these transitions, are provided in Fig. 2 of Paper II. The average uncertainties  $dT$  are of the order of 8.05%, 7.20%, 1.77%, and 0.28%, for C I-IV, respectively. Yet, when only looking at the strong transitions, with  $A > 10^6 \text{ s}^{-1}$ , the uncertainties  $dT$  appear to be remarkably decreased, especially for the C I-III ions. It should be noted that, for those strong transitions, the mean  $dT$  values are 1.68%, 1.53%, 0.297%, and 0.205%, in each of the C I-IV ions.

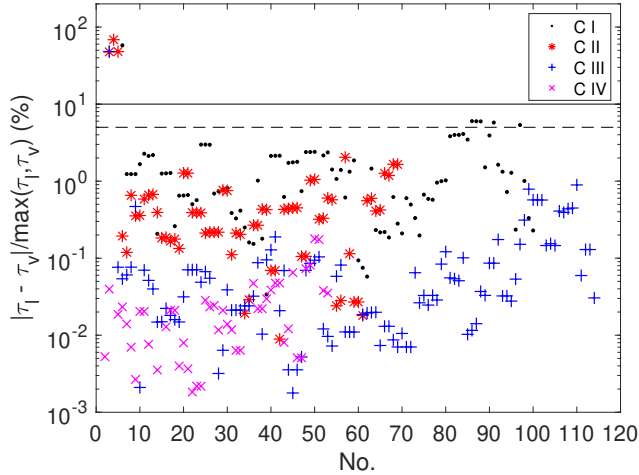


**Figure 3.3:** Left panel of Fig. 1 from Paper II, displaying the relative differences between the computed energy levels and the values suggested by the NIST database [84]. The numbers, No., in the  $x$ -axis correspond to the same labels provided in the second column of Table A1 in Paper II.

Considering that transitions with  $A > 10^6 \text{ s}^{-1}$  have the largest influences on the lifetimes, the latter properties are, ultimately, predicted with uncertainties  $dT$ , which are well below 5%, for almost all targeted excited states in C I-IV. The relative differences between the computed lifetimes in the Babushkin and Coulomb gauges, which define the  $dT$  values, are displayed in Fig.3.4, for all four carbon ions. By looking at the figure, we observe that there are a few outliers in the upper left corner, which correspond to the four long-lived states in C I-III. It must be pointed out that these states decay to the ground state only through intercombination (IC) transitions, which have small rates due to the large, but canceling, contributions (see also [85]).

One can say that the updated *ab initio* data contained in Paper II are, overall, of very high quality; also taking into consideration the total number of lines for which data were made available. The uncertainty evaluations of both computed energy separations and transition data, however, demonstrate the growing difficulties of the theoretical atomic structure studies with the increasing number of electrons that must be correlated. In carbon, this is observed when gradually going from  $N = 3$  to  $N = 6$  electrons and is also well illustrated in Figs. 3.3 and 3.4.

Finally, the computed transition data in C I were validated, in an astrophysical context, by performing a solar carbon abundance analysis. The dispersion of the line-by-line abundance results, generally, reflects the quality of the adopted atomic data. A solar carbon abundance analysis had recently been performed by Amarsi *et al.* [86], based



**Figure 3.4:** Right panel of Fig. 1 from Paper II, displaying the relative differences between the computed lifetimes in the Babushkin and Coulomb gauges, or else the quantity  $dT$ . The numbers, No., in the  $x$ -axis correspond to the same labels provided in the second column of Table A1 in Paper II.

on theoretical transition data provided by Hibbert *et al.* [87], which are commonly used in stellar spectroscopy applications. In Paper II, the solar carbon abundances were post-corrected by making use of the updated theoretical  $gf$  data in C I. It was deduced that the dispersion in the line-by-line abundance results are similar in the cases where the new and old sets of  $gf$  data are, respectively, used.

### 3.3 Al I-II

Aluminium is one of the interesting elements for chemical analysis of the Milky Way (see also Sec. 1 in Paper III), and one example is the *Gaia*-ESO Public Spectroscopic Survey (GES) [79, 80]. The common line list and corresponding atomic data that were used for abundance studies within GES, in the years 2012 to 2019, have just been published [88]. Within this recent work, the need for further improvements in atomic data for Al I was explicitly highlighted. The work of Paper III was motivated by the lack of reliable atomic transition data in aluminium ions. The MCDHF-RCI calculations of transition data that were performed in the paper targeted the 28 and 78 lowest energy levels, in Al I and Al II, respectively. The configurations of the targeted states are shown, for both systems, in Table 3.1.

**Table 3.1:** Summary of the computational schemes for Al I and Al II. The first column displays the configurations of the targeted states. MR and AS, respectively, denote the multi-reference space and the active sets of orbitals used in the MCDHF and RCI calculations, and  $N_{\text{CSFs}}$  are the numbers of generated CSFs in the final RCI calculations, for the even (e) and odd (o) parity states. The second computational scheme in Al II was applied in additional calculations, which go beyond Paper III.

Targeted configurations	MR	AS	$N_{\text{CSFs}}$
Al I, $N_{\text{levels}} = 28$			
$3s3p^2, 3s^2\{n_1s,$ $n_2p, n_3d, n_4f, 5g\}$ ( $4 \leq n_1 \leq 6, 3 \leq n_2 \leq 6,$ $3 \leq n_3 \leq 6, 4 \leq n_4 \leq 5$ )	$3s3p^2, \{3s^2, 3p^2\}\{n_1s,$ $n_2p, n_3d, n_4f, 5g\}$ ( $4 \leq n_1 \leq 6, 3 \leq n_2 \leq 6,$ $3 \leq n_3 \leq 6, 4 \leq n_4 \leq 5$ )	{12s,12p,12d 11f,11g,10h}	e: 4 362 628 o: 2 889 385
Al II, $N_{\text{levels}} = 78$			
$3s^2, 3p^2, 3s6h, 3p3d$ $3s\{n_1s, n_2p, n_3d, n_4f, n_5g\}$ ( $4 \leq n_1 \leq 7, 3 \leq n_2 \leq 7,$ $3 \leq n_3 \leq 6, 4 \leq n_4 \leq 6,$ $5 \leq n_5 \leq 6$ )	$3s^2, 3p^2, 3s6h, 3p3d$ $3s\{n_1s, n_2p, n_3d, n_4f, n_5g\}$ ( $4 \leq n_1 \leq 7, 3 \leq n_2 \leq 7,$ $3 \leq n_3 \leq 6, 4 \leq n_4 \leq 6,$ $5 \leq n_5 \leq 6$ )	{13s,13p,12d, 12f,12g,8h,7i}	e: 911 795 o: 1 269 797
Al II, $N_{\text{levels}} = 78$		(Beyond Paper III)	
$3s^2, 3p^2, 3s6h, 3p3d$ $3s\{n_1s, n_2p, n_3d, n_4f, n_5g\}$ ( $4 \leq n_1 \leq 7, 3 \leq n_2 \leq 7,$ $3 \leq n_3 \leq 6, 4 \leq n_4 \leq 6,$ $5 \leq n_5 \leq 6$ )	$3s^2, 3p^2, 3s6h, 3p3d$ $3s\{n_1s, n_2p, n_3d, n_4f, n_5g\}$ ( $4 \leq n_1 \leq 9, 3 \leq n_2 \leq 9,$ $3 \leq n_3 \leq 8, 4 \leq n_4 \leq 8,$ $5 \leq n_5 \leq 7$ )	{15s,15p,14d, 14f,13g,8h,7i}	e: 1 677 045 o: 2 143 943

The theoretical investigations of the Al I and Al II ions have been particularly challenging due to the perturbers that enter the Rydberg series, resulting in a strong mixing of some of the states. In Al II, the lower part of the spectrum is dominated by the strong interaction between the  $3s3d \ ^1D$  and  $3p^2 \ ^1D$  configuration states. This can readily be deduced by looking at the  $LS$ -composition of these states as, for instance, given in the NIST database [84]. Moving higher, the spectrum of Al II is governed by the strong configuration mixing of the  $3snf \ ^3F$  series with the  $3p3d \ ^3F$  states. As Al I has an additional electron in the valence shell, in this system the strong two-electron interaction between the  $3s3d \ ^1D$  and  $3p^2 \ ^1D$  states manifests itself in the interaction between the  $3s^23d \ ^2D$  and  $3s3p^2 \ ^2D$  states. In fact, the  $3s3p^2 \ ^2D$  perturber state is smeared out over the entire discrete part of the  $3s^2nd \ ^2D$  Rydberg series, resulting in the strong mixing of all these states [89].

The positions of strongly-mixed states are predicted correctly only if the wave functions are highly correlated, namely the atomic state expansions must contain a very large number of CSFs. At the same time, the CSF expansions should be generated so that the correlation orbitals are properly localized to adequately describe the wave functions of all targeted states. The computational strategies that were followed in Paper III aimed at facing these challenges. The computations in Al I and Al II are described below. A summary is also given in Table 3.1, displaying the MR spaces, ASs of orbitals, and numbers of CSFs that were generated in the final RCI calculations.

### 3.3.1 Computations

In the computations of Al I, static electron correlation was captured by extending the MR to include, besides the configurations of the targeted states, configurations of CSFs that give substantial contributions to the total wave functions (see also Table 3.1). Following the general methodology described in Sec. 2.5, the atomic state expansions were enlarged with CSFs that were formed by allowing single and restricted-double (SrD)-MR electron substitutions from the valence spectroscopic orbitals to six layers of correlation orbitals (see “AS” in Table 3.1). The applied restriction was that there was at most one substitution from orbitals with  $n = 3$ . By doing so, the correlation orbitals were localized, between the inner  $n = 3$  valence orbitals and the outer orbitals of the higher Rydberg states, to ably describe all states considered. This is a compromise we had to make due to the fact that we could not afford (computationally) to first saturate other types of substitutions before we get enough correlation orbitals overlapping with the outer orbitals of the higher Rydberg states (see also Sec. 2.5). Subsequent RCI calculations included CSF expansions produced by single, double, and triple (SDT) substitutions from all valence orbitals and SD substitutions from the valence orbitals and the  $2p^6$  core, with the limitation of allowing maximum one hole in  $2p^6$ .

Al II is less complex than Al I, and it is computationally feasible to build the radial orbital basis using CSF expansions that are produced by SrD-MR electron substitutions (the MR merely consists of the targeted configurations shown in Table 3.1), from the valence orbitals and the  $2p^6$  core, with the restriction that only one substitution is allowed from  $2p^6$ . In this manner, the CSFs capture both VV and CV electron correlation effects. The  $2pnl$  pair-correlation effect is, yet, relatively important, and the generated correlation orbitals are spatially localized between the  $2p$  core orbital and the inner valence orbitals. Hence, the wave functions are not properly described for all states, and in particular, not for the higher Rydberg states considered. This is also reflected in the large theoretical uncertainties of computed data associated with transitions that involve high Rydberg states.



A correct representation of all targeted states in Al II demands that the correlation orbitals occupy, instead, the space of the valence orbitals. Hence, the Al II data, presented in Paper III, were computed based on CSF expansions that were formed by only allowing VV substitutions of electrons to effectively build six layers of correlation orbitals (see “AS” in Table 3.1). This time, the resulting correlation orbitals are more extended, overlapping with orbitals of higher Rydberg states. In the subsequent RCI calculations, the CSF expansions were augmented by enabling SrD-MR electron substitutions from the valence orbitals and the 2s and 2p core orbitals, with the restriction that there was maximum one substitution from the  $n=2$  orbitals.

### 3.3.2 Results

The spectrum calculations that were performed in Paper III produced a great number of updated *ab initio* excitation energies and transition data. An important task was to evaluate the accuracy of these data. The computed excitation energies were compared with the critically evaluated energies proposed by NIST [84] and were found to be in very good agreement. On average, the relative differences between computed energies,  $E_{\text{RCI}}$ , and critically compiled energies,  $E_{\text{NIST}}$ , are  $< 0.6\%$  and  $< 0.2\%$ , in Al I and Al II, respectively. Additionally, we note that in the computations of Al II, all differences  $\Delta E = E_{\text{NIST}} - E_{\text{RCI}}$  maintain the same sign, and similar is the case for Al I, with the exceptions of the  $3s^2 4d^2 D_{3/2,5/2} a^1$  states. That being so, the uncertainties in the predicted excitation energies of two states associated with a transition most often cancel out, and the majority of the derived transition energies are in excellent agreement with the NIST recommended values.

The theoretical uncertainties of the computed transition data essentially arise from the disagreement of the radial transition integrals (3.5), evaluated in the Babushkin and the Coulomb gauges, respectively. These uncertainties are reflected in the  $dT$  values given by Eq. (3.8). For the strong transitions, with rates  $A > 10^6 \text{ s}^{-1}$ , the  $A$  values are subject to uncertainties  $dT$  that are typically of the order of 5% in Al I and 3% in Al II. It is, however, observed that, when the transitions involve high Rydberg states, the agreement between the  $A_B$  and  $A_C$  values is not as good. For instance, when the  $3s^2 6s^2 S_{1/2}$  state participates in a transition in Al I, the average uncertainty  $dT$  is about 8%. In Al II, for transitions involving the  $3s 7p^1,^3P$  states, the  $dT$  values are consistently large, ranging between 8% and 37%. Consequently, the lifetimes of the  $3s 7p^1,^3P$  states are computed with average uncertainties of the order of 13%. The latter uncertainties are by far the largest among all computed lifetimes in Al II.

---

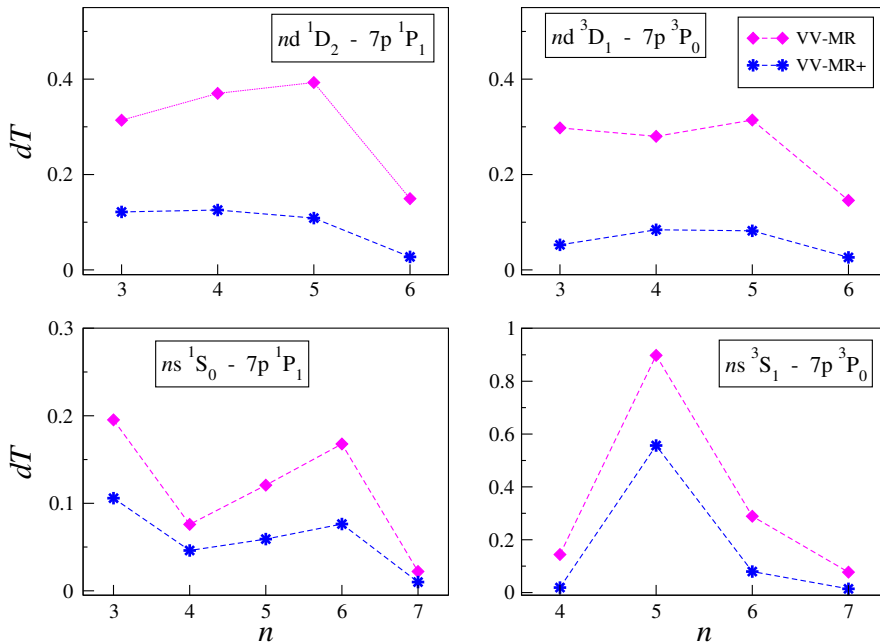
<sup>1</sup>The subscript  $a$  is used to distinguish the two terms that are assigned the same label after the computations.

### 3.3.3 Beyond Paper III

The computations of transition data in the Babushkin and the Coulomb forms, respectively, involve radial transition integrals given by (3.5), which probe separate parts of the wave functions (see also Appx. A). Obtaining transition data that are weakly sensitive to the choice of gauge, i.e.,  $dT \sim 0$ , requires that the radial parts of the wave functions are well approximated as a whole. In the computations of Al I and Al II, despite the specific optimization strategies, the correlation orbitals are, in most cases, rather contracted compared to the spectroscopic outer Rydberg orbitals, and the outer parts of the wave functions representing the high Rydberg states are not always effectively described. As a result, computed data for transitions involving high Rydberg states are often subject to unexpectedly large  $dT$  values.

To improve the overall accuracy of the computed transition data, a more balanced orbital basis, with correlation orbitals that occupy regions of space far from the atomic core, should be generated. To do so, one could consider to include in the MR set configurations that encompass orbitals with higher principal quantum numbers  $n$ , such as  $3s^2nl$  configurations with  $n = 7, 8$  in Al I and  $3snl$  configurations with  $n = 8, 9$  in Al II. A similar orbital optimization strategy has been applied in the past in spectrum calculations of Mg I [72].

Additional computations have now been performed in Al II, employing a similar approach to the aforementioned orbital optimization strategy, which is based on an “extended” MR configuration space. The extended MR space, together with the AS of orbitals and the numbers of CSFs generated in the final RCI calculations, are shown in the last segment of Table 3.1. The uncertainties  $dT$  of the transition rates computed in Paper III and in the additional –most recent– calculations are compared for a few groups of transitions in Fig. 3.5. Each group is selected to include transitions between a fixed state and Rydberg states described by electron distributions gradually localized farther from the atomic core. Looking at Fig. 3.5, we observe that, when the extended MR configuration space is used, the uncertainties in the transition rates are substantially reduced. In fact, in some of the cases, the reduction is remarkable.



**Figure 3.5:** The uncertainties  $dT$  of the computed transition rates for transitions between the  $3s7p\ ^1P_1$ , or  $3s7p\ ^3P_0$ , state and various successive Rydberg states in Al II. The magenta diamonds correspond to the resulting  $dT$  values from the computations based on the VV-MR approach that was applied in Paper III, whereas the blue circles indicate the  $dT$  values from the computations based on the VV-MR+ approach, which employed an “extended” set of MR configurations. In all cases, the uncertainties are significantly reduced. Yet, for the displayed transitions in the upper panels, the reduction is rather remarkable.

### 3.4 Landé g-factors

In intermediate coupling, i.e.,  $LS\ J$  approximation, the Landé  $g_{\Gamma J}$ -factor, for a state specified by  $|\Gamma P J M\rangle$ , is given by

$$g_{\Gamma J} = \sum_{LS} w(LS) g_J(LS), \quad (3.9)$$

where  $w(LS)$  are the weights of the  $LS$ -terms determining the  $LS$ -composition of the wave function. The Landé  $g_{\Gamma J}$ -factors are, therefore, valuable probes of the coupling conditions in atoms. When two states are close in energy, the knowledge of the  $g_{\Gamma J}$ -factors can be used to identify them, providing the values of the  $g_{\Gamma J}$ -factors are significantly different [14, 15]. Accordingly, information on  $g_{\Gamma J}$ -factors can be useful

for identifying strongly-interacting states with different  $LS$ -terms.

Since the Landé  $g_{\Gamma J}$ -factors are directly dependant on the mixing of the different  $LS$ -terms, they also depend on the predicted energy separations. The accuracy of the Landé  $g_{\Gamma J}$ -factors, computed in Paper IV, was, thus, evaluated based on the accuracy of the resulting energy separations. For this purpose, a new parameter, denoted  $\overline{dE_S}$ , was introduced to quantify the average relative differences between the computed energy separations and recommended values from the NIST database (for the exact definition of this parameter see Sec. 4.1 in Paper IV). As also seen in Table 4 of Paper IV, the  $\overline{dE_S}$  values, are below 0.5%, for both even and odd parity states in C I-IV and Al II, as well as for the odd states in Al I. For the even states in Al I, the  $\overline{dE_S}$  value is  $\sim 1.5\%$ .

Using Eq. (3.9), the mixing between different  $LS$ -terms can be evaluated by comparing the computed  $g_{\Gamma J}$ -factors with the corresponding  $g_J(LS)$  values from the pure  $LS$ -coupling. In Paper IV, this comparison was performed for all computed states in the studied ions, and it is visualized in Fig. 1 of the paper. The good agreement between the  $g_{\Gamma J}$  and  $g_J(LS)$  values, in C II-IV and Al I-II, indicates that the states of these atoms and ions are well described within the  $LS$ -coupling approximation. On the other hand, in C I, there are many states for which the discrepancies between the  $g_{\Gamma J}$  and  $g_J(LS)$  values reach  $\sim 15\%$ , calling for a more rigorous treatment.

## Chapter 4

# Hyperfine Structure - Extracting Nuclear Quadrupole Moments of Tin Isotopes

Nuclei with an odd proton number,  $Z$ , and/or an odd neutron number,  $N$ , have a non-zero total nuclear spin,  $I$ . Nuclei also possess electromagnetic multipole moments, higher than the electric monopole, representing the nuclear charge. The lowest non-trivial nuclear magnetic and electric multipoles are the magnetic dipole moment,  $\mu_I$ , and electric quadrupole moment,  $Q$ . The latter reflects the deviation –to first order– of a nuclear charge distribution from the spherical shape [90], constituting an important characteristic of the structure of a nucleus [91, Ch. 7]. In atomic systems containing nuclei with non-zero spin  $I$ , the nuclear electromagnetic moments interact with the magnetic field and inhomogeneous electric field, produced by the electrons at the position of the nucleus. As a result of this interaction, the nucleus experiences a torque, which generates orientation potential energy and gives rise to further splittings of the fine-structure energy levels. These splittings are about three orders of magnitude smaller than the fine-structure splittings and are, thus, known as the hyperfine structure (HFS) [92]. Theoretical investigations of the HFSs require that the computed electronic parts of the interactions are merged with trustworthy values of the respective nuclear electromagnetic moments.

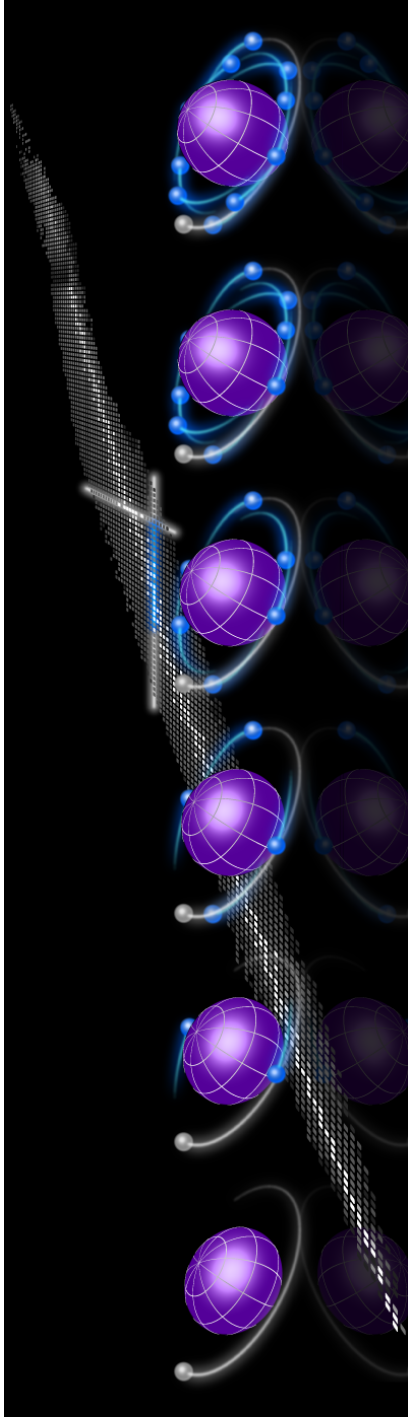
In general, experiments can, very accurately, determine the magnetic dipole moments  $\mu_I$ , which are, practically, considered to be known [93, 94]. On the other hand, it is rather difficult to measure the electric quadrupole moments  $Q$ , via direct experimental nuclear techniques. High-precision measurements of HFS splittings combined with computed hyperfine electronic factors can, alternatively, be used to semi-empirically

determine the nuclear quadrupole moments (see, e.g., [95–97]). The systematic tabulation of the  $Q$  values along the isotope sequences [98, 99] and their comparisons with the theoretical predictions allow the nuclear models to be thoroughly tested and the description of the effective nuclear interactions to be improved [100]. In Paper v, HFS measurements of the  $5s^25p6s\ ^3P_1^o$  and  $5s^25p6s\ ^1P_1^o$  states in neutral tin (Sn I) were combined with calculations of the corresponding electronic factors to extract the  $Q$  moments of the odd-mass tin isotopes in the range  $^{117-131}\text{Sn}$ .

The tin isotope sequence, with a magic number of protons at  $Z = 50$ , is particularly interesting for nuclear structure studies. Tin, besides being the chemical element with the largest number of stable isotopes, is the heaviest known element containing two isotopes with closed both proton and neutron shells. These are the neutron-deficient  $^{100}\text{Sn}$  [101] and neutron-rich  $^{132}\text{Sn}$  isotopes [102]. The intermediate tin isotopes, with only their proton core complete, may acquire quadrupole moments through the geometry of the valence neutron orbitals. In the odd-mass tin isotopes, the unpaired neutron, in principle, polarizes the spherical core, modifying its electromagnetic properties (see, e.g., [91, Fig. 7.8]). This matter polarization effect is visualized, for a portion of the studied isotopes, in Fig. 4.1. High-precision data on quadrupole moments along the tin isotopic chain can, thus, provide the required criteria for probing the shell structure predicted by nuclear models.

The extracted  $Q(\text{Sn})$  values, in Paper v, exhibit mass-dependent trends, which are remarkably smooth, namely linear, or, at most, quadratic (see also Fig. 3a, b in the paper). This observed global behavior of the extracted quadrupole moments was reproduced by the nuclear density functional theory (DFT) calculations that were performed in the paper, using recently optimized input parameters. Nonetheless, local patterns, including the crossover point at the neutron number  $N$  for which the valence shell becomes half-filled and the quadrupole moment vanishes, do not always conform to expectations. This suggests that further theoretical developments and a more dedicated microscopic modeling are required in the future.

As previously mentioned, in Paper v, the nuclear quadrupole moments were determined based on the theoretical evaluation of the electronic parts of the hyperfine interaction. The multiconfiguration calculations of the hyperfine electronic factors in neutral systems, such as Sn I, are particularly challenging due to their high sensitivity to different electron correlation effects and the large number of electrons to correlate. To be in a position to estimate the final values of these properties and their uncertainties, it is, therefore, common to perform multiple sets of large-scale calculations, employing different electron correlation models [58]. Paper VI reports on the specifics of the four separate *ab initio* calculations that were carried out to deduce the final value of the electronic part of the electric quadrupole interaction in the  $5s^25p6s\ ^1P_1^o$  state, which was, ultimately, used to extract the  $Q(\text{Sn})$  values. In Paper VI, the rigorous



**Figure 4.1:** The filling of a particular neutron shell in the (odd-mass) isotopes of tin results in a gradual elongation of the nucleus, modifying its electromagnetic properties. The neutrons that are added, in pairs, are shown as blue particles, while the single grey particle represents the unpaired odd neutron, which is present in each case. The rest of the neutrons are contained in the (purple) core, together with the 50 protons. The nuclear chart is depicted in perspective, where the isotopes studied in Paper v are illuminated in blue. The relevant shell closures at 50 protons and 82 neutrons are also highlighted in the chart. Image credits: [103].

assessment of the uncertainties of the latter computed electronic factor is further discussed in detail. Since the accuracy of the inferred  $Q(\text{Sn})$  values is affected by the uncertainties of the atomic structure calculations, ensuring the highest quality of the latter is an absolute requirement for interpreting the patterns that these experimental observables follow.

In Sec. 4.1, we describe the theory of the HFS interaction, demonstrating how the hyperfine splittings of the energy levels are, to the lowest orders, given by the magnetic dipole and electric quadrupole coupling constants  $A$  and  $B$ , respectively. The latter constants can simply be written as products of the nuclear magnetic dipole and electric quadrupole moments and the corresponding electronic contributions. The importance of different electron correlation effects in the computations of the hyperfine electronic factors is, subsequently, discussed in Sec. 4.2. Within this section, one of the three sets of separate MCDHF-RCI calculations that were carried out in Papers v-vi (reflecting the author's major contribution to these works) is analyzed, justifying the adopted computational strategy.

## 4.1 Hyperfine Structure

The Dirac-Coulomb Hamiltonian of Eq. (2.8) solely takes into account the central part of the nuclear charge density distribution. The non-central interaction between the electrons and the nuclear electromagnetic multipole moments gives rise to what is known as the hyperfine structure (HFS). The corresponding contribution to the Hamiltonian can be represented by a multipole expansion

$$\mathcal{H}_{\text{HFS}} = \sum_{k \geq 1} \mathbf{T}^{(k)} \cdot \mathbf{M}^{(k)}, \quad (4.1)$$

where  $\mathbf{T}^{(k)}$  and  $\mathbf{M}^{(k)}$  are two spherical tensor operators of the same rank  $k$ , which, separately, act on the electronic,  $|\Gamma P J M_J\rangle$ , and nuclear,  $|\eta \Pi I M_I\rangle$ , spaces [92]. The nuclear states are characterized by the parity  $\Pi$ , the total angular momentum  $I$  and its projection quantum number  $M_I$ , together with the label  $\eta$ , which contains additional information necessary to uniquely describe each state. In the expansion (4.1),  $k = 1$  represents the magnetic dipole (M1) part, while  $k = 2$  refers to the electric quadrupole (E2) component, of the hyperfine interaction. Higher than second-order terms are far less significant<sup>1</sup> and most often neglected.

The hyperfine interaction couples the nuclear spin,  $\mathbf{I}$ , and electronic angular momentum,  $\mathbf{J}$ , to a total angular quantum number  $\mathbf{F} = \mathbf{I} + \mathbf{J}$ . The coupled electronic

---

<sup>1</sup>Indicatively, we note that magnetic octupole (M3) shifts are typically  $\sim 10^8$  times smaller than M1 splittings [104].



and nuclear states, which are eigenfunctions of  $\mathbf{F}^2$  and  $F_z$ , are characterized by the quantum numbers  $F$  and  $M_F$  and are expressed as

$$|\eta\Gamma\Pi\Pi I J F M_F\rangle = \sum_{M_I, M_J} \langle I, J; M_I, M_J | F, M_F \rangle |\eta\Pi\Pi I M_I\rangle |\Gamma P J M_J\rangle, \quad (4.2)$$

with  $\langle I, J; M_I, M_J | F, M_F \rangle$  being the CG coefficients. Assuming that the HFS energies are small in comparison to the fine-structure splittings, the hyperfine interaction can be treated in first-order perturbation theory. In this case, for a specific state  $|\Gamma P J\rangle$ , the total HFS contribution to the fine-structure energy,  $E_{\Gamma J}$ , is given by

$$E_{\Gamma J}^{\text{HFS}} = \langle \eta\Gamma\Pi\Pi I J F M_F | \sum_{k=1,2} \mathbf{T}^{(k)} \cdot \mathbf{M}^{(k)} | \eta\Gamma\Pi\Pi I J F M_F \rangle, \quad (4.3)$$

which corresponds to the diagonal HFS effect. Following [51, § 11.8], the two terms of Eq. (4.3) are evaluated according to

$$\begin{aligned} & \langle \eta\Gamma\Pi\Pi I J F M_F | \mathbf{T}^{(k)} \cdot \mathbf{M}^{(k)} | \eta\Gamma\Pi\Pi I J F M_F \rangle = \\ & (-1)^{I+J+F} \left\{ \begin{array}{ccc} I & J & F \\ J & I & k \end{array} \right\} \langle \Gamma P J | \mathbf{T}^{(k)} | \Gamma P J \rangle \langle \eta\Pi\Pi | \mathbf{M}^{(k)} | \eta\Pi\Pi \rangle, \end{aligned} \quad (4.4)$$

where the dependence on the total momentum  $F$  is contained in the  $6j$ -symbol and the phase factor. Due to the properties of the  $6j$ -symbol in the expression above, Eq. (4.3) includes terms only up to  $k = 2 \min(I, J)$ . Papers v and vi exclusively considered  $J = 1$  states in neutral tin, which potentially, permit both M1 and E2 interactions. However, among the studied tin isotopes, there were a few isomers with nuclear spin  $I = 1/2$ , for which only the M1 components exist, and no nuclear quadrupole moments were extracted (see Table 1 in Paper v).

In the majority of cases, the nuclear operators,  $\mathbf{M}^{(1)}$  and  $\mathbf{M}^{(2)}$ , are not explicitly used—their expressions can yet be found in, e.g., [104]. Instead, the expectation values of the  $\mathbf{M}^{(1)}$  and  $\mathbf{M}^{(2)}$  operators in the state with the maximum component of the nuclear spin, i.e.,  $M_I = I$ , are directly connected to the conventional nuclear magnetic dipole moment,  $\mu_I$ , and electric quadrupole moment,  $Q$ , so that

$$\mu_I = \langle \eta\Pi\Pi I | M_0^{(1)} | \eta\Pi\Pi I \rangle \quad (4.5)$$

and

$$\frac{Q}{2} = \langle \eta\Pi\Pi I | M_0^{(2)} | \eta\Pi\Pi I \rangle. \quad (4.6)$$

By making use of the Wigner-Eckart theorem [51, § II.4] in Eqs. (4.5) and (4.6) and substituting the formulas for the respective  $3j$ -symbols as found in [105, §4.2], we get

$$\langle \eta\pi I \| \mathbf{M}^{(1)} \| \eta\pi I \rangle = \mu_I \sqrt{\frac{((2I+1)(I+1))}{I}} \quad (4.7)$$

and

$$\langle \eta\pi I \| \mathbf{M}^{(2)} \| \eta\pi I \rangle = \frac{Q}{2} \sqrt{\frac{(2I+3)(I+1)(2I+1)}{I(2I-1)}}. \quad (4.8)$$

To evaluate the expectation value (4.3), using Eq. (4.4), the nuclear reduced matrix elements are replaced by the expressions (4.7) and (4.8). After also utilizing the formulas for the  $6j$ -symbols found in [105, §4.2], the HFS energy corrections to the fine-structure levels are, finally, written as

$$E_{\Gamma J F}^{\text{HFS}} = \frac{1}{2} A_{\Gamma J} C + B_{\Gamma J} \frac{\frac{3}{4} C(C+1) - I(I+1)J(J+1)}{2I(2I-1)J(2J-1)}, \quad (4.9)$$

where  $C = F(F+1) - J(J+1) - I(I+1)$  and  $A_{\Gamma J}$ ,  $B_{\Gamma J}$  are the so-called HFS constants, which do not depend on the  $F$  quantum number, and, respectively, describe the intensities of the M1 and E2 interactions for a specific  $|\Gamma P J\rangle$  state. The HFS constants are expressed as

$$A_{\Gamma J} \equiv A = \frac{\mu_I}{I} \frac{1}{\sqrt{J(J+1)(2J+1)}} \langle \Gamma P J \| \mathbf{T}^{(1)} \| \Gamma P J \rangle, \quad (4.10)$$

and

$$B_{\Gamma J} \equiv B = 2Q \sqrt{\frac{J(2J-1)}{(J+1)(2J+1)(2J+3)}} \langle \Gamma P J \| \mathbf{T}^{(2)} \| \Gamma P J \rangle. \quad (4.11)$$

For an  $N$ -electron atom, the electronic operators for each of the M1 and E2 interactions are given by

$$\mathbf{T}^{(1)} = \sum_{i=1}^N \mathbf{t}^{(1)}(i) = \sum_{i=1}^N -i\sqrt{2} \alpha r_i^{-2} \left( \boldsymbol{\alpha}_i \mathbf{C}^{(1)}(\theta_i, \varphi_i) \right)^{(1)} \quad (4.12)$$

and

$$\mathbf{T}^{(2)} = \sum_{i=1}^N \mathbf{t}^{(2)}(i) = \sum_{i=1}^N -r_i^{-3} \mathbf{C}^{(2)}(\theta_i, \varphi_i), \quad (4.13)$$

where  $\alpha$  is the fine-structure constant,  $\boldsymbol{\alpha}$  is the Dirac matrix, and  $\mathbf{C}^{(1)}$  and  $\mathbf{C}^{(2)}$  are the renormalized spherical harmonics of rank 1 and 2, respectively. The M1 operator (4.12) represents the magnetic field produced at the region of the nucleus by the orbital motions and spins of the electrons, whereas the E2 operator (4.13) describes the rate of change in the electric field, or the electric field gradient (EFG), which is generated by the electrons at the site of the nucleus.

The  $A$  and  $B$  constants can be obtained by combining the computed values of the electronic factors,

$$A_{\text{el}} = AI/\mu_I, \quad B_{\text{el}} = B/Q, \quad (4.14)$$

with information on the nuclear electromagnetic moments  $\mu_I$  and  $Q$ . When high-precision measurements of the  $A$  and  $B$  constants, together with accurate values of nuclear magnetic dipole moments  $\mu_I$ , are available, the computed electronic factors  $A_{\text{el}}$  and  $B_{\text{el}}$  can be used to semi-empirically determine the nuclear electric quadrupole moments  $Q$  [98, 99].

## 4.2 Computing the Electronic Factors $A_{\text{el}}$ and $B_{\text{el}}$

The computations of the electronic  $A_{\text{el}}$  and  $B_{\text{el}}$  factors, in principle, rely on how accurately the generated magnetic fields and EFGs at the nuclear region are described. In an atomic state, an unpaired valence  $s$ -electron, with a finite probability density at the nucleus, is likely to give the largest contribution to the magnetic field near the origin. However, electron correlation effects, and especially, the polarization effects resulting from the Coulomb interaction between core and valence subshells, may provide significant corrections to the representations of the magnetic fields, as well as contributions to the EFGs.

Taking for convenience the non-relativistic limit, in the Hartree-Fock approximation, the closed electron core has a charge distribution, which is spherically symmetric and gives no contribution to the magnetic field and EFG. Closed subshells also have zero spin-densities due to the full cancellation of the spin-up and spin-down contributions, and as a result, no magnetic field is, overall, generated from the core. Yet, in reality, outer valence electrons polarize the electron core, resulting in a distortion of the spherically symmetric charge distribution. Further on, the interactions between an outer valence electron and the individual core electrons are, practically, different for spin-up and spin-down. As a general rule, the Coulomb exchange interaction weakens the repulsion between core and valence electrons with the same spin orientation, pulling the core electron towards the valence subshell [52, §8.14]. This interaction distorts the core, whose spin-density, eventually, becomes non-zero.

In the MCDHF calculations, the distortion, or else polarization, of the core can be represented by CSFs that are generated by single (S) electron substitutions from the core orbitals of the MR configurations. More particularly, the spin-polarization effects are largely captured by S substitutions from the core  $s$ -orbitals. It should be mentioned that, as inner  $s$ -electrons have very high spin-densities at the site of the nucleus, even small differences between the spin-densities of the two  $s$ -electrons in the same subshell can induce a net interaction, which is comparable to the effect from an open valence subshell. The orbital-polarization effects, which impact both magnetic field and EFG, are taken into account by the S substitutions from core orbitals with  $l \geq 1$ . The HFS interaction is described by one-particle operators (see Eqs. (4.12) and (4.13)), and when computing the hyperfine electronic factors  $A_{\text{el}}$  and  $B_{\text{el}}$ , the CSF expansions should, in principle, include S substitutions from all orbitals that are part of the MR configurations.

Although the spin- and orbital-polarization effects directly captured by S electron substitutions give the most substantial corrections to the computed electronic HFS factors, there are more effects, such as additional core-valence (CV) correlation effects and three-particle interactions, which are also critical. By including CSFs that capture CV electron correlation, in addition to valence-valence (VV) correlation, the valence orbitals will undergo a contraction. Since the operators  $\mathbf{T}^{(1)}$  and  $\mathbf{T}^{(2)}$  scale as  $r^{-3}$ , this effective contraction of the valence orbitals will raise the  $A_{\text{el}}$  and  $B_{\text{el}}$  values. It should be pointed out that, even though it is not directly obvious from Eqs. (4.12) and (4.13), the common  $r^{-3}$  dependence is explained by the different structures of the corresponding one-electron matrix elements in the non-relativistic limit [37, § 5.2]. CSFs produced by triple (T) substitutions from the MR configurations further increase the electronic HFS factors. As the HFS is described by one-particle operators, and the energy corrections are obtained by (one- and) two-particle operators, the CSFs built from T substitutions account for the spin- and orbital-polarization effects of the most energetically important configurations that are obtained by double (D) substitutions from the configurations in the MR (in the same way that CSFs built from D substitutions account for the polarization effects of the most energetically important configurations obtained by S substitutions from the MR configurations).

#### 4.2.1 The SrD-MR-MCDHF and RCI calculations

In Papers v-vi, three independent sets of MCDHF-RCI calculations (together with a fourth set of calculations based on the configuration interaction Dirac-Fock-Sturm theory [106]), were carried out to deduce the hyperfine electronic factors  $A_{\text{el}}$  and  $B_{\text{el}}$  of the  $5s5p6s\ ^{1,3}P_1^o$  states in Sn I. In each of the three independent MCDHF-RCI calculations, the wave functions representing the atomic states were obtained based

on various approximations with respect to the orbital basis and the CSF expansions. In this thesis, we focus on the set of multiconfiguration calculations, which applied an orbital optimization strategy based on CSF expansions that were built from S and restricted-double (rD) electron substitutions from a multi-reference (MR) configuration space and are, accordingly, denoted SrD-MR-MCDHF.

The HFS in Sn I is characterized by a large magnetic dipole splitting of the  $^3P_1^o$  state and a sizeable electric quadrupole splitting of the  $^1P_1^o$  state. The quadrupole moments of the studied tin isotopes were extracted by combining the measured  $B[{}^1P_1^o]$  constants, for each of the isotopes, with the calculated electronic factor  $B_{el}[{}^1P_1^o]$ . Additionally, by combining the knowledge on magnetic dipole moments (as obtained from the literature [107, 108]) with the measured  $A[{}^3P_1^o]$  constants, the electronic factor  $A_{el}[{}^3P_1^o]$  was experimentally determined (see also “Methods” in Paper v). The  $A_{el}^{expt}[{}^3P_1^o] = 2396.6(7)$  MHz/ $\mu_N$  value was used to benchmark the calculated  $A_{el}[{}^3P_1^o]$  value, further assisting the evaluation of the uncertainty in the calculated electronic factor  $B_{el}[{}^1P_1^o]$  (see Sec. IV B in Paper v). For this reason, we solely present and discuss the  $A_{el}[{}^3P_1^o]$  and  $B_{el}[{}^1P_1^o]$  values.

In what follows, the SrD-MR-MCDHF and RCI calculations are motivated by discussing, in brief, the captured electron correlation effects and by quantifying the impact that some of them had on the computed electronic factors  $A_{el}[{}^3P_1^o]$  and  $B_{el}[{}^1P_1^o]$ . For further details, the reader is referred to Sec. III A.3 in Paper vi.

The SrD-MR-MCDHF orbital optimization strategy mainly differs from the SrD-SR-MCDHF calculations, which are described in Sec. III A.2 of Paper vi, in choosing a set of MR configurations from which substitutions of electrons were allowed. By defining an MR space that produces a set of CSFs accounting for the major electron correlation effects, a better initial representation of the targeted atomic states was obtained. Moreover, when further generating CSFs by allowing S (and D) substitutions from the MR configurations, triple (and quadrupole) substitutions from the targeted  $5s5p6s$  configuration were also considered. As already mentioned, such CSFs play a critical role in the computation of the HFS constants.

More specifically, in the MCDHF calculations, the orbital basis was obtained based on CSF expansions that were built from SrD substitutions from the 4d, 5s, 5p, 5d, and 6s spectroscopic orbitals, with the limitation that there was at most one substitution from the 4d core subshell. In this way, besides VV electron correlation effects, CV correlation and polarization effects of the 4d orbital were also taken into account. To make sure that the values of all computed properties were converged, nine layers of correlation orbitals were generated, corresponding to more than one million of CSFs (see Table IV in the paper). That being said, during the optimization of the orbital basis, CSFs formed from S, or D, substitutions from orbitals deeper in the atomic

core were not generated, as the computational resources at our disposal did not allow us to do so.

After ensuring the convergence of the computed properties within the (CV-)SrD-MR-MCDHF orbital optimization scheme, a final RCI computation was carried out, in which the atomic state expansions were augmented to include CSFs accounting for additional correlation effects. Due to the limited computational power, the CSF expansions had to be generated so that the most crucial effects were captured. To assess the relative significance of the various correlation effects on the computation of the electronic factors  $A_{\text{el}}[{}^3\text{P}_1^0]$  and  $B_{\text{el}}[{}^1\text{P}_1^0]$ , preliminary RCI calculations (using an orbital basis restricted to four layers of correlation orbitals) were performed. In each of these RCI calculations, the atomic state expansions were, progressively, enlarged to include CSFs that had been generated by, first, allowing additional D substitutions from the 4d orbital and then, gradually, also enabling S substitutions from the 4p, 4s, 3d, and so on, orbitals, down to the innermost 1s orbital. The resulting  $A_{\text{el}}[{}^3\text{P}_1^0]$  and  $B_{\text{el}}[{}^1\text{P}_1^0]$  values are shown in Table 4.1. In addition, starting from the RCI calculations, which employed CSF expansions based on SD substitutions from the 4d, 5s, 5p, and 6s orbitals, further CV correlation effects were considered by, first, opening the 4p orbital and, then, the 4s orbital to generate CSFs based on D substitutions, with the restriction of allowing maximum one hole in  $4p^6$  and, then, also maximum one hole in  $4s^2$ . These results are displayed in the last two rows of Table 4.1.

As seen in Table 4.1, the CSFs formed by allowing D substitutions from the 4d orbital, accounting for core-core (CC) electron correlation effects, are clearly the most important. However, we observe that the effect of adding CC correlation is to decrease the value of the electronic factor  $A_{\text{el}}[{}^3\text{P}_1^0]$ . The effect of CC correlation in the computations of HFSs is mainly indirect. Due to their important contribution to the total energy, the CSFs accounting for CC correlation are expected to have relatively large mixing coefficients. As a result, the mixing coefficients of CSFs describing effects that are more important for HFS interactions, such as the orbital-polarization of the 4d subshell, take lower values. This is, eventually, counterbalanced by the inclusion of CSFs that are formed from S substitutions from the rest of the core subshells. All these classes of CSFs were considered in the atomic state expansions of the final RCI calculation.

Looking at the last portion of Table 4.1, it is confirmed that the contributions from the CV correlation effects of both 4p and 4s subshells are significant. Nonetheless, our computational resources allowed us to include CSFs based on rD substitutions only from the 4p orbital, and not from the 4s orbital, when constructing the final expansions of the atomic states. After including all nine layers of correlation orbitals, we note that the atomic state expansions contained more than 3.5 millions of CSFs (see also Table VI in the paper).

**Table 4.1:** The effect of different types of electron substitutions on the computation of the electronic factors  $A_{el}[^3P_1^o]$  and  $B_{el}[^1P_1^o]$ . The reference values displayed in the first row were computed after optimizing four correlation orbital layers in the SrD-MR-MCDHF calculations. Contributions from additional substitutions were evaluated in subsequent RCI calculations, where the CSF expansions were enlarged by, first, including D substitutions from the 4d orbital and, then, progressively adding S substitutions from the 4p orbital down to the 1s orbital. In the last portion of the table, contributions from CV correlation effects were evaluated in RCI calculations, where CSFs were generated by allowing SrD substitutions from  $n \geq 4$  orbitals, with the restriction that there was at most one substitution, initially, only from the 4p orbital, and then, from the 4s orbital as well.

Subst.	Orbital	$A_{el}[^3P_1^o]$	$B_{el}[^1P_1^o]$
SrD	4d	2 109	591
SD	4d	1 996	605
+ S	4p	2 058	671
+ S	4s	2 062	671
+ S	3d	2 061	672
+ S	3p	2 081	684
+ S	3s	2 086	684
+ S	2p	2 094	687
+ S	2s	2 097	687
+ S	1s	2 099	687
SD	4d	1 996	605
+ SrD	4p	2 087	674
+ SrD	4s	2 095	675





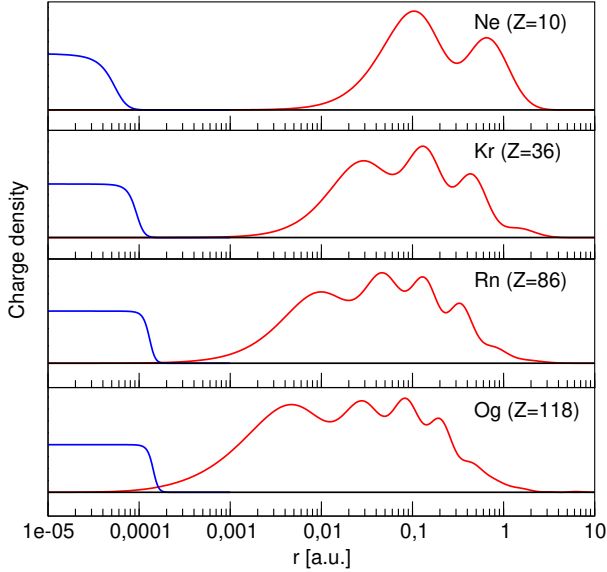
## Chapter 5

# Probing Nuclear Properties in Heavy Atoms via Isotope Shifts

Besides the hyperfine structure splittings of the atomic energy levels (taking place in systems with non-zero nuclear spin), the interplay between the atomic electrons and the nucleus further manifests itself in isotope-dependent energy shifts. When spectral lines from different isotopes of the same element are observed, the isotope specific properties of nuclei induce a small energy separation, known as the line isotope shift (IS). By far the most significant contributions to the observed IS are the mass shift (MS) and field shift (FS) effects [109]. The MS emerges from the difference in the nuclear recoil energies, due to the finite isotopic masses, whereas the FS arises from the different central field potentials that the electrons experience, owing to the unique nuclear charge density distributions. While the impact of the MS is the most prominent in light atoms, the FS dominates in middle- $Z$ , or heavier, systems. This is due to the increased nuclear radii for larger nuclear masses and simultaneous contraction of the atomic orbitals for higher  $Z$  (see Fig. 5.1).

Within the framework of perturbation theory, the MS and FS contributions to the IS are factorized into electronic and nuclear parts [111]. The electronic parts depend on the atomic states participating in the studied transitions, while the nuclear parts are evaluated based on relevant nuclear properties; for the MS and FS, these are, respectively, the nuclear masses and radial moments of the nuclear charge density distributions of the isotopes in question. For a charge density distribution  $\rho(\mathbf{r})$ , the radial moments, of order  $n$ , are given by

$$\langle r^n \rangle = \frac{\int_0^\infty dr^3 r^n \rho(\mathbf{r})}{\int_0^\infty dr^3 \rho(\mathbf{r})}, \quad (5.1)$$



**Figure 5.1:** Nuclear charge (blue) and radial electron (red) density distributions in ground states of selected noble gases. As the atomic number  $Z$  increases, the nuclear charge density distributions gradually expand, while at the same time, the atomic orbitals, and consequently the electron density distributions, become more and more contracted. Image credits: [110]

where the value of the denominator is determined by the normalization condition. The nuclear radial moments provide information about the specifics of the shapes of the nuclear charge density distributions, including their radial extent and the density diffuseness around the nuclear surfaces (surface thickness).

Experimental techniques, such as elastic electron scattering, typically yield precise information on nuclear radial moments, up to infinite order [112, 113]. Even so, electron scattering experiments are only possible for stable and long-lived isotopes. In radioactive and short-lived systems, the theoretical predictions of ISs might have to rely on radial moments that are obtained from models approximating the nuclear charge density distributions. In the studies of atomic structure, the most commonly adopted approximation is the Fermi model [40], which, yet, does not fully capture the details of the nuclear charge distributions. This was also demonstrated in Paper VII, where the Fermi distribution was compared with “realistic” nuclear charge density distributions, obtained from microscopic nuclear models [114, 115].

By making the assumption that the electron density is –to a very good approximation– constant within the nuclear volume, the FS contribution to the IS is simply given by

the product of the electronic parameter and the difference in the second-order radial moments  $\langle r^2 \rangle$  of the studied isotopes [116]. This means that from knowledge of an IS measurement, for one atomic transition, and computations of the corresponding electronic MS and FS parameters, the change in the  $\langle r^2 \rangle$  values between two isotopes can be extracted in a nuclear-model-independent way. In fact, combining high-precision measurements of ISs, via laser spectroscopy [27] or dielectronic recombination [28], with accurate predictions of the electronic MS and FS parameters, has proven to be a key approach for extracting the  $\delta\langle r^2 \rangle$  values in a large number of isotope pairs, including radioactive systems (see, e.g., [117–121]). Thanks to this combined effort from theory and experiment, data of variations in  $\langle r^2 \rangle$  have been made available for isotope sequences along, practically, the entire periodic table [122]. The data on mean-square charge radii, which contain information about the sizes and shapes of nuclei, can eventually be compared with predictions from state-of-the-art nuclear models to assess their ability to reproduce the global behaviour of these observables, as well as further microscopic features [123].

In relatively heavy systems, the constant electron density approximation, however, breaks down, and to obtain an accurate description of the observed ISs, it is necessary to take into account the variations of the electron densities across the nuclear volumes. This leads to the reformulation of the FS, which contribution is now expressed as an expansion over the differences in the first-four even nuclear radial moments of the two isotopes in question [124–126]. It has been shown that, in systems with  $Z \sim 90$ , the corrections in the description of the FS, due to the terms containing the variations in higher than second-order nuclear radial moments, can be of the order of 10% [124].

In Paper VII, it was further deduced that, provided the shape variation is large between the two isotopes, replacing the higher-order radial moments obtained from the Fermi model with radial moments from realistic charge density distributions can have a significant effect on the description of the FSs in systems with  $Z \gtrsim 50$ . In some cases, this effect is greater than the experimental uncertainties, suggesting the possibility to extract information about higher than second-order radial moments from IS measurements. In Paper VII, a promising method for the simultaneous extraction of the  $\delta\langle r^2 \rangle$  and  $\delta\langle r^4 \rangle$  values, using experimental ISs, was introduced, by also quantifying the statistical errors that arise from the uncertainties in the IS measurements. It was concluded that an increase in the experimental precision by 1 – 2 orders of magnitude is necessary to extract the  $\delta\langle r^2 \rangle$  and  $\delta\langle r^4 \rangle$  values with adequate accuracy. It was recently shown [127] that possible access to both  $\langle r^2 \rangle$  and  $\langle r^4 \rangle$  moments could establish more reliable constraints in the prediction of the surface thickness of the nuclear charge density distributions, which, in approximate models, such as the Fermi distribution, is set to be constant.

To be in a position to extract the information on the  $\langle r^2 \rangle$  and  $\langle r^4 \rangle$  radial moments from measurements of atomic transition energies, one must also bear in mind that the electronic parts that make up the MS and FS contributions must be evaluated with very high precision. Although, in highly-charged systems, this might be feasible, the accuracy of atomic structure calculations in neutral, or near-neutral, systems is often limited by the electron correlation effects, which might not be effectively captured. Besides the MS and FS contributions, there are additional effects, such as QED and nuclear polarization corrections, which also contribute to the observed ISs and must be accurately estimated. The nuclear polarization contribution refers to the interaction of a nucleus with the radiation field, which results in virtual excitations of collective nuclear states [128, Ch. 19]. This effect is always present in atomic transitions and, when identifying the various contributions to the observed ISs, it can be the largest uncertainty factor [129].

In Sec. 5.1, we describe how the observed ISs can be predicted by separately evaluating the MS and FS contributions. Sec. 5.2 summarizes the most important findings from the investigations that quantified the effect of using realistic nuclear charge density distributions when computing the FSs. The developed method for the simultaneous extraction of the  $\delta\langle r^2 \rangle$  and  $\delta\langle r^4 \rangle$  radial moment differences is presented in Sec. 5.3. Thereafter, Sec. 5.4 discusses the systematical (model) errors and statistical uncertainties that should be considered.

## 5.1 Isotope Shift

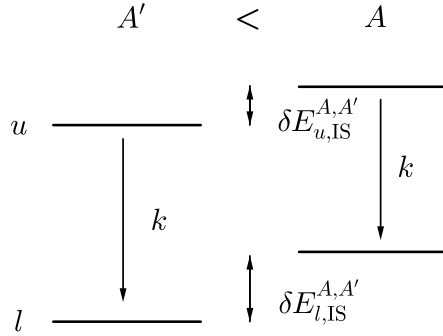
Given a transition  $k$ , the experimentally measurable line frequency IS, for a pair of isotopes  $A, A'$ , is given by

$$\delta\nu_{k,\text{IS}}^{A,A'} = \nu_k^A - \nu_k^{A'} = \frac{\delta E_{k,\text{IS}}^{A,A'}}{h} = \frac{\delta E_{u,\text{IS}}^{A,A'} - \delta E_{l,\text{IS}}^{A,A'}}{h}, \quad (5.2)$$

where  $\delta E_{u,\text{IS}}^{A,A'}$  and  $\delta E_{l,\text{IS}}^{A,A'}$  are, respectively, the shifts in the energies of the upper,  $u$ , and lower,  $l$ , levels taking part in the transition (see also Fig. 5.2). For a particular level, the IS is expressed as the sum of the MS and FS contributions. Accordingly, for a transition  $k$ , the line IS can be written as

$$\delta E_{k,\text{IS}}^{A,A'} = \delta E_{k,\text{MS}}^{A,A'} + \delta E_{k,\text{FS}}^{A,A'}. \quad (5.3)$$

Below, we describe how these two contributions are evaluated in atomic structure computations with the latest versions of GRASP [32, 34] and its extension code RIS 4 [111].



**Figure 5.2:** The upper  $u$  and lower  $l$  levels that are, respectively, associated with an atomic transition  $k$ , in the isotopes  $A$  and  $A'$  of an element. The shift in energy is different in magnitude for each of the upper,  $u$ , and lower,  $l$ , levels of the two isotopes, resulting in the observed IS for the transition  $k$ .

### 5.1.1 Mass shift

The Dirac-Coulomb Hamiltonian, presented earlier in Sec. 2.1, is based on the infinite (nuclear) mass approximation<sup>1</sup>. The finite nuclear mass  $M^A$ , of an isotope  $A$ , gives rise to a recoil effect, known as the mass shift (MS). The Hamiltonian accounting for the recoil motion of the nucleus, within the  $(\alpha Z)^4 m^2 / M^A$  approximation, as derived by Shabaev [130] and, in an independent way, by Palmer [131], is given by

$$\mathcal{H}_{\text{MS}}^A = \frac{1}{2M^A} \sum_{i,j}^N \left( \mathbf{p}_i \cdot \mathbf{p}_j - \frac{\alpha Z}{r_i} \left( \boldsymbol{\alpha}_i + \frac{(\boldsymbol{\alpha}_i \cdot \mathbf{r}_i) \mathbf{r}_i}{r_i^2} \right) \cdot \mathbf{p}_j \right). \quad (5.4)$$

After separating the one-body ( $i = j$ ) and two-body ( $i \neq j$ ) terms into the normal mass shift (NMS) and specific mass shift (SMS) contributions, respectively, the recoil Hamiltonian (5.4) splits into

$$\mathcal{H}_{\text{MS}}^A = \mathcal{H}_{\text{NMS}}^A + \mathcal{H}_{\text{SMS}}^A. \quad (5.5)$$

One may observe that each of the first terms in the operators  $\mathcal{H}_{\text{NMS}}^A$  and  $\mathcal{H}_{\text{SMS}}^A$  represents the NMS and SMS operators in the non-relativistic limit (see also Appx. B).

<sup>1</sup>This assumption relies on the fact that an atomic nucleus has a much larger mass than the electrons around it; the mass of nuclei range from  $1.672621777(74) \cdot 10^{-27}$  kg to about  $4.88 \cdot 10^{-25}$  kg for the heaviest nucleus known, while the electron's mass is  $9.10938291(40) \cdot 10^{-31}$  kg.

For a state specified by  $|\Gamma P J M\rangle$ , the (mass-independent) normal mass shift,  $K_{\Gamma J, \text{NMS}}$ , and specific mass shift,  $K_{\Gamma J, \text{SMS}}$ , parameters are, respectively, defined by

$$\frac{K_{\Gamma J, \text{NMS}}}{M^A} = \frac{1}{\sqrt{2J+1}} \langle \Gamma P J | \mathcal{H}_{\text{NMS}}^A | \Gamma P J \rangle \quad (5.6)$$

and

$$\frac{K_{\Gamma J, \text{SMS}}}{M^A} = \frac{1}{\sqrt{2J+1}} \langle \Gamma P J | \mathcal{H}_{\text{SMS}}^A | \Gamma P J \rangle, \quad (5.7)$$

where the expectation values of the NMS and SMS operators above are evaluated using the zero-order wave functions obtained according to Sec. 2.3.

Finally, the level MS between two isotopes  $A, A'$ , with masses  $M^A, M^{A'}$ , respectively, is given by

$$\delta E_{\Gamma J, \text{MS}}^{A, A'} = \left( \frac{1}{M^A} - \frac{1}{M^{A'}} \right) (K_{\Gamma J, \text{NMS}} + K_{\Gamma J, \text{SMS}}). \quad (5.8)$$

The corresponding line MS, for a transition  $k$ , can, then, be expressed as

$$\delta E_{k, \text{MS}}^{A, A'} = \left( \frac{1}{M^A} - \frac{1}{M^{A'}} \right) (\Delta K_{k, \text{NMS}} + \Delta K_{k, \text{SMS}}), \quad (5.9)$$

where  $\Delta K_{k, \text{NMS}}$  and  $\Delta K_{k, \text{SMS}}$  are the differences in the  $K_{\Gamma J, \text{NMS}}$  and  $K_{\Gamma J, \text{SMS}}$  parameters between the upper and lower states involved in the transition  $k$ .

### 5.1.2 Field shift

As also mentioned in Sec. 2.1, the nuclear potential of the Dirac-Coulomb Hamiltonian, implemented in GRASP, accounts for an extended nuclear charge density distribution. The FS effect is induced by the penetration of the electronic wave functions into the nuclear region (see also Fig. 5.1), and it is, consequently, more prominent for electrons moving in the  $s_{1/2}$  and  $p_{1/2}$  orbitals, which may have an appreciable electron density at the nucleus.

In atomic structure calculations using the infinite mass approximation, the level FS between two isotopes  $A, A'$  can be estimated by subtracting the level energies obtained from two separate calculations that use different sets of parameters describing the nuclear charge distributions of the two isotopes [132]. In the GRASP codes, the nuclear

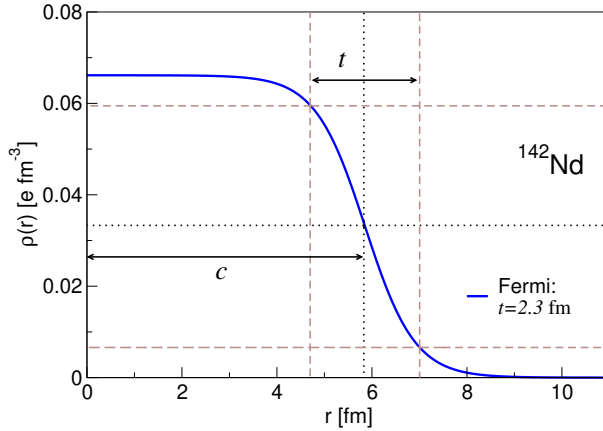
charge density distribution is approximated by the spherical two-parameter Fermi model

$$\rho(r) = \frac{\rho_0}{1 + e^{\frac{r-c}{a}}}, \quad (5.10)$$

where the normalization constant  $\rho_0$  can, e.g., be chosen so that

$$\int_0^\infty 4\pi r^2 \rho(r) dr = Z. \quad (5.11)$$

In the expression (5.10), the  $a$  parameter is related to the surface (skin) thickness  $t$  of the distribution by  $t = 4\ln(3)a$  [40]. The surface thickness, which defines the interval where the density decreases from 90% to 10% of  $\rho(0)$ , has a default value  $t = 2.3$  fm. The  $c$  parameter represents the half-density radius and is determined based on the value of  $a$  and the selected root-mean-square (rms) radius  $\sqrt{\langle r^2 \rangle}$ . A plot of the Fermi distribution, highlighting the  $t$  and  $c$  parameters, is shown in Fig. 5.3.



**Figure 5.3:** A spherical two-parameter Fermi nuclear charge density distribution for the neodymium (Nd) isotope with mass number  $A = 142$ . The Fermi distribution is determined by the surface thickness  $t$  and the half-density radius  $c$ , which is chosen so that it reproduces the rms radius  $\langle r^2 \rangle = 4.935$  fm, as predicted by microscopic nuclear structure calculations.

The Fermi model given by Eq. (5.10) can be generalized to also describe deformed nuclei. The half-radius  $c$  parameter is, then, replaced by

$$c(\theta) = c_0 \left( 1 + \sum_{l=2}^{\infty} \sum_{m=-l}^l \beta_{lm} Y_{lm}(\theta, \phi) \right), \quad (5.12)$$

where  $\beta_{lm}$  are the nuclear multipole deformation parameters, and  $Y_{lm}$  are the spherical harmonics. In many cases, only axially symmetric quadrupole nuclear deformation is considered, so that

$$c(\theta) = c_0 [1 + \beta_{20} Y_{20}(\theta)], \quad (5.13)$$

where  $c_0$  is adjusted to reproduce the selected  $\sqrt{\langle r^2 \rangle}$  value. The quadrupole deformation parameter  $\beta_{20}$  is related to the static nature (rigidity) of the nuclear deformation, contrary to the spectroscopic electric quadrupole moment  $Q$ , which probes the dynamic nature (softness) of the nuclear deformation and is separately obtained from HFS measurements. The nuclear parameters  $\beta_{20}$  and  $Q$  are, thus, complementary measures of deformation (see, e.g., [29]).

When several isotopes are considered, the above-mentioned “exact” calculations are cumbersome, computationally expensive, and, in general, the result of subtracting large numbers, which is likely to be unstable. Alternatively, we can use an approach based on perturbation theory. Within the framework of perturbation, the first-order level FS, for a state  $|\Gamma P J M\rangle$ , can be expressed as

$$\delta E_{\Gamma J, \text{FS}}^{(1)A, A'} = - \int_{R^3} \left( V_{\text{nuc}}^{A'}(\mathbf{r}) - V_{\text{nuc}}^A(\mathbf{r}) \right) \rho_{\Gamma J}^e(\mathbf{r}) d^3 \mathbf{r}, \quad (5.14)$$

where  $V_{\text{nuc}}^A(\mathbf{r})$  and  $V_{\text{nuc}}^{A'}(\mathbf{r})$  are the one-electron potentials arising from the different nuclear charge distributions of the two isotopes  $A$  and  $A'$ , and  $\rho_{\Gamma J}^e(\mathbf{r})$  is the level electron density distribution inside the nuclear volume of the reference isotope  $A$ . Averaging over the magnetic components  $M$ , the spherically symmetric electron density within the nucleus is evaluated as

$$\rho_{\Gamma J}^e(r) = \left\langle \Gamma P J \left| \left| \frac{\hat{\delta}(r)}{r^2} \right| \right| \Gamma P J \right\rangle, \quad (5.15)$$

where  $\hat{\delta}(r) = \sum_{i=1}^N \hat{\delta}(r - r_i)$ , with  $\hat{\delta}(r - r_i)$  probing the presence of the electron  $i$  at a particular distance  $r$  from the origin.

Assuming a finite nuclear charge distribution, the electron density within the nucleus can be expanded as an even polynomial function [124–126]. After keeping only the first few terms, the electron density around  $r = 0$  is given by

$$\rho_{\Gamma J}^e(\mathbf{r}) = \frac{\rho_{\Gamma J}^e(r)}{4\pi} \approx b_{\Gamma J}(r) = b_{\Gamma J,1} + b_{\Gamma J,2} r^2 + b_{\Gamma J,3} r^4 + b_{\Gamma J,4} r^6. \quad (5.16)$$



After inserting the expansion above in Eq. (5.14), we arrive at the expression for the reformulated (level) field shift (RFS) [III, 126], which is written as

$$\delta E_{\Gamma J, \text{FS}}^{(1)A, A'} \approx \delta E_{\Gamma J, \text{RFS}}^{(1)A, A'} = \sum_{n=1}^4 F_{\Gamma J, n} \delta \langle r^{2n} \rangle^{A, A'}, \quad (5.17)$$

where  $F_{\Gamma J, n}$  are the level electronic factors given by

$$F_{\Gamma J, n} = \frac{2\pi Z b_{\Gamma J, n}}{n(2n+1)}, \quad (5.18)$$

and

$$\delta \langle r^{2n} \rangle^{A, A'} = \langle r^{2n} \rangle^A - \langle r^{2n} \rangle^{A'} \quad (5.19)$$

are the differences in radial nuclear moments, of order  $2n$ , between the isotopes  $A$  and  $A'$ . These moments can be taken from any nuclear model, calculation, or experiment.

The computations of the electronic factors  $F_{\Gamma J, n}$ , together with the MS parameters  $K_{\Gamma J, \text{NMS}}$  and  $K_{\Gamma J, \text{SMS}}$ , are performed with the Ris 4 code [III]. In Ris 4, the polynomial expansion  $b_{\Gamma J}(r)$  is, for each level, fitted to the constructed electron density  $\rho_{\Gamma J}^e(r)$  using a least-squares method.

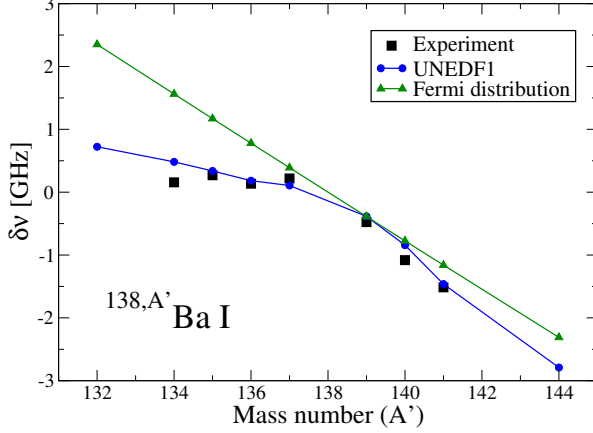
The corresponding line FS, for a transition  $k$ , can, then, be expressed as

$$\delta E_{k, \text{FS}}^{A, A'} = \sum_{n=1}^4 \frac{2\pi Z \Delta b_{k, n}}{n(2n+1)} \delta \langle r^{2n} \rangle^{A, A'}, \quad (5.20)$$

where  $\Delta b_{k, n}$  are the differences in the coefficients  $b_{\Gamma J, n}$  between the upper and lower states.

## 5.2 Realistic Nuclear Charge Distributions

In Sec. III.B of Paper VII, calculated FS values in Ba I ( $Z = 56$ ) are compared with experimental IS data [133], from which the theoretical MS contributions were subtracted [134]. To calculate the FSs according to Eq. (5.20), we used nuclear radial moments that resulted from: (i) the Fermi model given by (5.10) and (ii) the realistic nuclear charge distributions obtained from DFT calculations [135]. The comparison shows that the calculations based on the Fermi distribution fail to capture the general behavior of the observed FSs. On the other hand, the microscopic nuclear calculations capture both the right trend with neutron number and, in addition, some of the odd-even staggering (see also Fig. 5.4).



**Figure 5.4:** Figure 3 from Paper VII. The predicted absolute FS values are compared to the available experimental data [133]. The computed FSs are based on nuclear radial moments, which have resulted (1) from nuclear DFT calculations (UNEDF1) and (2) from the Fermi distribution.

The Fermi model was used with the rms radii given by

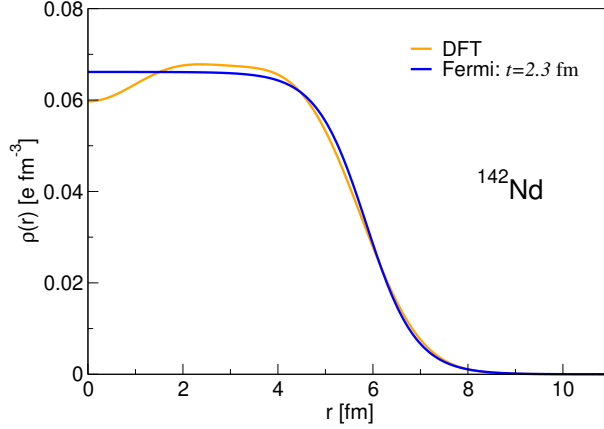
$$\sqrt{\langle r^2 \rangle} = 0.836 \cdot A^{\frac{1}{3}} + 0.570 \text{ fm} \quad (A > 9), \quad (5.21)$$

where  $A$  denotes the mass number of the isotope. The major correction to the descriptions of the observed FS values is clearly provided by the use of realistic rms radii. However, by also making use of realistic higher-order radial moments, the predicted FSs are further improved. In Fig. 5.5, the Fermi and realistic nuclear charge distributions are, for instance, compared for the system of neodymium ( $Z = 60$ ). The Fermi distribution, shown in the figure, is tuned so that it has the same  $\langle r^2 \rangle$  radial moment as the more realistic charge distribution denoted as “DFT”. Nonetheless, the density profiles differ to some extent. The Fermi model, with fixed skin thickness  $t = 2.3$  fm, does not properly describe the density wiggles and diffuseness of the distribution. These features are encoded in higher-order radial moments.

In Sec. IV of Paper VII, we further investigate the magnitude of the corrections when realistic higher-order radial moments are used, in Eq. (5.17), to predict the FS. This was done by evaluating the so-called *correction term*, which is defined as

$$\delta\nu_{\text{realistic}}^{A,A'} - \delta\nu_{\text{Fermi}}^{A,A'} = \sum_{n=2}^4 F_{k,n} [\delta \langle r^{2n} \rangle_{\text{realistic}}^{A,A'} - \delta \langle r^{2n} \rangle_{\text{Fermi}}^{A,A'}]. \quad (5.22)$$

The magnitude of (5.22) was estimated for a wide range of isotopes in Li-like systems and in Ba I. For isotope pairs  $A, A'$  of a specific element, the absolute value of (5.22)



**Figure 5.5:** Comparison between the nuclear charge density distributions resulting from the Fermi model (blue) and the DFT calculations (orange) in the spherical neodymium (Nd) with mass number  $A = 142$ . The Fermi model has a fixed skin thickness  $t = 2.3$  fm and is fitted to reproduce the  $\langle r^2 \rangle$  moment provided by the realistic DFT calculations. Discrepancies in the specifics of the distributions are observed. (Image credits: [110].)

typically grows with the difference between the neutron number  $\Delta N^{A,A'}$ . When more neutrons are added (or removed), they alter the protons' distribution, leading to changes in the diffuseness. As also seen in Fig. 5.5, this effect is not sufficiently captured by the Fermi model. In deformed nuclei, the corrections further depend on the quadrupole deformation parameter  $\beta_{20}$ , which is assumed to be zero in the Fermi model given by (5.10). The corrections increase when the difference in deformation between the reference and the target isotope gets larger. The same trends are observed in Ba I. When, instead, the axially symmetric deformed Fermi model is used, the correction term appears to be smaller.

Besides the IS measurements in Ba I, experimental ISs are also available for the first two resonance transitions in the  $^{142,150}\text{Nd}^{57+}$  isotope pair [136]. In highly-charged systems, the MS contribution is generally much smaller, and the uncertainties in the observed FS values are most often restricted to the experimental uncertainties. That being so, the uncertainties of the observed ISs in  $^{142,150}\text{Nd}^{57+}$  are compared with the estimated correction terms resulting from the use of realistic higher than second-order radial moments (see Fig. 6 in Paper VII). It is deduced that effects, such as deformation, which are captured by these nuclear radial moments, could be detected. In the next two sections, the developed method for possible simultaneous extraction of the  $\delta\langle r^2 \rangle$  and  $\delta\langle r^4 \rangle$  radial moment differences from IS measurements is outlined.

### 5.3 Simultaneous Extraction of $\delta\langle r^2 \rangle$ and $\delta\langle r^4 \rangle$

The RFS expression given by Eq. (5.20), combined with experimental IS data, in principle, enables the extraction of differences in higher-order radial moments. Given measurements for at least four transitions, a system of four equations can be solved, i.e.,

$$\delta\nu_{k,\text{RFS}} = F_{k,1}\delta\langle r^2 \rangle + F_{k,2}\delta\langle r^4 \rangle + F_{k,3}\delta\langle r^6 \rangle + F_{k,4}\delta\langle r^8 \rangle, \quad (5.23)$$

where  $k = 1, 2, 3, 4$ . However, it is rare that observed ISs are available for four transitions in the same pair of isotopes, and such systems of equations cannot be formed so that they give trustworthy solutions for higher than second-order moments.

The expansion (5.23) is truncated, and the set of  $r^{2n}$ , where  $n = 1, 2, 3, 4$ , does not form an orthonormal basis. By instead expanding in a set of orthogonal polynomials  $y_n$ , the RFS expression is written as

$$\delta\nu_{k,\text{RFS}} = c_{k,1}\delta\langle y_1 \rangle + c_{k,2}\delta\langle y_2 \rangle + c_{k,3}\delta\langle y_3 \rangle + c_{k,4}\delta\langle y_4 \rangle, \quad (5.24)$$

where the new expansion coefficients  $c_{k,n}$  are expressed in relation to the electronic factors  $F_{k,n}$  and the functions  $y_n$  are given in terms of the  $r^{2n}$  moments (see also Appendix in Paper VII). The expansion (5.24) converges substantially faster than the original summation (5.23). In fact, simply the  $\delta\langle y_1 \rangle$  and  $\delta\langle y_2 \rangle$ , which are given in terms of the  $\delta\langle r^2 \rangle$  and  $\delta\langle r^4 \rangle$ , need to be considered when the sum is rearranged. Then, for a pair of isotopes  $A, A'$  and a transition  $k$ , the RFS can, to a very good approximation, be expressed as

$$\delta\nu_{k,\text{RFS}} \approx c_{k,1}\delta\langle y_1 \rangle + c_{k,2}\delta\langle y_2 \rangle. \quad (5.25)$$

From knowledge of observed ISs for at least two transitions, a system of two equations is then solved for the unknowns  $\delta\langle y_1 \rangle$  and  $\delta\langle y_2 \rangle$ , from which the  $\delta\langle r^2 \rangle$  and  $\delta\langle r^4 \rangle$  values are determined. It is demonstrated in Paper VII that the expression (5.25) enables the determination of the differences in the  $\langle r^2 \rangle$  and  $\langle r^4 \rangle$  moments much more accurately than when the first two terms of the original expression (5.23) are considered. Yet, there are still systematical and statistical errors that must be taken into account, and their nature will be discussed next.

## 5.4 Errors in the Extraction of $\delta\langle r^2 \rangle$ and $\delta\langle r^4 \rangle$

### 5.4.1 Systematical errors

From observed ISs, experimental FS values can be obtained by estimating and subtracting the MS contributions and residual effects,  $\delta\nu_{k,\text{RES}}$ , so that

$$\delta\nu_{k,\text{FS}}^{\text{expt}} = \delta\nu_{k,\text{IS}}^{\text{expt}} - \delta\nu_{k,\text{MS}} - \delta\nu_{k,\text{RES}}. \quad (5.26)$$

The residual effects are related to QED corrections, as well as model errors induced by the perturbation treatment that led to the RFS expression<sup>2</sup>. They can be represented by the discrepancy between the “exact” variational solution  $\delta\nu_{k,\text{VA}}^{\text{exact}}$  and the RFS solution  $\delta\nu_{k,\text{RFS}}$ . Making a *qualified guess* for the unknown rms radii of the target (and perhaps also the reference) isotope, and assuming a spherical Fermi distribution that yields the higher-order moments for both isotopes, this discrepancy can be evaluated. A qualified guess of rms radii is provided by, e.g., the parametrization of Eq. (5.21). In heavy nuclei, the QED effects become significant and it is, thus, crucial to precisely determine the  $\delta\nu_{k,\text{RES}}$  term in these systems. In Sec. V.B of Paper VII, the contributions from QED effects were, indicatively, investigated for two different isotope pairs in uranium ( $Z=92$ ), and they were found to be of the order of 1.5%.

### 5.4.2 Statistical errors

The  $\delta\langle r^2 \rangle$  and  $\delta\langle r^4 \rangle$  moments are determined based on the  $\delta\langle y_1 \rangle$  and  $\delta\langle y_2 \rangle$  values, which are extracted by solving the matrix equation

$$\begin{bmatrix} \delta\nu_{1,\text{RFS}} \\ \delta\nu_{2,\text{RFS}} \end{bmatrix} = C \begin{bmatrix} \delta\langle y_1 \rangle \\ \delta\langle y_2 \rangle \end{bmatrix}. \quad (5.27)$$

where

$$C = \begin{bmatrix} c_{1,1} & c_{1,2} \\ c_{2,1} & c_{2,2} \end{bmatrix} \quad (5.28)$$

is the matrix containing the expansion coefficients of the equations that are formed based on Eq. (5.25). The unknown  $\delta\langle y_1 \rangle$  and  $\delta\langle y_2 \rangle$  are, thus, evaluated according to

$$\begin{bmatrix} \delta\langle y_1 \rangle \\ \delta\langle y_2 \rangle \end{bmatrix} = C^{-1} \begin{bmatrix} \delta\nu_{1,\text{RFS}} \\ \delta\nu_{2,\text{RFS}} \end{bmatrix}. \quad (5.29)$$

---

<sup>2</sup>It should be mentioned that contributions from nuclear polarization effects, which can often be an important source of systematical errors, have been neglected in the work of Paper VII.

To obtain the  $\delta \langle y_1 \rangle$  and  $\delta \langle y_2 \rangle$  values, the matrix  $C$  must be invertible. If the matrix determinant is zero, then the matrix is singular and cannot be inverted. Occasionally, the determinant of the matrix can approach zero, but still be non-zero. In this case, the matrix is close to singular and the extracted  $\delta \langle y_1 \rangle$  and  $\delta \langle y_2 \rangle$  will be hugely affected, even by a small change in the field shifts  $\delta\nu_{1,\text{RFS}}$  and  $\delta\nu_{2,\text{RFS}}$ . This means that the values of  $\delta \langle y_1 \rangle$  and  $\delta \langle y_2 \rangle$  and, in turn, the  $\delta \langle r^2 \rangle$  and  $\delta \langle r^4 \rangle$  moments, might be greatly affected by the uncertainties in the observed ISs, the computed MS contributions, and the evaluated residual effects represented by Eq. (5.26).

A matrix determinant equal to zero is obtained if the two equations are linearly dependent. To minimize the statistical errors when solving Eq. (5.29), the set of electronic factors  $F_{k,n}$ —which affect the values of the coefficients  $c_{k,n}$ —for the two transitions must be as linearly independent as possible.

## Chapter 6

# Outlook

The continuous advances in astronomical instrumentation constantly raise the demands on atomic transition data, which must now also cover the near-infrared wavelength region. In the long wavelength regime, lines of atoms are produced by transitions between states lying close in energy, which often correspond to transitions between highly excited states. In the latter instance, large-scale spectrum calculations of transition parameters must be carried out, which become all the more challenging when the targeted spectra include Rydberg series. In Paper I, it was demonstrated that by paying special attention to the construction of the radial orbital basis that builds the atomic state functions, reliable transition data can be obtained, including the transitions that involve high Rydberg states that were proven to be problematic.

Drawing on the detailed investigations of Paper I, specialized orbital optimization strategies were applied in Paper II to produce accurate and extended data of transition rates, weighted oscillator strengths, and lifetimes, for the C I-IV ions. By paying special attention to the applied orbital optimization strategies, a large amount of updated data, of the same aforementioned transition parameters, was also produced for the systems of Al I-II, and they are contained in Paper III. However, recent investigations have shown that the accuracy of the computed transition data in Al I-II can further be improved. Additionally, Paper IV contains extended data of Landé  $g$ -factors for several atoms and ions of astrophysical interest, including C I-IV and Al I-II.

As we move away from the valley of stability, data of nuclear structure properties are, generally, scarce. By combining high-resolution measurements of hyperfine structure splittings, or isotope shifts, with *ab initio* calculations of the electronic parts of these interactions, nuclear observables can be extracted for long isotopic sequences, which include radioactive systems. In Paper V, collinear laser spectroscopy measurements of

the hyperfine structure in neutral tin were combined with the computed electronic factors to extract the nuclear electric quadrupole moments,  $Q$ , of odd-mass tin isotopes in the range  $A = 117 - 131$ . To be in a position to determine the final value of the electronic part of the electric quadrupole hyperfine interaction and estimate the associated theoretical uncertainty, four separate *ab initio* calculations were carried out. The four different applied computational methodologies are described in Paper VI.

In Paper VII, a promising method for the extraction of both  $\delta\langle r^2 \rangle$  and  $\delta\langle r^4 \rangle$  radial moment differences, from measurements of isotope shifts, was presented and tested. Considering both systematical and statistical errors for isotope pairs in different lithium-like systems, it was deduced that an increase in experimental precision by 1–2 orders of magnitude, or/and access to data for more independent transitions is essential. From the theoretical side, effort to accurately compute the mass shift contributions, mainly in neutral and near-neutral systems, must be made. A combined theoretical and experimental progress would allow possible tabulation of changes in the  $\langle r^4 \rangle$  nuclear moments. It was recently shown that the  $\langle r^4 \rangle$  moment is directly related to the surface thickness of the nuclear charge density distribution, and thus, prediction of  $\langle r^4 \rangle$  values would allow more realistic estimates of nuclear structure corrections for the interpretation of new physics quests [127].



# Appendices



## Appendix A

# Non-relativistic Electric Dipole Transition Operators

In C I-IV, and also Al I-II, the relativistic effects are expected to be small, justifying an examination of the reduced matrix elements of the electric dipole (E1) transition operator within the non-relativistic framework. In the non-relativistic limit, the reduced matrix elements of the E1 operator are, in the length and velocity forms, respectively, expressed as

$$\langle \Gamma P J || \sum_{i=1}^N r_i \mathbf{C}^{(1)}(\theta_i, \phi_i) || \Gamma' P' J' \rangle \quad (\text{A.1})$$

and

$$\frac{1}{E_{\Gamma' J'} - E_{\Gamma J}} \langle \Gamma P J || \sum_{i=1}^N \nabla_i^{(1)} || \Gamma' P' J' \rangle, \quad (\text{A.2})$$

where  $\mathbf{C}^{(1)}$  is the renormalized spherical harmonic of rank 1,  $\nabla_i^{(1)}$  is the gradient tensor operator of rank 1, and  $E_{\Gamma' J'} - E_{\Gamma J}$  is the energy of the transition [137]. Each of the reduced matrix elements (A.1) and (A.2) involves sums over radial transition integrals of the kind

$$\int_0^\infty P(r) r P'(r) dr \quad (\text{A.3})$$

and

$$\int_0^\infty P(r) \frac{d}{dr} P'(r) dr, \quad (\text{A.4})$$

weighted with the products of the mixing coefficients of the CSFs (see Eq. (2.59)) and the angular coefficients [49, 50, 137]. In the integrals (A.3) and (A.4),  $P'(r)$  and  $P(r)$

are the radial functions of the large components of the Dirac orbitals (2.29), which, respectively, build the CSFs of the upper state  $|\Gamma' P' J'\rangle$  and the lower state  $|\Gamma P J\rangle$ . In the computation of the integrals (A.3), the emphasis is, evidently, given to the outer part of the radial orbitals. On the other hand, when computing the integrals (A.4), the emphasis is given to the inner part of the orbitals.

In the simple Hartree–Fock model, the approximate wave functions usually display a correct asymptotic behavior towards large  $r$  (see also Sec. 5 of Paper 1), and since the integrals (A.3) are also computationally simpler, the computed transition data are traditionally provided in the length form [p. 401–2; 51, 138–140]. It was, however, shown in Paper 1 that, when multiconfiguration methods concurrently target multiple atomic states, all wave functions are not always well approximated at large  $r$ , and the velocity form may, by contrast, give the most accurate results.

## Appendix B

# Non-relativistic Mass Shift

For an infinitely heavy, i.e.,  $M^A \rightarrow \infty$ , point charge nucleus, the zero-order non-relativistic (NR) many-electron Hamiltonian is given by

$$\mathcal{H}_\infty^{\text{NR}} = \sum_{i=1}^N \left( \frac{\mathbf{p}_i^2}{2m_e} - \frac{Z}{r_i} \right) + \sum_{i<j}^N \frac{1}{r_{ij}}, \quad (\text{B.1})$$

where the first term,

$$T_\infty = \sum_{i=1}^N \frac{\mathbf{p}_i^2}{2m_e}, \quad (\text{B.2})$$

simply is the kinetic energy of the  $N$ -electron atomic system<sup>1</sup>.

For a finite nuclear mass  $M^A$ , of an isotope  $A$ , the kinetic energy of the nucleus must be considered, and the total kinetic energy of the atomic system,  $T$ , in an arbitrary coordinate system, becomes

$$T = T_\infty + T_{MA} = \frac{1}{2m_e} \sum_{i=1}^N \mathbf{p}_i^2 + \frac{1}{2M^A} \mathbf{p}_{MA}^2. \quad (\text{B.3})$$

We want to transform to the *center-of-mass* ( $cm$ ) coordinate system, where the observer is at rest. From the momentum conservation law, in the  $cm$ -system, we get

$$\mathbf{p}_{MA}^{cm} = - \sum_{i=1}^N \mathbf{p}_i^{cm}. \quad (\text{B.4})$$

---

<sup>1</sup>In atomic units,  $m_e = 1$ , but it is explicitly included here to avoid any misunderstandings.

By inserting (B.4) into (B.3), the total kinetic energy,  $T^{cm}$ , in the  $cm$ -system becomes

$$\begin{aligned}
T^{cm} &= \frac{1}{2m_e} \sum_{i=1}^N (\mathbf{p}_i^{cm})^2 + \frac{1}{2M^A} \left( - \sum_{i=1}^N \mathbf{p}_i^{cm} \right)^2 \\
&= \frac{1}{2m_e} \sum_{i=1}^N (\mathbf{p}_i^{cm})^2 + \frac{1}{2M^A} \sum_{i=1}^N (\mathbf{p}_i^{cm})^2 + \frac{1}{2M^A} \sum_{i \neq j}^N \mathbf{p}_i^{cm} \cdot \mathbf{p}_j^{cm} \\
&= T_\infty^{cm} + \frac{1}{2M^A} \sum_{i=1}^N (\mathbf{p}_i^{cm})^2 + \frac{1}{2M^A} \sum_{i \neq j}^N \mathbf{p}_i^{cm} \cdot \mathbf{p}_j^{cm}. \tag{B.5}
\end{aligned}$$

The non-relativistic perturbation Hamiltonian, describing the mass shift (MS) when the finite nuclear mass  $M^A$  is taken into account, corresponds to the nuclear recoil energy, which, in the  $cm$ -system<sup>2</sup>, is given by

$$\mathcal{H}_{\text{MS}}^{\text{NR}} = \Delta T^{cm} = T^{cm} - T_\infty^{cm} = \frac{1}{2M^A} \sum_{i=1}^N \mathbf{p}_i^2 + \frac{1}{2M^A} \sum_{i \neq j}^N \mathbf{p}_i \cdot \mathbf{p}_j. \tag{B.6}$$

Hughes and Eckart [I41] suggested the division of the recoil Hamiltonian (B.6) into the normal mass shift (NMS) and specific mass shift (SMS) contributions, so that

$$\mathcal{H}_{\text{NMS}}^{\text{NR}} = \frac{1}{2M^A} \sum_{i=1}^N \mathbf{p}_i^2 \tag{B.7}$$

and

$$\mathcal{H}_{\text{SMS}}^{\text{NR}} = \frac{1}{2M^A} \sum_{i \neq j}^N \mathbf{p}_i \cdot \mathbf{p}_j. \tag{B.8}$$

The operators (B.7) and (B.8) resemble the leading-order terms of the relativistic NMS and SMS operators, discussed in Sec. 5.1.1. Evaluating the expectation values of the non-relativistic recoil operators with relativistic (zero-order) wave functions would, however, overestimate the relativistic corrections to the MS effect [I42]. When one works in the relativistic scheme, it is important to use the complete form of the operator (5.4).

---

<sup>2</sup>In the following, working in the  $cm$  coordinate system is implied and thus, the “ $cm$ ” superscripts in the electron momentum operators are omitted for brevity.

# References

- [1] Gilore G. and Wyse R. The chemical evolution of the galaxy. *Nature*, 322: 806–807, 1986. <https://doi.org/10.1038/322806a0>.
- [2] Gray D. *The Observation and Analysis of Stellar Photospheres*. Cambridge: Cambridge University Press, 2005.
- [3] Jabran Z. H., Geller M. J., Kewley L. J., Hwang H. S., Fabricant D. G., and Kurtz M. J. The chemical evolution of star-forming galaxies over the last 11 billion years. *Astrophys. J.*, 771(2):L19, 2013. <https://doi.org/10.1088/2041-8205/771/2/L19>.
- [4] Gerner T., Beuther H., Semenov D., Linz H., Vasyunina T., Bihr S., Shirley Y. L., and Henning Th. Chemical evolution in the early phases of massive star formation. I. *A&A*, 563:A97, 2014. <https://doi.org/10.1051/0004-6361/201322541>.
- [5] Thorsbro B. *Clues to galaxy evolution from spectroscopic observations of Galactic centre stars*. PhD Thesis, Lund: MediaTryck Lund, 2020. <https://lup.lub.lu.se/search/ws/files/82853814/ThorsbroThesisFinal.pdf>.
- [6] Henrik Jönsson. Personal communication on March 16, 2021.
- [7] Ekman J., Jönsson P., Gustafsson S., Hartman H., Gaigalas G., Godefroid M. R., and Froese Fischer C. Calculations with spectroscopic accuracy: energies, transition rates, and Landé  $g_j$ -factors in the carbon isoelectronic sequence from Ar XIII to Zn XXV. *A&A*, 564:A24, 2014. <https://doi.org/10.1051/0004-6361/201323163>.
- [8] Wang K., Song C. X., Jönsson P., et al. Benchmarking Atomic Data from Large-scale Multiconfiguration Dirac–Hartree–Fock Calculations for Astrophysics: S-like Ions from Cr IX to Cu XIV. *Astrophys. J. Suppl. S.*, 239(2):30, 2018. <https://doi.org/10.3847/1538-4365/aaedba>.

- [9] Osten R. A., Kowalski A., Drake S. A., et al. A very bright, very hot, and very long flaring event from the M dwarf binary system DG CVn. *Astrophys. J.*, 832(2):174, 2016. <https://iopscience.iop.org/article/10.3847/0004-637X/832/2/174>.
- [10] Si R., Brage T., Li W., Grumer J., Li M., and Hutton R. A First Spectroscopic Measurement of the Magnetic-field Strength for an Active Region of the Solar Corona. *Astrophys. J.*, 898(2):L34, 2020. <https://doi.org/10.3847/2041-8213/ab18c>.
- [11] Oskinova L., Nazé Y., Todt H., Huenemoerder D. P., Ignace R., Hubrig S., and Hamann W.-R. Discovery of X-ray pulsations from a massive star. *Nat. Commun.*, 5(1):4024, 2014. <https://doi.org/10.1038/ncomms5024>.
- [12] Yadav R. K., Gastine T., Christensen U. R., and Reiners A. Formation of starspots in self-consistent global dynamo models: Polar spots on cool stars. *A&A*, 573:A68, 2015. <https://doi.org/10.1051/0004-6361/201424589>.
- [13] Oudmajer R. and Harries T. Spectropolarimetry: probing the third dimension. *A&G*, 49(4):4.30–4.34, 2008. <https://doi.org/10.1111/j.1468-4004.2008.49430.x>.
- [14] Froese Fischer C. and Jönsson P. Landé  $g$  factors for  $2p^4$  ( $^3P$ ) $3p$  and  $2p^4$ ( $^3P$ ) $3d$  states of Ne II. *J. Mol. Struct. THEOCHEM*, 537(1):55–62, 2001. <https://www.sciencedirect.com/science/article/pii/S016612800004607>.
- [15] Schiffmann S. and Godefroid M. Electronic isotope shift factors for the Ir  $5d^7 6s^2$   $^4F_{9/2} \rightarrow$  (odd,  $J = 9/2$ ) line at 247.587 nm. *J. Quant. Spectrosc. Radiat. Transfer*, 258:107332, 2021. <https://www.sciencedirect.com/science/article/pii/S002240732030697X>.
- [16] Federman S. R., Lambert D. L., Cardelli J. A., and Sheffer Y. The boron isotope ratio in the interstellar medium. *Nature*, 381(6585):764–766, 1996. <http://dx.doi.org/10.1038/381764a0>.
- [17] Leckrone D. S., Proffitt C. R., Wahlgren G. M., Johansson S. G., and Brage T. Very High Resolution Ultraviolet Spectroscopy of a Chemically Peculiar Star: Results of the  $\chi$  Lupi Pathfinder Project. *Astron. J.*, 117(3):1454–1470, 1999. <https://doi.org/10.1086/300776>.
- [18] Proffitt C. R., Jönsson P., Litzén U., Pickering J. C., and Wahlgren G. M. Goddard high-resolution spectrograph observations of the B III resonance doublet in early B stars: abundances and isotope ratios. *Astrophys. J.*, 516:342–348, 1999. <https://doi.org/10.1086/307095>.
- [19] Hawkins I. and Jura M. The  $^{12}\text{C}/^{13}\text{C}$  isotope ratio of the interstellar medium in the neighborhood of the Sun. *Astrophys. J.*, 317:926–950, 1987. <http://dx.doi.org/10.1086/165342>.



- [20] Lundqvist M., Wahlgren G. M., and Hill V. Isotope structure of Sm II as an indicator of  $r$ - vs.  $s$ -process nucleosynthesis. *A&A*, 463:693–702, 2007. <https://doi.org/10.1051/0004-6361:20066231>.
- [21] Cayrel R., Steffen M., Chand H., Bonifacio P., Spite M., Spite F., Petitjean P., Ludwig H.-G., and Caffau E. Line shift, line asymmetry, and the  ${}^6\text{Li}/{}^7\text{Li}$  isotopic ratio determination. *A&A*, 473(3):L37–L40, 2007. <https://doi.org/10.1051/0004-6361:20078342>.
- [22] Kurucz R. L. Atomic data for interpreting stellar spectra: isotopic and hyperfine data. *Phys. Scr.*, T47:110, 1993. <https://doi.org/10.1088/0031-8949/1993/T47/017>.
- [23] Nielsen K., Karlsson H., and Wahlgren G. M. Analysis of the hyperfine and isotopic structure of Ga II in the optical spectrum of  $\kappa$  Cnc and HR 7775. *A&A*, 363:815–820, 2000. <http://adsabs.harvard.edu/full/2000A%26A...363..815N>.
- [24] Brage T., Judge P. G., Aboussaid A., Godefroid M. R., Jönsson P., Ynnerman A., Froese Fischer C., and Leckrone D. S. Hyperfine Induced Transitions as Diagnostics of Isotopic Composition and Densities of Low-Density Plasmas. *Astrophys. J.*, 500(1):507–521, 1998. <https://doi.org/10.1086/305690>.
- [25] Brage T., Judge P. G., and Proffitt C. R. Determination of Hyperfine-Induced Transition Rates from Observations of a Planetary Nebula. *Phys. Rev. Lett.*, 89: 281101, 2002. <https://link.aps.org/doi/10.1103/PhysRevLett.89.281101>.
- [26] Thorsbro B. *The Near-Infrared as a Spectral Hunting Ground*. Master Thesis, Lund University, 2016. <http://lup.lub.lu.se/student-papers/record/8890122>.
- [27] Borge M. J. G. Recent Highlights of the ISOLDE Facility. *J. Phys. Conf. Ser.*, 580:012049, 2015. <https://doi.org/10.1088/1742-6596/580/1/012049>.
- [28] Brandau C., Lestinsky M., Kozhuharov C., Müller A., Schippers S., and Stöhler Th. High-resolution dielectronic recombination experiments at the upcoming CRYRING@ESR facility. *J. Phys. Conf. Ser.*, 635(2):022084, 2015. <https://doi.org/10.1088/1742-6596/635/2/022084>.
- [29] Campbell P., Moore I. D., and Pearson M. R. Laser spectroscopy for nuclear structure physics. *Prog. Part. Nuc. Phys.*, 86:127–180, 2016. <https://www.sciencedirect.com/science/article/pii/S0146641015000915>.
- [30] Neugart R., Billowes J., Bissell M. L., Blaum K., Cheal B., Flanagan K. T., Neyens G., Nörtershäuser W., and Yordanov D. T. Collinear laser spectroscopy at ISOLDE: new methods and highlights. *J. Phys. G: Nucl. Partic. Phys.*, 44: 064002, 2017. <https://doi.org/10.1088/1361-6471/aa6642>.

- [31] Kozlov M. G., Porsev S. G., Safronova M. S., and Tupitsyn I. I. CI-MBPT: A package of programs for relativistic atomic calculations based on a method combining configuration interaction and many-body perturbation theory. *Comput. Phys. Commun.*, 195:199–213, 2015. <https://www.sciencedirect.com/science/article/pii/S001046551500185X>.
- [32] Froese Fischer C., Gaigalas G., Jönsson P., and Bieroń J. GRASP2018-A Fortran 95 version of the General Relativistic Atomic Structure Package. *Comput. Phys. Commun.*, 237:184–187, 2019. <https://doi.org/10.1016/j.cpc.2018.10.032>.
- [33] Kahl E. V. and Berengut J. C. AMBIT: A programme for high-precision relativistic atomic structure calculations. *Comput. Phys. Commun.*, 238:232–243, 2019. <https://www.sciencedirect.com/science/article/pii/S0010465518304302>.
- [34] Jönsson P., Gaigalas G., Bieroń J., Froese Fischer C., and Grant I. P. New version: GRASP2K relativistic atomic structure package. *Comput. Phys. Commun.*, 184:2197–2203, 2013. <https://doi.org/10.1016/j.cpc.2013.02.016>.
- [35] Grant I. P. *Relativistic Quantum Theory of Atoms and Molecules: Theory and Computation (Springer Series on Atomic, Optical, and Plasma Physics)*. Springer, New York, USA, 2007.
- [36] Papoulia A. *Computational Atomic Structure: Applications to Astrophysics and Nuclear Structure*. Licentiate Thesis, Lund: MediaTryck Lund, 2020. <https://lup.lub.lu.se/record/558a42e2-3233-4e7e-bd71-437cd3efe310>.
- [37] Johnson W. R. *Atomic Structure Theory: Lectures on Atomic Physics*. Springer Verlag, Berlin, Heidelberg, Springer-Verlag edition, 2007.
- [38] Dyall K. G., Grant I. P., Johnson C. T., Parpia F. A., and Plummer E. P. GRASP: A general-purpose relativistic atomic structure program. *Comput. Phys. Commun.*, 55(3):425–456, 1989. [https://doi.org/10.1016/0010-4655\(89\)90136-7](https://doi.org/10.1016/0010-4655(89)90136-7).
- [39] Froese Fischer C., Godefroid M., Brage T., Jönsson P., and Gaigalas G. Advanced multiconfiguration methods for complex atoms: I. energies and wave functions. *J. Phys. B: At. Mol. Opt. Phys.*, 49(18):182004, 2016. <http://stacks.iop.org/0953-4075/49/i=18/a=182004>.
- [40] Parpia F. A. and Mohanty A. K. Relativistic basis-set calculations for atoms with Fermi nuclei. *Phys. Rev. A*, 46(7):3735, 1992. <https://link.aps.org/doi/10.1103/PhysRevA.46.3735>.
- [41] Feynman R. P. *QED: The Strange Theory of Light and Matter*. Princeton University Press, 1985.

- [42] Grant I. P., McKenzie B. J., Norrington P. H., Mayers D. F., and Pyper N. C. An atomic multiconfiguration Dirac-Fock package. *Comput. Phys. Commun.*, 21(2):207–231, 1980. [https://doi.org/10.1016/0010-4655\(80\)90041-7](https://doi.org/10.1016/0010-4655(80)90041-7).
- [43] Mann J. B. and Johnson W. R. Breit Interaction in Multielectron Atoms. *Phys. Rev. A*, 4:41–51, 1971. <https://link.aps.org/doi/10.1103/PhysRevA.4.41>.
- [44] Löwdin P. Quantum Theory of Many-Particle Systems. III. Extension of the Hartree-Fock Scheme to Include Degenerate Systems and Correlation Effects. *Phys. Rev.*, 97:1509–1520, 1955. <https://link.aps.org/doi/10.1103/PhysRev.97.1509>.
- [45] Gaigalas G., Froese Fischer C., Rynkun P., and Jönsson P. JJ2LSJ Transformation and Unique Labeling for Energy Levels. *Atoms*, 5(1):6, 2017. <https://www.mdpi.com/2218-2004/5/1/6>.
- [46] Kemble E. C. *The Fundamental Principles of Quantum Mechanics*. Dover Publications, Inc., New York, USA, 1958.
- [47] Nesbet R. *Variational Principles and Methods in Theoretical Physics and Chemistry*. Cambridge University Press, Cambridge, UK, 2004.
- [48] Hartree D. *The Calculation of Atomic Structures*. Wiley, New York, USA, 1957.
- [49] Gaigalas G., Rudzikas Z., and Froese Fischer C. An efficient approach for spin-angular integrations in atomic structure calculations. *J. Phys. B: At. Mol. Opt. Phys.*, 30(17):3747–3771, 1997. <https://doi.org/10.1088/0953-4075/30/17/006>.
- [50] Gaigalas G., Fritzsche S., and Grant I. P. Program to calculate pure angular momentum coefficients in jj-coupling. *Comput. Phys. Commun.*, 139:263–278, 2001. [https://doi.org/10.1016/S0010-4655\(01\)00213-2](https://doi.org/10.1016/S0010-4655(01)00213-2).
- [51] Cowan R. D. *The Theory of Atomic Structure and Spectra*. Los Alamos Series in Basic and Applied Sciences, University California Press, USA, 1981.
- [52] Froese Fischer C., Brage T., and Jönsson P. *Computational atomic structure: An MCHF approach*. Institute of Physics Publishing, Bristol and Philadelphia, 1997.
- [53] Tew D. P., Klopper W., and Helgaker T. Electron correlation: The many-body problem at the heart of chemistry. *Journal of Computational Chemistry*, 28(8):1307–1320. <https://onlinelibrary.wiley.com/doi/abs/10.1002/jcc.20581>.
- [54] Olsen J., Roos B. O., Jørgensen P., and Jensen H. J. A. Determinant based configuration interaction algorithms for complete and restricted configuration interaction spaces. *J. Chem. Phys.*, 89(4):2185–2192, 1988. <https://doi.org/10.1063/1.455063>.

- [55] Sturesson L., Jönsson P., and Froese Fischer C. JJGEN: A flexible program for generating lists of jj-coupled configuration state functions. *Comput. Phys. Commun.*, 177(6):539–550, 2007. <https://doi.org/10.1016/j.cpc.2007.05.013>.
- [56] Oliver P. and Hibbert A. Accurate configuration-interaction calculation of transitions in Sn II. *J. Phys. B: At. Mol. Opt. Phys.*, 43(7):074013, 2010. <https://doi.org/10.1088/0953-4075/43/7/074013>.
- [57] Froese Fischer C., Jönsson P., and Godefroid M. Some two-electron properties of sodium. *Phys. Rev. A*, 57:1753–1758, 1998. <https://link.aps.org/doi/10.1103/PhysRevA.57.1753>.
- [58] Bieroń J., Filippin L., Gaigalas G., Godefroid M., Jönsson P., and Pyykkö P. *Ab initio* calculations of the hyperfine structure of zinc and evaluation of the nuclear quadrupole moment  $Q(^{67}\text{Zn})$ . *Phys. Rev. A*, 97:062505, 2018. <https://link.aps.org/doi/10.1103/PhysRevA.97.062505>.
- [59] Verdebout S., Jönsson P., Gaigalas G., Godefroid M., and Froese Fischer C. Exploring biorthonormal transformations of pair-correlation functions in atomic structure variational calculations. *J. Phys. B: At. Mol. Opt. Phys.*, 43(7):074017, 2010. <https://doi.org/10.1088/0953-4075/43/7/074017>.
- [60] Godefroid M. R., Jönsson P., and Froese Fischer C. Atomic Structure Variational Calculations in Spectroscopy. *Phys. Scr.*, T78(1):33–46, 1998. <https://doi.org/10.1238/physica.topical.078a00033>.
- [61] Nave G., Barklem P., Belmonte M. T., et al. Atomic data for astrophysics: Needs and challenges. *Bulletin of the AAS*, 51(7), 2019. <https://baas.aas.org/pub/2020n71001>.
- [62] Käuff H-U., Ballester P., Biereichel P., et al. CRIRES: A high-resolution infrared spectrograph for ESO’s VLT. *Ground-based Instrum. Astron.*, 5492:1218–1227, 2004. <https://doi.org/10.1117/12.551480>.
- [63] Young E. T., Becklin E., Marcum P. M., et al. Early Science with SOFIA, the Stratospheric Observatory for Infrared Astronomy. *Astrophys. J. Lett.*, 749:L17, 2012. <https://doi.org/10.1088/2041-8205/749/2/L17>.
- [64] Dorn R. J., Anglada-Escude G., Baade D., et al. CRIRES+: Exploring the Cold Universe at High Spectral Resolution. *The Messenger*, 156:7–11, 2014.
- [65] Wahlgren G. M. Atomic data for stellar astrophysics: from the UV to the IR. *Can. J. Phys.*, 89(4):345–356, 2011. <https://doi.org/10.1139/p10-125>.

- [66] Hibbert A. Recent Progress in Atomic Structure Calculations. *Phys. Scr.*, T112 (1):39, 2004. <https://doi.org/10.1238/physica.topical.112a00039>.
- [67] Gálvez F. J., Buendía E., and Sarsa A.  $1s^22p^3$  and  $1s^22s^23l$ ,  $l = s, p, d$ , excited states of boron isoelectronic series from explicitly correlated wave functions. *J. Chem Phys.*, 123(3):34302, 2005. <https://aip.scitation.org/doi/pdf/10.1063/1.1869468>.
- [68] Andersson M., Brage T., Hutton R., Kink I., and Engström L. Systematic studies of highly excited Rydberg states in ions with two valence electrons. *J. Phys. B: At. Mol. Phys.*, 39(12):2815–2826, 2006. <https://doi.org/10.1088/0953-4075/39/12/015>.
- [69] Andersson M. *Theoretical Studies of Atomic Structure, Radiative Transitions and Interference Effects*. PhD Thesis, Department of Physics, Lund University, 2006. <https://lup.lub.lu.se/record/547629>.
- [70] Bhalla C. P. Relativistic Hartree-Fock-Slater oscillator strengths for Ti. *Nucl. Instrum. Methods*, 90:149–155, 1970. [https://doi.org/10.1016/0029-554X\(70\)90664-6](https://doi.org/10.1016/0029-554X(70)90664-6).
- [71] Grant I. P. Gauge invariance and relativistic radiative transitions. *J. Phys. B: At. Mol. Phys.*, 7(12):1458–1475, 1974. <https://doi.org/10.1088/0022-3700/7/12/007>.
- [72] Pehlivan Rhodin A., Hartman H., Nilsson H., and Jönsson P. Experimental and theoretical oscillator strengths of Mg I for accurate abundance analysis. *A&A*, 598:A102, 2017. <https://doi.org/10.1051/0004-6361/201629849>.
- [73] Froese Fischer C. Evaluating the accuracy of theoretical transition data. *Phys. Scr.*, T134:014019, 2009. <https://doi.org/10.1088/0031-8949/2009/t134/014019>.
- [74] Ekman J., Godefroid M., and Hartman H. Validation and Implementation of Uncertainty Estimates of Calculated Transition Rates. *Atoms*, 2(2):215–224, 2014. <https://doi.org/10.3390/atoms2020215>.
- [75] Asplund M., Grevesse N., Sauval A. J., and Scott P. The Chemical Composition of the Sun. *ARA&A*, 47(1):481–522, 2009. <https://doi.org/10.1146/annurev.astro.46.060407.145222>.
- [76] Franchini M., Morossi C., Di Marcantonio P., et al. The *Gaia*–ESO Survey: Carbon Abundance in the Galactic Thin and Thick Disks. *Astrophys. J.*, 888(2): 55, 2020. <https://doi.org/10.3847/1538-4357/ab5dc4>.
- [77] Stonkutė E., Chorniy Y., Tautvaišienė G., et al. High-resolution Spectroscopic Study of Dwarf Stars in the Northern Sky: Lithium, Carbon, and Oxygen Abundances. *Astron. J.*, 159(3):90, 2020. <https://doi.org/10.3847/1538-3881/ab6a19>.

- [78] Marigo P., Cummings J. D., Curtis J. L., et al. Carbon star formation as seen through the non-monotonic initial–final mass relation. *Nat. Astron.*, 4:1102–1110, 2020. <https://doi.org/10.1038/s41550-020-1132-1>.
- [79] Gilmore G., Randich S., Asplund M. *et al.*, and Gaia-ESO Survey Team. The Gaia-ESO Public Spectroscopic Survey. *The Messenger*, 147:25–31, 2012. <https://ui.adsabs.harvard.edu/abs/2012Msngr.147...25G>.
- [80] Randich S., Gilmore G., and Gaia-ESO Consortium. The Gaia-ESO Large Public Spectroscopic Survey. *The Messenger*, 154:47–49, 2013. <https://ui.adsabs.harvard.edu/abs/2013Msngr.154...47R>.
- [81] Majewski S. R., Schiavon R. P., Frinchaboy P. M., et al. The Apache Point Observatory Galactic Evolution Experiment (APOGEE). *Astron. J.*, 154(3):94, 2017. <https://ui.adsabs.harvard.edu/abs/2017AJ....154...94M>.
- [82] De Silva G. M., Freeman K. C., Bland-Hawthorn J., et al. The GALAH survey: scientific motivation. *MNRAS*, 449(3):2604–2617, 2015. <https://ui.adsabs.harvard.edu/abs/2015MNRAS.449.2604D>.
- [83] Mihalas D. *Stellar Atmospheres*. San Francisco: W. H. Freeman Company, 1970.
- [84] Kramida A., Ralchenko Yu., Reader J., and NIST ASD Team. NIST Atomic Spectra Database (ver. 5.8), [Online]. Available: <https://physics.nist.gov/asd> [2021, March 6]. National Institute of Standards and Technology, Gaithersburg, MD., 2020.
- [85] Ynnerman A. and Froese Fischer C. Multiconfigurational-Dirac-Fock calculation of the  $2s^2\ ^1S_0-2s2p\ ^3P_1$  spin-forbidden transition for the Be-like isoelectronic sequence. *Phys. Rev. A*, 51:2020–2030, 1995. <https://link.aps.org/doi/10.1103/PhysRevA.51.2020>.
- [86] Amarsi A. M., Barklem P. S., Collet R., Grevesse N., and Asplund M. 3D non-LTE line formation of neutral carbon in the Sun. *A&A*, 624:A111, 2019. <https://doi.org/10.1051/0004-6361/201833603>.
- [87] Hibbert A., Biemont E., Godefroid M., and Vaeck N. Accurate  $f$  values of astrophysical interest for neutral carbon. *A&AS*, 99(1):179–204, 1993. <https://ui.adsabs.harvard.edu/abs/1993A&AS...99..179H>.
- [88] Heiter U., Lind K., Bergemann M., et al. Atomic data for the *Gaia*-ESO Survey. *A&A*, 645:A106, 2021. <https://doi.org/10.1051/0004-6361/201936291>.

- [89] Weiss A. W. Series perturbations in atomic spectra: Superposition-of-configurations calculations on Al I and Al II. *Phys. Rev. A*, 9:1524–1536, 1974. <https://link.aps.org/doi/10.1103/PhysRevA.9.1524>.
- [90] Bohr A. and Mottelson B. R. *Nuclear Structure, Vol. 2: Nuclear deformations*. W. A. Benjamin, Inc., Singapore, 1975.
- [91] Ragnarsson I. and Nilsson S. G. *Shapes and Shells in Nuclear Structure*. Cambridge University Press, Cambridge, 1995.
- [92] Lindgren I. and Rosen A. Relativistic self-consistent-field calculations with application to atomic hyperfine interaction. II. Relativistic theory of atomic hyperfine interaction. *Case Stud. At. Phys.*, 4(3):150–196, 1974. <https://www.osti.gov/biblio/4210365>.
- [93] Raghavan P. Table of nuclear moments. *At. Data Nucl. Data Tables*, 42(2): 189–291, 1989. [https://doi.org/10.1016/0092-640X\(89\)90008-9](https://doi.org/10.1016/0092-640X(89)90008-9).
- [94] Stone N. J. Table of nuclear magnetic dipole and electric quadrupole moments. *At. Data Nucl. Data Tables*, 90(1):75 – 176, 2005. <http://www.sciencedirect.com/science/article/pii/S0092640X05000239>.
- [95] Yordanov D. T., Balabanski D. L., Bieroń J., et al. Spins, Electromagnetic Moments, and Isomers of  $^{107-129}\text{Cd}$ . *Phys. Rev. Lett.*, 110:192501, 2013. <https://link.aps.org/doi/10.1103/PhysRevLett.110.192501>.
- [96] Wraith C., Yang X. F., Xie L., et al. Evolution of nuclear structure in neutron-rich odd-Zn isotopes and isomers. *Phys. Lett. B*, 771:385–391, 2017. <https://doi.org/10.1016/j.physletb.2017.05.085>.
- [97] Kanellakopoulos A., Yang X. F., Bissell M. L., et al. Nuclear moments of germanium isotopes near  $N = 40$ . *Phys. Rev. C*, 102:054331, 2020. <https://link.aps.org/doi/10.1103/PhysRevC.102.054331>.
- [98] Stone N. J. Table of nuclear electric quadrupole moments. *At. Data Nucl. Data Tables*, 111-112:1–28, 2016. <https://doi.org/10.1016/j.adt.2015.12.002>.
- [99] Pyykkö P. Year-2017 nuclear quadrupole moments. *Molecular Physics*, 116(10): 1328–1338, 2018. <https://doi.org/10.1080/00268976.2018.1426131>.
- [100] Neyens G. Nuclear magnetic and quadrupole moments for nuclear structure research on exotic nuclei. *Rep. Progr. Phys.*, 66(4):633–689, 2003. <https://doi.org/10.1088/0034-4885/66/4/205>.

- [101] Morris T. D., Simonis J., Stroberg S. R., et al. Structure of the Lightest Tin Isotopes. *Phys. Rev. Lett.*, 120:152503, 2018. <https://link.aps.org/doi/10.1103/PhysRevLett.120.152503>.
- [102] Gorges C., Rodríguez L. V., Balabanski D. L., et al. Laser Spectroscopy of Neutron-Rich Tin Isotopes: A Discontinuity in Charge Radii across the  $N = 82$  Shell Closure. *Phys. Rev. Lett.*, 122:192502, 2019. <https://link.aps.org/doi/10.1103/PhysRevLett.122.192502>.
- [103] Deyan T. Yordanov. This image appeared in the Communications Physics journal homepage shortly after the publication of “Paper v ”, on June 25, 2020.
- [104] Schwartz C. Theory of Hyperfine Structure. *Phys. Rev.*, 97:380–395, 1955. <https://link.aps.org/doi/10.1103/PhysRev.97.380>.
- [105] Sobelman I. *Atomic spectra and radiative transitions*. Springer-Verlag Berlin Heidelberg, 1979.
- [106] Tupitsyn I. I. and Loginov A. V. Use of Sturmian expansions in calculations of the hyperfine structure of atomic spectra. *Opt. Spectrosc.*, 94:319–326, 2003. <https://doi.org/10.1134/1.1563671>.
- [107] Malkin E., Komorovsky S., Repisky M., Demissie T. B., and Ruud K. The Absolute Shielding Constants of Heavy Nuclei: Resolving the Enigma of the  $^{119}\text{Sn}$  Absolute Shielding. *J. Phys. Chem. Lett.*, 4(3):459–63, 2013. <https://pubs.acs.org/doi/10.1021/jz302146m>.
- [108] Włodzimierz M. Tetramethyltin study by NMR spectroscopy in the gas and liquid phase. *J. Mol. Struct.*, 1017:45–50, 2012. <https://www.sciencedirect.com/science/article/pii/S0022286012002104>.
- [109] King W. H. *Isotope Shifts in Atomic Spectra*. Plenum Press, New York, USA, 1984.
- [110] Jörgen Ekman. ECT Workshop held in Trento, Italy, on August 25, 2015.
- [111] Ekman J., Jönsson P., Godefroid M., Nazé C., Gaigalas G., and Bieroń J. Rts 4: A program for relativistic isotope shift calculations. *Comput. Phys. Commun.*, 235:433–446, 2019. <https://doi.org/10.1016/j.cpc.2018.08.017>.
- [112] De Vries H., De Jager C. W., and De Vries C. Nuclear charge-density-distribution parameters from elastic electron scattering. *At. Data Nucl. Data Tables*, 36:495–536, 1987. [https://doi.org/10.1016/0092-640X\(87\)90013-1](https://doi.org/10.1016/0092-640X(87)90013-1).



- [113] Anni R., Co G., and Pellegrino P. Nuclear charge density distributions from elastic electron scattering data. *Nucl. Phys. A*, 584:35–39, 1995. <https://www.sciencedirect.com/science/article/abs/pii/037594749400508K?via%3Dihub>.
- [114] Chabanat E., Bonche P., Haensel P., Meyer J., and Schaeffer R. A Skyrme parametrization from subnuclear to neutron star densities Part II. Nuclei far from stabilities. *Nucl. Phys. A*, 635(1):231–256, 1998. <https://www.sciencedirect.com/science/article/pii/S0375947498001808>.
- [115] Alex Brown B. New Skyrme interaction for normal and exotic nuclei. *Phys. Rev. C*, 58:220–231, 1998. <https://link.aps.org/doi/10.1103/PhysRevC.58.220>.
- [116] Nazé C., Gaidamauskas E., Gaigalas G., Godefroid M., and Jönsson P. R1S3: A program for relativistic isotope shift calculations. *Comput. Phys. Commun.*, 184(9):2187–2196, 2013. <https://doi.org/10.1016/j.cpc.2013.02.015>.
- [117] Parthey C. G., Matveev A., Alnis J., et al. Improved Measurement of the Hydrogen  $1S - 2S$  Transition Frequency. *Phys. Rev. Lett.*, 107:203001, 2011. <https://link.aps.org/doi/10.1103/PhysRevLett.107.203001>.
- [118] Nörtershäuser W., Tiedemann D., Žáková M., et al. Nuclear Charge Radii of  ${}^{7,9,10}\text{Be}$  and the One-Neutron Halo Nucleus  ${}^{11}\text{Be}$ . *Phys. Rev. Lett.*, 102:062503, 2009. <https://link.aps.org/doi/10.1103/PhysRevLett.102.062503>.
- [119] Procter T. J., Billowes J., Bissell M. L., et al. Nuclear mean-square charge radii of  ${}^{63,64,66,68-82}\text{Ga}$  nuclei: No anomalous behavior at  $N = 32$ . *Phys. Rev. C*, 86:034329, 2012. <https://link.aps.org/doi/10.1103/PhysRevC.86.034329>.
- [120] Müller P., König K., Imgram P., Krämer J., and Nörtershäuser W. Collinear laser spectroscopy of  $\text{Ca}^+$ : Solving the field-shift puzzle of the  $4s^2 S_{1/2} \rightarrow 4p^2 P_{1/2,3/2}$  transitions. *Phys. Rev. Research*, 2:043351, 2020. <https://link.aps.org/doi/10.1103/PhysRevResearch.2.043351>.
- [121] Heylen H., Devlin C. S., Gins W., et al. High-resolution laser spectroscopy of  ${}^{27-32}\text{Al}$ . *Phys. Rev. C*, 103:014318, 2021. <https://link.aps.org/doi/10.1103/PhysRevC.103.014318>.
- [122] Angeli I. and Marinova K. P. Table of experimental nuclear ground state charge radii: An update. *At. Data and Nucl. Data Tables*, 99:69–95, 2013. <https://doi.org/10.1016/j.adt.2011.12.006>.
- [123] Cheal B., Cocolios T. E., and Fritzsche S. Laser spectroscopy of radioactive isotopes: Role and limitations of accurate isotope-shift calculations. *Phys. Rev. A*, 86:042501, 2012. <https://link.aps.org/doi/10.1103/PhysRevA.86.042501>.

- [124] Seltzer E. C. *K X-Ray Isotope Shifts*. *Phys. Rev.*, 188:1916, 1969. <https://link.aps.org/doi/10.1103/PhysRev.188.1916>.
- [125] Torbohm G., Fricke B., and Rosén A. State-dependent volume isotope shifts of low-lying states of group-IIa and -IIb elements. *Phys. Rev. A*, 31:2038–2053, 1985. <https://link.aps.org/doi/10.1103/PhysRevA.31.2038>.
- [126] Blundell S. A., Baird P. E. G., Palmer C. W. P., Stacey D. N., and Woodgate G. K. A reformulation of the theory of field isotope shift in atoms. *J. Phys. B: At. Mol. Phys.*, 20(15):3663, 1987. <https://doi.org/10.1088/0022-3700/20/15/015>.
- [127] Reinhard P.-G., Nazarewicz W., and Garcia Ruiz R. F. Beyond the charge radius: The information content of the fourth radial moment. *Phys. Rev. C*, 101:021301, 2020. <https://link.aps.org/doi/10.1103/PhysRevC.101.021301>.
- [128] Povh B., Rith K., Scholz C., Zetsche F., and Rodejohann W. *Particles and nuclei*. Springer-Verlag Berlin Heidelberg, 2015.
- [129] Pálffy A. Nuclear effects in atomic transitions. *Contemp. Phys.*, 51(6):471–496, 2010. <https://doi.org/10.1080/00107514.2010.493325>.
- [130] Shabaev V. M. Mass corrections in a strong nuclear field. *Theor. Math. Phys.*, 63:588–596, 1985. <https://doi.org/10.1007/BF01017505>.
- [131] Palmer C. W. P. Reformulation of the theory of the mass shift. *J. Phys. B: At. Mol. Phys.*, 20:5987–5996, 1987. <https://doi.org/10.1088/0022-3700/20/22/011>.
- [132] Grant I. P. Many-Electron Effects in the Theory of Nuclear Volume Isotope Shift. *Phys. Scr.*, 21(3-4):443–447, 1980. <https://doi.org/10.1088/0031-8949/21/3-4/033>.
- [133] Van Wijngaarden W. A. and Li J. Hyperfine splittings and isotope shifts of  $(6s)^2\ ^1S_0 \rightarrow (6s6p)\ ^1P_1$  transition in barium. *Can. J. Phys.*, 73:484, 1995. <https://cdnsiencepub.com/doi/abs/10.1139/p95-069>.
- [134] Nazé C., Li J. G., and Godefroid M. Theoretical isotope shifts in neutral barium. *Phys. Rev. A*, 91:032511, 2015. <https://link.aps.org/doi/10.1103/PhysRevA.91.032511>.
- [135] Stoitsov M. V., Schunck N., Kortelainen M., Michel N., Nam H., Olsen E., Sarich J., and Wild S. Axially deformed solution of the Skyrme-Hartree-Fock-Bogoliubov equations using the transformed harmonic oscillator basis (II) HFBTHO v2.00d: A new version of the program. *Comput. Phys. Commun.*, 184:1592–1604, 2013. <https://www.sciencedirect.com/science/article/abs/pii/S0010465513000301?via%3Dihub>.

- [136] Brandau C., Kozhuharov C., Harman Z., et al. Isotope Shift in the Dielectronic Recombination of Three-Electron  $^A\text{Nd}^{57+}$ . *Phys. Rev. Lett.*, 100:073201, 2008. <https://link.aps.org/doi/10.1103/PhysRevLett.100.073201>.
- [137] Froese Fischer C. and Godefroid M. R. Programs for computing  $LS$  and  $LSJ$  transitions from MCHF wave functions. *Comput. Phys. Commun.*, 64(3):501–519, 1991. [https://doi.org/10.1016/0010-4655\(91\)90141-7](https://doi.org/10.1016/0010-4655(91)90141-7).
- [138] Crossley R. J. S. The Calculation of Atomic Transition Probabilities. *Adv. At.*, 5:237–296, 1969. <https://www.sciencedirect.com/science/article/pii/S0065219908601591>.
- [139] Starace A. F. Length and Velocity Formulas in Approximate Oscillator-Strength Calculations. *Phys. Rev. A*, 3:1242–1245, 1971. <https://link.aps.org/doi/10.1103/PhysRevA.3.1242>.
- [140] Starace A. F. Comment on "Length and Velocity Formulas in Approximate Oscillator-Strength Calculations". *Phys. Rev. A*, 8:1141–1142, 1973. <https://link.aps.org/doi/10.1103/PhysRevA.8.1141>.
- [141] Hughes D. S. and Eckart C. The Effect of the Motion of the Nucleus on the Spectra of Li I and Li II. *Phys. Rev.*, 36:694–698, 1930. <https://link.aps.org/doi/10.1103/PhysRev.36.694>.
- [142] Tupitsyn I. I., Shabaev V. M., Crespo López-Urrutia J. R., Draganić I., Orts R. S., and Ullrich J. Relativistic calculations of isotope shifts in highly charged ions. *Phys. Rev. A*, 68:022511, 2003. <https://link.aps.org/doi/10.1103/PhysRevA.68.022511>.
- [143] Papoulia A. *The effect of realistic nuclear charge distributions on atomic levels and transitions*. Master Thesis, Lund University, 2015. <http://lup.lub.lu.se/student-papers/record/7360031>.



# Scientific Publications

## Author contributions

### **Paper I: Coulomb (Velocity) Gauge Recommended in Multiconfiguration Calculations of Transition Data Involving Rydberg Series**

I contributed to the conceptualization of this project, developed the methodology together with PJ, and took part in the computations. I analyzed the results, which were also discussed with JE and PJ, and produced the tables and most of the figures. I was the main responsible for the preparation of the manuscript. I presented this work (in a poster) at the 13th International Colloquium on Atomic Spectra and Oscillator Strengths (ASOS2019) for Astrophysical and Laboratory Plasmas<sup>3</sup> and (orally) at the 2019 meeting of the Computational Atomic Structure (CompAS) international group<sup>4</sup>. This paper is included in the PhD thesis of SS.

### **Paper II: Extended theoretical transition data in C I-IV**

I took part in the development of the applied computational methodologies, contributed to the computations in the C IV and C III systems and participated in the discussions and analysis of the results. I also reviewed several versions of the manuscript before submission and publication and contributed to its editing.

---

<sup>3</sup><https://asos2019.fudan.edu.cn/>

<sup>4</sup><http://ddwap.mah.se/tsjoek/compas/>

### **Paper III: Extended transition rates and lifetimes in Al I and Al II from systematic multiconfiguration calculations**

I carried out the computations in both Al I and Al II. The computational methods and strategies were also discussed with JE and PJ. As part of this project, I wrote an additional computer program for handling the expansions of the atomic state functions that facilitated and sped up the final computations. I performed a thorough review of previous theoretical and experimental works on these two atomic systems, and I was the main responsible for the preparation of the manuscript. I produced the figure and all tables. I presented this work (orally) at the 2018 CompAS meeting and at the 11th International Conference on Atomic and Molecular Data and Their Applications (ICAMDATA 2018)<sup>5</sup>.

### **Paper IV: Multiconfiguration Dirac-Hartree-Fock calculations of Landé g-factors for ions of astrophysical interest: B II, C I-IV, Al I-II, Si I-IV, P II, S II, Cl III, Ar IV, Ca I, Ti II, Zr III and Sn II**

I performed the calculations in the systems of C III, C IV, Al I, and Al II. I also reviewed the final versions of the manuscript before submission and publication.

### **Paper V: Structural trends in atomic nuclei from laser spectroscopy of tin**

I carried out one of the three sets of large-scale atomic structure calculations based on the MCDHF theory. I took part in the assessment of the reliability of the computed electronic factors of the  $A$  and  $B$  hyperfine constants, which had a substantial influence on the assigned errors of the extracted  $Q$ -values presented in Table 1 of the paper. Finally, I provided input that was necessary to compose the “Atomic structure calculations” section of the manuscript. This paper is included in the PhD thesis of SS. There are other PhD students performing the experimental work, which might also include this paper in their theses.

### **Paper VI: Ab initio electronic factors of the $A$ and $B$ hyperfine structure constants for the $5s^25p6s\ 1,3P_1^o$ states in Sn I**

I performed the calculations described in Sec. III.A 3, in collaboration with SS, and took part in the discussions for determining the final value, presented in Sec. IV, and its accuracy. I produced Figure 3, Table III, and (together with SS) Table IV, and I

---

<sup>5</sup><https://projects.iq.harvard.edu/icamdata>

wrote Sec. III.A 3. I also wrote substantial parts of Secs. I, IV, and V, after discussing their content with SS. By receiving input from the rest of the co-authors, I finalized the entire Sec. III, describing all sets of calculations performed in this work, as well as the other parts of the manuscript, until it was brought to its final form. This work was presented (in a poster) at the 2019 Solvay Workshop on “New Frontiers in Atomic, Nuclear, Plasma and Astrophysics”<sup>6</sup>. This paper is included in the PhD thesis of SS.

### **Paper VII: Effect of realistic nuclear charge distributions on isotope shifts and progress towards the extraction of higher-order nuclear radial moments**

The majority of the results and figures presented in Secs. III, IV, and V.A-B were produced in the course of my master thesis project [143], performing both nuclear and atomic structure calculations. I further produced the results shown in Secs. V.C-D and generated all tables and figures. All computational steps were carried out under the guidance of GC and JE. I was the main responsible for the preparation of the core of the manuscript, i.e., Secs. II-V. I presented this work (orally) at the 2017 CompAS meeting and at the 12th International Conference on Relativistic Effects in Heavy-Element Chemistry and Physics (REHE 2017)<sup>7</sup>.

---

<sup>6</sup>[http://www.solvayinstitutes.be/event/workshop/new\\_frontiers\\_2019/new\\_frontiers\\_2019.html](http://www.solvayinstitutes.be/event/workshop/new_frontiers_2019/new_frontiers_2019.html)

<sup>7</sup><https://www.online.uni-marburg.de/rehe2017/>










A. Papoulia, J. Ekman, G. Gaigalas, M. Godefroid, S. Gustafsson, H. Hartman, W. Li, L. Radžiūtė, P. Rynkun, S. Schiffmann, K. Wang, and P. Jönsson  
Coulomb (Velocity) Gauge Recommended in Multiconfiguration Calculations of Transition Data Involving Rydberg Series  
*Atoms*, 2019, 7(4), 106  
Copyright 2019 The Authors.



Article

# Coulomb (Velocity) Gauge Recommended in Multiconfiguration Calculations of Transition Data Involving Rydberg Series

Asimina Papoulia<sup>1,2,\*</sup>, Jörgen Ekman<sup>1</sup>, Gediminas Gaigalas<sup>3</sup>, Michel Godefroid<sup>4</sup>, Stefan Gustafsson<sup>1</sup>, Henrik Hartman<sup>1</sup>, Wenxian Li<sup>1</sup>, Laima Radžiūtė<sup>3</sup>, Pavel Rynkun<sup>3</sup>, Sacha Schiffmann<sup>2,4</sup>, Kai Wang<sup>5</sup> and Per Jönsson<sup>1</sup>

<sup>1</sup> Department of Materials Science and Applied Mathematics, Malmö University, SE-20506 Malmö, Sweden; jorgen.ekman@mau.se (J.E.); stefan.gustafsson@mau.se (S.G.); henrik.hartman@mau.se (H.H.); wenxian.li@mah.se (W.L.); per.jonsson@mau.se (P.J.)

<sup>2</sup> Division of Mathematical Physics, Department of Physics, Lund University, SE-22100 Lund, Sweden; saschiff@ulb.ac.be

<sup>3</sup> Institute of Theoretical Physics and Astronomy, Vilnius University, Saulėtekio av. 3, LT-10222 Vilnius, Lithuania; gediminas.gaigalas@tfai.vu.lt (G.G.); laima.radiute@tfai.vu.lt (L.R.); pavel.rynkun@tfai.vu.lt (P.R.)

<sup>4</sup> Chimie Quantique et Photophysique, Université libre de Bruxelles, B-1050 Brussels, Belgium; michel.godefroid@ulb.be

<sup>5</sup> Hebei Key Lab of Optic-electronic Information Materials, College of Physics Science and Technology, Hebei University, Baoding 071002, China; kaiwang1128@aliyun.com

\* Correspondence: asimina.papoulia@mau.se; Tel.: +46-40-66-58268

Received: 23 October 2019; Accepted: 21 November 2019; Published: 26 November 2019



**Abstract:** Astronomical spectroscopy has recently expanded into the near-infrared (nIR) wavelength region, raising the demands on atomic transition data. The interpretation of the observed spectra largely relies on theoretical results, and progress towards the production of accurate theoretical data must continuously be made. Spectrum calculations that target multiple atomic states at the same time are by no means trivial. Further, numerous atomic systems involve Rydberg series, which are associated with additional difficulties. In this work, we demonstrate how the challenges in the computations of Rydberg series can be handled in large-scale multiconfiguration Dirac–Hartree–Fock (MCDHF) and relativistic configuration interaction (RCI) calculations. By paying special attention to the construction of the radial orbital basis that builds the atomic state functions, transition data that are weakly sensitive to the choice of gauge can be obtained. Additionally, we show that the Babushkin gauge should not always be considered as the preferred gauge, and that, in the computations of transition data involving Rydberg series, the Coulomb gauge could be more appropriate for the analysis of astrophysical spectra. To illustrate the above, results from computations of transitions involving Rydberg series in the astrophysically important C IV and C III ions are presented and analyzed.

**Keywords:** infrared spectra; spectrum calculations; multiconfiguration methods; Rydberg series; Rydberg states; electric dipole transitions; transition rates; Babushkin gauge; Coulomb gauge; length form; velocity form

## 1. Introduction

The starlight emitted at optical or shorter wavelengths is efficiently scattered by intervening interstellar and intergalactic dust particles. To observe stars deeper into the galactic center and go even beyond the Milky Way, astrophysical missions and spectrographs were recently designed to observe

nIR radiation, which has higher transmission through dust clouds [1–3]. Accurate transition data from the IR part of the spectrum are thus required to interpret the spectra of distant astronomical objects observed, and to carry out chemical abundance studies.

The interest in the nIR region is relatively recent, and atomic data corresponding to wavelengths from 1 to 5  $\mu\text{m}$  are scarce. Due to the limited resources and the numerous possible transitions, laboratory measurements are insufficient to provide astrophysicists with complete sets of atomic transition data. Critically evaluated theoretical data are, therefore, necessary to complement experiments and to allow for accurate chemical abundance analyses of stars. In the long wavelength IR regime, lines of atoms are produced by transitions between states lying close in energy, which often correspond to transitions between highly excited states. The latter instance necessitates atomic structure calculations over a large portion of a spectrum. Extensive spectrum calculations that produced transition data in the nIR region were formerly carried out as part of the Opacity Project [4]. The latter non-relativistic calculations were based on the close-coupling approximation of the R-matrix theory.

Performing spectrum calculations, in which multiple atomic states are targeted at the same time, is generally not trivial. In multiconfiguration calculations, the correlation between the electrons is taken into account by expanding the targeted states in a number of symmetry adapted basis functions, which are built from products of spin-orbitals. To accurately predict the energies of all the targeted states, the shapes of the radial parts of the spin-orbitals must be such that they account for the *LS*-term dependencies; i.e., the way the electrons are coupled to form different terms from the same configuration [5]. Additionally, many studies involve states that are part of Rydberg series. Perturbers often enter the Rydberg series and the atomic state expansions must correctly predict their positions [6]. Computations of Rydberg series have to further describe states with electron distributions occupying different regions in space, extending far out from the atomic core. The above challenges require that special attention is paid to the optimization scheme of the wave functions; i.e., how the orbital basis is generated. The challenges in the computations of Rydberg series become more apparent when computing transition data.

The transition parameters (line strengths, oscillator strengths, and transition rates) are expressed in terms of reduced matrix elements of the transition operator. Different choices of gauge, Babushkin and Coulomb, for the transition operator lead to alternative expressions for the reduced matrix elements, and consequently, the transition parameters. Gauge invariance of the transition data is a straightforward matter for hydrogenic systems. Yet, the use of approximate wave functions results in different values for transition data expressed in different gauges. During the past years, recommendations for choosing the appropriate gauge became contradictory, suggesting further work in the field [7–12]. The Babushkin gauge (or length form) is sensitive to the outer part of the wave functions that governs the atomic transitions, and transition data expressed in this gauge are often considered to be more reliable than transition data expressed in the Coulomb gauge (or velocity form) [13]. It is, however, argued that provided reasonably accurate approximate wave functions, the Coulomb gauge (or velocity form) may give the best results when the transition energy is not very small [14]. Recent work suggests that the Coulomb gauge gives more accurate results and is the preferred gauge for transitions involving high Rydberg states [15].

In this paper, we present and analyze results from computations of Rydberg series in the C IV and C III ions. Although the latter are of astrophysical interest, the goal of the paper is not benchmarking transition data for these two ions against other theoretical methods, but instead assessing the relative reliability of the MCDHF/RCI results obtained with the two different gauges. Using the MCDHF method, we apply different computational strategies for optimizing the radial orbital basis used for constructing the wave functions and compare the results. For transitions involving low-lying states, the transition data are accurately computed in both the Babushkin and the Coulomb gauge, independently of how the radial orbitals are optimized. On the other hand, transitions involving high Rydberg states are problematic, and the Babushkin gauge does not provide trustworthy results when conventional optimization strategies are applied. However, by paying special attention to the

construction of the radial orbital basis that builds the atomic state functions, transition data that are weakly sensitive to the choice of gauge are produced for all the computed transitions in the ions we study. The present article is an extended transcript of the poster presentation given on 24 June 2019 at the 13th International Colloquium on Atomic Spectra and Oscillator Strengths (ASOS2019) for Astrophysical and Laboratory Plasmas that took place at Fudan University in Shanghai, China (<https://asos2019.fudan.edu.cn>).

## 2. Theory

### 2.1. MultiConfiguration Calculations

Numerical representations of atomic state functions (ASFs), which are approximations to the exact wave functions, are obtained using the fully relativistic MCDHF method [16,17]. In the MCDHF method, the ASFs  $\Psi(\gamma\pi JM_J)$  are expanded over  $N_{CSF}$  antisymmetrized basis functions  $\Phi(\gamma_v\pi JM_J)$ , which are known as configuration state functions (CSFs), i.e.,

$$\Psi(\gamma\pi JM_J) = \sum_{\nu=1}^{N_{CSF}} c_{\nu} \Phi(\gamma_{\nu}\pi JM_J). \tag{1}$$

In the expression above,  $J$  and  $M_J$  are the angular momentum quantum numbers,  $\pi$  is the parity, and  $\gamma_{\nu}$  denotes other appropriate labeling of the CSF  $\nu$ , such as orbital occupancy and angular coupling tree. The CSFs are coupled products of one-electron Dirac orbitals  $\psi_{n\kappa,m}$ , which have the general form:

$$\psi_{n\kappa,m}(\mathbf{r}) = \frac{1}{r} \begin{pmatrix} P_{n\kappa}(r)\chi_{\kappa,m}(\theta, \varphi) \\ iQ_{n\kappa}(r)\chi_{-\kappa,m}(\theta, \varphi) \end{pmatrix}, \tag{2}$$

where  $\chi_{\pm\kappa,m}(\theta, \varphi)$  are the two-component spin-angular functions and  $\{P_{n\kappa}(r), Q_{n\kappa}(r)\}$  are, respectively, the radial functions of the large and small components, which are represented on a logarithmic grid. The selection of the CSFs to be included in the expansion (1) depends on the shell structure of the atom at hand and the computed properties, as explained in Section 3. The shape of the radial functions  $\{P_{n\kappa}(r), Q_{n\kappa}(r)\}$  is determined by the effective field in which the considered electron moves, which is in turn established by the included CSFs [18].

The expansion coefficients  $c_{\nu}$ , together with the radial parts of the spin-orbitals, are obtained in a self-consistent field (SCF) procedure. The set of SCF equations to be iteratively solved results from applying the variational principle on a weighted energy functional of all the targeted atomic states according to the extended optimal level (EOL) scheme [19]. In fully relativistic calculations, the energy functional is estimated from the expectation value of the Dirac-Coulomb Hamiltonian [17]. The angular integrations needed for the construction of the energy functional are based on the second quantization formalism in the coupled tensorial form [20,21].

The MCDHF method is employed to generate an orbital basis. Given this basis, the final wave functions  $\Psi(\gamma\pi JM_J)$  of the targeted states are determined in subsequent RCI calculations. In the RCI calculations, the spin-orbitals defining the basis are fixed and only the expansion coefficients  $c_{\nu}$  are evaluated by diagonalizing the Hamiltonian matrix. At this step, the expansions based on Equation (1) can be augmented to include CSFs that account for additional electron correlation effects. All MCDHF and RCI calculations were performed using the relativistic atomic structure package GRASP2018 [22].

### 2.2. Transition Parameters

Once the wave functions  $\Psi(\gamma\pi JM_J)$  have been determined, transition parameters can be computed. In this work, we focus on the computation of transition rates (or probabilities) for electric dipole (E1) transitions. Electric dipole transitions are much stronger than electric quadrupole (E2) and magnetic

multipole (Mk) transitions. For the transition rate  $A^{(k)}$  of electric dipole ( $k = 1$ ) emission from an upper state  $\gamma' \pi' J' M'_J$  to any of the  $2J + 1$  states  $\gamma \pi J M_J$  of lower energy, we have the following proportionality

$$A^{(1)}(\gamma' \pi' J', \gamma \pi J) \sim (E_{\gamma' \pi' J'} - E_{\gamma \pi J})^3 \frac{S^{(1)}(\gamma \pi J, \gamma' \pi' J')}{2J' + 1}, \tag{3}$$

where  $E_{\gamma' \pi' J'} - E_{\gamma \pi J}$  is the transition energy and  $S^{(1)}(\gamma \pi J, \gamma' \pi' J')$  is the line strength given by

$$S^{(1)}(\gamma \pi J, \gamma' \pi' J') = |\langle \Psi(\gamma \pi J) || \mathbf{O}^{(1)} || \Psi(\gamma' \pi' J') \rangle|^2. \tag{4}$$

The E1 transition rates are therefore expressed in terms of reduced matrix elements of the electric dipole transition operator  $\mathbf{O}^{(1)}$ . From Equation (1), it follows that

$$\langle \Psi(\gamma \pi J) || \mathbf{O}^{(1)} || \Psi(\gamma' \pi' J') \rangle = \sum_{k,l} c_k c'_l \langle \Phi(\gamma k \pi J) || \mathbf{O}^{(1)} || \Phi(\gamma' l \pi' J') \rangle. \tag{5}$$

The choice of gauge parameter determines whether the electric dipole matrix elements are computed in the Babushkin or the Coulomb gauge, which in non-relativistic calculations correspond to the length and the velocity form, respectively [10]. The two forms are equivalent for hydrogenic wave functions, but they result in different values when approximate many-electron wave functions are used. As shown later, in Section 4, these values reveal a strong dependence on the generated orbital basis and the captured correlation effects. Although the present results arise from fully relativistic calculations, similar behavior is observed when non-relativistic multiconfiguration calculations are performed [15].

The explicit expressions of the electric dipole reduced matrix elements in the Babushkin and the Coulomb gauge are given in [10]. Taking for convenience the non-relativistic limit, the electric dipole reduced matrix elements are, in the length and the velocity form, respectively, given by

$$\langle \Psi(\gamma \pi J) || \sum_{i=1}^N r_i \mathbf{C}^{(1)}(i) || \Psi(\gamma' \pi' J') \rangle \tag{6}$$

and

$$\frac{1}{E_{\gamma' \pi' J'} - E_{\gamma \pi J}} \langle \Psi(\gamma \pi J) || \sum_{i=1}^N \nabla^{(1)}(i) || \Psi(\gamma' \pi' J') \rangle, \tag{7}$$

where the summation runs over the number  $N$  of electrons and  $\mathbf{C}^{(1)}$  is the renormalized spherical harmonic of rank 1 [23]. The reduced matrix elements of (6) and (7) involve, respectively, sums over radial transition integrals of the kind

$$\int_0^\infty P(r) r P'(r) dr \tag{8}$$

and

$$\int_0^\infty P(r) \frac{d}{dr} P'(r) dr, \tag{9}$$

weighted with the products of the expansion coefficients of the CSFs and the angular coefficients [20,21,23].  $P'(r)$  and  $P(r)$  are the radial functions of the large components of the Dirac one-electron spin-orbitals (2) that build the CSFs of the initial state  $\gamma' \pi' J'$  and the final state  $\gamma \pi J$ , respectively. In the present work, the initial and final states belonging to different parities are built from a common orbital basis.

In the computation of the integrals (8), the emphasis is given to the tail of the radial orbitals, while in the integrals (9) the emphasis is given instead to the inner part of the radial orbitals. In the simple Hartree–Fock (HF) model, the approximate wave functions usually display a correct asymptotic behavior towards large  $r$  (see also Section 5), and since the former integrals are also computationally simpler, the transition rates are traditionally provided in the length form [7–9,14]. As discussed in

Section 5, when multiconfiguration methods concurrently target multiple atomic states, all wave functions are not always well approximated at large  $r$ ; and the velocity form, or correspondingly, the Coulomb gauge, may by contrast, give the best results.

The agreement between the transition rates  $A_B$  and  $A_C$ , respectively, evaluated in the Babushkin and the Coulomb gauge is used as an indicator of accuracy. This is particularly useful when laboratory measurements are not available for comparison. The uncertainty of the computed transition rates in the preferred gauge can be estimated as

$$dT = \frac{|A_B - A_C|}{\max(A_B, A_C)}, \quad (10)$$

which reflects the relative discrepancy between the Babushkin and the Coulomb gauge of the computed line strengths [24,25]. Although the accuracy indicators  $dT$  should be used in a statistical manner for a group of transitions with similar properties (see [6]), individual  $dT$  values can point out problematic transitions, which could further be analyzed.

### 3. Computational Methodology—Optimization of the Orbital Basis

The accuracy of multiconfiguration calculations relies on the CSF expansion of Equation (1). A first approximation of the ASFs is acquired by performing an MCDHF calculation on expansions that are built from the configurations that define what is known as the multi-reference (MR) [17]. The orbitals that take part in this initial calculation are called spectroscopic orbitals and are kept frozen in all subsequent calculations. The initial approximation of the ASFs is improved by augmenting the expansion with CSFs that interact with the ones that are generated by the MR configurations. Such CSFs are built from configurations that differ by either a single (S) or a double (D) electron substitution from the configurations in the MR [17,26]. Following the SD-MR scheme, the interacting configurations are obtained by allowing substitutions of electrons from the spectroscopic orbitals to an active set of correlation orbitals, which is systematically increased (each step introducing an additional correlation orbital layer) [27,28]. These configurations produce CSFs that can be classified, based on the nature of the substitutions, into CSFs that capture valence–valence (VV), core–valence (CV), and core–core (CC) electron correlation effects.

Building accurate wave functions requires a very large orbital basis. Even so, a large but incomplete orbital basis does not ensure that the wave functions give accurate properties other than energies. In the MCDHF calculations, the correlation orbitals are obtained by applying the variational principle on the weighted energy functional of all the targeted atomic states. Thus, the orbitals of the first correlation layers will overlap with the spectroscopic orbitals that account for the effects that minimize the energy the most [18,29]. The energetically dominant effects must first be saturated to obtain orbitals localized in other regions of space, which might describe effects that do not lower the energy much, but are important for, e.g., transition parameters. One must, therefore, carefully choose the orbital basis with respect to the computed properties [30].

Valence atomic transitions are governed by the outer part of the wave functions and this part must be properly described by the correlation orbitals to obtain reliable transition parameters. States that are part of Rydberg series encompass valence orbitals of increasing principal quantum number  $n$ . Spectrum calculations that involve Rydberg series need, thus, to describe states with electron distributions localized in different regions of space extending far out from the atomic core. Since the overlap between orbitals describing Rydberg states is in some cases minor, generating an optimal orbital basis is not straightforward [6]. This raises the need to explore different computational strategies.

#### 3.1. CIV

In lithium-like carbon, the configurations being studied are  $1s^2nl$  with  $n = 2$  to 8 and  $l = 0$  to 4 and  $1s^26h$ . These configurations define the MR and correspond to 53 targeted atomic states of both even and odd parity, which are simultaneously optimized. For simple systems such as three-electron systems,

the MCDHF calculations are conventionally performed using CSF expansions that are produced by SD-MR electron substitutions from all spectroscopic orbitals. In this manner, the CSFs capture all valence (V), CV, and CC correlation effects. The 1s1s pair-correlation effect is energetically very important and the orbitals of the first correlation layers overlap with the 1s core orbital accounting for this effect (see Table 1). After building six correlation layers by utilizing this conventional approach, we see that all correlation orbitals up to 14s, 14p, 14d, 12f, 12g, 8h, and 7i are rather contracted in comparison with the outer Rydberg orbitals. As a consequence, the wave functions are not properly described for all states, and in particular, not for the higher Rydberg states considered.

**Table 1.** The mean radii  $\langle r \rangle$  (a.u.) of the spectroscopic and correlation orbitals that belong to the s and p symmetries in C IV. The correlation orbitals result from two different optimization schemes, the conventional and the alternative, and they occupy different regions in space.

Spectroscopic		Correlation			Spectroscopic		Correlation		
		Conventional	Alternative				Conventional	Alternative	
1s	0.27	9s	0.51	1.12			9p	0.44	0.87
2s	1.31	10s	0.43	0.92	2p	1.28	10p	0.41	1.03
3s	3.00	11s	0.42	0.84	3p	2.95	11p	0.40	1.00
4s	5.55	12s	0.46	0.87	4p	5.64	12p	0.45	1.18
5s	8.81	13s	0.56	0.87	5p	8.99	13p	0.48	2.59
6s	12.82	14s	0.40	1.26	6p	13.10	14p	0.77	5.94
7s	17.58				7p	17.94			
8s	23.09				8p	23.54			

For a more appropriate description of the wave functions, the correlation orbitals must occupy the space between the 1s core orbital and the inner valence orbitals. This can be accomplished by imposing restrictions on the allowed substitutions for obtaining the orbital basis. Thus, the MCDHF calculations are alternatively performed using CSF expansions that are produced by SD-MR substitutions with the restriction of allowing maximum one hole in the 1s core shell. In this case, the shape of the correlation orbitals is established by CSFs accounting for V and CV correlation effects. The resulting correlation orbitals are, as shown in Table 1, more extended, overlapping with orbitals of higher Rydberg states.

The final wave functions of the targeted states are determined in subsequent RCI calculations, where D substitutions from the 1s core orbital and triple (T) substitutions from all the spectroscopic orbitals, are included. The number of CSFs in the final even and odd state expansions are, respectively, 1,077,872 and 1,287,706, distributed over the different J symmetries.

### 3.2. C III

In beryllium-like carbon, the configurations in question are  $1s^2 2snl$  with  $n = 2$  to 7 and  $l = 0$  to 4 and  $1s^2 2p^2$ ,  $1s^2 2p3s$ ,  $1s^2 2p3p$ , and  $1s^2 2p3d$ . These configurations define the MR and correspond to 114 targeted atomic states of both even and odd parity, which are simultaneously optimized. Having introduced two correlation orbitals, 8s and 8p—specifically targeted to account for the LS-term dependence [31], i.e., the difference between the ns orbitals for  $2sns \ ^3S$  and  $2sns \ ^1S$  and the difference between the np orbitals for  $2snp \ ^3P^\circ$  and  $2snp \ ^1P^\circ$ —the MCDHF calculations are conventionally performed using CSF expansions that are produced by SD-MR electron substitutions from all spectroscopic orbitals with the restriction that only one excitation is allowed from the  $1s^2$  atomic core. In this manner, the CSFs capture VV and CV correlation effects. The  $1snl$  pair-correlation effect is comparatively important, and the orbitals of the first correlation layers are spatially localized between the 1s orbital and the 2s and 2p orbitals. As the CV correlation effects start to saturate, the correlation orbitals are gradually located further away from the  $1s^2$  atomic core (see Table 2). The correlation orbitals up to 12s, 12p, 12d, 12f, 11g, and 8h are, however, still contracted in comparison with the outer Rydberg orbitals.



**Table 2.** Same as Table 1, but for radial orbitals in C III. The correlation orbitals 8s and 8p, which are introduced to account for the *LS*-term dependencies, are the same in both optimization schemes and fairly diffuse in comparison with the rest of the correlation orbitals.

Spectroscopic		Correlation			Spectroscopic		Correlation		
		Conventional		Alternative			Conventional		Alternative
1s	0.26	9s	1.05	4.86			9p	1.00	3.56
2s	1.28	10s	1.48	3.67	2p	1.23	10p	1.24	3.37
3s	3.57	11s	1.88	3.25	3p	3.74	11p	1.56	3.37
4s	6.63	12s	1.87	8.40	4p	7.04	12p	1.52	9.04
5s	10.80				5p	11.37			
6s	15.95				6p	16.71			
7s	22.10				7p	23.04			
<b>term corr.</b>					<b>term corr.</b>				
8s	8.22				8p	5.55			

For a more appropriate description of the wave functions, the correlation orbitals must occupy the space of the valence orbitals. In the alternative approach, this is accomplished by allowing SD substitutions only from the outer valence orbitals accounting for VV correlation. The resulting correlation orbitals are, as shown in Table 2, more extended, overlapping with orbitals of higher Rydberg states.

The final wave functions of the targeted states are determined in subsequent RCI calculations, where SDT substitutions from all the spectroscopic orbitals are included, with the restriction that only one substitution is allowed from the  $1s^2$  atomic core. The number of CSFs in the final even and odd state expansions are, respectively, 1,578,620 and 1,274,147, distributed over the different *J* symmetries.

#### 4. Results

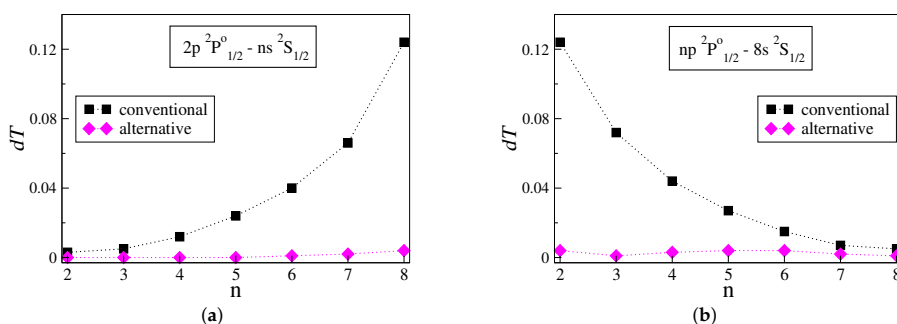
Excitation energies are produced, based on the conventional and alternative computational strategies that were described in Section 3, and are compared with the critically evaluated data from the National Institute of Standards and Technology's (NIST's) Atomic Spectra Database (ASD) [32]. In C IV, the computed excitation energies are in excellent agreement with the NIST's recommended values. Both computational approaches give similar energies and the relative differences from the NIST values are less than 0.01%. For the more complex system of C III, the computed excitation energies agree also well with the energies proposed by NIST. The relative differences between theoretical and critically compiled energies are, on average, of the order of 0.1% and 0.02%, when following the conventional and the alternative approach, respectively. The NIST database does not provide excitation energies for the  $2s6s\ ^2S$ ,  $2s7s\ ^2S$ , and  $2s7p\ ^3P^o$  states, which are included in the computations.

Transition rates *A* are produced based on the two different computational strategies. In the present computations, the uncertainties in the predicted excitation energies of two states associated with a transition most often cancel out, and consequently, the majority of the evaluated transition energies are ultimately in perfect agreement with the NIST values. The uncertainties of the computed transition rates solely emerge from the disagreement of the computed line strengths in the Babushkin and the Coulomb gauge, which are then reflected in the *dT* values. When the conventional strategy is applied, most of the transition rates are predicted with uncertainties *dT* lower than 1% and 5%, in lithium-like and beryllium-like carbon, respectively. Yet, for transitions involving high Rydberg states, the uncertainties increase remarkably, especially for the more complex C III ion. The alternative strategy for optimizing the radial orbitals yields transition rates that are overall more accurate. The improvement in accuracy is significant for transitions that involve high Rydberg states.

The uncertainties *dT* of the transition rates computed with the conventional and alternative approaches are presented and analyzed for groups of transitions in the studied carbon ions. Each group is selected to include transitions between a fixed state and Rydberg states described by electron

distributions that are gradually localized farther from the atomic core. Accordingly, Figure 1a,b illustrates the uncertainties  $dT$  for the  $2p^2P_{1/2}^\circ - ns^2S_{1/2}$  and  $np^2P_{1/2}^\circ - 8s^2S_{1/2}$  groups of transitions in C IV. Similarly, Figure 2a,b illustrates the  $dT$  values for the  $2s^2^1S_0 - 2snp^1P_1^\circ$  and  $2sns^1S_0 - 2s7p^1P_1^\circ$  groups of transitions in C III.

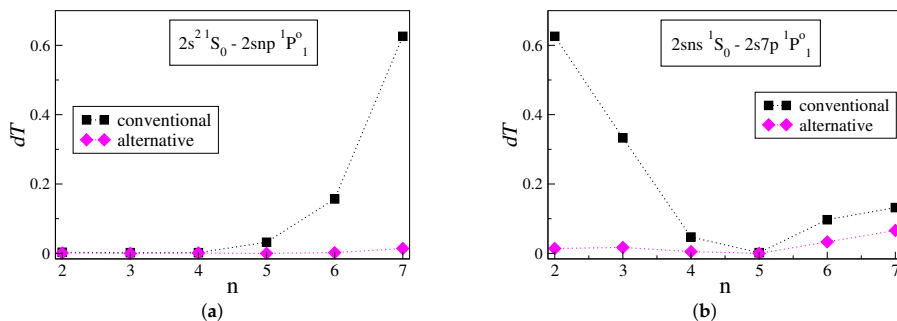
Figure 1a demonstrates the uncertainties for the series of transitions between the low-lying  $2p^2P_{1/2}^\circ$  state and successively higher Rydberg  $ns^2S_{1/2}$  states. The uncertainty  $dT$  of the transition rates computed with the conventional approach grows almost exponentially with the increasing principal quantum number  $n$ . The transition rate for the  $2p^2P_{1/2}^\circ - 8s^2S_{1/2}$  transition, which is the transition between the two states with the largest energy difference in the plot, eventually exhibits the highest uncertainty—12.4%. When the alternative approach is utilized instead, the uncertainties range between 0% and 0.4% for the respective transitions. The same trends are also observed in other groups of transitions in C IV, such as the  $2p^2P^\circ - nd^2D$ , the  $2s^2S - np^2P^\circ$ , and so forth.



**Figure 1.** (a) The uncertainty  $dT$  of the computed transition rates for transitions between the  $2p^2P_{1/2}^\circ$  state and Rydberg  $ns^2S_{1/2}$  states of increasing principal quantum number  $n$  in C IV. The black squares and magenta diamonds, respectively, correspond to the results from the conventional and the alternative strategies for optimizing the radial orbitals. (b) Same as the first panel, but for transitions between the  $8s^2S_{1/2}$  state and successive Rydberg  $np^2P_{1/2}^\circ$  states in C IV.

Having as a starting point the  $2p^2P_{1/2}^\circ - 8s^2S_{1/2}$  transition, Figure 1b demonstrates the uncertainties for the series of transitions between the high Rydberg  $8s^2S_{1/2}$  state and successively higher Rydberg  $np^2P_{1/2}^\circ$  states. As  $n$  increases, the transition energy gets smaller. The uncertainties of the transition rates computed with the conventional approach exhibit a nearly exponential decay with increasing  $n$ . Similarly to Figure 1a, when following the alternative strategy, the uncertainties in the transition rates are substantially reduced, ranging between 0.1% and 0.4%. Other groups of transitions in C IV, such as the  $np^2P^\circ - 8d^2D$  series and the  $ns^2S - 8p^2P^\circ$  series, follow analogous trends.

Figure 2a displays the  $dT$  values for transitions between the low-lying  $2s^2^1S_0$  state and successively higher Rydberg  $2snp^1P_1^\circ$  states. Looking at Figure 2a, when the conventional approach is applied the uncertainties  $dT$  increase sharply for  $n > 5$ . For the  $2s^2^1S_0 - 2s7p^1P_1^\circ$  transition, i.e., the transition between the two states with the largest energy difference, the  $dT$  rises to 63%. The latter is about five times larger than the highest estimated  $dT$  value in the figures above. Once more, when the radial orbitals are optimized using the alternative strategy, the uncertainties drop dramatically, ranging between 0% and 1.4% for the respective transitions. More groups of transitions in C III that reveal similar behavior are the  $2s2p^1P_1^\circ - 2sns^1S_0$  series and the  $2p^2^3P_0 - 2snp^3P_1^\circ$  series.



**Figure 2.** (a) The uncertainty  $dT$  of the computed transition rates for transitions between the  $2s^2\ ^1S_0$  state and Rydberg  $2snp\ ^1P_1^\circ$  states of increasing principal quantum number  $n$  in C III. The black squares and magenta diamonds, respectively, correspond to the results from the conventional and alternative strategies for optimizing the radial orbitals. (b) Same as the first panel, but for transitions between the  $2s7p\ ^1P_1^\circ$  state and successive Rydberg  $2sns\ ^1S_0$  states in C III.

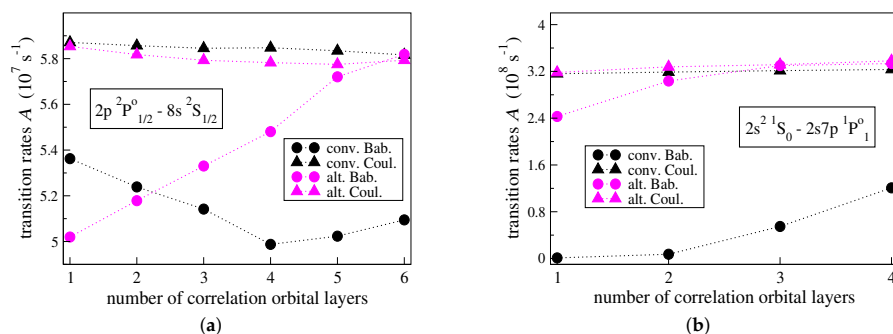
Starting with the  $2s^2\ ^1S_0 - 2s7p\ ^1P_1^\circ$  transition, Figure 2b displays the  $dT$  values for transitions between the high Rydberg  $2s7p\ ^1P_1^\circ$  state and successively higher Rydberg  $2sns\ ^1S_0$  states. Likewise, in Figure 1b, the increase in  $n$  corresponds to transitions between states that gradually come closer in energy. The uncertainties of the transition rates computed with the conventional approach reduce rapidly as  $n$  increases. Applying the alternative strategy results in much lower uncertainties, which extend between 0.5% and 6.6%. A similar trend is also observed in the  $2snp\ ^1P_1^\circ - 2s7s\ ^1S_0$  series of transitions in C III. Although the last two points in Figure 2b correspond to transitions between states lying close in energy, the uncertainties are comparatively high. Nevertheless, the alternative strategy still predicts the transition rates with lower uncertainties.

Altogether, for transitions between low-lying states, the transition rates are accurately predicted independently of whether the conventional or the alternative computational strategy is employed. Further, when both states involved in a transition in C IV are high Rydberg states, the transition rates are also predicted with high accuracy in both computations. On average, the same holds for transitions between high Rydberg states in C III. The line strengths of transitions between two states close in energy, and with the outer electrons occupying nearly the same region of space, are relatively large, and therefore, weakly affected by the optimization strategy of the radial orbitals. Quite the contrary, transitions between a low-lying state and a high Rydberg state are problematic in both carbon ions. The line strength of transitions between two states with large energy differences, and with the outer electrons occupying different parts of space, take smaller values, which are more sensitive to how the radial orbitals are optimized with regard to correlation.

To better understand the origins of the large  $dT$  values in transitions between low-lying states and high Rydberg states, the convergences of the individual transition rates  $A_B$  and  $A_C$ , computed in the Babushkin and the Coulomb gauges respectively, are studied with respect to the increasing active set of correlation orbitals. In connection with the figures above, this is done for the  $2p\ ^2P_{1/2}^\circ - 8s\ ^2S_{1/2}$  transition in C IV (see Figure 3a) and  $2s^2\ ^1S_0 - 2s7p\ ^1P_1^\circ$  transition in C III (see Figure 3b); i.e., the transitions with the highest uncertainties  $dT$ . In Figure 3a,b, the convergences of the  $A_B$  and  $A_C$  values are illustrated for the two different computational approaches.

As seen in Figure 3a,b, when the computations are performed in the alternative manner, the transition rates given by  $A_B$  and  $A_C$  ultimately come really close in value. Considering the small final  $dT$  value, the agreement between the  $A_B$  and  $A_C$  values is expected. One observes that the transition rate given by  $A_C$  is rather stable with respect to the increasing orbital set. The  $A_C$  value varies by only 1% and 6.2% for each of the transitions displayed in the figures below. On the contrary,

the  $A_B$  value varies by 13.7% and 27.2%, respectively. In the  $2p^2P_{1/2}^o - 8s^2S_{1/2}$  transition, it takes five correlation layers for the  $A_B$  value to start converging, while in the  $2s^2^1S_0 - 2s7p^1P_1^o$  transition it takes three layers of correlation orbitals for the  $A_B$  value to converge.



**Figure 3.** (a) The transition rates  $A$  in the Babushkin (circles) and the Coulomb (triangles) gauges for the  $2p^2P_{1/2}^o - 8s^2S_{1/2}$  transition in C IV, as a function of the increasing number of correlation layers. The transition rates computed in the conventional and the alternative manner are respectively shown in black and magenta. (b) Same as the first panel, but for the  $2s^2^1S_0 - 2s7p^1P_1^o$  transition in C III.

Looking at Figure 3a,b, when the conventional approach is applied, the individual  $A_B$  and  $A_C$  values do not converge, as the large final uncertainties  $dT$  reveal. The transition rate given by  $A_C$  is, however, again stable and is also consistent with the  $A_B$  and  $A_C$  values provided by the alternative computational strategy. Throughout the optimization of the radial orbitals in the conventional manner, the  $A_C$  value varies by only 0.9% and 2.3% for each of the transitions displayed in Figure 3a,b, respectively. Although it seems that the  $A_B$  values will eventually approach the  $A_C$  ones, this would require a very large orbital basis, which is beyond the reach of the available computational resources. One may deduce that when the conventional computational strategy is applied the transition rates  $A_B$ , computed in the Babushkin gauge, are problematic and unreliable.

### 5. Discussion

Transition data, such as transition rates  $A$ , are expressed in terms of reduced matrix elements of the transition operator (see Equation (5)), which can be computed in different gauges. According to Equation (10), the uncertainty of the computed  $A$  values is assessed by the agreement of the transition rates computed in the different gauges. Computations of reduced matrix elements in different gauges, however, probe separate parts of the wave functions. Hence, the radial parts of the wave functions must be well approximated as a whole to obtain gauge invariant transition rates.

For transitions between low-lying states, both computational strategies yield reduced matrix elements of the transition operator that almost reach gauge invariance, and the transition rates are, overall, accurately predicted. There are enough correlation orbitals spatially localized between the core and the inner valence orbitals that make up the low-lying states. As a result, the inner parts of the wave functions are adequately approximated. Moreover, the spectroscopic outer valence orbitals, which make up the higher Rydberg states and are localized farther from the atomic core, improve the description of the outer parts of the wave functions for representing the low-lying states, ensuring that they have the correct asymptotic behavior. The radial parts of the latter wave functions are then effectively described at all  $r$  values, being insensitive to the choice of the optimization strategy with regard to correlation.

For transitions between a low-lying state and a high Rydberg state, the conventional computational strategy fails to produce accurate transition rates. The correlation orbitals are significantly contracted compared to the outer Rydberg orbitals. Further, there are no spectroscopic orbitals farther localized

to correct for the fact that the asymptotic behavior of the tail of the wave functions that represent the higher Rydberg states is not well approximated. Thus, the Babushkin gauge that probes the outer part of the wave functions does not produce trustworthy results. The inner parts of the wave functions representing the higher Rydberg states are, however, adequately approximated, and as a result, the Coulomb gauge yields transition rates that are more reliable (see also, Figure 3a,b).

The alternative computational strategy generates correlation orbitals that are more extended, increasing the overlap with the spectroscopic orbitals that make up the higher Rydberg states. In this case, the correlation orbitals are properly localized to ably describe the asymptotic behavior of the outer part of the wave functions representing the higher Rydberg states. That being so, after the final MCDHF and RCI computations in the alternative manner, the reduced matrix elements of the transition operator are practically gauge invariant and the transition rates are also accurately predicted for the transitions between low-lying states and high Rydberg states (see also, Figure 3a,b).

The radial transition integrals (8) and (9) that take part in the computations of the reduced matrix elements of the transition operator have an upper integration bound that goes to infinity. In (8) and (9),  $P(r)$  and  $P'(r)$  are the radial parts of the spectroscopic and correlation orbitals that are included in the computations. If we express the transition integrals as a function of the upper integration bound  $R$ , we get

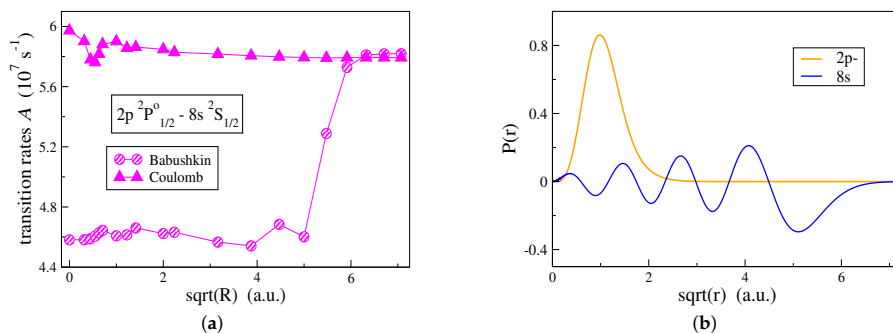
$$\int_0^R P(r)rP'(r) dr \quad (11)$$

and

$$\int_0^R P(r) \frac{d}{dr} P'(r) dr, \quad (12)$$

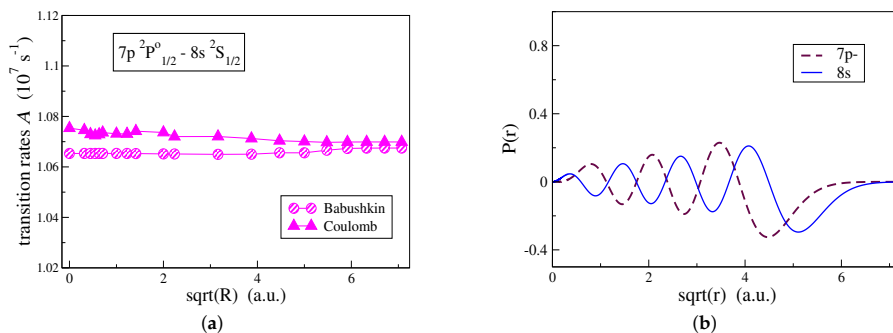
respectively. We can keep  $R = \infty$  for the spectroscopic orbitals so that they extend to their full values and only introduce a cut-off value for  $R$  in the transition integrals involving correlation orbitals. In this manner, the effect on the transition rate values, from correlation orbitals gradually localized farther from the origin, can be studied. In connection with Figure 3a, the effect that the shape of the correlation orbitals has on the computation of transition rates is, in Figure 4a, examined for the  $2p^2P_{1/2}^o - 8s^2S_{1/2}$  transition in C IV. In Figure 4a, the transition rates are computed by employing the alternative computational strategy and both Babushkin and Coulomb gauges are displayed. One observes that the two gauges are affected differently by the outer parts of the correlation orbitals.

In Figure 4a, the transition rate computed in the Coulomb gauge is mainly influenced by the correlation orbitals that are localized close to the origin and in the vicinity of the atomic core. Correlation orbitals occupying regions with  $\sqrt{R} > 1$  have an insignificant effect on the Coulomb gauge. This explains the fact that the conventional computational strategy, which generates more contracted orbitals, still predicts with accuracy, the transition rates in the Coulomb gauge. Oppositely, the Babushkin gauge is hugely affected by the correlation orbitals occupying the region between  $\sqrt{R} = 5$  and  $\sqrt{R} = 6$ . Looking at Figure 4b, the  $8s$  radial orbital, which extends far out from the  $1s^2$  atomic core, begins its asymptotic decay at about  $\sqrt{R} = 5$  and dies out at  $\sqrt{R} \approx 6$ . Only when we have orbitals extending into this region, the asymptotic behavior of the wave function representing the  $8s^2S_{1/2}$  state is well described, and thus, the Babushkin gauge will yield accurate transition rates. As previously seen, the conventional computational strategy fails to do so.



**Figure 4.** (a) The transition rates  $A$  in the Babushkin and the Coulomb gauges for the  $2p^2P_{1/2}^o - 8s^2S_{1/2}$  transition in C IV, as a function of the square root of the upper integration bound  $R$  in the radial transition integrals (11) and (12) involving correlation orbitals. The radial transition integrals involving spectroscopic orbitals extend to their full values, so that  $R = 0$  corresponds to transition rates computed from wave functions exclusively built from spectroscopic orbitals. The wave functions are produced by the alternative computational strategy. (b) The spectroscopic  $2p$  and  $8s$  radial orbitals in C IV as a function of  $\sqrt{r}$ . The two orbitals occupy different regions in space and their overlap is minor. The  $8s$  orbital extends far out from the atomic core.

A similar study was performed for a transition between two high Rydberg states. In Figure 5a, the effect of the shape of the correlation orbitals on the computed transition rates is examined for the  $7p^2P_{1/2}^o - 8s^2S_{1/2}$  transition in C IV. As seen in Figure 5a, correlation has nearly the same effect on both gauges. Although the  $7p$  and  $8s$  orbitals extend far out from the atomic core (see Figure 5b), correlation orbitals occupying the large  $R$  region remain unimportant in the Babushkin gauge. For transitions between states close in energy, the line strengths take large values and the change in the transition rates due to correlation is very small. For this reason, the conventional computational strategy also yields accurate transition rates for transitions between high Rydberg states.



**Figure 5.** (a) Same as Figure 4a, but for the  $7p^2P_{1/2}^o - 8s^2S_{1/2}$  transition in C IV. (b) The spectroscopic  $7p$  and  $8s$  radial orbitals in C IV as functions of  $\sqrt{r}$ . Both orbitals occupy nearly the same regions in space, overlapping to a great extent.

To clarify the fact that the asymptotic behavior of the wave function at large distances is (or is not) well approximated, depending on the alternative (or the conventional) optimization strategy, Brillouin’s theorem [33,34] can be put forward to emphasize the importance of the variational content of the wave functions. When being interested into the description of Rydberg states  $1s^2nl^2L$  ( $L = l$ ) in the

single-configuration non-relativistic HF approximation, node counting of the valence radial function,  $nc = n - l - 1$ , provides a simple and efficient way to select the desired state in the self-consistent procedure [34]. Each separately optimized state implicitly contains all single-electron excitations  $nl \rightarrow n'l$  of both lower and upper parts of the spectrum, including the continuum  $1s^2\epsilon l$ , with the associated interesting property

$$\langle \Phi^{\text{HF}}(1s^2nl \ ^2L) | \mathcal{H} | \Phi(1s^2n'l \ ^2L) \rangle = \langle \Phi^{\text{HF}}(1s^2nl \ ^2L) | \mathcal{H} | \Phi(1s^2\epsilon l \ ^2L) \rangle = 0, \quad \forall (n', \epsilon) \quad (13)$$

where  $\mathcal{H}$  is the scalar non-relativistic Hamiltonian that is used in the energy functional to derive the HF equations. The annihilation property of the  $(M_L, M_S)$ -independent interaction matrix elements between the reference HF CSF built with the optimized HF orbitals, i.e.,  $\Phi^{\text{HF}}$ , and all single-electron excitation CSFs  $\Phi$ , defines Brillouin's theorem and explains the reasonable accuracy of the HF approximation through the richness of its variational content. The above discussion can be extended to the relativistic framework by considering  $n\kappa \rightarrow (n', \epsilon)\kappa$  single-electron excitations and taking for  $\mathcal{H}$  the relativistic Hamiltonian that is used for deriving the DHF equations [17].

In the present work, it is hard to define the variational content of the MCDHF approach due to the complexity of the energy functional, but one should keep in mind that the optimization strategy is based (i) on a layer-by-layer approach in which only the last layer is variational while the previous ones are kept frozen, and (ii) on the use of the EOL method targeting, simultaneously, a large number of states for a spectrum calculation. The resulting lack of variational freedom for the individual states can (partially) be counterbalanced by the inclusion of enough interacting states in the Hamiltonian matrix. Going back to the single-configuration approximation case mentioned above, any member of a Rydberg series can be described through configuration interaction involving Brillouin one-electron excitations with a resulting CI-expansion strictly equivalent to the single approximation HF wave function if the basis of single-excitation CSFs is large and rich enough. This equivalence has been exploited to solve convergence problems encountered in the MCHF study of Rydberg series in strontium [35] or to demonstrate the correspondence between different orbital optimization schemes for describing the discrete-continuum interactions in complex systems [36]. In the context of our work, one illustrates the inadequacy of the orbitals obtained in the conventional approach that are used to compensate the lack of variational freedom in the representation of the high-lying Rydberg members. On the contrary, the alternative strategy proposed produces orbitals that have a better localization for describing the single-electron excitations, which would have been implicitly included with a fully optimized MCDHF wave function targeting a single Rydberg state.

## 6. Summary and Conclusions

The computations of transition data in the systems of lithium-like and beryllium-like carbon are examples of spectrum calculations that involve Rydberg series. In this work, we showed that, independently of the optimization scheme of the radial orbitals, transition parameters corresponding to the lower part of the spectrum are computed with high accuracy. As astronomical spectroscopy raises the demand on atomic data, highly accurate transition parameters are, however, also required for transitions that involve high Rydberg states. We demonstrated how this can be achieved by paying special attention to the optimization scheme of the radial orbitals with respect to correlation. Finally, we showed that the Babushkin gauge should not, by default, be considered as the preferred gauge, and that, in the computations of Rydberg series, it might be required that the transition rates in the Coulomb gauge are used as a reference for the interpretation of astrophysical observations.

**Author Contributions:** All authors contributed jointly to conceptualization, investigation, validation, and writing—reviewing and editing. A.P. and P.J. cooperatively took part in the methodology and visualization. A.P., P.J., and J.E. conducted the formal analysis. A.P. performed the writing—original draft preparation and data curation.

**Funding:** This research was funded by the Swedish Research Council (VR) under contract 2015-04842 and 2016-04185. A.P. was financially supported by the Royal Physiographic Society of Lund (<https://www.fysiografen.se/en/>) to attend the ASOS 2019 conference in Shanghai. M.G. acknowledges support from the FWO-FNRS

Excellence of Science Programme (grant number EOS-O022818F). S.S. is a FRIA grantee of the Fonds de la Recherche Scientifique—FNRS.

**Acknowledgments:** M.G., G.G., and P.J., were research associates at Vanderbilt University in 1981, 1994–97, and 1995–97, respectively. They are grateful to Charlotte for her endless training and encouragement in many atomic physics research projects over the years, for which her deep knowledge in computational and mathematical physics was crucial. Her outstanding contribution to theoretical atomic physics has been a boundless source of inspiration for all of us.

**Conflicts of Interest:** The authors declare no conflict of interest.

## References

- Käufel, H.-U.; Ballester, P.; Biereichel, P.; Delabre, B.; Donaldson, R.; Dorn, R.; Fedrigo, E.; Finger, G.; Fischer, G.; Franza, F.; et al. CRIRES: A high-resolution infrared spectrograph for ESO's VLT. *Ground-Based Instrum. Astron.* **2004**, *5492*, 1218–1227.
- Young, E.T.; Becklin, E.; Marcum, P.M.; Roellig, T.L.; Buizer, J.M.D.; Herter, T.L.; Güsten, R.; Dunham, E.W.; Temi, P.; Andersson, B.-G.; et al. Early Science with SOFIA, the Stratospheric Observatory for Infrared Astronomy. *Astrophys. J. Lett.* **2012**, *749*, L17. [[CrossRef](#)]
- Dorn, R.J.; Anglada-Escude, G.; Baade, D.; Bristow, P.; Follert, R.; Gojak, D.; Grunhut, J.; Hatzes, A.; Heiter, U.; Hilker, M.; et al. CRIRES+: Exploring the Cold Universe at High Spectral Resolution. *Messenger* **2014**, *156*, 7–11.
- Atomic Databases from the Opacity Project and the Iron Project. Available online: <http://cdsweb.u-strasbg.fr/topbase/testop/home.html> (accessed on 13 November 2019).
- Galvez, F.J.; Buendia, E.; Sarsa, A.  $1s^2 2p^3$  and  $1s^2 2s^2 3l$ ,  $l = s, p, d$ , excited states of boron isoelectronic series from explicitly correlated wave functions. *J. Chem. Phys.* **2005**, *123*, 034302.
- Papoulia, A.; Ekman, J.; Jönsson, P. Extended transition rates and lifetimes in Al I and Al II from systematic multiconfiguration calculations. *Astron. Astrophys.* **2019**, *621*, A16. [[CrossRef](#)]
- Crossley, R.J.S. The Calculation of Atomic Transition Probabilities. *Adv. At. Mol. Phys.* **1969**, *5*, 237–296. [[CrossRef](#)]
- Starace, A.F. Length and Velocity Formulas in Approximate Oscillator-Strength Calculations. *Phys. Rev. A* **1971**, *3*, 1242.
- Starace, A.F. Comment on “Length and Velocity Formulas in Approximate Oscillator-Strength Calculations”. *Phys. Rev. A* **1973**, *8*, 1141. [[CrossRef](#)]
- Grant, I.P. Gauge invariance and relativistic radiative transitions. *J. Phys. B At. Mol. Opt. Phys.* **1974**, *7*, 1458. [[CrossRef](#)]
- Grant, I.P.; Starace, A.F. Gauge invariance and radiative transition probabilities. *J. Phys. B At. Mol. Opt. Phys.* **1975**, *8*, 1999. [[CrossRef](#)]
- Crossley, R.J.S. Fifteen Years On—The Calculation of Atomic Transition Probabilities Revisited. *Phys. Scr.* **1984**, *T8*, 117–128. [[CrossRef](#)]
- Hibbert, A. Oscillator strengths of transitions in the beryllium sequence. *J. Phys. B At. Mol. Opt. Phys.* **1974**, *7*, 1417. [[CrossRef](#)]
- Cowan, R.D. Electric dipole radiation. In *The Theory of Atomic Structure and Spectra*; University of California Press: London, UK, 1981; pp. 400–402. [[CrossRef](#)]
- Pehlivan Rhodin, A.; Hartman, H.; Nilsson, H.; Jönsson, P. Experimental and theoretical oscillator strengths of Mg I for accurate abundance analysis. *Astron. Astrophys.* **2017**, *598*, A102.
- Grant, I.P. *Relativistic Quantum Theory of Atoms and Molecules*; Springer: New York, NY, USA, 2007. [[CrossRef](#)]
- Froese Fischer, C.; Godefroid, M.; Brage, T.; Jönsson, P.; Gaigalas, G. Advanced multiconfiguration methods for complex atoms: I. Energies and wave functions. *J. Phys. B At. Mol. Opt. Phys.* **2016**, *49*, 182004.
- Verdebout, S.; Jönsson, P.; Gaigalas, G.; Godefroid, M.; Froese Fischer, C. Exploring biorthonormal transformations of pair-correlation functions in atomic structure variational calculations. *J. Phys. B At. Mol. Opt. Phys.* **2010**, *43*, 074017. [[CrossRef](#)]
- Dyall, K.G.; Grant, I.P.; Johnson, C.T.; Parpia, F.A.; Plummer, E.P. GRASP: A general-purpose relativistic atomic structure program. *Comput. Phys. Commun.* **1989**, *55*, 425–456. [[CrossRef](#)]
- Gaigalas, G.; Rudzikas, Z.; Froese Fischer, C. An efficient approach for spin-angular integrations in atomic structure calculations. *J. Phys. B At. Mol. Opt. Phys.* **1997**, *30*, 3747–3771. [[CrossRef](#)]



21. Gaigalas, G.; Fritzsche, S.; Grant, I.P. Program to calculate pure angular momentum coefficients in jj-coupling. *Comput. Phys. Commun.* **2001**, *139*, 263–278. [[CrossRef](#)]
22. Froese Fischer, C.; Gaigalas, G.; Jönsson, P.; Bieroń, J. GRASP2018-A Fortran 95 version of the General Relativistic Atomic Structure Package. *Comput. Phys. Commun.* **2019**, *237*, 184–187. [[CrossRef](#)]
23. Froese Fischer, C.; Godefroid, M.R. Programs for computing *LS* and *LSJ* transitions from MCHF wave functions. *Comput. Phys. Commun.* **1991**, *64*, 501–519. [[CrossRef](#)]
24. Froese Fischer, C. Evaluating the accuracy of theoretical transition data. *Phys. Scr.* **2009**, *T134*, 014019. [[CrossRef](#)]
25. Ekman, J.; Godefroid, M.; Hartman, H. Validation and Implementation of Uncertainty Estimates of Calculated Transition Rates. *Atoms* **2014**, *2*, 215–224. [[CrossRef](#)]
26. Froese Fischer, C.; Brage, T.; Jönsson, P. Structure of  $\psi_1$ . In *Computational Atomic Structure—An MCHF Approach*; CRC Press: Boca Raton, FL, USA, 1997; pp. 70–71. [[CrossRef](#)]
27. Olsen, J.; Roos, B.O.; Jørgensen, P.; Jensen, H.J.A. Determinant based configuration interaction algorithms for complete and restricted configuration interaction spaces. *J. Chem. Phys.* **1988**, *89*, 2185.
28. Stuesson, L.; Jönsson, P.; Froese Fischer, C. JJGEN: A flexible program for generating lists of jj-coupled configuration state functions. *Comput. Phys. Commun.* **2007**, *177*, 539–550. [[CrossRef](#)]
29. Godefroid, M.; Jönsson, P.; Froese Fischer, C. Atomic structure variational calculations in spectroscopy. *Phys. Scr.* **1998**, *T78*, 33–46. [[CrossRef](#)]
30. Froese Fischer, C.; Jönsson, P.; Godefroid, M. Some two-electron properties of sodium. *Phys. Rev. A* **1998**, *57*, 1753. [[CrossRef](#)]
31. Froese Fischer, C.; Brage, T.; Jönsson, P. Term dependence. In *Computational Atomic Structure—An MCHF Approach*; CRC Press: Boca Raton, FL, USA, 1997; pp. 55–56. [[CrossRef](#)]
32. Kramida, A.; Ralchenko, Y.U.; Reader, J.; NIST ASD Team. *NIST Atomic Spectra Database (ver. 5.6.1)*; National Institute of Standards and Technology: Gaithersburg, MD, USA, 2018. Available online: <https://physics.nist.gov/asd> (accessed on 24 September 2019).
33. Godefroid, M.; Liévin, J.; Metz, J.-Y. Brillouin’s theorem for complex atomic configurations. *J. Phys. B At. Mol. Opt. Phys.* **1987**, *20*, 3283–3296.
34. Froese Fischer, C. *The Hartree-Fock Method for Atoms. A Numerical Approach*; John Wiley and Sons: New York, NY, USA, 1977. [[CrossRef](#)]
35. Vaeck, N.; Godefroid, M.; Hansen, J.E. Multiconfiguration Hartree-Fock calculations for singlet terms in neutral strontium. *Phys. Rev. A* **1988**, *38*, 2830–2845.
36. Cowan, R.D.; Hansen, J.E. Discrete-continuum interactions in CI I and S I. *JOSA* **1981**, *71*, 60. [[CrossRef](#)]



© 2019 by the authors. Licensee MDPI, Basel, Switzerland. This article is an open access article distributed under the terms and conditions of the Creative Commons Attribution (CC BY) license (<http://creativecommons.org/licenses/by/4.0/>).



W. Li, A. M. Amarsi, **A. Papoulia**, J. Ekman, and P. Jönsson

Extended theoretical transition data in C I-IV

*Monthly Notices of the Royal Astronomical Society*, 2021, 502(3), 3780-3799

Copyright 2021 The Authors - Published by Oxford University Press on  
behalf of the Royal Astronomical Society.



# Extended theoretical transition data in C I–IV

W. Li<sup>1,3</sup>★, A. M. Amarsi<sup>2</sup>, A. Papoulia<sup>1,3</sup>, J. Ekman<sup>1</sup> and P. Jönsson<sup>1</sup><sup>1</sup>Department of Materials Science and Applied Mathematics, Malmö University, SE-205 06 Malmö, Sweden<sup>2</sup>Theoretical Astrophysics, Department of Physics and Astronomy, Uppsala University, Box 516, SE-751 20 Uppsala, Sweden<sup>3</sup>Division of Mathematical Physics, Lund University, P.O. Box 118, SE-221 00 Lund, Sweden

Accepted 2021 January 15. Received 2021 January 9; in original form 2020 December 7

## ABSTRACT

Accurate atomic data are essential for opacity calculations and for abundance analyses of the Sun and other stars. The aim of this work is to provide accurate and extensive results of energy levels and transition data for C I–IV. The Multiconfiguration Dirac–Hartree–Fock and relativistic configuration interaction methods were used in this work. To improve the quality of the wavefunctions and reduce the relative differences between length and velocity forms for transition data involving high Rydberg states, alternative computational strategies were employed by imposing restrictions on the electron substitutions when constructing the orbital basis for each atom and ion. Transition data, for example, weighted oscillator strengths and transition probabilities, are given for radiative electric dipole (E1) transitions involving levels up to  $1s^22s^22p6s$  for C I, up to  $1s^22s^27f$  for C II, up to  $1s^22s7f$  for C III, and up to  $1s^28g$  for C IV. Using the difference between the transition rates in length and velocity gauges as an internal validation, the average uncertainties of all presented E1 transitions are estimated to be 8.05 per cent, 7.20 per cent, 1.77 per cent, and 0.28 per cent, respectively, for C I–IV. Extensive comparisons with available experimental and theoretical results are performed and good agreement is observed for most of the transitions. In addition, the C I data were employed in a re-analysis of the solar carbon abundance. The new transition data give a line-by-line dispersion similar to the one obtained when using transition data that are typically used in stellar spectroscopic applications today.

**Key words:** atomic data – atomic processes – radiative transfer – Sun: abundances.

## 1 INTRODUCTION

Accurate atomic data are of fundamental importance to many different fields of astronomy and astrophysics. This is particularly true for carbon. As the fourth-most abundant metal in the cosmos (Asplund et al. 2009), carbon is a major source of opacity in the atmospheres and interiors of stars. Complete and reliable sets of atomic data for carbon are essential for stellar opacity calculations, because of their significant impact on stellar structure and evolution (e.g. Vandenberg et al. 2012; Chen et al. 2020).

Accurate atomic data for carbon are also important in the context of spectroscopic abundance analyses and Galactic Archaeology. Carbon abundances measured in late-type stars help us to understand the nucleosynthesis of massive and asymptotic giant branch stars, and thus the Galactic chemical evolution (e.g. Franchini et al. 2020; Jofré, Jackson & Tucci Maia 2020; Stonkutė et al. 2020). In early-type stars, carbon abundances help constrain the present-day Cosmic Abundance Standard (e.g. Nieva & Przybilla 2008, 2012; Alexeeva et al. 2019). In the Sun, the carbon abundance is precisely measured in order to put different cosmic objects on to a common scale (e.g. Caffau et al. 2010; Amarsi et al. 2019). In all of these cases, oscillator strengths for C I (cool stars) and for C I–IV (hot stars) underpin the spectroscopic analyses; this is especially the case for studies that relax the assumption of local thermodynamic equilibrium (LTE, e.g. Przybilla, Butler & Kudritzki 2001; Nieva & Przybilla

2006), in which case much larger sets of reliable atomic data are needed.

On the experimental side, a number of studies of transition data have been presented in the literature. Neutral C I transition probabilities for the  $2p4p \rightarrow 2p3s$  transition array have been studied by Miller et al. (1974) using a spectroscopic shock tube and by Jones & Wiese (1984) using a wall-stabilized arc. The measurements of relative oscillator strengths for  $2p3p \rightarrow 2p3s$ ,  $2p3d \rightarrow 2p3p$ , and  $2p4s \rightarrow 2p3p$  have been performed by Musielok, Veres & Wiese (1997), Bacawski, Wujec & Musielok (2001), and Golly, Jazgara & Wujec (2003) using a wall-stabilized arc. Older measurements of oscillator strengths are also available using the same technique (Maecker 1953; Richter 1958; Foster 1962; Boldt 1963; Goldbach & Nollez 1987; Goldbach, Martin & Nollez 1989). By analysing the high-resolution spectra obtained with the Goddard High Resolution Spectrograph on the *Hubble Space Telescope*, Federman & Zsargo (2001) derived oscillator strengths for C I lines below 1200 Å.

For C II, a number of measurements have also been performed. Träbert et al. (1999) measured the radiative decay rates for the intercombination (IC) transitions  $2s2p^2\ ^4P \rightarrow 2s^22p^2\ ^2P^o$  at a heavy-ion storage ring, and the total measured radiative decay rates to the ground term were  $125.8 \pm 0.9\ \text{s}^{-1}$  for  $^4P_{1/2}$ ,  $9.61 \pm 0.05\ \text{s}^{-1}$  for  $^4P_{3/2}$ , and  $45.35 \pm 0.15\ \text{s}^{-1}$  for  $^4P_{5/2}$ . The aforementioned results are, however, not in agreement with the values measured by Fang et al. (1993) using a radio-frequency ion trap, that is,  $146.4(+8.3, -9.2)\ \text{s}^{-1}$  for  $^4P_{1/2}$ ,  $11.6(+0.8, -1.7)\ \text{s}^{-1}$  for  $^4P_{3/2}$ , and  $51.2(+2.6, -3.5)\ \text{s}^{-1}$  for  $^4P_{5/2}$ . Goly & Weniger (1982) measured the transition probabilities from a helium–carbon arc for some multiplets of  $\{2p^3, 2s^23p\} \rightarrow$

★ E-mail: wenxian.li@mau.se

$2s2p^2$  and  $2s^24s \rightarrow 2s^23p$  with estimated relative uncertainty of 50 per cent. Using an electric shock tube, Roberts & Eckerle (1967) provided the relative oscillator strengths of some C II multiplets with relative uncertainties of 7 per cent. Reistad et al. (1986) gave lifetimes for 11 C II levels using the beam-foil excitation technique and extensive cascade analyses.

For C III, the IC decay rate of the  $2s2p\ ^3P_1^o \rightarrow 2s^2\ ^1S_0$  transition was measured to be  $121.0 \pm 7\ \text{s}^{-1}$  by Kwong et al. (1993) using a radio-frequency ion trap and  $102.94 \pm 0.14\ \text{s}^{-1}$  by Doerfert et al. (1997) using a heavy-ion storage ring. The discrepancy between the values obtained from the two different methods is quite large, that is, of the order of 15 per cent. The result given by the latter measurement is closer to earlier *ab initio* calculations ranging between 100 and  $104\ \text{s}^{-1}$  (Fischer 1994; Fleming, Hibbert & Stafford 1994; Ynnerman & Fischer 1995). Several measurements have also been performed for the lifetimes of the low-lying levels of C III (Mickey 1970; Buchet-Poulizac & Buchet 1973; Reistad & Martinson 1986; Nandi et al. 1996).

For the system of Li-like C IV, the transition probabilities of the  $1s^22p\ ^2P_{1/2,3/2}^o \rightarrow 1s^22s\ ^2S_{1/2}$  transitions were measured by Berkner et al. (1965) using the foil-excitation technique and by Knystautas et al. (1971) using the beam-foil technique, respectively. There are also a number of measurements of lifetimes in C IV using the beam-foil technique (Buchet-Poulizac & Buchet 1973; Donnelly, Kernahan & Pinnington 1978; Jacques et al. 1980).

On the theoretical side, Froese Fischer et al. have performed detailed studies of C I–IV, focusing on the low-lying levels. They carried out Multiconfiguration Hartree–Fock (MCHF) calculations and used the Breit–Pauli (MCHF-BP) approximation for computing energy levels and transition properties, for example, transition probabilities, oscillator strengths, and lifetimes, in C I (Tachiev & Fischer 2001; Fischer & Tachiev 2004; Fischer 2006), C II (Tachiev & Fischer 2000), C III (Tachiev & Fischer 1999; Fischer 2000), and C IV (Fischer et al. 1998; Godefroid, Fischer & Jönsson 2001).

Hibbert et al. have presented extensive calculations for optical transitions. They used the cIv3 code (Hibbert 1975) to calculate oscillator strengths and transition probabilities in C I (Hibbert et al. 1993), C II (Corr eg e & Hibbert 2004), and C III (Kingston & Hibbert 2000). In the calculations of Hibbert et al. (1993) and Corr eg e & Hibbert (2004), empirical adjustments were introduced to the diagonal matrix elements in order to accurately reproduce energy splittings. Their C I oscillator strengths are frequently used in the abundance analyses of cool stars (Section 5).

A number of other authors have also presented theoretical transition data for carbon. Zatsarinyi & Fischer (2002) calculated the oscillator strengths for transitions to high-lying excited states of C I using a spline frozen-cores (FCS) method. Nussbaumer & Storey (1984) provided the radiative transition probabilities using the *LS*- and intermediate-coupling approximations, respectively, for the six energetically lowest configurations of C I. Nussbaumer & Storey (1981) calculated the transition probabilities for C II, from terms up to  $2s^24f\ ^2F^o$ , using the *LS*- and close coupling approximation, respectively.

In view of the great astrophysical interest for large sets of homogeneous atomic data, extensive spectrum calculations of transition data in the carbon atom and carbon ions were carried out under the umbrella of the Opacity Project using the close coupling approximation of the R-matrix theory, and the results are available in the Opacity Project online data base (TOPbase, Cunto & Mendoza 1992; Cunto et al. 1993). The latest compilation of C I transition probabilities was made available by Haris & Kramida (2017), and

those of C II–IV can be found in earlier compilations by Wiese & Fuhr (2007a, b) and Fuhr (2006).

In this context, the General-purpose Relativistic Atomic Structure Package (GRASP) has, more recently, been used by Aggarwal & Keenan (2015) to predict the radiative decay rates and lifetimes of 166 levels belonging to the  $n \leq 5$  configurations in C III. Using an updated and extended version of this code (GRASP2K), J onsson et al. (2010) determined transition data involving 26 levels in C II.

Although for the past decades, a considerable amount of research has been conducted for carbon, there is still a need for extended sets of reliable theoretical transition data. To address this, we have carried out new calculations based on the fully relativistic Multiconfiguration Dirac–Hartree–Fock (MCDHF) and relativistic configuration interaction (RCI) methods, as implemented in the newest version of the GRASP code, GRASP2018 (J onsson et al. 2013; Fischer et al. 2019). We performed energy spectrum calculations for 100, 69, 114, and 53 states, in C I–IV, respectively. Electric dipole (E1) transition data (wavelengths, transition probabilities, line strengths, and oscillator strengths) were computed along with the corresponding lifetimes of these states.

This paper is structured into six sections, including the Introduction. Our theoretical methods are described in Section 2, and computational details are given in Section 3. In Section 4, we present our results and the validation of the data. As a complementary method of validation, in Section 5, we use the derived data in a re-analysis of the solar carbon abundance. Finally, we present our conclusions in Section 6.

## 2 THEORY

In the MCDHF method (Grant 2007; Fischer et al. 2016), wavefunctions for atomic states  $\gamma^{(j)} P J M$ ,  $j = 1, 2, \dots, N$  with angular momentum quantum numbers  $JM$  and parity  $P$  are expanded over  $N_{\text{CSFs}}$  configuration state functions (CSFs)

$$\Psi(\gamma^{(j)} P J M) = \sum_i^{N_{\text{CSFs}}} c_i^{(j)} \Phi(\gamma_i P J M). \quad (1)$$

The CSFs are *jj*-coupled many-electron functions, recursively built from products of one-electron Dirac orbitals. As for the notation,  $\gamma_i$  specifies the occupied subshells of the CSF with their complete angular coupling tree information. The radial large and small components of the one-electron orbitals and the expansion coefficients  $\{c_i^{(j)}\}$  of the CSFs are obtained, for a number of targeted states, by solving the Dirac–Hartree–Fock radial equations and the configuration interaction eigenvalue problem resulting from applying the variational principle on the statistically weighted energy functional of the targeted states with terms added for preserving the orthonormality of the one-electron orbitals. The energy functional is based on the Dirac–Coulomb (DC) Hamiltonian and accounts for relativistic kinematic effects.

Once the radial components of the one-electron orbitals are determined, higher order interactions, such as the transverse photon interaction and quantum electrodynamic (QED) effects (vacuum polarization and self-energy), are added to the DC Hamiltonian. Keeping the radial components fixed, the expansion coefficients  $\{c_i^{(j)}\}$  of the CSFs for the targeted states are obtained by solving the configuration interaction eigenvalue problem.

The evaluation of radiative E1 transition data (transition probabilities AND oscillator strengths) between two states:  $\gamma' P' J' M'$  and  $\gamma P J M$  is non-trivial. The transition data can be expressed in terms

of reduced matrix elements of the transition operator  $\mathbf{T}^{(1)}$ :

$$\langle \Psi(\gamma_j P J) \| \mathbf{T}^{(1)} \| \Psi(\gamma'_j P' J') \rangle = \sum_{j,k} c_j c'_k \langle \Phi(\gamma_j P J) \| \mathbf{T}^{(1)} \| \Phi(\gamma'_k P' J') \rangle, \quad (2)$$

where  $c_j$  and  $c'_k$  are, respectively, the expansion coefficients of the CSFs for the lower and upper states, and the summation occurs over all the CSFs for the lower and upper states. The reduced matrix elements are expressed via spin-angular coefficients  $d_{ab}^{(1)}$  and operator strengths as:

$$\langle \Phi(\gamma_j P J) \| \mathbf{T}^{(1)} \| \Phi(\gamma'_k P' J') \rangle = \sum_{a,b} d_{ab}^{(1)} \langle n_a l_a j_a \| \mathbf{T}^{(1)} \| n_b l_b j_b \rangle. \quad (3)$$

Allowing for the fact that we are now using Brink-and-Satchler type reduced matrix elements, we have

$$\langle n_a l_a j_a \| \mathbf{T}^{(1)} \| n_b l_b j_b \rangle = \left( \frac{(2j_b + 1)\omega}{\pi c} \right)^{1/2} (-1)^{j_a - 1/2} \begin{pmatrix} j_a & 1 & j_b \\ \frac{1}{2} & 0 & -\frac{1}{2} \end{pmatrix} \overline{M}_{ab}, \quad (4)$$

where  $\overline{M}_{ab}$  is the radiative transition integral defined by Grant (1974). The factor in front of  $\overline{M}_{ab}$  is the Wigner 3-j symbol that gives the angular part of the matrix element. The  $\overline{M}_{ab}$  integral can be written  $\overline{M}_{ab} = \overline{M}_{ab}^e + G \overline{M}_{ab}^l$ , where  $G$  is the gauge parameter. When  $G = 0$  we get the Coulomb gauge, whereas for  $G = \sqrt{2}$  we get the Babushkin gauge. The Babushkin gauge corresponds to the length gauge in the non-relativistic limit and puts weight on the outer part of the wavefunctions (Grant 1974; Hibbert 1974). The Coulomb gauge corresponds to the velocity gauge and puts more weight on the inner part of the wavefunctions (Papoulia et al. 2019). For E1 transitions, the Babushkin and Coulomb gauges give the same value of the transition moment for exact solutions of the Dirac equation (Grant 1974). For approximate solutions, the transition moments differ, and the quantity  $dT$ , defined as (Froese Fischer 2009; Ekman, Godefroid & Hartman 2014)

$$dT = \frac{|A_l - A_v|}{\max(A_l, A_v)}, \quad (5)$$

where  $A_l$  and  $A_v$  are transition rates in length and velocity form, can be used as an estimation of the uncertainty of the computed rate.

### 3 COMPUTATIONAL SCHEMES

Calculations were performed in the extended optimal level scheme (Dyall et al. 1989) for the weighted average of the even and odd parity states. The CSF expansions were determined using the multireference-single-double (MR-SD) method, allowing single and double (SD) substitutions from a set of important configurations, referred to as the MR, to orbitals in an active set (AS, Olsen et al. 1988; Stuesson, Jönsson & Froese Fischer 2007; Fischer et al. 2016). The orbitals in the AS are divided into spectroscopic orbitals, which build the configurations in the MR, and correlation orbitals, which are introduced to correct the initially obtained wavefunctions. During the different steps of the calculations for C I–IV, the CSF expansions were systematically enlarged by adding layers of correlation orbitals.

MCDHF calculations aim to generate an orbital set. The orbital set is then used in RCI calculations based on CSF expansions that can be enlarged to capture additional electron correlation effects. For the same CSF expansion, different orbital sets give different results for both energy levels and transition data. Conventionally, MCDHF calculations are performed for CSF expansions obtained by allowing

substitutions not only from the valence subshells, but also from the subshells deeper in the core, accounting for valence–valence (VV), core–valence (CV), and core–core (CC) electron correlation effects. Using orbital sets from such calculations, Pehlivan Rhodin et al. (2017) predicted large  $dT$  values for transitions between low-lying states and high Rydberg states, indicating substantial uncertainties in the corresponding transition data. For transitions involving high Rydberg states, it was shown that the velocity gauge gave the more accurate results, which is contradictory to the general belief that the length gauge is the preferred one (Hibbert 1974). Analysing the situation more carefully, Papoulia et al. (2019) found that correlation orbitals resulting from MCDHF calculations based on CSF expansions obtained by allowing substitutions from deeper subshells are very contracted in comparison with the outer Rydberg orbitals. As a consequence, the outer parts of the wavefunctions for the Rydberg states are not accurately described. Thus, the length form that probes the outer part of the wavefunctions does not produce trustworthy results, while the velocity form that probes the inner part of the wavefunctions yields more reliable transition rates. In the same work, the authors showed how transition rates that are only weakly sensitive to the choice of gauge can be obtained, by paying close attention to the CSF generation strategies for the MCDHF calculations.

In this work, following the suggestion by Papoulia et al. (2019), the MCDHF calculations were based on CSF expansions for which we impose restrictions on the substitutions from the inner subshells and obtain, as a consequence, correlation orbitals that overlap more with the spectroscopic orbitals of the higher Rydberg states, adding to a better representation of the outer parts of the corresponding wavefunctions. The MR and orbital sets for each atom and ion are presented in Table 1. The computational scheme, including CSF generation strategies, for each atom and ion is discussed in detail below. The MCDHF calculations were followed by RCI calculations, including the Breit interaction and leading QED effects.

#### 3.1 C I

As seen in Table 1, in the computations of neutral carbon, configurations with  $n = 7$  ( $l = s$ ); 6 ( $l = p, d$ ), which are not of direct relevance, were included in the MR set to obtain orbitals that are spatially extended, improving the quality of the outer parts of the wavefunctions of the higher Rydberg states. The MCDHF calculations were performed using CSF expansions that were produced by SD substitutions from the valence orbitals of the configurations in the MR to the active set of orbitals, with the restriction of allowing maximum one substitution from orbitals with  $n = 2$ . The  $1s^2$  core was kept closed and, at this point, the expansions of the atomic states accounted for VV electron correlation. As a final step, an RCI calculation was performed for the largest SD valence expansion augmented by a CV expansion. The CV expansion was obtained by allowing SD substitutions from the valence orbitals and the  $1s^2$  core of the configurations in the MR, with the restriction that there should be at most one substitution from  $1s^2$ . The numbers of CSFs in the final even and odd state expansions are, respectively, 14 941 842 and 15 572 953, distributed over the different  $J$  symmetries.

#### 3.2 C II

Similarly to the computations in C I, in the computations of the singly-ionized carbon, the configurations  $2s^2\{8s, 8p, 9s, 9p\}$ , which are not our prime targets, were included in the MR set (see also Table 1). In this manner, we generated orbitals that are localized farther from the atomic core. The MCDHF calculations were performed

**Table 1.** Summary of the computational schemes for C I–IV. The first column displays the configurations of the targeted states. MR and AS, respectively, denote the multireference and the active sets of orbitals used in the MCDHF and RCI calculations, and  $N_{\text{CSFs}}$  are the numbers of generated CSFs in the final RCI calculations, for the even (e) and the odd (o) parity states.

Targeted configurations	MR	AS	$N_{\text{CSFs}}$
C I, $N_{\text{levels}} = 100$			
$2s2p^3$	$2s2p^3$	{11s, 10p, 10d, 9f, 7g, 6h}	e: 14 941 842 o: 15 572 953
$2s^22p\{n_1s, n_2p, n_3d, 4f\}$ ( $3 \leq n_1 \leq 6, 2 \leq n_2 \leq 5, 3 \leq n_3 \leq 5$ )	$2s^22p\{n_1s, n_2p, n_3d, 4f\}$ ( $3 \leq n_1 \leq 6, 2 \leq n_2 \leq 6, 3 \leq n_3 \leq 5$ ) $2p^3\{n_1s, n_2p, n_3d\}$ ( $3 \leq n_1 \leq 6, 3 \leq n_2 \leq 5, 3 \leq n_3 \leq 6$ ) $2s2p^2\{3s, 3p, 4p, 6p, 6d, 7s\}$ $2s2p\{n_1s, n_2p, n_3d, 4f\}6d$ ( $3 \leq n_1 \leq 6, 3 \leq n_2 \leq 5, 3 \leq n_3 \leq 5$ )		
C II, $N_{\text{levels}} = 69$			
$2s^2nl(n \leq 6, l \leq 4)$	$2s2p^2, 2s^2\{n_1s, n_2p, n_3d, n_4f, n_5g\}$ ( $3 \leq n_1 \leq 9, 2 \leq n_2 \leq 9, 3 \leq n_3 \leq 7,$ $4 \leq n_4 \leq 7, 5 \leq n_5 \leq 6$ )	{14s, 14p, 12d, 12f, 10g, 8h}	e: 6 415 798 o: 4 988 973
$2s^27l(l \leq 3)$	$2p^3, 2p^2\{n_1s, n_2p, n_3d, n_4f, n_5g\}$ ( $3 \leq n_1 \leq 9, 4 \leq n_2 \leq 9, 3 \leq n_3 \leq 7,$ $4 \leq n_4 \leq 7, 5 \leq n_5 \leq 6$ )		
$2s2p^2, 2p^3,$ $2s2p3s, 2s2p3p$	$2s2p3s, 2s2p3p$		
C III, $N_{\text{levels}} = 114$			
$2snl(n \leq 7, l \leq 4)$	$2snl(n \leq 7, l \leq 4)$	{12s, 12p, 12d, 12f, 11g, 8h}	e: 1 578 620 o: 1 274 147
$2p^2, 2p\{3s, 3p, 3d\}$	$2p^2, 2p\{3s, 3p, 3d\}$		
C IV, $N_{\text{levels}} = 53$			
$1s^2nl(n \leq 8, l \leq 4)$	$1s^2nl(n \leq 8, l \leq 4)$	{14s, 14p, 14d, 12f, 12g, 8h, 7i}	e: 1 077 872 o: 1 287 706
$1s^26h$	$1s^26h$		

using CSF expansions obtained by allowing SD substitutions from the valence orbitals of the MR configurations. During this stage, the  $1s^2$  core remained frozen and the CSF expansions accounted for VV correlation. The final wavefunctions of the targeted states were determined in an RCI calculation, which included CSF expansions that were formed by allowing SD substitution from all subshells of the MR configurations, with the restriction that there should be at most one substitution from the  $1s^2$  core. The numbers of CSFs in the final even and odd state expansions are, respectively, 6 415 798 and 4 988 973, distributed over the different  $J$  symmetries.

### 3.3 C III

In the computations of beryllium-like carbon, the MR simply consisted of the targeted configurations (see also Table 1). The CSF expansions used in the MCDHF calculations were obtained by allowing SD substitutions from the valence orbitals, accounting for VV correlation effects. The final wavefunctions of the targeted states were determined in subsequent RCI calculations, which included CSFs that were formed by allowing single, double, and triple (SDT) substitutions from all orbitals of the MR configurations, with the limitation of leaving no more than one hole in the  $1s^2$  atomic core. The final even and odd state expansions, respectively, contained 1 578 620 and 1 274 147 CSFs, distributed over the different  $J$  symmetries.

### 3.4 C IV

Likewise the computations in C III, the MR in the computations of lithium-like carbon was solely represented by the targeted configurations (see also Table 1). In the MCDHF calculations, the CSF

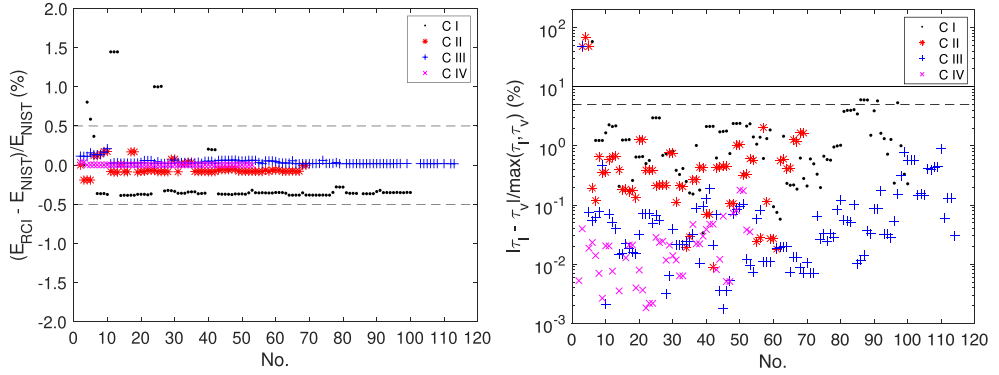
expansions were acquired by implementing SD electron substitutions from the configurations in the MR, with the restriction of allowing maximum one hole in the  $1s^2$  core. In this case, the shape of the correlation orbitals was established by CSFs accounting for valence (V) and CV correlation effects. In the subsequent RCI calculations, the CSF expansions were enlarged by enabling all SDT substitutions from the orbitals in the MR to the active set of orbitals. The final expansions of the atomic states gave rise to 1 077 872 CSFs with even parity and 1 287 706 CSFs with odd parity, respectively, shared among the different  $J$  symmetry blocks.

## 4 RESULTS

The energy spectra and wavefunction composition in  $LS$ -coupling for the 100, 69, 114, and 53 lowest states, respectively, for C I–IV are given in Table A1. In the tables, the states are given with unique labels (Gaigalas et al. 2017), and the labelling is determined by the CSFs with the largest coefficient in the expansion of equation (1). We first summarize the results here, before discussing the individual ions in detail in Sections 4.1–4.4, below.

The accuracy of the wavefunctions from the present calculations was evaluated by comparing the calculated energy levels with experimental data provided via the National Institute of Standards and Technology (NIST) Atomic Spectra Database (Kramida et al. 2019). In the left-hand panel of Fig. 1, energy levels computed in this work are compared with the NIST data. A closer inspection of the figure reveals that the relative discrepancies between the experimental and the computed in this work energies are, in most cases, about  $-0.35$  per cent,  $-0.08$  per cent,  $0.03$  per cent, and  $0.003$  per cent,





**Figure 1.** Left-hand panel: comparison of computed energy levels in this work with data from the NIST data base, for C I–IV. The dashed lines indicate the  $-0.5$  per cent and  $0.5$  per cent relative discrepancies. Right-hand panel: the relative differences between the lifetimes in length and velocity forms, for C I–IV. The dashed and solid lines indicate the 5 per cent and 10 per cent relative differences, respectively. No., as label in the  $x$ -axis, corresponds to the numbers in Table A1.

respectively, for C I–IV. Only for levels of the  $2s2p^3$  configuration in C I, the disagreements are larger than 1.0 per cent. The average difference of the computed energy levels relative to the energies from the NIST data base is 0.41 per cent, 0.081 per cent, 0.041 per cent, and 0.0044 per cent, respectively, for C I–IV. In Table A1, lifetimes in length and velocity gauges are also presented. The right-hand panel of Fig. 1 presents the relative differences between the lifetimes in length and velocity forms for C I–IV. Except for a few long-lived states that can decay to the ground state only through IC transitions, the relative differences are well below 5 per cent.

The accuracy of calculated transition rates can be estimated either by comparisons with other theoretical works and experimental results, when available, or by the quantity  $dT$ , which is defined in equation (5) as the agreement between the values in length and velocity gauges (Froese Fischer 2009; Ekman et al. 2014). The latter is particularly useful when no experimental measurements are available. Transition data, for example, wavenumbers, wavelengths, line strengths, weighted oscillator strengths, transition probabilities of E1 transitions, and the accuracy indicators  $dT$ , are given in Tables A2–A5, respectively, for C I–IV. Note that the wavenumbers and wavelengths are adjusted to match the level energy values in the NIST data base, which are critically evaluated by Haris & Kramida (2017) for C I and Moore & Gallagher (1993) for C II–IV. When no NIST values are available, the wavenumbers and wavelengths are from the present MCDHF/RCI calculations and marked with \* in the tables.

To better display the uncertainties  $dT$  of the computed transition rates and their distribution in relation to the magnitude of the transition rate values  $A$ , the transitions are organized in five groups based on the magnitude of the  $A$  values. A statistical analysis of the uncertainties  $dT$  of the transitions is performed for the 1553, 806, 1805, and 386 E1 transitions, respectively, for C I–IV. In Table 2, the mean value of the uncertainties ( $dT$ ) and standard deviations  $\sigma$  are given for each group of transitions. As seen in Table 2, most of the estimated uncertainties  $dT$  are well below 10 per cent. Most of the strong transitions with  $A > 10^6 \text{ s}^{-1}$  are associated with small uncertainties  $dT$ , less than 2 per cent, especially for C III and C IV, for which ( $dT$ ) is 0.297 per cent ( $\sigma = 0.01$ ) and 0.205 per cent ( $\sigma = 0.0041$ ), respectively. It is worth noting that, by employing the alternative optimization scheme of the radial orbitals in the present calculations, the uncertainties

$dT$  for transitions involving high Rydberg states are significantly reduced.

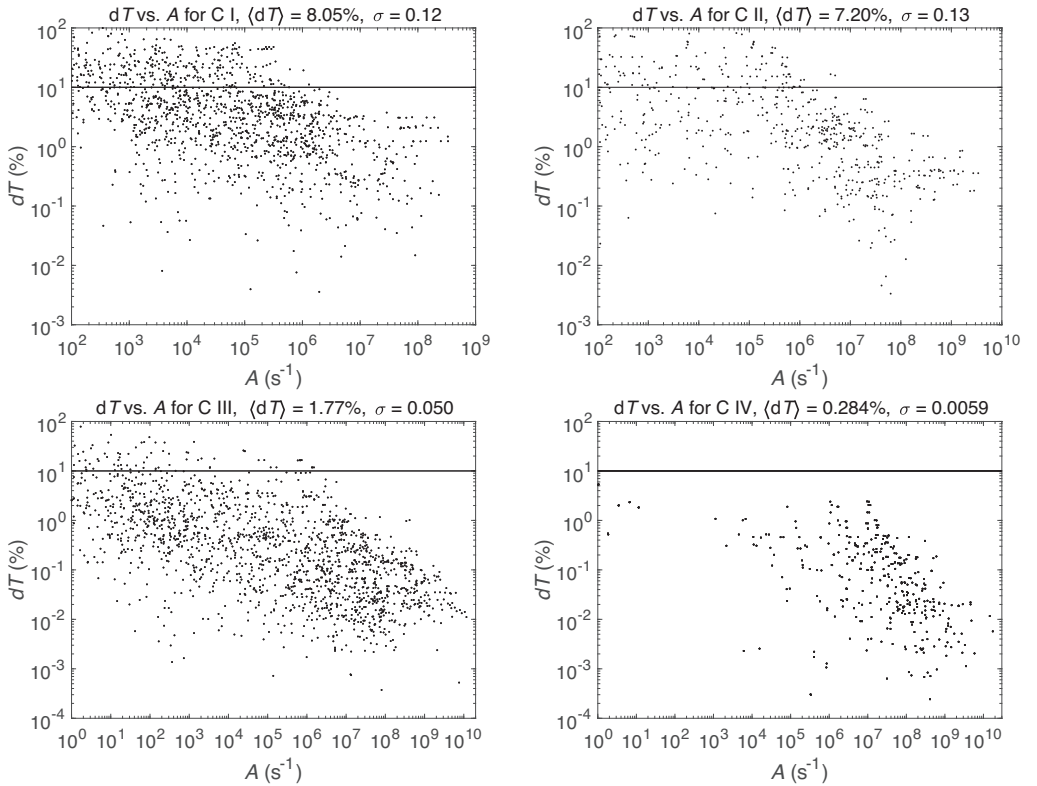
Contrary to the strong transitions, the weaker transitions are associated with relatively large  $dT$  values. This is even more pronounced for the first two groups of transitions in C I and C II, where  $A$  is less than  $10^2 \text{ s}^{-1}$ . These weak E1 transitions are either IC or two-electron one-photon transitions. The rates of the former transitions, in relativistic calculations, are small due to the strong cancellation contributions to the transition moment (Ynnerman & Fischer 1995), whereas the rates of the latter transitions are identically zero in the simplest approximation of the wavefunction and only induced by correlation effects (Bogdanovich, Karpuškiene & Rancova 2007; Li et al. 2010). These types of transitions are extremely challenging, and therefore interesting from a theoretical point of view, and improved methodology is needed to further decrease the uncertainties of the respective transition data.

Fortunately, the weak transitions tend to be of lesser astrophysical importance, either for opacity calculations, or for spectroscopic abundance analyses. Thus, only the transitions with  $A \geq 10^2 \text{ s}^{-1}$  for C I and C II, and  $A \geq 10^0 \text{ s}^{-1}$  for C III and C IV, are discussed in the paper; although the complete transition data tables, for all computed E1 transitions in C I–IV, are available online. The scatterplots of  $dT$  versus  $A$  are given in Fig. 2. The mean  $dT$  for all presented E1 transitions shown in Fig. 2 is 8.05 per cent ( $\sigma = 0.12$ ), 7.20 per cent ( $\sigma = 0.13$ ), 1.77 per cent ( $\sigma = 0.05$ ), and 0.28 per cent ( $\sigma = 0.0059$ ), respectively, for C I–IV. A statistical analysis of the proportions of the transitions with  $dT$  less than 20 per cent, 10 per cent, and 5 per cent in all the presented E1 transitions is also performed and shown in the last three rows of Table 2.

Finally, this work can be compared with other theoretical calculations. In Fig. 3,  $\log gf$  values from this work are compared with results from MCHF-BP (Fischer 2006; Tachiev & Fischer 2000, 1999; Fischer et al. 1998), CIV3 (Hibbert et al. 1993; Corrége & Hibbert 2004), and TOPbase data (Cunto & Mendoza 1992), when available. As shown in the figure, the differences between the  $\log gf$  values computed in this work and respective results from other sources are rather small for most of the transitions. Comparing the MCDHF/RCI results with those from CIV3 calculations by Hibbert et al. (1993), which are frequently used in the abundance analyses, 292(228) out of 378 transitions are in agreement within 20 per cent

**Table 2.** Distribution of the uncertainties  $dT$  (in per cent) of the computed transition rates in C I–IV depending on the magnitude of the rates. The transition rates are arranged in five groups based on the magnitude of the  $A$  values (in  $s^{-1}$ ). The number of transitions, No., the mean  $dT$ ,  $\langle dT \rangle$ , (in per cent), and the standard deviations,  $\sigma$ , are given for each group of transitions, in C I–IV, respectively. The last three rows show the proportions (in percentages) of the transitions with  $dT$  less than 20 per cent, 10 per cent, and 5 per cent in all the transitions with  $A \geq 10^2 s^{-1}$  for C I and C II and  $A \geq 10^0 s^{-1}$  for C III and C IV, respectively.

Group	C I			C II			C III			C IV		
	No.	$\langle dT \rangle$ (per cent)	$\sigma$	No.	$\langle dT \rangle$ (per cent)	$\sigma$	No.	$\langle dT \rangle$ (per cent)	$\sigma$	No.	$\langle dT \rangle$ (per cent)	$\sigma$
$<10^0$	62	52.6	0.34	80	29.6	0.32	137	10.8	0.18	20	5.92	0.061
$10^0$ – $10^2$	156	34.0	0.25	134	17.1	0.24	239	5.57	0.096	10	2.38	0.017
$10^2$ – $10^4$	451	13.2	0.15	128	14.4	0.19	354	2.48	0.050	6	0.667	0.0047
$10^4$ – $10^6$	600	7.20	0.11	167	11.8	0.15	360	1.44	0.034	43	0.267	0.0035
$>10^6$	284	1.68	0.020	297	1.53	0.023	715	0.297	0.010	307	0.205	0.0041
$dT < 20$ per cent		87.4			89.5			98.4			100	
$dT < 10$ per cent		77.3			80.7			95.7			100	
$dT < 5$ per cent		62.0			68.7			91.7			99.4	

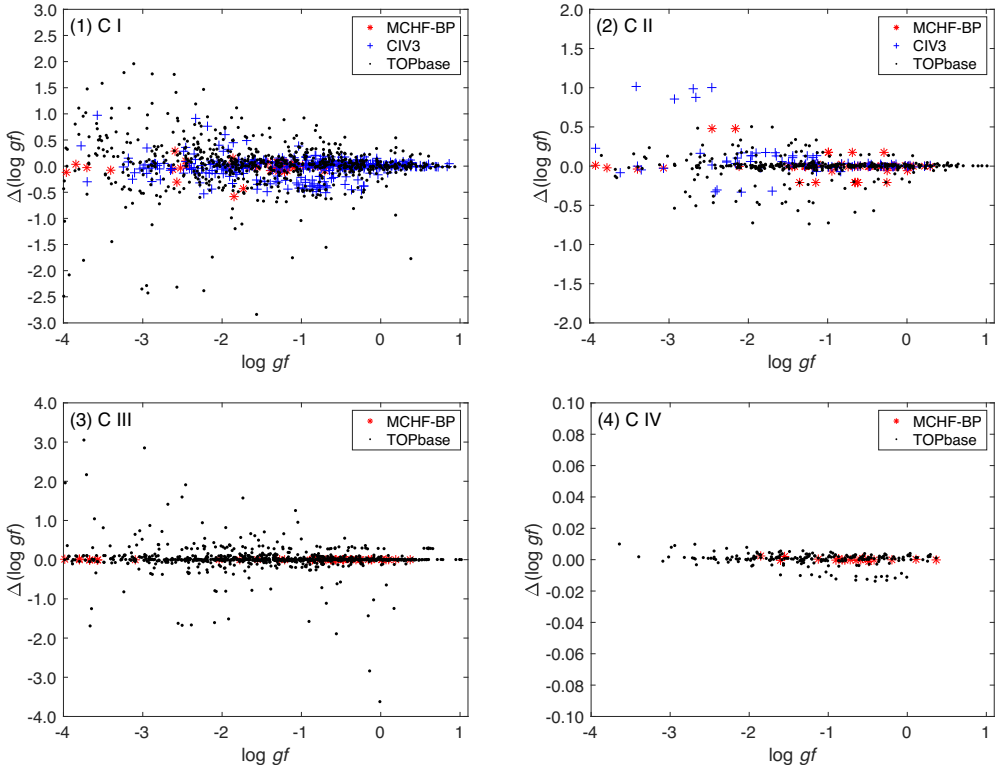


**Figure 2.** Scatterplot of  $dT$  values versus transition rates  $A$  of E1 transitions, for C I–IV. The solid lines indicate the 10 per cent relative agreement between the length and velocity gauges.

(10 per cent) for C I, and 78(66) out of 87 transitions are within the same range for C II. The results from the MCDHF/RCI and MCHF-BP calculations are found to be in very good agreement for C III–IV, with the relative differences being less than 5 per cent for all the computed transitions. More details about the comparisons with other theoretical calculations, as well as with experimental results, are given in Sections 4.1–4.4.

#### 4.1 C I

The computed excitation energies, given in Table A1, are compared with results from NIST (Kramida et al. 2019). With the exception of the levels belonging to the  $2s2p^3$  configuration, for which the average relative difference between theory and experiment is 1.22 per cent, the mean relative difference for the rest of the states is 0.35 per cent.



**Figure 3.** Differences between the calculated  $\log gf$  values in this work and results from other theoretical calculations: MCHF-BP (red asterisk), CIV3 (blue plus sign), and TOPbase (black point), for C I–IV.

The complete transition data, for all computed E1 transitions in C I, can be found in Table A2. Based on the statistical analysis of the uncertainties  $dT$  shown in Table 2, out of the 1335 transitions with  $A \geq 10^2 \text{ s}^{-1}$ , the proportions of the transitions with  $dT$  less than 20 per cent, 10 per cent, and 5 per cent are, respectively, 87.4 per cent, 77.3 per cent, and 62.0 per cent.

In C I, experimental transition data are available for the  $2p3p \rightarrow 2p3s$ ,  $2p3d \rightarrow 2p3p$ , and  $2p4s \rightarrow 2p3p$  transition arrays using a stabilized arc source (Musielok et al. 1997; Golly et al. 2003; Bacawski et al. 2001). In Table A6, the experimental relative line strengths, together with their uncertainties, are compared with the present MCDHF/RCI theoretical values and with values from the non-relativistic CIV3 calculations by Hibbert et al. (1993) that included semi-empirical diagonal energy shifts by  $LS$  configuration in the interaction matrix in the determination of the wavefunctions. The estimated uncertainties  $dT$  of the MCDHF/RCI line strengths are given as percentages in parentheses. In most cases, the theoretical values fall into, or only slightly outside, the range of the estimated uncertainties of the experimental values.

Comparing the MCDHF/RCI results with the results from the CIV3 calculations by Hibbert et al. (1993), we see that 41 out of the 50 transitions in common are in good agreement, with the relative differences being less than 10 per cent (see Table A6). For the  $2p4s \ ^3P^o \rightarrow 2p3p \ ^3P$  transitions and the  $2p4s \ ^3P^o \rightarrow 2p3p \ ^3D_1$  transition, the  $S$  values deduced from the present MCDHF/RCI calculations differ substantially from the experimental values, that

is, by more than 20 per cent, while the values from the CIV3 calculations appear to be in better agreement with the corresponding experimental values. Based on the agreement between the length and velocity forms, the estimated uncertainties  $dT$  of the present MCDHF/RCI calculations for the above-mentioned transitions are of the order of 8.5 per cent and 1.4 per cent, respectively. For the  $2p3d \ ^3P^o \rightarrow 2p3p \ ^3P_1$ ,  $2p4s \ ^3P^o \rightarrow 2p3p \ ^3D_2$ , and  $2p3d \ ^3D_2^o \rightarrow 2p3p \ ^3D_3$  transitions, both theoretical results are outside the range of the estimated uncertainties of the experimental values. For the  $2p3d \ ^3D^o \rightarrow 2p3p \ ^3P$  transitions, the evaluated relative line strengths by Golly et al. (2003) slightly differ from the observations by Bacawski et al. (2001). The latter seem to be in better overall agreement with the transition rates predicted by the present calculations.

In Table A7, the computed line strengths and transition rates are compared with values from the spline FCS method by Zatsarinny & Fischer (2002) and the MCHF-BP calculations by Fischer (2006). Zatsarinny & Fischer (2002) presented oscillator strengths for transitions from the  $2p^2 \ ^3P$  term to high-lying excited states, while Fischer (2006) considered only transitions from  $2p^2 \ ^3P$ ,  $^1D$ , and  $^1S$  to odd levels up to  $2p3d \ ^3P^o$ . As seen in the table, the present MCDHF/RCI results seem to be in better agreement with the values from spline FCS calculations. 76 out of 98 transitions from Zatsarinny & Fischer (2002) agree with present values within 10 per cent, while only 38 out of 78 transitions from Fischer (2006) are within the same range. The relatively large differences with Fischer (2006) may be due

to the fact that limited electron correlations were included in their calculations. In the MCHF-BP calculations, two types of correlation, that is, VV, CV, have been accounted for; however, the CC correlation has not been considered. Additionally, CSF expansions obtained from SD substitutions are not as large as the CSF expansions used in the present calculations. For the majority of the strong transitions with  $A > 10^6 \text{ s}^{-1}$ , there is a very good agreement between the MCDHF/RCI results and the spline FCS values, with the relative difference being less than 5 per cent. On the other hand, for the  $2p3d \ ^3F \rightarrow 2p^2 \ ^3P$  and  $2p4s \ ^1P_1 \rightarrow 2p^2 \ ^3P$  transitions, the observed discrepancies between these three methods, that is, MCDHF/RCI, spline FCS, and MCHF-BP, are quite large. These transitions are all *LS*-forbidden transitions, the former is with  $\Delta L = 2$  and the latter is spin-forbidden transition; these types of transitions are challenging for computations and are always with large uncertainties. For example, for the  $2p3d \ ^3F_3 \rightarrow 2p^2 \ ^3P_2$  transition, the  $A$  values from MCDHF/RCI, spline FCS, and MCHF-BP calculations are, respectively,  $7.92\text{E}+06$ ,  $6.24\text{E}+06$ , and  $1.14\text{E} + 07 \text{ s}^{-1}$ , with the relative difference between each two of them being greater than 20 per cent. Experimental data are, therefore, needed for validating these theoretical results. On the contrary, based on the agreement between the length and velocity forms displayed in the parentheses, the estimated uncertainties of the MCDHF/RCI calculations for the above-mentioned transitions are all less than 0.5 per cent.

#### 4.2 C II

The relative differences between theory and experiment for all the energy levels of  $2s2p^2$  are 0.16 per cent, while the mean relative difference for the rest of the states is 0.071 per cent (see Table A1). The complete transition data, for all computed E1 transitions in C II, can be found in Table A3. Out of the presented 592 E1 transitions with  $A \geq 10^2 \text{ s}^{-1}$ , the proportions of the transitions with  $dT$  less than 20 per cent, 10 per cent, and 5 per cent are, respectively, 89.5 per cent, 80.7 per cent, and 68.7 per cent.

In Table A6, the lifetimes from the present MCDHF/RCI calculations are compared with available results from the MCHF-BP calculations by Tachiev & Fischer (2000) and observations by Reistad et al. (1986) and Träbert et al. (1999). Träbert et al. (1999) measured lifetimes for the three fine-structure components of the  $2s2p^2 \ ^4P$  term in an ion storage ring. For the measured lifetimes by Reistad et al. (1986) of the doublets terms using the beam-foil technique, a single value for the two fine-structure levels is provided. It can be seen that, in all cases, the MCDHF/RCI computed lifetimes agree with the experimental values by Reistad et al. (1986) within the experimental errors. For the  $2s2p^2 \ ^4P_{1/2, 3/2, 5/2}$  states, as discussed in Introduction, the discrepancies between the measured transition rates by Fang et al. (1993) and by Träbert et al. (1999) are quite large. It is found that the MCDHF/RCI values are in better agreement with the results given by the latter measurements, with a relative difference less than 3 per cent. For these long-lived states, the measured lifetimes are better represented by the MCDHF/RCI results than by the MCHF-BP values.

The computed line strengths and transition rates are compared with values from the MCHF-BP calculations by Tachiev & Fischer (2000) and the CIV3 calculations by Corrége & Hibbert (2004) in Table A8. We note that the agreement between the present MCDHF/RCI and the MCHF-BP transition rates exhibits a broad variation. In the earlier MCHF-BP and our MCDHF/RCI calculations, the same correlation effects, that is, VV and CV, have been accounted for. However, the CSF expansions obtained from SD substitutions in the MCHF-BP calculations are not as large as the CSF expansions used in the present calculations, and as a consequence, the *LS*-composition of the configurations might not be predicted as accurately in the former

calculations. The MCDHF/RCI results seem to be in better overall agreement with the values from the CIV3 calculations, except for transitions from  $2p^3 \ ^2P^o$  to  $2s2p^2 \ \{^1P, ^2S\}$  and to  $2s^23d \ ^2D$ . For these transitions, involving  $2p^3 \ ^2P^o$  as the upper level, the transition rates  $A$  are of the order of  $10^2$ – $10^4 \text{ s}^{-1}$ . The  $dT$  values are relatively large in the present calculations. This is due to the strong cancellation effects caused by, for example, the strong mixing between the  $2p^3 \ ^2P^o$  and  $2s2p3s \ ^2P^o$  levels for  $2p^3 \ ^2P^o \rightarrow 2s2p^2 \ ^2S$ , and the mixing between the  $2p^3 \ ^2P^o$  and  $2s^24p \ ^2P^o$  levels for  $2p^3 \ ^2P^o \rightarrow 2s^23d \ ^2D$ . Large discrepancies are also observed between the MCDHF/RCI and MCHF-BP results, as well as between the MCHF-BP and CIV3 results for these transitions. Experimental data are, therefore, crucial for validating the aforementioned theoretical results. On the contrary, for the majority of the strong transitions with  $A > 10^6 \text{ s}^{-1}$ , there is a very good agreement between the MCDHF/RCI results and those from the two previous calculations, with the relative differences being less than 5 per cent.

#### 4.3 C III

The average relative discrepancy between the computed excitation energies, shown in Table A1, and the NIST recommended values is 0.041 per cent. The complete transition data, for all computed E1 transitions in C III, can be found in Table A4. Out of the 1668 transitions with  $A \geq 10^0 \text{ s}^{-1}$ , 91.7 per cent (98.4 per cent) of them have  $dT$  values less than 5 per cent (20 per cent). Further, the mean  $dT$  for all transitions with  $A \geq 10^0 \text{ s}^{-1}$  is 1.8 per cent with  $\sigma = 0.05$ .

The lifetimes of the  $2s2p \ ^1P_1$ ,  $2p^2 \ \{^1S_0, ^1D_2\}$ , and  $2s3s \ ^1S_0$  states were measured by Reistad et al. (1986) using the beam-foil technique, and the oscillator strengths for the  $2s2p \ ^1P_1 \rightarrow 2s^2 \ ^1S_0$  and  $2p^2 \ \{^1S_0, ^1D_2\} \rightarrow 2s2p \ ^1P_1$  transitions were also provided. Table A6 gives the comparisons between the observed and computed oscillator strengths and lifetimes in C III. Looking at the table, we see an excellent agreement between the present calculations and those from the MCHF-BP calculations (Tachiev & Fischer 1999) with the relative difference being less than 0.7 per cent. In all cases, the computed oscillator strengths and lifetimes agree with experiment within the experimental errors. The exceptions are the oscillator strength of the  $2p^2 \ ^1S_0 \rightarrow 2s2p \ ^1P_1$  transition and the lifetime of the  $2p^2 \ ^1S_0$  state, for which the computed values slightly differ from the observations.

In Table A9, the computed line strengths and transition rates are compared with values from the MCHF-BP calculations by Tachiev & Fischer (1999) and the GRASP calculations by Aggarwal & Keenan (2015). For the majority of the transitions, there is an excellent agreement between the MCDHF/RCI and MCHF-BP values with the relative differences being less than 1 per cent. Only 4 out of 60 transitions display discrepancies that are greater than 20 per cent. These large discrepancies are observed for the IC transitions, for example,  $2s3d \ ^3D_2 \rightarrow 2s2p \ ^1P_1$  and  $2s3d \ ^3D_2 \rightarrow 2s2p \ ^1P_1$ , for which the  $dT$  is relatively large. The discrepancies between the MCDHF/RCI and GRASP values are overall large; this is due to the fact that limited electron correlations were included in their calculations. Based on the excellent agreement between the MCDHF/RCI and MCHF-BP results as well as with experiment, we believe that the present transition rates together with the MCHF-BP transition data are more reliable than the ones provided by Aggarwal & Keenan (2015).

#### 4.4 C IV

The mean relative discrepancy between the computed excitation energies, given in Table A1, and the NIST values is 0.0044 per cent. Out of the presented 366 transitions with  $A \geq 10^0 \text{ s}^{-1}$  shown in Table A5, only two of them have  $dT$  values greater than 5 per cent;

**Table 3.** The 14 permitted C I lines used as abundance diagnostics in Amarsi et al. (2019). Shown are the upper and lower configurations, oscillator strengths obtained from the present calculations, and oscillator strengths from NIST; the latter being based on the calculations from CIV3 (Hibbert et al. 1993). The estimated uncertainties  $dT$  of the oscillator strengths are given as percentages in parentheses. The final two columns show the abundances derived in Amarsi et al. (2019), and the post-corrected values derived here based on the formula  $\Delta \log \epsilon_C^{\text{line}} = -\Delta \log gf^{\text{line}}$ .

Upper	Lower	$\lambda_{\text{air}}(\text{nm})$	NIST	$\log gf$		$\log \epsilon_C^{\text{A19}}$	$\log \epsilon_C^{\text{L20}}$
				MCDHF/RCI( $dT$ , per cent)			
2p4p $^1D_2$	2p3s $^1P_1^o$	505.217	-1.30	-1.36(0.8)	8.41	8.47	
2p4p $^1P_1$	2p3s $^1P_1^o$	538.034	-1.62	-1.71(1.4)	8.43	8.52	
2p4d $^1P_1^o$	2p3p $^1P_1$	658.761	-1.00	-1.05(0.2)	8.33	8.38	
2p4d $^3F_2^o$	2p3p $^3D_1$	711.148	-1.08	-1.24(0.9)	8.31	8.47	
2p4d $^3F_4^o$	2p3p $^3D_3$	711.318	-0.77	-0.94(1.5)	8.41	8.58	
2p3p $^3D_1$	2p3s $^3P_2^o$	1075.40	-1.61	-1.62(1.3)	8.49	8.50	
2p3d $^3F_2^o$	2p3p $^3D_2$	1177.75	-0.52	-0.46(0.9)	8.46	8.40	
2p3d $^3P_1^o$	2p3p $^3P_0$	1254.95	-0.57	-0.65(3.3)	8.51	8.59	
2p3d $^3P_0^o$	2p3p $^3P_1$	1256.21	-0.52	-0.61(3.3)	8.51	8.60	
2p3d $^3P_2^o$	2p3p $^3P_1$	1256.90	-0.60	-0.70(3.2)	8.46	8.56	
2p3d $^3P_2^o$	2p3p $^3P_1$	1258.16	-0.54	-0.61(3.4)	8.46	8.53	
2p3d $^1P_1^o$	2p3p $^1S_0$	2102.31	-0.40	-0.39(0.5)	8.47	8.46	
2p4p $^1D_2$	2p3d $^1F_3^o$	3085.46	+0.10	+0.07(0.2)	8.41	8.44	
2p4d $^1D_2^o$	2p4p $^1P_1$	3406.58	+0.44	+0.45(3.1)	8.47	8.46	

94.0 per cent of them with  $dT$  being less than 1 per cent. The mean  $dT$  for all transitions with  $A \geq 10^0 \text{ s}^{-1}$  is 0.28 per cent with  $\sigma = 0.0059$ .

For C IV, there are a number of measurements of transition properties. The transition rates of the  $2p \ ^2P_{1/2,3/2}^o \rightarrow 2s \ ^2S_{1/2}$  transitions were measured by Knystautas et al. (1971) using the beam-foil technique. By using the same technique, the lifetimes for a number of excited states were measured in four different experimental works (Donnelly et al. 1978; Buchet-Poulizac & Buchet 1973; Jacques et al. 1980; Peach, Saraph & Seaton 1988). In Table A6, we compare the theoretical results, from present calculations and MCHF-BP calculations, with the NIST recommended values and observed values. The transition rates of the  $2p \ ^2P_{1/2,3/2}^o \rightarrow 2s \ ^2S_{1/2}$  transitions from this work agree perfectly with the values from the MCHF-BP calculations by Fischer et al. (1998), while they are slightly smaller than the NIST data and the values by Knystautas et al. (1971). A comparison of the lifetimes of the  $\{3s, 4s, 2p, 3p, 4p, 3d, 4d, 5d\}$  states is made with other theoretical results, that is, from the MCHF-BP calculations and the Model Potential method. The agreements between these different theoretical results are better than 1 per cent for all these states. Furthermore, the agreement between the computed values and those from observations is also very good except for the  $3s \ ^2S_{1/2}$  level, for which the MCDHF/RCI calculations give a slightly smaller lifetime of 0.2350 ns than the observed value of  $0.25 \pm 0.01$  ns.

In Table A10, the computed line strengths and transition rates are compared with available values from the MCHF-BP calculations by Fischer et al. (1998). There is an excellent agreement between the two methods with the relative differences being less than 1 per cent for all transitions.

## 5 RE-ANALYSIS OF THE SOLAR CARBON ABUNDANCE

One can also attempt to verify the present atomic data empirically, in an astrophysical context. To demonstrate this, a solar carbon abundance analysis was carried out, based on permitted C I lines. Larger errors in the atomic data usually impart a larger dispersion

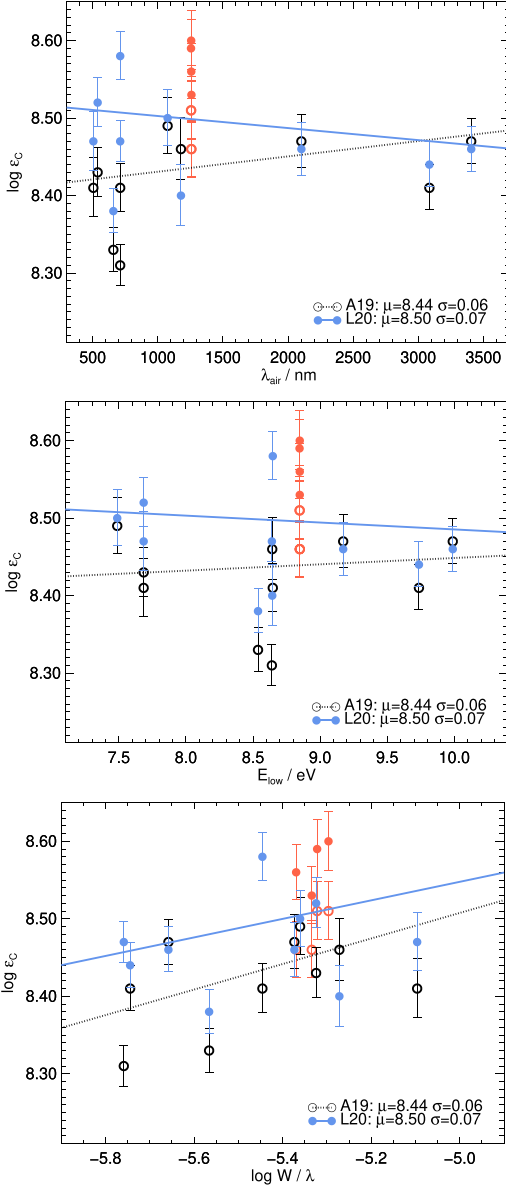
in the line-by-line abundance results, as well as trends in the results with respect to the line parameters.

The solar carbon abundance analysis recently presented in Amarsi et al. (2019) was taken as the starting point. Their analysis is based on equivalent widths measured in the solar disc-centre intensity, for 14 permitted C I lines in the optical and near-infrared, as well as a single forbidden [C I] line at 872.7 nm. Their analysis draws on a 3D hydrodynamic model solar atmosphere and 3D non-LTE radiative transfer, that reflects the current state-of-the-art in stellar elemental abundance determinations (e.g. Asplund et al. 2009). For the 14 permitted C I lines, the authors adopted transition probabilities from NIST, that are based on those of Hibbert et al. (1993) but normalized to a different scale (Haris & Kramida 2017), corresponding to differences of the order  $\pm 0.01$  dex.

Here, we post-correct the solar carbon abundances inferred in Amarsi et al. (2019) from the 14 permitted C I lines, using the new atomic data derived in the present study (see Table 3). To first order, for a given spectral line, the change in the inferred abundances are related to the difference in the adopted transition probabilities simply as  $\Delta \log \epsilon_C^{\text{line}} = -\Delta \log gf^{\text{line}}$ . We briefly note that second-order effects on the inferred abundances, propagated forward from changes to the non-LTE statistical equilibrium when adopting the full set of new  $\log gf$  data in the non-LTE model atom, were also tested; these were found to be negligible.

The results of this post-correction are illustrated in Fig. 4. We find that the dispersion in the line-by-line abundance results are similar when using the new and the old sets of  $\log gf$  data. We also find that the trends in the results with respect to the line parameters are of similar gradients. This is consistent with the finding in Section 4.1, that the precision of this new, much larger atomic data set is comparable to that of Hibbert et al. (1993).

This new analysis implies a solar carbon abundance of 8.50 dex, which is 0.06 dex larger than that inferred in Amarsi et al. (2019) from C I lines, and 0.07 dex larger than the current standard value from Asplund et al. (2009) that is based on C I lines as well as on molecular diagnostics. This increase in the mean abundance is due to 12 of the 14 permitted C I lines having lower oscillator strengths in the present calculations, compared to the NIST data set. Six of the lines give



**Figure 4.** Inferred solar carbon abundances. Black points (A19) are the 3D non-LTE results of Amarsi et al. (2019) for 14 permitted C I lines. Blue points (L20) are these same results but post-corrected using the new  $\log gf$  data. Error bars reflect  $\pm 5$  per cent uncertainties in the measured equivalent widths as stipulated by those authors. The four lines between 1254 and 1259 nm discussed in the text have been highlighted in red. The unweighted means  $\mu$  (including all 14 lines) and the standard deviations of the samples  $\sigma$  are stated in each panel.

results that are larger than the mean ( $\log \varepsilon \geq 8.51$ ); included in this set are all four of the lines between 1254 and 1259 nm, which give rise to values of between 8.53 and 8.60 dex. These four lines have the same upper level configuration,  $2p3d^3P^o$ , and a closer inspection of the *LS*-composition reveals that these states are strongly mixed (of the order of 26 per cent) with  $2s2p^3^3P^o$  states, which are less accurately described in the present calculations. As a consequence, as shown in Table 3, these transitions appear to be associated with slightly larger uncertainties  $dT$  than most of the other lines. Omitting these four lines, or adopting NIST oscillator strengths for them, would reduce the mean abundance from 8.50 to 8.47 dex.

Given that the scatter and trends in the results do not support one set of data over the other, we refrain from advocating a higher solar carbon abundance at this point. Nevertheless, this quite drastic change in the resulting solar carbon abundance highlights the importance of having accurate atomic data for abundance analyses. This is especially relevant in the context of the solar modelling problem, wherein standard models of the solar interior, adopting the solar chemical composition of Asplund et al. (2009), fail to reproduce key empirical constraints, including the depth of the convection zone and interior sound speed that are precisely inferred from helioseismic observations (Basu & Antia 2008; Zhang, Li & Christensen-Dalsgaard 2019). Extra opacity in the solar interior near the boundary of the convection zone would resolve the problem (Bailey et al. 2015). Carbon contributes about 5 per cent of the opacity in this region (Blancard, Cossé & Faussurier 2012), so a higher carbon abundance would help alleviate the problem, albeit only very slightly.

## 6 CONCLUSIONS

In this work, energy levels and transition data of E I transitions are computed for C I–IV using the MCDHF and RCI methods. Special attention is paid to the computation of transition data involving high Rydberg states by employing an alternative orbital optimization approach.

The accuracy of the predicted excitation energies is evaluated by comparing with experimental data provided by the NIST data base. The average relative differences of the computed energy levels compared with the NIST data are 0.41 per cent, 0.081 per cent, 0.041 per cent, and 0.0044 per cent, respectively, for C I–IV. The accuracy of the transition data is evaluated based on the relative differences of the computed transition rates in the length and velocity gauges, which is given by the quantity  $dT$ , and by extensive comparisons with previous theoretical and experimental results. For most of the strong transitions in C I–IV, the  $dT$  values are less than 5 per cent. The mean  $dT$  for all presented E I transitions are 8.05 per cent ( $\sigma = 0.12$ ), 7.20 per cent ( $\sigma = 0.13$ ), 1.77 per cent ( $\sigma = 0.050$ ), and 0.28 per cent ( $\sigma = 0.0059$ ), respectively, for C I–IV. Particularly, for strong transitions with  $A > 10^6 \text{ s}^{-1}$ , the mean  $dT$  is 1.68 per cent ( $\sigma = 0.020$ ), 1.53 per cent ( $\sigma = 0.023$ ), 0.297 per cent ( $\sigma = 0.010$ ), and 0.205 per cent ( $\sigma = 0.0041$ ), respectively, for C I–IV. By employing alternative optimization schemes of the radial orbitals, the uncertainties  $dT$  of the computed transition data for transitions involving high Rydberg states are significantly reduced. The agreement between computed transition properties, for example, line strengths, transition rates, and lifetimes, and experimental values is overall good. The exception is the weak transitions, e.g. the IC transitions, for which the strong cancellation effects are important; however, these effects cannot be properly considered in the present calculations. The present calculations are extended to high Rydberg



states that are not covered by previous accurate calculations and this is of special importance in various astrophysical applications.

The accurate and extensive sets of atomic data for C I–IV are publicly available for use by the astronomy community. These data should be useful for opacity calculations and for models of stellar structures and interiors. They should also be useful to non-LTE spectroscopic analyses of both early- and late-type stars.

## ACKNOWLEDGEMENTS

This work is supported by the Swedish Research Council under contracts 2015-04842, 2016-04185, 2016-03765, and 2020-03940, and by the Knut and Alice Wallenberg Foundation under the project grant KAW 2013.0052. Some of the computations were enabled by resources provided by the Swedish National Infrastructure for Computing (SNIC) at the Multidisciplinary Center for Advanced Computational Science (UPPMAX) and at the High Performance Computing Center North (HPC2N) partially funded by the Swedish Research Council through grant agreement no. 2018-05973. This work was also supported by computational resources provided by the Australian Government through the National Computational Infrastructure (NCI) under the National Computational Merit Allocation Scheme (NCMAS), under project y89. We thank Nicolas Grevesse for insightful comments on an earlier version of this manuscript. We would also like to thank the anonymous referee for her/his useful comments that helped improve the original manuscript.

## DATA AVAILABILITY

The full tables of energy levels (Table A1) and transition data (Tables A2–A5) are available in the online Supporting Information.

## REFERENCES

Aggarwal K. M., Keenan F. P., 2015, *MNRAS*, 450, 1151  
 Alexeeva S., Sadakane K., Nishimura M., Du J., Hu S., 2019, *ApJ*, 884, 150  
 Amarsi A. M., Barklem P. S., Collet R., Grevesse N., Asplund M., 2019, *A&A*, 624, A111  
 Asplund M., Grevesse N., Sauval A. J., Scott P., 2009, *ARA&A*, 47, 481  
 Bacawski A., Wujec T., Musielok J., 2001, *Phys. Scr.*, 64, 314  
 Bailey J. E. et al., 2015, *Nature*, 517, 56  
 Basu S., Antia H. M., 2008, *Phys. Rep.*, 457, 217  
 Berkner K., Cooper W., Kaplan S., Pyle R., 1965, *Phys. Lett.*, 16, 35  
 Blancard C., Cossé P., Faussurier G., 2012, *ApJ*, 745, 10  
 Bogdanovich P., Karpuškiene R., Rancova O., 2007, *Phys. Scr.*, 75, 669  
 Boldt G., 1963, *Z. Nat. Teil A*, 18, 1107  
 Buchet-Poullizac M. C., Buchet J. P., 1973, *Phys. Scr.*, 8, 40  
 Caffau E., Ludwig H. G., Bonifacio P., Faraggiana R., Steffen M., Freytag B., Kamp I., Ayres T. R., 2010, *A&A*, 514, A92  
 Chen X. et al., 2020, *ApJ*, 889, 157  
 Corrége G., Hibbert A., 2004, *At. Data Nucl. Data Tables*, 86, 19  
 Cunto W., Mendoza C., 1992, *Rev. Mex. Astron. Astrofis.*, 23, 107  
 Cunto W., Mendoza C., Ochsenbein F., Zeippen C. J., 1993, *A&A*, 275, L5  
 Doerfert J., Träbert E., Wolf A., Schwalm D., Uwira O., 1997, *Phys. Rev. Lett.*, 78, 4355  
 Donnelly K. E., Kernahan J. A., Pinnington E. H., 1978, *J. Opt. Soc. Am.*, 68, 1000  
 Dyall K., Grant I., Johnson C., Parpia F., Plummer E., 1989, *Comput. Phys. Commun.*, 55, 425  
 Ekman J., Godefroid M., Hartman H., 2014, *Atoms*, 2, 215  
 Fang Z., Kwong V. H. S., Wang J., Parkinson W. H., 1993, *Phys. Rev. A*, 48, 1114  
 Federman S. R., Zsargo J., 2001, *ApJ*, 555, 1020

Fischer C. F., 1994, *Phys. Scr.*, 49, 323  
 Fischer C. F., 2000, *Phys. Scr.*, 62, 458  
 Fischer C. F., 2006, *J. Phys. B: At. Mol. Opt. Phys.*, 39, 2159  
 Fischer C. F., Tachiev G., 2004, *At. Data Nucl. Data Tables*, 87, 1  
 Fischer C., Saporov M., Gaigalas G., Godefroid M., 1998, *At. Data Nucl. Data Tables*, 70, 119  
 Fischer C. F., Godefroid M., Brage T., Jönsson P., Gaigalas G., 2016, *J. Phys. B: At. Mol. Opt. Phys.*, 49, 182004  
 Fischer C. F., Gaigalas G., Jönsson P., Bieroń J., 2019, *Comput. Phys. Commun.*, 237, 184  
 Fleming J., Hibbert A., Stafford R. P., 1994, *Phys. Scr.*, 49, 316  
 Foster E. W., 1962, *Proc. Phys. Soc.*, 79, 94  
 Franchini M. et al., 2020, *ApJ*, 888, 55  
 Froese Fischer C., 2009, *Phys. Scr. Vol. T*, 134, 014019  
 Fuhr J. R., 2006, *J. Am. Chem. Soc.*, 128, 5585  
 Gaigalas G., Fischer C. F., Rynkun P., Jönsson P., 2017, *Atoms*, 5, 6  
 Godefroid M., Fischer C. F., Jönsson P., 2001, *J. Phys. B: At. Mol. Opt. Phys.*, 34, 1079  
 Goldbach C., Nollez G., 1987, *A&A*, 181, 203  
 Goldbach C., Martin M., Nollez G., 1989, *A&A*, 221, 155  
 Golly A., Jazgara A., Wujec T., 2003, *Phys. Scr.*, 67, 485  
 Goly A., Weniger S., 1982, *J. Quant. Spec. Radiat. Transf.*, 28, 389  
 Grant I. P., 1974, *J. Phys. B: At. Mol. Opt. Phys.*, 7, 1458  
 Grant I. P., 2007, *Relativistic Quantum Theory of Atoms and Molecules*. Springer, New York  
 Haris K., Kramida A., 2017, *ApJS*, 233, 16  
 Hibbert A., 1974, *J. Phys. B: At. Mol. Phys.*, 7, 1417  
 Hibbert A., 1975, *Comput. Phys. Commun.*, 9, 141  
 Hibbert A., Biemont E., Godefroid M., Vaecq N., 1993, *A&AS*, 99, 179  
 Jönsson P., Li J., Gaigalas G., Dong C., 2010, *At. Data Nucl. Data Tables*, 96, 271  
 Jacques C., Knystautas E. J., Drouin R., Berry H. G., 1980, *Can. J. Phys.*, 58, 1093  
 Jofré P., Jackson H., Tucci Maia M., 2020, *A&A*, 633, L9  
 Jones D. W., Wiese W. L., 1984, *Phys. Rev. A*, 29, 2597  
 Jönsson P., Gaigalas G., Bieroń J., Fischer C. F., Grant I., 2013, *Comput. Phys. Commun.*, 184, 2197  
 Kingston A. E., Hibbert A., 2000, *J. Phys. B: At. Mol. Opt. Phys.*, 33, 693  
 Knystautas E., Barrette L., Neveu B., Drouin R., 1971, *J. Quant. Spectrosc. Radiat. Transfer*, 11, 75  
 Kramida A., Yu. Ralchenko Reader J., and NIST ASD Team, 2019, NIST Atomic Spectra Database (ver. 5.7.1). National Institute of Standards and Technology, Gaithersburg, MD [Online]. Available: <https://physics.nist.gov/asd> [2020, February 11]  
 Kwong V. H. S., Fang Z., Gibbons T. T., Parkinson W. H., Smith P. L., 1993, *ApJ*, 411, 431  
 Li J., Jönsson P., Dong C., Gaigalas G., 2010, *J. Phys. B: At. Mol. Opt. Phys.*, 43, 035005  
 Maecker H., 1953, *Z. Phys.*, 135, 13  
 Mickey D., 1970, *Nucl. Instrum. Methods*, 90, 77  
 Miller M. H., Wilkerson T. D., Roig R. A., Bengtson R. D., 1974, *Phys. Rev. A*, 9, 2312  
 Moore C. E., Gallagher J. W., 1993, Tables of Spectra of Hydrogen, Carbon, Nitrogen, and Oxygen Atoms and Ions. CRC Press, Boca Raton  
 Musielok J., Veres G., Wiese W., 1997, *J. Quant. Spectrosc. Radiat. Transfer*, 57, 395  
 Nandi T., Bhattacharya N., Kurup M. B., Prasad K. G., 1996, *Phys. Scr.*, 54, 179  
 Nieva M. F., Przybilla N., 2006, *ApJ*, 639, L39  
 Nieva M. F., Przybilla N., 2008, *A&A*, 481, 199  
 Nieva M. F., Przybilla N., 2012, *A&A*, 539, A143  
 Nussbaumer H., Storey P. J., 1981, *A&A*, 96, 91  
 Nussbaumer H., Storey P. J., 1984, *A&A*, 140, 383  
 Olsen J., Roos B. O., Jørgensen P., Jensen H. J. A., 1988, *J. Chem. Phys.*, 89, 2185  
 Papoula A. et al., 2019, *Atoms*, 7, 106  
 Peach G., Saraph H. E., Seaton M. J., 1988, *J. Phys. B: At. Mol. Opt. Phys.*, 21, 3669

Pehlivan Rhodin A., Hartman H., Nilsson H., Jönsson P., 2017, *A&A*, 598, A102  
 Przybilla N., Butler K., Kudritzki R. P., 2001, *A&A*, 379, 936  
 Reistad N., Martinson I., 1986, *Phys. Rev. A*, 34, 2632  
 Reistad N., Hutton R., Nilsson A. E., Martinson I., Mannervik S., 1986, *Phys. Scr.*, 34, 151  
 Richter J., 1958, *Z. Phys.*, 151, 114  
 Roberts J. R., Eckerle K. L., 1967, *Phys. Rev.*, 153, 87  
 Stonkutė E. et al., 2020, *AJ*, 159, 90  
 Sturesson L., Jönsson P., Froese Fischer C., 2007, *Comput. Phys. Commun.*, 177, 539  
 Tachiev G., Fischer C. F., 1999, *J. Phys. B: At. Mol. Opt. Phys.*, 32, 5805  
 Tachiev G., Fischer C. F., 2000, *J. Phys. B: At. Mol. Opt. Phys.*, 33, 2419  
 Tachiev G., Fischer C. F., 2001, *Can. J. Phys.*, 79, 955  
 Träbert E., Gwinner G., Knystautas E. J., Tordoix X., Wolf A., 1999, *J. Phys. B: At. Mol. Opt. Phys.*, 32, L491  
 VandenBerg D. A., Bergbusch P. A., Dotter A., Ferguson J. W., Michaud G., Richer J., Proffitt C. R., 2012, *ApJ*, 755, 15  
 Wiese W. L., Fuhr J. R., 2007a, *J. Phys. Chem. Ref. Data*, 36, 1287  
 Wiese W. L., Fuhr J. R., 2007b, *J. Phys. Chem. Ref. Data*, 36, 1737  
 Ynnerman A., Fischer C. F., 1995, *Phys. Rev. A*, 51, 2020  
 Zatsarinny O., Fischer C. F., 2002, *J. Phys. B: At. Mol. Opt. Phys.*, 35, 4669  
 Zhang Q.-S., Li Y., Christensen-Dalsgaard J., 2019, *ApJ*, 881, 103

## SUPPORTING INFORMATION

Supplementary data are available at [MNRAS](https://www.mnras.org) online.

**Table A1.** Wavefunction composition (up to three *LS* components with a contribution > 0.02 of the total wavefunction) in *LS*-coupling, energy levels (in  $\text{cm}^{-1}$ ), and lifetimes (in s; given in length ( $\tau_l$ ) and velocity ( $\tau_v$ ) gauges) for C I–IV.

**Table A2.** Electric dipole transition data for C I from present calculations.

**Table A3.** Electric dipole transition data for C II from present calculations.

**Table A4.** Electric dipole transition data for C III from present calculations.

**Table A5.** Electric dipole transition data for C IV from present calculations.

Please note: Oxford University Press is not responsible for the content or functionality of any supporting materials supplied by the authors. Any queries (other than missing material) should be directed to the corresponding author for the article.

## APPENDIX A: ADDITIONAL TABLES

**Table A1.** Wavefunction composition (up to three *LS* components with a contribution > 0.02 of the total wavefunction) in *LS*-coupling, energy levels (in  $\text{cm}^{-1}$ ), and lifetimes (in s; given in length ( $\tau_l$ ) and velocity ( $\tau_v$ ) gauges) for C I–IV. Energy levels are given relative to the ground state and compared with NIST data (Kramida et al. 2019). The full table is available online.

Species	No.	State	<i>LS</i> -composition	$E_{\text{RCI}}$	$E_{\text{NIST}}$	$\tau_l$	$\tau_v$
C I	1	$2s^2 2p^2 ({}^3P) {}^3P_0$	$0.88 + 0.03 2s^2 2p^2 2P 7p {}^3P$	0	0	–	–
C I	2	$2s^2 2p^2 ({}^3P) {}^3P_1$	$0.88 + 0.03 2s^2 2p^2 2P 7p {}^3P$	16	16	–	–
C I	3	$2s^2 2p^2 ({}^3P) {}^3P_2$	$0.88 + 0.03 2s^2 2p^2 2P 7p {}^3P$	43	43	–	–
C I	4	$2s^2 2p^2 ({}^1D) {}^1D_2$	$0.85 + 0.05 2s^2 2p^2 2P 7p {}^1D + 0.03 2s^2 2p^2 2P 3p {}^1D$	10 275	10 193	–	–
C I	5	$2s^2 2p^2 ({}^1S) {}^1S_0$	$0.78 + 0.06 2s^2 2p^2 2P 7p {}^1S + 0.06 2p^4 ({}^1S) {}^1S$	21 775	21 648	–	–
C I	6	$2s^2 2p^3 ({}^4S) {}^4S^{\circ}_2$	$0.93 + 0.04 2s^2 2p^2 2P ({}^3P) {}^4P 7p {}^3S^{\circ}$	33 859	33 735	3.00E-02	1.26E-02
C I	7	$2s^2 2p^2 2P 3s {}^3P^{\circ}_0$	$0.91 + 0.04 2p^3 ({}^3P) {}^2P 3s {}^3P^{\circ}$	60 114	60 333	3.00E-09	3.04E-09
C I	8	$2s^2 2p^2 2P 3s {}^3P^{\circ}_1$	$0.91 + 0.04 2p^3 ({}^3P) {}^2P 3s {}^3P^{\circ}$	60 133	60 353	3.00E-09	3.04E-09
C I	9	$2s^2 2p^2 2P 3s {}^3P^{\circ}_2$	$0.91 + 0.04 2p^3 ({}^3P) {}^2P 3s {}^3P^{\circ}$	60 174	60 393	3.00E-09	3.04E-09
C I	10	$2s^2 2p^2 2P 3s {}^1P^{\circ}_1$	$0.92 + 0.04 2p^3 ({}^1P) {}^2P 3s {}^1P^{\circ}$	61 750	61 982	2.78E-09	2.83E-09
–	–	–	–	–	–	–	–

**Table A2.** Electric dipole transition data for C I from present calculations. Upper and lower states, wavenumber,  $\Delta E$ , wavelength,  $\lambda$ , line strength, *S*, weighted oscillator strength, *gf*, transition probability, *A*, together with the relative difference between two gauges of *A* values, *dT*, provided by the present MCDHF/RCI calculations are shown in the table. Wavelength and wavenumber values are from the NIST data base (Kramida et al. 2019) when available. Wavelengths and wavenumbers marked with \* are from the present calculations. Only the first 10 rows are shown; the full table is available online.

Upper	Lower	$\Delta E(\text{cm}^{-1})$	$\lambda (\text{\AA})$	<i>S</i> (au of $a_0^2 e^2$ )	<i>gf</i>	<i>A</i> ( $\text{s}^{-1}$ )	<i>dT</i>
$2s^2 2p5d {}^3D^{\circ}_2$	$2s^2 2p^2 {}^3P_1$	86373	1157.769	1.025E-01	2.679E–02	2.647E + 07	0.004
$2s^2 2p5d {}^3D^{\circ}_1$	$2s^2 2p^2 {}^3P_0$	86362	1157.909	8.568E-02	2.240E–02	3.689E + 07	0.003
$2s^2 2p5d {}^3D^{\circ}_3$	$2s^2 2p^2 {}^3P_2$	86354	1158.018	3.197E-01	8.358E–02	5.897E + 07	0.003
$2s^2 2p6s {}^3P^{\circ}_2$	$2s^2 2p^2 {}^3P_1$	86352	1158.038	1.273E-01	3.328E–02	3.287E + 07	0.002
$2s^2 2p5d {}^3D^{\circ}_1$	$2s^2 2p^2 {}^3P_1$	86346	1158.130	4.687E-02	1.225E–02	2.017E + 07	0.002
$2s^2 2p5d {}^3D^{\circ}_2$	$2s^2 2p^2 {}^3P_2$	86346	1158.131	1.049E-01	2.742E–02	2.708E + 07	0.000
$2s^2 2p6s {}^3P^{\circ}_1$	$2s^2 2p^2 {}^3P_0$	86331	1158.324	2.442E-02	6.380E–03	1.050E + 07	0.001
$2s^2 2p6s {}^3P^{\circ}_2$	$2s^2 2p^2 {}^3P_2$	86325	1158.400	2.619E-02	6.844E–03	6.756E + 06	0.001
$2s^2 2p5d {}^3D^{\circ}_1$	$2s^2 2p^2 {}^3P_2$	86319	1158.492	1.367E-03	3.571E–04	5.875E + 05	0.002
$2s^2 2p6s {}^3P^{\circ}_0$	$2s^2 2p^2 {}^3P_1$	86315	1158.544	6.630E-03	1.732E–03	2.849E + 06	0.004
–	–	–	–	–	–	–	–



**Table A3.** Electric dipole transition data for C II from present calculations. Upper and lower states, wavenumber,  $\Delta E$ , wavelength,  $\lambda$ , line strength,  $S$ , weighted oscillator strength,  $gf$ , transition probability,  $A$ , together with the relative difference between two gauges of  $A$  values,  $dT$ , provided by the present MCDHF/RCI calculations are shown in the table. Wavelength and wavenumber values are from the NIST data base (Kramida et al. 2019) when available. Only the first 10 rows are shown; the full table is available online.

Upper	Lower	$\Delta E$ (cm <sup>-1</sup> )	$\lambda$ (Å)	$S$ (au of $a_0^2 e^2$ )	$gf$	$A$ (s <sup>-1</sup> )	$dT$
2s2p3p <sup>2</sup> D <sub>3/2</sub>	2s <sup>2</sup> 2p <sup>2</sup> P <sub>1/2</sub>	188581	530.275	8.159E-02	4.673E-02	2.771E+08	0.015
2s2p3p <sup>2</sup> D <sub>5/2</sub>	2s <sup>2</sup> 2p <sup>2</sup> P <sub>3/2</sub>	188551	530.359	1.515E-01	8.678E-02	3.430E+08	0.015
2s2p3p <sup>2</sup> D <sub>3/2</sub>	2s <sup>2</sup> 2p <sup>2</sup> P <sub>3/2</sub>	188517	530.454	1.661E-02	9.511E-03	5.636E+07	0.015
2s <sup>2</sup> 7d <sup>2</sup> D <sub>3/2</sub>	2s <sup>2</sup> 2p <sup>2</sup> P <sub>1/2</sub>	187353	533.752	1.094E-01	6.223E-02	3.637E+08	0.007
2s <sup>2</sup> 7d <sup>2</sup> D <sub>5/2</sub>	2s <sup>2</sup> 2p <sup>2</sup> P <sub>3/2</sub>	187289	533.933	1.943E-01	1.104E-01	4.300E+08	0.007
2s <sup>2</sup> 7d <sup>2</sup> D <sub>3/2</sub>	2s <sup>2</sup> 2p <sup>2</sup> P <sub>3/2</sub>	187289	533.933	2.205E-02	1.254E-02	7.321E+07	0.007
2s2p3p <sup>4</sup> P <sub>3/2</sub>	2s <sup>2</sup> 2p <sup>2</sup> P <sub>1/2</sub>	186443	536.355	1.779E-07	1.007E-07	5.830E+02	0.017
2s2p3p <sup>4</sup> P <sub>1/2</sub>	2s <sup>2</sup> 2p <sup>2</sup> P <sub>1/2</sub>	186427	536.402	6.007E-07	3.400E-07	3.936E+03	0.039
2s2p3p <sup>4</sup> P <sub>5/2</sub>	2s <sup>2</sup> 2p <sup>2</sup> P <sub>3/2</sub>	186402	536.473	1.227E-05	6.942E-06	2.678E+04	0.020
2s2p3p <sup>4</sup> P <sub>3/2</sub>	2s <sup>2</sup> 2p <sup>2</sup> P <sub>3/2</sub>	186380	536.537	1.327E-06	7.506E-07	4.343E+03	0.027
–	–	–	–	–	–	–	–

**Table A4.** Electric dipole transition data for C III from present calculations. Upper and lower states, wavenumber,  $\Delta E$ , wavelength,  $\lambda$ , line strength,  $S$ , weighted oscillator strength,  $gf$ , transition probability,  $A$ , together with the relative difference between two gauges of  $A$  values,  $dT$ , provided by the present MCDHF/RCI calculations are shown in the table. Wavelength and wavenumber values are from the NIST data base (Kramida et al. 2019) when available. Wavelengths and wavenumbers marked with \* are from the present calculations. Only the first 10 rows are shown; the full table is available online.

Upper	Lower	$\Delta E$ (cm <sup>-1</sup> )	$\lambda$ (Å)	$S$ (au of $a_0^2 e^2$ )	$gf$	$A$ (s <sup>-1</sup> )	$dT$
2s7p <sup>3</sup> P <sub>1</sub> <sup>o</sup>	2s <sup>2</sup> <sup>1</sup> S <sub>0</sub>	365034*	273.947*	7.670E-07	8.505E-07	2.520E+04	0.005
2s7p <sup>1</sup> P <sub>1</sub> <sup>o</sup>	2s <sup>2</sup> <sup>1</sup> S <sub>0</sub>	364896	274.051	1.043E-02	1.156E-02	3.423E+08	0.010
2s6p <sup>1</sup> P <sub>1</sub> <sup>o</sup>	2s <sup>2</sup> <sup>1</sup> S <sub>0</sub>	357109	280.026	1.593E-02	1.728E-02	4.901E+08	0.001
2s6p <sup>3</sup> P <sub>1</sub> <sup>o</sup>	2s <sup>2</sup> <sup>1</sup> S <sub>0</sub>	357050	280.073	5.265E-06	5.711E-06	1.619E+05	0.004
2p3d <sup>1</sup> P <sub>1</sub> <sup>o</sup>	2s <sup>2</sup> <sup>1</sup> S <sub>0</sub>	346712	288.423	9.317E-04	9.818E-04	2.627E+07	0.003
2s5p <sup>3</sup> P <sub>1</sub> <sup>o</sup>	2s <sup>2</sup> <sup>1</sup> S <sub>0</sub>	344236	290.498	3.900E-07	4.079E-07	1.075E+04	0.018
2s5p <sup>1</sup> P <sub>1</sub> <sup>o</sup>	2s <sup>2</sup> <sup>1</sup> S <sub>0</sub>	343258	291.326	4.551E-02	4.747E-02	1.244E+09	0.000
2p3d <sup>3</sup> P <sub>1</sub> <sup>o</sup>	2s <sup>2</sup> <sup>1</sup> S <sub>0</sub>	340127	294.007	7.645E-07	7.903E-07	2.035E+04	0.005
2p3d <sup>3</sup> D <sub>1</sub> <sup>o</sup>	2s <sup>2</sup> <sup>1</sup> S <sub>0</sub>	337655	296.159	7.267E-07	7.458E-07	1.893E+04	0.005
2s4p <sup>1</sup> P <sub>1</sub> <sup>o</sup>	2s <sup>2</sup> <sup>1</sup> S <sub>0</sub>	322404	310.170	3.480E-02	3.409E-02	7.884E+08	0.000
–	–	–	–	–	–	–	–

**Table A5.** Electric dipole transition data for C IV from present calculations. Upper and lower states, wavenumber,  $\Delta E$ , wavelength,  $\lambda$ , line strength,  $S$ , weighted oscillator strength,  $gf$ , transition probability,  $A$ , together with the relative difference between two gauges of  $A$  values,  $dT$ , provided by the present MCDHF/RCI calculations are shown in the table. Wavelength and wavenumber values are from the NIST data base (Kramida et al. 2019). Only the first 10 rows are shown; the full table is available online.

Upper	Lower	$\Delta E$ (cm <sup>-1</sup> )	$\lambda$ (Å)	$S$ (au of $a_0^2 e^2$ )	$gf$	$A$ (s <sup>-1</sup> )	$dT$
8p <sup>2</sup> P <sub>3/2</sub> <sup>o</sup>	2s <sup>2</sup> S <sub>1/2</sub>	492479	203.054	5.029E-03	7.523E-03	3.043E+08	0.004
8p <sup>2</sup> P <sub>1/2</sub> <sup>o</sup>	2s <sup>2</sup> S <sub>1/2</sub>	492477	203.055	2.517E-03	3.766E-03	3.046E+08	0.004
7p <sup>2</sup> P <sub>3/2</sub> <sup>o</sup>	2s <sup>2</sup> S <sub>1/2</sub>	483950	206.633	7.885E-03	1.159E-02	4.527E+08	0.001
7p <sup>2</sup> P <sub>1/2</sub> <sup>o</sup>	2s <sup>2</sup> S <sub>1/2</sub>	483948	206.634	3.946E-03	5.801E-03	4.532E+08	0.001
6p <sup>2</sup> P <sub>3/2</sub> <sup>o</sup>	2s <sup>2</sup> S <sub>1/2</sub>	470778	212.414	1.349E-02	1.930E-02	7.132E+08	0.000
6p <sup>2</sup> P <sub>1/2</sub> <sup>o</sup>	2s <sup>2</sup> S <sub>1/2</sub>	470775	212.416	6.753E-03	9.657E-03	7.139E+08	0.000
5p <sup>2</sup> P <sub>3/2</sub> <sup>o</sup>	2s <sup>2</sup> S <sub>1/2</sub>	448862	222.785	2.644E-02	3.604E-02	1.211E+09	0.000
5p <sup>2</sup> P <sub>1/2</sub> <sup>o</sup>	2s <sup>2</sup> S <sub>1/2</sub>	448855	222.789	1.323E-02	1.804E-02	1.212E+09	0.000
8d <sup>2</sup> D <sub>3/2</sub>	2p <sup>2</sup> P <sub>1/2</sub> <sup>o</sup>	428244	233.511	1.264E-02	1.644E-02	5.027E+08	0.002
8d <sup>2</sup> D <sub>5/2</sub>	2p <sup>2</sup> P <sub>3/2</sub> <sup>o</sup>	428136	233.570	2.275E-02	2.958E-02	6.028E+08	0.002
–	–	–	–	–	–	–	–

**Table A6.** Comparison of relative line strengths ( $S$ ), weighted oscillator strengths ( $gf$ ), and lifetimes ( $\tau$ ), or transition probabilities ( $A$ ), with other theoretical work and experimental results for C I–IV. The present values from the MCDHF/RCI calculations are given in the Babushkin(length) gauge. The values in the parentheses are the relative differences between the length and velocity gauges. The references for the experiments are shown in the last column. Note that the sums of the line strengths  $S$  have been normalized to 100 for each multiplet in C I.

		C I		$S$ (au of $a_0^2 e^2$ )			
Transition array	Mult.	$J_u - J_l$					
			MCDHF/RCI	civ3 <sup>(a)</sup>	Expt.	Expt.	
$2s^2 2p3p - 2s^2 2p3s$	$^3D - ^3P^o$	3 – 2	46.67(1.3 per cent)	46.72	$46.3 \pm 1.8$ <sup>(b)</sup>		
		2 – 1	25.29(1.2 per cent)	25.43	$25.5 \pm 1.2$ <sup>(b)</sup>		
		1 – 0	11.25(1.2 per cent)	11.29	$11.8 \pm 0.5$ <sup>(b)</sup>		
		2 – 2	8.047(1.3 per cent)	7.898	$7.67 \pm 0.38$ <sup>(b)</sup>		
		1 – 1	8.213(1.3 per cent)	8.153	$8.42 \pm 0.46$ <sup>(b)</sup>		
$2s^2 2p3p - 2s^2 2p3s$	$^3P - ^3P^o$	2 – 2	42.15(0.2 per cent)	41.92	$40.6 \pm 0.9$ <sup>(b)</sup>	41.3 <sup>(d)</sup>	
		1 – 1	7.812(0.3 per cent)	7.873	$7.98 \pm 0.23$ <sup>(b)</sup>	8.1 <sup>(d)</sup>	
		1 – 2	15.07(0.2 per cent)	14.79	$15.1 \pm 0.4$ <sup>(b)</sup>	15.1 <sup>(d)</sup>	
		0 – 1	11.11(0.2 per cent)	11.11	$11.3 \pm 0.3$ <sup>(b)</sup>	11.6 <sup>(d)</sup>	
		2 – 1	13.41(0.2 per cent)	13.67	$14.0 \pm 0.35$ <sup>(b)</sup>	13.0 <sup>(d)</sup>	
$2s^2 2p3p - 2s^2 2p3s$	$^3S - ^3P^o$	1 – 0	10.44(0.2 per cent)	10.64	$10.9 \pm 0.3$ <sup>(b)</sup>	10.9 <sup>(d)</sup>	
		1 – 2	51.96(0.3 per cent)	51.43	$52.4 \pm 1.1$ <sup>(b)</sup>		
		1 – 1	35.49(0.2 per cent)	35.80	$34.8 \pm 0.9$ <sup>(b)</sup>		
		1 – 0	12.54(0.2 per cent)	12.77	$12.8 \pm 0.38$ <sup>(b)</sup>		
		2 – 1	57.27(3.0 per cent)	56.85	$59.0 \pm 3.2$ <sup>(c)</sup>		
$2s^2 2p3d - 2s^2 2p3p$	$^3P^o - ^3S$	1 – 1	32.30(2.9 per cent)	32.56	$32.1 \pm 4.1$ <sup>(c)</sup>		
		0 – 1	10.43(2.9 per cent)	10.59	$8.9 \pm 2.1$ <sup>(c)</sup>		
		2 – 2	42.67(3.3 per cent)	42.63	$43.5 \pm 0.4$ <sup>(c)</sup>		
		1 – 1	9.465(3.2 per cent)	9.669	$10.2 \pm 0.6$ <sup>(c)</sup>		
		1 – 2	13.91(3.3 per cent)	13.84	$14.9 \pm 0.8$ <sup>(c)</sup>		
$2s^2 2p3d - 2s^2 2p3p$	$^3P^o - ^3P$	0 – 1	11.57(3.3 per cent)	11.69	$11.2 \pm 0.5$ <sup>(c)</sup>		
		2 – 1	11.72(3.4 per cent)	11.47	$10.2 \pm 0.5$ <sup>(c)</sup>		
		1 – 0	10.66(3.3 per cent)	10.70	$10.0 \pm 0.4$ <sup>(c)</sup>		
		2 – 2	62.05(5.7 per cent)	50.76	$51.2 \pm 5.0$ <sup>(c)</sup>		
		1 – 1	9.312(7.1 per cent)	8.778	$8.4 \pm 1.6$ <sup>(c)</sup>		
$2s^2 2p4s - 2s^2 2p3p$	$^3P - ^3P$	1 – 2	13.79(7.0 per cent)	14.08	$14.3 \pm 2.0$ <sup>(c)</sup>		
		0 – 1	7.335(8.7 per cent)	9.670	$10.2 \pm 1.5$ <sup>(c)</sup>		
		2 – 1	3.113(11.9 per cent)	8.440	$10.1 \pm 2.0$ <sup>(c)</sup>		
		1 – 0	4.397(10.3 per cent)	8.271	$5.8 \pm 1.0$ <sup>(c)</sup>		
		3 – 2	47.89(1.2 per cent)	46.50	$45.5 \pm 2.0$ <sup>(c)</sup>	45.1 <sup>(d)</sup>	
$2s^2 2p3d - 2s^2 2p3p$	$^3D^o - ^3P$	2 – 1	26.70(1.2 per cent)	26.59	$27.5 \pm 1.2$ <sup>(c)</sup>	24.2 <sup>(d)</sup>	
		1 – 0	9.708(1.2 per cent)	11.11	$11.0 \pm 0.6$ <sup>(c)</sup>	13.6 <sup>(d)</sup>	
		2 – 2	8.170(0.9 per cent)	7.559	$7.5 \pm 0.4$ <sup>(c)</sup>	8.0 <sup>(d)</sup>	
		1 – 1	7.100(1.1 per cent)	7.792	$8.1 \pm 0.5$ <sup>(c)</sup>	9.1 <sup>(d)</sup>	
		2 – 3	44.42(3.2 per cent)	44.77	$44.5 \pm 2.0$ <sup>(c)</sup>		
$2s^2 2p4s - 2s^2 2p3p$	$^3P^o - ^3D$	1 – 2	23.65(3.1 per cent)	24.14	$24.8 \pm 1.2$ <sup>(c)</sup>		
		0 – 1	11.10(3.0 per cent)	11.24	$11.5 \pm 0.6$ <sup>(c)</sup>		
		2 – 2	9.145(2.6 per cent)	9.424	$8.4 \pm 0.6$ <sup>(c)</sup>		
		1 – 1	9.301(2.7 per cent)	9.071	$9.5 \pm 0.5$ <sup>(c)</sup>		
		2 – 1	2.373(1.4 per cent)	1.356	$1.3 \pm 0.2$ <sup>(c)</sup>		
$2s^2 2p3d - 2s^2 2p3p$	$^3D^o - ^3D$	3 – 3	50.31(1.5 per cent)	49.19	$50.0 \pm 5.0$ <sup>(c)</sup>		
		2 – 2	25.28(1.6 per cent)	25.72	$25.4 \pm 2.2$ <sup>(c)</sup>		
		1 – 1	11.50(1.7 per cent)	12.68	$12.3 \pm 0.7$ <sup>(c)</sup>		
		2 – 3	8.250(0.9 per cent)	7.291	$6.6 \pm 0.6$ <sup>(c)</sup>		
		1 – 2	4.043(1.8 per cent)	4.621	$4.7 \pm 0.5$ <sup>(c)</sup>		
$2s^2 2p3d - 2s^2 2p3p$	$^3P^o - ^3D$	4 – 3	43.41(0.4 per cent)	43.53	$44.9 \pm 2.0$ <sup>(c)</sup>		
		3 – 2	30.86(0.4 per cent)	30.92	$30.0 \pm 1.5$ <sup>(c)</sup>		
		2 – 1	20.77(0.3 per cent)	21.09	$20.4 \pm 1.0$ <sup>(c)</sup>		
		3 – 3	1.961(1.2 per cent)	1.743	$1.9 \pm 0.2$ <sup>(c)</sup>		
		2 – 2	2.999(0.9 per cent)	2.722	$2.7 \pm 0.2$ <sup>(c)</sup>		

		C II		$\tau$ (ns)			Ref.
Configuration	Term	$J$					
			MCDHF/RCI	MCHF-BP <sup>(e)</sup>	Expt.		
$2s2p^2$	$^3S$	1/2	0.4497 (0.7 per cent)	0.4523	$0.44 \pm 0.02$	(f)	
$2s^2 3s$	$^3S$	1/2	2.292 (0.6 per cent)	2.266	$2.4 \pm 0.3$	(f)	
$2s^2 4s$	$^2S$	1/2	2.017 (0.1 per cent)		$1.9 \pm 0.1$	(f)	
$2s^2 5s$	$^2S$	1/2	3.774 (0.1 per cent)		$3.7 \pm 0.2$	(f)	
$2s2p^2$	$^2P^o$	1/2	0.2446(0.3 per cent)	0.2445	$0.25 \pm 0.01$	(f)	
		3/2	0.2445(0.3 per cent)	0.2449	$0.25 \pm 0.01$	(f)	
$2s^2 3p$	$^2P^o$	1/2	9.265(0.7 per cent)	8.973	$8.9 \pm 0.4$	(f)	
		3/2	9.255(0.7 per cent)	8.963	$8.9 \pm 0.4$	(f)	
$2s^2 4p$	$^2P^o$	1/2	3.838(1.3 per cent)		$3.8 \pm 0.2$	(f)	
		3/2	3.854(1.3 per cent)		$3.8 \pm 0.2$	(f)	
$2p^3$	$^2P^o$	1/2	0.4998(0.8 per cent)	0.4966	$0.48 \pm 0.02$	(f)	

Table A6 – continued

C I							
Transition array	Mult.	$J_u - J_l$	$S$ (au of $a_0^2 e^2$ )				
			MCDHF/RCI	CIv3 <sup>(a)</sup>	Expt.	Expt.	
2s <sup>2</sup> 5p	2p <sup>o</sup>	3/2	0.4981(0.8 per cent)	0.4944	0.48 ± 0.02	(f)	
		1/2	5.044(0.2 per cent)		5.2 ± 0.3	(f)	
		3/2	5.099(0.2 per cent)		5.2 ± 0.3	(f)	
2s <sup>2</sup> 3d	2D	3/2	0.3490(0.2 per cent)	0.3493	0.34 ± 0.01	(f)	
		5/2	0.3491(0.2 per cent)	0.3494	0.34 ± 0.01	(f)	
		3/2	0.7299(0.2 per cent)		0.75 ± 0.03	(f)	
2s <sup>2</sup> 4d	2D	5/2	0.7304(0.2 per cent)		0.75 ± 0.03	(f)	
Configuration	Term	$J$	$\tau$ (ms)			Ref.	
			MCDHF/RCI	MCHF-BP <sup>(e)</sup>	Expt.		
2s2p <sup>2</sup>	4P	1/2	8.151 (47.6 per cent)	7.654	7.95 ± 0.07	(g)	
		3/2	106.1 (68.5 per cent)	96.93	104.1 ± 0.5	(g)	
		5/2	22.66 (48.0 per cent)	22.34	22.05 ± 0.07	(g)	
C III							
Transition array	Mult.	$J_u - J_l$	$gf$			Ref.	
			MCDHF/RCI	MCHF-BP <sup>(h)</sup>	Expt.		
2s2p - 2s <sup>2</sup>	1p <sup>o</sup> - 1S	1-0	0.7592(0.1 per cent)	0.7583	0.75 ± 0.03	(f)	
2p <sup>2</sup> - 2s2p	1S - 1p <sup>o</sup>	0-1	0.1623(<0.05 per cent)	0.1622	0.152 ± 0.009	(f)	
2p <sup>2</sup> - 2s2p	1D - 1p <sup>o</sup>	2-1	0.1815(0.5 per cent)	0.1819	0.183 ± 0.005	(f)	
Configuration	Term	$J$	$\tau$ (ns)			Ref.	
			MCDHF/RCI	MCHF-BP <sup>(h)</sup>	Expt.		
2s2p	1p <sup>o</sup>	1	0.5638(0.1 per cent) ns	0.5651	0.57 ± 0.02	(f)	
2p <sup>2</sup>	1S	0	0.4766(<0.05 per cent) ns	0.4764	0.51 ± 0.01	(f)	
2p <sup>2</sup>	1D	2	7.240(0.5 per cent) ns	7.191	7.2 ± 0.2	(f)	
2s3s	1S	0	1.164(<0.05 per cent) ns	1.171	1.17 ± 0.05	(f)	
C IV							
Transition array	Mult.	$J_u - J_l$	$A(10^8 s^{-1})$			Ref.	
			MCDHF/RCI	MCHF-BP <sup>(j)</sup>	NIST		Expt.
2p-2s	2p <sup>o</sup> - 2S	1/2 - 1/2	2.632(<0.05 per cent)	2.6320	2.65	2.72 ± 0.07	(k)
2p-2s	2p <sup>o</sup> - 2S	3/2 - 1/2	2.646(<0.05 per cent)	2.6459	2.64	2.71 ± 0.07	(k)
Configuration	Term	$J$	$\tau$ (ns)			Ref.	
			MCDHF/RCI	MCHF-BP <sup>(j)</sup>	Model Potential <sup>(o)</sup>	Expt.	
3s	2S	1/2	0.2350(<0.05 per cent)	0.2350	0.236	0.25 ± 0.1	(l)
4s	2S	1/2	0.3755(<0.05 per cent)	0.3747	0.377	0.34 ± 0.035	(m)
2p	2p <sup>o</sup>	1/2	3.799 (<0.05 per cent)	3.799	3.79	3.7 ± 0.1	(k)
		3/2	3.779 (<0.05 per cent)	3.779	3.79		
3p	2p <sup>o</sup>	1/2	0.2146(<0.05 per cent)	0.2142	0.216	0.226 ± 0.03	(n)
		3/2	0.2149(<0.05 per cent)	0.2145	0.216		
4p	2p <sup>o</sup>	1/2	0.3435(<0.05 per cent)		0.344	0.32 ± 0.03	(m)
		3/2	0.3440(<0.05 per cent)		0.344		
3d	2D	3/2	0.05717(<0.05 per cent)	0.05716	0.0572	0.0575 ± 0.006	(n)
		5/2	0.05719(<0.05 per cent)	0.05719	0.0572		
4d	2D	3/2	0.1312 (<0.05 per cent)		0.130	0.14 ± 0.015	(m)
		5/2	0.1313 (<0.05 per cent)		0.130		
5d	2D	3/2	0.2511 (<0.05 per cent)		0.251	0.23 ± 0.023	(m)
		5/2	0.2512 (<0.05 per cent)		0.251		

Notes: <sup>(a)</sup>Hibbert et al. (1993); <sup>(b)</sup>Musielok et al. (1997); <sup>(c)</sup>Bacawski et al. (2001); <sup>(d)</sup>Golly et al. (2003); <sup>(e)</sup>Tachiev & Fischer (2000); <sup>(f)</sup>Reistad et al. (1986); <sup>(g)</sup>Träbert et al. (1999); <sup>(h)</sup>Tachiev & Fischer (1999); <sup>(i)</sup>Fischer et al. (1998); <sup>(j)</sup>Knystautas et al. (1971); <sup>(k)</sup>Donnelly et al. (1978); <sup>(l)</sup>Buchet-Pouilzac & Buchet (1973); <sup>(m)</sup>Jacques et al. (1980); and <sup>(n)</sup>Peach et al. (1988).

**Table A7.** Comparison of line strengths ( $S$ ) and transition rates ( $A$ ) with other theoretical results for C I. The present values from the MCDHF/RCI calculations are given in the Babushkin(length) gauge. The wavenumber  $\Delta E$  and wavelength  $\lambda$  values are taken from the NIST data base. The estimated uncertainties  $dT$  of the transition rates are given as percentages in parentheses.

Transition array	Mult.	$J_u - J_l$	$\Delta E$ ( $\text{cm}^{-1}$ )	$\lambda$ ( $\text{\AA}$ )	MCDHF/RCI		Spline FCS <sup>(a)</sup>		MCHF-BP <sup>(b)</sup>	
					$S$ (au of $a_0^2 e^2$ )	$A$ ( $\text{s}^{-1}$ )	$S$ (au of $a_0^2 e^2$ )	$A$ ( $\text{s}^{-1}$ )	$S$ (au of $a_0^2 e^2$ )	$A$ ( $\text{s}^{-1}$ )
$2s^2 2p3d - 2s^2 2p^2$	$^3\text{F}^\circ - ^3\text{P}$	3-2	78172	1279.228	5.79E-02	7.92E+06(0.1 per cent)	4.52E-02	6.24E+06	8.20E-02	1.14E+07
		2-2	78155	1279.498	1.27E-02	2.43E+06(0.3 per cent)	9.62E-03	1.86E+06	1.16E-02	2.25E+06
		2-1	78182	1279.056	1.08E-02	2.07E+06(0.1 per cent)	8.95E-03	1.73E+06	2.08E-02	4.04E+06
$2s^2 2p4d - 2s^2 2p^2$	$^3\text{F}^\circ - ^3\text{P}$	3-2	83717	1194.488	4.48E-02	7.52E+06(0.1 per cent)	3.99E-02	6.77E+06		
		2-2	83709	1194.614	1.59E-03	3.74E+05(0.5 per cent)	1.44E-03	3.42E+05		
		2-1	83736	1194.229	1.97E-02	4.64E+06(0.2 per cent)	1.73E-02	4.10E+06		
$2s^2 2p5d - 2s^2 2p^2$	$^3\text{F}^\circ - ^3\text{P}$	3-2	86283	1158.966	4.17E-02	7.67E+06(0.3 per cent)	3.88E-02	7.21E+06		
		2-2	86274	1159.094	1.38E-03	3.55E+05(0.3 per cent)	1.36E-03	3.54E+05		
		2-1	86301	1158.731	2.20E-02	5.66E+06(0.3 per cent)	1.96E-02	5.11E+06		
$2s^2 2p3s - 2s^2 2p^2$	$^3\text{P}^\circ - ^3\text{P}$	2-2	60349	1657.008	2.84E+00	2.50E+08(1.2 per cent)	2.69E+00	2.41E+08	2.93E+00	2.61E+08
		1-2	60309	1658.121	9.46E-01	1.39E+08(1.2 per cent)	8.95E-01	1.33E+08	9.75E-01	1.45E+08
		2-1	60376	1656.267	9.47E-01	8.35E+07(1.2 per cent)	8.97E-01	8.05E+07	9.78E-01	8.73E+07
		1-1	60336	1657.379	5.67E-01	8.32E+07(1.2 per cent)	5.37E-01	8.01E+07	5.84E-01	8.67E+07
		0-1	60317	1657.907	7.57E-01	3.33E+08(1.2 per cent)	7.17E-01	3.20E+08	7.80E-01	3.47E+08
		1-0	60352	1656.928	7.57E-01	1.11E+08(1.2 per cent)	7.17E-01	1.07E+08	7.81E-01	1.16E+08
$2s^2 2p3s - 2s^2 2p^2$	$^1\text{P}^\circ - ^3\text{P}$	1-2	61938	1614.507	1.80E-04	2.86E+04(1.6 per cent)	2.72E-04	4.40E+04	1.85E-04	2.97E+04
		1-1	61965	1613.803	1.65E-04	2.61E+04(1.0 per cent)	1.62E-04	2.62E+04	1.74E-04	2.81E+04
		1-0	61981	1613.376	2.21E-04	3.51E+04(1.1 per cent)	2.34E-04	3.79E+04	2.26E-04	3.65E+04
$2s^2 2p^3 - 2s^2 2p^2$	$^3\text{D}^\circ - ^3\text{P}$	3-2	64043	1561.437	1.53E+00	1.22E+08(2.3 per cent)	1.42E+00	1.14E+08	1.54E+00	1.19E+08
		2-2	64046	1561.366	2.72E-01	3.03E+07(2.1 per cent)	2.52E-01	2.84E+07	2.75E-01	2.96E+07
		1-2	64047	1561.339	1.81E-02	3.35E+06(2.0 per cent)	1.67E-02	3.14E+06	1.83E-02	3.28E+06
		2-1	64073	1560.708	8.22E-01	9.14E+07(2.2 per cent)	7.60E-01	8.59E+07	8.28E-01	8.91E+07
		1-1	64074	1560.681	2.73E-01	5.06E+07(2.1 per cent)	2.53E-01	4.96E+07	7.6E-01	4.94E+07
		1-0	64090	1560.282	3.65E-01	6.78E+07(2.1 per cent)	3.38E-01	6.37E+07	3.68E-01	6.61E+07
$2s^2 2p^3 - 2s^2 2p^2$	$^3\text{P}^\circ - ^3\text{P}$	2-2	75212	1329.562	7.98E-01	1.42E+08(3.1 per cent)	7.44E-01	1.35E+08	9.54E-01	1.66E+08
		1-2	75210	1329.600	2.69E-01	9.95E+07(3.1 per cent)	2.51E-01	7.57E+07	3.20E-01	9.28E+07
		2-1	75239	1329.085	2.58E-01	4.58E+07(3.1 per cent)	2.40E-01	4.34E+07	3.12E-01	5.44E+07
		1-1	75237	1329.123	1.64E-01	4.85E+07(3.1 per cent)	1.53E-01	4.63E+07	1.93E-01	5.60E+07
		0-1	75238	1329.100	2.17E-01	1.93E+08(3.1 per cent)	2.04E-01	1.85E+08	2.57E-01	2.24E+08
		1-0	75254	1328.833	2.13E-01	6.30E+07(3.1 per cent)	1.99E-01	6.00E+07	2.54E-01	7.37E+07
$2s^2 2p3d - 2s^2 2p^2$	$^1\text{D}^\circ - ^3\text{P}$	1-2	77636	1288.055	4.63E-04	8.69E+04(1.4 per cent)	4.27E-04	8.10E+04	3.51E-04	6.68E+04
		2-1	77663	1287.608	8.40E-04	1.58E+05(1.2 per cent)	7.68E-04	1.46E+05	7.84E-04	1.49E+05
		2-2	78104	1280.333	3.23E-01	6.17E+07(0.7 per cent)	3.21E-01	6.21E+07	3.30E-01	6.40E+07
$2s^2 2p4s - 2s^2 2p^2$	$^3\text{P}^\circ - ^3\text{P}$	1-2	78073	1280.847	1.13E-01	3.59E+07(0.5 per cent)	1.10E-01	3.55E+07	1.13E-01	3.63E+07
		2-1	78131	1279.890	1.96E-01	3.76E+07(0.5 per cent)	1.81E-01	3.50E+07	1.77E-01	3.44E+07
		1-1	78100	1280.404	5.55E-02	1.77E+07(0.6 per cent)	5.57E-02	1.79E+07	5.83E-02	1.88E+07
		0-1	78088	1280.597	9.23E-02	8.82E+07(0.5 per cent)	8.91E-02	8.61E+07	9.14E-02	8.84E+07
		1-0	78116	1280.135	1.16E-01	3.71E+07(0.5 per cent)	1.81E-01	3.57E+07	1.10E-01	3.56E+07
		3-2	78274	1277.550	1.68E+00	2.31E+08(0.2 per cent)	1.61E+00	2.23E+08	1.64E+00	2.28E+08
$2s^2 2p3d - 2s^2 2p^2$	$^3\text{D}^\circ - ^3\text{P}$	2-2	78264	1277.723	3.44E-01	6.61E+07(0.1 per cent)	3.22E-01	6.26E+07	3.24E-01	6.32E+07
		1-2	78250	1277.954	1.47E-02	4.70E+06(<0.05 per cent)	1.72E-02	5.58E+06	1.84E-02	5.95E+06
		2-1	78291	1277.282	8.75E-01	1.68E+08(0.2 per cent)	8.42E-01	1.64E+08	8.73E-01	1.70E+08
		1-1	78277	1277.513	2.43E-01	7.80E+07(0.1 per cent)	2.66E-01	6.16E+07	2.85E-01	9.26E+07
		1-0	78293	1277.245	3.42E-01	1.10E+08(0.2 per cent)	3.59E-01	1.17E+08	3.88E-01	1.26E+08
		1-2	78296	1277.190	1.14E-02	3.64E+06(0.4 per cent)	6.78E-03	2.20E+06	5.59E-03	1.82E+06
$2s^2 2p4s - 2s^2 2p^2$	$^1\text{P}^\circ - ^3\text{P}$	1-1	78323	1276.750	7.84E-02	2.52E+07(0.2 per cent)	3.90E-02	1.77E+07	2.89E-02	9.41E+06
		1-0	78340	1276.482	5.97E-02	1.92E+07(0.1 per cent)	2.48E-02	8.05E+06	1.55E-02	5.05E+06
		3-2	78486	1274.109	1.00E-02	1.39E+06(0.1 per cent)	1.18E-02	1.65E+06	8.60E-03	1.21E+06
$2s^2 2p3d - 2s^2 2p^2$	$^3\text{P}^\circ - ^3\text{P}$	1-2	78687	1270.844	1.77E-06	5.75E+02(0.4 per cent)	3.03E-07	9.97E+01	1.28E-05	4.23E+03
		1-1	78714	1270.408	6.02E-04	1.96E+05(0.3 per cent)	5.66E-04	1.87E+05	6.50E-04	2.15E+05
		1-0	78731	1270.143	1.65E-03	5.39E+05(0.1 per cent)	1.61E-03	5.32E+05	1.38E-03	4.55E+05
$2s^2 2p3d - 2s^2 2p^2$	$^3\text{P}^\circ - ^3\text{P}$	2-2	79267	1261.552	8.17E-01	1.66E+08(2.1 per cent)	8.13E-01	1.67E+08	6.65E-01	1.35E+08
		1-2	79275	1261.425	2.74E-01	9.26E+07(2.1 per cent)	2.72E-01	9.31E+07	2.23E-01	7.55E+07
		2-1	79294	1261.122	2.54E-01	5.15E+07(2.1 per cent)	5.22E-01	5.19E+07	1.98E-01	4.02E+07
		1-1	79302	1260.996	1.69E-01	5.72E+07(2.1 per cent)	1.68E-01	5.75E+07	1.39E-01	4.70E+07
		0-1	79306	1260.926	2.20E-01	2.24E+08(2.1 per cent)	2.18E-01	2.24E+08	1.79E-01	1.82E+08
		1-0	79318	1260.735	2.12E-01	7.19E+07(2.1 per cent)	2.11E-01	7.23E+07	1.69E-01	5.73E+07
$2s^2 2p3d - 2s^2 2p^2$	$^3\text{F}^\circ - ^1\text{D}$	2-2	68006	1470.449	4.71E-04	5.91E+04(1.4 per cent)			4.22E-04	5.36E+04
		3-2	68022	1470.094	1.52E-02	1.36E+06(0.2 per cent)			1.55E-02	1.41E+06
$2s^2 2p3s - 2s^2 2p^2$	$^3\text{P}^\circ - ^1\text{D}$	1-2	50160	1993.620	1.04E-03	8.67E+04(1.4 per cent)			9.65E-04	8.18E+04
		2-2	50200	1992.012	1.97E-05	9.90E+02(3.2 per cent)			1.50E-05	7.66E+02
$2s^2 2p3s - 2s^2 2p^2$	$^1\text{P}^\circ - ^1\text{D}$	1-2	51789	1930.905	3.59E+00	3.30E+08(1.5 per cent)			3.62E+00	3.37E+08
		3-2	53894	1855.483	9.91E-06	4.71E+02(24.2 per cent)			6.60E-06	3.01E+02
$2s^2 2p^3 - 2s^2 2p^2$	$^3\text{D}^\circ - ^1\text{D}$	1-2	65061	1537.011	8.58E-06	1.65E+03(1.7 per cent)			8.59E-06	1.60E+01
		2-2	65063	1536.960	2.51E-05	2.89E+03(6.9 per cent)			7.15E-06	8.02E+02
$2s^2 2p3d - 2s^2 2p^2$	$^1\text{D}^\circ - ^1\text{D}$	2-2	67487	1481.763	3.03E-01	3.72E+07(1.2 per cent)			2.77E-01	3.45E+07
		1-2	67924	1472.231	4.55E-03	9.48E+05(1.6 per cent)			3.68E-03	7.77E+05
$2s^2 2p4s - 2s^2 2p^2$	$^3\text{P}^\circ - ^1\text{D}$	2-2	67955	1471.552	2.02E-04	2.53E+04(1.0 per cent)			1.77E-04	2.25E+04

Table A7 – continued

Transition array	Mult.	$J_u - J_l$	$\Delta E$ (cm <sup>-1</sup> )	$\lambda$ (Å)	MCDHF/RCI		Spline FCS <sup>(a)</sup>		MCHF-BP <sup>(b)</sup>	
					$S$ (au of $a_0^2 e^2$ )	$A$ (s <sup>-1</sup> )	$S$ (au of $a_0^2 e^2$ )	$A$ (s <sup>-1</sup> )	$S$ (au of $a_0^2 e^2$ )	$A$ (s <sup>-1</sup> )
2s <sup>2</sup> 2p3d – 2s <sup>2</sup> 2p <sup>2</sup>	<sup>3</sup> D <sup>o</sup> – <sup>1</sup> D	3 – 2	68125	1467.877	7.46E–03	6.72E + 05(0.2 per cent)			5.35E–03	4.88E + 05
		2 – 2	68114	1468.106	5.36E–05	6.76E + 03(2.9 per cent)			7.36E–05	9.40E + 03
		1 – 2	68100	1468.410	4.59E–02	9.64E + 06(2.2 per cent)			1.13E–02	2.40E + 06
2s <sup>2</sup> 2p4s – 2s <sup>2</sup> 2p <sup>2</sup>	<sup>1</sup> P <sup>o</sup> – <sup>1</sup> D	1 – 2	68147	1467.402	2.36E–01	4.97E + 07(2.0 per cent)			2.57E–01	5.48E + 07
		3 – 2	68336	1463.336	1.99E + 00	1.81E + 08(0.3 per cent)			1.94E + 00	1.78E + 08
		1 – 2	68538	1459.031	2.18E–01	4.66E + 07(0.1 per cent)			2.51E–01	5.44E + 07
2s <sup>2</sup> 2p3d – 2s <sup>2</sup> 2p <sup>2</sup>	<sup>3</sup> P <sup>o</sup> – <sup>1</sup> D	2 – 2	69118	1446.797	1.83E–05	2.46E + 03(5.2 per cent)			3.09E–05	4.13E + 03
		1 – 2	69126	1446.630	4.50E–06	1.01E + 03(5.4 per cent)			2.65E–06	5.92E + 02
		1 – 0	38704	2583.670	1.61E–04	6.13E + 03(5.2 per cent)			1.48E–04	5.72E + 03
2s <sup>2</sup> 2p3s – 2s <sup>2</sup> 2p <sup>2</sup>	<sup>1</sup> P <sup>o</sup> – <sup>1</sup> S	1 – 0	40333	2479.310	6.69E–01	2.89E + 07(3.7 per cent)			6.31E–01	2.76E + 07
		3 – 2	53605	1865.464	6.83E–06	7.36E + 02(23.2 per cent)			2.71E–06	2.83E + 02
		1 – 0	56468	1770.891	9.52E–05	1.13E + 04(6.6 per cent)			8.80E–05	1.06E + 04
2s <sup>2</sup> 2p3d – 2s <sup>2</sup> 2p <sup>2</sup>	<sup>3</sup> D <sup>o</sup> – <sup>1</sup> S	1 – 0	56645	1765.366	1.32E–02	1.59E + 06(2.9 per cent)			6.33E–03	7.72E + 05
		1 – 0	56692	1763.909	1.72E–02	2.07E + 06(5.0 per cent)			1.99E–02	2.43E + 06
		1 – 0	57083	1751.827	7.32E–01	9.00E + 07(<0.05 per cent)			6.67E–01	8.33E + 07
2s <sup>2</sup> 2p3d – 2s <sup>2</sup> 2p <sup>2</sup>	<sup>3</sup> P <sup>o</sup> – <sup>1</sup> S	1 – 0	57670	1733.980	4.99E–05	6.48E + 03(8.1 per cent)			1.18E–04	1.53E + 04
		2 – 2	83454	1198.262	3.73E–04	8.70E + 04(0.8 per cent)	2.87E–04	6.75E + 04		
		2 – 1	83481	1197.875	1.03E–03	2.39E + 05(0.8 per cent)	8.64E–04	2.04E + 05		
2s <sup>2</sup> 2p5s – 2s <sup>2</sup> 2p <sup>2</sup>	<sup>3</sup> P <sup>o</sup> – <sup>3</sup> P	2 – 2	83747	1194.063	1.18E–01	2.78E + 07(0.9 per cent)			1.25E–01	2.98E + 07
		1 – 2	83704	1194.686	4.34E–02	1.70E + 07(0.8 per cent)			4.47E–02	1.77E + 07
		2 – 1	83774	1193.678	1.17E–01	2.75E + 07(0.6 per cent)			1.07E–01	2.54E + 07
2s <sup>2</sup> 2p4d – 2s <sup>2</sup> 2p <sup>2</sup>	<sup>3</sup> D <sup>o</sup> – <sup>3</sup> P	1 – 1	83731	1194.301	1.95E–02	7.67E + 06(0.9 per cent)			2.10E–02	8.34E + 06
		0 – 1	83723	1194.405	3.64E–02	4.29E + 07(0.7 per cent)			3.70E–02	4.40E + 07
		1 – 0	83747	1194.066	4.98E–02	1.95E + 07(0.7 per cent)			4.90E–02	1.94E + 07
2s <sup>2</sup> 2p4d – 2s <sup>2</sup> 2p <sup>2</sup>	<sup>3</sup> D <sup>o</sup> – <sup>3</sup> P	1 – 2	83805	1193.240	6.80E–01	1.15E + 08(0.1 per cent)			6.52E–01	1.11E + 08
		2 – 2	83794	1193.393	1.57E–01	3.70E + 07(0.1 per cent)			1.45E–01	3.46E + 07
		1 – 2	83776	1193.649	5.60E–03	2.20E + 06(0.1 per cent)			2.67E–03	2.25E + 06
2s <sup>2</sup> 2p5s – 2s <sup>2</sup> 2p <sup>2</sup>	<sup>1</sup> P <sup>o</sup> – <sup>3</sup> P	2 – 1	83821	1193.009	3.37E–01	7.95E + 07(<0.05 per cent)			3.31E–01	7.90E + 07
		1 – 1	83803	1193.264	1.10E–01	4.31E + 07(<0.05 per cent)			1.08E–01	4.29E + 07
		1 – 0	83820	1193.030	1.65E–01	6.50E + 07(0.1 per cent)			1.61E–01	6.39E + 07
2s <sup>2</sup> 2p5s – 2s <sup>2</sup> 2p <sup>2</sup>	<sup>1</sup> P <sup>o</sup> – <sup>3</sup> P	1 – 2	83833	1192.835	6.48E–03	2.55E + 06(0.5 per cent)			5.50E–03	2.19E + 06
		1 – 1	83860	1192.451	2.38E–02	9.38E + 06(0.3 per cent)			1.91E–02	7.61E + 06
		1 – 0	83877	1192.218	7.36E–03	2.90E + 06(0.3 per cent)			5.39E–03	2.15E + 06
2s <sup>2</sup> 2p4d – 2s <sup>2</sup> 2p <sup>2</sup>	<sup>1</sup> F <sup>o</sup> – <sup>3</sup> P	3 – 2	83903	1191.841	1.54E–02	2.61E + 06(0.1 per cent)			1.70E–02	2.90E + 06
		1 – 2	83988	1190.636	3.47E–05	1.37E + 04(0.3 per cent)			3.15E–05	1.26E + 04
		1 – 1	84015	1190.253	1.25E–03	4.93E + 05(0.1 per cent)			1.20E–03	4.79E + 05
2s <sup>2</sup> 2p4d – 2s <sup>2</sup> 2p <sup>2</sup>	<sup>3</sup> P <sup>o</sup> – <sup>3</sup> P	1 – 0	84032	1190.021	2.39E–03	9.48E + 05(<0.05 per cent)			2.26E–03	9.05E + 05
		2 – 2	84059	1189.631	2.38E–01	5.68E + 07(1.0 per cent)			2.19E–01	5.28E + 07
		1 – 2	84072	1189.447	8.04E–02	3.20E + 07(1.0 per cent)			7.37E–02	2.96E + 07
2s <sup>2</sup> 2p5d – 2s <sup>2</sup> 2p <sup>2</sup>	<sup>1</sup> D <sup>o</sup> – <sup>3</sup> P	2 – 1	84086	1189.249	5.07E–02	1.21E + 07(1.1 per cent)			4.53E–02	1.09E + 07
		1 – 1	84099	1189.065	5.43E–02	2.16E + 07(1.0 per cent)			5.01E–02	2.02E + 07
		0 – 1	84104	1188.993	6.52E–02	7.79E + 07(1.0 per cent)			5.96E–02	7.19E + 07
2s <sup>2</sup> 2p5d – 2s <sup>2</sup> 2p <sup>2</sup>	<sup>1</sup> D <sup>o</sup> – <sup>3</sup> P	1 – 0	84116	1188.833	5.35E–02	2.13E + 07(1.1 per cent)			4.86E–02	1.96E + 07
		2 – 2	86141	1160.876	6.52E–04	1.67E + 05(<0.05 per cent)			4.58E–04	1.19E + 05
		2 – 1	86168	1160.513	1.50E–03	3.86E + 05(0.8 per cent)			1.26E–03	3.27E + 05
2s <sup>2</sup> 2p6s – 2s <sup>2</sup> 2p <sup>2</sup>	<sup>3</sup> P <sup>o</sup> – <sup>3</sup> P	2 – 2	86325	1158.400	2.62E–02	6.76E + 06(0.1 per cent)			3.15E–02	8.19E + 06
		1 – 2	86288	1158.907	1.78E–02	7.62E + 06(0.2 per cent)			1.93E–02	8.36E + 06
		2 – 1	86352	1158.038	1.27E–01	3.29E + 07(0.2 per cent)			1.19E–01	3.10E + 07
2s <sup>2</sup> 2p5d – 2s <sup>2</sup> 2p <sup>2</sup>	<sup>3</sup> D <sup>o</sup> – <sup>3</sup> P	1 – 1	86315	1158.544	6.63E–03	2.85E + 06(0.4 per cent)			7.73E–03	3.36E + 06
		0 – 1	86305	1158.674	1.57E–02	2.02E + 07(0.3 per cent)			1.68E–02	2.19E + 07
		1 – 0	86331	1158.324	2.44E–02	1.05E + 07(0.1 per cent)			2.50E–02	1.09E + 07
2s <sup>2</sup> 2p5d – 2s <sup>2</sup> 2p <sup>2</sup>	<sup>3</sup> D <sup>o</sup> – <sup>3</sup> P	3 – 2	86354	1158.018	3.20E–01	5.90E + 07(0.3 per cent)			2.99E–01	5.56E + 07
		2 – 2	86346	1158.131	1.05E–01	2.71E + 07(<0.05 per cent)			9.90E–02	2.58E + 07
		1 – 2	86319	1158.492	1.37E–03	5.88E + 05(0.2 per cent)			1.45E–03	6.29E + 05
2s <sup>2</sup> 2p5d – 2s <sup>2</sup> 2p <sup>2</sup>	<sup>3</sup> D <sup>o</sup> – <sup>3</sup> P	2 – 1	86373	1157.769	1.03E–01	2.65E + 07(0.4 per cent)			1.00E–01	2.62E + 07
		1 – 1	86346	1158.130	4.69E–02	2.02E + 07(0.2 per cent)			4.55E–02	1.98E + 07
		1 – 0	86362	1157.909	8.57E–02	3.69E + 07(0.3 per cent)			8.08E–02	3.51E + 07

Notes: <sup>(a)</sup> Zatsarinny & Fischer (2002); and <sup>(b)</sup> Fischer (2006).

**Table A8.** Comparison of line strengths ( $S$ ) and transition rates ( $A$ ) with other theoretical results for C II. The present values from the MCDHF/RCI calculations are given in the Babushkin(length) gauge. The wavenumber  $\Delta E$  and wavelength  $\lambda$  values are taken from the NIST data base. The estimated uncertainties  $dT$  of the transition rates are given as percentages in parentheses.

Transition array	Mult.	$J_u - J_l$	$\Delta E$ ( $\text{cm}^{-1}$ )	$\lambda$ ( $\text{\AA}$ )	MCDHF/RCI		MCHF-BP <sup>(a)</sup>		civ3 <sup>(b)</sup>
					$S$ (au of $a_0^2 e^2$ )	$A$ ( $\text{s}^{-1}$ )	$S$ (au of $a_0^2 e^2$ )	$A$ ( $\text{s}^{-1}$ )	$A$ ( $\text{s}^{-1}$ )
2s2p <sup>2</sup> – 2s <sup>2</sup> 2p	2D – 2P <sup>o</sup>	5/2 – 3/2	74866	1335.708	2.03E+00	2.89E+08(0.2 per cent)	2.03E+00	2.90E+08	2.89E+08
		3/2 – 3/2	74869	1335.663	2.24E–01	4.79E+07(<0.05 per cent)	2.24E–01	4.80E+07	4.79E+07
2s2p <sup>2</sup> – 2s <sup>2</sup> 2p	2S – 2P <sup>o</sup>	3/2 – 1/2	74932	1334.532	1.13E+00	2.42E+08(0.1 per cent)	1.13E+00	2.43E+08	2.42E+08
		1/2 – 3/2	96430	1037.018	1.62E+00	1.48E+09(0.7 per cent)	1.61E+00	1.47E+09	1.47E+09
2s2p <sup>2</sup> – 2s <sup>2</sup> 2p	2P – 2P <sup>o</sup>	3/2 – 1/2	96493	1036.337	8.18E–01	7.48E+08(0.6 per cent)	8.11E–01	7.43E+08	7.46E+08
		1/2 – 3/2	110560	904.480	9.96E–01	1.37E+09(0.3 per cent)	9.96E–01	1.37E+09	1.36E+09
2s <sup>2</sup> 3s – 2s <sup>2</sup> 2p	2S – 2P <sup>o</sup>	3/2 – 3/2	110602	904.142	4.95E+00	3.41E+09(0.4 per cent)	4.94E+00	3.41E+09	3.38E+09
		1/2 – 1/2	110624	903.962	1.97E+00	2.72E+09(0.4 per cent)	1.97E+00	2.72E+09	2.69E+09
2s <sup>2</sup> 3s – 2s <sup>2</sup> 2p	2S – 2P <sup>o</sup>	3/2 – 1/2	110665	903.623	9.88E–01	6.82E+08(0.4 per cent)	9.87E–01	6.82E+08	6.76E+08
		1/2 – 1/2	116474	858.559	1.81E–01	2.89E+08(0.6 per cent)	1.83E–01	2.93E+08	2.83E+08
2s <sup>2</sup> 3d – 2s <sup>2</sup> 2p	2D – 2P <sup>o</sup>	3/2 – 3/2	145485	687.352	3.03E–01	4.71E+08(0.2 per cent)	3.02E–01	4.70E+08	4.60E+08
		3/2 – 3/2	145487	687.345	2.72E+00	2.82E+08(0.2 per cent)	2.71E+00	2.82E+09	2.76E+09
2s <sup>2</sup> 3p – 2s2p <sup>2</sup>	2P <sup>o</sup> – 4P	3/2 – 1/2	145549	687.053	1.51E+00	2.35E+09(0.2 per cent)	1.51E+00	2.35E+09	2.30E+09
		3/2 – 5/2	88681	1127.626	6.13E–07	2.16E+02(2.0 per cent)	5.04E–07	1.79E+02	1.80E+02
2p <sup>3</sup> – 2s2p <sup>2</sup>	4S <sup>o</sup> – 4P	3/2 – 5/2	98973	1010.371	3.45E+00	1.70E+09(0.4 per cent)	3.44E+00	1.70E+09	1.71E+09
		3/2 – 3/2	99001	1010.083	2.30E+00	1.13E+09(0.4 per cent)	2.30E+00	1.13E+09	1.14E+09
2p <sup>3</sup> – 2s2p <sup>2</sup>	2D <sup>o</sup> – 4P	3/2 – 1/2	99023	1009.858	1.15E+00	5.67E+08(0.4 per cent)	1.15E+00	5.67E+08	5.69E+08
		5/2 – 5/2	107407	931.030	4.41E–06	1.86E+03(21.1 per cent)	3.52E–06	1.48E+03	1.50E+03
2s <sup>2</sup> 3s – 2s2p <sup>2</sup>	4P <sup>o</sup> – 4P	3/2 – 3/2	107441	930.740	1.04E–06	6.59E+02(22.2 per cent)	8.44E–07	5.33E+02	5.39E+02
		3/2 – 5/2	123937	806.861	6.36E–01	6.13E+08(0.4 per cent)	3.93E–01	3.79E+08	
2s <sup>2</sup> 3s – 2s2p <sup>2</sup>	4P <sup>o</sup> – 4P	1/2 – 3/2	123941	806.830	5.88E–01	1.13E+09(0.4 per cent)	3.64E–01	7.02E+08	
		1/2 – 1/2	123963	806.687	1.18E–01	2.27E+08(0.4 per cent)	7.27E–02	1.40E+08	
2s <sup>2</sup> 3s – 2s2p <sup>2</sup>	4P <sup>o</sup> – 4P	3/2 – 3/2	123965	806.677	1.88E–01	1.81E+08(0.4 per cent)	1.16E–01	1.12E+08	
		5/2 – 5/2	123982	806.568	1.48E+00	9.53E+08(0.4 per cent)	9.16E–01	5.90E+08	
2s <sup>2</sup> 3s – 2s2p <sup>2</sup>	4P <sup>o</sup> – 4P	3/2 – 1/2	123987	806.533	5.88E–01	5.67E+08(0.4 per cent)	3.63E–01	3.51E+08	
		5/2 – 3/2	124010	806.834	6.35E–01	4.09E+08(0.4 per cent)	3.92E–01	2.53E+08	
2p <sup>3</sup> – 2s2p <sup>2</sup>	2P <sup>o</sup> – 4P	3/2 – 5/2	125924	794.125	2.69E–05	2.72E+04(3.2 per cent)	7.77E–06	7.83E+03	1.72E+02
		1/2 – 3/2	125953	793.947	4.39E–06	8.88E+03(0.3 per cent)	3.80E–06	7.65E+03	1.88E+02
2p <sup>3</sup> – 2s2p <sup>2</sup>	2P <sup>o</sup> – 4P	3/2 – 3/2	125953	793.947	1.60E–06	1.62E+03(8.6 per cent)	8.35E–06	8.42E+03	1.57E+03
		1/2 – 1/2	125975	793.808	1.51E–06	3.06E+03(10.2 per cent)	1.73E–06	3.50E+03	2.04E+01
2s <sup>2</sup> 3p – 2s2p <sup>2</sup>	2P <sup>o</sup> – 2D	3/2 – 1/2	125975	793.808	1.44E–05	1.46E+04(2.7 per cent)	2.48E–05	2.50E+04	6.67E+02
		1/2 – 3/2	56791	1760.819	2.23E–01	4.09E+07(1.6 per cent)	2.20E–01	4.08E+07	4.37E+07
2s <sup>2</sup> 3p – 2s2p <sup>2</sup>	2P <sup>o</sup> – 2D	3/2 – 3/2	56802	1760.473	4.45E–02	4.09E+06(1.6 per cent)	4.40E–02	4.07E+06	4.37E+06
		3/2 – 5/2	56805	1760.395	4.01E–01	3.68E+07(1.6 per cent)	3.96E–01	3.67E+07	3.94E+07
2p <sup>3</sup> – 2s2p <sup>2</sup>	2D <sup>o</sup> – 2D	5/2 – 3/2	75528	1323.995	2.27E–01	3.33E+07(0.2 per cent)	2.25E–01	3.28E+07	3.50E+07
		5/2 – 5/2	75531	1323.951	3.16E+00	4.63E+08(0.1 per cent)	3.13E+00	4.56E+08	4.88E+08
2s <sup>2</sup> 3s – 2s2p <sup>2</sup>	4P <sup>o</sup> – 2D	3/2 – 3/2	75534	1323.906	2.03E+00	4.45E+08(0.1 per cent)	2.01E+00	4.39E+08	4.69E+08
		3/2 – 5/2	75536	1323.862	2.30E–01	5.05E+07(<0.05 per cent)	2.27E–01	4.96E+07	5.31E+07
2s <sup>2</sup> 3s – 2s2p <sup>2</sup>	4P <sup>o</sup> – 2D	1/2 – 3/2	92034	1086.549	1.55E–05	1.21E+04(1.0 per cent)	2.45E–05	1.93E+04	
		3/2 – 3/2	92058	1086.270	1.50E–05	5.88E+03(1.4 per cent)	2.13E–05	8.39E+03	
2s <sup>2</sup> 3s – 2s2p <sup>2</sup>	4P <sup>o</sup> – 2D	3/2 – 5/2	92060	1086.241	9.46E–05	3.71E+04(0.9 per cent)	1.50E–04	5.93E+04	
		5/2 – 5/2	92105	1085.710	3.20E–06	8.38E+02(3.6 per cent)	2.45E–06	6.45E+02	
2p <sup>3</sup> – 2s2p <sup>2</sup>	2P <sup>o</sup> – 2D	1/2 – 3/2	94045	1063.313	1.97E+00	1.65E+09(0.9 per cent)	1.73E–00	1.45E+09	1.63E+09
		3/2 – 3/2	94045	1063.313	3.97E–01	1.66E+08(0.9 per cent)	3.44E–01	1.44E+08	1.64E+08
2s <sup>2</sup> 3p – 2s2p <sup>2</sup>	2P <sup>o</sup> – 2S	3/2 – 5/2	94048	1063.284	3.55E+00	1.49E+09(0.8 per cent)	3.11E+00	1.30E+09	1.46E+09
		1/2 – 1/2	35230	2838.439	7.05E–01	3.06E+07(0.1 per cent)	7.44E–01	3.27E+07	3.32E+07
2p <sup>3</sup> – 2s2p <sup>2</sup>	2D <sup>o</sup> – 2S	3/2 – 1/2	35241	2837.541	1.41E+00	3.06E+07(0.1 per cent)	1.49E+00	3.28E+07	3.32E+07
		3/2 – 1/2	53972	1852.780	1.78E–05	1.43E+03(1.8 per cent)	1.55E–05	1.23E+03	1.46E+03
2p <sup>3</sup> – 2s2p <sup>2</sup>	2P <sup>o</sup> – 2S	1/2 – 1/2	72484	1379.603	1.55E–05	5.92E+03(59.0 per cent)	1.02E–01	3.87E+07	2.50E+04
		3/2 – 1/2	72484	1379.603	1.78E–04	3.39E+04(31.6 per cent)	2.13E–01	4.05E+07	6.94E+04
2s <sup>2</sup> 3p – 2s2p <sup>2</sup>	2P <sup>o</sup> – 2P	1/2 – 3/2	21058	4748.606	2.62E–03	2.37E+04(5.9 per cent)	2.46E–03	2.31E+04	2.52E+04
		3/2 – 3/2	21069	4746.093	1.35E–02	6.12E+04(5.6 per cent)	1.26E–02	5.92E+04	6.53E+04
2p <sup>3</sup> – 2s2p <sup>2</sup>	2D <sup>o</sup> – 2P	1/2 – 1/2	21100	4739.292	6.33E–03	5.76E+04(5.2 per cent)	5.75E–03	5.42E+04	6.12E+04
		3/2 – 1/2	21111	4736.789	1.87E–03	8.54E+03(6.5 per cent)	1.90E–03	8.96E+03	9.23E+03
2p <sup>3</sup> – 2s2p <sup>2</sup>	2D <sup>o</sup> – 2P	5/2 – 3/2	39796	2512.814	2.68E+00	5.73E+07(2.7 per cent)	2.64E+00	5.62E+07	6.20E+07
		3/2 – 3/2	39801	2512.491	2.95E–01	9.45E+06(2.6 per cent)	2.90E–01	9.28E+06	1.02E+07
2s <sup>2</sup> 3s – 2s2p <sup>2</sup>	4P <sup>o</sup> – 2P	3/2 – 1/2	39842	2509.881	1.49E+00	4.81E+07(2.6 per cent)	1.47E+00	4.72E+07	5.21E+07
		1/2 – 3/2	56301	1776.149	4.38E–06	7.80E+02(0.4 per cent)	9.53E–06	1.71E+03	
2p <sup>3</sup> – 2s2p <sup>2</sup>	2P <sup>o</sup> – 2P	3/2 – 3/2	56325	1775.405	5.90E–05	5.25E+03(0.4 per cent)	1.53E–04	1.37E+04	
		1/2 – 1/2	56342	1774.845	4.89E–06	8.72E+02(0.5 per cent)	1.53E–05	2.78E+03	
2p <sup>3</sup> – 2s2p <sup>2</sup>	2P <sup>o</sup> – 2P	3/2 – 1/2	56366	1774.102	1.29E–05	1.15E+03(0.3 per cent)	3.19E–05	2.88E+03	
		1/2 – 3/2	58312	1714.890	5.79E–01	1.14E+08(0.3 per cent)	8.67E–01	1.71E+08	1.12E+08
2p <sup>3</sup> – 2s2p <sup>2</sup>	2P <sup>o</sup> – 2P	3/2 – 3/2	58312	1714.890	2.91E+00	2.88E+08(0.3 per cent)	4.36E+00	4.31E+08	2.83E+08
		1/2 – 1/2	58354	1713.674	1.16E+00	2.30E+08(0.3 per cent)	1.74E+00	3.44E+08	2.26E+08
2s <sup>2</sup> 3p – 2s <sup>2</sup> 3s	2P <sup>o</sup> – 2S	3/2 – 1/2	58354	1713.674	5.79E–01	5.74E+07(0.3 per cent)	8.70E–01	8.62E+07	5.63E+07
		1/2 – 1/2	15186	6584.700	1.03E+01	3.64E+07(0.2 per cent)	1.03E+01	3.78E+07	3.70E+07
2s <sup>2</sup> 3p – 2s <sup>2</sup> 3s	2P <sup>o</sup> – 2S	3/2 – 1/2	15197	6579.869	2.06E+01	3.65E+07(0.3 per cent)	2.06E+01	3.79E+07	3.71E+07

**Table A8** – *continued*

Transition array	Mult.	$J_u - J_l$	$\Delta E$ (cm <sup>-1</sup> )	$\lambda$ (Å)	MCDHF/RCI		MCHF-BP <sup>(a)</sup>		CI3 <sup>(b)</sup>
					$S$ (au of $a_0^2 e^2$ )	$A$ (s <sup>-1</sup> )	$S$ (au of $a_0^2 e^2$ )	$A$ (s <sup>-1</sup> )	
2p <sup>3</sup> – 2s <sup>2</sup> 3s	2P <sup>o</sup> – 2S	1/2 – 1/2	52440	1906.916	2.19E+02	3.19E + 06(0.1 per cent)	6.60E–02	9.58E + 06	3.35E + 06
		3/2 – 1/2	52440	1906.916	4.31E–02	3.15E + 06(0.1 per cent)	1.30E–01	9.45E + 06	3.32E + 06
2s <sup>2</sup> 3d – 2s <sup>2</sup> 3p	2D – 2P <sup>o</sup>	3/2 – 3/2	13813	7239.164	5.20E+00	6.94E + 06(0.6 per cent)	5.21E+00	6.73E + 06	7.09E + 06
		5/2 – 3/2	13815	7238.415	4.68E+01	4.17E + 07(0.6 per cent)	4.69E + 01	4.04E + 07	4.25E + 07
2p <sup>3</sup> – 2s <sup>2</sup> 3d	2P <sup>o</sup> – 2D	3/2 – 1/2	13824	7233.325	2.60E+01	3.48E + 07(0.6 per cent)	2.60E+01	3.37E + 07	3.55E + 07
		5/2 – 5/2	23429	4268.202	9.99E–05	1.30E + 03(27.0 per cent)	3.11E–01	3.99E + 06	4.08E + 04
		3/2 – 5/2	23427	4268.462	1.15E–04	7.49E + 02(32.7 per cent)	5.57E–01	3.58E + 06	3.33E + 04

Notes: <sup>(a)</sup> Tachiev & Fischer (2000); and <sup>(b)</sup> Corrégé & Hibbert (2004).

**Table A9.** Comparison of line strengths ( $S$ ) and transition rates ( $A$ ) with other theoretical results for C III. The present values from the MCDHF/RCI calculations are given in the Babushkin(length) gauge. The wavenumber  $\Delta E$  and wavelength  $\lambda$  values are taken from the NIST data base. The estimated uncertainties  $dT$  of the transition rates are given as percentages in parentheses.

Transition array	Mult.	$J_u - J_l$	$\Delta E$ (cm <sup>-1</sup> )	$\lambda$ (Å)	MCDHF/RCI		MCHF-BP <sup>(a)</sup>		GRASP <sup>(b)</sup>	
					$S$ (au of $a_0^2 e^2$ )	$A$ (s <sup>-1</sup> )	$S$ (au of $a_0^2 e^2$ )	$A$ (s <sup>-1</sup> )	$S$ (au of $a_0^2 e^2$ )	$A$ (s <sup>-1</sup> )
2s2p – 2s <sup>2</sup>	1P <sup>o</sup> – 1S	1 – 0	102352	977.020	2.44E+00	1.77E + 09(0.1 per cent)	2.44E+00	1.77E + 09	2.38E + 00	2.15E + 09
		1 – 0	258931	386.203	3.06E–01	3.59E + 09(<0.05 per cent)	3.06E–01	3.59E + 09	2.70E–01	3.16E + 09
2s3p – 2s <sup>2</sup>	1P <sup>o</sup> – 1S	1 – 0	259711	385.043	4.29E–05	5.08E + 05(0.5 per cent)	4.37E–05	5.18E + 05	1.17E–02	1.36E + 08
2s3p – 2s <sup>2</sup>	3P <sup>o</sup> – 1S	1 – 0	85007	1176.370	1.32E+00	5.48E + 08(<0.05 per cent)	1.32E+00	5.50E+08	1.33E+00	5.95E+08
2p <sup>2</sup> – 2s2p	3P – 3P <sup>o</sup>	0 – 1	85034	1175.987	1.05E+00	1.32E + 09(0.1 per cent)	1.05E+00	1.32E + 09	1.07E+00	1.43E+09
		2 – 2	85054	1175.711	3.95E+00	9.89E + 08(0.1 per cent)	3.95E+00	9.91E + 08	4.00E+00	1.07E+09
2p <sup>2</sup> – 2s2p	1D – 3P <sup>o</sup>	1 – 1	85063	1175.590	7.90E–01	3.30E + 08(0.1 per cent)	7.89E–01	3.31E + 08	8.00E–01	3.58E + 08
		1 – 0	85087	1175.263	1.05E+00	4.40E + 08(0.1 per cent)	1.05E+00	4.41E + 08	1.07E+00	4.78E + 08
2p <sup>2</sup> – 2s2p	3S – 3P <sup>o</sup>	2 – 1	85111	1174.933	1.32E+00	3.30E + 08(0.1 per cent)	1.32E+00	3.31E + 08	1.33E+00	3.59E + 08
		2 – 2	93429	1070.331	9.42E–05	3.13E + 04(5.3 per cent)	9.51E–05	3.17E + 04	3.74E–05	1.51E + 04
2p <sup>2</sup> – 2s2p	1S – 3P <sup>o</sup>	2 – 1	93485	1069.686	1.36E–05	4.52E + 03(7.8 per cent)	1.49E–05	4.97E + 03	3.37E–06	1.37E + 03
		0 – 1	130129	768.467	4.58E–07	2.06E + 03(17.8 per cent)	4.71E–07	2.12E + 03	2.01E–07	1.14E + 03
2s3s–2s2p	3S – 3P <sup>o</sup>	1 – 2	185765	538.312	4.73E–01	2.05E + 09(0.1 per cent)	4.73E–01	2.05E + 09	5.03E–01	2.11E + 09
1 – 1		185822	538.149	2.83E–01	1.23E + 09(0.1 per cent)	2.84E–01	1.23E + 09	3.01E–01	1.27E + 09	
2s3s–2s2p	1S – 3P <sup>o</sup>	1 – 0	185845	538.080	9.43E–02	4.09E + 08(0.1 per cent)	9.45E–02	4.10E + 08	1.00E–01	4.22E + 08
		0 – 1	194779	513.401	1.45E–08	2.17E + 02(25.2 per cent)	1.76E–08	2.64E + 02	2.46E–08	3.60E + 02
2s3d–2s2p	3D – 3P <sup>o</sup>	1 – 2	217563	459.635	4.24E–02	2.95E + 08(<0.05 per cent)	4.24E–02	2.95E + 08	4.24E–02	2.88E + 08
2 – 2		217564	459.633	6.36E–01	2.65E + 09(<0.05 per cent)	6.36E–01	2.66E + 09	6.36E–01	2.60E + 09	
2s3d–2s2p	3P – 3P <sup>o</sup>	3 – 2	217567	459.627	3.56E+00	1.06E + 10(<0.05 per cent)	3.56E+00	1.06E + 10	3.56E+00	1.04E + 10
		1 – 1	217620	459.516	6.36E–01	4.43E + 09(<0.05 per cent)	6.36E–01	4.43E + 09	6.36E–01	4.33E + 09
2s3d–2s2p	1D – 3P <sup>o</sup>	2 – 1	217621	459.514	1.91E+00	7.96E + 09(<0.05 per cent)	1.91E+00	7.97E + 09	1.91E+00	7.79E + 09
		1 – 0	217643	459.466	8.47E–01	5.90E + 09(<0.05 per cent)	8.47E–01	5.91E + 09	8.48E–01	5.77E + 09
2s3d–2s2p	1D – 3P <sup>o</sup>	2 – 1	224092	446.245	4.65E–07	2.12E + 03(0.3 per cent)	2.80E–07	1.28E + 03	2.48E–07	1.14E + 03
2p <sup>2</sup> – 2s2p		3P – 1P <sup>o</sup>	0 – 1	35073	2851.142	2.69E–06	2.36E + 02(37.5 per cent)	2.99E–06	2.65E + 02	1.85E–06
2p <sup>2</sup> – 2s2p	1D – 1P <sup>o</sup>		2 – 1	35149	2844.953	7.79E–05	1.37E + 03(8.2 per cent)	8.02E–05	1.43E + 03	2.85E–05
		2 – 1	43524	2297.578	4.11E+00	1.38E + 08(0.5 per cent)	4.11E+00	1.39E + 08	4.18E+00	1.34E + 08
2p <sup>2</sup> – 2s2p	1S – 1P <sup>o</sup>	0 – 1	80167	1247.383	1.99E+00	2.10E + 09(<0.05 per cent)	1.99E+00	2.10E + 09	2.24E+00	2.69E+09
2s3s–2s2p		3S – 1P <sup>o</sup>	1 – 1	135860	736.047	4.69E–07	7.92E + 02(5.0 per cent)	5.42E–07	9.17E + 02	3.76E–07
2s3s–2s2p	1S – 1P <sup>o</sup>		0 – 1	144818	690.521	1.40E–01	8.59E + 08(0.1 per cent)	1.39E–01	8.54E + 08	1.77E–01
2s3d–2s2p		3D – 1P <sup>o</sup>	1 – 1	167658	596.449	5.91E–07	1.88E + 03(6.5 per cent)	7.50E–07	2.39E + 03	4.14E–07
2s3d–2s2p	1D – 1P <sup>o</sup>		2 – 1	167659	596.446	9.30E–07	1.77E + 03(6.2 per cent)	4.89E–07	9.34E + 02	3.79E–07
		2 – 1	174130	574.281	2.93E+00	6.25E + 09(<0.05 per cent)	2.92E+00	6.25E + 09	3.37E+00	6.40E+09
2s3p – 2p <sup>2</sup>	1P <sup>o</sup> – 3P	1 – 2	121429	823.525	1.05E–05	1.27E + 04(0.3 per cent)	1.07E–05	1.29E + 04	7.12E–06	7.96E + 03
2s3p – 2p <sup>2</sup>		3P <sup>o</sup> – 3P	1 – 1	121476	823.202	1.76E–07	2.12E + 02(1.0 per cent)	8.87E–08	1.07E + 02	1.41E–05
	1 – 2		122209	818.269	7.20E–04	8.84E + 05(0.2 per cent)	7.05E–04	8.65E + 05	6.36E–04	7.10E + 05
2s3p – 2p <sup>2</sup>	1P <sup>o</sup> – 1D	2 – 2	122222	818.181	2.17E–03	1.60E + 06(0.2 per cent)	2.15E–03	1.58E + 06	1.91E–03	1.28E + 06
		0 – 1	122251	817.988	5.76E–04	2.13E + 06(0.2 per cent)	5.65E–04	2.08E + 06	5.08E–04	1.70E + 06
2s3p–2s3s	1P <sup>o</sup> – 3S	1 – 1	122256	817.950	4.29E–04	5.27E + 05(0.2 per cent)	4.26E–04	5.23E + 05	3.63E–04	4.06E + 05
		2 – 1	122269	817.863	7.30E–04	5.39E + 05(0.3 per cent)	7.20E–04	5.31E + 05	6.43E–04	4.31E + 05
2s3p–2s3s	3P <sup>o</sup> – 3S	1 – 0	122285	817.758	5.78E–04	7.12E + 05(0.2 per cent)	5.69E–04	7.00E + 05	4.86E–04	5.44E + 05
		1 – 2	113055	884.524	3.77E–01	3.66E + 08(<0.05 per cent)	3.69E–01	3.59E + 08	7.16E–01	5.67E + 08
2s3p – 2p <sup>2</sup>	3P <sup>o</sup> – 1D	1 – 2	113835	878.464	6.05E–05	6.00E + 04(0.1 per cent)	6.32E–05	6.27E + 04	3.07E–02	2.43E + 07
2s3p – 2p <sup>2</sup>		1P <sup>o</sup> – 1S	1 – 0	76411	1308.705	7.24E–02	2.16E + 07(0.1 per cent)	7.20E–02	2.15E + 07	1.54E–01
2s3p – 2p <sup>2</sup>	3P <sup>o</sup> – 1S		1 – 0	77191	1295.482	1.04E–05	3.19E + 03(0.2 per cent)	1.05E–05	3.23E + 03	6.65E–03
2s3p–2s3s		1P <sup>o</sup> – 3S	1 – 1	20718	4826.653	1.65E–03	9.96E + 03(1.7 per cent)	1.69E–03	1.02E + 04	4.51E–01
2s3p–2s3s	3P <sup>o</sup> – 3S		0 – 1	21492	4652.775	3.57E+00	7.20E + 07(<0.05 per cent)	3.57E+00	7.19E + 07	3.65E+00
		1 – 1	21498	4651.548	1.07E+01	7.20E + 07(<0.05 per cent)	1.07E+01	7.20E + 07	1.05E+01	7.14E + 07
2s3p–2s3s	1P <sup>o</sup> – 1S	2 – 1	21511	4648.720	1.78E+01	7.22E + 07(<0.05 per cent)	1.78E+01	7.21E + 07	1.83E+01	7.46E + 07
		1 – 0	11761	8502.657	9.25E+00	1.02E + 07(<0.05 per cent)	9.25E+00	1.02E + 07	8.59E+00	1.02E + 07
2s3p–2s3s	3P <sup>o</sup> – 1S	1 – 0	12540	7973.871	1.42E–03	1.89E + 03(2.6 per cent)	1.45E–03	1.92E + 03	3.69E–01	4.33E + 05

Table A9 – continued

Transition array	Mult.	$J_u - J_l$	$\Delta E$ ( $\text{cm}^{-1}$ )	$\lambda$ ( $\text{\AA}$ )	MCDHF/RCI		MCHF-BP <sup>(a)</sup>		GRASP <sup>(b)</sup>	
					$S$ (au of $a_0^2 e^2$ )	$A$ ( $\text{s}^{-1}$ )	$S$ (au of $a_0^2 e^2$ )	$A$ ( $\text{s}^{-1}$ )	$S$ (au of $a_0^2 e^2$ )	$A$ ( $\text{s}^{-1}$ )
2s3d–2s3p	$^3\text{D} - ^1\text{P}^o$	1 – 1	11079	9025.645	6.66E–04	6.10E + 02(1.6 per cent)	6.87E–04	6.35E + 02	1.86E–01	1.44E + 05
		2 – 1	11080	9024.749	2.12E–03	1.17E + 03(1.4 per cent)	2.23E–03	1.24E + 03	5.55E–01	2.58E + 05
2s3d–2s3p	$^1\text{D} - ^1\text{P}^o$	2 – 1	17551	5697.496	1.94E + 01	4.26E + 07(<0.05 per cent)	1.94E + 01	4.28E + 07	1.88E + 01	5.15E + 07
		1 – 2	10286	9721.451	2.94E–01	2.16E + 05(<0.05 per cent)	2.94E–01	2.18E + 05	3.00E–01	2.35E + 05
2s3d–2s3p	$^3\text{D} - ^3\text{P}^o$	2 – 2	10287	9720.412	4.40E + 00	1.95E + 06(<0.05 per cent)	4.41E + 00	1.97E + 06	4.51E + 00	2.11E + 06
		3 – 2	10290	9717.757	2.47E + 01	7.79E + 06(<0.05 per cent)	2.47E + 01	7.87E + 06	2.52E + 01	8.46E + 06
		1 – 1	10299	9709.105	4.40E + 00	3.25E + 06(<0.05 per cent)	4.41E + 00	3.29E + 06	4.32E + 00	3.39E + 06
		2 – 1	10300	9708.069	1.32E + 01	5.86E + 06(<0.05 per cent)	1.32E + 01	5.92E + 06	1.30E + 01	6.10E + 06
		1 – 0	10305	9703.764	5.87E + 00	4.35E + 06(<0.05 per cent)	5.88E + 00	4.39E + 06	6.01E + 00	4.72E + 06
2s3d–2s3p	$^1\text{D} - ^3\text{P}^o$	2 – 1	16771	5962.446	3.11E–03	5.97E + 03(0.4 per cent)	3.23E–03	6.24E + 03	8.04E–01	2.22E + 06

Notes: <sup>(a)</sup> Tachiev & Fischer (1999); and <sup>(b)</sup> Aggarwal & Keenan (2015).

**Table A10.** Comparison of line strengths ( $S$ ) and transition rates ( $A$ ) with other theoretical results for C IV. The present values from the MCDHF/RCI calculations are given in the Babushkin (length) gauge. The wavenumber  $\Delta E$  and wavelength  $\lambda$  values are taken from the NIST data base. The estimated uncertainties  $dT$  of the transition rates are given as percentages in parentheses.

Transition array	Mult.	$J_u - J_l$	$\Delta E$ ( $\text{cm}^{-1}$ )	$\lambda$ ( $\text{\AA}$ )	MCDHF/RCI		MCHF-BP <sup>(a)</sup>	
					$S$ (au of $a_0^2 e^2$ )	$A$ ( $\text{s}^{-1}$ )	$S$ (au of $a_0^2 e^2$ )	$A$ ( $\text{s}^{-1}$ )
2p–2s	$^2\text{P}^o - ^2\text{S}$	1/2 – 1/2	64484	1550.772	9.68E–01	2.63E + 08(<0.05 per cent)	9.68E–01	2.63E + 08
		3/2 – 1/2	64591	1548.187	1.94E + 00	2.65E + 08(<0.05 per cent)	1.94E + 00	2.65E + 08
3p–2s	$^2\text{P}^o - ^2\text{S}$	1/2 – 1/2	320050	312.451	1.39E–01	4.63E + 09(<0.05 per cent)	1.40E–01	4.64E + 09
		3/2 – 1/2	320081	312.420	2.78E–01	4.62E + 09(<0.05 per cent)	2.79E–01	4.63E + 09
3s–2p	$^2\text{S} - ^2\text{P}^o$	1/2 – 3/2	238257	419.714	2.07E–01	2.84E + 09(<0.05 per cent)	2.07E–01	2.84E + 09
		1/2 – 1/2	238365	419.525	1.03E–01	1.42E + 09(<0.05 per cent)	1.03E–01	1.42E + 09
3d–2p	$^2\text{D} - ^2\text{P}^o$	3/2 – 3/2	260288	384.190	3.26E–01	2.91E + 09(<0.05 per cent)	3.26E–01	2.91E + 09
		5/2 – 3/2	260298	384.174	2.94E + 00	1.75E + 10(<0.05 per cent)	2.94E + 00	1.75E + 10
		3/2 – 1/2	260395	384.031	1.63E + 00	1.46E + 10(<0.05 per cent)	1.63E + 00	1.46E + 10
4s–2p	$^2\text{S} - ^2\text{P}^o$	1/2 – 3/2	336756	296.951	2.74E–02	1.06E + 09(<0.05 per cent)	2.75E–02	1.06E + 09
		1/2 – 1/2	336864	296.856	1.37E–02	5.30E + 08(<0.05 per cent)	1.38E–02	5.32E + 08
3p–3s	$^2\text{P}^o - ^2\text{S}$	1/2 – 1/2	17201	5813.582	6.10E + 00	3.15E + 07(<0.05 per cent)	6.11E + 00	3.15E + 07
		3/2 – 1/2	17232	5802.921	1.22E + 01	3.17E + 07(<0.05 per cent)	1.22E + 01	3.16E + 07
3d–3p	$^2\text{D} - ^2\text{P}^o$	3/2 – 3/2	4798	20841.583	1.71E + 00	9.54E + 04(<0.05 per cent)	1.71E + 00	9.51E + 04
		5/2 – 3/2	4808	20796.074	1.54E + 01	5.76E + 05(<0.05 per cent)	1.54E + 01	5.74E + 05
		3/2 – 1/2	4829	20705.220	8.54E + 00	4.87E + 05(<0.05 per cent)	8.54E + 00	4.85E + 05
4s–3p	$^2\text{S} - ^2\text{P}^o$	1/2 – 3/2	81266	1230.521	1.32E + 00	7.16E + 08(<0.05 per cent)	1.31E + 00	7.14E + 08
		1/2 – 1/2	81298	1230.043	6.57E–01	3.58E + 08(<0.05 per cent)	6.57E–01	3.57E + 08

Note: <sup>(a)</sup> Fischer et al. (1998).

This paper has been typeset from a  $\text{T}_{\text{E}}\text{X}/\text{L}^{\text{A}}\text{T}_{\text{E}}\text{X}$  file prepared by the author.



## Paper III



A. Papoulia, J. Ekman and P. Jönsson

Extended transition rates and lifetimes in Al I and Al II from systematic multiconfiguration calculations

*Astronomy & Astrophysics*, 2019, 621(A16)

Reproduced with permission from *A & A*

Copyright 2019 ESO.



# Extended transition rates and lifetimes in Al I and Al II from systematic multiconfiguration calculations<sup>\*</sup>

A. Papoulia (Ασημίνα Παπούλια)<sup>1,2</sup>, J. Ekman<sup>1</sup>, and P. Jönsson<sup>1</sup>

<sup>1</sup> Materials Science and Applied Mathematics, Malmö University, 20506 Malmö, Sweden  
e-mail: [asimina.papoulia@mau.se](mailto:asimina.papoulia@mau.se)

<sup>2</sup> Division of Mathematical Physics, Lund University, Post Office Box 118, 22100 Lund, Sweden

Received 3 July 2018 / Accepted 22 September 2018

## ABSTRACT

MultiConfiguration Dirac-Hartree-Fock (MCDHF) and relativistic configuration interaction (RCI) calculations were performed for 28 and 78 states in neutral and singly ionized aluminium, respectively. In Al I, the configurations of interest are  $3s^2nl$  for  $n = 3, 4, 5$  with  $l = 0$  to 4, as well as  $3s3p^2$  and  $3s^26l$  for  $l = 0, 1, 2$ . In Al II, in addition to the ground configuration  $3s^2$ , the studied configurations are  $3snl$  with  $n = 3$  to 6 and  $l = 0$  to 5,  $3p^2$ ,  $3s7s$ ,  $3s7p$ , and  $3p3d$ . Valence and core-valence electron correlation effects are systematically accounted for through large configuration state function (CSF) expansions. Calculated excitation energies are found to be in excellent agreement with experimental data from the National Institute of Standards and Technology (NIST) database. Lifetimes and transition data for radiative electric dipole (E1) transitions are given and compared with results from previous calculations and available measurements for both Al I and Al II. The computed lifetimes of Al I are in very good agreement with the measured lifetimes in high-precision laser spectroscopy experiments. The present calculations provide a substantial amount of updated atomic data, including transition data in the infrared region. This is particularly important since the new generation of telescopes are designed for this region. There is a significant improvement in accuracy, in particular for the more complex system of neutral Al I. The complete tables of transition data are available at the CDS.

**Key words.** atomic data

## 1. Introduction

Aluminium is an important element in astrophysics. In newly born stars the galactic [Al/H] abundance ratio and the [Al/Mg] ratio are found to be increased in comparison to early stars (Clayton 2003). The aluminium abundance and its anti-correlation with that of magnesium is the best tool to determine which generation a globular cluster star belongs to. The abundance variations of different elements and the relative numbers of first- and second-generation stars can be used to determine the nature of polluting stars, the timescale of the star formation episodes, and the initial mass function of the stellar cluster (Carretta et al. 2010). The aluminium abundance is of importance for other types and groups of stars as well. A large number of spectral lines of neutral and singly ionized aluminium are observed in the solar spectrum and in many stellar spectra. Aluminium is one of the interesting elements for chemical analysis of the Milky Way, and one example is the *Gaia*-ESO Survey<sup>1</sup>; medium- and high-resolution spectra from more than  $10^5$  stars are analysed to provide public catalogues with astrophysical parameters. As part of this survey, Smiljanic et al. (2014) analysed high-resolution UVES<sup>2</sup> spectra of FGK-type stars and derived abundances for 24 elements, including aluminium.

<sup>\*</sup> The data are only available available at the CDS via anonymous ftp to [cdsarc.u-strasbg.fr](http://cdsarc.u-strasbg.fr) (130.79.128.5) or via <http://cdsarc.u-strasbg.fr/viz-bin/qcat?J/A+A/621/A16>

<sup>1</sup> <http://casu.ast.cam.ac.uk/surveys-projects/ges>

<sup>2</sup> <http://www.eso.org/sci/facilities/paranal/instruments/uves.html>

In addition, aluminium abundances have been determined in local disk and halo stars by Gehren et al. (2004), Reddy et al. (2006), Mishenina et al. (2008), Adibekyan et al. (2012), and Bensby et al. (2014). However, chemical evolution models still have problems reproducing the observed behaviour of the aluminium abundance in relation to abundances of other elements. Such examples are the observed trends of the aluminium abundances in relation to metallicity [Fe/H], which are not well reproduced at the surfaces of stars, for example giants and dwarfs (Smiljanic et al. 2016). In light of the above issues, Smiljanic et al. (2016) redetermined aluminium abundances within the *Gaia*-ESO Survey. Furthermore, strong deviations from local thermodynamic equilibrium (LTE) are found to significantly affect the inferred aluminium abundances in metal poor stars, which was highlighted in the work by Gehren et al. (2006). Nordlander & Lind (2017) presented a non-local thermodynamic equilibrium (NLTE) modelling of aluminium and provided abundance corrections for lines in the optical and near-infrared regions.

Correct deduction of aluminium abundances and chemical evolution modelling is thus necessary to put together a complete picture of the stellar and Galactic evolution. Obtaining the spectroscopic reference data to achieve this goal is demanding. A significant amount of experimental research has been conducted to probe the spectra of Al II and Al I and to facilitate the analysis of the astrophysical observations. Even so, some laboratory measurements still lack reliability and in many cases, especially when going to higher excitation energies, only theoretical values of transition properties exist. Accurate computed atomic data are

therefore essential to make abundance analyses in the Sun and other stars possible.

For the singly ionized Al II, there are a number of measurements of transition properties. The radiative lifetime of the  $3s3p\ ^3P_1$  level was measured by Johnson et al. (1986) using an ion storage technique and the transition rate value for the inter-combination  $3s3p\ ^3P_1 \rightarrow 3s^2\ ^1S_0$  transition was provided. Träbert et al. (1999) measured lifetimes in an ion storage ring and the result for the lifetime of the  $3s3p\ ^3P_1$  level is in excellent agreement with the value measured by Johnson et al. (1986). Using the beam-foil technique, Andersen et al. (1971) measured lifetimes for the  $3snf\ ^3F$  series with  $n = 4-7$ , although these measurements are associated with significant uncertainties. By using the same technique, the lifetime of the singlet  $3s3p\ ^1P_1$  level was measured in four different experimental works (Kernahan et al. 1979; Head et al. 1976; Berry et al. 1970; Smith 1970), which are in very good agreement.

In the case of neutral Al I, several measurements have also been performed. Following a sequence of earlier works (Jönsson & Lundberg 1983; Jönsson et al. 1984), Buurman et al. (1986) used laser spectroscopy to obtain experimental values for the oscillator strengths of the lowest part of the spectrum. A few years later, Buurman & Dönszelmann (1990) redetermined the lifetime of the  $3s24p\ ^2P$  level and separated the different fine-structure components. Using similar laser techniques, Davidson et al. (1990) measured the natural lifetimes of the  $3s^2nd\ ^2D$  Rydberg series and obtained oscillator strengths for transitions to the ground state. In a more recent work, Vujnović et al. (2002) used the hollow cathode discharge method to measure relative intensities of spectral lines of both neutral and singly ionized aluminium. Absolute transition probabilities were evaluated based on available results from previous studies, such as the ones mentioned above.

Al II is a nominal two-electron system and the lower part of its spectrum is strongly influenced by the interaction between the  $3s3d\ ^1D$  and  $3p^2\ ^1D$  configuration states. Contrary to neutral Mg I where no level is classified as  $3p^2\ ^1D$ , in Al II the  $3p^2$  configuration dominates the lowest  $^1D$  term and yields a well-localized state below the  $3s3d\ ^1D$  term. The interactions between the  $3snd\ ^1D$  Rydberg series and the  $3p^2\ ^1D$  perturber were investigated by Tayal & Hibbert (1984). Going slightly further up, the spectrum of Al II is governed by the strong mixing of the  $3snf\ ^3F$  Rydberg series with the  $3p3d\ ^3F$  term. Despite the widespread mixing,  $3p3d\ ^3F$  is also localized, between the  $3s6f\ ^3F$  and  $3s7f\ ^3F$  states. The configuration interaction between doubly excited states (e.g. the  $3p^2\ ^1D$  and  $3p3d\ ^3F$  states) and singly excited  $3snl\ ^{1,3}L$  states was thoroughly investigated by Chang & Wang (1987). However, the extreme mixing of the  $3p3d\ ^3F$  term in the  $3snf\ ^3F$  series and its effect on the computation of transition properties was first investigated by Weiss (1974). Although the work by Chang & Wang (1987) was more of a qualitative nature, computed transition data were provided based on configuration interaction (CI) calculations. Using the B-spline configuration interaction (BSCI) method, Chang & Fang (1995) also predicted transition properties and lifetimes of Al II excited states.

Despite the large number of measured spectral lines in Al I, the  $3s3p^2\ ^2D$  state could not be experimentally identified and for a long time theoretical calculations had been trying to localize it and predict whether it lies above or below the first-ionization limit. Al I is a system with three valence electrons, and the correlation effects are even stronger than in the singly ionized Al II. Especially strong is the two-electron interaction of  $3s3d\ ^1D$  with  $3p^2\ ^1D$ , which becomes evident between the  $3s^23d\ ^2D$  and

$3s3p^2\ ^2D$  states. The  $3s3p^2\ ^2D$  state is strongly coupled to the  $3s^23d\ ^2D$  state, but it is also smeared out over the entire discrete part of the  $3s^2nd\ ^2D$  series and contributes to a significant mixing of all those states (Weiss 1974). Asking for the position of the  $3s3p^2\ ^2D$  level is thus meaningless since it does not correspond to any single spectral line (Lin 1974; Trefftz 1988). Due to this strong two-electron interaction, the line strength of one of the  $^2D$  states involved in a transition appears to be enhanced, while the line strength of the other  $^2D$  state is suppressed. This makes the computation of transition properties in Al I far from trivial (Froese Fischer et al. 2006). More theoretical studies on the system of neutral aluminium were conducted by Taylor et al. (1988) and Theodosiou (1992).

In view of the great astrophysical interest for accurate atomic data, close coupling (CC) calculations were carried out for the systems of Al II and Al I by Butler et al. (1993) and Mendoza et al. (1995), respectively, as part of the Opacity Project. These extended spectrum calculations produced transition data in the infrared region (IR), which had been scarce until then. However, the neglected relativistic effects and the insufficient amount of correlation included in the calculations constitute limiting factors to the accuracy of the results. Later on, Froese Fischer et al. (2006) performed MultiConfiguration Hartree-Fock (MCHF) calculations and used the Breit-Pauli (BP) approximation to also capture relativistic effects for Mg- and Al-like sequences. Focusing more on correlation, relativistic effects were kept to lower order. Even so, in Al I, correlation in the core and core-valence effects were not included due to limited computational resources. The latest compilation of Al II and Al I transition probabilities was made available by Kelleher & Podobedova (2008a). Wiese & Martin (1980) had earlier updated the first critical compilation of atomic data by Wiese et al. (1969).

Although for the past decades a considerable amount of research has been conducted for the systems of Al II and Al I, there is still a need for extended and accurate theoretical transition data. The present study is motivated by such a need. To obtain energy separations and transition data, the fully relativistic MultiConfiguration Dirac-Hartree-Fock (MCDHF) scheme has been employed. Valence and core-valence electron correlation is included in the computations of both systems. Spectrum calculations have been performed to include the first 28 and 78 lowest states in neutral and singly ionized aluminium, respectively. Transition data corresponding to IR lines have also been produced. The excellent description of energy separations is an indication of highly accurate computed atomic properties, which can be used to improve the interpretation of abundances in stars.

## 2. Theory

### 2.1. MultiConfiguration Dirac-Hartree-Fock approach

The wave functions describing the states of the atom, referred to as atomic state functions (ASFs), are obtained by applying the MCDHF approach (Grant 2007; Froese Fischer et al. 2016). In the MCDHF method, the ASFs are approximate eigenfunctions of the Dirac-Coulomb Hamiltonian given by

$$H_{DC} = \sum_{i=1}^N [c \boldsymbol{\alpha}_i \cdot \mathbf{p}_i + (\beta_i - 1)c^2 + V_{\text{nuc}}(r_i)] + \sum_{i < j}^N \frac{1}{r_{ij}}, \quad (1)$$

where  $V_{\text{nuc}}(r_i)$  is the potential from an extended nuclear charge distribution,  $\boldsymbol{\alpha}$  and  $\beta$  are the  $4 \times 4$  Dirac matrices,  $c$  the speed of light in atomic units, and  $\mathbf{p} \equiv -i\nabla$  the electron momentum

operator. An ASF  $\Psi(\gamma PJM_J)$  is given as an expansion over  $N_{\text{CSF}}$  configuration state functions (CSFs),  $\Phi(\gamma_i PJM_J)$ , characterized by total angular momentum  $J$  and parity  $P$ :

$$\Psi(\gamma PJM_J) = \sum_{i=1}^{N_{\text{CSF}}} c_i \Phi(\gamma_i PJM_J). \quad (2)$$

The CSFs are anti-symmetrized many-electron functions built from products of one-electron Dirac orbitals and are eigenfunctions of the parity operator  $P$ , the total angular momentum operator  $J^2$  and its projection on the  $z$ -axis  $J_z$  (Grant 2007; Froese Fischer et al. 2016). In the expression above,  $\gamma_i$  represents the configuration, coupling, and other quantum numbers necessary to uniquely describe the CSFs.

The radial parts of the Dirac orbitals together with the mixing coefficients  $c_i$  are obtained in a self-consistent field (SCF) procedure. The set of SCF equations to be iteratively solved results from applying the variational principle on a weighted energy functional of all the studied states according to the extended optimal level (EOL) scheme (Dyall et al. 1989). The angular integrations needed for the construction of the energy functional are based on the second quantization method in the coupled tensorial form (Gaigalas et al. 1997, 2001).

The transverse photon (Breit) interaction and the leading quantum electrodynamic (QED) corrections (vacuum polarization and self-energy) can be accounted for in subsequent relativistic configuration interaction (RCI) calculations (McKenzie et al. 1980). In the RCI calculations, the Dirac orbitals from the previous step are fixed and only the mixing coefficients of the CSFs are determined by diagonalizing the Hamiltonian matrix. All calculations were performed using the relativistic atomic structure package GRASP2K (Jönsson et al. 2013).

In the MCDHF relativistic calculations, the wave functions are expansions over  $jj$ -coupled CSFs. To identify the computed states and adapt the labelling conventions followed by the experimentalists, the ASFs are transformed from  $jj$ -coupling to a basis of  $LSJ$ -coupled CSFs. In the GRASP2K code this is done using the methods developed by Gaigalas et al. (2003, 2004, 2017).

## 2.2. Transition parameters

In addition to excitation energies, lifetimes  $\tau$  and transition parameters, such as emission transition rates  $A$  and weighted oscillator strengths  $gf$ , were also computed. The transition parameters between two states  $\gamma'P'J'$  and  $\gamma PJ$  are expressed in terms of reduced matrix elements of the transition operator  $\mathbf{T}$  (Grant 1974):

$$\langle \Psi(\gamma PJ) || \mathbf{T} || \Psi(\gamma'P'J') \rangle = \sum_{k,l} c_k c'_l \langle \Phi(\gamma_k PJ) || \mathbf{T} || \Phi(\gamma'_l P'J') \rangle. \quad (3)$$

For electric multipole transitions, there are two forms of the transition operator: the length, which in fully relativistic calculations is equivalent to the Babushkin gauge, and the velocity form, which is equivalent to the Coulomb gauge. The transitions are governed by the outer part of the wave functions. The length form is more sensitive to this part of the wave functions and it is generally considered to be the preferred form. Regardless, the agreement between the values of these two different forms can be used to indicate the accuracy of the wave functions (Froese Fischer 2009; Ekman et al. 2014). This is particularly useful when no experimental measurements are available. The transitions can be organized in groups determined, for

instance, by the magnitude of the transition rate value. A statistical analysis of the uncertainties of the transitions can then be performed. For each group of transitions the average uncertainty of the length form of the computed transition rates is given by

$$\langle \delta T \rangle = \frac{1}{N} \sum_{i=1}^N \frac{|A_i^l - A_i^v|}{\max(A_i^l, A_i^v)}, \quad (4)$$

where  $A_i^l$  and  $A_i^v$  are respectively the transition rates in length and velocity form for a transition  $i$  and  $N$  is the number of the transitions belonging to a group. In this work, we only computed transition parameters for the electric dipole (E1) transitions. The electric quadrupole (E2) and magnetic multipole (Mk) transitions are much weaker and therefore less likely to be observed.

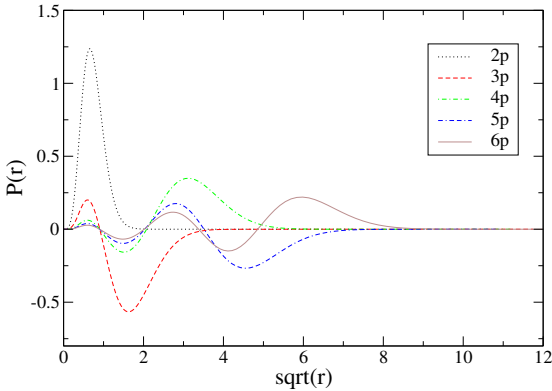
## 3. Calculations

### 3.1. Al I

In neutral aluminium, calculations were performed in the EOL scheme (Dyall et al. 1989) for 28 targeted states. These states belong to the  $3s^2ns$  configurations with  $n = 4, 5, 6$ , the  $3s^2nd$  configurations with  $n = 3, \dots, 6$ , and the  $3s3p^2$  and  $3s^25g$  configurations, characterized by even parity, and on the other hand the  $3s^2np$  configurations with  $n = 3, \dots, 6$  and the  $3s^24f$  and  $3s^25f$  configurations, characterized by odd parity. These configurations define what is known as the multireference (MR). From initial calculations and analysis of the eigenvector compositions, we deduced that all  $3p^2nl$  configurations, in addition to the targeted  $3s^2nl$ , give considerable contributions to the total wave functions and should be included in the MR. Following the active set (AS) approach (Olsen et al. 1988; Sturesson et al. 2007), the CSF expansions (see Eq. (2)) were obtained by allowing single and restricted double (SD) substitutions of electrons from the reference (MR) orbitals to an AS of correlation orbitals. The AS is systematically increased by adding layers of orbitals to effectively build nearly complete wave functions. This is achieved by keeping track of the convergence of the computed excitation energies, and of the other physical quantities of interest, such as the transition parameters here.

As a first step an MCDHF calculation was performed for the orbitals that are part of the MR. States with both even and odd parity were simultaneously optimized. Following this step, we continued to optimize six layers of correlation orbitals based on valence (VV) substitutions. The VV expansions were obtained by allowing SD substitutions from the three outer valence orbitals in the MR, with the restriction that there will be at most one substitution from orbitals with  $n = 3$ . In this manner, the correlation orbitals will occupy the space between the inner  $n = 3$  valence orbitals and the outer orbitals involved in the higher Rydberg states (see Fig. 1). These orbitals have been shown to be of crucial importance for the transition probabilities, which are weighted towards this part of the space (Pehlivan Rhodin et al. 2017; Pehlivan Rhodin 2018). The six correlation layers correspond to the 12s, 12p, 12d, 11f, 11g, and 10h set of orbitals.

Each MCDHF calculation was followed by an RCI calculation for an extended expansion, obtained by single, double, and triple (SDT) substitutions from the valence orbitals. As a final step, an RCI calculation was performed for the largest SDT valence expansion augmented by a core-valence (CV) expansion. The CV expansion was obtained by allowing SD substitutions from the valence orbitals and the  $2p^6$  core, with the restriction that there will be at most one substitution from



**Fig. 1.** Al I Dirac-Fock radial orbitals for the  $p$  symmetry, as a function of  $\sqrt{r}$ . The 2p orbital is part of the core and the orbitals from  $n = 3$  to  $n = 6$  are part of the valence electron cloud. These orbitals occupy different regions in space and the overlap between some of the Rydberg states is minor.

2p<sup>6</sup>. All the RCI calculations included the Breit interaction and the leading QED effects. Accounting for CV correlation does not lower the total energies significantly, but it can have large effects on the energy separations and thus we considered it crucial. Core-valence correlation is also important for transition properties (Hibbert 1989). Core-core (CC) correlation, obtained by allowing double excitations from the core, is known to be less important and has not been considered in the present work. The number of CSFs in the final even and odd state expansions, accounting for both VV and CV electron correlation, were 4 362 628 and 2 889 385, respectively, distributed over the different J symmetries.

### 3.2. Al II

In the singly ionized aluminium, the calculations were more extended, including 78 targeted states. These states belong to the 3s<sup>2</sup> ground configuration, and to the 3p<sup>2</sup>; the 3sns configurations with  $n = 4, \dots, 7$ ; the 3snd with  $n = 3, \dots, 6$ ; and the 3s5g and 3s6g configurations, characterized by even parity, and on the other hand, the 3snp configurations with  $n = 3, \dots, 7$ ; the 3snf with  $n = 4, 5, 6$ ; and the 3s6h and 3p3d configurations, characterized by odd parity. These configurations define the multireference (MR). In the computations of Al II, the EOL scheme was applied and the CSF expansions were obtained following the active set (AS) approach, accounting for VV and CV correlation. Al II is less complex and the CSF expansions generated from (SD) substitutions are not as large as those in Al I. Hence, we can afford both 2s and 2p orbitals to account for CV correlation. The 1s core orbital remained closed and, as it was for Al I, core-core correlation was neglected. The MCDHF calculations were performed in a similar way to the calculations in Al I, yet no particular restrictions were imposed on the VV substitutions. We optimized six correlation layers corresponding to the 13s, 13p, 12d, 12f, 12g, 8h, and 7i set of orbitals. Each MCDHF calculation was followed by an RCI calculation. Finally, an RCI calculation was performed for the largest SD valence expansion augmented by the CV expansion. The number of CSFs in the final even and odd state expansions, accounting for both VV and CV electron correlation, were 911 795 and 1 269 797, respectively, distributed over the different J symmetries.

## 4. Results

### 4.1. Al I

In Table 1 the computed excitation energies, based on VV correlation, are given as a function of the increasing active set of orbitals. After adding the  $n = 11$  correlation layer, we note that the energy values for all 28 targeted states have converged. For comparison, in the second last column the observed energies from the National Institute of Standards and Technology (NIST) Atomic Spectra Database (Kramida et al. 2018) are displayed. All energies but those belonging to the 3s3p<sup>2</sup> configuration are already in good agreement with the NIST recommended values. The relative differences between theory and experiment for all three levels of the quartet 3s3p<sup>2</sup> 4P state is 3.1%, while the mean relative difference for the rest of the states is less than 0.2%. In the third last column, the computed excitation energies after accounting for CV correlation are displayed. When taking into account CV effects the agreement with the observed values is better overall. Most importantly, for the 3s3p<sup>2</sup> 4P levels the relative differences between observed and computed values decrease to less than 0.6%. The likelihood that the 1s<sup>2</sup>2s<sup>2</sup>2p<sup>6</sup> core overlaps with the 3s3p<sup>2</sup> cloud of electrons is much less than that for 3s<sup>2</sup>n $l$ . Consequently, when CV correlation is taken into account the lowering of the 3s3p<sup>2</sup> energy levels is much smaller than for levels belonging to any 3s<sup>2</sup>n $l$  configuration. Thus, the adjustments to the separation energies will be minor between the ground state 3s<sup>2</sup>3p and 3s<sup>2</sup>n $l$  levels, but significant between the 3s<sup>2</sup>3p and 3s3p<sup>2</sup> levels. In the last column of Table 1 the differences  $\Delta E = E_{\text{obs}} - E_{\text{theor}}$ , between the final (CV) computed and the observed energies, are also displayed. In principle, there are two groups of values; the one consisting of the 3s<sup>2</sup>n $l$  configurations exhibits the smallest absolute discrepancies from the observed energies. For the rest, the absolute discrepancies are somewhat larger.

In the calculations, the labelling of the eigenstates is determined by the CSF with the largest coefficient in the expansion of Eq. (2). When the same label is assigned to different eigenstates, a detailed analysis can be performed by displaying their  $LS$ -compositions. In Table 1, we note that two of the states have been assigned the same label, i.e. 3s<sup>2</sup>4d<sup>2</sup>D, and thus the subscripts  $a$  and  $b$  are used to distinguish them. In Table 2, we give the  $LS$ -composition of all computed 3s<sup>2</sup>nd<sup>2</sup>D states, including the three most dominant CSFs. The 3s<sup>2</sup>4d<sup>2</sup>D term appears twice as the CSF with the largest  $LS$ -composition. Moreover, the admixture of the 3s3p<sup>2</sup> 2D in the four lowest 3s<sup>2</sup>nd<sup>2</sup>D states is rather strong and adds up to 65%. That being so, the 3s3p<sup>2</sup> 2D does not exist in the calculated spectrum as a localized state. For comparison, in the last column of Table 2 the labelling of the observed 3s<sup>2</sup>nd<sup>2</sup>D states is also given. In the observed configurations presented by NIST (Kramida et al. 2018), the second highest 3s<sup>2</sup>nd<sup>2</sup>D term has not been given any specific label and it is therefore designated as  $y$  2D. The higher 2D terms are designated as 3s<sup>2</sup>4d, 3s<sup>2</sup>5d, and so on.

In Table 3, the current results for the lowest excitation energies are compared with the values from the MCHF-BP calculations by Froese Fischer et al. (2006). The latter calculations are extended up to levels corresponding to the doublet 3s<sup>2</sup>4p<sup>2</sup>P state. The differences  $\Delta E$  between observed and computed energies are given in the last two columns for the different computational approaches. As can be seen, when using the current MCDHF and RCI method the agreement with the observed energies is substantially improved for all levels and in particular, for those belonging to the quartet 3s3p<sup>2</sup> 4P state. In the MCHF-BP calculations, core-valence correlation was neglected. As

**Table 1.** Computed excitation energies in  $\text{cm}^{-1}$  for the 28 lowest states in Al I.

Pos.	Conf.	$LSJ$	VV						CV	$E_{\text{obs}}^a$	$\Delta E$
			$n = 7$	$n = 8$	$n = 9$	$n = 10$	$n = 11$	$n = 12$			
1	$3s^2 3p$	$2P_{1/2}^o$	0	0	0	0	0	0	0	0	0
2		$2P_{3/2}^o$	108	108	108	108	108	108	104	112	8
3	$3s^2 4s$	$2S_{1/2}$	25 318	25 377	25 416	25 419	25 427	25 429	25 196	25 348	152
4	$3s 3p^2$	$4P_{1/2}$	27 788	27 966	28 073	28 085	28 109	28 111	28 863	29 020	157
5		$4P_{3/2}$	27 833	28 011	28 118	28 130	28 154	28 156	28 907	29 067	160
6		$4P_{5/2}$	27 906	28 085	28 191	28 204	28 227	28 230	28 981	29 143	162
7	$3s^2 3d$	$2D_{3/2}$	32 211	32 077	32 135	32 139	32 150	32 150	32 414	32 435	21
8		$2D_{5/2}$	32 212	32 079	32 137	32 141	32 152	32 152	32 416	32 437	21
9	$3s^2 4p$	$2P_{1/2}^o$	32 770	32 879	32 935	32 937	32 946	32 949	32 801	32 950	149
10		$2P_{3/2}^o$	32 786	32 894	32 951	32 952	32 962	32 964	32 814	32 966	152
11	$3s^2 5s$	$2S_{1/2}$	37 493	37 637	37 693	37 694	37 704	37 706	37 512	37 689	177
12	$3s^2 4d$	$2D_{3/2 a}$	38 733	38 659	38 711	38 707	38 717	38 718	38 951	38 929	-22
13		$2D_{5/2 a}$	38 736	38 664	38 717	38 712	38 722	38 724	38 957	38 934	-23
14	$3s^2 5p$	$2P_{1/2}^o$	40 038	40 187	40 252	40 249	40 259	40 262	40 101	40 272	171
15		$2P_{3/2}^o$	40 043	40 193	40 258	40 255	40 265	40 268	40 106	40 278	172
16	$3s^2 4f$	$2F_{5/2}^o$	41 050	41 209	41 282	41 287	41 297	41 300	41 163	41 319	156
17		$2F_{7/2}^o$	41 050	41 209	41 282	41 287	41 297	41 300	41 163	41 319	156
18	$3s^2 6s$	$2S_{1/2}$	41 897	42 069	42 133	42 135	42 144	42 143	41 964	42 144	180
19	$3s^2 4d$	$2D_{3/2 b}$	42 105	42 071	42 121	42 108	42 119	42 121	42 232	42 234	2
20		$2D_{5/2 b}$	42 109	42 075	42 126	42 112	42 123	42 125	42 237	42 238	1
21	$3s^2 6p$	$2P_{1/2}^o$	43 076	43 246	43 316	43 311	43 321	43 324	43 160	43 335	175
22		$2P_{3/2}^o$	43 079	43 249	43 318	43 313	43 324	43 326	43 162	43 338	176
23	$3s^2 5f$	$2F_{5/2}^o$	43 549	43 721	43 795	43 801	43 811	43 813	43 660	43 831	171
24		$2F_{7/2}^o$	43 549	43 721	43 795	43 801	43 811	43 813	43 660	43 831	171
25	$3s^2 5g$	$2G_{7/2}$	43 576	43 763	43 838	43 845	43 856	43 859	43 687	43 876	189
26		$2G_{9/2}$	43 576	43 763	43 838	43 845	43 856	43 859	43 687	43 876	189
27	$3s^2 5d$	$2D_{3/2}$	44 034	44 059	44 115	44 096	44 106	44 109	44 126	44 166	40
28		$2D_{5/2}$	44 036	44 062	44 117	44 099	44 109	44 111	44 129	44 169	40

**Notes.** The energies are given as a function of the increasing active set of orbitals, accounting for VV correlation, where  $n$  indicates the maximum principle quantum number of the orbitals included in the active set. In Col. 10, the final energy values are displayed after accounting for CV correlation. The differences  $\Delta E$  between the final computations and the observed values are shown in the last column. The sequence and labelling of the configurations and  $LSJ$ -levels are in accordance with the final (CV) computed energies. The  $3s^2 4d^2$  D term is assigned twice throughout the calculations (see also Table 2) and the subscripts  $a$  and  $b$  are used to distinguish them. See text for details.

**References.** <sup>(a)</sup>NIST Atomic Spectra Database 2018 (Kramida et al. 2018).

**Table 2.**  $LS$ -composition of the computed states belonging to the strongly mixed  $3s^2 nd$  Rydberg series in Al I.

Pos.	Conf.	$LSJ$	$LS$ -composition	Label used in NIST <sup>(1)</sup>
7,8	$3s^2 3d$	$2D_{3/2,5/2}$	$0.67 + 0.19 3s 3p^2 \ ^2D + 0.04 3s^2 4d \ ^2D$	$3s^2 3d \ ^2D_{3/2,5/2}$
12,13	$3s^2 4d$	$2D_{3/2,5/2 a}$	$0.41 + 0.22 3s^2 3d \ ^2D + 0.21 3s 3p^2 \ ^2D$	$3s^2 nd \ y \ ^2D_{3/2,5/2}$
19,20	$3s^2 4d$	$2D_{3/2,5/2 b}$	$0.44 + 0.25 3s^2 5d \ ^2D + 0.15 3s 3p^2 \ ^2D$	$3s^2 4d \ ^2D_{3/2,5/2}$
27,28	$3s^2 5d$	$2D_{3/2,5/2}$	$0.58 + 0.19 3s^2 6d \ ^2D + 0.10 3s 3p^2 \ ^2D$	$3s^2 5d \ ^2D_{3/2,5/2}$

**Notes.** The three most dominant  $LS$ -components are displayed. The first percentage value corresponds to the assigned configuration and term. In all these cases, the percentages for the two different  $LSJ$ -levels are the same and are therefore given in the same line. In the last column we provide the labelling of the corresponding observed terms as given in the NIST Database. The first column refers to the positions according to Table 1.

**References.** <sup>(1)</sup>Kramida et al. (2018).

mentioned above and also acknowledged by Froese Fischer et al. (2006), capturing such correlation effects is crucial for  $3s$ -hole states, such as states with significant  $3s3p^2$  composition. Furthermore, the  $\Delta E_{\text{MCHF-BP}}$  values do not always have the same sign, while the  $\Delta E_{\text{RCI}}$  differences are consistently positive. This is particularly important when calculating transition properties.

On average, properties for transitions between two levels for which the differences  $\Delta E_{\text{MCHF-BP}}$  have opposite signs are estimated less accurately.

The complete transition data tables, for all computed E1 transitions in Al I, can be found at the CDS. In the CDS table, the transition energies, wavelengths and the length form of the



**Table 3.** Observed and computed excitation energies in  $\text{cm}^{-1}$  for the 10 and 20 lowest states in Al I and Al II, respectively.

Pos.	Conf.	$LSJ$	$E_{\text{obs}}^a$	$E_{\text{RCI}}^b$	$\Delta E_{\text{RCI}}^b$	$\Delta E_{\text{MCHF-BP}}^c$
Al I						
1	3s <sup>2</sup> 3p	<sup>2</sup> P <sub>1/2</sub> <sup>o</sup>	0	0	0	0
2		<sup>2</sup> P <sub>3/2</sub> <sup>o</sup>	112	104	8	22
3	3s <sup>2</sup> 4s	<sup>2</sup> S <sub>1/2</sub>	25 348	25 196	152	-235
4	3s 3p <sup>2</sup>	<sup>4</sup> P <sub>1/2</sub>	29 020	28 863	157	940
5		<sup>4</sup> P <sub>3/2</sub>	29 067	28 907	160	949
6		<sup>4</sup> P <sub>5/2</sub>	29 143	28 981	162	964
7	3s <sup>2</sup> 3d	<sup>2</sup> D <sub>3/2</sub>	32 435	32 414	21	250
8		<sup>2</sup> D <sub>5/2</sub>	32 437	32 416	21	251
9	3s <sup>2</sup> 4p	<sup>2</sup> P <sub>1/2</sub> <sup>o</sup>	32 950	32 801	149	-98
10		<sup>2</sup> P <sub>3/2</sub> <sup>o</sup>	32 966	32 814	152	-94
Al II						
1	3s <sup>2</sup>	<sup>1</sup> S <sub>0</sub>	0	0	0	0
2	3s 3p	<sup>3</sup> P <sub>0</sub> <sup>o</sup>	37 393	37 445	-52	9
3		<sup>3</sup> P <sub>1</sub> <sup>o</sup>	37 454	37 503	-49	8
4		<sup>3</sup> P <sub>2</sub> <sup>o</sup>	37 578	37 626	-48	6
5		<sup>1</sup> P <sub>1</sub> <sup>o</sup>	59 852	59 982	-130	-177
6	3p <sup>2</sup>	<sup>1</sup> D <sub>2</sub>	85 481	85 692	-211	-305
7	3s 4s	<sup>3</sup> S <sub>1</sub>	91 275	91 425	-150	-376
8	3p <sup>2</sup>	<sup>3</sup> P <sub>0</sub>	94 085	94 211	-126	-107
9		<sup>3</sup> P <sub>1</sub>	94 147	94 264	-117	-111
10		<sup>3</sup> P <sub>2</sub>	94 269	94 375	-106	-113
11	3s 4s	<sup>1</sup> S <sub>0</sub>	95 351	95 543	-192	-400
12	3s 3d	<sup>3</sup> D <sub>2</sub>	95 549	95 791	-242	-527
13		<sup>3</sup> D <sub>1</sub>	95 551	95 794	-243	-527
14		<sup>3</sup> D <sub>3</sub>	95 551	95 804	-253	-529
15	3s 4p	<sup>3</sup> P <sub>0</sub> <sup>o</sup>	105 428	105 582	-154	-357
16		<sup>3</sup> P <sub>1</sub> <sup>o</sup>	105 442	105 594	-152	-360
17		<sup>3</sup> P <sub>2</sub> <sup>o</sup>	105 471	105 623	-152	-363
18		<sup>1</sup> P <sub>1</sub> <sup>o</sup>	106 921	107 132	-211	-365
19	3s 3d	<sup>1</sup> D <sub>2</sub>	110 090	110 330	-240	-475
20	3p <sup>2</sup>	<sup>1</sup> S <sub>0</sub>	111 637	112 086	-449	-445

**Notes.** In the last two columns, the difference  $\Delta E$  between observed and computed energies is compared for the current RCI and previous MCHF-BP calculations.

**References.** <sup>(a)</sup>Kramida et al. (2018); <sup>(b)</sup>present calculations; <sup>(c)</sup>Froese Fischer et al. (2006).

**Table 4.** Statistical analysis of the uncertainties of the computed transition rates in Al I and Al II.

$A_{\text{RCI}}^{\text{low}}$	$A_{\text{RCI}}^{\text{high}}$	No. Trans.	$\langle dT \rangle$	$Q_3$	Max	
Al I						
1	1.00E+05	31	0.62	0.83	0.98	
2	1.00E+05	1.00E+06	25	0.29	0.37	0.81
3	1.00E+06	1.00E+07	24	0.055	0.076	0.15
4	1.00E+07	20	0.043	0.073	0.14	
Al II						
1	1.00E+05	109	0.07	0.11	0.61	
2	1.00E+05	1.00E+06	81	0.09	0.11	0.67
3	1.00E+06	1.00E+07	99	0.043	0.036	0.39
4	1.00E+07	141	0.011	0.009	0.12	

**Notes.** The transition rates are arranged in four groups and in Col. 4, the number of transitions belonging to each group is given. In the last three columns, the average value, the value  $Q_3$  containing 75% of the lowest computed  $dT$  values, and the maximum value are given for each group of transitions. All transition rates are given in  $\text{s}^{-1}$ .

transition rates  $A$ , and weighted oscillator strengths  $gf$  are given. Based on the agreement between the length and velocity forms of the computed transition rates  $A_{\text{RCI}}$ , a statistical analysis of the uncertainties can be performed. The transitions were arranged in four groups based on the magnitude of the  $A_{\text{RCI}}$  values. The first two groups contain all the weak transitions with transition rates up to  $A = 10^6 \text{ s}^{-1}$ , while the next two groups contain the strong transitions with  $A > 10^6 \text{ s}^{-1}$ . In Table 4, the average value of the uncertainties  $\langle dT \rangle$  (see Eq. (4)) is given for each group of transitions. To better understand how the individual uncertainties  $dT$  are distributed, the maximum value and the value  $Q_3$  containing 75% of the lowest computed  $dT$  values (third quartile) are also given in Table 4. When examining the predicted uncertainties of the individual groups, we deduce that for all the strong transitions  $dT$  always remains below 15%. Most of the strong transitions are associated with small uncertainties, which justifies the low average values. Contrary to the strong transitions, the weaker transitions are associated with considerably larger uncertainties. This is even more pronounced for the first group of transitions where  $A$  is less than  $10^5 \text{ s}^{-1}$ . The weak EI transitions are challenging, and therefore interesting, from a theoretical point



**Table 5.** Comparison between computed and observed transition rates  $A$  in  $\text{s}^{-1}$  for selected transitions in Al I.

Upper	Lower	$A_{\text{RCI}}^a$	$A_{\text{MCHF-BP}}^b$	$A_{\text{CC}}^c$	$A_{\text{obs}}^{d,e,f}$	$A_{\text{obs}}^g$
$3s^2 4s \ ^2S_{1/2}$	$3s^2 3p \ ^2P_{1/2}^o$	4.966E+07	5.098E+07		4.93E+07 <sup>d C</sup>	4.70E+07 <sup>B</sup>
	$3s^2 3p \ ^2P_{3/2}^o$	9.884E+07	10.15E+07		9.80E+07 <sup>d C</sup>	9.90E+07 <sup>B</sup>
$3s^2 5s \ ^2S_{1/2}$	$3s^2 3p \ ^2P_{1/2}^o$	1.277E+07			1.33E+07 <sup>d C</sup>	1.42E+07 <sup>C+</sup>
	$3s^2 3p \ ^2P_{3/2}^o$	2.534E+07			2.64E+07 <sup>d C</sup>	2.84E+07 <sup>C+</sup>
$3s^2 5s \ ^2S_{1/2}$	$3s^2 4p \ ^2P_{1/2}^o$	3.815E+06				3.00E+06 <sup>D</sup>
	$3s^2 4p \ ^2P_{3/2}^o$	7.599E+06				6.00E+06 <sup>D</sup>
$3s^2 4p \ ^2P_{1/2}^o$	$3s^2 4s \ ^2S_{1/2}$	1.580E+07	1.507E+07		1.69E+07 <sup>e C+</sup>	1.60E+07 <sup>A</sup>
$3s^2 4p \ ^2P_{3/2}^o$	$3s^2 4s \ ^2S_{1/2}$	1.587E+07	1.514E+07		1.69E+07 <sup>e C+</sup>	1.50E+07 <sup>B</sup>
$3s^2 3d \ ^2D_{3/2}$	$3s^2 3p \ ^2P_{1/2}^o$	6.542E+07	5.651E+07		6.30E+07 <sup>d C</sup>	5.90E+07 <sup>C+</sup>
	$3s^2 3p \ ^2P_{3/2}^o$	1.321E+07	1.140E+07			(1.20)E+07
$3s^2 3d \ ^2D_{5/2}$	$3s^2 3p \ ^2P_{3/2}^o$	7.877E+07	6.806E+07		7.40E+07 <sup>d C</sup>	7.10E+07 <sup>A</sup>
	$3s^2 3p \ ^2P_{1/2}^o$	1.722E+07			1.92E+07 <sup>f C+</sup>	
$3s^2 4d \ ^2D_{3/2 \ a}$	$3s^2 3p \ ^2P_{3/2}^o$	3.293E+06		5.99E+06	2.30E+07 <sup>d C</sup>	
					3.80E+06 <sup>f C+</sup>	
					4.40E+06 <sup>d C</sup>	
$3s^2 4d \ ^2D_{5/2 \ a}$	$3s^2 3p \ ^2P_{3/2}^o$	2.010E+07		3.60E+07	2.30E+07 <sup>f</sup>	
					2.80E+07 <sup>d C</sup>	
$3s^2 4d \ ^2D_{3/2 \ b}$	$3s^2 3p \ ^2P_{1/2}^o$	7.128E+07		7.61E+07	7.20E+07 <sup>d C</sup>	
	$3s^2 3p \ ^2P_{3/2}^o$	1.386E+07		1.51E+07	5.26E+07 <sup>f</sup>	
$3s^2 4d \ ^2D_{5/2 \ b}$	$3s^2 3p \ ^2P_{3/2}^o$	8.412E+07		9.07E+07	1.40E+07 <sup>d C</sup>	
					1.05E+07 <sup>f A</sup>	
$3s^2 5d \ ^2D_{3/2}$	$3s^2 3p \ ^2P_{1/2}^o$	8.204E+07			8.60E+07 <sup>d C</sup>	
	$3s^2 3p \ ^2P_{3/2}^o$	1.596E+07		1.26E+07	6.31E+07 <sup>f</sup>	
$3s^2 5d \ ^2D_{5/2}$	$3s^2 3p \ ^2P_{3/2}^o$	9.706E+07		7.58E+07	6.60E+07 <sup>d C</sup>	
					5.76E+07 <sup>f</sup>	
					1.30E+07 <sup>d C</sup>	
					1.15E+07 <sup>f</sup>	
					7.90E+07 <sup>d C</sup>	
					6.91E+07 <sup>f</sup>	

**Notes.** The present values from the RCI calculations are given in Col. 3. In the next two columns, theoretical values from former MCHF-BP and close coupling (CC) calculations are displayed. The CC values complement the MCHF-BP values, which are restricted to transitions between levels in the lower part of the Al I spectrum. All theoretical transition rates are presented in length form. The last two columns contain the results from experimental observations. The experimental results go along with a letter grade, whenever accessible, which indicates the accuracy level. The correspondence between the accuracy ratings and the estimated relative uncertainty of the experimental results is  $A \leq 3\%$ ,  $B \leq 10\%$ ,  $C+ \leq 15\%$ ,  $C \leq 25\%$ ,  $D+ \leq 30\%$ ,  $D \leq 50\%$ .

**References.** <sup>(a)</sup>Present calculations; <sup>(b)</sup>Froese Fischer et al. (2006); <sup>(c)</sup>Mendoza et al. (1995); <sup>(d)</sup>Wiese & Martin (1980); <sup>(e)</sup>Buurman et al. (1986); <sup>(f)</sup>Davidson et al. (1990); <sup>(g)</sup>Vujnović et al. (2002).

of view, although they are less likely to be observed. The computation of transition properties in the system of Al I is overall far from trivial due to the extreme mixing of the  $3s^2nd \ ^2D$  series. Transitions involving any  $^2D$  state as upper or lower level appear to be associated with large uncertainties. However, the predicted energy separations are in excellent agreement with observations, meaning that the  $LS$ -composition of the  $3s^2nd \ ^2D$  states is well described. This should serve as a quality indicator of the computed transition data.

Transition rates  $A_{\text{obs}}$  evaluated from experimental measurements are compared with the current RCI theoretical values (see Table 5) and with values from the MCHF-BP calculations by Froese Fischer et al. (2006) and the close coupling (CC) calculations by Mendoza et al. (1995). Even though the measurements by Davidson et al. (1990) are more recent than the compiled values by Wiese & Martin (1980), the latter seem to be in

better overall agreement with the transition rates predicted by the RCI calculations. In all cases the  $A_{\text{RCI}}$  values fall into the range of the estimated uncertainties by Wiese & Martin (1980). The only exceptions are the transitions with  $3s^2 4d \ ^2D_{3/2,5/2 \ a}$  as upper levels, for which the  $A_{\text{RCI}}$  values agree better with the ones suggested by Davidson et al. (1990). Although the evaluated transition rates by Vujnović et al. (2002) slightly differ from the other observations, they are still in fairly good agreement with the present work. For the  $3s^2 4p \ ^2P_{3/2}^o \rightarrow 3s^2 4s \ ^2S_{1/2}$  and  $3s^2 3d \ ^2D_{5/2} \rightarrow 3s^2 3p \ ^2P_{3/2}^o$  transitions, the values by Vujnović et al. (2002) are better reproduced by the  $A_{\text{MCHF-BP}}$  results, yet not enough correlation is included in the calculations by Froese Fischer et al. (2006) and the transition rates predicted by the RCI calculations should be considered more accurate. Whenever values from the close coupling (CC) calculations are presented to complement the MCHF-BP

**Table 6.** Comparison between computed and observed lifetimes  $\tau$  in seconds for the 26 lowest excited states in AlI.

Pos.	Conf.	$LSJ$	RCI <sup>a</sup>		MCHF-BP <sup>b</sup>	Expt. <sup>c,d,e</sup>
			$\tau_l$	$\tau_v$	$\tau_l$	$\tau_{\text{obs}}$
1	3s <sup>2</sup> 4s	<sup>2</sup> S <sub>1/2</sub>	6.734E-09	6.745E-09	6.558E-09	6.85(6)E-09 <sup>c</sup>
2	3s 3p <sup>2</sup>	<sup>4</sup> P <sub>1/2</sub>	1.652E-03	1.182E-03	4.950E-03	
3		<sup>4</sup> P <sub>3/2</sub>	6.702E-03	6.911E-03	13.24E-03	
4		<sup>4</sup> P <sub>5/2</sub>	2.604E-03	3.681E-03	9.486E-03	
5	3s <sup>2</sup> 3d	<sup>2</sup> D <sub>3/2</sub>	1.272E-08	1.372E-08	1.472E-08	1.40(2)E-08 <sup>c</sup>
6		<sup>2</sup> D <sub>5/2</sub>	1.270E-08	1.371E-08	1.469E-08	1.40(2)E-08 <sup>c</sup>
7	3s <sup>2</sup> 4p	<sup>2</sup> P <sub>1/2</sub> <sup>o</sup>	6.329E-08	6.357E-08	6.621E-08	6.05(9)E-08 <sup>e</sup>
8		<sup>2</sup> P <sub>3/2</sub> <sup>o</sup>	6.300E-08	6.328E-08	6.590E-08	6.5 (2) E-08 <sup>e</sup>
9	3s <sup>2</sup> 5s	<sup>2</sup> S <sub>1/2</sub>	2.019E-08	2.027E-08		1.98(5)E-08 <sup>c</sup>
10	3s <sup>2</sup> 4d	<sup>2</sup> D <sub>3/2</sub> a	3.117E-08	2.919E-08		2.95(7)E-08 <sup>c</sup>
11		<sup>2</sup> D <sub>5/2</sub> a	3.158E-08	2.953E-08		2.95(7)E-08 <sup>c</sup>
12	3s <sup>2</sup> 5p	<sup>2</sup> P <sub>1/2</sub> <sup>o</sup>	2.448E-07	2.532E-07		2.75(8)E-07 <sup>c</sup>
13		<sup>2</sup> P <sub>3/2</sub> <sup>o</sup>	2.429E-07	2.512E-07		2.75(8)E-07 <sup>c</sup>
14	3s <sup>2</sup> 4f	<sup>2</sup> F <sub>5/2</sub> <sup>o</sup>	6.041E-08	6.162E-08		
15		<sup>2</sup> F <sub>7/2</sub> <sup>o</sup>	6.041E-08	6.160E-08		
16	3s <sup>2</sup> 6s	<sup>2</sup> S <sub>1/2</sub>	4.812E-08	4.885E-08		
17	3s <sup>2</sup> 4d	<sup>2</sup> D <sub>3/2</sub> b	1.136E-08	1.083E-08		1.32(3)E-08 <sup>d</sup>
18		<sup>2</sup> D <sub>5/2</sub> b	1.150E-08	1.093E-08		1.32(3)E-08 <sup>d</sup>
19	3s <sup>2</sup> 6p	<sup>2</sup> P <sub>1/2</sub> <sup>o</sup>	4.886E-07	6.952E-07		
20		<sup>2</sup> P <sub>3/2</sub> <sup>o</sup>	4.845E-07	6.882E-07		
21	3s <sup>2</sup> 5f	<sup>2</sup> F <sub>7/2</sub> <sup>o</sup>	1.176E-07	1.172E-07		
22		<sup>2</sup> F <sub>5/2</sub> <sup>o</sup>	1.175E-07	1.172E-07		
23	3s <sup>2</sup> 5g	<sup>2</sup> G <sub>7/2</sub>	2.301E-07	2.315E-07		
24		<sup>2</sup> G <sub>9/2</sub>	2.301E-07	2.315E-07		
25	3s <sup>2</sup> 5d	<sup>2</sup> D <sub>3/2</sub>	1.011E-08	9.855E-09		14.0(2)E-09 <sup>d</sup>
26		<sup>2</sup> D <sub>5/2</sub>	1.020E-08	9.921E-09		14.0(2)E-09 <sup>d</sup>

**Notes.** For the current RCI calculations both length  $\tau_l$  and velocity  $\tau_v$  forms are displayed. In Col. 6, the predicted lifetimes from MCHF-BP calculations are given in length form. The last column contains available lifetimes from experimental measurements together with their uncertainties.

**References.** <sup>(a)</sup>Present calculations; <sup>(b)</sup>Froese Fischer et al. (2006); <sup>(c)</sup>Buurman et al. (1986); <sup>(d)</sup>Davidson et al. (1990); <sup>(e)</sup>Buurman & Dönszelmann (1990).

results, the  $A_{\text{RCI}}$  values appear to be in better agreement with the experimental values. Exceptionally, for the  $3s^2 5d \ ^2D_{3/2,5/2} \rightarrow 3s^2 3p \ ^2P_{3/2}^o$  transitions, the  $A_{\text{CC}}$  values by Mendoza et al. (1995) approach the corresponding experimental values more closely. Even so, the  $A_{\text{RCI}}$  values are still within the given experimental uncertainties. One should bear in mind that according to the estimation of uncertainties by Kelleher & Podobedova (2008b) the  $A_{\text{CC}}$  values carry relative uncertainties up to 30%. On the contrary, based on the agreement between length and velocity forms, the estimated uncertainties of the current RCI calculations for the above-mentioned transitions are of the order of 3% percent. Therefore, we suggest that the current transition rates are used as a reference.

From the computed E1 transition rates, the lifetimes of the excited states are estimated. Transition data for transitions other than E1 have not been computed in this work since the contributions to the lifetimes from magnetic or higher electric multipoles are expected to be negligible. In Table 6 the currently computed lifetimes are given in both length  $\tau_l$  and velocity  $\tau_v$  forms. The agreement between these two forms probes the level of accuracy of the calculations. Because of the poor agreement between the length and velocity form of the quartet  $3s3p^2 \ ^4P$  and doublet  $3s^2 6p \ ^2P$  states, the average relative difference appears overall to

be  $\sim 8\%$ . The differences between the length and velocity gauges of the quartet  $3s3p^2 \ ^4P$  states are of the order of 25% on average. These long-lived states are associated with weak transitions and computations involving such transitions are, as mentioned above, rather challenging. In addition, we note that the relative differences corresponding to the  $3s^2 6p \ ^2P$  states exceed 40%. As the computations involve Rydberg series, states between the lowest and highest computed levels might not occupy the same region in space. Nevertheless, these states are part of the same multireference (MR). The highest computed levels correspond to configurations with orbitals up to  $n = 6$ , such as  $3s^2 6p$ . To obtain a better description of these levels it is probably necessary to perform initial calculations including in the MR  $3s^2 n l$  configurations with  $n = 7$  and perhaps even  $n = 8$ . This would lead to a more complete and balanced orbital set (Pehlivan Rhodin et al. 2017). When excluding the above-mentioned states, the mean relative difference between  $\tau_l$  and  $\tau_v$  is  $\sim 3\%$ , which is satisfactory.

In Table 6, the lifetimes from the current RCI calculations are compared with results from the MCHF-BP calculations by Froese Fischer et al. (2006) and observations. Only for the  $3s^2 4p \ ^2P$  state are separated observed values of the lifetimes given for the two fine-structure components. For the rest of the

measured lifetimes, a single value for the two fine-structure levels is provided. As can be seen, the overall agreement between the theoretical and the measured lifetimes  $\tau_{\text{obs}}$  is rather good. However, the measured lifetimes are better represented by the current RCI results than by the MCHF-BP values. For most of the states, the differences between the RCI and MCHF-BP values are small, except for the levels of the quartet  $3s3p^2\ ^4P$  state. For these long-lived states, no experimental lifetimes exist for comparison.

#### 4.2. Al II

In Table A.1, the computed excitation energies, based on VV correlation, are given as a function of the increasing active set of orbitals. When adding the  $n = 12$  correlation layer, the values for all computed energy separations have converged. The agreement with the NIST observed energies (Kramida et al. 2018) is, at this point, fairly good. The mean relative difference between theory and experiment is of the order of 1.2%. However, when accounting for CV correlation, the agreement with the observed values is significantly improved, resulting in a mean relative difference being less than 0.2%. Accounting for CV effects also results in a labelling of the eigenstates that matches observations. For instance, when only VV correlation is taken into account, the  $^3F$  triplet with the highest energy is labelled as a  $3s6f$  level. After taking CV effects into account, the eigenstates of this triplet are assigned the  $3p3d$  configuration, now the one with the largest expansion coefficient, which agrees with observations. There are no experimental excitation energies for the singlet and triplet  $3s6h\ ^{1,3}H$  terms. In the last column of Table A.1, the differences  $\Delta E$  between computed and observed energies are displayed. All  $\Delta E$  values maintain the same sign, being negative.

In Table 3, a comparison between the present computed excitation energies and those from the MCHF-BP calculations by Froese Fischer et al. (2006) is also performed for Al II. The latter spectrum calculations are extended up to levels corresponding to the singlet  $3p^2\ ^1S$  state and all types of correlation, i.e. VV, CV, and CC, were accounted for. Both computational approaches are highly accurate, yet the majority of the levels is better represented by the current RCI results. The average relative difference for the RCI values is  $\sim 0.2\%$  and for the MCHF-BP  $\sim 0.3\%$ . Moreover, the  $\Delta E_{\text{MCHF-BP}}$  values do not always maintain the same sign, while the  $\Delta E_{\text{RCI}}$  values do. Hence, in general, the MCHF-BP calculations do not predict the transition energies as precisely as the present RCI method.

For all computed E1 transitions in Al II, transition data tables can also be found at the CDS. In Table 4, a statistical analysis of the uncertainties to the computed transition rates  $A_{\text{RCI}}$  is performed in a similar way to that for Al I. The transitions are also arranged here in four groups. Following the conclusions by Pehlivan Rhodin et al. (2017) and Pehlivan Rhodin (2018), the transitions involving any of the  $3s7p\ ^{1,3}P$  states have been excluded from this analysis. The discrepancies between the length and velocity forms for transitions including the  $3s7p\ ^{1,3}P$  states are consistently large, and thus the computed transition rates are not trustworthy. We note that overall the average uncertainty, as well as the value that includes 75% of the data, appear to be smaller, for each group of transitions, than the predicted values in Al I. Nevertheless, the maximum values of the uncertainties for the last two groups are larger in comparison to Al I. This is due to some transitions involving  $3p3d\ ^3F$  as the upper level. The strong mixing between the  $3p3d\ ^3F$  and the  $3s6f\ ^3F$  levels results in strong cancellation effects. Such effects often

hamper the accuracy of the computed transition data and result in large discrepancies between the length and velocity forms.

In Table 7, current RCI theoretical transition rates are compared with the values from the MCHF-BP calculations by Froese Fischer et al. (2006) and, whenever available, results from the B-spline configuration interaction (BSCI) calculations by Chang & Fang (1995). For the majority of the transitions, there is an excellent agreement between the RCI and MCHF-BP values with the relative difference being less than 1%. Some of the largest discrepancies are observed for the  $3s3d, 3p^2\ ^1D \rightarrow 3s3p\ ^{1,3}P^o$  transitions. According to Froese Fischer et al. (2006), correlation is extremely important for transitions from such  $^1D$  states. In the MCHF-BP calculations, all three types of correlation, i.e. VV, CV, and CC, have been accounted for; however, the CSF expansions obtained from SD-substitutions are not as large as in the present calculations and the  $LS$ -composition of the configurations might not be predicted as accurately. Hence, the evaluation of line strengths for transitions involving  $^1D$  states and in turn the computation of transition rates involving these states will be affected. Computed transition rates using the BSCI approach are provided for transitions that involve only singlet states. The BSCI calculations do not account for the relativistic interaction and no separate values are given for the different fine-structure components of triplet states. For the  $3p^2\ ^1D \rightarrow 3s3p\ ^1P^o$  transition, the discrepancy between the RCI and BSCI values is also quite large. On the other hand, for the  $3s3d\ ^1D \rightarrow 3s3p\ ^1P^o$  transition, the BSCI result is in perfect agreement with the present  $A_{\text{RCI}}$  value. The agreement between the current RCI and BSCI transition rates exhibits a broad variation. The advantage of the BSCI approach is that it takes into account the effect of the positive-energy continuum orbitals in an explicit manner. Nevertheless, the parametrized model potential that is being used in the work by Chang & Fang (1995) is not sufficient to describe states that are strongly mixed. Finally, we note the discrepancy for the  $3s4p\ ^1P^o \rightarrow 3s^2\ ^1S_0$  transition, which is quite large between the RCI and MCHF-BP values and inexplicably large between the RCI and BSCI values.

In singly ionized aluminium, measurements of transition properties are available only for a few transitions. In Table 7, the available experimental results are compared with the theoretical results from the current RCI calculations, and with the former calculations by Froese Fischer et al. (2006) and Chang & Fang (1995). Transition rates have been experimentally observed for the  $3s3p\ ^{1,3}P^o \rightarrow 3s^2\ ^1S_0$  transitions in the works by Kernahan et al. (1979), Smith (1970), Berry et al. (1970) and Head et al. (1976), and by Träbert et al. (1999) and Johnson et al. (1986), respectively. In Table 7, the average value of these works is displayed. The agreement with the current RCI results is fairly good. Nonetheless, the averaged  $A_{\text{obs}}$  by Träbert et al. (1999) and Johnson et al. (1986) is in better agreement with the value by Froese Fischer et al. (2006). Additionally, Vujnović et al. (2002) provided experimental transition rates for the  $3p^2\ ^1D_2 \rightarrow 3s3p\ ^1P_1$  and  $3p^2\ ^1D_2 \rightarrow 3s3p\ ^3P_{1,2}$  transitions by measuring relative intensities of spectral lines. These experimental results, however, differ from the theoretical values.

In the last portion of Table 7, current rates for transitions between states with higher energies are compared with the results from the close coupling (CC) calculations by Butler et al. (1993) and the early results from the configuration interaction (CI) calculations by Chang & Wang (1987). The results from the latter two calculations are found to be in very good agreement. Furthermore, the agreement between the RCI results and those from the CC and CI calculations is also very good

**Table 7.** Comparison between computed and observed transition rates  $A$  in  $\text{s}^{-1}$  for selected transitions in Al II.

Upper	Lower	$A_{\text{RCI}}^a$	$A_{\text{theor}}^{b,c}$	$A_{\text{theor}}^{e,f}$	$A_{\text{obs}}^{d,h,g}$
3s3p $^3\text{P}_1^o$	3s $^2$ $^1\text{S}_0$	3.054E+03	3.277E+03 <sup>b</sup>		3.30E+03 <sup>h</sup>
3s3p $^1\text{P}_1^o$	3s $^2$ $^1\text{S}_0$	1.404E+09	1.400E+09 <sup>b</sup>	1.486E+09 <sup>f</sup>	1.45E+09 <sup>g</sup>
3s4s $^3\text{S}_1$	3s3p $^3\text{P}_0^o$	8.612E+07	8.572E+07 <sup>b</sup>		
	3s3p $^3\text{P}_1^o$	2.555E+08	2.547E+08 <sup>b</sup>		
	3s3p $^3\text{P}_2^o$	4.173E+08	4.162E+08 <sup>b</sup>		
3s4s $^1\text{S}_0$	3s3p $^1\text{P}_1^o$	3.422E+08	3.455E+08 <sup>b</sup>	3.408E+08 <sup>f</sup>	
3p $^2$ $^1\text{D}_2$	3s3p $^1\text{P}_1^o$	2.523E+05	3.804E+05 <sup>b</sup>	3.980E+05 <sup>f</sup>	1.84E+04 <sup>d</sup>
	3s3p $^3\text{P}_1^o$	1.790E+04	2.016E+04 <sup>b</sup>		0.19E+04 <sup>d</sup>
	3s3p $^3\text{P}_2^o$	2.827E+04	3.141E+04 <sup>b</sup>		0.30E+04 <sup>d</sup>
3p $^2$ $^3\text{P}_0$	3s3p $^3\text{P}_0^o$	1.236E+09	1.235E+09 <sup>b</sup>		
3p $^2$ $^3\text{P}_1$	3s3p $^3\text{P}_0^o$	4.148E+08	4.144E+08 <sup>b</sup>		
	3s3p $^3\text{P}_1^o$	3.058E+08	3.062E+08 <sup>b</sup>		
	3s3p $^3\text{P}_2^o$	5.170E+08	5.167E+08 <sup>b</sup>		
3p $^2$ $^3\text{P}_2$	3s3p $^3\text{P}_1^o$	3.145E+08	3.144E+08 <sup>b</sup>		
	3s3p $^3\text{P}_2^o$	9.264E+08	9.272E+08 <sup>b</sup>		
3p $^2$ $^1\text{S}_0$	3s3p $^1\text{P}_1^o$	1.020E+09	6.738E+08 <sup>b</sup>		
	3s3p $^3\text{P}_1^o$	5.021E+08	3.399E+07 <sup>b</sup>		
3s3d $^3\text{D}_2$	3s3p $^3\text{P}_1^o$	8.977E+08	9.072E+08 <sup>b</sup>		
	3s3p $^3\text{P}_2^o$	3.019E+08	3.046E+08 <sup>b</sup>		
3s3d $^3\text{D}_3$	3s3p $^3\text{P}_2^o$	1.197E+09	1.208E+09 <sup>b</sup>		
3s3d $^1\text{D}_2$	3s3p $^1\text{P}_1^o$	1.388E+09	1.429E+09 <sup>b</sup>	1.388E+09 <sup>f</sup>	
3s4p $^3\text{P}_0^o$	3s4s $^3\text{S}_1$	5.639E+07	5.705E+07 <sup>b</sup>		
	3s3d $^3\text{D}_1$	1.556E+07	1.520E+07 <sup>b</sup>		
3s4p $^3\text{P}_1^o$	3s4s $^3\text{S}_1$	5.649E+07	5.724E+07 <sup>b</sup>		
	3s3d $^3\text{D}_1$	3.905E+06	3.816E+06 <sup>b</sup>		
	3s3d $^3\text{D}_2$	1.172E+07	1.146E+07 <sup>b</sup>		
3s4p $^3\text{P}_2^o$	3s4s $^3\text{S}_1$	5.683E+07	5.762E+07 <sup>b</sup>		
	3s3d $^3\text{D}_1$	1.568E+05	1.541E+05 <sup>b</sup>		
	3s3d $^3\text{D}_2$	2.361E+06	2.312E+06 <sup>b</sup>		
	3s3d $^3\text{D}_3$	1.319E+07	1.294E+07 <sup>b</sup>		
3s4p $^1\text{P}_1^o$	3s $^2$ $^1\text{S}_0$	1.527E+06	0.981E+06 <sup>b</sup>	5.079E+06 <sup>f</sup>	
	3p $^2$ $^1\text{D}_2$	5.835E+07	5.897E+07 <sup>b</sup>	6.307E+07 <sup>f</sup>	
	3s4s $^1\text{S}_0$	3.109E+07	2.965E+07 <sup>b</sup>	3.111E+07 <sup>f</sup>	
3p3d $^3\text{F}_2^o$	3s3d $^3\text{D}_1$	2.956E+08	2.07E+08 <sup>c</sup>	2.14E+08 <sup>e</sup>	
3p3d $^3\text{F}_3^o$	3s3d $^3\text{D}_2$	3.174E+08	2.19E+08 <sup>c</sup>	2.25E+08 <sup>e</sup>	
3p3d $^3\text{F}_4^o$	3s3d $^3\text{D}_3$	3.794E+08	2.47E+08 <sup>c</sup>	2.54E+08 <sup>e</sup>	
3s4f $^3\text{F}_2^o$	3s3d $^3\text{D}_1$	1.981E+08	1.97E+08 <sup>c</sup>	1.98E+08 <sup>e</sup>	
3s4f $^3\text{F}_3^o$	3s3d $^3\text{D}_2$	2.096E+08	2.09E+08 <sup>c</sup>	2.07E+08 <sup>e</sup>	
3s4f $^3\text{F}_4^o$	3s3d $^3\text{D}_3$	2.360E+08	2.35E+08 <sup>c</sup>	2.33E+08 <sup>e</sup>	
3s5f $^3\text{F}_2^o$	3s3d $^3\text{D}_1$	2.801E+07	2.40E+07 <sup>c</sup>	2.50E+07 <sup>e</sup>	
3s5f $^3\text{F}_3^o$	3s3d $^3\text{D}_3$	3.438E+07	2.85E+07 <sup>c</sup>	2.90E+07 <sup>e</sup>	
3s6f $^3\text{F}_2^o$	3s3d $^3\text{D}_1$	1.957E+07	2.90E+07 <sup>c</sup>	3.10E+07 <sup>e</sup>	
	3s4d $^3\text{D}_1$	1.116E+07	1.07E+07 <sup>c</sup>	1.00E+07 <sup>e</sup>	
3s6f $^3\text{F}_3^o$	3s3d $^3\text{D}_2$	1.910E+07	3.07E+07 <sup>c</sup>	3.30E+07 <sup>e</sup>	
	3s4d $^3\text{D}_2$	1.200E+07	1.14E+07 <sup>c</sup>	1.10E+07 <sup>e</sup>	
3s6f $^3\text{F}_4^o$	3s3d $^3\text{D}_3$	1.920E+07	3.46E+07 <sup>c</sup>	3.70E+07 <sup>e</sup>	
	3s4d $^3\text{D}_3$	1.367E+07	1.28E+07 <sup>c</sup>	1.20E+07 <sup>e</sup>	

**Notes.** The present values from the RCI calculations are given in Col. 3. In the next two columns, theoretical values from former MCHF-BP, close coupling (CC), configuration interaction (CI), and B-spline configuration interaction (BSCI) calculations are given. The last column contains the results from experimental observations. All theoretical transition rates are presented in length form.

**References.** <sup>(a)</sup>Present calculations; <sup>(b)</sup>Froese Fischer et al. (2006); <sup>(c)</sup>Butler et al. (1993); <sup>(d)</sup>Vujnović et al. (2002); <sup>(e)</sup>Chang & Wang (1987); <sup>(f)</sup>Chang & Fang (1995); <sup>(g)</sup>Kernahan et al. (1979), Smith (1970), Berry et al. (1970), Head et al. (1976); <sup>(h)</sup>Träbert et al. (1999), Johnson et al. (1986).

for the 3s4f  $^3\text{F} \rightarrow 3s3d$   $^3\text{D}$  transitions and fairly good for the 3s5f  $^3\text{F} \rightarrow 3s3d$   $^3\text{D}$  transitions. On the other hand, for the 3p3d, 3s6f  $^3\text{F} \rightarrow 3s3d$   $^3\text{D}$  transitions, the observed discrepancy between the current RCI values and those from the two pre-

vious calculations is substantial. This outcome indicates that the calculations by Butler et al. (1993) and Chang & Wang (1987) are insufficient to properly account for correlation and further emphasizes the quality of the present work.

In the same way as for Al I, the lifetimes of Al II excited states were also estimated based on the computed EI transitions. In Table A.2, both length  $\tau_l$  and velocity  $\tau_v$  forms of the currently computed lifetimes are displayed. As already mentioned, the agreement between these two forms serves as an indication of the quality of the results. The average relative difference between the two forms is  $\sim 2\%$ . The largest discrepancies are observed between the length and velocity gauges of the singlet  $3p^2\ ^1D$  state, and between the singlet and triplet  $3s7p\ ^1,^3P$  states. The highest computed levels in the calculations of Al II correspond to configuration states with orbitals up to  $n = 7$ , such as  $3s7p$ . Similarly to the conclusions for the lifetimes of Al I, better agreement between the length and velocity forms of the  $3s7p\ ^1,^3P$  states could probably be obtained by including  $3snl$  configurations with  $n > 7$  in the MR.

In Table A.2, the lifetimes from the current RCI calculations are compared with results from previous MCHF-BP and BSCI calculations by Froese Fischer et al. (2006) and Chang & Fang (1995), respectively. Except for the lifetimes of the triplet  $3s3p\ ^3P_1^o$  and singlet  $3p^2\ ^1D_2$  states, the agreement between the RCI and MCHF-BP calculations is very good. Furthermore, the overall agreement between the RCI and BSCI calculations is sufficiently good. Despite the poor agreement between the RCI and BSCI values for the  $3p^2\ ^1D_2$  and  $3s7p\ ^1,^3P$  states, for the rest of the states the discrepancies are small. The BSCI results are more extended. However, no separate values are provided for the different  $LSJ$ -components of the triplet states and the average lifetime is presented for them instead.

In Table A.2, the theoretical lifetimes are also compared with available measurements. The measured lifetime of the  $3s3p\ ^3P_1^o$  state by Träbert et al. (1999) and Johnson et al. (1986) agrees remarkably well with the calculated value by Froese Fischer et al. (2006). The agreement with the current results is fairly good too. The lifetime of the  $3s3p\ ^1P_1^o$  state measured by Kernahan et al. (1979), Head et al. (1976), Berry et al. (1970), and Smith (1970) is well represented by all theoretical values. On the other hand, the results from the measurements of the  $3snf\ ^3F$  states by Andersen et al. (1971) differ substantially from the theoretical RCI values. For the  $3snf\ ^3F$  Rydberg series, only theoretical lifetimes using the current MCDHF and RCI approach are available. Given the large uncertainties associated with early beam-foil measurements, the discrepancies between theoretical and experimental values are in some way expected. The only exception is the lifetime of the  $3s5f\ ^3F$  state, which is in rather good agreement with the RCI values. In the experiments by Andersen et al. (1971) the different fine-structure components have not been separated and a single value is provided for all three different  $LSJ$ -levels.

## 5. Summary and conclusions

In the present work, updated and extended transition data and lifetimes are made available for both Al I and Al II. The computations of transition properties in these two systems are challenging mainly due to the strong two-electron interaction between the  $3s3d\ ^1D$  and  $3p^2\ ^1D$  states, which dominates the lowest part of their spectra. Thus, some of the states are strongly mixed and highly correlated wave functions are needed to accurately predict their  $LS$ -composition. We are confident that in this work enough correlation has been included to affirm the reliability of the results. The predicted excitation energies are in excellent agreement with the experimental data provided by the NIST database, which is a good indicator of the quality of the produced transition data and lifetimes.

We have performed an extensive comparison of the computed transition rates and lifetimes with the most recent theoretical and experimental results. There is a significant improvement in accuracy, in particular for the more complex system of neutral Al I. The computed lifetimes of Al I are in very good agreement with the measured lifetimes in high-precision laser spectroscopy experiments. The same holds for the measured lifetimes of Al II in ion storage rings. The present calculations are extended to higher energies and many of the computed transitions fall in the infrared spectral region. The new generation of telescopes are designed for this region and these transition data are of high importance. The objective of this work is to make available atomic data that could be used to improve the interpretation of abundances in stars. Lists of trustworthy elemental abundances will permit the tracing of stellar evolution, as well as the formation and chemical evolution of the Milky Way.

The agreement between the length and velocity gauges of the transition operator serves as a criterion for the quality of the transition data and for the lifetimes. For most of the strong transitions in both Al I and Al II, the agreement between the two gauges is very good. For transitions involving states with the highest  $n$  quantum number for the  $s$  and  $p$  symmetries, we observe that the agreement between the length and velocity forms is not as good. This becomes more evident when estimating lifetimes of excited levels that are associated with those transitions.

*Acknowledgements.* The authors have been supported by the Swedish Research Council (VR) under contract 2015-04842. The authors acknowledge H. Hartman, Malmö University, and H. Jönsson, Lund University, for discussions.

## References

- Adibekyan, V. Z., Sousa, S. G., Santos, N. C., et al. 2012, *A&A*, 545, A32  
 Andersen, T., Roberts, J. R., & Sørensen, G. 1971, *Phys. Scr.*, 4, 52  
 Bensby, T., Feltzing, S., & Oey, M. S. 2014, *A&A*, 562, A71  
 Berry, H. G., Bromander, J., & Buchta, R. 1970, *Phys. Scr.*, 1, 181  
 Butler, K., Mendoza, C., & Zeppen, C. 1993, *J. Phys. B*, 26, 4409  
 Buurman, E., & Dönszelmann, A. 1990, *A&A*, 227, 289  
 Buurman, E., Dönszelmann, A., Hansen, J. E., & Snoek, C. 1986, *A&A*, 164, 224  
 Carretta, E., Bragaglia, A., Gratton, R. G., et al. 2010, *A&A*, 516, A55  
 Chang, T. N., & Fang, T. K. 1995, *Phys. Rev. A*, 52, 2638  
 Chang, T. N., & Wang, R. 1987, *Phys. Rev. A*, 36, 3535  
 Clayton, D. D. 2003, *Handbook of Isotopes in the Cosmos: Hydrogen to Gallium* (Cambridge: Cambridge University Press)  
 Davidson, M. D., Volten, H., & Dönszelmann, A. 1990, *A&A*, 238, 452  
 Dyall, K. G., Grant, I. P., Johnson, C., Parpia, F. A., & Plummer, E. P. 1989, *Comput. Phys. Commun.*, 55, 425  
 Ekman, J., Godefroid, M., & Hartman, H. 2014, *Atoms*, 2, 215  
 Froese Fischer, C. 2009, *Phys. Scr.*, T134, 014019  
 Froese Fischer, C., Tachiev, G., & Irimia, A. 2006, *At. Data Nucl. Data Tables*, 92, 607  
 Froese Fischer, C., Godefroid, M., Brage, T., Jönsson, P., & Gaigalas, G. 2016, *J. Phys. B: At. Mol. Opt. Phys.*, 49, 182004  
 Gaigalas, G., Rudzikas, Z., & Froese Fischer, C. 1997, *J. Phys. B: At. Mol. Opt. Phys.*, 30, 3747  
 Gaigalas, G., Fritzsche, S., & Grant, I. P. 2001, *Comput. Phys. Commun.*, 139, 263  
 Gaigalas, G., Zalandauskas, T., & Rudzikas, Z. 2003, *At. Data Nucl. Data Tables*, 84, 99  
 Gaigalas, G., Zalandauskas, T., & Fritzsche, S. 2004, *Comput. Phys. Commun.*, 157, 239  
 Gaigalas, G., Froese Fischer, C., Rynkun, P., & Jönsson, P. 2017, *Atoms*, 5, 6  
 Gehren, T., Liang, Y. C., Shi, J. R., Zhang, H. W., & Zhao, G. 2004, *A&A*, 413, 1045  
 Gehren, T., Shi, J. R., Zhang, H. W., Zhao, G., & Korn, A. J. 2006, *A&A*, 451, 1065  
 Grant, I. P. 1974, *J. Phys. B*, 7, 1458

- Grant, I. P. 2007, *Relativistic Quantum Theory of Atoms and Molecules* (New York: Springer)
- Head, M. E. M., Head, C. E., & Lawrence, J. N. 1976, in *Atomic Structure and Lifetimes*, eds. F. A. Sellin, & D. J. Pegg (NY: Plenum), 147
- Hibbert, A. 1989, *Phys. Scr.*, 39, 574
- Jönsson, G., & Lundberg, H. 1983, *Z. Phys. A*, 313, 151
- Johnson, B. C., Smith, P. L., & Parkinson, W. H. 1986, *ApJ*, 308, 1013
- Jönsson, G., Kröll, S., Persson, A., & Svanberg, S. 1984, *Phys. Rev. A*, 30, 2429
- Jönsson, P., Gaigalas, G., Bieroń, J., Froese Fischer, C., & Grant, I. P. 2013, *Phys. Commun.*, 184, 2197
- Kelleher, D. E., & Podobedova, L. I. 2008a, *J. Phys. Chem. Ref. Data*, 37, 709
- Kelleher, D. E., & Podobedova, L. I. 2008b, *J. Phys. Chem. Ref. Data*, 37, 267
- Kernahan, J. A., Pinnington, E. H., O'Neill, J. A. M., Brooks, R. L., & Donnelly, K. E. 1979, *Phys. Scripta*, 19, 267
- Kramida, A., Ralchenko, Y. u., & Reader, J. NIST ASD Team 2018, *NIST Atomic Spectra Database, ver. 5.5.3 (Online)*, available: <https://physics.nist.gov/asd> (2018, March 15), National Institute of Standards and Technology, Gaithersburg, MD
- Lin, C. D. 1974, *ApJ*, 187, 385
- McKenzie, B. J., Grant, I. P., & Norrington, P. H. 1980, *Comput. Phys. Commun.*, 21, 233
- Mendoza, C., Eissner, W., Le Dourneuf, M., & Zeppen, C. J. 1995, *J. Phys. B*, 28, 3485
- Mishenina, T. V., Soubiran, C., Bienaymé, O., et al. 2008, *A&A*, 489, 923
- Nordlander, T., & Lind, K. 2017, *A&A*, 607, A75
- Olsen, J., Roos, B. O., Jorgensen, P., & Jensen, H. J. A. a. 1988, *J. Chem. Phys.*, 89, 2185
- Pehlivan Rhodin, A., Hartman, H., Nilsson, H., & Jönsson, P. 2017, *A&A*, 598, A102
- Pehlivan Rhodin, A. 2018, Ph. D. Thesis, Lund Observatory
- Reddy, B. E., Lambert, D. L., & Allende Prieto, C. 2006, *MNRAS*, 367, 1329
- Smiljanic, R., Korn, A. J., Bergemann, M., Frasca, A., et al. 2014, *A&A*, 570, A122
- Smiljanic, R., Romano, D., Bragaglia, A., Donati, P., et al. 2016, *A&A*, 589, A115
- Smith, W. H. 1970, *NIM*, 90, 115
- Sturesson, L., Jönsson, P., & Fischer, C. F. 2007, *Comput. Phys. Commun.*, 177, 539
- Tayal, S. S., & Hibbert, A. 1984, *J. Phys. B*, 17, 3835
- Taylor, P. R. C. W., Bauschlicher, J., & Langhoff, S. 1988, *J. Phys. B*, 21, L333
- Theodosiou, C. E. 1992, *Phys. Rev. A*, 45, 7756
- Treffitz, E. 1988, *J. Phys. B: At. Mol. Opt. Phys.*, 21, 1761
- Träbert, E., Wolf, A., & Linkemann, J. 1999, *J. Phys. B*, 32, 637
- Vujnović, V., Blagoev, K., Fürböck, C., Neger, T., & Jäger, H. 2002, *A&A*, 338, 704
- Weiss, A. W. 1974, *Phys. Rev.*, 9, 1524
- Wiese, W. L., Smith, M. W., & Miles, B. M. 1969, *NSRDS-NBS*, 22, 47
- Wiese, W. L., & Martin, G. A. 1980, in *Transition Probabilities, Part II*, Vol. Natl. Stand. Ref. Data System., (Washington DC), Natl. Bur. Std., 68



## Appendix A: Additional tables

Table A.1. Computed excitation energies in  $\text{cm}^{-1}$  for the 78 lowest states in Al II.

Pos.	Conf.	LSJ	VV						CV	$E_{\text{obs}}^a$	$\Delta E$
			$n = 8$	$n = 9$	$n = 10$	$n = 11$	$n = 12$	$n = 13$			
1	3s <sup>2</sup>	<sup>1</sup> S <sub>0</sub>	0	0	0	0	0	0	0	0	0
2	3s 3p	<sup>3</sup> P <sub>0</sub> <sup>o</sup>	36 227	36 280	36 298	36 318	36 332	36 335	37 445	37 393	-52
3		<sup>3</sup> P <sub>1</sub> <sup>o</sup>	36 286	36 339	36 357	36 377	36 391	36 394	37 503	37 454	-49
4		<sup>3</sup> P <sub>2</sub> <sup>o</sup>	36 405	36 459	36 477	36 496	36 511	36 514	37 626	37 578	-48
5		<sup>1</sup> P <sub>1</sub> <sup>o</sup>	59 810	59 698	59 617	59 619	59 606	59 602	59 982	59 852	-130
6	3p <sup>2</sup>	<sup>1</sup> D <sub>2</sub>	83 542	83 596	83 620	83 641	83 657	83 660	85 692	85 481	-211
7	3s 4s	<sup>3</sup> S <sub>1</sub>	89 965	90 028	90 059	90 082	90 099	90 102	91 425	91 275	-150
8	3p <sup>2</sup>	<sup>3</sup> P <sub>0</sub>	92 679	92 709	92 716	92 736	92 750	92 752	94 211	94 085	-126
9		<sup>3</sup> P <sub>1</sub>	92 739	92 769	92 776	92 795	92 809	92 812	94 264	94 147	-117
10		<sup>3</sup> P <sub>2</sub>	92 855	92 885	92 892	92 912	92 926	92 928	94 375	94 269	-106
11	3s 4s	<sup>1</sup> S <sub>0</sub>	94 003	94 057	94 084	94 101	94 111	94 114	95 543	95 351	-192
12	3s 3d	<sup>3</sup> D <sub>2</sub>	94 262	94 243	94 241	94 262	94 278	94 280	95 791	95 549	-242
13		<sup>3</sup> D <sub>1</sub>	94 261	94 243	94 242	94 263	94 279	94 281	95 794	95 551	-243
14		<sup>3</sup> D <sub>3</sub>	94 263	94 242	94 239	94 261	94 276	94 279	95 804	95 551	-253
15	3s 4p	<sup>3</sup> P <sub>0</sub> <sup>o</sup>	103 935	104 003	104 030	104 053	104 070	104 073	105 582	105 428	-154
16		<sup>3</sup> P <sub>1</sub> <sup>o</sup>	103 948	104 017	104 044	104 067	104 084	104 087	105 594	105 442	-152
17		<sup>3</sup> P <sub>2</sub> <sup>o</sup>	103 976	104 045	104 073	104 095	104 112	104 115	105 623	105 471	-152
18		<sup>1</sup> P <sub>1</sub> <sup>o</sup>	105 597	105 643	105 655	105 673	105 683	105 685	107 132	106 921	-211
19	3s 3d	<sup>1</sup> D <sub>2</sub>	109 010	108 919	108 897	108 910	108 918	108 918	110 330	110 090	-240
20	3p <sup>2</sup>	<sup>1</sup> S <sub>0</sub>	111 100	110 804	110 659	110 643	110 618	110 608	112 086	111 637	-449
21	3s 5s	<sup>3</sup> S <sub>1</sub>	118 564	118 632	118 661	118 685	118 702	118 705	120 259	120 093	-166
22		<sup>1</sup> S <sub>0</sub>	119 807	119 878	119 908	119 931	119 946	119 948	121 544	121 367	-177
23	3s 4d	<sup>3</sup> D <sub>2</sub>	120 013	120 034	120 045	120 068	120 085	120 088	121 684	121 484	-200
24		<sup>3</sup> D <sub>1</sub>	120 013	120 034	120 046	120 068	120 085	120 088	121 685	121 484	-201
25		<sup>3</sup> D <sub>3</sub>	120 014	120 034	120 045	120 068	120 084	120 087	121 688	121 484	-204
26	3s 4f	<sup>3</sup> F <sub>2</sub> <sup>o</sup>	121 657	121 739	121 772	121 797	121 815	121 818	123 606	123 418	-188
27		<sup>3</sup> F <sub>3</sub> <sup>o</sup>	121 659	121 742	121 775	121 799	121 817	121 820	123 608	123 420	-188
28		<sup>3</sup> F <sub>4</sub> <sup>o</sup>	121 663	121 745	121 778	121 802	121 820	121 824	123 612	123 423	-189
29		<sup>1</sup> F <sub>3</sub> <sup>o</sup>	121 735	121 818	121 852	121 876	121 894	121 898	123 657	123 471	-186
30	3s 4d	<sup>1</sup> D <sub>2</sub>	123 606	123 489	123 461	123 473	123 482	123 483	125 049	124 794	-255
31	3s 5p	<sup>3</sup> P <sub>0</sub> <sup>o</sup>	124 108	124 185	124 212	124 236	124 254	124 257	125 869	125 703	-166
32		<sup>3</sup> P <sub>1</sub> <sup>o</sup>	124 114	124 190	124 218	124 242	124 259	124 262	125 874	125 709	-165
33		<sup>3</sup> P <sub>2</sub> <sup>o</sup>	124 126	124 203	124 231	124 254	124 272	124 275	125 887	125 722	-165
34		<sup>1</sup> P <sub>1</sub> <sup>o</sup>	124 302	124 375	124 401	124 424	124 440	124 443	126 078	125 869	-209
35	3s 6s	<sup>3</sup> S <sub>1</sub>	130 615	130 689	130 716	130 740	130 758	130 761	132 386	132 216	-170

**Notes.** The energies are given as a function of the increasing active set of orbitals, accounting for VV correlation, where  $n$  indicates the maximum principle quantum number of the orbitals included in the active set. In Col. 10, the final energy values are displayed after accounting for CV correlation. The differences  $\Delta E$  between the final computations and the observed values are shown in the last column. The sequence and naming of the configurations and LSJ-levels are in accordance with the final (CV) computed energies. The levels of the singlet and triplet 3s6h <sup>1,3</sup>H and the 3p3d <sup>1</sup>D level have not yet been observed, and so the  $\Delta E$  values are not available.

**References.** <sup>(a)</sup>NIST Atomic Spectra Database 2018 (Kramida et al. 2018).

Table A.1. continued.

Pos.	Conf.	<i>LSJ</i>	VV						CV	$E_{\text{obs}}^a$	$\Delta E$
			<i>n</i> = 8	<i>n</i> = 9	<i>n</i> = 10	<i>n</i> = 11	<i>n</i> = 12	<i>n</i> = 13			
36		$^1S_0$	131 160	131 237	131 268	131 291	131 308	131 311	132 953	132 779	-174
37	3s 5d	$^3D_2$	131 265	131 307	131 326	131 348	131 365	131 368	133 013	132 823	-190
38		$^3D_1$	131 265	131 307	131 327	131 348	131 365	131 368	133 013	132 823	-190
39		$^3D_3$	131 266	131 307	131 326	131 347	131 365	131 368	133 017	132 823	-194
40	3s 5f	$^3F_2^o$	131 641	131 712	131 745	131 769	131 787	131 790	133 639	133 438	-201
41		$^3F_3^o$	131 647	131 718	131 751	131 776	131 794	131 797	133 644	133 443	-201
42		$^3F_4^o$	131 655	131 727	131 760	131 785	131 803	131 806	133 654	133 450	-204
43		$^1F_3^o$	131 968	132 048	132 082	132 106	132 124	132 128	133 866	133 682	-184
44	3s 5d	$^1D_2$	132 490	132 447	132 445	132 460	132 474	132 476	134 143	133 916	-227
45	3s 5g	$^3G_3$	132 487	132 577	132 611	132 636	132 654	132 657	134 359	134 184	-175
46		$^3G_4$	132 487	132 577	132 611	132 636	132 654	132 658	134 360	134 184	-176
47		$^3G_5$	132 487	132 577	132 611	132 636	132 654	132 657	134 360	134 184	-176
48		$^1G_4$	132 487	132 577	132 611	132 636	132 654	132 658	134 360	134 184	-176
49	3s 6p	$^1P_1^o$	133 288	133 366	133 387	133 411	133 428	133 431	135 132	134 919	-213
50		$^3P_0^o$	133 378	133 459	133 485	133 509	133 526	133 530	135 183	135 012	-171
51		$^3P_1^o$	133 381	133 462	133 488	133 512	133 530	133 533	135 186	135 016	-170
52		$^3P_2^o$	133 388	133 468	133 494	133 518	133 536	133 539	135 192	135 022	-170
53	3s 7s	$^3S_1$	136 870	136 949	136 975	136 999	137 014	137 017	138 675	138 500	-175
54	3s 6f	$^3F_2^o$	136 665	136 628	136 655	136 678	136 695	136 698	138 810	138 521	-289
55		$^3F_3^o$	136 684	136 649	136 677	136 699	136 717	136 720	138 829	138 539	-290
56		$^3F_4^o$	136 709	136 677	136 704	136 727	136 745	136 748	138 862	138 562	-300
57	3s 7s	$^1S_0$	137 154	137 236	137 267	137 291	137 307	137 311	138 974	138 801	-173
58	3s 6d	$^3D_2$	137 217	137 273	137 297	137 314	137 331	137 333	139 005	138 815	-190
59		$^3D_1$	137 217	137 273	137 297	137 314	137 331	137 333	139 005	138 815	-190
60		$^3D_3$	137 218	137 273	137 297	137 314	137 331	137 333	139 010	138 815	-195
61	3s 6f	$^1F_3^o$	137 562	137 625	137 657	137 681	137 699	137 702	139 437	139 245	-192
62	3s 6d	$^1D_2$	137 753	137 754	137 767	137 786	137 801	137 803	139 497	139 289	-208
63	3s 6g	$^3G_3$	137 898	137 988	138 022	138 046	138 065	138 067	139 766	139 591	-175
64		$^3G_4$	137 898	137 988	138 022	138 046	138 065	138 068	139 766	139 591	-175
65		$^3G_5$	137 898	137 988	138 022	138 046	138 065	138 067	139 766	139 591	-175
66		$^1G_4$	137 898	137 988	138 022	138 047	138 065	138 068	139 766	139 591	-175
67	3s 6h	$^3H_4^o$	137 965	138 043	138 079	138 103	138 121	138 125	139 817		
68		$^3H_5^o$	137 965	138 043	138 079	138 103	138 121	138 125	139 817		
69		$^1H_5^o$	137 965	138 043	138 079	138 103	138 121	138 125	139 817		
70		$^3H_6^o$	137 965	138 043	138 079	138 103	138 121	138 125	139 817		
71	3s 7p	$^1P_1^o$	138 286	138 364	138 360	138 384	138 401	138 402	140 148	139 919	-229
72		$^3P_0^o$	138 439	138 522	138 545	138 569	138 587	138 589	140 266	140 090	-176
73		$^3P_1^o$	138 441	138 524	138 547	138 571	138 589	138 591	140 268	140 092	-176
74		$^3P_2^o$	138 445	138 529	138 552	138 575	138 593	138 595	140 272	140 096	-176
75	3p 3d	$^3F_2^o$	136 665	136 628	136 655	136 678	136 695	139 291	141 615	141 085	-531
76		$^3F_3^o$	136 684	136 649	136 677	136 699	136 717	139 311	141 665	141 110	-555
77		$^3F_4^o$	136 709	136 677	136 704	136 727	136 745	139 338	141 768	141 143	-625
78	3p 3d	$^1D_2^o$	140 333	140 372	140 385	140 408	140 425	140 428	142 964		



**Table A.2.** Comparison between computed and observed lifetimes  $\tau$  in seconds for 75 excited states in Al II.

Pos.	Conf.	LSJ	RCI <sup>a</sup>		MCHF-BP <sup>b</sup>	BSCI <sup>c</sup>	Expt. <sup>d,e,f</sup>
			$\tau_l$	$\tau_v$	$\tau_l$		$\tau_{\text{obs}}$
1	3s3p	<sup>3</sup> P <sub>1</sub> <sup>o</sup>	3.274E-04	2.965E-04	3.051E-04		3.02 (2) E-04 <sup>e</sup>
2		<sup>1</sup> P <sub>1</sub> <sup>o</sup>	7.120E-10	7.089E-10	7.141E-10	6.70 E-10	6.90(13)E-10 <sup>d</sup>
3	3p <sup>2</sup>	<sup>1</sup> D <sub>2</sub>	3.351E-06	2.630E-06	2.270E-06	2.51 E-06	
4	3s4s	<sup>3</sup> S <sub>1</sub>	1.318E-09	1.325E-09	1.322E-09	1.32 E-09	
5	3p <sup>2</sup>	<sup>3</sup> P <sub>0</sub>	8.091E-10	8.032E-10	8.098E-10		
6		<sup>3</sup> P <sub>1</sub>	8.081E-10	8.023E-10	8.082E-10		
7		<sup>3</sup> P <sub>2</sub>	8.059E-10	8.000E-10	8.054E-10		
8	3s4s	<sup>1</sup> S <sub>0</sub>	2.921E-09	2.922E-09	2.893E-09	2.93 E-09	
9	3s3d	<sup>3</sup> D <sub>2</sub>	8.337E-10	8.346E-10	8.252E-10	8.00 E-10	
10		<sup>3</sup> D <sub>1</sub>	8.319E-10	8.328E-10	8.233E-10	8.00 E-10	
11		<sup>3</sup> D <sub>3</sub>	8.358E-10	8.357E-10	8.277E-10	8.00 E-10	
12	3s4p	<sup>3</sup> P <sub>0</sub> <sup>o</sup>	1.390E-08	1.394E-08	1.384E-08	1.403E-08	
13		<sup>3</sup> P <sub>1</sub> <sup>o</sup>	1.386E-08	1.391E-08	1.379E-08	1.403E-08	
14		<sup>3</sup> P <sub>2</sub> <sup>o</sup>	1.379E-08	1.384E-08	1.369E-08	1.403E-08	
15		<sup>1</sup> P <sub>1</sub> <sup>o</sup>	1.099E-08	1.113E-08	1.116E-08	1.007E-08	
16	3s3d	<sup>1</sup> D <sub>2</sub>	7.204E-10	7.192E-10	6.994E-10	7.20 E-10	
17	3p <sup>2</sup>	<sup>1</sup> S <sub>0</sub>	9.804E-10	9.758E-10	9.720E-10	9.50 E-10	
18	3s5s	<sup>3</sup> S <sub>1</sub>	2.767E-09	2.785E-09		2.78 E-09	
19		<sup>1</sup> S <sub>0</sub>	4.059E-09	4.055E-09		4.33 E-09	
20	3s4d	<sup>3</sup> D <sub>2</sub>	3.862E-09	3.872E-09		3.71 E-09	
21		<sup>3</sup> D <sub>1</sub>	3.850E-09	3.860E-09		3.71 E-09	
22		<sup>3</sup> D <sub>3</sub>	3.880E-09	3.889E-09		3.71 E-09	
23	3s4f	<sup>3</sup> F <sub>2</sub> <sup>o</sup>	4.235E-09	4.254E-09			6.4 (5)E-09 <sup>f</sup>
24		<sup>3</sup> F <sub>3</sub> <sup>o</sup>	4.230E-09	4.248E-09			6.4 (5)E-09 <sup>f</sup>
25		<sup>3</sup> F <sub>4</sub> <sup>o</sup>	4.230E-09	4.256E-09			6.4 (5)E-09 <sup>f</sup>
26		<sup>1</sup> F <sub>3</sub> <sup>o</sup>	3.428E-09	3.438E-09			
27	3s4d	<sup>1</sup> D <sub>2</sub>	1.366E-09	1.368E-09		1.31 E-09	
28	3s5p	<sup>3</sup> P <sub>0</sub> <sup>o</sup>	4.903E-08	4.941E-08		4.928E-08	
29		<sup>3</sup> P <sub>1</sub> <sup>o</sup>	4.862E-08	4.899E-08		4.928E-08	
30		<sup>3</sup> P <sub>2</sub> <sup>o</sup>	4.850E-08	4.903E-08		4.928E-08	
31		<sup>1</sup> P <sub>1</sub> <sup>o</sup>	1.315E-08	1.377E-08		1.263E-08	
32	3s6s	<sup>3</sup> S <sub>1</sub>	5.196E-09	5.242E-09		5.19 E-09	
33		<sup>1</sup> S <sub>0</sub>	7.265E-09	7.254E-09		7.61 E-09	
34	3s5d	<sup>3</sup> D <sub>2</sub>	1.077E-08	1.081E-08		1.03 E-08	
35		<sup>3</sup> D <sub>1</sub>	1.073E-08	1.077E-08		1.03 E-08	

**Notes.** For the current RCI calculations length  $\tau_l$  and velocity  $\tau_v$  forms are both displayed. In Cols. 6 and 7, the predicted lifetimes from MCHF-BP and BSCI calculations are, respectively, given in length form. The last column contains available lifetimes from experimental measurements, together with their uncertainties.

**References.** <sup>(a)</sup>Present calculations; <sup>(b)</sup>Froese Fischer et al. (2006); <sup>(c)</sup>Chang & Fang (1995); <sup>(d)</sup>Kernahan et al. (1979), Smith (1970), Berry et al. (1970), Head et al. (1976); <sup>(e)</sup>Träbert et al. (1999), Johnson et al. (1986); <sup>(f)</sup>Andersen et al. (1971).

Table A.2. continued.

Pos.	Conf.	$LSJ$	RCI <sup>a</sup>		MCHF-BP <sup>b</sup>	BSCI <sup>c</sup>	Expt. <sup>d,e,f</sup>
			$\tau_l$	$\tau_u$	$\tau_l$		$\tau_{\text{obs}}$
36		$^3D_3$	1.085E-08	1.090E-08		1.03 E-08	
37	3s5f	$^3F_2^0$	1.337E-08	1.356E-08			1.4 (2)E-08 <sup>f</sup>
38		$^3F_3^0$	1.328E-08	1.348E-08			1.4 (2)E-08 <sup>f</sup>
39		$^3F_4^0$	1.320E-08	1.345E-08			1.4 (2)E-08 <sup>f</sup>
40		$^1F_3^0$	5.981E-09	6.015E-09			
41	3s5d	$^1D_2$	3.523E-09	3.525E-09		3.37 E-09	
42	3s5g	$^3G_3$	1.389E-08	1.390E-08			
43		$^3G_4$	1.389E-08	1.389E-08			
44		$^3G_5$	1.389E-08	1.390E-08			
45		$^1G_4$	1.383E-08	1.384E-08			
46	3s6p	$^1P_1^0$	1.322E-08	1.425E-08		1.211E-08	
47		$^3P_0^0$	1.147E-07	1.171E-07		1.105E-07	
48		$^3P_1^0$	1.097E-07	1.122E-07		1.105E-07	
49		$^3P_2^0$	1.137E-07	1.173E-07		1.105E-07	
50	3s7s	$^3S_1$	9.039E-09	9.167E-09		8.78 E-09	
51	3s6f	$^3F_2^0$	2.041E-08	2.051E-08			1.5 (1)E-08 <sup>f</sup>
52		$^3F_3^0$	2.111E-08	2.125E-08			1.5 (1)E-08 <sup>f</sup>
53		$^3F_4^0$	2.222E-08	2.236E-08			1.5 (1)E-08 <sup>f</sup>
54	3s7s	$^1S_0$	1.174E-08	1.170E-08			
55	3s6d	$^3D_2$	2.386E-08	2.399E-08		2.234E-08	
56		$^3D_1$	2.376E-08	2.391E-08		2.234E-08	
57		$^3D_3$	2.423E-08	2.445E-08		2.234E-08	
58	3s6f	$^1F_3^0$	9.655E-09	9.720E-09			
59	3s6d	$^1D_2$	7.546E-09	7.518E-09		7.46 E-09	
60	3s6g	$^3G_3$	2.415E-08	2.417E-08			
61		$^3G_4$	2.412E-08	2.413E-08			
62		$^3G_5$	2.417E-08	2.415E-08			
63		$^1G_4$	2.373E-08	2.375E-08			
64	3s6h	$^3H_4^0$	3.753E-08	3.759E-08			
65		$^3H_5^0$	3.753E-08	3.759E-08			
66		$^1H_5^0$	3.753E-08	3.759E-08			
67		$^1H_6^0$	3.753E-08	3.759E-08			
68	3s7p	$^1P_1^0$	1.238E-08	1.450E-08		1.081E-08	
69		$^3P_0^0$	1.904E-07	2.090E-07		1.608E-07	
70		$^3P_1^0$	1.897E-07	2.078E-07		1.608E-07	
71		$^3P_2^0$	1.865E-07	2.148E-07		1.608E-07	
72	3p3d	$^3F_2^0$	2.769E-09	2.735E-09			3.5 (3)E-09 <sup>f</sup>
73		$^3F_3^0$	2.736E-09	2.701E-09			3.5 (3)E-09 <sup>f</sup>
74		$^3F_4^0$	2.586E-09	2.539E-09			3.5 (3)E-09 <sup>f</sup>
75		$^1D_2^0$	8.207E-10	8.198E-10			

## Paper IV

W. Li, P. Rynkun, L. Radžiūtė, G. Gaigalas, B. Atalay, A. Papoulia, K. Wang, H. Hartman, J. Ekman, T. Brage, C. Y. Chen, and P. Jönsson  
Multiconfiguration DiracHartreeFock calculations of Landé g-factors for ions of astrophysical interests: B II, C I-IV, Al I-II, Si I-IV, P II, S II, Cl III, Ar IV, Ca I, Ti II, Zr III and Sn II

*Astronomy & Astrophysics*, 2020, 639, A25

Copyright 2020 ESO



# Multiconfiguration Dirac-Hartree-Fock calculations of Landé $g$ -factors for ions of astrophysical interest: B II, C I–IV, Al I–II, Si I–IV, P II, S II, Cl III, Ar IV, Ca I, Ti II, Zr III, and Sn II<sup>\*</sup>

W. Li<sup>1</sup>, P. Rynkun<sup>2</sup>, L. Radžiūtė<sup>2</sup>, G. Gaigalas<sup>2</sup>, B. Atalay<sup>3,4</sup>, A. Papoulia<sup>1,3</sup>, K. Wang<sup>5</sup>, H. Hartman<sup>1</sup>, J. Ekman<sup>1</sup>, T. Brage<sup>3</sup>, C. Y. Chen<sup>6</sup>, and P. Jönsson<sup>1</sup>

<sup>1</sup> Department of Materials Science and Applied Mathematics, Malmö University, 20506 Malmö, Sweden  
e-mail: [wenxian.li@mau.se](mailto:wenxian.li@mau.se)

<sup>2</sup> Institute of Theoretical Physics and Astronomy, Vilnius University, Saulėtekio Av. 3, 10222 Vilnius, Lithuania

<sup>3</sup> Division of Mathematical Physics, Lund University, Post Office Box 118, 22100 Lund, Sweden

<sup>4</sup> Department of Physics, Çanakkale Onsekiz Mart University, Çanakkale, Turkey

<sup>5</sup> Hebei Key Lab of Optic-electronic Information and Materials, The College of Physics Science and Technology, Hebei University, Baoding 071002, PR China

<sup>6</sup> Shanghai EBIT Lab, Key Laboratory of Nuclear Physics and Ion-beam Application, Institute of Modern Physics, Department of Nuclear Science and Technology, Fudan University, Shanghai 200433, PR China

Received 21 February 2020 / Accepted 4 May 2020

## ABSTRACT

**Aims.** The Landé  $g$ -factor is an important parameter in astrophysical spectropolarimetry, used to characterize the response of a line to a given value of the magnetic field. The purpose of this paper is to present accurate Landé  $g$ -factors for states in B II, C I–IV, Al I–II, Si I–IV, P II, S II, Cl III, Ar IV, Ca I, Ti II, Zr III, and Sn II.

**Methods.** The multiconfiguration Dirac-Hartree-Fock and relativistic configuration interaction methods, which are implemented in the general-purpose relativistic atomic structure package GRASP2K, are employed in the present work to compute the Landé  $g$ -factors for states in B II, C I–IV, Al I–II, Si I–IV, P II, S II, Cl III, Ar IV, Ca I, Ti II, Zr III, and Sn II. The accuracy of the wave functions for the states, and thus the accuracy of the resulting Landé  $g$ -factors, is evaluated by comparing the computed excitation energies and energy separations with the National Institute of Standards and Technology (NIST) recommended data.

**Results.** All excitation energies are in very good agreement with the NIST values except for Ti II, which has an average difference of 1.06%. The average uncertainty of the energy separations is well below 1% except for the even states of Al I; odd states of Si I, Ca I, Ti II, Zr III; and even states of Sn II for which the relative differences range between 1% and 2%. Comparisons of the computed Landé  $g$ -factors are made with available NIST data and experimental values. Analysing the  $LS$ -composition of the wave functions, we quantify the departures from  $LS$ -coupling and summarize the states for which there is a difference of more than 10% between the computed Landé  $g$ -factor and the Landé  $g$ -factor in pure  $LS$ -coupling. Finally, we compare the computed Landé  $g$ -factors with values from the Kurucz database.

**Key words.** atomic data – magnetic fields

## 1. Introduction

Magnetic fields play a fundamental role in astrophysical systems, and thus in the evolution of the Universe. Measurement of the polarization of light as a function of wavelength, known as spectropolarimetry, is the most powerful tool for the accurate determination of magnetic fields in astrophysics. Highly accurate atomic data (e.g. excitation energies, transition rates, oscillator strengths, and Landé  $g$ -factors) are essential for interpreting and modelling the spectropolarimetric observations (Judge 2017). The need for atomic data have increased tremendously over the last 20 years with the development of new instrumentation like the *Daniel K. Inoué* Solar Telescope (DKIST, formerly ATST; Keil et al. 2009). The next generation ground-based solar telescopes will also offer spectropolarimetric capa-

bilities covering a broad wavelength range from the visible into the near-infrared, the latter of which is largely unexplored spectroscopically.

When an atom or ion is placed in a magnetic field, level splitting occurs that breaks the degeneracy of the energy levels for the different magnetic quantum numbers. This splitting, known as the Zeeman effect, is caused by the interaction between the magnetic moment of the atom and an external magnetic field (Cowan 1981) and is expressed in terms of the Landé  $g$ -factor. Accordingly, the effective Landé  $g$ -factor of a spectral line, which can be expressed in terms of the Landé  $g$ -factors of the lower and upper levels, is an important parameter in astrophysical spectropolarimetry used to characterize the response of the line to a given value of the magnetic field (Landi Degl’Innocenti 1982; Landi Degl’Innocenti & Landolfi 2004). The effective Landé  $g$ -factor,  $\bar{g}$ , and the second order effective Landé  $g$ -factor,  $\bar{G}$ , are respectively related to the circular and the linear polarization of a spectral line produced by

\* Tables 5–23 are only available at the CDS via anonymous ftp to [cdsarc.u-strasbg.fr](http://cdsarc.u-strasbg.fr) (130.79.128.5) or via <http://cdsarc.u-strasbg.fr/viz-bin/cat/J/A+A/639/A25>

the Zeeman effect (Landi Degl'Innocenti & Landolfi 2004). For this reason, detailed investigations of the magnetic fields require knowledge of accurate Landé  $g$ -factors.

There are a number of measurements of Landé  $g$ -factors. In the first half of 20th century massive efforts were made by atomic physicists to establish the energy level structures of atoms and ions from the observed spectral lines. The experimental Landé  $g$ -factors were derived from the analysis of Zeeman patterns in individual spectral lines produced in the magnetic fields. These  $g$ -factors were collected and made available in the critical compilation by Moore (1949). However, there was a surprising scarcity of reliable data on observed Zeeman patterns among the spectra of the light elements. For example, among the elements studied in this work, the observed  $g$ -factors compiled in Moore (1949) are available only for a few states in Ca I and Ti II, which reveals a glaring need of further observations. Later on, Lott et al. (1966) studied the Zeeman effect using strong pulsed magnetic fields and derived the  $g$ -factors for a number of states in B I, C I, C III, O II, O III, Mg I, Mg II, Si I, Si III, Si IV, Ca II, and Cu II. Li (1972) measured the Zeeman effect of P II using the electrodeless discharge tubes operated in a field of 32 215 G. The Landé  $g$ -factor of the Sn II  $5s5p^2\ ^4P_{1/2}$  level was measured by David et al. (1980) by direct magnetic resonance. As of today there are, to the knowledge of the authors, no experimental efforts to cover the needs of Landé  $g$ -factors, and thus they have to be calculated.

If there are no experimental or calculated data available, the Landé  $g$ -factors in pure  $LS$ -coupling are sometimes used (see Sect. 2). While in many cases this is a good approximation, there are many cases where this fails, thus giving erroneous polarization profiles. One example is the Fe I transition  $3d^74p\ ^5F_1^o - 3d^75s\ ^5F_1^o$  at 7389.398 Å, where the circular polarization is produced by the Zeeman effect due to the non-zero experimental Landé  $g$ -factor value, which is instead missing under the  $LS$ -coupling scheme because of the zero Landé  $g$ -factor (Li et al. 2017). More accurate values of the Landé  $g$ -factors are obtained in the intermediate coupling approximation, as described in Sect. 2 below. Using the Cowan code in the intermediate coupling approximation, Biémont et al. (2010) calculated Landé  $g$ -factors for elements along the sixth row of the periodic table. These data were collected in the DESIRE database<sup>1</sup>. In this context we should also mention the MCHF/MCDHF database of Froese Fischer for which the Landé  $g$ -factors are provided for a few collections<sup>2</sup>. Fully relativistic calculations of Landé  $g$ -factors were pioneered by Cheng & Childs (1985) for states of the  $4f^N6s^2$  configurations in rare-earth elements. More recently relativistic  $g$ -factor calculations have been performed for states in Ne I and Ne II (Fischer et al. 2004) and Si IX (Brage et al. 2000). A full set of  $g$ -factors was also calculated for the  $n = 2$  states in beryllium-, boron-, carbon-, and nitrogen-like ions (Verdehout et al. 2014).

The purpose of the present work is to compute accurate Landé  $g$ -factors for states in B II, C I–IV, Al I–II, Si I–IV, P II, S II, Cl III, Ar IV, Ca I, Ti II, Zr III, and Sn II within the fully relativistic scheme. Looking at the ions and states studied in this work, the National Institute of Standards and Technology (NIST) database (Kramida et al. 2019) reports Landé  $g$ -factors for only 3 out of 100 states for C I, 76 out of 106 for P II, 15 out of 99 for Ti II, and 1 out of 22 for Sn II (see Table 1 for a summary).

<sup>1</sup> <http://hosting.umons.ac.be/html/agif/databases/desire.html>

<sup>2</sup> <https://nlte.nist.gov/MCHF/>

## 2. Theory

We start the theory section with a brief discussion of the Breit–Pauli and intermediate coupling approximations, which provide the necessary background for understanding the validity and limitations of the often used pure  $LS$ -coupling approximation of the Landé  $g$ -factors. The Breit–Pauli and intermediate coupling approximations also provide the theoretical background for the labelling and description of states by the  $LS$ -composition, for example as done in the NIST Atomic Spectra Database (Kramida et al. 2019). After this brief discussion we present the fully relativistic theory and show how it links to the Breit–Pauli and intermediate coupling approximations.

### 2.1. Multiconfiguration wave functions

In the non-relativistic multiconfiguration Hartree–Fock (MCHF) approach the wave function  $\Psi$  for a state labelled  $\gamma LS$ , where  $L$  and  $S$  are the total orbital and spin angular quantum numbers and  $\gamma$  represents the configuration and other quantum numbers needed to specify the state, is expanded in terms of configuration state functions (CSFs) with the same  $LS$  term:

$$\Psi(\gamma LS) = \sum_j c_j \Phi(\gamma_j LS). \quad (1)$$

The CSFs are constructed from products of one-electron spin orbitals. The radial orbitals and the expansion coefficients of the CSFs are determined by iteratively solving a set of coupled differential equation resulting from the stationary condition of the energy functional of the non-relativistic Hamiltonian (Fischer et al. 2016). Once radial orbitals have been obtained, Breit–Pauli configuration interaction (CI) calculations can be performed where the wave function is expanded in  $LS$   $J$ -coupled CSFs:

$$\Psi(\gamma LS J) = \sum_j c_j \Phi(\gamma_j L_j S_j J). \quad (2)$$

In the CI calculation the expansion coefficients,  $c_j$ , are obtained by diagonalizing the Hamiltonian interaction matrix with respect to the Breit–Pauli operators. This is the intermediate coupling or  $LS$   $J$  approximation. If the interaction matrix is ordered according to  $LS$  terms the interaction has a block structure. Diagonal blocks represent interaction within CSFs of a given  $LS$  and off-diagonal blocks between CSFs of different  $LS$  terms. If off-diagonal interactions occur for a specific  $J$  we say that the  $LS$  terms interact and as a result of this interaction the terms mix in the wave function expansion.

In the fully relativistic multiconfiguration Dirac–Hartree–Fock (MCDHF) approach the wave function  $\Psi$  for a state labelled  $\gamma J$  is expanded in terms of  $jj$ -coupled CSFs:

$$\Psi(\gamma J) = \sum_j c_j \Phi(\gamma_j J). \quad (3)$$

The CSFs,  $\Psi(\gamma J)$ , are constructed from products of relativistic one-electron spin orbitals. The radial orbitals and the expansion coefficients of the CSFs are determined by iteratively solving a set of coupled differential equations resulting from the stationary condition of energy functional of the relativistic Dirac–Coulomb Hamiltonian (Grant 2007; Fischer et al. 2016). Once the radial orbitals have been obtained, relativistic configuration interaction (RCI) calculations can be performed where the Breit interaction and quantum electrodynamic (QED) effects can be added to the Hamiltonian. Relativistic wave functions are given in terms

**Table 1.** Summary of ions, the number of computed energy levels  $N_{\text{cal-levels}}$ , and the number of Landé  $g$ -factors in NIST  $N_{\text{NIST-}g_J}$ .

Ions	$N_{\text{cal-levels}}$	$N_{\text{NIST-}g_J}$	Ions	$N_{\text{cal-levels}}$	$N_{\text{NIST-}g_J}$	Ions	$N_{\text{cal-levels}}$	$N_{\text{NIST-}g_J}$
B II	100	0	Si I	168	0	Ar IV	103	0
C I	100	3	Si II	56	0	Ca I	45	0
C II	69	0	Si III	106	0	Ti II	99	15
C III	114	0	Si IV	45	0	Zr III	88	0
C IV	53	0	P II	106	76	Sn II	22	1
Al I	28	0	S II	134	0			
Al II	78	0	Cl III	87	0			

of  $jj$ -coupled CSFs. In order to have a labelling that is consistent with the one from the intermediate coupling approximation, CSFs are transformed from  $jj$ -coupling to  $LS$   $J$ -coupling using the methods developed by Gaigalas et al. (2003, 2017).

## 2.2. Zeeman effect

The Zeeman effect is caused by the interaction between the magnetic moment of the atom and an external magnetic field. The operator representing the interaction is given by

$$\mathcal{H}_M = -\boldsymbol{\mu} \cdot \mathbf{B}, \quad (4)$$

where  $\boldsymbol{\mu}$  is the magnetic moment of the electrons and  $\mathbf{B}$  is the magnetic field. If the external magnetic field is weak such that the magnetic interaction energy is small compared to the fine structure separations, the interaction can be treated in first-order perturbation theory with the wave functions from the Breit–Pauli approximation or from the fully relativistic theory as zero-order functions.

In the Breit–Pauli approximation the magnetic moment can be written as

$$\boldsymbol{\mu} = -\mu_B(\mathbf{L} + g_s\mathbf{S}), \quad (5)$$

where  $\mu_B$  is the Bohr magneton and  $g_s \approx 2.00160$  is the  $g$ -factor of the electron spin corrected for QED effects. Using the Wigner–Eckart theorem to relate the matrix elements of  $\mathbf{L} + g_s\mathbf{S}$  with the matrix element of  $\mathbf{J}$ , it can be shown that the magnetic moment is proportional to  $\mathbf{J}$ , i.e.

$$\mu_B(\mathbf{L} + g_s\mathbf{S}) = \mu_B g_{\gamma J} \mathbf{J}, \quad (6)$$

where the factor of proportionality,  $g_{\gamma J}$ , is the Landé  $g$ -factor. Choosing the direction of the external field as the  $z$ -direction of the operator for the interaction can, using tensor-operator notation, be written as

$$\mathcal{H}_M = \mu_B (\mathbf{L}_0^{(1)} + g_s \mathbf{S}_0^{(1)}) B = \mu_B g_{\gamma J} \mathbf{J}_0^{(1)} B. \quad (7)$$

Inserting the wave function expansion from Eq. (2) and computing the reduced matrix elements of the interaction gives the Landé  $g$ -factor in intermediate coupling, i.e.

$$g_{\gamma J} = \sum_{i,j} c_i c_j \frac{\langle \gamma_i L_i S_i J_i | (\mathbf{L}^{(1)} + g_s \mathbf{S}^{(1)}) | \gamma_j L_j S_j J_j \rangle}{\sqrt{J(J+1)(2J+1)}}. \quad (8)$$

The matrix elements between the  $LS$   $J$ -coupled CSFs can be analytically evaluated to give

$$\frac{\langle \gamma LS J | (\mathbf{L}^{(1)} + g_s \mathbf{S}^{(1)}) | \gamma' L' S' J' \rangle}{\sqrt{J(J+1)(2J+1)}} = \delta_{\gamma\gamma'} \delta_{LL'} \delta_{SS'} g_J(LS), \quad (9)$$

where

$$g_J(LS) = 1 + (g_s - 1) \frac{J(J+1) + S(S+1) - L(L+1)}{2J(J+1)} \quad (10)$$

is the Landé  $g$ -factor in pure  $LS$ -coupling (Cowan 1981). Summing up the contributions from the different  $LS$  terms, we have

$$g_{\gamma J} = \sum_{LS} w(LS) g_J(LS), \quad (11)$$

where  $w(LS)$  is the accumulated squared expansion coefficients for the CSFs with the specified  $LS$  term (Jönsson & Gustafsson 2002). The set of  $w(LS)$  determine the  $LS$   $J$ -composition of the wave function. The Landé  $g$ -factor in intermediate coupling thus provides a valuable probe of the coupling conditions in the atom (Fawcett 1990). To summarize, the full sum in Eq. (11) gives the Landé  $g$ -factor,  $g_{\gamma J}$ , in the intermediate coupling approximation. Truncating the sum to a single dominating  $LS$  term, often the one used to label the state, gives the Landé  $g$ -factor,  $g_J(LS)$ , in pure  $LS$ -coupling.

In the relativistic theory the interaction between the magnetic moment of the atom and an external field can be written as

$$\mathcal{H}_M = \frac{1}{2} \mathbf{N} \cdot \mathbf{B}, \quad (12)$$

where

$$\mathbf{N}_q^{(1)} = - \sum_{j=1}^N i \sqrt{\frac{8\pi}{3}} r_j \boldsymbol{\alpha}_j \cdot \mathbf{Y}_{1q}^{(0)}(\hat{r}_j) \quad (13)$$

is an operator of the same tensorial form as the magnetic dipole hyperfine operator (Cheng & Childs 1985). Just as in the Breit–Pauli approximation, we express the operator  $\mathcal{H}_M$  in terms of  $\mathbf{J}$  and the Landé  $g$ -factor, i.e.

$$\mathcal{H}_M = \frac{1}{2} \mathbf{N}_0^{(1)} B = \mu_B g_{\gamma J} \mathbf{J}_0^{(1)} B. \quad (14)$$

Inserting the wave function expansion from Eq. (3) and evaluating the matrix elements of the interaction gives

$$g_{\gamma J} = \sum_{i,j} c_i c_j \frac{1}{2\mu_B} \frac{\langle \gamma_i J_i | \mathbf{N}^{(1)} | \gamma_j J_j \rangle}{\sqrt{J(J+1)(2J+1)}}. \quad (15)$$

In the relativistic Dirac theory the electron  $g$ -factor is exactly 2. The QED corrections to this factor lead to a correction of the Landé  $g$ -factor. Defining the operator  $\Delta \mathbf{N}$  by

$$\Delta \mathbf{N}_q^{(1)} = \sum_{j=1}^N \frac{g_s - 2}{2} \beta_j \boldsymbol{\Sigma}_{qj}, \quad (16)$$

the correction to the Landé  $g$ -factor is given by

$$\Delta g_{\gamma J} = \sum_{i,j} c_i c_j \frac{(g_s - 2)}{2} \frac{\langle \gamma_i J_i | \Delta \mathbf{N}^{(1)} | \gamma_j J_j \rangle}{\sqrt{J(J+1)(2J+1)}}. \quad (17)$$

### 3. Computational scheme

The accuracy of the computed Landé  $g$ -factors depends on the quality of the wave functions. From Eq. (11) we see that the  $g$ -factors require the mixing of  $LS$ -terms in the wave functions to be accurately determined (Fischer et al. 2004). This in turn depends on the CSFs expansions, what electron correlation effects are captured, and how well the resulting wave functions reproduce measured energy separations. For the studied atoms and ions the CSF expansions, aimed at producing accurate energies, are based on the multireference-single-double (MR-SD) approach (Fischer et al. 2016). In the MR-SD approach, the CSF expansions are obtained first by defining a set of important configurations referred to as the MR and then by allowing SD substitutions, according to some rules, of the orbitals in the MR configurations to orbitals in an active set (AS) (see Olsen et al. 1988; Stuesson et al. 2007; Fischer et al. 2016). Depending on the rules, substitutions for the CSF expansion will account for valence–valence (VV), core–valence (CV), and core–core (CC) electron correlation effects. The CSF expansions are systematically enlarged by increasing the active set along with the MR. A number of studies show that expansions accounting for VV and CV effects and based on reasonably large MR and active orbital sets often are sufficient for reproducing energy separations with high accuracy (Jönsson et al. 2017). The Breit interaction and leading QED effects (e.g. vacuum polarization and self-energy) can be accounted for in the following RCI calculations.

The computational schemes, as well as the evaluation of the wave functions and atomic data for each atomic system, are described in detail in Wang et al. (2018) (for B II), Papoulia et al. (2019a) (for C III–IV), Papoulia et al. (2019b) (for Al I–II), Pehlivan Rhodin et al. (2019) (for Si I–II), Atalay et al. (2019) (for Si III–IV), Rynkun et al. (2019a) (for P II), Rynkun et al. (2019b) (for S II, Cl III and Ar IV), and Rynkun et al. (2020) (for Zr III). The corresponding manuscripts of C I–C IV by Li et al., Ti II by Li et al., and Sn II by Atalay et al. (in prep.). The ions, as well as the details of the computational schemes and correlation effects (e.g. targeted configuration states, MR for RCI calculations, definition of core orbitals, correlation model for final RCI calculations, AS, and the number of generated CSFs) are summarized in Table 2.

All calculations of the wave functions were done using the MCDHF and RCI programs (Grant 2007; Fischer et al. 2016), which are parts of general relativistic atomic structure package GRASP2K (Jönsson et al. 2013; Fischer et al. 2019). The evaluation of the Landé  $g$ -factors was then done with the HFSZEE-MAN programs (Andersson & Jönsson 2008; Li et al. 2020).

### 4. Evaluation of data

The accuracy of the Landé  $g$ -factors is to a large extent determined by the accuracy of the energy separations. In this section we evaluate the accuracy of the calculated energy levels by comparing them with the NIST recommended data. We then present the results for the Landé  $g$ -factors,  $g_{yJ}$ , and compare them with the Landé  $g$ -factors in pure  $LS$ -coupling,  $g_J(LS)$ . Finally, we compare the Landé  $g$ -factors with values from Kurucz’s atomic database (Kurucz 2017).

#### 4.1. Energy levels

The computed excitation energies and wave function composition in  $LS$ -coupling of the targeted atomic states in the B II, C I–IV, Al I–II, Si I–IV, P II, S II, Cl III, Ar IV, Ca I, Ti II,

Zr III, and Sn II ions are displayed in Tables 5–23, respectively, and are available at the CDS. In the calculations the labelling of the eigenstates is determined by the  $LS$   $J$ -coupled CSF with the largest coefficient in the expansion resulting from the transformation from  $jj$ -coupling to  $LS$   $J$ -coupling using the methods by Gaigalas et al. (2017).

One of the quality indicators of calculations is the ability to reproduce the energy structure. Therefore, the accuracy of the wave functions from the calculations can be evaluated by comparing the calculated energy levels with data from the NIST database (Kramida et al. 2019). Here we define the average percentage difference between the present calculations and NIST as “Av. accuracy” to indicate the accuracy of the calculations. In Table 3 a summary of the Av. accuracy is presented for the targeted atoms and ions. As seen from Table 3, all energies are in very good agreement with the NIST recommended values. In particular, the Av. accuracy values are less than 0.1%; they are 0.089%, 0.088%, 0.044%, 0.004%, 0.05%, and 0.09%, respectively, for the Be II, C II–IV, Si III, and Si IV ions. The Av. accuracy values are less than 0.68% for C I, Al I–II, Si I–II, P II, S II, Cl III, Ar IV, Ca I, Zr III, and Sn II. For Ti II the average difference is larger, about 1.06%. The excellent agreement of the excitation energies with the NIST recommended values allows us to infer that the corresponding wave functions are very accurate (see the references given in Sect. 3 for each atom or ion for more details on how to estimate the accuracy.)

As we have already discussed, the Landé  $g$ -factor depends on the mixing of different  $LS$  terms, which in turn depends on the separation of these terms. The accuracy of the energy separation of the terms is thus a more proper measure of the accuracy of the Landé  $g$ -factors than the excitation energies. To evaluate the accuracy of the energy separation of the terms, we define a new average accuracy parameter  $\overline{dE_S}$  by (i) classifying the states into different blocks by  $J$ -values and parity, one for each symmetry block; (ii) computing the energy separation relative to the lowest state of each block,  $E_S = E_i - E_{\min}$ , where  $E_i$  is the excitation energy and  $E_{\min}$  is the lowest energy of each block; (iii) computing the relative difference with the NIST values,  $dE_S = \frac{|E_S - E_{S-NIST}|}{E_S}$ , where  $E_{S-NIST}$  is the energy separation from the NIST database; and (iv) averaging the difference,  $\overline{dE_S} = \frac{\sum dE_S}{N_{E_S}}$ , where  $N_{E_S}$  is the number of the energy separations. The results are shown in Table 4 for even and odd states. Generally, the uncertainties of the energy separations are larger than those of the excitation energies, especially when the energy separations are very small. However, for most of the levels,  $\overline{dE_S}$  is well below 1%. For a few levels for which  $E_S$  is small,  $\overline{dE_S}$  is higher than 5% and these data have been excluded to obtain the average difference values shown in Table 4 (one level for C I, one for C III, one for Si I, one for Si II, one for Si III, one for Ar IV, one for Ca I, and five levels for Ti II). Table 4 shows that the average uncertainty  $\overline{dE_S}$  is well below 1%, except for even states of Al I; odd states of Si I, Ca I, Ti II, Zr III; and even states of Sn II. For these levels the relative difference is between 1% and 2%. The good agreement of the energy separations of the terms with the NIST data confirms the reliable values of the mixing between the relativistic CSFs, which is a good indicator of the quality of the produced Landé  $g$ -factors.

#### 4.2. Landé $g$ -factors

Tables 5–23 display the Landé  $g$ -factors,  $g_{yJ}$ , for the lowest states (shown in Table 1) in the B II, C I–IV, Al I–II, Si I–IV, P II, S II, Cl III, Ar IV, Ca I, Ti II, Zr III, and Sn II ions, respectively.



**Table 2.** Summary of the computational schemes of B II, C I–IV, Al I–II, Si I–IV, P II, S II, Cl III, Ar IV, Ca I, Ti II, Zr III, and Sn II.

Configurations	MR-RCI	Core orbitals	Correlation	AS	$N_{\text{NCFs}}$
	B II <sup>(1)</sup> , $N_{\text{levels}} = 100$				
$2s^2, 2p^2$ , {2s,2p}nl ( $n \leq 6, l \leq 5$ )	$2s^2, 2p^2$ , {2s,2p}nl ( $n \leq 6, l \leq 5$ )	1s	VV + CV + CC (1s)	{11s,11p,11d,11f, 11g,11h,11i,11k}	e: 777 325 o: 800 410
	C I, $N_{\text{levels}} = 100$				
$2s2p^3$ $2s^2 2p\{n_1s, n_2p, n_3d, 4f\}$ ( $3 \leq n_1 \leq 6, 2 \leq n_2 \leq 5, 3 \leq n_3 \leq 5$ )	$2s2p^3$ $2s^2 2p\{n_1s, n_2p, n_3d, 4f\}$ ( $3 \leq n_1 \leq 6, 2 \leq n_2 \leq 6, 3 \leq n_3 \leq 5$ ) $2p^3\{n_1s, n_2p, n_3d\}$ ( $3 \leq n_1 \leq 6, 3 \leq n_2 \leq 5, 3 \leq n_3 \leq 6$ ) $2s2p^2\{3s, 3p, 4p, 6p, 6d, 7s\}$ $2s2p\{n_1s, n_2p, n_3d, 4f\}6d$ ( $3 \leq n_1 \leq 6, 3 \leq n_2 \leq 5, 3 \leq n_3 \leq 5$ )	1s	VV + CV (1s)	{11s,10p,10d,9f, 7g,6h}	e: 14 941 842 o: 15 572 953
	C II, $N_{\text{levels}} = 69$				
$2s^2 nl$ ( $n \leq 6, l \leq 4$ ) $2s^2 7l$ ( $l \leq 3$ ) $2s2p^2, 2p^3$ , $2s2p3s, 2s2p3p$	$2s2p^2, 2s^2\{n_1s, n_2p, n_3d, n_4f, n_5g\}$ ( $3 \leq n_1 \leq 7, 2 \leq n_2 \leq 8, 3 \leq n_3 \leq 7$ $4 \leq n_4 \leq 7, 5 \leq n_5 \leq 6$ ) $2p^3, 2p^2\{n_1s, n_2p, n_3d, n_4f, n_5g\}$ ( $3 \leq n_1 \leq 7, 4 \leq n_2 \leq 7, 3 \leq n_3 \leq 7$ $4 \leq n_4 \leq 7, 5 \leq n_5 \leq 6$ ) $2s2p\{3s, 4s, 8s, 3p, 3d, 4d, 5d, 6d, 8d\}$ $2s3s\{3p, 8p\}$	1s	VV + CV (1s)	{13s,13p,13d,13f, 10g,8h}	e: 6 623 511 o: 4 768 481
	C III <sup>(2)</sup> , $N_{\text{levels}} = 114$				
$2snl$ ( $n \leq 7, l \leq 4$ ) $2p^2, 2p\{3s, 3p, 3d\}$	$2snl$ ( $n \leq 7, l \leq 4$ ) $2p^2, 2p\{3s, 3p, 3d\}$	1s	VV + CV (1s)	{12s,12p,12d,12f, 11g,8h}	e: 1 578 620 o: 1 274 147
	C IV <sup>(2)</sup> , $N_{\text{levels}} = 53$				
$1s^2 nl$ ( $n \leq 8, l \leq 4$ ) $1s^2 6h$	$1s^2 nl$ ( $n \leq 8, l \leq 4$ ) $1s^2 6h$	1s	CV + CC (1s)	{14s,14p,14d,12f,12g, 8h,7i}	e: 1 077 872 o: 1 287 706
	Al I <sup>(3)</sup> , $N_{\text{levels}} = 28$				
$3s3p^2, 3s^2\{n_1s, n_2p, n_3d, n_4f, 5g\}$ ( $4 \leq n_1 \leq 6, 3 \leq n_2 \leq 6, 3 \leq n_3 \leq 6$ , $4 \leq n_4 \leq 5$ )	$3s3p^2, \{3s^2, 3p^2\}\{n_1s, n_2p, n_3d, n_4f, 5g\}$ ( $4 \leq n_1 \leq 6, 3 \leq n_2 \leq 6, 3 \leq n_3 \leq 6$ , $4 \leq n_4 \leq 5$ )	1s,2s,2p	VV + CV (2p)	{12s,12p,12d,11f, 11g,10h}	e: 4 362 628 o: 2 889 385
	Al II <sup>(3)</sup> , $N_{\text{levels}} = 78$				
$3s^2, 3p^2, 3s6h, 3p3d$ $3s\{n_1s, n_2p, n_3d, n_4f\}$ ( $4 \leq n_1 \leq 7, 3 \leq n_2 \leq 7, 3 \leq n_3 \leq 6$ , $4 \leq n_4 \leq 6$ )	$3s^2, 3p^2, 3s6h, 3p3d$ $3s\{n_1s, n_2p, n_3d, n_4f\}$ ( $4 \leq n_1 \leq 7, 3 \leq n_2 \leq 7, 3 \leq n_3 \leq 6$ , $4 \leq n_4 \leq 6$ )	1s,2s,2p	VV + CV (2s,2p)	{13s,13p,12d,12f,12g, 8h,7i}	e: 911 795 o: 1 269 797
	Si I <sup>(4)</sup> , $N_{\text{levels}} = 168$				
$3s^2 3p^2, 3s3p^3, 3s^2 3p5g$ $3s^2 3p\{n_1s, n_2p, n_3d, n_4f\}$ ( $4 \leq n_1 \leq 8, 4 \leq n_2 \leq 7, 3 \leq n_3 \leq 6$ , $4 \leq n_4 \leq 6$ )	$3s^2 3p^2, 3s3p^3, 3p^4, 3s^2 3p5g, 3s3p^2 3d$ , $3p^3 7d, 3s3p7d^2, 3s^2 3p3d, 3p^3 5g$ , $\{3s^2 3p, 3p^3, 3s3p3d\}\{n_1s, n_2p, n_3d, n_4f\}$ ( $4 \leq n_1 \leq 8, 4 \leq n_2 \leq 7, 3 \leq n_3 \leq 6$ $4 \leq n_4 \leq 6$ ), $3s3p3d5g$	1s,2s,2p	VV + CV (2s,2p)	{13s,12p,12d,11f,10g, 9h,7i} for VV {9p,7d,6f,5g} for CV	e: 8 789 575 o: 9 097 389
	Si II <sup>(4)</sup> , $N_{\text{levels}} = 56$				
$3s3p^2, 3s3p3d, 3s3p4s, 3s^2\{5g,6g\}$ $3s^2\{n_1s, n_2p, n_3d, n_4f\}$ ( $4 \leq n_1 \leq 8, 3 \leq n_2 \leq 7, 3 \leq n_3 \leq 7$ , $4 \leq n_4 \leq 7$ )	$3s3p^2, 3s3p3d, 3s3p4s, 3s^2\{5g,6g\}$ $3s^2\{n_1s, n_2p, n_3d, n_4f\}$ ( $4 \leq n_1 \leq 8, 3 \leq n_2 \leq 7, 3 \leq n_3 \leq 7$ , $4 \leq n_4 \leq 7$ )	1s,2s,2p	VV + CV (2s,2p)	{13s,12p,12d,11f,10g, 9h,7i} for VV {9p,7d,6f,5g} for CV	e: 5 267 943 o: 6 582 233
	Si III <sup>(5)</sup> , $N_{\text{levels}} = 106$				
$3s^2, 3p^2, 3p4s, 3p4p$ , $3s\{n_1s, n_2p, n_3d, n_4f, n_5g\}$ ( $4 \leq n_1 \leq 7, 3 \leq n_2 \leq 7, 3 \leq n_3 \leq 7$ , $4 \leq n_4 \leq 7, 5 \leq n_5 \leq 7$ ) $3pnd$ ( $3 \leq n_2 \leq 4$ )	$3s^2, 3p^2, 3p4s, 3p4p$ , $3s\{n_1s, n_2p, n_3d, n_4f, n_5g\}$ ( $4 \leq n_1 \leq 9, 3 \leq n_2 \leq 9, 3 \leq n_3 \leq 8$ , $4 \leq n_4 \leq 8, 5 \leq n_5 \leq 8$ ) $3pnd$ ( $3 \leq n_2 \leq 4$ )	1s,2s,2p	VV + CV (2s,2p)	{13s,13p,12d,12f,12g, 9h}	e: 1 401 150 o: 1 760 209
	Si IV <sup>(5)</sup> , $N_{\text{levels}} = 45$				
$2s^2 2p^6 nl$ ( $n \leq 7, l \leq 6$ )	$2s^2 2p^6 nl$ ( $n \leq 9, l \leq 6$ )	1s,2s,2p	CV + CC (2s,2p)	{13s,13p,13d,12f,12g, 12h,12i}	e: 995 020 o: 993 501

**Notes.**  $N_{\text{levels}}$  is the number of the targeted levels computed in this work. Configuration denotes the targeted configuration states. MR-RCI denotes multireference for relativistic configuration interaction calculations. Core orbitals denotes core orbitals defined in the calculations. Correlation denotes correlation effects included in the calculation. The orbitals included in the CV and CC correlation effects are shown in parentheses and the remaining core orbitals define an inactive closed core. AS denotes active set of orbitals;  $N_{\text{NCFs}}$  is the number of generated configuration state functions for the relativistic configuration interaction calculations.

**References.** (1) Wang et al. (2018); (2) Papoulia et al. (2019a); (3) Papoulia et al. (2019b); (4) Pehlivan Rhodin et al. (2019); (5) Atalay et al. (2019); (6) Rynkun et al. (2019a); (7) Rynkun et al. (2019b); (8) Rynkun et al. (2020).

Table 2. continued.

Configurations	MR-RCI	Core orbitals	Correlation	AS	$N_{\text{NCFs}}$
	P II <sup>(6)</sup> , $N_{\text{levels}} = 106$				
$3s^2 3p^2, 3s 3p^2 3d, 3s 3p^3,$ $3s^2 3p \{n_1 s, n_2 p, n_3 d, n_4 f\}$ ( $4 \leq n_1 \leq 6, 4 \leq n_2 \leq 6, 3 \leq n_3 \leq 5,$ $4 \leq n_4 \leq 5$ )	$3s^2 3p^2, 3s 3p^2 3d, 3s 3p^3, 3s^2 3d^2, 3p^4,$ $3s^2 3d 7d, 3s 3p^2 7d, 3s 3p^2 4p, 3p^3 7d,$ $3s^2 3p \{n_1 s, n_2 p, n_3 d, n_4 f\}$ ( $4 \leq n_1 \leq 7, 4 \leq n_2 \leq 6, 3 \leq n_3 \leq 7,$ $4 \leq n_4 \leq 5$ ) $3p^3 \{n_1 s, n_2 p, n_3 d, n_4 f\}$ ( $4 \leq n_1 \leq 7,$ $4 \leq n_2 \leq 6, 3 \leq n_3 \leq 7, 4 \leq n_4 \leq 5$ )	1s,2s,2p	VV + CV (2p)	{12s,11p,11d,10f,9g, 7h,7i}	e: 5 954 032 o: 4 815 663
	S II <sup>(7)</sup> , $N_{\text{levels}} = 134$				
$3s 3p^4, 3s^2 3p^3, 3s 3p^3 3d$ $3s^2 3p^2 \{n_1 s, n_2 p, n_3 d, n_4 f\}$ ( $4 \leq n_1 \leq 5, 4 \leq n_2 \leq 5$ $3 \leq n_3 \leq 4, n_4 = 4$ )	$3s 3p^4, 3s^2 3p^3, 3s 3p^3 3d, 3p^5$ $3s^2 3p^2 \{n_1 s, n_2 p, n_3 d, n_4 f\}$ ( $4 \leq n_1 \leq 5, 4 \leq n_2 \leq 5$ $3 \leq n_3 \leq 5, n_4 = 4$ ) $3p^3 \{3d, 4s, 4p, 4d, 4f, 5s, 5p\}$ $3s 3p^2 3d \{3d, 4s, 4p, 4d, 4f, 5s, 5p\}$ Cl III <sup>(7)</sup> , $N_{\text{levels}} = 87$	1s,2s,2p	VV + CV (2p)	{9s,9p,9d,8f,8g,8h,8i} {6s,6p,5d,5f} for S from 2p	e: 6 220 422 o: 7 329 546
$3s 3p^4, 3s^2 3p^3, 3s 3p^3 3d, 3p^5$ $3s^2 3p^2 \{3d, 4s, 4p, 4d\}$	$3s 3p^4, 3s^2 3p^3, 3s 3p^3 3d, 3p^5$ $3p^3 \{3d, 4p\}, 3s 3p^3 4s, 3s 3p^2 3d^2$ $3s 3p^2 3d \{4s, 4p, 4d\}, 3s^2 3p 3d^2$	1s,2s,2p	VV + CV (2p)	{9s,9p,9d,8f,8g,8h,8i} {6s,6p,5d,5f} for S from 2p	e: 6 466 816 o: 4 111 005
	Ar IV <sup>(7)</sup> , $N_{\text{levels}} = 103$				
$3s 3p^4, 3s^2 3p^3, 3s 3p^3 3d, 3p^5$ $3s^2 3p^2 \{3d, 4s, 4p\}$	$3s 3p^4, 3s^2 3p^3, 3s 3p^3 3d, 3p^5$ $3s^2 3p^2 \{3d, 4s, 4p, 4d, 4f\}, 3p^4 3d$ $3s 3p^2 3d \{3d, 4s, 4p\}, 3s 3d^2 4s, 3s^2 3d^3$ $3s^2 3p 3d^2, 3s 3p^3 4s, 3p^4 4p, 3p^3 3d^2$	1s,2s,2p	VV + CV (2p)	{9s,9p,9d,8f,8g,8h,8i} {7s,6p,6d,6f,5g} for S from 2p	e: 4 946 496 o: 7 329 546
	Ca I, $N_{\text{levels}} = 45$				
$4s^2, 4p^2, 3d \{4s, 4p\},$ $4s \{4p, 4d, 4f, 5s, 5p, 6s, 6p\}$	$4s^2, 4p^2, 3d^2$ $4s \{5s, 6s, 4p, 5p, 6p, 4d, 5d, 4f\}$ $4p \{5p, 7p, 4d, 5d\}$ $3d \{4s, 5s, 4p, 5p, 4d, 5d\}$	1s,2s,2p, 3s,3p	VV + CV + CC (3s,3p)	{10s, 10p, 8d, 8f, 8g, 6h} {10s,10p,8d} for CC	e: 2 916 533 o: 3 021 057
	Ti II, $N_{\text{levels}} = 99$				
$3d^2 \{4s, 4p\}, 3d^3, 3d 4s^2$ $3d 4s 4p$	$3d^2 \{4s, 4p, 4d\}, 3d^3, 3d \{4s^2, 4p^2, 4d^2\}$ $3d 4s \{4p, 4d, 5s\}, 4s^2 \{4p, 4d\}, 4s \{4p^2, 4d^2\}$ $4s 4p 4d, 3d 4s 5p, 3d 4p 4d, 4p 4d^2$ $3p^4 \{3d^4 4s, 3d^3, 3d^3 4s^2, 3d^4 4p, 3d^3 4s 4p\}$	1s,2s,2p, 3s,3p	VV + CV + CC (3s,3p)	{8s,8p,8d,8f,8g,8h,7i} {8s,8p,8d} for CC	e: 14 089 101 o: 15 573 967
	Zr III <sup>(8)</sup> , $N_{\text{levels}} = 88$				
$4d^2, 5s^2, 5p^2, 5s 5p,$ $4d \{4f, 5s, 5p, 5d, 6s, 6p\}$	$4d^2, 5s^2, 5p^2, 5p 5d, 5s \{5p, 5d\},$ $4d \{4f, 5s, 5p, 5d, 6s, 6p, 6d\}$	1s,2s,2p,3s, 3p,4s,4p	VV + CV + CC (4s,4p)	{11s,11p,10d,9f,7g,7h}	e: 14 255 953 o: 16 514 844
	Sn II, $N_{\text{levels}} = 22$				
$5s^2 \{4f, 5p, 5d, 6s, 6p, 6d, 7s, 7p\},$ $5s 5p^2$	$5s^2 \{4f, 5p, 5d, 6s, 6p, 6d, 7s, 7p\},$ $7d, 8s, 8p\}, 5s 5p^2$	1s,2s,2p,3s, 3p,4s,4p,4d	VV + CV (4s, 4p,4d)	{14s,14p,13d,10f,10g, 8h,8i}	e: 1 329 994 o: 674 998

Table 3. Comparison of computed energy levels in the present work with data from the NIST database.

Ions	Av. accuracy (%)	Ions	Av. accuracy (%)	Ions	Av. accuracy (%)
B II	0.089	Si I	0.25	Ar IV	0.21
C I	0.26	Si II	0.16	Ca I	0.68
C II	0.088	Si III	0.05	Ti II	1.06
C III	0.044	Si IV	0.09	Zr III	0.57
C IV	0.0044	P II	0.19	Sn II	0.22
Al I	0.60	S II	0.22		
Al II	0.17	Cl III	0.18		

In Table A.1, the computed  $g_{J,J}$  values are compared with the available experimental values for C I (Lott et al. 1966), C III (Lott et al. 1966), P II (Li 1972), Si I (Lott et al. 1966), Si III (Lott et al. 1966), Si IV (Lott et al. 1966), Ti II (Moore 1949), and Sn II (David et al. 1980). The corresponding  $g_J(LS)$  values are also displayed in the third column for a comparison. From

Eq. (11) it is clear that there is a significant change in  $g_{J,J}$  when there is a strong mixing between terms with greatly different  $g_J(LS)$  values. For C I, C III, Si I, Si III, Si IV, and Sn II the relative differences between  $g_{J,J}$  and  $g_J(LS)$  are rather small, within 0.7%, meaning that the mixing between terms is either small or occurs between terms with nearly the same  $g_J(LS)$ ,

**Table 4.** Comparison of computed energy separations with NIST data.

Ions	$\overline{dE_S}$ (%)		Ions	$\overline{dE_S}$ (%)		Ions	$\overline{dE_S}$ (%)	
	Even	Odd		Even	Odd		Even	Odd
B II	0.24	0.28	Si I	0.35	1.37 <sup>(*)</sup>	Ar IV	0.41 <sup>(*)</sup>	0.23
C I	0.42	0.95 <sup>(*)</sup>	Si II	0.30 <sup>(*)</sup>	0.24	Ca I	1.94	1.29 <sup>(*)</sup>
C II	0.23	0.49	Si III	0.18 <sup>(*)</sup>	0.89 <sup>(*)</sup>	Ti II	1.81 <sup>(*)</sup>	1.55 <sup>(*)</sup>
C III	0.059 <sup>(*)</sup>	0.14	Si IV	0.062	0.050	Zr III	0.89	1.01
C IV	0.0051	0.0043	P II	0.23	0.82	Sn II	1.17	0.22
Al I	1.47	0.46	S II	0.82	0.45			
Al II	0.24	0.47	Cl III	0.44	0.31			

**Notes.** <sup>(\*)</sup>The values are obtained by excluding the levels with  $dE_S$  higher than 5%.

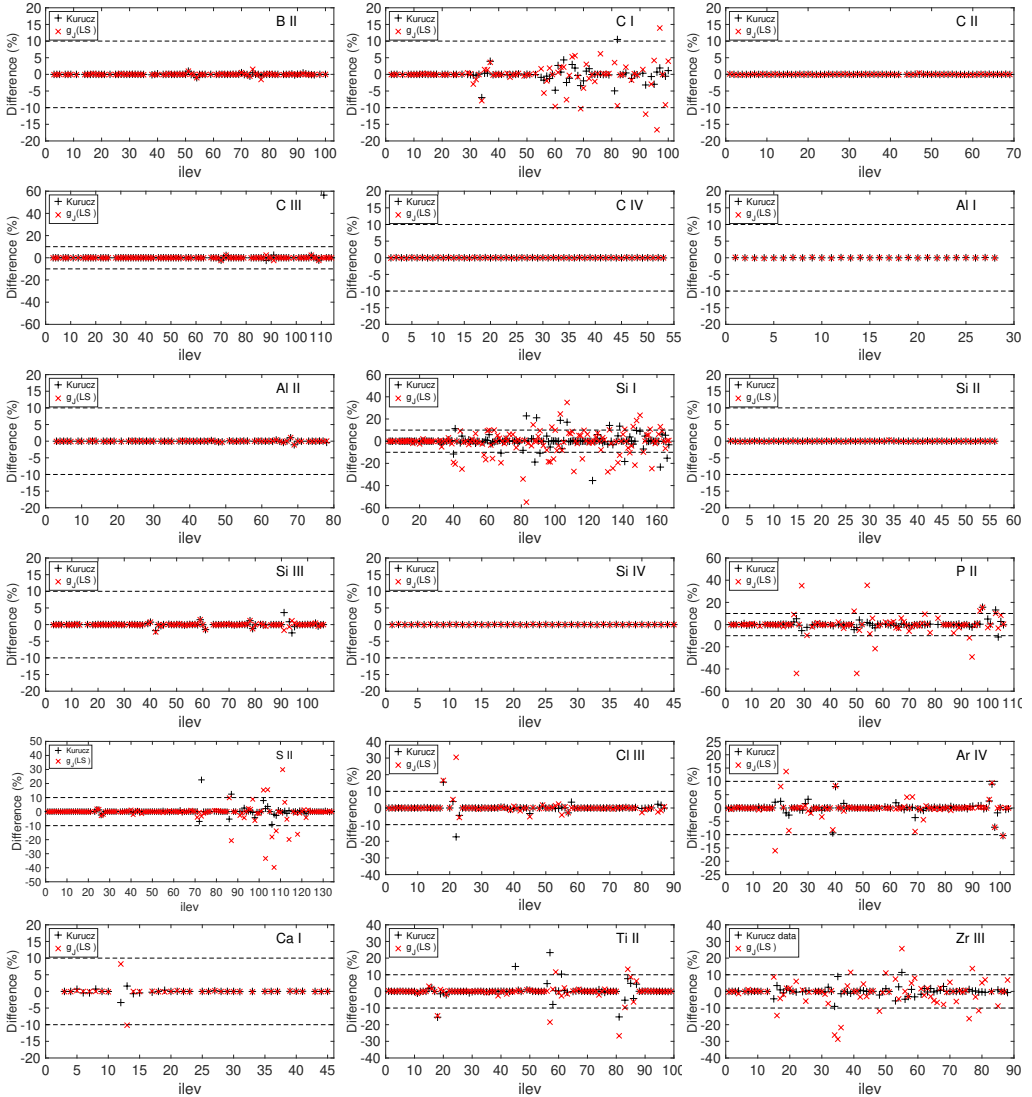
which will not change  $g_{\gamma J}$  appreciably (Fischer et al. 2004). The experimental values for the C and Si ions, displayed in the last column, are obtained from observations of atomic Zeeman patterns using strong pulsed magnetic fields (Lott et al. 1966). For most of the levels the computed and the experimental  $g_{\gamma J}$ -values agree within the experimental errors, i.e. 1%–3% for C I, C III, Si I, and Si III, and a factor of two higher for Si IV due to the broad spectra lines. The good agreement between theory and experiment, and with the  $g_J(LS)$ , indicates that these states of C I, C III, Si I, Si III, and Si IV are well described in  $LS$ -coupling. One exception is level 7 of Si IV for which the  $LS$ -composition (see Table 15) is dominated by one term, giving  $g_{\gamma J} = 0.66583$  in close agreement with the value  $g_J(LS) = 0.66667$  in pure  $LS$ -coupling. These values differ by more than 8% from the measured value  $g_{\gamma J} = 0.72$ . Since there is excellent agreement with the NIST recommended data, for the excitation energies and for energy separations, we are confident in our value and suggest a re-measurement for this level.

Some states of P II are strongly mixed in  $LS$ -coupling. Out of the 76 levels in P II for which experimental Landé  $g$ -factors are available, 23 levels have relative differences between  $g_{\gamma J}$  and  $g_J(LS)$  greater than 3%. We especially note a 44% difference for levels 27 and 50, a 30% difference for levels 29 and 54, a 29% difference for level 94, and a 22% difference for level 57. The departure from  $LS$ -coupling is quantified in Table 16, for example level 27, labelled  $^3D_1^o$ , has the composition 45%  $3s^2 3p^2 3d^3 3D_1^o$ , 26%  $3s^2 3p^2 3d^3 3P^o$ , and 8%  $3s^2 S 3p^3 3D$   $^3D^o$ . The  $g_J(LS)$  of  $^3D_1$  has the relatively small value of 0.50000, whereas the value for  $^3P_1$  is 1.50000, and so the mixing results in an appreciable increase in the smaller value. The experimental Landé  $g$ -factors of P II are from measurements of the Zeeman effect using the electrodeless discharge tubes operated in a given magnetic field (Li 1972). Comparisons between the computed  $g_{\gamma J}$  and measured values show that there is a good agreement for most of the levels within the experimental uncertainties of 0.01 (0.02 for most of the  $g_{\gamma J}$  values of  $3p5d$  levels), except for levels 27 and 29 for which the relative difference is about 5%, and for levels 49 and 51 for which the relative difference is about 4%.

For Ti II there are 15 levels for which experimental data are available. Of these 15 levels, 7 have relative differences between  $g_{\gamma J}$  and  $g_J(LS)$  greater than 1%, especially 18% for level 18 and 23% for level 57. From the  $LS$ -percentage composition shown in Table 21, level 18 has the composition 61%  $3d^3 3P$   $^2P_{1/2}$ , 26%  $3d^2 3P$   $^3P 4s^2 2P_{1/2}$ , and 3%  $3d^2 3P$   $^3P 4s^2 4P_{1/2}$ . The  $g_J(LS)$  for  $^2P_{1/2}$  has a relatively small value of 0.66607, whereas the value for  $^4P_{1/2}$  is 2.63809 and the mixing results in a 17%

increase in the smaller value. Level 57 has the composition of 51%  $3d^2 3D$   $^1D 4p^2 D_{3/2}^o$ , 29%  $3d^2 3D$   $^1D 4p^2 P^o$ , and 5%  $3d^2 3P$   $^3P 4p^2 D^o$ . The  $g_J(LS)$  for  $^2D_{3/2}$  has a relatively small value of 0.8, whereas the value for  $^2P_{3/2}$  is 1.33333, and the mixing results in an appreciable change in the  $3d^2 4p^2 D_{3/2}^o$  value to 0.98131. Compared with the NIST recommended Landé  $g$ -factors of Ti II (Corliss & Sugar 1979; Sugar & Corliss 1985; Saloman 2012), levels 18, 45, 56, and 57 have relative differences of 15%, 15%, 5%, and 23%, respectively. The suggested  $LS$ -percentage compositions are from the calculations of Huldt et al. (1982). The experimental  $g$ -values were determined by Catalán from the Zeeman patterns observed by King and Babcock and quoted by Russell (1927). They were published by Moore (1949). For level 18, NIST gives similar values of the leading compositions with present calculation, 62%  $3d^3 3P$   $^2P_{1/2}$  and 24%  $3d^2 3P$   $^3P 4s^2 2P_{1/2}$ , but not for that of  $3d^2 3P$   $^3P 4s^2 4P_{1/2}$ , which mainly contributes to the changes in  $g_{\gamma J}$ . The same happens for level 45. The labelling of level 56 identifies the dominant component of the composition with 94%  $3d^2 3P$   $^3P 4p^2 S_{1/2}^o$ , which indicates a good description in  $LS$ -coupling. The weak mixing results in  $g_{\gamma J} = 1.99657$  in relative to  $g_J(LS) = 2.00000$ . However, NIST suggests 99%  $^2S_{1/2}^o$ , but gives an even larger  $g_{\gamma J}$  value of 2.09. For level 57, NIST suggests 48%  $3d^2 1D$   $^1D 4p^2 D_{3/2}^o$  and 36%  $3d^2 1D$   $^1D 4p^2 P^o$  and  $g_{\gamma J} = 1.21$  in relative to the computed value  $g_{\gamma J} = 0.98131$ . As stated in Russell (1927), due to the limitations inherent in old laboratory analyses, very few patterns have been resolved which resulted in large uncertainties of the observed  $g$ -values. It is highly desirable to redo the measurements by using the current high-resolution instruments and techniques. For level 3 of Sn II,  $LS$ -coupling is a good approximation and the computed  $g_{\gamma J} = 2.65984$  agrees well with the measured value of 2.66085 within the experimental uncertainty of 5% (David et al. 1980).

In Fig. 1, we compare the computed  $g_{\gamma J}$  values with  $g_J(LS)$ , and with available results in Kurucz's atomic database (Kurucz 2017) for all the atoms and ions presented in this work. The good agreement between  $g_{\gamma J}$  and  $g_J(LS)$  in B II, C II, C III, C IV, Al I, Al II, Si II, Si III, Si IV, and Ca I, indicates that these atoms and ions are well described in  $LS$ -coupling approximation. For some states of the rest of the atom and ions, the strong mixing of  $LS$ -terms results in large differences between  $g_{\gamma J}$  and  $g_J(LS)$  by >10%. Kurucz's atomic data (Kurucz 2017), which are widely adopted by the solar scientists for the spectropolarimetric modelling, are either taken from the experimental results or, when no experimental values are available, from semi-empirical values. From Fig. 1 we see that there is good agreement between



**Fig. 1.** Comparison of computed Landé  $g$ -factors,  $g_{J,I}$ , in the present work with values in  $LS$ -coupling,  $g_{J,I}(LS)$  (red cross sign) and with Kurucz's data (black plus sign). Differences  $((g_{\text{other}} - g_{J,I})/g_{J,I})$  are given in percentage. The dashed lines indicate the  $\pm 10\%$  deviations.

the computed  $g_{J,I}$  values and Kurucz's data, except for a number of energy levels in C III, Si I, Ti II, and Zr III with relative differences  $>10\%$ . In Table A.2, we display all these states with a relative difference between  $g_{J,I}$  and  $g_{J,I}(LS)$  of more than  $10\%$ . Additionally, we present the  $g_{J,I}$  values in the last column for comparison. Except for the levels of P II and level 18 and 57 of Ti II, for which the Kurucz's data are from experimental results (see discussion above), the others are semi-empirical determinations of the Landé  $g$ -factor in intermediate coupling. The computed  $g_{J,I}$  using the fully relativistic MCDHF approach differ from the semi-empirical values by more than  $10\%$  for several cases, e.g. level 82 of C I; levels 40, 41, 68, 83, 138, and 144 of Si I; level 87 of S II; levels 18 and 22 of Cl III; and levels 18

and 101 of Ar IV. The data for Sn II are absent in Kurucz's database.

## 5. Summary

In the present work Landé  $g$ -factors are computed for the B II, C I–IV, Al I–II, Si I–IV, P II, S II, Cl III, Ar IV, Ca I, Ti II, Zr III, and Sn II ions, all of which are of astrophysical interest. The MCDHF and RCI methods, which are implemented in the general-purpose relativistic atomic structure package GRASP2K, are used in the present work. The accuracy of the present calculations is validated by extensive comparisons of the excitation energies and energy separations with the NIST

recommended data. All excitation energies are in good agreement with the NIST values. The Av. accuracy values are within 0.1%, 0.089%, 0.088%, 0.044%, 0.004%, 0.05%, and 0.09%, respectively, for the Be II, C II–IV, Si III, and Si IV ions, and are less than 0.68% for the C I, Al I–II, Si I–II, P II, S II, Cl III, Ar IV, Ca I, Zr III, and Sn II ions. For Ti II, the average difference is about 1.06%.

The Landé  $g$ -factor depends on the mixing of  $LS$  terms, which in turn, depends on the separation of these terms. The accuracy of the energy separations in each symmetry block is thus a more proper measure of the accuracy of the Landé  $g$ -factors than the excitation energies. The average accuracy of the energy separations is well below 1% except for even states of Al I; odd states of Si I, Ca I, Ti II, Zr III; and even states of Sn II, all of which show a relative difference of between 1% and 2%.

The computed  $g_{J,J}$  values are compared with available experimental values, and with the values in pure  $LS$ -coupling. The differences with the values in  $LS$ -coupling are explained by analysing wave function  $LS$ -compositions. The observed and theoretical  $g$ -values differ by a small percentage in some cases, which may be due to the limitations in old laboratory analyses. It is highly recommended to redo the measurements for these cases. We summarize the levels with a difference of more than 10% between the  $g_{J,J}$  and  $g_J(LS)$  values, and make a comparison with the semi-empirical values from the Kurucz's database. The present calculations provide a substantial amount of critically evaluated Landé  $g$ -factors that are useful for modelling and diagnostics of astrophysical plasmas.

**Acknowledgements.** This work is supported by the Swedish research council under contracts 2015-04842 and 2016-04185. Betül Atalay acknowledges financial support from the Scientific and Technological Research Council of Turkey (TUBITAK) – BİDEB 2219 International Post-Doctoral Research Fellowship Program.

## References

- Andersson, M., & Jönsson, P. 2008, *Comput. Phys. Commun.*, **178**, 156
- Atalay, B., Brage, T., Jönsson, P., & Hartman, H. 2019, *A&A*, **631**, A29
- Biémont, É., Palmeri, P., & Quinet, P. 2010, *J. Phys. B: At. Mol. Opt. Phys.*, **43**, 074010
- Brage, T., Judge, P. G., Jönsson, P., & Edwards, D. P. 2000, *ApJ*, **540**, 1114
- Cheng, K. T., & Childs, W. J. 1985, *Phys. Rev. A*, **31**, 2775
- Corliss, C., & Sugar, J. 1979, *J. Phys. Chem. Ref. Data*, **8**, 1
- Cowan, R. D. 1981, *The Theory of Atomic Structure and Spectra* (Berkeley, CA: University of California Press)
- David, D., Hamel, J., & Barrat, J.-P. 1980, *Opt. Commun.*, **32**, 241
- Fawcett, B. C. 1990, *Phys. Scr.*, **42**, 173
- Fischer, C. F., Jönsson, P., & Tachiev, G. 2004, *Mol. Phys.*, **102**, 1177
- Fischer, C. F., Godefroid, M., Brage, T., Jönsson, P., & Gaigalas, G. 2016, *J. Phys. B: At. Mol. Opt. Phys.*, **49**, 182004
- Fischer, C. F., Gaigalas, G., Jönsson, P., & Bieroń, J. 2019, *Comput. Phys. Commun.*, **237**, 184
- Gaigalas, G., Žalandauskas, T., & Rudzikas, Z. 2003, *At. Data Nucl. Data Tables*, **84**, 99
- Gaigalas, G., Fischer, C. F., Rynkun, P., & Jönsson, P. 2017, *Atoms*, **5**, 6
- Grant, I. P. 2007, *Relativistic Quantum Theory of Atoms and Molecules* (New York: Springer)
- Huldt, S., Johansson, S., Litzén, U., & Wyart, J.-F. 1982, *Phys. Scr.*, **25**, 401
- Jönsson, P., & Gustafsson, S. 2002, *Comput. Phys. Commun.*, **144**, 188
- Jönsson, P., Gaigalas, G., Bieroń, J., Fischer, C. F., & Grant, I. 2013, *Comput. Phys. Commun.*, **184**, 2197
- Jönsson, P., Gaigalas, G., Rynkun, P., et al. 2017, *Atoms*, **5**, 16
- Judge, P. G. 2017, *Can. J. Phys.*, **95**, 847
- Keil, S. L., Rimmele, T. R., & Wagner, J. 2009, *Earth Moon Planets*, **104**, 77
- Kramida, A., Ralchenko, Yu., Reader, J., & NIST ASD Team 2019, *NIST Atomic Spectra Database (ver. 5.7.1)*. [Online]. Available: <https://physics.nist.gov/asd> [2020, February 11]. National Institute of Standards and Technology, Gaithersburg, MD
- Kurucz, R. L. 2017, *On-line Database of Observed and Predicted Atomic Transitions* (Cambridge, MA: Harvard-Smithsonian Center for Astrophysics), <http://kurucz.harvard.edu>
- Landi Degl'Innocenti, E. 1982, *Sol. Phys.*, **77**, 285
- Landi Degl'Innocenti, E., & Landolfi, M. 2004, in *Polarization in Spectral Lines* (Dordrecht: Kluwer Academic Publishers), *Astrophys. Space Sci. Lib.*, **307**
- Li, H. 1972, *J. Opt. Soc. Am.*, **62**, 1483
- Li, W., Casini, R., del Pino Alemán, T., & Judge, P. G. 2017, *ApJ*, **848**, 82
- Li, W., Grumer, J., Brage, T., & Jönsson, P. 2020, *Comput. Commun. Phys.*, **107211**
- Lott, S. H., Roos, C. E., & Ginter, M. L. 1966, *J. Opt. Soc. Am.*, **56**, 775
- Martin, W. C., Zalubas, R., & Musgrove, A. 1985, *J. Phys. Chem. Ref. Data*, **14**, 751
- Moore, C. E. 1949, *Atomic Energy Levels*. 1949, *Nat. Bur. Stand. (U.S.) Circ.* **467**, Vol. I, 309 pp.; 1952, Vol. II, 227 pp.; 1958, Vol. III, 245 pp.; 1971, *Reprinted in Three Volumes as Nat. Stand. Ref. Data Ser., Nat. Bur. Stand. (U.S.)*, 35
- Olsen, J., Roos, B. O., Jørgensen, P., & Jensen, H. J. A. 1988, *J. Chem. Phys.*, **89**, 2185
- Papouliou, A., Ekman, J., Gaigalas, G., et al. 2019a, *Atoms*, **7**, 106
- Papouliou, A., Ekman, J., & Jönsson, P. 2019b, *A&A*, **621**, A16
- Pehlivan Rhodin, A., Hartman, H., Nilsson, H., & Jönsson, P. 2019, *A&A*, submitted
- Russell, H. N. 1927, *ApJ*, **66**, 283
- Rynkun, P., Radžičtė, L., Gaigalas, G., & Jönsson, P. 2019a, *A&A*, **622**, A167
- Rynkun, P., Gaigalas, G., & Jönsson, P. 2019b, *A&A*, **623**, A155
- Rynkun, P., Gaigalas, G., & Jönsson, P. 2020, *A&A*, **637**, A10
- Saloman, E. B. 2012, *J. Phys. Chem. Ref. Data*, **41**, 013101
- Stursson, L., Jönsson, P., & Froese Fischer, C. 2007, *Comput. Phys. Commun.*, **177**, 539
- Sugar, J., & Corliss, C. 1985, *J. Phys. Chem. Ref. Data*, **14**
- Verdebut, S., Naze, C., Jönsson, P., et al. 2014, *At. Data Nucl. Data Tables*, **100**, 1111
- Wang, K., Chen, Z. B., Zhang, C. Y., et al. 2018, *ApJS*, **234**, 40

## Appendix A: Additional tables

Table A.1. continued.

Table A.1. Comparison of computed Landé g-factors,  $g_{J,J}$ , with their  $LS$ -coupling values  $g_J(LS)$  and experimental values (Exp.).

No.	State	$g_J(LS)$	$g_{J,J}$	Exp.
C I <sup>(1)</sup>				
2	$2p^2(^3P) ^3P_1$	1.50000	1.50109	1.5010623(50)
3	$2p^2(^3P) ^3P_2$	1.50000	1.50107	1.5010469(50)
10	$2p^2P 3s^1P_1$	1.00000	1.00007	0.97
C III <sup>(1)</sup>				
5	$2s^2S 2p^1P_1$	1.00000	0.99990	1.01
9	$2p^2(^1D) ^1D_2$	1.00000	0.99991	1.01
P II <sup>(2)(3)</sup>				
7	$3s^2S 3p^3(^3D) ^3D_0^o$	0.50000	0.49910	0.504
8	$3s^2S 3p^3(^3D) ^3D_1^o$	1.16667	1.16713	1.16
9	$3s^2S 3p^3(^3D) ^3D_2^o$	1.33333	1.33399	1.329
10	$3s^2S 3p^3(^1P) ^3P_0$	1.50000	1.48750	1.486
11	$3s^2S 3p^3(^1P) ^3P_1$	1.50000	1.50077	1.5
13	$3s^2 3p^2P 3d^1D_2^o$	1.00000	1.01330	1.014
15	$3s^2 3p^2P 4s^1P_1^o$	1.50000	1.49450	1.495
16	$3s^2 3p^2P 4s^1P_2^o$	1.50000	1.50106	1.499
17	$3s^2 3p^2P 3d^1F_2^o$	0.66667	0.66594	0.666
18	$3s^2 3p^2P 3d^1F_3^o$	1.08333	1.08347	1.083
19	$3s^2 3p^2P 3d^1F_4^o$	1.25000	1.25051	1.25
20	$3s^2 3p^2P 4s^1P_1^o$	1.00000	1.00644	1.006
21	$3s^2 3p^2P 4p^1P_1$	1.00000	0.99420	0.998
22	$3s^2 3p^2P 4p^1D_1$	0.50000	0.50942	0.511
23	$3s^2 3p^2P 3d^1P_1^o$	1.00000	0.99699	1
24	$3s^2 3p^2P 4p^1D_2$	1.16667	1.16808	1.166
25	$3s^2 3p^2P 4p^1D_3$	1.33333	1.33404	1.334
26	$3s^2 3p^2P 3d^1P_2^o$	1.50000	1.37568	1.408
27	$3s^2 3p^2P 3d^1D_1^o$	0.50000	0.89293	0.94
28	$3s^2 3p^2P 3d^1D_2^o$	1.33333	1.33335	1.326
29	$3s^2 3p^2P 3d^1P_1^o$	1.50000	1.11039	1.05
31	$3s^2 3p^2P 3d^1D_2^o$	1.16667	1.29222	1.26
33	$3s^2 3p^2P 4p^1P_1$	1.50000	1.53101	1.525
34	$3s^2 3p^2P 4p^1P_2$	1.50000	1.49802	1.499
35	$3s^2 3p^2P 4p^1S_1$	2.00000	1.96742	1.968
36	$3s^2 3p^2P 3d^1F_3^o$	1.00000	1.00063	1.004
37	$3s^2 3p^2P 4p^1D_2$	1.00000	1.00189	1.002
40	$3s^2S 3p^3(^3D) ^1D_2^o$	1.00000	1.00010	0.998
41	$3s^2S 3p^3(^1P) ^1P_1^o$	1.00000	1.00064	0.99
43	$3s^2 3p^2P 5s^1P_1$	1.50000	1.46648	1.465
44	$3s^2 3p^2P 5s^1P_2$	1.50000	1.50104	1.497
45	$3s^2 3p^2P 5s^1P_1^o$	1.00000	1.03443	1.036
46	$3s^2 3p^2P 4d^1F_2^o$	0.66667	0.66790	0.664
47	$3s^2 3p^2P 4d^1F_3^o$	1.08333	1.08425	1.081
48	$3s^2 3p^2P 4d^1F_4^o$	1.25000	1.25053	1.25
49	$3s^2 3p^2P 4d^1P_2^o$	1.50000	1.33882	1.278
50	$3s^2 3p^2P 4d^1D_1^o$	0.50000	0.89316	0.87
51	$3s^2 3p^2P 4d^1D_2^o$	1.00000	1.05416	1.098
52	$3s^2 3p^2P 4d^1D_3^o$	1.33333	1.33185	1.33
54	$3s^2 3p^2P 4d^1P_1^o$	1.50000	1.10772	1.129
55	$3s^2 3p^2P 4d^1D_2^o$	1.16667	1.27311	1.284
56	$3s^2 3p^2P 5p^1P_1$	1.00000	0.94599	0.94
57	$3s^2 3p^2P 5p^1D_1$	0.50000	0.63857	0.62
58	$3s^2 3p^2P 5p^1D_2$	1.16667	1.18244	1.187
59	$3s^2 3p^2P 5p^1D_3$	1.33333	1.33383	1.34
61	$3s^2 3p^2P 5p^1P_1$	1.50000	1.46729	1.473
62	$3s^2 3p^2P 4d^1F_3^o$	1.00000	1.00138	1
63	$3s^2 3p^2P 5p^1P_2$	1.50000	1.47622	1.47
64	$3s^2 3p^2P 5p^1S_1$	2.00000	1.95020	1.96
65	$3s^2 3p^2P 4f^1F_3$	1.00000	1.02861	1.02
66	$3s^2 3p^2P 4f^1F_2$	0.66667	0.69005	0.674
67	$3s^2 3p^2P 4f^1F_3$	1.08333	1.02328	1.03
68	$3s^2 3p^2P 4f^1F_4$	1.25000	1.21827	1.22
69	$3s^2 3p^2P 5p^1D_2$	1.00000	1.00737	1.005

No.	State	$g_J(LS)$	$g_{J,J}$	Exp.
70	$3s^2 3p^2P 4f^1G_3$	0.75000	0.79709	0.79
71	$3s^2 3p^2P 4f^1G_4$	1.05000	1.07055	1.06
72	$3s^2 3p^2P 4f^1G_5$	1.20000	1.20042	1.2
73	$3s^2 3p^2P 4d^1P_1^o$	1.00000	0.99914	0.999
74	$3s^2 3p^2P 4f^1G_4$	1.00000	1.01177	1.01
75	$3s^2 3p^2P 4f^1D_3$	1.33333	1.31820	1.32
76	$3s^2 3p^2P 4f^1D_2$	1.16667	1.06628	1.063
77	$3s^2 3p^2P 4f^1D_1$	0.50000	0.49893	0.5
78	$3s^2 3p^2P 4f^1D_2$	1.00000	1.07863	1.083
81	$3s^2 3p^2P 6s^1P_1^o$	1.50000	1.41849	1.42
85	$3s^2 3p^2P 6s^1P_2^o$	1.50000	1.50082	1.5
87	$3s^2 3p^2P 6s^1P_1^o$	1.00000	1.08220	1.08
89	$3s^2 3p^2P 5d^1F_2^o$	0.66667	0.68597	0.69
90	$3s^2 3p^2P 5d^1F_3^o$	1.08333	1.09022	1.08
91	$3s^2 3p^2P 5d^1F_4^o$	1.25000	1.25053	1.25
93	$3s^2 3p^2P 5d^1D_2^o$	1.00000	1.13551	1.12
94	$3s^2 3p^2P 5d^1D_1^o$	0.50000	0.70581	0.69
95	$3s^2 3p^2P 5d^1D_2^o$	1.16667	1.17731	1.18
96	$3s^2 3p^2P 5d^1D_3^o$	1.33333	1.32274	1.33
97	$3s^2 3p^2P 5d^1P_2^o$	1.50000	1.33546	1.34
98	$3s^2 3p^2P 5d^1P_1^o$	1.50000	1.29786	1.3
101	$3s^2 3p^2P 5d^1F_3^o$	1.00000	1.00454	1.01
Si I <sup>(1)</sup>				
2	$3p^2(^3P) ^3P_1$	1.50000	1.50110	1.52
3	$3p^2(^3P) ^3P_2$	1.50000	1.50095	1.50
4	$3p^2(^1D) ^1D_2$	1.00000	1.00009	1.01
8	$3p^2P 4s^1P_1$	1.50000	1.49593	1.52
9	$3p^2P 4s^1P_2$	1.50000	1.50110	1.49
10	$3p^2P 4s^1P_1^o$	1.00000	1.00509	0.99
15	$3p^2P 3d^1D_2^o$	1.00000	1.00005	1.02
32	$3p^2P 3d^1P_1^o$	1.00000	0.99476	1.00
Si III <sup>(1)</sup>				
5	$3s 3p^1P_1^o$	1.00000	0.99995	0.98
6	$3p^2^1D_2$	1.00000	1.00010	0.98
13	$3s 4s^1S_1$	2.00000	2.00221	2.00
16	$3s 3d^1D_2$	1.00000	0.99996	0.99
18	$3s 4p^1P_1^o$	1.50000	1.50050	1.55
19	$3s 4p^1P_2^o$	1.50000	1.50109	1.49
20	$3s 4p^1P_1^o$	1.00000	1.00054	1.01
27	$3s 4d^1D_2$	1.00000	1.00000	1.00
Si IV <sup>(1)</sup>				
6	$4s^2S_{1/2}$	2.00000	2.00225	1.98
7	$4p^2P_{1/2}^o$	0.670000	0.66583	0.72
8	$4p^2P_{3/2}^o$	1.33000	1.33405	1.34
9	$4d^2D_{3/2}^o$	1.20000	1.20043	1.16
15	$5p^2P_{3/2}^o$	1.33000	1.33407	1.34
Ti II <sup>(4)</sup>				
11	$3d^2(^1D) ^1D 4s^2D_{3/2}$	0.800000	0.80900	0.80
15	$3d^3(^3P) ^4P_{1/2}$	2.66667	2.58681	2.63
16	$3d^3(^3P) ^4P_{3/2}$	1.73333	1.70373	1.74
18	$3d^3(^3P) ^2P_{1/2}$	0.666667	0.78123	0.66
19	$3d^3(^3P) ^3P 4s^1P_{1/2}$	2.66667	2.63809	2.60
21	$3d^3(^3P) ^2P_{3/2}$	1.33333	1.35842	1.33
29	$3d^3(^3P) ^3P 4s^1P_{1/2}$	0.666667	0.66607	0.66
30	$3d^3(^3P) ^3P 4s^1P_{3/2}$	1.33333	1.33324	1.33
45	$3d^2(^3F) ^3F 4p^2D_{3/2}^o$	0.800000	0.80021	0.92
46	$3d^2(^3F) ^3F 4p^2D_{5/2}^o$	1.20000	1.19159	1.20
48	$3d^2(^3F) ^3F 4p^4D_{1/2}^o$	0.000000	1.02735E-04	0.00
49	$3d^2(^3F) ^3F 4p^4D_{3/2}^o$	1.20000	1.18881	1.20
50	$3d^2(^3F) ^3F 4p^4D_{5/2}^o$	1.37143	1.36075	1.37
56	$3d^2(^3P) ^3P 4p^2S_{1/2}^o$	2.00000	1.99657	2.09
57	$3d^2(^1D) ^1D 4p^2D_{3/2}^o$	0.800000	0.98131	1.21
Sn II <sup>(5)</sup>				
3	$5s 5p^2P_{1/2}$	2.66667	2.65984	2.6609

References. (1) Lott et al. (1966); (2) Li (1972); (3) Martin et al. (1985); (4) Moore (1949); (5) David et al. (1980).

**Table A.2.** Summary of levels with a relative difference  $\geq 10\%$  with respect to  $g_J(LS)$ . **Table A.2.** continued.

No.	State	$g_J(LS)$	$g_{yJ}$	Kurucz
C I				
60	$2p^2P4d^3D_1^o$	0.50000	0.55335	0.527
69	$2p^2P4f^3G_3$	0.75000	0.83619	0.808
82	$2p^2P5p^3D_1$	0.50000	0.55210	0.610
92	$2p^2P5d^3F_2^o$	0.66667	0.75711	0.733
96	$2p^2P5d^3D_1^o$	0.50000	0.59981	0.604
97	$2p^2P6s^3P_2^o$	1.50000	1.31673	1.342
99	$2p^2P5d^3D_2^o$	1.16667	1.28419	1.277
Si I				
40	$3p^2P4d^1D_{2a}^o$	1.00000	1.23605	1.093
41	$3p^2P4d^1D_{2b}^o$	1.00000	1.26057	1.403
45	$3p^2P5p^3D_1$	0.50000	0.66751	0.698
58	$3p^2P4f^3F_2$	0.66667	0.76027	0.755
59	$3p^2P4f^3G_{3a}$	0.75000	0.89982	0.910
63	$3p^2P4f^3G_{3b}$	0.75000	0.88920	0.881
68	$3p^2P4d^3D_1^o$	0.50000	0.62064	0.554
81	$3p^2P6p^3D_{1a}$	0.50000	0.75851	0.696
83	$3p^2P6p^3D_{1b}$	0.50000	1.10995	1.363
96	$3p^2P5f^3F_{2a}$	0.66667	0.81795	0.814
97	$3p^2P5f^3G_3$	0.75000	0.92167	0.873
99	$3p^2P5g^3G_{3a}^o$	0.75000	0.89339	0.894
111	$3p^2P5f^3F_{2b}$	0.66667	0.91694	0.923
116	$3p^2P5g^3G_{3b}^o$	0.75000	0.89222	0.891
131	$3p^2P7p^3D_1$	0.50000	0.69044	0.672
134	$3p^2P6d^3F_{3a}^o$	0.66667	0.88297	0.866
137	$3p^2P6d^3F_{3b}^o$	0.66667	0.82644	0.855
138	$3p^2P7p^1P_1$	1.00000	1.14422	1.299
144	$3p^2P6f^3G_3$	0.75000	0.83711	1.147
147	$3p^2P6f^3F_{2a}$	0.66667	0.85004	0.850
152	$3p^2P6d^1F_3^o$	1.00000	1.10913	1.031
157	$3p^2P6f^3F_{2b}$	0.66667	0.88535	0.892
P II				
27	$3s^23p^2P3d^3D_1^o$	0.50000	0.89293	0.940
29	$3s^23p^2P3d^3P_1^o$	1.50000	1.11039	1.050
31	$3s^23p^2P3d^3D_2^o$	1.16667	1.29222	1.260
49	$3s^23p^2P4d^3P_2^o$	1.50000	1.33882	1.278
50	$3s^23p^2P4d^3D_1^o$	0.50000	0.89316	0.870
54	$3s^23p^2P4d^3P_1^o$	1.50000	1.10772	1.129
57	$3s^23p^2P5p^3D_1$	0.50000	0.63857	0.620
93	$3s^23p^2P5d^1D_2^o$	1.00000	1.13551	1.120
94	$3s^23p^2P5d^3D_1^o$	0.50000	0.70581	0.690
97	$3s^23p^2P5d^3P_2^o$	1.50000	1.33546	1.340
98	$3s^23p^2P5d^3P_1^o$	1.50000	1.29786	1.300
S II				
87	$3s^23p^2(1S)1S4p^2P_{1/2}^o$	0.66667	0.84052	0.945
102	$3s^2S3p^4(3P)2P_{3/2}$	1.33333	1.15616	
104	$3s^23p^2(3P)3P4f^4D_{7/2}^o$	1.42857	1.23570	1.281
106	$3s^23p^2(3P)3P4d^2D_{3/2}$	0.80000	0.97639	0.887
107	$3s^23p^2(3P)3P4f^2D_{5/2}^o$	1.20000	0.94834	0.930
108	$3s^23p^2(3P)3P4f^4G_{7/2}^o$	0.98413	1.14087	1.109
111	$3s^23p^2(3P)3P4f^4D_{5/2}^o$	1.20000	0.92391	0.919
114	$3s^23p^2(3P)3P4f^2D_{3/2}^o$	0.80000	0.99823	1.005
118	$3s^23p^2(3P)3P4f^4F_{3/2}^o$	0.40000	0.47703	0.475
Cl III				
18	$3s^23p^2(3P)3P3d^4D_{5/2}$	1.37143	1.17635	1.359
22	$3s^23p^2(1D)1D3d^2F_{5/2}$	0.85714	1.05128	0.873
Ar IV				
18	$3s^23p^2(1D)1D3d^2F_{5/2}$	0.85714	1.02081	0.861
22	$3s^23p^2(3P)3P3d^4D_{5/2}$	1.37143	1.20618	1.184
101	$3s^2S3p^4(1P)3P3d^2D_{5/2}^o$	1.20000	1.34088	1.202
Ca I				
13	$3s^23p^63d^2D4p^3F_2^o$	0.66667	0.74211	0.754
Ti II				
18	$3d^4(3P)2P_{1/2}$	0.66667	0.78123	0.660
57	$3d^2(1D)1D4p^2D_{3/2}^o$	0.80000	0.98131	1.210

No.	State	$g_J(LS)$	$g_{yJ}$	Kurucz
59	$3d^2(1D)1D4p^2P_{3/2}^o$	1.33333	1.19437	1.200
81	$3d^2D4s^3D4p^4F_{3/2}^o$	0.40000	0.54562	0.462
83	$3d^2D4s^3D4p^4F_{5/2}^o$	1.02857	1.13809	1.078
84	$3d^2D4s^3D4p^4D_{3/2}^o$	1.20000	1.05899	1.140
Zr III				
16	$4d^2D5p^3F_2^o$	0.66667	0.77976	0.807
34	$4d^2D5d^3G_{3a}$	0.75000	1.01649	0.925
35	$4d^2D5d^3G_{3b}$	0.75000	1.05195	1.146
36	$4d^2D6s^3D_1$	0.50000	0.63883	0.630
39	$4d^2D5d^1P_1$	1.00000	0.89734	0.887
48	$4d^2D5d^1D_2$	1.00000	1.13456	1.110
50	$4d^2D5d^3P_2$	1.50000	1.35112	1.373
55	$4d^2D6p^3D_2^o$	1.16667	0.92822	1.034
76	$4d^2D4f^3D_7^o$	0.50000	0.59790	0.605
77	$4d^2D4f^3D_5^o$	1.33333	1.17260	1.175
79	$4d^2D4f^1F_3^o$	1.00000	1.13107	1.126
Sn II				
13	$5s5p^22S_{1/2}$	2.00000	1.36349	
14	$5s5p^22P_{1/2}$	0.66667	1.31877	

**Notes.** Kurucz's data (Kurucz 2017) are shown in the last column for comparison.





## Paper v



D. T. Yordanov, L. V. Rodriguez, D. L. Balabanski, J. Bieroń, M. L. Bissell, K. Blaum, B. Cheal, J. Ekman, G. Gaigalas, R. F. Garcia Ruiz, G. Georgiev, W. Gins, M. R. Godefroid, C. Gorges, Z. Harman, H. Heylen, P. Jönsson, A. Kanellakopoulos, S. Kaufmann, C. H. Keitel, V. Lagaki, S. Lechner, B. Maaß, S. Malbrunot-Ettenauer, W. Nazarewicz, R. Neugart, G. Neyens, W. Nörtershäuser, N. S. Oreshkina, **A. Pappouli**a, P. Pyykkö, P.-G. Reinhard, S. Sailer, R. Sánchez, S. Schiffmann, S. Schmidt, L. Wehner, C. Wraith, L. Xie, Z. Xu, and X. Yang


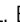

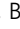



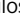
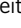
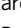
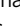
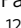
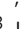

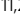
Structural trends in atomic nuclei from laser spectroscopy of tin

*Communications Physics*, 2020, 3(1), 107

Copyright 2020 The Authors.



# Structural trends in atomic nuclei from laser spectroscopy of tin

Deyan T. Yordanov <sup>1,2,✉</sup>, Liss V. Rodríguez<sup>1,3</sup>, Dimiter L. Balabanski <sup>4</sup>, Jacek Bieroń <sup>5</sup>, Mark L. Bissell<sup>6</sup>, Klaus Blaum <sup>3</sup>, Bradley Cheal<sup>7</sup>, Jörgen Ekman<sup>8</sup>, Gediminas Gaigalas <sup>9</sup>, Ronald F. Garcia Ruiz <sup>2,24</sup>, Georgi Georgiev <sup>10</sup>, Wouter Gins<sup>11,25</sup>, Michel R. Godefroid<sup>12</sup>, Christian Gorges<sup>13,26</sup>, Zoltán Harman<sup>3</sup>, Hanne Heylen<sup>2,3</sup>, Per Jönsson<sup>8</sup>, Anastasios Kanellakopoulos <sup>11</sup>, Simon Kaufmann<sup>13</sup>, Christoph H. Keitel <sup>3</sup>, Varvara Lagaki<sup>2,14</sup>, Simon Lechner<sup>2,15</sup>, Bernhard Maaß<sup>13</sup>, Stephan Malbrunot-Ettenauer<sup>2</sup>, Witold Nazarewicz <sup>16</sup>, Rainer Neugart<sup>3,17</sup>, Gerda Neyens<sup>2,11</sup>, Wilfried Nörtershäuser <sup>13</sup>, Natalia S. Oreshkina <sup>3</sup>, Asimina Papoulia <sup>8,18</sup>, Pekka Pyykkö <sup>19</sup>, Paul-Gerhard Reinhard<sup>20</sup>, Stefan Sailer<sup>21</sup>, Rodolfo Sánchez <sup>22</sup>, Sacha Schiffmann<sup>12,18</sup>, Stefan Schmidt<sup>13</sup>, Laura Wehner<sup>17</sup>, Calvin Wraith<sup>7</sup>, Liang Xie<sup>6</sup>, Zhengyu Xu<sup>11,27</sup> & Xiaofei Yang <sup>11,23</sup>

Tin is the chemical element with the largest number of stable isotopes. Its complete proton shell, comparable with the closed electron shells in the chemically inert noble gases, is not a mere precursor to extended stability; since the protons carry the nuclear charge, their spatial arrangement also drives the nuclear electromagnetism. We report high-precision measurements of the electromagnetic moments and isomeric differences in charge radii between the lowest  $1/2^+$ ,  $3/2^+$ , and  $11/2^-$  states in  $^{117-131}\text{Sn}$ , obtained by collinear laser spectroscopy. Supported by state-of-the-art atomic-structure calculations, the data accurately show a considerable attenuation of the quadrupole moments in the closed-shell tin isotopes relative to those of cadmium, with two protons less. Linear and quadratic mass-dependent trends are observed. While microscopic density functional theory explains the global behaviour of the measured quantities, interpretation of the local patterns demands higher-fidelity modelling.

<sup>1</sup>Institut de Physique Nucléaire, CNRS-IN2P3, Université Paris-Sud, Université Paris-Saclay, Orsay, France. <sup>2</sup>Experimental Physics Department, CERN, Geneva, Switzerland. <sup>3</sup>Max-Planck-Institut für Kernphysik, Heidelberg, Germany. <sup>4</sup>ELI-NP, Horia Hulubei National Institute for R&D in Physics and Nuclear Engineering, Magurele, Romania. <sup>5</sup>Instytut Fizyki imienia Mariana Smoluchowskiego, Uniwersytet Jagielloński, Kraków, Poland. <sup>6</sup>School of Physics and Astronomy, The University of Manchester, Manchester, UK. <sup>7</sup>Oliver Lodge Laboratory, University of Liverpool, Liverpool, UK. <sup>8</sup>Department of Materials Science and Applied Mathematics, Malmö University, Malmö, Sweden. <sup>9</sup>Institute of Theoretical Physics and Astronomy, Vilnius University, Vilnius, Lithuania. <sup>10</sup>CSNSM, CNRS-IN2P3, Université Paris-Sud, Université Paris-Saclay, Orsay, France. <sup>11</sup>Instituut voor Kern-en Stralingsfysica, KU Leuven, Leuven, Belgium. <sup>12</sup>Chimie Quantique et Photophysique, Université libre de Bruxelles, Brussels, Belgium. <sup>13</sup>Institut für Kernphysik, Technische Universität Darmstadt, Darmstadt, Germany. <sup>14</sup>Institut für Physik, Universität Greifswald, Greifswald, Germany. <sup>15</sup>Technische Universität Wien, Vienna, Austria. <sup>16</sup>Department of Physics and Astronomy and FRIB Laboratory, Michigan State University, East Lansing, MI, USA. <sup>17</sup>Institut für Kernchemie, Universität Mainz, Mainz, Germany. <sup>18</sup>Division of Mathematical Physics, Department of Physics, Lund University, Lund, Sweden. <sup>19</sup>Department of Chemistry, University of Helsinki, Helsinki, Finland. <sup>20</sup>Institut für Theoretische Physik II, Universität Erlangen-Nürnberg, Erlangen, Germany. <sup>21</sup>Technische Universität München, Munich, Germany. <sup>22</sup>GSI Helmholtzzentrum für Schwerionenforschung GmbH, Darmstadt, Germany. <sup>23</sup>School of Physics and State Key Laboratory of Nuclear Physics and Technology, Peking University, Beijing, China. <sup>24</sup>Present address: Massachusetts Institute of Technology, Cambridge, MA, USA. <sup>25</sup>Present address: Department of Physics, University of Jyväskylä, Jyväskylä, Finland. <sup>26</sup>Present address: Institut für Kernchemie, Universität Mainz, Mainz, Germany. <sup>27</sup>Present address: Department of Physics and Astronomy, University of Tennessee, Knoxville, TN, USA. ✉email: [Deyan.Yordanov@cern.ch](mailto:Deyan.Yordanov@cern.ch)

Nuclear science greatly relies on observations, not only in naturally-occurring, but also in laboratory-synthesized nuclides, which represent the majority of approximately 3000 species discovered to date<sup>1</sup>. Either type can be studied by laser spectroscopy, a non-destructive experimental technique probing the hyperfine splitting of atomic energy levels induced by the nuclear electromagnetism. An electric quadrupole moment, for instance, reflects an anisotropic (deformed) charge distribution within the nucleus<sup>2</sup>. Appreciable nuclear deformation is primarily found in species with open shells for both protons and neutrons<sup>3,4</sup>. The tin isotopes, with their proton core complete (spherical), may still acquire quadrupole moments through the geometry of valence neutron orbitals. Those can be discussed in terms of schematic theoretical descriptions such as the seniority or generalized-seniority models<sup>5,6</sup>, which explain the striking regularities previously observed, e.g., the nearly-constant energy of excited states and simple patterns exhibited by other quantities<sup>7–9</sup>. When looking into details, however, deviations from regular behavior are revealed as fingerprints of the underlying nucleonic shell structure and many-body correlations<sup>10–13</sup>.

Here we study the odd-mass isotopes <sup>117–131</sup>Sn. An  $11/2^-$  state with an unpaired neutron confined by the rules of quantum mechanics to the unique-parity  $h_{11/2}$  orbital is present in each case. The remaining valence orbitals in the neutron shell have the opposite parity and considerably lower angular momenta, which results in isomerism (metastability of an excited nuclear state). Quadrupole moments in the closed-shell tin isotopes are found at variance with those in the cadmium isotopes having two protons less. Differences in radii between nuclear ground and isomeric states, on the other hand, are shown to remain surprisingly similar. Calculations in the framework of nuclear density functional theory with recently optimized input describe the global behavior of the experimental observables. Interpretation of the local patterns, however, calls for a dedicated microscopic modeling.

## Results and discussion

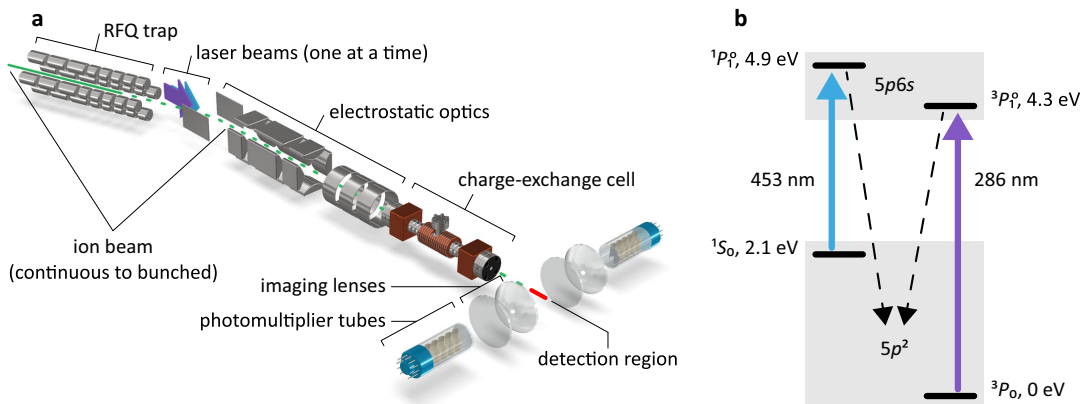
**Measurements.** Short-lived nuclei, naturally occurring only in astrophysical phenomena such as supernovae explosions<sup>14</sup>, are synthesized on Earth using particle accelerators. The tin isotopes for this study were produced at the CERN-ISOLDE laboratory<sup>15</sup> by uranium fission using fast protons traveling with more than 90% of the speed of light. Prior conversion to neutrons increased the fission purity<sup>16</sup>. Tin atoms were laser ionized, accelerated to an energy of 40 or 50 keV to form a continuous beam of fast-traveling ions, and mass separated. Typically, each 100-ms segment of the beam was compressed into an ion bunch with a temporal width of less than 10 μs using a linear Paul trap<sup>17</sup>. Individual bunches were subsequently released, re-accelerated, and guided with a dedicated set of electrostatic optics into a volume of vaporized sodium for neutralization. Narrow-bandwidth continuous-wave laser light was introduced along the axis of ion/atom propagation. The atomic-beam energy and the associated Doppler-shifted laser frequency were defined at the sodium charge-exchange cell, whose electrostatic potential was scanned in search of resonant atomic-beam fluorescence. The latter was collected by telescopes of aspheric lenses and imaged onto the photocathodes of photomultiplier tubes for single-photon counting. The measurements were correlated with the timing structure of the atomic beam, which allowed substantial background suppression and high sensitivity. A sketch of the experimental arrangement is shown in Fig. 1a.

Laser excitation of tin atoms was performed using the two complementary transitions in Fig. 1b to resolve the nuclear properties, as described in “Methods”. The laser system comprised

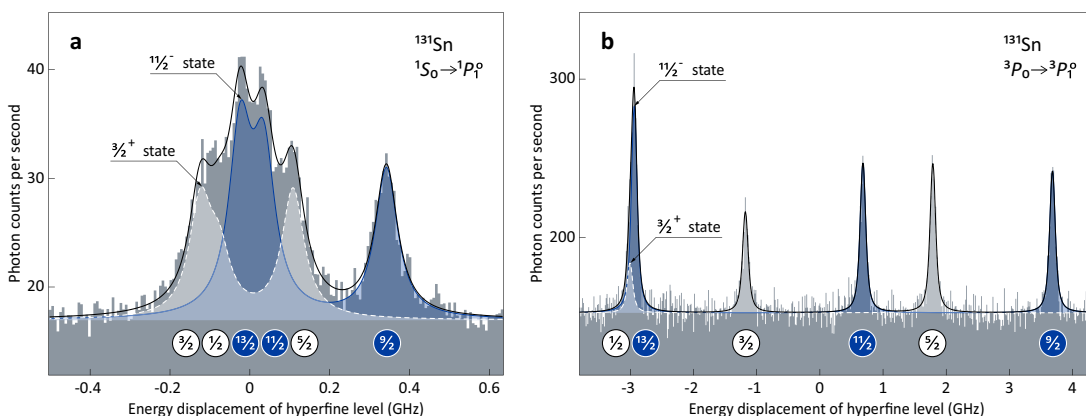
a diode-pumped solid-state laser, a tunable laser using either dye or titanium-sapphire as the active medium, and a second-harmonic-generation cavity. Two nuclear states were detected for each odd-mass isotope in the range <sup>117–131</sup>Sn, as shown in Fig. 2. The hyperfine structure is characterized by a sizeable quadrupole splitting in the  $5p6s\ ^1P_1^o$  state and a large magnetic splitting in the  $5p6s\ ^3P_1^o$  state. The two are correlated through the nuclear electromagnetic properties and are thus fitted simultaneously. All results are shown in Table 1. The magnetic moments therein incorporate the latest computation of the absolute shielding constant in tin<sup>18</sup>. The accuracy of quadrupole moments is ensured by the theoretical work outlined in the following.

**Atomic structure calculations.** The fully relativistic multi-configuration Dirac–Hartree–Fock (MCDHF) method was employed to calculate the magnetic dipole hyperfine-structure constants and electric-field gradients in the  $5p6s\ ^1P_1^o$  and  $5p6s\ ^3P_1^o$  states of tin (see “Methods” for the definition of these quantities). Three independent series of large-scale calculations were performed, adopting different computational strategies and correlation models using the General Relativistic Atomic Structure Package computer codes GRASP2K<sup>19</sup> and GRASP2018<sup>20</sup>, based on the same relativistic MCDHF theory and methodology<sup>21,22</sup>. Classes of electron excitations adopting different multireference spaces and active orbital sets were investigated in detail to clarify the role of electron correlation in the relevant matrix elements. A combined effort was put in assessing the reliability of the resulting ab initio electronic factors involved in M1 and E2 hyperfine interactions for both levels (Papoulia, A. & Schiffman, S. et al. manuscript in preparation). The quadrupole moments from this work are obtained with the electric-field gradient 706(50) MHz/b in the singlet state, which is the mean value resulting from the aforementioned calculations. With regard to the dipole hyperfine constants in the triplet state, cross-checking calculations were performed using the configuration interaction Dirac–Fock–Sturm (CI-DFS) method<sup>23</sup>. The hyperfine anomaly (see “Methods”) was estimated in separate multireference calculations for each isotope using a Fermi charge distribution with adopted root mean square radius and a parametrized squared harmonic-oscillator wave function of the last unpaired neutron as magnetization distribution<sup>24</sup>. It reaches a maximum at  $^{119}\text{g}\Delta^{131\text{m}} = 0.05\%$  due to the limited overlap between the  $3s$  and  $1h$  nuclear wave functions and partly due to the increase in the charge radius between the two isotopes. The anomaly between positive-parity states was found to be negligible with respect to the experimental precision.

**Experimental trends.** The data on quadrupole moments and differences in mean square charge radii between nuclear ground and isomeric states are compared in Fig. 3 with values measured in the cadmium isotones<sup>25–27</sup>. A number of key observations are worth being pointed out: (i) There is a significant attenuation of the quadrupole moments of tin ( $Z = 50$ ) with respect to cadmium ( $Z = 48$ ). Note that the observed charge (proton) quadrupole moment originates from the nuclear response to an odd neutron in a  $d_{3/2}$  or an  $h_{11/2}$  single-particle state. (ii) The fitted trends in Fig. 3a, b cross each other close to zero, i.e., the  $h_{11/2}$  orbital is half full<sup>5,6</sup> for both tin and cadmium at  $N = 73$ , as is  $d_{3/2}$  at  $N = 75$ . (iii) The quadrupole moments of tin in the  $11/2^-$  states are by a factor of about two larger in magnitude than those in the  $3/2^+$  states. This is consistent with a stronger quadrupole polarization exerted by unique-parity  $h_{11/2}$  nucleons. (iv) All trends are remarkably smooth, often near linear, at most quadratic. (v) The quadrupole moments of the  $11/2^-$  states in tin exhibit a quadratic behavior with changing neutron number, strikingly different from the linear trend observed along the cadmium chain. (vi) The



**Fig. 1** Experimental arrangement and level scheme in the neutral atom of Sn. **a** From left to right: linear Paul trap for ion-beam bunching; continuous-wave laser beams; electrostatic elements: deflector, quadrupole triplet, cylinder lens; alkali-vapor cell; optical detection: fused-silica aspheric lenses, photomultiplier tubes. **b** Partial energy level scheme of neutral tin indicating the studied excitations and the subsequent fluorescence used for detection. The shaded areas indicate the groups of  $5p^2$  and  $5p6s$  levels.

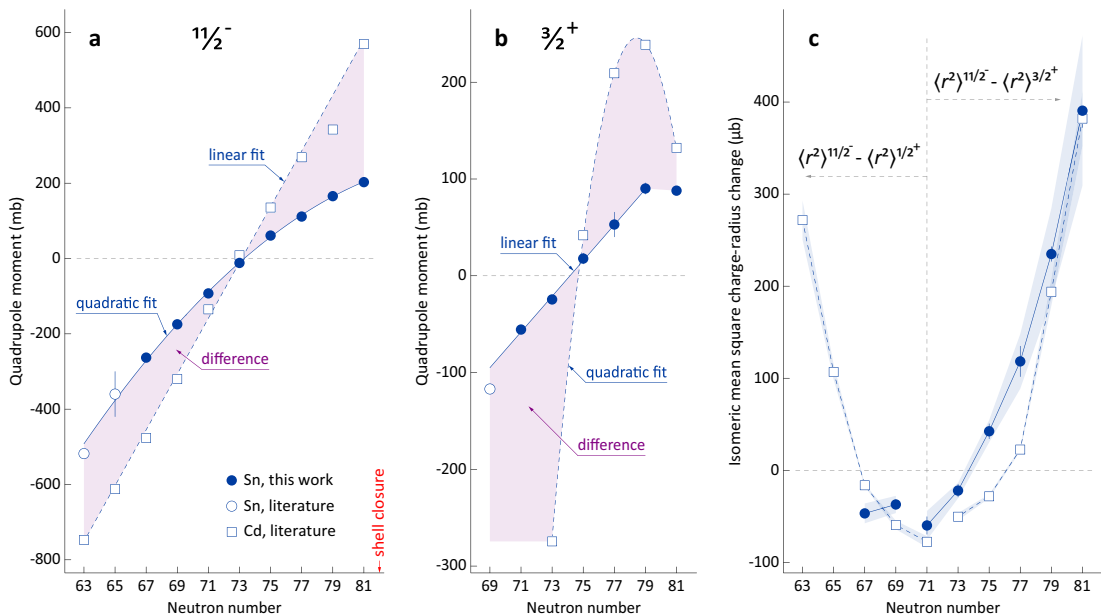


**Fig. 2** Fluorescence spectra of  $^{131}\text{Sn}$ . Hyperfine structure in the **a**  $5p6s\ ^1P_1$  state and **b**  $5p6s\ ^3P_1$  state. The fitted black curves comprise a  $3/2^+$  nuclear ground state, represented by the dashed white lines, and an  $11/2^-$  isomer, represented by the solid blue lines. Hyperfine levels are denoted by the individual total angular-momentum quantum number.

pattern is unexpectedly reversed for the  $3/2^+$  states whose quadrupole moments change linearly for tin and quadratically for cadmium. (vii) Re-evaluated values for  $^{113,115,119}\text{Sn}$ <sup>28</sup> in Fig. 3a, b are consistent with the trends defined by the heavier isotopes. These are independently calibrated to experimental  $\gamma$ -decay rates, thus showing consistency between nuclear data and atomic theory. (viii) The measured mean square charge-radii changes in Fig. 3c are fairly similar for tin and cadmium. All these features are discussed in the following.

**Nuclear structure calculations.** The theoretical analysis at the level of nuclear density functional theory<sup>29</sup> (DFT) employs the standard Skyrme functional SV-min<sup>30</sup> and the recently optimized Fayans functional  $Fy(\Delta r, \text{HFB})$ <sup>31</sup>, the latter containing gradient terms in surface and pairing energies<sup>32,33</sup>. Both models are optimized to the same large set of basic ground-state nuclear data<sup>30</sup>. In addition,  $Fy(\Delta r, \text{HFB})$  accommodates the isotopic

shifts of charge radii in the calcium chain, a feature which could only be achieved by invoking the Fayans gradient terms<sup>31,34</sup>. The calculations for the charge radius, which is an isotropic observable, were done in spherical approximation with pairing handled at Hartree–Fock–Bogoliubov (HFB) level. The odd nucleons were treated within the blocking ansatz<sup>35</sup>. In principle, the odd nucleon polarizes the nucleus and so perturbs the spherical shape. The impact of this polarization effect on charge radii and correlations beyond mean field are small for heavier spherical species as the tin isotopes<sup>36,37</sup>. To check the uncertainty from the spherical mean-field approximation, we performed more elaborate blocked HFB calculations allowing axial deformations and spin polarization for the case of the SV-min model. In this variant, each magnetic sub-state produces a slightly different radius whose average is very close to the spherical result. This supports our spherical calculations and the variance of charge radii within a  $jm$  shell delivers an estimate of their theoretical uncertainties.



**Fig. 3 Sn vs. Cd. a**  $11/2^-$  quadrupole moments. **b**  $3/2^+$  quadrupole moments. Correlated uncertainties originating from the electric-field gradients are smaller than the dots. **c** Mean square charge-radii changes for the  $11/2^-$  states relative to the  $1/2^+$  ( $N \leq 71$ ) and  $3/2^+$  ( $N \geq 71$ ) states. Shaded bands represent systematic uncertainties originating from the field-shift coefficients. The literature values are taken from refs. [25,26,28](#).

Figure 4a shows the quadrupole moments of  $11/2^-$  states in tin and cadmium which were obtained by blocking the  $m = 11/2$  magnetic substate of the  $h_{11/2}$  orbital in calculations that break spherical symmetry. It is satisfactory to see that the general experimental pattern in Fig. 3a is reproduced. Namely, the quadrupole moments exhibit a smooth increase as a function of the neutron number, with the quadrupole moments of tin being reduced in magnitude relative to cadmium. The enhanced quadrupole correlations in cadmium stem from the enhanced polarizability through the two  $g_{9/2}$  proton holes<sup>38,39</sup>. Indeed, in the nuclear shell model<sup>40</sup> and in nuclear DFT<sup>41</sup>, deformation is primarily driven by the isoscalar neutron-proton (quadrupole) interaction, acting against the sphericity-favoring monopole force, which includes the isovector pairing interaction. According to the seniority coupling scheme<sup>5-7</sup>, the spectroscopic quadrupole moment should vanish at mid-shell. In SV-min, the neutron  $h_{11/2}$  shell becomes half-filled at  $N = 75$ , as seen in Fig. 4a. Experimentally, the zero crossover point is at  $N = 73$ , which suggests that the single-particle energy of the  $h_{11/2}$  shell is perhaps not optimal in our model. This nicely demonstrates that the present high-precision data on quadrupole moments deliver extremely sensitive criteria for probing the shell structure of a model.

Theoretical values for the isomeric charge-radii shifts of the odd-mass tin isotopes are displayed in Fig. 4b, c. The error bars on the SV-min results indicate the estimated uncertainty of the spherical approach as compared to calculations allowing shape deformation as well as spin polarization and subsequent angular momentum projection, as explained above. We expect similar uncertainty for the Fy( $\Delta r$ , HFB) model. One finds an acceptable agreement for the charge radii difference between the  $11/2^-$  and the  $3/2^+$  states, with a preference towards the Fy( $\Delta r$ , HFB) description, especially when considering the theoretical uncertainty. This is not the case for the radii

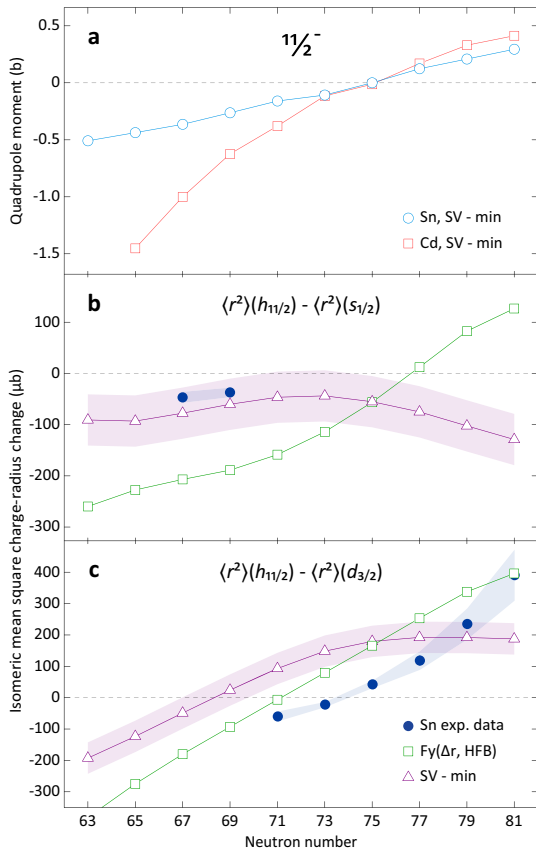
changes between the  $11/2^-$  and the  $1/2^+$  states, since the experimental data approach the upper end of theoretical results in Fig. 4b. A word of caution is in order here: the  $1/2^+$  state is particularly prone to a dynamical coupling with low-energy quadrupole vibrations which is expected to enhance the charge radius.

The trends of quadrupole moments, linear vs. quadratic, are different for cadmium and tin owing to a significant configuration dependence. The latter does not cause a substantial deviation between the corresponding mean square charge-radii changes. The future theoretical analysis would need to address these features in greater detail together with variations of the magnetic moments shown in Fig. 5. Any connection with the quadrupole moments of the lowest  $2^+$  states in the even-even isotopes<sup>42,43</sup> should also be examined.

**Perspective.** Complex systems often display regular patterns. Atomic nuclei, composite structures consisting of hundreds of nucleons, are no exception; they often behave as ordered systems obeying elementary rules<sup>5</sup>. The reason for such simplicities is the presence of many-body symmetries resulting in a collective nucleonic motion. A challenge for the modern microscopic theory is to explain the origin of underlying symmetries.

In this work, we showed that electromagnetic properties of tin nuclei evolve from one isotope to another in a simple way: along a line or parabola. The microscopic mechanisms behind the observed behavior are rooted in many-body polarization effects. While the general trends are explained by theory, the regularities seen at high experimental resolution provide a strong motivation for further theoretical developments.

Similar effects are expected to be common for nuclei whose valence nucleons move in a unique-parity shell. Dedicated studies would be required to refine the systematics in lead and mercury



**Fig. 4** Theoretical calculations. **a**  $11/2^-$  quadrupole moments in tin and cadmium isotopes computed with the Skyrme density functional SV-min<sup>31</sup>. **b, c** Mean square charge-radii changes for the  $11/2^-$  states relative to the  $1/2^+$  and  $3/2^+$  states in tin obtained with SV-min and the Fayans functional Fy( $\Delta r$ , HFB)<sup>31</sup>.

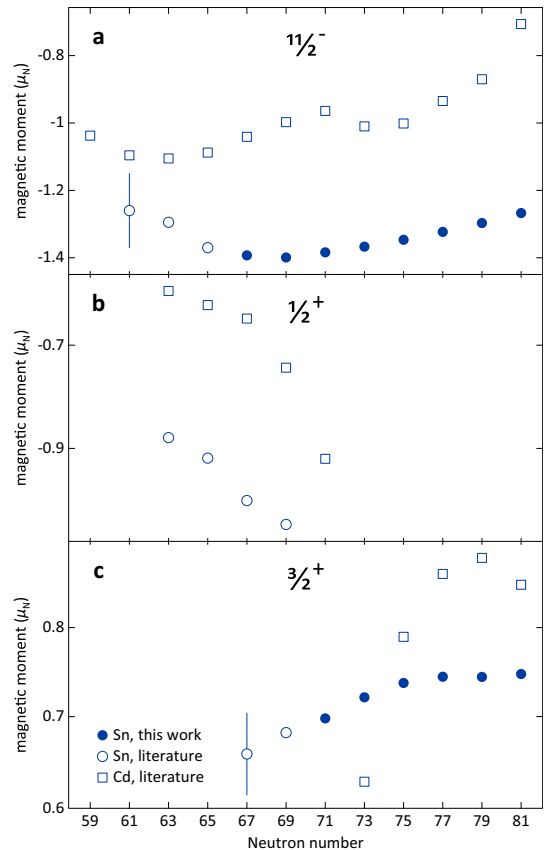
isotopes<sup>44</sup>, which are the closest analogues of tin and cadmium in terms of nuclear structure. While initial assessments could be made by in-source measurements<sup>45,46</sup>, the high-resolution spectroscopic techniques employed here, in combination with advanced atomic calculations, will be essential for developing further understanding of complex nuclear systems.

**Methods**

**Hyperfine structure.** The electromagnetic interaction of the nucleus with the electron environment in an atom causes splitting of the energy levels which is about a millionth of the fine-structure splitting, hence the term hyperfine structure. The energy shift of the individual hyperfine components equals

$$E_F - E_J = A \frac{k}{2} + B \frac{3k(k+1) - 4I(I+1)J(J+1)}{8I(2I-1)J(2J-1)},$$

where  $A = \mu B_0 / (IJ)$  is proportional to the nuclear magnetic moment  $\mu$  and the average magnetic-flux density at the origin  $B_0$ ,  $B = eQV_{JJ}$  is proportional to the nuclear quadrupole moment  $Q$  and the average electric-field gradient at the origin  $V_{JJ}$ ,  $\mathbf{F} = \mathbf{I} + \mathbf{J}$  is the total angular momentum of the atom, and  $k = F(F+1) - I(I+1) - J(J+1)$ . The hyperfine-structure splitting is determined by the  $A$  and  $B$  parameters whose values are obtained from the experiment. The decay rate per



**Fig. 5** Sn vs. Cd: magnetic moments. **a** Of the  $11/2^-$  states, **b** of the  $3/2^+$  states, and **c** of the  $1/2^+$  states. The literature values are taken from refs. 26,57. The current high-resolution data correspond to former measurements in refs. 53,54. The magnetic moment of the  $3/2^+$  state in  $^{123}\text{Sn}$  is reported for the first time.

atom, commonly referred to as Racah intensities<sup>47</sup>, is given by

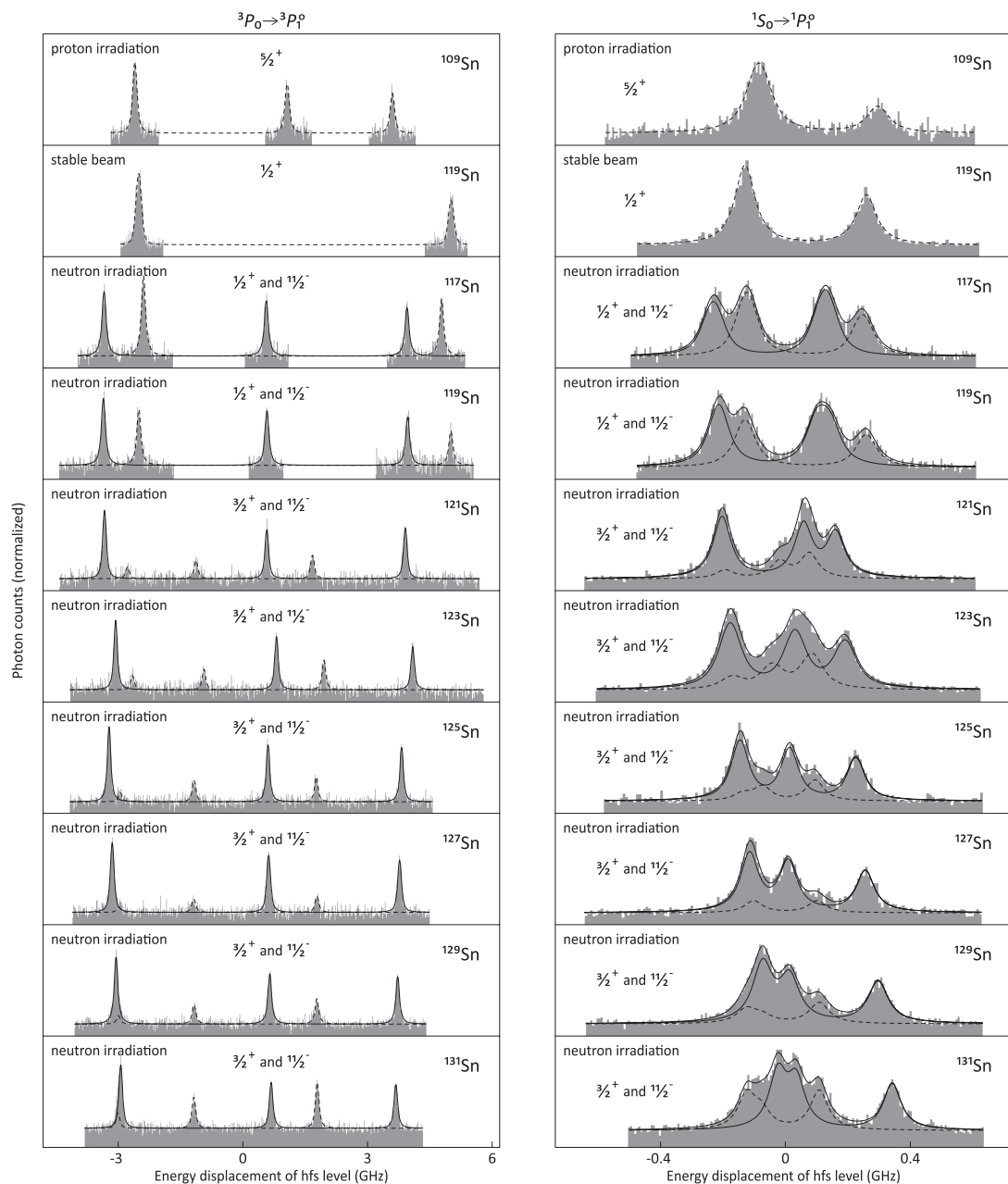
$$\frac{R}{n} = \frac{\gamma}{3\tau} \frac{(2J_1 + 1)(2F_1 + 1)(2F_2 + 1)}{(2I + 1)(2J_2 + 1)} \begin{Bmatrix} J_2 & F_2 & I \\ F_1 & J_1 & 1 \end{Bmatrix}^2,$$

where  $\tau$  is the lifetime of the excited atomic state and  $\gamma$  is the ratio between the induced and spontaneous emission coefficients, which incorporates the laser intensity and the spectral lineshape.

**Hyperfine anomaly.** The  $A$  hyperfine constant is influenced by the extended nuclear magnetization, known as Bohr-Weisskopf effect, and the extended nuclear charge distribution, known as Breit-Rosenthal-Crawford-Schawlow correction. Both contribute to the hyperfine anomaly:

$$^1\Delta^2 = \frac{A_1 I_1 \mu_2}{A_2 I_2 \mu_1} - 1.$$

Following justification by atomic calculations, the anomaly is neglected in our analysis. However, its estimated contribution to the  $11/2^-$  magnetic moments is predicted to be on the level of the experimental precision and it is therefore incorporated into the final uncertainties quoted in Table 1, as further discussed.



**Fig. 6 Fitted fluorescence spectra of  $^{109,117-131}\text{Sn}$ .** The common frequency scales are relative to the fine-structure splittings in the transitions  $5p^2\ ^3P_0 \rightarrow 5p6s\ ^3P_0$  and  $5p^2\ ^1S_0 \rightarrow 5p6s\ ^1P_1$ . Positive- and negative-parity states are represented by dashed and solid lines, respectively. Solid lines in the right column also show the sum fit function.  $^{119}\text{Sn}$  is studied from a mass marker to observe only the stable  $1/2^+$  g.s., and after target irradiation to detect the radioactive  $11/2^-$  state. Spectra of the stable g.s. in  $^{115,117}\text{Sn}$  (similar to  $^{119}\text{Sn}$  g.s.) are not shown.  $^{133}\text{Sn}$ , used together with  $^{109}\text{Sn}$  for calibration of the  $B$ -ratio, will be published elsewhere.



**Table 1** Experimental results on  $^{109,115-131}\text{Sn}$ .

	$I^\pi$	$A$ (MHz)	$\delta\nu^{e,o}$ (MHz)	$B$ (MHz)	$\mu$ ( $\mu_N$ )	$\delta\langle r^2 \rangle^{e,o}$ ( $\mu\text{b}$ )	$Q$ (mb)
$^{109}\text{Sn}$	$5/2^+$	−1035.8(6)		+154(5)	−1.081(1)		+218(7)(15)
$^{115}\text{Sn}$	$1/2^+$	−4394(2)			−0.9167(1)		
$^{117}\text{Sn}$	$1/2^+$	−4783(2)			−0.9983(1)		
$^{117}\text{Sn}$	$11/2^-$	−606.9(3)	−12(2)	−186(4)	−1.393(1)	−46(5)(11)	−263(6)(19)
$^{119}\text{Sn}$	$1/2^+$	−5011(3)			−1.0448(1)		
$^{119}\text{Sn}$	$11/2^-$	−609.6(4)	−10(2)	−123(3)	−1.399(1)	−37(5)(9)	−175(4)(12)
$^{121}\text{Sn}$	$3/2^+$	+1115(2)		−39(3)	+0.698(1)		−56(4)(4)
$^{121}\text{Sn}$	$11/2^-$	−603.0(3)	−16(3)	−65(2)	−1.384(1)	−60(10)(16)	−93(3)(7)
$^{123}\text{Sn}$	$3/2^+$	+1153(2)		−17(3)	+0.722(1)		−24(4)(2)
$^{123}\text{Sn}$	$11/2^-$	−595.7(3)	−6(2)	−8(2)	−1.367(1)	−22(7)(8)	−12(3)(1)
$^{125}\text{Sn}$	$3/2^+$	+1179(2)		+13(4)	+0.738(1)		+18(6)(1)
$^{125}\text{Sn}$	$11/2^-$	−586.8(2)	+12(2)	+43(2)	−1.347(1)	+42(8)(12)	+61(2)(4)
$^{127}\text{Sn}$	$3/2^+$	+1190(3)		+37(9)	+0.745(2)		+53(13)(4)
$^{127}\text{Sn}$	$11/2^-$	−576.6(3)	+32(5)	+79(2)	−1.323(1)	+118(17)(30)	+111(3)(8)
$^{129}\text{Sn}$	$3/2^+$	+1190(2)		+64(4)	+0.745(2)		+90(6)(6)
$^{129}\text{Sn}$	$11/2^-$	−565.1(2)	+64(2)	+117(2)	−1.297(1)	+235(8)(50)	+166(3)(12)
$^{131}\text{Sn}$	$3/2^+$	+1195(1)		+62(2)	+0.748(1)		+88(2)(6)
$^{131}\text{Sn}$	$11/2^-$	−552.2(2)	+107(1)	+143(2)	−1.267(1)	+391(4)(81)	+203(3)(14)
		$5p6s\ ^3P_1^o$	$5p^2\ ^3P_0 \rightarrow 5p6s\ ^3P_1^o$	$5p6s\ ^1P_1^o$			
		$\frac{A(^1P_1^o)}{A(^3P_0^o)} = 0.0517(2)$	$\frac{B(^3P_0^o)}{B(^1P_1^o)} = -0.25(2)$			$\frac{\delta\nu(^1S_0 \rightarrow ^1P_1^o)}{\delta\nu(^3P_0 \rightarrow ^3P_1^o)} = 0.91(2)$	

Content of each column, from left to right: isotopes; measured nuclear spins  $I$  with parity assignments  $\pi$ ; magnetic dipole hyperfine constants  $A$  in the  $5p6s\ ^3P_1^o$  state; isomer shifts relative to the unique-parity state  $\delta\nu^{e,o} = \nu^{\text{odd-parity state}} - \nu^{\text{even-parity state}}$ , i.e., odd “o”–even “e”; electric quadrupole hyperfine constants  $B$  in the  $5p6s\ ^1P_1^o$  state; magnetic dipole moments  $\mu$  in nuclear magnetons  $\mu_N$ ; mean square charge-radii changes relative to the unique-parity state  $\delta\langle r^2 \rangle^{e,o} = \langle r^2 \rangle^{\text{odd-parity state}} - \langle r^2 \rangle^{\text{even-parity state}}$ ; electric quadrupole moments  $Q$  with systematic uncertainties from the computed electric-field gradient and the experimental field-shift factor shown in the second sets of parentheses. In the SI system of units,  $1\text{b} = 100\text{fm}^2 = 10^{-28}\text{m}^2$ .

**Isomer shifts.** A change in the nuclear mean square charge radius between a nuclear ground state and an isomer results in a common energy displacement of all levels in a given hyperfine multiplet. The combined effect in a transition between two atomic levels is manifested in spectra from laser spectroscopy as an apparent “isomer shift”. For example, in Fig. 6, this causes the pattern of peaks associated with the  $11/2^-$  state in the right column to “walk” towards higher frequencies in the heavier isotopes. The isomer (frequency) shift is a product of the electronic factor, related to a change in the total electronic charge density at the site of the nucleus, and a change in the nuclear mean square charge radius:

$$\delta\nu = F_1\delta\langle r^2 \rangle.$$

Distinction should be made between  $F_1$  and the total angular-momentum quantum number  $F$  introduced earlier. The effect from a change in the nuclear mass is negligible.

**Fitting of multiple spectra.** Routines for fitting multiple spectra were developed in the ROOT data analysis framework<sup>48</sup>, making use of the WrappedMultiTF1 class for enveloping individual fit functions under a common  $\chi^2$ . Spectra of the stable  $1/2^+$  ground states in  $^{115,117,119}\text{Sn}$ , free of quadrupole splitting, were used to determine the proportionality of  $A$  factors between the singlet and the triplet state. With this condition applied to the spectra of  $^{109}\text{Sn}$  and  $^{133}\text{Sn}$ , which are unperturbed by the presence of an isomer, one obtained the ratio of  $B$  factors. Individual masses were used for ground and isomeric states<sup>49</sup>. The isomer shifts were constrained to one another by a King plot<sup>50</sup> of data on the even–even isotopes. The three aforementioned ratios are presented in Table 1. Voigt line-shapes were used with a predominant Lorentzian component emerging from the fits. Resolved lines were fitted with free intensities. The heights of overlapping lines were locked to each other, or to other resolved lines when available, by using the Racah intensities. As constrained above, the fits fully determine the nuclear spins.

**Nuclear properties.** Using frequency ratios from the nuclear magnetic resonance of the  $1/2^+$  states in  $^{115,117,119}\text{Sn}$ <sup>51</sup>, and the latest evaluation of the magnetic moment of  $^{119}\text{Sn}$ <sup>18</sup> with an adopted uncertainty of 0.01%<sup>52</sup>, one arrives at a high-precision magnetic moment for each of the three isotopes, as given in Table 1. These in combination with their corresponding  $A$  factors in the triplet

state are used to determine the ratio  $A|\mu_N|/(h\mu) = 2396.6(7)$  MHz through a weighted mean, which is then used to extract magnetic moments for the rest of the isotopes. A small hyperfine-anomaly contribution of 0.05% (see the main text) is added in quadrature to the uncertainties of the  $11/2^-$  magnetic moments. The quadrupole moments are determined in the singlet state with the electric-field gradient  $B/(hQ) = 706(50)$  MHz/b from this work. Using the  $B$  ratio reported in Table 1, the electric-field gradient in the triplet state is found to be  $-173(17)$  MHz/b. Both are substantially stronger in comparison with semi-empirical estimates adopted in former studies<sup>53–55</sup>. This has had an impact on the results of a recent phenomenological analysis<sup>56</sup>. Mean square charge-radii changes are extracted in the triplet state with the field shift  $\delta\nu/\delta\langle r^2 \rangle = 0.274(57)$  MHz/ $\mu\text{b}$ <sup>37</sup>.

## Data availability

The authors declare that the data supporting this study are published within the paper as histograms in Fig. 6.

Received: 4 March 2020; Accepted: 2 April 2020;

Published online: 08 June 2020

## References

- Thoennessen, M. *The Discovery of Isotopes*. (Springer: Cham, Switzerland, 2016).
- Bohr, A. & Mottelson, B. R. *Nuclear Structure*, Vol. 2 (W. A. Benjamin, Inc.: Singapore, 1975).
- Reinhard, P.-G. & Otten, E. W. Transition to deformed shapes as a nuclear Jahn–Teller effect. *Nucl. Phys. A* **420**, 173 (1984).
- Nazarewicz, W. Microscopic origin of nuclear deformations. *Nucl. Phys. A* **574**, 27 (1994).
- Casten, R. F. *Nuclear Structure from a Simple Perspective*. (Oxford University Press: New York, 1990).
- Talmi, I. *Simple Models of Complex Nuclei*. (Harwood Academic Publishers: Switzerland, 1993).
- Talmi, I. The shell model—simplicity from complexity: some of my best nuclei are spherical. *Phys. Scr.* **92**, 083001 (2017).

8. Morales, I. O., Van Isacker, P. & Talmi, I. Generalized seniority and E2 transitions in the tin isotopes. *Phys. Lett. B* **703**, 606 (2011).
9. Stuchbery, A. E. Simple structures in complex nuclei versus complex structures in simple nuclei: a nuclear moments perspective. *J. Phys.: Conf. Ser.* **366**, 012042 (2012).
10. Morris, T. D. et al. Structure of the lightest tin isotopes. *Phys. Rev. Lett.* **120**, 152503 (2018).
11. Togashi, T., Tsunoda, Y., Otsuka, T., Shimizu, N. & Honma, M. Novel shape evolution in Sn isotopes from magic numbers 50 to 82. *Phys. Rev. Lett.* **121**, 062501 (2018).
12. Siciliano, M. et al. Pairing-quadrupole interplay in the neutron deficient tin nuclei: first lifetime measurements of low-lying states in  $^{106,108}\text{Sn}$ . Preprint at <https://arxiv.org/abs/1905.10313> (2019).
13. Zuker, A. P. Quadrupole dominance in light Cd and Sn isotopes. Preprint at <https://arxiv.org/abs/1905.11479> (2019).
14. Burbidge, E. M., Burbidge, G. R., Fowler, W. A. & Hoyle, F. Synthesis of the elements in stars. *Rev. Mod. Phys.* **29**, 547 (1957).
15. Neugart, R. et al. Collinear laser spectroscopy at ISOLDE: new methods and highlights. *J. Phys. G* **44**, 064002 (2017).
16. Köster, U. et al. Progress in ISOL target-ion source systems. *Nucl. Instrum. Methods Phys. Res., Sect. B* **266**, 4229 (2008).
17. Mané, E. et al. An ion cooler-buncher for high-sensitivity collinear laser spectroscopy at isolde. *Eur. Phys. J. A* **42**, 503 (2009).
18. Malkin, E., Komorovsky, S., Repisky, M., Demissie, T. B. & Ruud, K. The absolute shielding constants of heavy nuclei: resolving the enigma of the  $^{119}\text{Sn}$  absolute shielding. *J. Phys. Chem. Lett.* **4**, 459 (2013).
19. Jönsson, P., Gaigalas, G., Bieroń, J., Froese Fischer, C. & Grant, I. P. New version: GRASP2K relativistic atomic structure package. *Comput. Phys. Commun.* **184**, 2197 (2013).
20. Froese Fischer, C., Gaigalas, G., Jönsson, P. & Bieroń, J. GRASP2018—A Fortran 95 version of the general relativistic atomic structure package. *Comput. Phys. Commun.* **237**, 184 (2019).
21. Froese Fischer, C., Godefroid, M., Brage, T., Jönsson, P. & Gaigalas, G. Advanced multiconfiguration methods for complex atoms: I. Energies and wave functions. *J. Phys. B* **49**, 182004 (2016).
22. Grant, I. P. *Relativistic Quantum Theory of Atoms and Molecules. Theory and Computation.* (Springer-Verlag: NY, USA, 2007).
23. Tupitsyn, I. I. & Loginov, A. V. Use of Sturmian expansions in calculations of the hyperfine structure of atomic spectra. *Opt. Spectrosc.* **94**, 319 (2003).
24. Ekman, J., Li, J., Jönsson P., Godefroid M. & Gaigalas G. Modeling hyperfine anomalies using GRASP. *Proc. EOS workshop on Electronic Atomic Factors and Hyperfine Anomalies for Nuclear Physics* (Brussels, Belgium, 2019).
25. Yordanov, D. T. et al. Spins, electromagnetic moments, and isomers of  $^{107-129}\text{Cd}$ . *Phys. Rev. Lett.* **110**, 192501 (2013).
26. Yordanov, D. T. et al. Simple nuclear structure in  $^{111-129}\text{Cd}$  from atomic isomer shifts. *Phys. Rev. Lett.* **116**, 032501 (2016).
27. Frömngen, N. et al. Collinear laser spectroscopy of atomic cadmium. *Eur. Phys. J. D* **69**, 164 (2015).
28. Haas, H. Data re-evaluation. Private Communication (2019).
29. Bender, M., Heenen, P.-H. & Reinhard, P.-G. Self-consistent mean-field models for nuclear structure. *Rev. Mod. Phys.* **75**, 121 (2003).
30. Klüpfel, P., Reinhard, P.-G., Bürvenich, T. J. & Maruhn, J. A. Variations on a theme by Skyrme: a systematic study of adjustments of model parameters. *Phys. Rev. C* **79**, 034310 (2009).
31. Miller, A. J., Minamisono, K. & Klose, A. et al. Proton superfluidity and charge radii in proton-rich calcium isotopes. *Nat. Phys.* **15**, 432 (2019).
32. Fayans, S. A. Towards a universal nuclear density functional. *JETP Lett.* **68**, 169 (1998).
33. Fayans, S. A., Tolokonnikov, S. V., Trykov, E. L. & Zawischa, D. Nuclear isotope shifts within the local energy-density functional approach. *Nucl. Phys. A* **676**, 49 (2000).
34. Reinhard, P.-G. & Nazarewicz, W. Toward a global description of nuclear charge radii: exploring the Fayans energy density functional. *Phys. Rev. C* **95**, 064328 (2017).
35. Ring, P. & Schuck, P. *The Nuclear Many-Body Problem.* (Springer-Verlag: Berlin, 1980).
36. Hammen, M. & Nörtershäuser, W. et al. From calcium to cadmium: testing the pairing functional through chargeradii measurements of  $^{100-130}\text{Cd}$ . *Phys. Rev. Lett.* **121**, 102501 (2018).
37. Gorges, C. et al. Laser spectroscopy of neutron-rich tin isotopes: a discontinuity in charge radii across the  $N = 82$  shell closure. *Phys. Rev. Lett.* **122**, 192502 (2019).
38. Zhao, P. W., Zhang, S. Q. & Meng, J. Explanation of the simplicity of the quadrupole moments recently observed in Cd isotopes from covariant density functional theory. *Phys. Rev. C* **89**, 011301(R) (2014).
39. Yordanov, D. T. et al. Spins and electromagnetic moments of  $^{101-109}\text{Cd}$ . *Phys. Rev. C* **98**, 011303(R) (2018).
40. Federman, P. & Pittel, S. Unified shell-model description of nuclear deformation. *Phys. Rev. C* **20**, 820 (1979).
41. Dobaczewski, J., Nazarewicz, W., Skalski, J. & Werner, T. Nuclear deformation: a proton–neutron effect? *Phys. Rev. Lett.* **60**, 2254 (1988).
42. Esat, M. T., Kean, D. C., Spear, R. H. & Baxter, A. M. Mass dependence of the static quadrupole moments of the first  $2^+$  states in the cadmium isotopes. *Nucl. Phys. A* **274**, 237 (1976).
43. Allmond, J. M. et al. Investigation into the semimagic nature of the tin isotopes through electromagnetic moments. *Phys. Rev. C* **92**, 041303(R) (2015).
44. Neyens, G. Nuclear magnetic and quadrupole moments for nuclear structure research on exotic nuclei. *Rep. Prog. Phys.* **66**, 633 (2003).
45. Ferrer, R. et al. Towards high-resolution laser ionization spectroscopy of the heaviest elements in supersonic gas jet expansion. *Nat. Commun.* **8**, 14520 (2017).
46. Sels, S. et al. Shape staggering of midshell mercury isotopes from in-source laser spectroscopy compared with density-functional-theory and Monte Carlo shell-model calculations. *Phys. Rev. C* **99**, 044306 (2019).
47. Magnante, P. C. & Stroke, H. H. Isotope shift between  $^{209}\text{Bi}$  and 6.3-day  $^{206}\text{Bi}$ . *J. Opt. Soc. Am.* **59**, 836 (1969).
48. Brun, R. & Rademakers, F. ROOT—an object oriented data analysis framework. *Nucl. Instrum. Methods Phys. Res., Sect. A* **389**, 81 (1997).
49. Audi, G., Kondev, F. G., Wang, M., Huang, W. J. & Naimi, S. The NUBASE2016 evaluation of nuclear properties. *Chin. Phys. C* **41**, 030001 (2017).
50. King, W. H. Comments on the article: Peculiarities of the isotope shift in the samarium spectrum. *J. Opt. Soc. Am.* **53**, 638 (1963).
51. Makulski, W. Tetramethyltin study by NMR spectroscopy in the gas and liquid phase. *J. Mol. Struct.* **1017**, 45 (2012).
52. Makulski, W., Jackowski, K., Antušek, A. & Jaszuski, M. Gas-phase NMR measurements, absolute shielding scales, and magnetic dipole moments of  $^{29}\text{Si}$  and  $^{73}\text{Ge}$  nuclei. *J. Phys. Chem. A* **110**, 11462 (2006).
53. Anselmetti, M. et al. Charge radii and moments of tin nuclei by laser spectroscopy. *Phys. Rev. C* **34**, 1052 (1986).
54. Le Blanc, F. et al. Charge-radius change and nuclear moments in the heavy tin isotopes from laser spectroscopy: charge radius of  $^{132}\text{Sn}$ . *Phys. Rev. C* **72**, 034305 (2005).
55. Eberz, J. et al. Nuclear spins, moments and charge radii of  $^{108-111}\text{Sn}$ . *Z. Phys. A* **326**, 121 (1987).
56. Maheshwari, B., Abu Kassim, H., Yusuf, N. & Jain, A. K. Evolution of nuclear structure in and around  $Z = 50$  closed shell: generalized seniority in Cd, Sn and Te isotopes. *Nucl. Phys. A* **992**, 121619 (2019).
57. Raghavan, P. Table of nuclear moments. *At. Data Nucl. Data Tables* **42**, 189 (1989).

## Acknowledgements

The authors thank the ISOLDE technical group for their professional assistance and Heinz Haas for re-evaluating the quadrupole moments of the very short-lived isomers in  $^{113,115,119}\text{Sn}$ . This work has been supported by the Max Planck Society, the German Federal Ministry for Education and Research under Contract No. 05P15RDCIA, the Helmholtz International Center for FAIR within the LOEWE program by the State of Hesse, the Belgian IAP Project No. P7/12, the FWO-Vlaanderen, GOA 15/010 from KU Leuven, the European Union seventh framework through ENSAR under Contract No. 262010, the Science and Technology Facilities Council (ST/P004423/1 and ST/P004598/1), and by the Office of Science, U.S. Department of Energy under Grant Nos. DE-SC0013365 and DE-SC0018083 (NUCLEI SciDAC-4 Collaboration). D.L.B. acknowledges support from the EU Development Fund and Competitiveness Operational Program for the ELI-NP Project Phase II (1/07.07.2016, COP, ID1334), M.R.G. from the FWO & FNRS Excellence of Science Programme (EOS-0022818F), A.P., J.E., and P.J. from the Swedish Research Council (VR) under Contract No. 2015-04842, and P.P. from the Magnus Ehrnrooth Foundation.

## Author contributions

M.L.B., R.F.G.R., C.G., H.H., S.K., V.L., S.L., S.M.-E., L.V.R., S. Sailer, L.X., X.Y., and D.T.Y. prepared the instrumentation and contributed to the on-line measurements along with D.L.B., K.B., B.C., G. Georgiev, W.G., A.K., B.M., R.N., G.N., W. Nörtershäuser, R.S., S. Schmidt, L.W., C.W., and Z.X. L.V.R. developed routines for the fitting of multiple spectra. Nuclear DFT analysis was carried out by W. Nazarewicz and P.-G.R. J.B., J.E., G. Gaigalas, M.R.G., Z.H., P.J., C.H.K., N.S.O., A.P., P.P., and S. Schifffmann contributed to the ab initio large-scale MCDHF and CI-DFS calculations of the relevant electronic parameters and to their reliability assessment. J.E. computed the hyperfine anomalies.

D.T.Y. proposed the measurements and prepared the manuscript with input from all authors. These results are part of the PhD theses of C.G. and L.V.R.

### Competing interests

The authors declare no competing interests.

### Additional information

**Correspondence** and requests for materials should be addressed to D.T.Y.

**Reprints and permission information** is available at <http://www.nature.com/reprints>

**Publisher's note** Springer Nature remains neutral with regard to jurisdictional claims in published maps and institutional affiliations.



**Open Access** This article is licensed under a Creative Commons Attribution 4.0 International License, which permits use, sharing, adaptation, distribution and reproduction in any medium or format, as long as you give appropriate credit to the original author(s) and the source, provide a link to the Creative Commons license, and indicate if changes were made. The images or other third party material in this article are included in the article's Creative Commons license, unless indicated otherwise in a credit line to the material. If material is not included in the article's Creative Commons license and your intended use is not permitted by statutory regulation or exceeds the permitted use, you will need to obtain permission directly from the copyright holder. To view a copy of this license, visit <http://creativecommons.org/licenses/by/4.0/>.

© The Author(s) 2020



## Paper VI

A. Papoulia, S. Schiffmann, J. Bieroń, G. Gaigalas, M. Godefroid, Z. Harman, P. Jönsson, N. S. Oreshkina, P. Pyykkö, and I. I. Tupitsyn

*Ab initio* electronic factors of the *A* and *B* hyperfine structure constants for the  $5s^25p6s\ ^1,^3P_1^o$  states in Sn I

*Physical Review A*, 2021, 103(2), 022815

Copyright 2021 American Physical Society



## *Ab initio* electronic factors of the *A* and *B* hyperfine structure constants for the $5s^25p6s\ 1^3P_1^o$ states in Sn I

Asimina Papoulia<sup>1,2,\*</sup>, Sacha Schiffmann<sup>2,3,\*</sup>, Jacek Bieroń<sup>4</sup>, Gediminas Gaigalas<sup>5</sup>, Michel Godefroid<sup>3</sup>, Zoltán Harman<sup>6</sup>, Per Jönsson<sup>1</sup>, Natalia S. Oreshkina<sup>6,§</sup>, Pekka Pyykkö<sup>7</sup>, and Ilya I. Tupitsyn<sup>8</sup>

<sup>1</sup>Department of Materials Science and Applied Mathematics, Malmö University, SE-20506 Malmö, Sweden

<sup>2</sup>Division of Mathematical Physics, Department of Physics, Lund University, SE-22100 Lund, Sweden

<sup>3</sup>Spectroscopy, Quantum Chemistry and Atmospheric Remote Sensing (SQUARES), CP160/09, Université libre de Bruxelles (ULB), 1050 Brussels, Belgium

<sup>4</sup>Instytut Fizyki Teoretycznej, Uniwersytet Jagielloński, ul. prof. Stanisława Łojasiewicza 11, Kraków, Poland

<sup>5</sup>Institute of Theoretical Physics and Astronomy, Vilnius University, Saulėtekio av. 3, LT-10222, Vilnius, Lithuania

<sup>6</sup>Max Planck Institute for Nuclear Physics, Saupfercheckweg 1, 69117 Heidelberg, Germany

<sup>7</sup>Department of Chemistry, University of Helsinki, PO Box 55 (A. I. Virtasen aukio 1), FIN-00014 Helsinki, Finland

<sup>8</sup>Department of Physics, St. Petersburg State University, 198504 St. Petersburg, Russia



(Received 22 July 2020; revised 18 December 2020; accepted 11 January 2021; published 12 February 2021)

Large-scale *ab initio* calculations of the electronic contribution to the electric quadrupole hyperfine constant *B* were performed for the  $5s^25p6s\ 1^3P_1^o$  excited states of neutral tin. To probe the sensitivity of *B* to different electron correlation effects, three sets of variational multiconfiguration Dirac-Hartree-Fock and relativistic configuration interaction calculations employing different strategies were carried out. In addition, a fourth set of calculations was based on the configuration interaction Dirac-Fock-Sturm theory. For the  $5s^25p6s\ 1^3P_1^o$  state, the final value of  $B/Q = 703(50)$  MHz/b differs by 0.4% from the one recently used by Yordanov *et al.* [*Commun. Phys.* **3**, 107 (2020)] to extract the nuclear quadrupole moments *Q* for tin isotopes in the range  $^{117-131}\text{Sn}$  from collinear laser spectroscopy measurements. Efforts were made to provide a realistic theoretical uncertainty for the final  $B/Q$  value of the  $5s^25p6s\ 1^3P_1^o$  state based on statistical principles and on correlation with the electronic contribution to the magnetic dipole hyperfine constant *A*.

DOI: 10.1103/PhysRevA.103.022815

### I. INTRODUCTION

The uninterrupted developments of computational methodologies [1–3], together with the growing computational resources at the disposal of atomic physicists, have increased tremendously the accuracy of atomic structure calculations in the past decades [4–11]. Theoretical predictions of atomic properties have, therefore, become efficient tools to support the corresponding experimental measurements. This is exemplified by the recent precision measurements of hyperfine structures [12–15]. In atoms, the hyperfine structure splittings are, to the lowest orders, described by the magnetic dipole (M1) and electric quadrupole (E2) hyperfine coupling constants *A* and *B*, respectively. The *A* constant arises from the interaction of the nuclear magnetic dipole moment  $\mu_I$ , with the magnetic field generated by the electrons at the site of the nucleus. At the same time, the *B* constant is the result of the interaction between the nuclear electric quadrupole moment *Q* and the electric field gradient (EFG), which reflects the electronic charge distribution in the vicinity of the nucleus.

The quadrupole moments *Q* are important characteristics of nuclei that provide a measure of the deviation of the nuclear charge distribution from a spherical shape. In general, they can be determined from nuclear, atomic, molecular, or solid-state spectroscopies, such as high-resolution laser spectroscopy [12], muonic or pionic x-ray spectroscopy [16], nuclear magnetic resonance (NMR) [17,18], nuclear quadrupole resonance (NQR) [19,20], Mössbauer measurements [21,22], or perturbed angular correlation (PAC) of nuclei passing thin foils [23,24]. Most of these techniques require to evaluate the electronic contribution  $B/Q$  to the E2 hyperfine constant. The accuracy of the extracted *Q* values is, therefore, strongly affected by the uncertainties in the calculations of this electronic property. Three compilations of available *Q* values are provided by Raghavan [25], Stone [26], and Pyykkö [27].

In this work, we focus on tin, with an atomic number  $Z = 50$ . All proton shells at this magic number are closed, but the incomplete neutron shells can still induce a *Q* with quadratic dependence on the neutron number *N*, which will not become magic until the  $^{132}\text{Sn}$  isotope, with  $N = 82$  and nuclear spin  $I = 0$ . The nuclear trends of the *Q* moments among 8 isotopes in the range  $^{117-131}\text{Sn}$ , which is below the doubly magic isotope, have just recently been published by Yordanov *et al.* [12]. The  $Q(\text{Sn})$  values given in Ref. [12] were based on measured atomic hyperfine structures for odd-*N* isotopes. More specifically, they were obtained by combining

\*These authors contributed equally to this work.

†asimina.papoulia@mau.se

‡saschiff@ulb.ac.be

§natalia.oreshkina@mpi-hd.mpg.de

the measured  $B$  constant in the  $[\text{Pd}]5s^25p6s\ ^1P_1^o$  state<sup>1</sup> of the neutral atom (Sn I), for each isotope, with the calculated electronic contribution  $B/Q$ . The  $B/Q$  value resulted from the three independent multiconfiguration Dirac-Hartree-Fock (MCDHF) and relativistic configuration interaction (RCI) calculations [28,29] reported in this work. The relative accuracy of the calculated  $B/Q$  is of the order of 7%, while the accuracy of the measured  $B$  constants varies, depending on the isotope, between 1.5% for  $^{131}\text{Sn}$  and 33% for  $^{125}\text{Sn}$ , as also reflected in Table 1 of Ref. [12]. As a result, the accuracy of the evaluated  $Q(\text{Sn})$  values ranges between 7% and 34%.

In Ref. [12], the focus was on the description of the experimental methods and the interpretation of the nuclear physics results. The aim of this work is to provide the details of the employed MCDHF-RCI computational methodologies for evaluating the electronic contribution  $B/Q$  for the  $5s^25p6s\ ^1,^3P_1^o$  excited states in Sn I. Additionally, the inferred  $B/Q$  values from averaging the individual results of the three independent series of MCDHF-RCI calculations are validated by a fourth set of calculations, based on the configuration interaction Dirac-Fock-Sturmian (CI-DFS) theory [30–34]. After taking into account the results from this new set of calculations, the final  $B/Q$  value for the  $^1P_1^o$  state is slightly shifted from 706(50) MHz/b in Ref. [12]<sup>2</sup> to 703(50) MHz/b in this work. Aside from the E2 hyperfine electronic contributions, the electronic parts  $A_I/\mu_I$  of the M1 hyperfine constants were also calculated for the same  $^1,^3P_1^o$  states. The correlation between the M1 and E2 hyperfine structures was used as a tool to evaluate the theoretical uncertainty of the  $B/Q$  value for the  $^1P_1^o$  state.

Due to the sensitivity of the hyperfine electronic factors to different electron correlation effects, one must often perform more than one set of calculations, which follow different computational strategies and correlation models, to be in a position to evaluate the accuracy of the results [35]. That being the case, a detailed description of the employed computational strategies is deemed necessary to better understand the contributions from the different correlation effects in systems with similar electronic structure and to, eventually, advance the current computational methods and computer codes.

In Sec. II, the underlying theories of the MCDHF-RCI and CI-DFS methods are briefly described. In the same section, the forms of the M1 and E2 hyperfine interaction operators that are used to compute the electronic contributions to the hyperfine structure constants  $A$  and  $B$  are given. In Sec. III, the computational details and results from the four independent sets of calculations are discussed. These results are combined in Sec. IV to provide the final  $B/Q$  value for the  $^1P_1^o$  state and its associated theoretical uncertainty. The resulting  $B/Q$  value is, then, used in Sec. V to reextract the nuclear quadrupole moment  $Q$  of the  $^{119}\text{Sn}$  isotope. Finally, our concluding remarks are presented in Sec. VI.

<sup>1</sup>[Pd] is used, for brevity, to indicate the 46-electron palladiumlike core and will be omitted in the following.

<sup>2</sup>Although the electronic contribution  $B/Q$  is proportional to the computed EFG value (see also Sec. II C), one should note that, in Ref. [12], the quantities EFG and  $B/Q$  are used interchangeably.

## II. THEORY

### A. MCDHF-RCI multiconfiguration methods

The principles of the MCDHF-RCI method are fully discussed in, e.g., the book by Grant [28] and the review article by Froese Fischer *et al.* [29]. With this section, we provide the reader with a short introduction of the main concepts, as implemented in the GRASP2K [36] and GRASP2018 [1] computer packages that were used to perform the calculations presented in Sec. III A.

In the relativistic framework, the MCDHF method describes an atomic state function (ASF),  $\Psi(\gamma\Pi JM)$ , as an expansion over a set of  $jj$ -coupled relativistic CSFs,  $\Phi_\mu(\gamma_\mu\Pi JM)$ , characterized by the parity  $\Pi$ , the total electronic angular momentum  $J$ , and the projection quantum numbers  $M$ , i.e.,

$$\Psi(\gamma\Pi JM) = \sum_{\mu=1}^{N_{\text{CSFs}}} c_\mu \Phi_\mu(\gamma_\mu\Pi JM), \quad (1)$$

$$\text{where } \sum_{\mu=1}^{N_{\text{CSFs}}} c_\mu^2 = 1.$$

The CSFs are antisymmetrized many-electron functions built from one-electron Dirac orbitals. In the expression above,  $\gamma_\mu$  represents the configuration, the angular momentum coupling tree, and other quantum numbers that are necessary to uniquely describe each CSF.

In the MCDHF method, the radial parts of the Dirac orbitals and the mixing coefficients  $c_\mu$  are computed in a self-consistent field (SCF) procedure. The SCF radial equations to be iteratively solved are derived from the application of the variational principle on a weighted Dirac-Coulomb energy functional of the targeted atomic states according to the extended optimal level scheme (EOL) [37]. The angular integrations needed for the construction of the energy functional are based on the second quantization formalism in the coupled tensorial form [38,39].

The MCDHF calculations provide the one-electron orbital basis, which, in the subsequent relativistic configuration interaction (RCI) calculations, is used to determine the final wave functions  $\Psi(\gamma\Pi JM)$  by diagonalizing the interaction matrix. At this RCI step, the transverse photon interaction, which reduces to the Breit interaction at the low-frequency limit, and the leading quantum electrodynamic (QED) corrections are added to the Dirac-Coulomb Hamiltonian (see Refs. [40,41] for more details). In the RCI calculations, the atomic-state expansions are usually augmented by CSFs that capture additional electron correlation effects.

### B. CI-DFS method

The detailed description of the CI-DFS method can be found in Refs. [30–34]. We highlight hereafter the most important underlying theoretical background.

Dirac-Fock-Sturm orbitals of a general type  $\varphi_j$  can be obtained as the solutions of the following eigenvalue problem:

$$(h_D - \varepsilon)\varphi_j = \lambda_j W(r)\varphi_j, \quad (2)$$



where  $h_D$  is the one-electron Dirac Hamiltonian,  $W(r)$  is a weight function,  $\varepsilon$  is a reference energy, and  $\lambda_j$  is the eigenvalue. Following Refs. [30,31], we adopt the weight function

$$W(r) = \left[ \frac{1 - \exp[-(\beta r)^2]}{(\beta r)^2} \right], \quad (3)$$

where the parameter  $\beta$  is chosen to speed up the convergence of the Sturmian series. The set of Sturmian eigenfunctions forms a discrete and complete orthonormalized basis set of one-electron wave functions with weight  $W(r)$ , which are used as virtual orbitals in subsequent calculations.

The next step is the construction of an orthonormalized set of one-electron wave functions from the solutions of the DF equations in the DFS orbital basis. One-electron wave functions that were previously obtained using the DF method stay intact, whereas the virtual Sturmian orbitals are modified to be eigenfunctions of the DF operator and they can, thus, be used for the construction of determinants in the configuration interaction (CI) method.

### C. Hyperfine structure

The hyperfine structure contribution to the Hamiltonian is represented by a multipole expansion

$$H_{\text{hfs}} = \sum_{k \geq 1} \mathbf{T}^{(k)} \cdot \mathbf{M}^{(k)}, \quad (4)$$

where  $\mathbf{T}^{(k)}$  and  $\mathbf{M}^{(k)}$  are spherical tensor operators of rank  $k$  in the electronic and nuclear spaces, respectively. The  $k = 1$  and 2 terms represent the M1 and E2 interactions. In the fully relativistic approach, the electronic contributions are obtained from the expectation values of the irreducible spherical tensor operators [42,43]

$$\mathbf{T}^{(1)} = -i\alpha \sum_{j=1}^{N_e} (\boldsymbol{\alpha}_j \cdot \mathbf{I}_j) \mathbf{C}^{(1)}(j) \frac{1}{r_j^2} \quad (5)$$

and

$$\mathbf{T}^{(2)} = - \sum_{j=1}^{N_e} \mathbf{C}^{(2)}(j) \frac{1}{r_j^3}, \quad (6)$$

where  $\mathbf{I}$  is the electronic orbital angular momentum and  $\mathbf{C}^{(1)}$  and  $\mathbf{C}^{(2)}$  are the renormalized spherical harmonics of rank 1 and 2, respectively.

The hyperfine structure splitting for a state  $J$  is normally expressed in terms of the  $A$  and  $B$  hyperfine constants, respectively, given by

$$A = \frac{\mu_I}{I} \frac{1}{\sqrt{J(J+1)(2J+1)}} \langle \Psi || \mathbf{T}^{(1)} || \Psi \rangle \quad (7)$$

and

$$B = 2Q \sqrt{\frac{J(2J-1)}{(J+1)(2J+1)(2J+3)}} \langle \Psi || \mathbf{T}^{(2)} || \Psi \rangle \quad (8)$$

In the equations above, we adopted the definition of the reduced matrix element, which is compatible with the Wigner-Eckart theorem of Edmonds [44], as used in most of the

atomic physics textbooks. For later use, we introduce the  $A_{\text{el}}$  and  $B_{\text{el}}$  electronic factors of the hyperfine constants, i.e.,

$$A_{\text{el}} = AI/\mu_I \text{ [MHz}/\mu_N], \quad (9)$$

$$B_{\text{el}} = B/Q \text{ [MHz/b]}, \quad (10)$$

assuming that  $A$  and  $B$  are expressed in MHz,  $\mu_I$  in nuclear magnetons ( $\mu_N$ ) and  $Q$  in barns (b). Given the electronic factors, the hyperfine constants  $A$  and  $B$  can easily be evaluated for a given isotope characterized by the  $(\mu_I, I, Q)$  set of nuclear parameters.

Due to the extended magnetic and charge distributions of the nucleus, respectively, resulting in the Bohr-Weisskopf (BW) and the Breit-Rosenthal-Crawford-Schawlow (BR) corrections, the quantity  $A_{\text{el}}$  is not purely electronic. A change in these nuclear structure properties for different isotopes contributes to the hyperfine anomaly, which is particularly important for extracting magnetic dipole moments from experimental measurements [45]. However, the BW effect was estimated, in the CI-DFS calculations, to be  $<0.1\%$  for both considered states (see also Sec. III B). Additionally, as shown in Ref. [12], the hyperfine anomaly along the tin isotope sequence remains small. An analogous effect takes place when computing the quantity  $B_{\text{el}}$  and it was also estimated to be  $<0.1\%$  for the states in question (see Sec. III B for details). In all four independent sets of calculations presented in this work, the BR correction was included by using the Fermi model approximation for the nuclear charge distribution. It should be mentioned that the  $B_{\text{el}}$  factor is proportional to the EFG, also denoted  $q$ . Expressing the latter in  $a_0^{-3}$  and  $B_{\text{el}}$  in MHz/b, the conversion factor should be

$$B_{\text{el}}[\text{MHz/b}] = 234.9646 q [a_0^{-3}] \quad (11)$$

where the latter is often given in theoretical works [46].

## III. CALCULATIONS

In this section, we report the computational details of the three independent sets of MCDHF-RCI calculations and the fourth set of CI-DFS calculations that were carried out. The respective values of the computed isotope-independent hyperfine structure constants  $A_{\text{el}}$  and  $B_{\text{el}}$  are, then, presented and analyzed. Experimental data (see, e.g., Ref. [12]) and state compositions indicate that the hyperfine structure in Sn 1 is characterized by a substantial E2 splitting in the  $^1P_1^0$  state and a large M1 splitting in the  $^3P_1^0$  state. For this reason, in what follows, we only display the  $A_{\text{el}}[^3P_1^0]$  and  $B_{\text{el}}[^1P_1^0]$  values. Nonetheless, the computed  $A_{\text{el}}[^1P_1^0]$  and  $B_{\text{el}}[^3P_1^0]$  values are still used (see Sec. III A 4) for evaluating the ratios of the  $A_{\text{el}}$  and  $B_{\text{el}}$  factors between the two states and for further comparing with the corresponding experimental values deduced in Ref. [12].

### A. MCDHF-RCI calculations

The accuracy of the MCDHF-RCI multiconfiguration calculation relies on how the atomic-state expansions of Eq. (1) are built. A first approximation of the atomic states is obtained by performing a MCDHF calculation on expansions that are built from one, or more, reference configurations. These configurations are associated with the targeted atomic states

TABLE I. The sequence of layers of correlation orbitals optimized in the S-MR3-MCDHF and S-MR4-MCDHF calculations. The former optimization scheme is based on S substitutions from the MR3 set of reference configurations, i.e.,  $\{5s^25p6s, 5s^25p5d, 5s5p^3\}$ , whereas the latter scheme also includes the  $5s^25p7s$  configuration in the so-called MR4 multireference. When all four configurations are included in the MR, the  $7s$  orbital is part of the spectroscopic orbitals and it is, thus, placed in parentheses in row 3, which displays the  $i = 2$  correlation orbital layer. In columns 3 and 4, the numbers of generated CSFs,  $N_{\text{CSFs}}$ , are, respectively, given for each of the two different optimization schemes. Columns 5 and 6 display the number of CSFs for the subsequent RCI calculations when additional VV correlations have been accounted for by D substitutions from the valence orbitals.

$i$	Layers of correlation orbitals	$N_{\text{CSFs}}$		$N_{\text{CSFs, RCI}}$	
		MR3	MR4	MR3	MR4
	None (MR)	9	11		
1	$6p, 4f$	2097	2479	2570	3093
2	$(7s), 7p, 6d, 5f$	4349	4820	6574	7295
3	$8s, 8p, 7d, 6f, 5g$	7054	7886	13 195	14 789
4	$9s, 9p, 8d, 7f, 6g$	9759	10 952	21 904	24 689
5	$10s, 10p, 9d, 8f, 7g, 6h$	12 563	14 120	34 056	38 498
6	$11s, 11p, 10d, 9f, 8g, 7h$	15 367	17 288	49 038	55 551
7	$12s, 12p, 11d, 10f, 9g, 8h, 7i$	18 242	20 529	68 286	77 435
8	$13s, 13p, 12d, 11f, 10g, 9h, 8i$	21 117	23 770	91 108	103 403

and can be merged with important closely degenerate configurations, forming the multi-reference (MR) space. When only one configuration is considered, the latter reduces to a single-reference (SR) space. Applying the rules for coupling angular momenta, the reference configurations produce a number of CSFs that account for the major electron correlation effects or else what is known as static correlation [29]. The spectroscopic (occupied) orbitals that take part in this initial calculation are kept frozen in all following MCDHF and RCI calculations.

The initial approximation of the wave functions is improved by gradually augmenting the atomic-state expansions with CSFs that interact, i.e., have nonzero matrix elements, with the ones that are generated by the reference configurations. These CSFs are, due to the one- and two-body character of the Hamiltonian, obtained from configurations generated by allowing single (S) and, possibly, double (D) substitutions from orbitals of the configurations in the MR to an active set (AS) of correlation orbitals. The AS is systematically increased by introducing, at each step, a layer of correlation orbitals consisting of at most one orbital per angular symmetry. The correlation orbital layers in the AS are optimized in successive MCDHF calculations, in which the previously generated orbitals are kept frozen. It should, therefore, be highlighted that the correlation orbitals of the MCDHF-RCI methods differ from the virtual orbitals of the CI-DFS method in that the former orbitals are variationally optimized through the MCDHF procedure, while the latter orbitals are generated according to Eq. (2).

The CSFs can, based on the nature of the SD substitutions, be classified into CSFs that capture valence-valence (VV), core-valence (CV), and core-core (CC) electron correlation effects [[47], p.71]. The radial orbital basis is obtained by performing MCDHF calculations, where all, or some, of these classes of CSFs are taken into account. Additional electron correlation effects, captured by CSFs formed from higher-order substitutions, i.e., triple (T), quadruple (Q), etc., can be considered in the subsequent RCI calculations. In general, the selection of the CSFs that take part in the MCDHF and RCI

calculations depends on the shell structure of the atom at hand and the atomic properties under investigation.

The computations of the hyperfine factors  $A_{\text{el}}$  and  $B_{\text{el}}$  are usually challenging due to their high sensitivity to different electron correlation effects. To investigate and assess the role of the separate electron correlation contributions, three alternative MCDHF-RCI computational approaches were employed in this work. Below, we describe the three independent multiconfiguration calculations and present their individual results.

### 1. S-MR-MCDHF calculations

In this first computational approach, the MCDHF calculations were performed with CSF expansions that were produced by allowing S substitutions from an MR set of configurations. Due to the one-body nature of the hyperfine operators (5) and (6), the S substitutions play an important role in the calculations of hyperfine structures. This also agrees with the perturbative analysis conducted, e.g., in Ref. [48]. CSFs generated by S substitutions interact with at least one of the CSFs built from the MR configurations. By using more than one reference configuration, the current computational strategy further takes into account important D and T substitutions from the targeted  $5s^25p6s$  configuration. The T substitutions are quite crucial. The latter may be decomposed into D substitutions followed by S substitutions. CSFs built from configurations that differ by T substitutions from the targeted configuration, thus, interact through the one-body hyperfine operators with the energetically important CSFs generated by D substitutions.

Two separate S-MR-MCDHF calculations were performed, using different MR spaces, which are, respectively, denoted MR3 and MR4. Aside from the  $5s^25p6s$  configuration of the targeted states, the MR3 set incorporates the  $5s^25p5d$  and  $5s5p^3$  configurations. The  $5s5p^3$  configuration was found to strongly influence the odd levels of Sn I due to its large mixing [49]. The MR4 set further includes the  $5s^25p7s$  configuration accounting for the  $LS$ -term dependence [47],

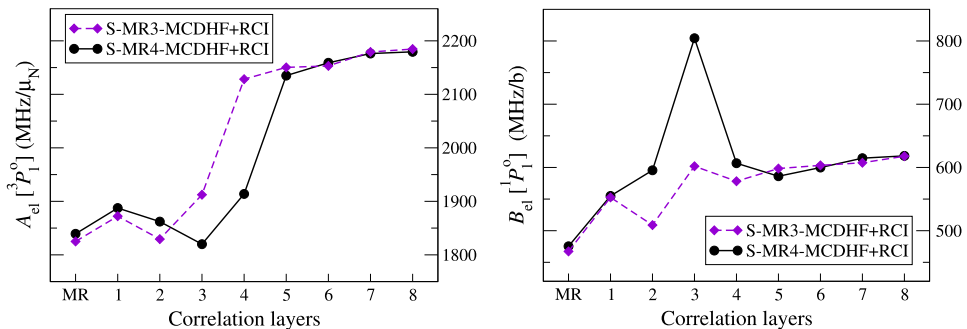


FIG. 1. The convergence patterns of the electronic hyperfine factors  $A_{el}[{}^3P_1^0]$  (in MHz/ $\mu_N$ ) and  $B_{el}[{}^1P_1^0]$  (in MHz/b) as functions of the correlation orbital layers. The radial orbital basis was obtained by applying two different optimization schemes with respect to the selected MR spaces. The purple dashed lines connect the values resulting from the S-MR3-MCDHF optimization, where three reference configurations are included in the MR, and the black solid lines link the resulting values from the S-MR4-MCDHF optimization, where the MR was extended to include four reference configurations. Both sets of values are the results from the RCI calculations that followed the orbital optimization step. For further details, see text in Sec. III A 1.

i.e., the difference between the  $6s$  orbital of the  $5s^25p6s\ {}^3P_1^0$  and  $5s^25p6s\ {}^1P_1^0$  states. The calculations are performed in the EOL scheme for the average of the configuration states included in the MR.

In both S-MR-MCDHF calculations, all spectroscopic orbitals were opened for S substitutions. The layers of correlation orbitals that were progressively added to the AS are shown in column 2 of Table I. In total, eight correlation orbital layers were built, corresponding to the  $13s13p12d11f10g9h8i$  set of orbitals. For every additional correlation orbital layer  $i$ , the resulting numbers of CSFs,  $N_{CSFs}$ , in the MR3 and MR4 optimization schemes are, respectively, given in columns 3 and 4 of Table I. As seen in Table I, the configurations in each of the MR3 and MR4 sets generate 9 and 11 CSFs.

The RCI calculations included CSFs that were produced by allowing D substitutions from the valence orbitals of the configurations in the MR. In this manner, VV electron correlation effects were ultimately captured. D substitutions from core orbitals were not considered to keep the number of CSFs at a manageable level. The numbers of CSFs for the RCI calculations are given in columns 5 and 6 of Table I.

The resulting values of the hyperfine electronic factors  $A_{el}[{}^3P_1^0]$  and  $B_{el}[{}^1P_1^0]$  from applying the two different optimization schemes are shown in Fig. 1 with the labels S-MR3-MCDHF+RCI and S-MR4-MCDHF+RCI, respectively. As seen in Fig. 1, both computed electronic factors are effectively converged. For the largest CSF expansions, the variations between the S-MR3-MCDHF+RCI and S-MR4-MCDHF+RCI results are insignificant. As the final results of this first MCDHF-RCI computational approach, we take the resulting values from the largest S-MR4-MCDHF+RCI calculation, corresponding to expansions with 103 403 CSFs, so that

$$A_{el}[{}^3P_1^0] = 2180 \text{ MHz}/\mu_N; \quad B_{el}[{}^1P_1^0] = 622 \text{ MHz/b.} \quad (12)$$

## 2. SrD-SR-MCDHF calculations

In the second computational approach, the MCDHF calculations were performed in the EOL scheme for the average of the  $5s^25p6s\ {}^1,3P_1^0$  states using CSF expansions that were produced by S and restricted double (rD) substitutions from the SR configuration of the targeted states, i.e.,  $5s^25p6s$ .

More specifically, S substitutions from all spectroscopic orbitals and D substitutions, restricted by the limitation of leaving maximum one hole in core orbitals with  $n < 5$ , were enabled. In this manner, the generated CSFs in the orbital optimization phase also captured CV correlation effects. The AS was systematically increased to include layers with one additional correlation orbital of the  $s$ ,  $p$ ,  $d$ ,  $f$ , and  $g$  angular symmetries, respectively, apart from the very last, eighth, layer, which only contained the  $s$ ,  $p$ ,  $d$ , and  $f$  symmetries. The largest multiconfiguration expansions were then built on the  $14s13p12d11f11g$  set of orbitals. For every layer of correlation orbitals that was added in the SrD orbital optimization phase, the resulting values of the electronic factors  $A_{el}[{}^3P_1^0]$  and  $B_{el}[{}^1P_1^0]$  are shown in Fig. 2 (magenta circles). We note that, after adding the sixth layer of correlation orbitals, both the  $A_{el}[{}^3P_1^0]$  and  $B_{el}[{}^1P_1^0]$  values were converged. For this reason, the CSFs produced during this first phase by allowing SrD substitutions to the seventh and eighth layers were not considered in the subsequent RCI calculations.

The RCI calculations were performed in two phases, which, respectively, allowed SD and SDT substitutions. In the so-called SD and SDT phases, the multiconfiguration expansions were obtained by systematically increasing the AS, the maximum angular momentum quantum number  $l$  within the AS, and the number of opened spectroscopic orbital shells. The computed electronic factors  $A_{el}[{}^3P_1^0]$  and  $B_{el}[{}^1P_1^0]$  for the different multiconfiguration expansions that were used in the SD and SDT phases are given in Table II. The  $A_{el}[{}^3P_1^0]$  and  $B_{el}[{}^1P_1^0]$  values are also plotted in Fig. 2 for both SD (green squares) and SDT (blue triangles) approaches. The numbers 10–26 on the  $x$  axis of Fig. 2 are equivalent to the labels

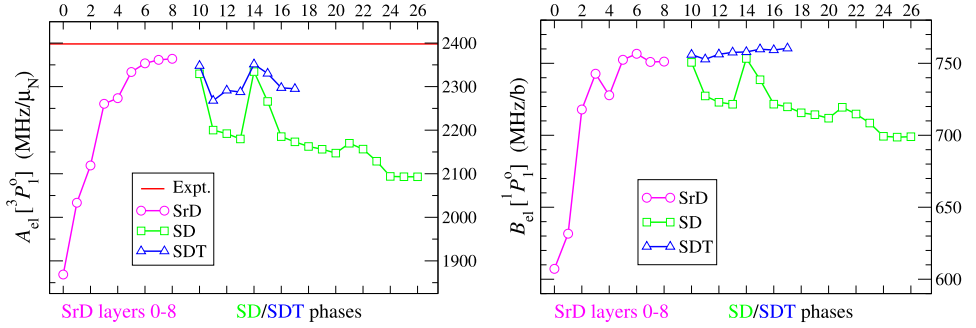


FIG. 2. The electronic hyperfine factors  $A_{el}[^3P_1^0]$  (in MHz/ $\mu_N$ ) and  $B_{el}[^1P_1^0]$  (in MHz/b) based on three computational approaches: the SrD (magenta circles), SD (green squares), and SDT (blue triangles). On the  $x$  axes, the number 0 indicates the DHF computation, the numbers 1–8 represent the consecutive layers of correlation orbitals developed in the SrD phase of the calculations, and the numbers 10–26 match the labels of the multiconfiguration expansions presented in column 1 of Table II, corresponding to the calculations performed in the SD and SDT phases. The red straight horizontal line on the left graph represents the experimental value  $A_{el}^{expt}[^3P_1^0] = 2398$  MHz/ $\mu_N$  from Ref. [12]. See also text in Sec. III A 2.

displayed in column 1 of Table II. For each calculation, column 2 of Table II provides the principal quantum number  $n$  of the deepest orbital shell that was opened for substitutions, e.g.,  $n \geq 4$  involves substitutions from  $4s$ ,  $4p$ ,  $4d$ ,  $5s$ ,  $5p$ ,  $6s$ , and column 3 displays the AS of orbitals to which the substitutions were allowed. As a reference, the  $A_{el}[^3P_1^0]$  and  $B_{el}[^1P_1^0]$  values resulting from the sixth layer of the SrD phase are

presented in the second row of Table II, while the first row displays the electronic factors from the DHF computation, restricted to two CSFs.

After generating CSF expansions by allowing substitutions from the  $n \geq 3$  spectroscopic shells to the  $12s11p10d9f10g$  set of orbitals in the label 24 calculation, the electronic factors computed in the SD phase were ultimately converged.

TABLE II. The computed electronic factors  $A_{el}[^3P_1^0]$  (in MHz/ $\mu_N$ ) and  $B_{el}[^1P_1^0]$  (in MHz/b) for various multiconfiguration expansions that were used in the RCI phases following the SrD-SR-MCDHF calculations. In each RCI phase, the considered CSFs were, respectively, generated based on SD (columns 4 and 6) and SDT (columns 5 and 7) substitutions from the opened spectroscopic shells displayed in column 2 to the AS of correlation orbitals given in column 3. The first row contains the resulting  $A_{el}[^3P_1^0]$  and  $B_{el}[^1P_1^0]$  values from the DHF computation, where only the CSFs of the two targeted states were considered, and the second row displays the converged results from the SrD orbital optimization phase after the sixth correlation orbital layer was added. The labels given in column 1 correspond to the labels used on the horizontal axes of Fig. 2.

Label	Open shells	Active orbital set	$A_{el}[^3P_1^0]$ (MHz/ $\mu_N$ )		$B_{el}[^1P_1^0]$ (MHz/b)	
			SD	SDT	SD	SDT
0	Phase 1: DHF computation		1869		607	
6	Phase 1: SrD correlation layer 6		2353		757	
10	$n \geq 5$	$8s7p$	2329	2348	751	756
11	$n \geq 4$	$7s6p5d4f$	2200	2268	727	753
12	$n \geq 4$	$8s7p5d4f$	2192	2291	723	756
13	$n \geq 4$	$8s7p5d4f5g$	2180	2288	722	758
14	$n \geq 4$	$9s8p$	2335	2351	753	758
15	$n \geq 4$	$9s8p5d$	2266	2330	739	760
16	$n \geq 4$	$9s8p5d4f$	2185	2297	722	759
17	$n \geq 4$	$9s8p5d4f5g$	2173	2295	720	760
18	$n \geq 4$	$10s9p6d5f6g$	2163		716	
19	$n \geq 4$	$11s10p7d6f7g$	2156		714	
20	$n \geq 4$	$12s11p10d9f10g$	2147		712	
21	$n \geq 3$	$9s8p5d4f5g$	2170		719	
22	$n \geq 3$	$10s9p6d5f6g$	2157		715	
23	$n \geq 3$	$11s10p7d6f7g$	2129		709	
24	$n \geq 3$	$12s11p10d9f10g$	2094		699	
25	$n \geq 3$	$13s12p11d10f11g$	2093		699	
26	$n \geq 2$	$12s11p10d9f10g$	2089		698	
	Expt. [12]		2398(2)			

Extending further the multiconfiguration expansions by either adding one more layer of correlation orbitals (label 25 calculation) or opening the  $n = 2$  spectroscopic shells (label 26 calculation) has nearly no effect on the  $A_{\text{el}}[{}^3P_1^0]$  and  $B_{\text{el}}[{}^1P_1^0]$  values (see columns 4 and 6 in Table II). The multiconfiguration expansions used in the label 24 calculation of the SD phase constituted the starting point for the RCI calculations of the SDT phase, which followed a pattern similar to the SD approach for generating the CSFs. Yet, the number of CSFs produced by T substitutions grew very rapidly, and the limits of the computational resources available to us were reached after performing the label 17 calculation. It should be pointed out that the latter calculation included 4 406 086 CSFs and took 37 days of wall time on the computer cluster at our disposal ( $6 \times 96$  CPU @ 2.4 GHz with  $6 \times 256$  GB RAM). For the next calculation, the label 18 calculation, 17 817 617 CSFs were generated, which exceeded the capacity of the cluster. The  $A_{\text{el}}[{}^3P_1^0]$  and  $B_{\text{el}}[{}^1P_1^0]$  values computed in the SDT phase were, thus, not fully converged.

The dependence of the resulting  $A_{\text{el}}[{}^3P_1^0]$  and  $B_{\text{el}}[{}^1P_1^0]$  values on CSF expansions formed from different classes of electron substitutions is well illustrated in Fig. 2. We notice that, in the SD phase, the values of the computed hyperfine factors decrease compared to the SrD results. On the other hand, when T substitutions are also considered, the values of the computed properties increase in relation to the respective calculations of the SD phase. This behavior has also been observed in many earlier calculations of hyperfine structures [35,50–55]. When performing RCI calculations by allowing D substitutions from core orbitals, CSFs that account for CC correlation effects are included in the atomic-state expansions. These CSFs have relatively large mixing coefficients due to their important contribution to the total energy and, as a result, the mixing coefficients of CSFs describing effects, such as spin and orbital polarization, that are more important for hyperfine interactions take lower values. This is eventually counterbalanced by the inclusion of CSFs generated from T substitutions.

Further, the comparison between the two graphs in Fig. 2 illustrates the similar synchronous dependence of the computed  $A_{\text{el}}[{}^3P_1^0]$  and  $B_{\text{el}}[{}^1P_1^0]$  values on the increasing multiconfiguration expansions in the SrD (magenta circles) and SD (green squares) phases of the computations. This correlated behavior between computed  $A_{\text{el}}$  and  $B_{\text{el}}$  hyperfine interaction factors has also been observed in numerous previous works [13,56–59]. The M1 and E2 hyperfine factors are obtained by evaluating the expectation values of the operators (5) and (6), respectively. These expectation values are expressed in terms of reduced matrix elements of the operators above, involving radial integrals that have a common dependence on the radial factor  $r^{-3}$ . Although it is not directly obvious from Eqs. (5) and (6), the common  $r^{-3}$  dependence is explained by the different structures of the relevant one-electron matrix elements in the nonrelativistic limit [[60], Sec. 5.2]. For this reason, when, at each step of the computations, the same CSF expansions are considered, the values of the  $A_{\text{el}}[{}^3P_1^0]$  and  $B_{\text{el}}[{}^1P_1^0]$  factors will most likely synchronously oscillate (see also, e.g., the curves  $a_{\text{dip}}$  and  $b_{\text{quad}}$  in Fig. 8 of Ref. [48]).

In consideration of the foregoing, the relative shifts in the  $A_{\text{el}}[{}^3P_1^0]$  and  $B_{\text{el}}[{}^1P_1^0]$  values induced by an additional MCDHF, or RCI, calculation are expected to be proportional, i.e.,

$$\Delta A_{\text{el}}/A_{\text{el}} \approx \Delta B_{\text{el}}/B_{\text{el}}. \quad (13)$$

The equation above may be transformed into a relation in which the computed  $A_{\text{el}}[{}^3P_1^0]$  and  $B_{\text{el}}[{}^1P_1^0]$  values are related to the corresponding experimental  $A_{\text{el}}^{\text{expt}}[{}^3P_1^0]$  and  $B_{\text{el}}^{\text{expt}}[{}^1P_1^0]$  values according to

$$|A_{\text{el}} - A_{\text{el}}^{\text{expt}}|/A_{\text{el}}^{\text{expt}} \approx |B_{\text{el}} - B_{\text{el}}^{\text{expt}}|/B_{\text{el}}^{\text{expt}}. \quad (14)$$

The latter equation can then be used to adjust the computed  $B_{\text{el}}[{}^1P_1^0]$  factor by applying a semiempirical shift based on the known error in the computed  $A_{\text{el}}[{}^3P_1^0]$  factor. Given the experimental result  $A_{\text{el}}^{\text{expt}}[{}^3P_1^0] = 2398$  MHz/ $\mu_N$  from Ref. [12], Eq. (14) was used to adjust the resulting  $B_{\text{el}}[{}^1P_1^0]$  values from all three phases of the calculations, i.e., SrD, SD, and SDT. This leads to the following “shifted” values:  $B_{\text{el}}(\text{SrD})^{\text{shifted}} = 759$  MHz/b,  $B_{\text{el}}(\text{SD})^{\text{shifted}} = 800$  MHz/b, and  $B_{\text{el}}(\text{SDT})^{\text{shifted}} = 793$  MHz/b.

Looking at Fig. 2 and Table II, one notices that the  $B_{\text{el}}[{}^1P_1^0]$  value (in contrast to the  $A_{\text{el}}[{}^3P_1^0]$  value) is overall insensitive to T substitutions. That being so, the result from the largest completed calculation in the SDT phase, i.e.,  $B_{\text{el}}[{}^1P_1^0] \equiv B_{\text{el}}(\text{SDT}) = 760$  MHz/b, is considered reliable and taken into account in the evaluation of the final  $B_{\text{el}}[{}^1P_1^0]$  result for the current SrD-SR-MCDHF+RCI approach. By taking the average of the above-mentioned four values, we ultimately arrive at

$$B_{\text{el}}[{}^1P_1^0] = 778 \text{ MHz/b}. \quad (15)$$

### 3. SrD-MR-MCDHF calculations

In the third computational approach, the MCDHF calculations were performed in the EOL scheme for the average of the  $5s^2 5p 6s \ 1^3P_1^0$  states using CSF expansions produced by allowing SrD substitutions from a set of MR configurations and are, therefore, denoted SrD-MR-MCDHF. By allowing S and D substitutions from the MR space, important T and Q substitutions from the targeted  $5s^2 5p 6s$  configuration were also taken into account. To determine the MR space, a preliminary SD-SR-MCDHF calculation was carried out, using CSFs that were formed by enabling SD substitutions from the valence orbitals ( $n \geq 5$ ) to a first layer of correlation orbitals, i.e.,  $7s$ ,  $6p$ ,  $6d$ , and  $4f$ . After analyzing the  $LS$  composition of the two targeted states (see Table III), we defined an MR composed of the  $5s^2 5p 6s$ ,  $5p^3 6s$ , and  $5s 5p 5d 6s$  configurations. The MR was restricted to the three leading configurations due to the limitations of our computational resources. This strategy for defining the reference configurations differs from the one used in Sec. III A 1, thus leading to different MR sets.

In the SrD-MR-MCDHF calculations, the  $4d$ ,  $5s$ ,  $5p$ ,  $5d$ , and  $6s$  spectroscopic orbitals were opened for SD substitutions, with the restriction that there was at most one substitution from the  $4d$  core orbital. All other inner-core subshells were kept closed. The polarization of the  $4d$  orbital was, thereby, taken into account together with VV correlation effects. The AS was systematically increased to include layers

TABLE III. The  $LS$  composition of the two targeted  $5s^25p6s\ ^1\ ^3P_1^o$  states after performing an initial SD-SR-MCDHF calculation. The percentages of the four most dominant  $LS$  components are solely displayed. The first percentage value corresponds to the assigned configuration and term.

Pos.	Conf.	$LSJ$	$LS$ composition
1	$5s^25p6s$	$^3P_1^o$	$0.761 + 0.186\ 5s^25p6s\ ^1P^o + 0.016\ 5p^36s\ ^3P^o + 0.010\ 5s5p5d6s\ ^3P^o$
2	$5s^25p6s$	$^1P_1^o$	$0.761 + 0.185\ 5s^25p6s\ ^3P^o + 0.017\ 5p^36s\ ^1P^o + 0.009\ 5s5p5d6s\ ^1P^o$

with one additional correlation orbital of the  $s$ ,  $p$ ,  $d$ , and  $f$  symmetries. The effects of orbitals with higher angular symmetries on the computation of hyperfine structures are generally known to be small, justifying the choice of the “ $f$  limit” [61]. Overall, nine correlation orbital layers were built, corresponding to the  $15s14p14d12f$  set of orbitals.

Table IV displays the computed excitation energies  $E[^3P_1^o]$  and  $E[^1P_1^o]$ , energy separations  $\Delta E = E[^1P_1^o] - E[^3P_1^o]$ , hyperfine electronic factors  $A_{el}[^3P_1^o]$  and  $B_{el}[^1P_1^o]$ , and numbers of CSFs,  $N_{CSFs}$ , as functions of the increasing AS of correlation orbitals. The values associated with the initial MR calculation that corresponds to 17 CSFs are given in the first row of Table IV. After optimizing nine layers of correlation orbitals, all computed properties were effectively converged. One should note that the number of CSFs in the expansions of the final SrD-MR-MCDHF calculation exceeded one million. At this point, the predicted energy separation agrees with the observed value to within 3%, which provides an initial assessment of the computed hyperfine factors. The convergence patterns of the computed  $A_{el}[^3P_1^o]$  and  $B_{el}[^1P_1^o]$  values with respect to the increasing number of correlation orbital layers optimized in the SrD-MR-MCDHF calculations are also graphically illustrated in Fig. 3.

As a final step, an RCI calculation was carried out using the  $15s14p14d12f$  orbital set. For this RCI calculation, the CSFs were produced by enabling S substitutions from all spectroscopic orbitals, along with D substitutions from the

$4p$ ,  $4d$ ,  $5s$ ,  $5p$ ,  $5d$ , and  $6s$  orbitals, with the two following restrictions: (1) at most one substitution from the  $4p$  orbital and (2) no simultaneous substitutions from the  $4p$  and  $4d$  orbitals. Hence, CC correlation effects were solely captured by the allowed D substitutions from the  $4d$  orbital. Based on preliminary RCI calculations that used a smaller orbital basis, the polarization effect of the  $4s$  core orbital was deduced to be significant too. However, the capacity of the computer cluster at our disposal did not allow us to include it. The SrD-MR-MCDHF+RCI results are presented in the second last row of Table IV and correspond to atomic-state expansions with 3 583 001 CSFs.

At each step of the calculations that followed this third MCDHF-RCI computational approach, the atomic-state expansions were restricted to CSFs that interact with the ones generated by the MR configurations. Indicatively, we mention that the number of CSFs in the atomic-state expansions of the final RCI calculation, initially, were 5 313 860. It has been shown, in previous works, that such reduction of CSFs does not bring any major losses in accuracy [64–66]. In any case, the effect of limiting the number of CSFs to the “interacting” ones was also evaluated in this work. It was deduced that utilizing the full CSF space causes the  $A_{el}[^3P_1^o]$  and  $B_{el}[^1P_1^o]$  values to rise by  $\sim 7$  MHz/ $\mu_N$  and  $\sim 1$  MHz/b, respectively. In addition, it was estimated that when orbitals of the  $g$  and  $h$  angular symmetries are added to the orbital basis, the  $A_{el}[^3P_1^o]$  value further increases by  $\sim 3$  MHz/ $\mu_N$ , while the change in

TABLE IV. The convergence of the energies and hyperfine factors  $A_{el}$  (in MHz/ $\mu_N$ ) and  $B_{el}$  (in MHz/b) for the  $^1\ ^3P_1^o$  states as the MR orbital basis extends to include nine layers of correlation orbitals optimized in the SrD-MR-MCDHF calculations. The results after the subsequent RCI calculations are also presented in the second last row. The computed excitation energies of the  $^3P_1^o$  and  $^1P_1^o$  states are, respectively, presented (in  $\text{cm}^{-1}$ ) in columns 2 and 3, whereas the evaluated energy separations are displayed in column 4. For comparison, the observed energies are shown in the last row. In each of the columns 5 and 6, the values of the  $A_{el}[^3P_1^o]$  and  $B_{el}[^1P_1^o]$  factors are given. The last column exhibits the numbers of generated CSFs for every additional correlation orbital layer.

Correlation layer	Energies ( $\text{cm}^{-1}$ )			$A_{el}[^3P_1^o]$	$B_{el}[^1P_1^o]$	$N_{CSFs}$
	$^3P_1^o$	$^1P_1^o$	$^1P_1^o - ^3P_1^o$			
None (MR)	33 301	38 002	4701	1869	613	17
1	34 327	38 990	4663	2044	586	16 593
2	34 789	39 323	4534	2055	586	57 086
3	34 644	39 154	4510	2092	587	122 610
4	34 587	39 072	4485	2109	591	212 946
5	34 544	39 020	4476	2120	596	328 094
6	34 529	39 004	4475	2117	590	468 054
7	34 521	38 993	4472	2121	593	632 826
8	34 519	38 987	4468	2119	590	822 410
9	34 517	38 984	4467	2120	592	1 036 806
+ RCI	34 374	38 938	4565	2169	716	3 583 001
Expt. [62,63]	34 914	39 257	4343			



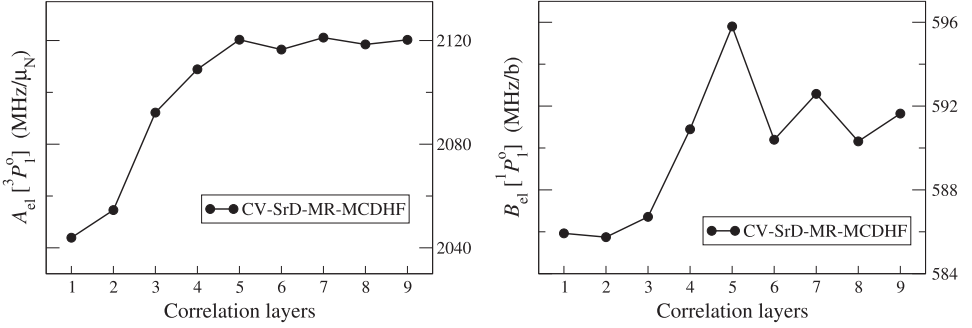


FIG. 3. The convergence patterns of the electronic hyperfine factors  $A_{el}[^3P_1^0]$  (in MHz/ $\mu_N$ ) and  $B_{el}[^3P_1^0]$  (in MHz/b) with the increasing number of correlation orbital layers optimized in the SrD-MR-MCDHF calculations. For the computational details, see text in Sec. III A 3.

the  $B_{el}[^1P_1^0]$  value is negligible. Considering the above corrections to the final SrD-MR-MCDHF+RCI results, we finally arrive at

$$A_{el}[^3P_1^0] = 2179 \text{ MHz}/\mu_N; \quad B_{el}[^1P_1^0] = 717 \text{ MHz/b}. \quad (16)$$

#### 4. Sensitivity to orbital bases and CSF expansions

As previously seen, different calculations based on the same general method, i.e., the MCDHF-RCI, and performed with the same program, the GRASP2018 computer package, lead to different results. The  $A_{el}[^3P_1^0]$  and  $B_{el}[^1P_1^0]$  values obtained with the three approaches do agree within approximately 10%. The differences in the S-MR-MCDHF, SrD-SR-MCDHF, and SrD-MR-MCDHF approaches lie in the choice of their respective orbital bases and CSF expansions, each with its benefits and drawbacks. In this subsection, we investigate the sensitivity of the SrD-SR-MCDHF and SrD-MR-MCDHF approaches by arbitrarily interchanging their orbital bases and CSF expansions. In addition to the  $A_{el}[^3P_1^0]$  and  $B_{el}[^1P_1^0]$  values, we also discuss the  $A_{el}[^1P_1^0]/A_{el}[^3P_1^0]$  and  $B_{el}[^3P_1^0]/B_{el}[^1P_1^0]$  ratios, as it was recently done with the experimental results presented in Ref. [12], to provide additional information about the sensitivity of our calculations.

For each of the two above-mentioned methods, the final results were obtained by performing RCI computations. These results are shown in the first two rows of Table V using

the labels SrD-MR/SrD-MR and SrD-SR/SrD-SR, for the SrD-MR-MCDHF and SrD-SR-MCDHF approaches, respectively (the notation X/Y defines the orbital basis from X and CSF expansion from Y). Two additional sets of computations were performed: one combining the SrD-MR-MCDHF orbital basis and the SrD-MR-MCDHF CSF space (see SrD-SR/SrD-MR in Table V) and one combining the SrD-MR-MCDHF orbital basis and the SrD-SR-MCDHF CSF space (see SrD-MR/SrD in Table V). Minor changes in the CSF spaces were required. The SR active space was restricted to the  $s$ ,  $p$ ,  $d$ , and  $f$  symmetries as the MR orbital basis is limited to  $l_{\max} = 3$ , and the SrD-MR-MCDHF CSF space was limited to only six correlation layers.

Although far from being in perfect agreement, the results presented in Table V are consistent. The effect of replacing the orbital set, for a given CSF expansion, is surprisingly small. Additionally, the  $A_{el}[^1P_1^0]/A_{el}[^3P_1^0]$  and  $B_{el}[^3P_1^0]/B_{el}[^1P_1^0]$  values are also presented in Table V, where it is seen that the former ratio is less stable than the latter. The computed  $A_{el}[^1P_1^0]/A_{el}[^3P_1^0]$  values vary from 0.124 to 0.185, which corresponds to a deviation of 50% from the lowest value. By considering a simple term mixing between the  $^3P_0$  and  $^1P_0$  terms, it is shown in the Appendix that this sensitivity is expected. Using the same model, one further explains the steadier values of the  $B_{el}[^3P_1^0]/B_{el}[^1P_1^0]$  ratio. The computed  $B_{el}[^3P_1^0]/B_{el}[^1P_1^0]$  values range from  $-0.240$  to  $-0.270$ , which is in very good agreement with the experimental value of

TABLE V. The electronic hyperfine factors  $A_{el}[^3P_1^0]$  (in MHz/ $\mu_N$ ) and  $B_{el}[^1P_1^0]$  (in MHz/ $\mu_N$ ) as well as the  $A_{el}[^1P_1^0]/A_{el}[^3P_1^0]$  and  $B_{el}[^3P_1^0]/B_{el}[^1P_1^0]$  ratios, computed for six different combinations of orbital basis sets and CSF spaces. The SrD-SR-MCDHF and SrD-MR-MCDHF computational approaches are compared by expanding the total wave function over the largest CSF expansion of the one method and using the orbital basis of the other method. Adjustments were made in the CSF expansions due to the specific properties of the orbital bases obtained in the two different approaches. For details, see text in Sec. III A 4.

Orb. basis	CSF expansions	$A_{el}[^3P_1^0]$	$A_{el}[^1P_1^0]/A_{el}[^3P_1^0]$	$B_{el}[^1P_1^0]$	$B_{el}[^3P_1^0]/B_{el}[^1P_1^0]$
SrD-MR	SrD-MR	2179	0.185	717	-0.240
SrD-SR	SrD-SR	2295	0.124	760	-0.250
SrD-MR	SrD-SR ( <i>spdf</i> limit)	2303	0.126	739	-0.254
SrD-SR	SrD-MR ( <i>spdf</i> limit)	2297	0.126	722	-0.263
SrD-MR	SrD-MR (6 layers)	2161	0.183	709	-0.243
SrD-SR	SrD-MR (6 layers)	2168	0.158	718	-0.270

TABLE VI. The numbers of CSFs and the resulting energy separations between the targeted  $^3P_1^o$  and  $^1P_1^o$  states for each virtual orbital layer used in the CI-DFS calculations. Two approaches, the direct (full basis) and the one based on perturbation theory (PT), were implemented. The numbers of additional determinants  $ND_{PT}$ , built using PT, are displayed in parentheses.  $\Delta E = E[{}^1P_1^o] - E[{}^3P_1^o]$  are the energy separations in  $\text{cm}^{-1}$ . The numbers of virtual orbital layers given in column 1 correspond to the labels used on the horizontal axes of Fig. 4, and column 2 displays the respective orbital basis sets. For details see Sec. III B.

Virtual layer	Orbital basis set	Full basis		Perturbation theory		
		$N_{\text{CSFs}}$	$\Delta E$ ( $\text{cm}^{-1}$ )	$ND_{PT}$	$N_{\text{CSFs}}$	$\Delta E$ ( $\text{cm}^{-1}$ )
1	6s5p4d	1 520	4 537	(1184)	886	4 538
2	6s5p5d4f	39 021	4 868	(69 759)	23 504	4 868
3	7s6p5d4f	80 018	4 930	(123 905)	47 828	4 930
4	7s6p6d5f	198 543	4 880	(341 769)	119 338	4 880
5	8s7p6d5f	282 859	4 888	(452 698)	169 363	5 102
6	8s7p7d6f	482 408	4 859	(819 851)	289 765	5 069
7	9s8p7d6f	610 043	4 858	(987 563)	365 491	5 279
8	9s8p8d7f	890 616	4 842	(2 343 509)	534 785	5 268
9	10s9p8d7f	1 061 570	4 848	(2 942 992)	636 212	5 495
10	10s9p9d8f			(4 691 292)	854 398	5 508
Expt. [62,63]			4 343			4 343

$-0.25(2)$  [12]. On the other hand, the  $A_{\text{el}}[{}^1P_1^o]/A_{\text{el}}[{}^3P_1^o]$  values (ranging from 0.124 to 0.185) do not agree with the experimental result of 0.0517(2) [12].

### B. CI-DFS calculations

In this last set of calculations, which is based on the CI-DFS theory, we used for all Sturmian functions the same reference energy, namely, the one of the hydrogenic  $5s$  state. Allowing SD substitutions from all spectroscopic orbitals with  $n \leq 5$ , together with the  $6s$  and  $6p$  orbitals, to an increasing AS of virtual orbitals results in a large number of configurations and huge matrices for the numerical diagonalization. By freezing the  $1s$ ,  $2s$ , and  $2p$  orbitals and by using perturbation theory (PT) to build low-lying closed shells and highly excited states, we were able to extend the one-electron basis to the  $12s11p10d9f$  set of orbitals. For the three smallest orbital basis sets, T substitutions from the  $n = 4, 5$  orbitals, in addition to the  $6s$  and  $6p$  orbitals, were included, although their influence was smaller than the uncertainty level we aim at.

In the CI-DFS calculations of the hyperfine electronic factors  $A_{\text{el}}$ , the nuclear dipole moment distribution, or else Bohr-Weisskopf (BW) effect, was also taken into account. This was done by multiplying the operator  $\mathbf{T}^{(1)}$  in Eq. (7) by a nuclear distribution function  $F_{\text{BW}}(r)$ . In the homogeneous-nuclear-current-distribution approximation, this function is determined by the nuclear radius  $R_N$  so that [67]

$$F_{\text{BW}}(r) = \begin{cases} (r/R_N)^3, & r \leq R_N \\ 1, & r > R_N. \end{cases} \quad (17)$$

The calculated BW correction was  $\lesssim 0.001\%$  and  $\lesssim 0.1\%$ , for the  $^3P_1^o$  and  $^1P_1^o$  states, respectively. Analogously, a nuclear quadrupole moment distribution function can be introduced for the  $B_{\text{el}}$  property as a factor to the operator  $\mathbf{T}^{(2)}$  in Eq. (8). For the shell model, i.e., assuming that the quadrupole distribution is concentrated around the nuclear radius, this function

is given by [67]

$$F_Q(r) = \begin{cases} (r/R_N)^5, & r \leq R_N \\ 1, & r > R_N. \end{cases} \quad (18)$$

The latter effect is on the level of 0.1% for both considered states, which is in good agreement with the estimations made for the Cd ground state in [68].

For each virtual orbital layer that was used in the CI-DFS calculations, the corresponding orbital basis set, numbers of CSFs, and computed energy separations  $\Delta E$  between the targeted  $^3P_1^o$  and  $^1P_1^o$  states are listed in Table VI. One can see that the resulting energy difference  $\Delta E = E[{}^1P_1^o] - E[{}^3P_1^o]$  from the direct (full basis) calculations is well converged, in contrast to the PT calculations, where the  $\Delta E$  value is not saturated. In Fig. 4, the convergence patterns of the computed  $A_{\text{el}}[{}^3P_1^o]$  and  $B_{\text{el}}[{}^1P_1^o]$  values are shown for both non-PT (solid circles) and PT (empty circles) bases. It is seen in the figure that the E2 hyperfine electronic factor  $B_{\text{el}}[{}^1P_1^o]$  is more sensitive to variations of the orbital basis set, in comparison to the M1 electronic factor  $A_{\text{el}}[{}^3P_1^o]$  and, for that reason, its theoretical uncertainty is larger. In addition, we observe that the results from the non-PT and PT calculations progressively diverge as the number of virtual PT orbitals increases. That being so, and taking also into account the weaker stability of the PT energy separation value, the results from the perturbative treatment can only be used for estimating the theoretical error bars (see Sec. IV A), and not for extending the basis further. The final results of the CI-DFS calculations based on the largest non-PT orbital basis set, which corresponds to 1 061 570 CSFs, are

$$A_{\text{el}}[{}^3P_1^o] = 2082 \text{ MHz}/\mu_N; \quad B_{\text{el}}[{}^1P_1^o] = 693 \text{ MHz/b}. \quad (19)$$

### IV. FINAL VALUE AND EVALUATION OF ACCURACY

In Secs. III A 1–III B, four different computational approaches for evaluating the electronic hyperfine factors  $A_{\text{el}}$



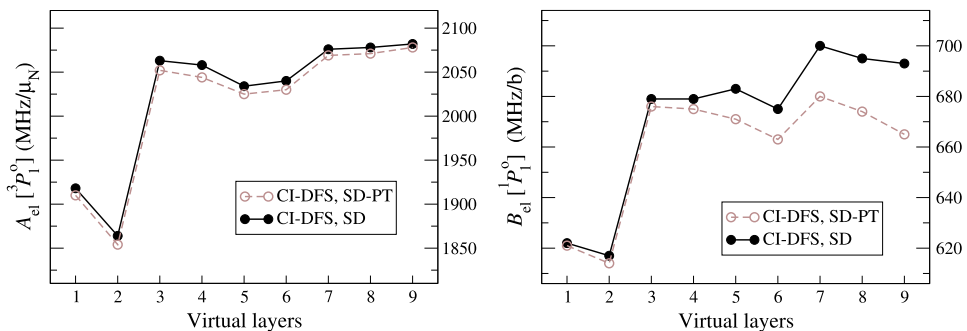


FIG. 4. The convergence of the electronic hyperfine factors  $A_{el}[^1P_1^0]$  (in MHz/ $\mu_N$ ) and  $B_{el}[^1P_1^0]$  (in MHz/b) with the increasing number of virtual orbital layers, optimized by employing the CI-DFS method. The solid black circles represent the results from the direct (full basis) calculations, while the empty brown circles illustrate the values obtained using perturbation theory (PT). The numbers of virtual orbital layers on the x axes are equivalent to the numbers given in column 1 of Table VI. See also text in Sec. III B.

and  $B_{el}$  of the  $1^1P_1^0$  excited states in neutral tin were presented. In this section, we solely focus on  $B_{el}[^1P_1^0]$  that can be used to extract the quadrupole moments  $Q$  of tin isotopes for which spectroscopic data are available. The  $B_{el}[^1P_1^0]$  values obtained from the four independent sets of calculations are summarized in Table VII. By taking their average, we ultimately arrive at  $B_{el}[^1P_1^0] = 703$  MHz/b.

As a crude estimate of the uncertainty of the concluding  $B_{el}[^1P_1^0]$  value, we can consider the half-range of the aforementioned individual results, i.e., 78 MHz/b. Yet, if one wants to be in a position to discuss atomic, or nuclear, properties and their underlying physics, a rigorous assessment of the uncertainties of the computed values is required. In recent years, atomic physicists have been putting great efforts into providing reliable uncertainties on their theoretical results [6,35,69–71]. In line with these efforts, the following subsections take into account a number of considerations to determine the accuracy of the final  $B_{el}[^1P_1^0]$  value. Some of these considerations are only applicable to one (or more) particular set(s) of calculations (see Sec. IV A), while others are analogously applied to all four separate results (see Sec. IV B). Statistical principles are implemented (see Sec. IV C), and former outcomes from computations of electronic hyperfine factors, regarding atomic states with electronic structure similar to the structure of the  $5s^25p6s\ 1^1P_1^0$  states in Sn I, are also used as an estimate of the accuracy of the  $B_{el}[^1P_1^0]$  value deduced in this work (see Sec. IV D).

TABLE VII. The resulting  $B_{el}[^1P_1^0]$  values (in MHz/b) from the four independent sets of calculations presented in Secs. III A 1–III B. The last row displays their average.

Methods	$B_{el}[^1P_1^0]$ (MHz/b)
S-MR-MCDHF+RCI	622
SrD-SR-MCDHF+RCI	778
SrD-MR-MCDHF+RCI	717
CI-DFS	693
Average	703

### A. Model-specific uncertainties

In each of the four independent approaches that were discussed in the previous sections, the wave functions (radial orbitals and configuration-mixing coefficients) that describe the atomic states were obtained based on various approximations with respect to the orbital basis and the list of configuration states. In Sec. III A 4, the sensitivity of the SrD-SR-MCDHF+RCI and SrD-MR-MCDHF+RCI results to the orbital basis was investigated by combining the radial orbital basis obtained in one of these two computational approaches with the CSF expansions used in the RCI computations of the other approach. As seen in Table V, these combinations gave rise to  $B_{el}[^1P_1^0]$  values that range from 709 MHz to 760 MHz/b. The half-range of these values yields an uncertainty of 26 Hz/b. Further, in the CI-DFS calculations, the electronic hyperfine factors were computed using both non-PT and PT orbital bases. The comparison between the non-PT and PT results for different orbital basis sets suggests an uncertainty of 70 MHz/b in the deduced  $B_{el}[^1P_1^0]$ . Lastly, in the instance of the SrD-SR-MCHDF calculations, the outcome for the  $B_{el}[^1P_1^0]$  value is the average of four separate values. One can, thus, assume an error bar corresponding to the half-range of these values, i.e., 20 MHz/b.

### B. Difference between the theoretical $A_{el}[^3P_1^0]$ and experimental $A_{el}^{exp}[^3P_1^0]$ values

The deviation of the calculated M1 hyperfine constant from the experimental value  $|A_{theor} - A_{expt}|$  is often assumed to be a measure of the overall accuracy of the hyperfine structure calculations [35,50,72]. In Sec. III A 2, the experimental  $A_{el}^{exp}[^3P_1^0]$  value was used to accordingly shift the resulting  $B_{el}[^1P_1^0]$  values from all three approximations, i.e., SrD, SD, and SDT, that were used in the SrD-SR-MCDHF+RCI calculations. Considering only the  $B_{el}[^1P_1^0]$  result from the most extensive SDT calculation and evaluating the difference  $B_{el}(SDT) - B_{el}(SDT)^{shifted}$  yields an error estimate of 32 MHz/b. When applying this shift to the final results of the remaining calculations, we acquire three more error bars: 54 MHz/b from the S-MR-MCDHF calculations, 64 MHz/b

from the SrD-MR-MCDHF calculations, and 91 MHz/b from the CI-DFS calculations.

### C. Statistical standard deviation

The individual results provided by the four independent sets of calculations could be regarded as a statistical sample and, in that case, the average value  $\mu$  and the standard deviation  $\sigma$  can be evaluated. For the {622, 693, 717, 778} set of  $B_{\text{el}}[{}^1P_1^o]$  values, it is  $\mu \pm \sigma = 703 \pm 56$  MHz/b, which places  $B_{\text{el}}[{}^1P_1^o]$  between 591 and 815 MHz/b within the  $2\sigma$  condition (95%). In this manner, we obtain another uncertainty estimate equivalent to 56 MHz.

### D. Zinc analogy

In a recent paper [35], the quadrupole moment  $Q({}^{67}\text{Zn})$  was evaluated based on 11 independent multiconfiguration calculations of the EFG  $\propto B_{\text{el}}$  for the  $4s4p\ {}^3P_1^o$  and  $4s4p\ {}^3P_2^o$  states in Zn I. The final accuracy of the calculated EFGs was estimated using the scatter of the individual results of these 11 calculations, resulting in a relative error of about 8%. The valence structure of the  $4s4p\ {}^3P_{1,2}^o$  states in neutral zinc is quite similar to the structure of the  $5s^25p6s\ {}^1,3P_1^o$  tin states, which are of interest in this work; in both cases, there are two electrons outside the closed shells, and the orbitals of these valence electrons have similar angular symmetries. Thereby, one expects that, for atomic calculations using similar computational approaches, the relative error bars of the computed hyperfine factors will be comparable. Adopting the 8% relative error bar, an uncertainty of 56 MHz/b is inferred for the  $B_{\text{el}}[{}^1P_1^o]$  value deduced in this paper.

### E. Final accuracy

The considerations above lead to diverse error bars, which, according to the order of their appearance in the text, are (in units of MHz/b): 78, 26, 70, 20, 32, 54, 64, 91, 56, and 56. The largest of these uncertainties, i.e., 91 MHz/b, places  $B_{\text{el}}[{}^1P_1^o]$  between 521 and 885 MHz/b within the  $2\sigma$  condition, which is a rather conservative choice. On the other hand, the smallest of all these error estimates, i.e., 20 MHz/b, positions  $B_{\text{el}}[{}^1P_1^o]$  between 663 and 743 MHz/b within the  $2\sigma$  condition. This interval does not overlap with all individual  $B_{\text{el}}[{}^1P_1^o]$  values resulting from the four independent sets of calculations and, therefore, such an error bar is not appropriate. Assuming that some of the obtained error bars possibly overestimate the uncertainty in our concluding  $B_{\text{el}}[{}^1P_1^o]$  value, and that a few others might underestimate it, the rounded value of 50 MHz/b is a reasonable choice. The final result of this paper, then, becomes

$$B_{\text{el}}[{}^1P_1^o] = 703 \pm 50 \text{ MHz/b}, \quad (20)$$

localizing  $B_{\text{el}}[{}^1P_1^o]$  between 603 and 803 MHz/b with 95% confidence.

Recent calculations performed in [73] based on Fock-space coupled-cluster theory resulted in a slightly smaller value of  $B_{\text{el}}[{}^1P_1^o] = 645(58)$  MHz/b, lying within our error bars. The only other available value is the one given by Eberz *et al.* [74], i.e.,  $B_{\text{el}}[{}^1P_1^o] = 593$  MHz/b, which is approximately 15% smaller than the result of this work. It is, therefore, seen that

the recent rigorous reinvestigations of the hyperfine electronic factors of excited states in Sn I yield, independently of the method used,  $B_{\text{el}}[{}^1P_1^o]$  values, which are larger than the initially computed value a few decades ago.

## V. QUADRUPOLE MOMENTS

The computed  $B_{\text{el}}[{}^1P_1^o]$  value can be used to deduce the nuclear quadrupole moments  $Q({}^A\text{Sn}) = B/B_{\text{el}}$  of the tin isotopes for which the E2 hyperfine constant  $B$  was measured. The  $B_{\text{el}}[{}^1P_1^o]$  value resulting from the present multiconfiguration calculations was recently employed by Yordanov *et al.* [12] to extract the nuclear quadrupole moments of odd- $A$  tin isotopes. As mentioned in the Introduction, the final  $B_{\text{el}} \propto$  EFG value for the  $5s^25p6s\ {}^1P_1^o$  state has been slightly shifted from 706(50) MHz/b that was reported and used in Ref. [12] to 703(50) MHz/b in this paper. The  $Q$  values listed in the last column of Table 1 in Ref. [12] should, therefore, be increased by a tiny factor of 706/703.

For a few tin isotopes, more than one experimental value of E2 hyperfine constants is available, allowing us to compare the extracted quadrupole moments. The E2 hyperfine constant  $B[{}^1P_1^o]$  for the  $I = 5/2$  state of  ${}^{109}\text{Sn}$  was measured independently in Refs. [12,74], and their results are, respectively,  $B[{}^1P_1^o] = 212.0(27.0)$  MHz and  $B[{}^1P_1^o] = 154(5)$  MHz. In Ref. [74], the computed  $B_{\text{el}}[{}^1P_1^o] = 593$  MHz/b value is also available, despite the fact that they used the data related to the  ${}^3P_1^o$  state, i.e.,  $B[{}^3P_1^o] = -43.0(12.0)$  MHz and  $B_{\text{el}}[{}^3P_1^o] = -138$  MHz/b, to extract the quadrupole moment  $Q({}^{109}\text{Sn}) = 310(100)$  mb. By combining the experimental  $B[{}^1P_1^o]$  result of Ref. [12] with the presently computed  $B_{\text{el}}[{}^1P_1^o] = 703(50)$ , we obtain  $Q({}^{109}\text{Sn}) = 219(7)(16)$ , which significantly differs from the above-mentioned value of  $Q({}^{109}\text{Sn}) = 310(100)$  mb. These two quadrupole moments merely overlap with each other due to the large uncertainty of 100 mb in the latter value. Further, the  $B_{\text{el}}[{}^1P_1^o]$  value given in Ref. [74] barely overlaps with the present  $B_{\text{el}}[{}^1P_1^o]$  value, which strengthens the need to improve the accuracy of the electronic hyperfine factors.

Finally, taking the  ${}^{119}\text{Sn}$  isotope as an example, we propose

$$Q({}^{119}\text{Sn}) = -0.176(4)(12)\text{ b}, \quad (21)$$

where (12) represents the theoretical uncertainty of 7% of the  $B_{\text{el}}[{}^1P_1^o]$  deduced in this work and (4) represents the experimental uncertainty of the measured  $B[{}^1P_1^o]$  in Ref. [12]. We notice that the theoretical uncertainty suggested above is about three times larger than the experimental uncertainty. In the previous section, a number of considerations were taken into account to provide a well-grounded estimate of the theoretical uncertainties in our final  $B_{\text{el}}[{}^1P_1^o]$  value. Nonetheless, one should always remain cautious toward error estimates of electronic hyperfine factors deduced from atomic calculations and of the corresponding error bars in the evaluated nuclear quadrupole moments  $Q$ . The element bismuth is a good example of the difficulties in estimating such error bars. Table I in Ref. [56] lists the proposed values of the nuclear quadrupole moment  $Q$  for the  ${}^{209}\text{Bi}$  isotope. The error bars of several of those values not only do not overlap, but they do not even touch each other (to make all of the error bars overlap, the relative uncertainties would have to exceed 50%). We should, however, also note here that the valence structure of the tin

atom is less complicated and less demanding computationally than the valence structure of the bismuth atom, and we are confident enough that the deduced error bars in this paper are trustworthy.

### VI. CONCLUSIONS

We presented the details of the theoretical calculations of the isotope-independent E2 hyperfine factor  $B_{el}$  ( $\propto$  EFG), which was recently used to extract nuclear quadrupole moments  $Q$  of tin isotopes [12]. Four independent computational approaches were employed to finally provide the value of  $B_{el} = 703(50)$  MHz/b for the  $5s^2 5p 6s \ ^1P_1^0$  excited state of Sn I. Three of these approaches were based on the MCDHF-RCI method as implemented in the GRASP packages, while the fourth approach relied on the CI-DFS theory. The convergence of the  $B_{el}[\ ^1P_1^0]$  values was monitored as the CSF expansions were enlarged by allowing single, double, and, depending on the correlation model, also triple electron substitutions from the reference configuration(s). Efforts were made to provide a realistic theoretical uncertainty for the final  $B_{el}[\ ^1P_1^0]$  value by accounting for statistical principles, the correlation with the isotope-independent M1 hyperfine factor  $A_{el}$ , and previous calculations of electronic hyperfine factors on systems with electronic structure similar to that of Sn I.

The deduced relative accuracy of the present atomic *ab initio* calculations of the EFG is of the order of 7%, leading to even larger uncertainties in the extracted  $Q(\text{Sn})$  values due to the uncertainty in the measured  $B$ . This level of accuracy is certainly inferior to the deduced  $Q(\text{Sn})$  values from the solid-state density functional calculations performed by Barone *et al.* [75], which are about an order of magnitude more accurate. In general, the accuracy of the atomic *ab initio* calculations of EFGs strongly depends on the valence structure of the atom, or ion, in question. We should note that, in the extreme case of lithiumlike systems, the relative uncertainties of the atomic calculations of hyperfine structures can be limited to 0.001%–0.01% [58,59,76–81]. Even though the tin atom is far more demanding computationally than the lithiumlike systems, an atomic calculation of hyperfine structures with lower uncertainty would be possible for singly ionized tin, with one electron outside closed shells, and it would be even more accurate, for triply ionized tin, which has one electron outside the  $n < 5$  core. Such calculations, as the latter, would likely challenge the accuracy of the solid-state methods. We hereby encourage experimentalists to consider one, or both, of the above-mentioned ions.

Interestingly, we observe that all computed  $A_{el}[\ ^3P_1^0]$  values are smaller than the experimental  $A_{el}^{\text{expt}}[\ ^3P_1^0] = 2398$  MHz/ $\mu_N$  value, independently of the computational method, or the correlation model. This could be explained by the lack of variational freedom intrinsic to the layer-by-layer optimization strategy, which hinders the contraction of spectroscopic orbitals when core-valence correlation is accounted for. In the specific case of Sn I, the spectroscopic  $4d$  soft shell, i.e., lying between the core and the valence orbitals, is expected to be highly sensitive to core-valence correlation that might not be effectively captured. Natural orbitals were recently used, as an efficient tool to overcome the limitation of the layer-by-layer optimization scheme, to estimate hyperfine

structure constants in Na I. Thanks to the radial reorganization of the orbitals, the spectroscopic orbitals are ultimately contracted, which affects both M1 and E2 electronic hyperfine factors [72]. Further investigations on the usefulness of the natural orbitals in the calculations of hyperfine structures are in progress.

### ACKNOWLEDGMENTS

S.S. is a FRIA grantee of the F.R.S-FNRS Fonds de la Recherche Scientifique (FNRS). M.G. acknowledges support from the FWO & FNRS Excellence of Science Programme (EOS-O022818F), P.J. acknowledges support from the Swedish Research Council (VR) under Contract No. 2015-04842, and I.I.T. acknowledges support by the RFBR Grant No. 18-03-01220.

### APPENDIX: SENSITIVITY OF THE HYPERFINE FACTORS AND STABILITY OF THE $B_{el}$ RATIO

As shown in Table V, where the influence of the choice of the CSF expansion and the orbital basis was investigated, the  $A_{el}[\ ^1P_1^0]/A_{el}[\ ^3P_1^0]$  ratio displays a much higher sensitivity in comparison to the  $B_{el}[\ ^3P_1^0]/B_{el}[\ ^1P_1^0]$  ratio. Also according to Table V, the computed  $A_{el}[\ ^3P_1^0]$  values range from 2161 to 2303 MHz/ $\mu_N$  (6%–7%). Hence, the sensitivity of the  $A_{el}[\ ^1P_1^0]/A_{el}[\ ^3P_1^0]$  ratio, which takes values from 0.124 to 0.185 (30%–50%), must arise from the computed  $A_{el}[\ ^1P_1^0]$  values.

The extreme sensitivity of  $A_{el}[\ ^1P_1^0]$  to correlation models is not really surprising if one performs calculations using the quasirelativistic Hartree-Fock and Breit-Pauli [47] method in the single-configuration approximation. In the Breit-Pauli (BP) scheme, the low value of the ratio  $A_{el}[\ ^1P_1^0]/A_{el}[\ ^3P_1^0]$  can indeed be understood. The  $A_{el}$  value of the *pure*  $\ ^3P_1^0$ , i.e., without considering any relativistic  $LS$ -term mixing, arises from the addition of the three contributions [82] (orbital, spin-dipole, and contact term), which interfere positively. On the other hand, the  $A_{el}$  value of the *pure*  $\ ^1P_1^0$  is only made of a (larger) orbital contribution, the total spin value ( $S = 0$ ) forbidding the two other contributions. For  $J = 1$ , the two singlet and triplet symmetries are mixed with relative phases that result from the orthogonality constraints. The eigenvector dominated by the triplet character has the same signs of both components, which makes the  $A_{el}[\ ^3P_1^0]$  value even larger than the one of the pure triplet (increase of 40%). For the state dominated by the singlet, strong cancellation occurs due to the triplet contamination, reducing the  $A_{el}[\ ^1P_1^0]$  value by 61%. Strong cancellation in the estimation of a property usually involves high uncertainty.

The “sharing rule” [83,84] that is used to quantify configuration mixing from the measured isotope shifts can be applied to the term-mixing analysis of the  $B_{el}$ . In the single-configuration approximation, the ratio  $B_{el}[\ ^3P_1^0]/B_{el}[\ ^1P_1^0]$  is exactly  $-\frac{1}{2} = -0.5$ , resulting from angular momentum algebra, when using the same orbital sets for describing both levels. Assuming a simple  $\ ^3P_0^0 - \ ^1P_0^0$  mixing for  $J = 1$ , we have

$$\begin{aligned} \Psi(\text{“} \ ^3P_1^0 \text{”}) &= a|\ ^3P_1^0\rangle + b|\ ^1P_1^0\rangle, \\ \Psi(\text{“} \ ^1P_1^0 \text{”}) &= b|\ ^3P_1^0\rangle - a|\ ^1P_1^0\rangle, \end{aligned} \tag{A1}$$

where  $|^{1,3}P_1^0\rangle$  are the two lowest  $J^\Pi = 1^-$  states resulting from pure  $LS$  terms and  $\Psi(|^{1,3}P_1^0\rangle)$  are the corresponding mixed states. Using the analytical ratio  $B_{el}[^1P_1^0]/B_{el}[^3P_1^0] = -2$ , one can estimate

$$\begin{aligned} B_{el}[|^3P_1^0\rangle] &= B_{el}[^3P_1^0](a^2 - 2b^2), \\ B_{el}[|^1P_1^0\rangle] &= B_{el}[^3P_1^0](b^2 - 2a^2), \end{aligned} \quad (\text{A2})$$

from which we deduce

$$R = B_{el}[|^3P_1^0\rangle]/B_{el}[|^1P_1^0\rangle] = \frac{a^2 - 2b^2}{b^2 - 2a^2}. \quad (\text{A3})$$

Adopting for this ratio a reasonable guess that is guided by the experimental result from Ref. [12] and that offers numerical simplicity,  $R = -\frac{1}{4}$ , one gets the following analytical eigenvector compositions:

$$\begin{aligned} \Psi(|^3P_1^0\rangle) &= \frac{\sqrt{7}}{3} |^3P_1^0\rangle + \frac{\sqrt{2}}{3} |^1P_1^0\rangle, \\ \Psi(|^1P_1^0\rangle) &= \frac{\sqrt{2}}{3} |^3P_1^0\rangle - \frac{\sqrt{7}}{3} |^1P_1^0\rangle. \end{aligned} \quad (\text{A4})$$

In other terms, the ratio  $B_{el}[|^3P_1^0\rangle]/B_{el}[|^1P_1^0\rangle]$  only reflects the singlet-triplet mixing in this simple model. We should not be surprised by its relative stability when more elaborate models are used. Extracting the  $^3P^0$  character ( $a^2$ ) from the lowest ( $^3P_1^0$ ) BP eigenvector obtained in a simple MR model mixing the  $\{5s^25p6s, 5s5p5d6s, 5p^36s\}$  configurations, we get after renormalization  $a^2 = 0.77617$  from which we determine  $B_{el}[|^3P_1^0\rangle]/B_{el}[|^1P_1^0\rangle] = -0.247$  according to

$$B_{el}[|^3P_1^0\rangle]/B_{el}[|^1P_1^0\rangle] = \frac{a^2 - 2b^2}{b^2 - 2a^2} = -\frac{3a^2 - 2}{3a^2 - 1}. \quad (\text{A5})$$

For the other BP eigenvector ( $^1P_1^0$ ), we have  $a^2 = 0.77641$  from which one confirms the ratio  $B_{el}[|^3P_1^0\rangle]/B_{el}[|^1P_1^0\rangle] = -0.248$ . The latter value is not too far from the above  $R = -\frac{1}{4}$  ratio value that would be obtained from the hypothetical ( $a^2 = \frac{7}{9}$ ;  $b^2 = \frac{2}{9}$ ) singlet-triplet mixing, taking into account that (i) one trusts the nonrelativistic ratio  $B_{el}[^3P_1^0]/B_{el}[^1P_1^0] = -\frac{1}{2}$  of the single-configuration approximation, (ii) the BP eigenvector has to be renormalized, and (iii) one assumes no contamination by other  $LS$  symmetries ( $^3D_1^0, ^3P_1^0, ^5D_1^0, ^5F_1^0, ^7D_1^0, \dots, ^{25}X_1^0$ ).

- [1] C. Froese Fischer, G. Gaigalas, P. Jönsson, and J. Bieroń, *Comput. Phys. Commun.* **237**, 184 (2019).
- [2] E. Kahl and J. Berengut, *Comput. Phys. Commun.* **238**, 232 (2019).
- [3] M. G. Kozlov, S. G. Porsev, M. S. Safronova, and I. I. Tupitsyn, *Comput. Phys. Commun.* **195**, 199 (2015).
- [4] A. Hibbert, *Phys. Scr.* **2004**, 39 (2004).
- [5] M. S. Safronova, D. Budker, D. DeMille, D. F. Jackson Kimball, A. Derevianko, and C. W. Clark, *Rev. Mod. Phys.* **90**, 025008 (2018).
- [6] K. Wang, C. X. Song, P. Jönsson, G. D. Zanna, S. Schiffmann, M. Godefroid, G. Gaigalas, X. H. Zhao, R. Si, C. Y. Chen, and J. Yan, *Astrophys. J., Suppl. Ser.* **239**, 30 (2018).
- [7] J. Ekman, P. Jönsson, S. Gustafsson, H. Hartman, G. Gaigalas, M. R. Godefroid, and C. Froese Fischer, *Astron. Astrophys.* **564**, A24 (2014).
- [8] L. Filippin, R. Beerwerth, J. Ekman, S. Fritzsche, M. Godefroid, and P. Jönsson, *Phys. Rev. A* **94**, 062508 (2016).
- [9] V. A. Dzuba, J. C. Berengut, C. Harabati, and V. V. Flambaum, *Phys. Rev. A* **95**, 012503 (2017).
- [10] S. Verdebout, C. Názé, P. Jönsson, P. Rynkun, M. Godefroid, and G. Gaigalas, *At. Data Nucl. Data Tables* **100**, 1111 (2014).
- [11] M. G. Kozlov, M. S. Safronova, J. R. Crespo López-Urrutia, and P. O. Schmidt, *Rev. Mod. Phys.* **90**, 045005 (2018).
- [12] D. T. Yordanov, L. V. Rodríguez, D. L. Balabanski, J. Bieroń, M. L. Bissell, K. Blaum, B. Cheal, J. Ekman, G. Gaigalas, R. F. Garcia Ruiz, G. Georgiev, W. Gins, M. R. Godefroid, C. Gorges, Z. Harman, H. Heylen, P. Jönsson, A. Kanellakopoulos, S. Kaufmann, C. H. Keitel, V. Lagaki, S. Lechner *et al.*, *Commun. Phys.* **3**, 107 (2020).
- [13] N. Frömmgen, D. L. Balabanski, M. L. Bissell, J. Bieroń, K. Blaum, B. Cheal, K. Flanagan, S. Fritzsche, C. Geppert, M. Hammen, M. Kowalska, K. Kreim, A. Krieger, R. Neugart, G. Neyens, M. M. Rajabali, W. Nörtershäuser, J. Papuga, and D. T. Yordanov, *Eur. Phys. J. D* **69**, 164 (2015).
- [14] D. T. Yordanov, D. L. Balabanski, J. Bieroń, M. L. Bissell, K. Blaum, I. Budinčević, S. Fritzsche, N. Frömmgen, G. Georgiev, C. Geppert, M. Hammen, M. Kowalska, K. Kreim, A. Krieger, R. Neugart, W. Nörtershäuser, J. Papuga, and S. Schmidt, *Phys. Rev. Lett.* **110**, 192501 (2013).
- [15] C. Wraith, X. F. Yang, L. Xie, C. Babcock, J. Biero, J. Billowes, M. L. Bissell, K. Blaum, B. Cheal, L. Filippin, R. F. G. Ruiz, W. Gins, L. K. Grob, G. Gaigalas, M. Godefroid, C. Gorges, H. Heylen, M. Honma, P. Jönsson, S. Kaufmann *et al.*, *Phys. Lett. B* **771**, 385 (2017).
- [16] A. Antognini, N. Berger, T. E. Cocolios, R. Dressler, R. Eichler, A. Eggenberger, P. Indelicato, K. Jungmann, C. H. Keitel, K. Kirch, A. Knecht, N. Michel, J. Nuber, N. S. Oreshkina, A. Ouf, A. Papa, R. Pohl, M. Pospelov, E. Rapisarda, N. Ritjoho *et al.*, *Phys. Rev. C* **101**, 054313 (2020).
- [17] M. Cohen and F. Reif, in *Solid State Physics Series, Volume 5*, edited by F. Seitz and D. Turnbull (Academic, New York, 1957), pp. 321–438.
- [18] P. Schwerdtfeger, M. Pernpointner, and W. Nazarewicz, in *Calculation of NMR and EPR Parameters. Theory and Applications*, edited by M. Kaupp, M. Bühl, and V. G. Malkin (Wiley, Weinheim, 2004), pp. 279–291.
- [19] E. A. C Lucken, *Nuclear Quadrupole Coupling Constants* (Academic, London, 1969).
- [20] T. Das and E. Hahn, *Solid State Physics: Supplement 1: Nuclear Quadrupole Resonance Spectroscopy* (Academic, New York, 1958).
- [21] *Mössbauer Spectroscopy*, edited by D. Dickson and F. Berry (Cambridge University Press, Cambridge, 2005).
- [22] Y. Chen and D. Yang, *Mössbauer Effect in Lattice Dynamics: Experimental Techniques and Applications* (Wiley, Hoboken, NJ, 2007).
- [23] H. Haas and D. A. Shirley, *J. Chem. Phys.* **58**, 3339 (1973).
- [24] H. Haas, S. P. A. Sauer, L. Hemmingsen, V. Kellö, and P. W. Zhao, *Europhys. Lett.* **117**, 62001 (2017).

- [25] P. Raghavan, *At. Data Nucl. Data Tables* **42**, 189 (1989).
- [26] N. J. Stone, *At. Data Nucl. Data Tables* **111-112**, 1 (2016).
- [27] P. Pyykkö, *Mol. Phys.* **116**, 1328 (2018).
- [28] I. P. Grant, *Relativistic Quantum Theory of Atoms and Molecules: Theory and Computation* (Springer, New York, 2007).
- [29] C. Froese Fischer, M. Godefroid, T. Brage, P. Jönsson, and G. Gaigalas, *J. Phys. B: At., Mol. Opt. Phys.* **49**, 182004 (2016).
- [30] I. I. Tupitsyn and A. V. Loginov, *Opt. Spectrosc.* **94**, 319 (2003).
- [31] I. I. Tupitsyn, V. M. Shabaev, J. R. Crespo López-Urrutia, I. Draganić, R. S. Orts, and J. Ullrich, *Phys. Rev. A* **68**, 022511 (2003).
- [32] I. I. Tupitsyn, A. V. Volotka, D. A. Glazov, V. M. Shabaev, G. Plunien, J. R. Crespo López-Urrutia, A. Lapierre, and J. Ullrich, *Phys. Rev. A* **72**, 062503 (2005).
- [33] R. Soria Orts, Z. Harman, J. R. Crespo López-Urrutia, A. N. Artemyev, H. Bruhns, A. J. González Martínez, U. D. Jentschura, C. H. Keitel, A. Lapierre, V. Mironov, V. M. Shabaev, H. Tawara, I. I. Tupitsyn, J. Ullrich, and A. V. Volotka, *Phys. Rev. Lett.* **97**, 103002 (2006).
- [34] I. Tupitsyn, Dirac-Fock-Sturm method in relativistic calculations for atoms and two-atomic molecules, Ph.D. thesis, Saint-Petersburg State University, Saint-Petersburg, 2008 (in Russian).
- [35] J. Bieroń, L. Filippin, G. Gaigalas, M. Godefroid, P. Jönsson, and P. Pyykkö, *Phys. Rev. A* **97**, 062505 (2018).
- [36] P. Jönsson, G. Gaigalas, J. Bieroń, C. Froese Fischer, and I. P. Grant, *Comput. Phys. Commun.* **184**, 2197 (2013).
- [37] I. P. Grant, B. J. McKenzie, P. H. Norrington, D. F. Mayers, and N. C. Pyper, *Comput. Phys. Commun.* **21**, 207 (1980).
- [38] G. Gaigalas, Z. Rudzikas, and C. Froese Fischer, *J. Phys. B: At., Mol. Opt. Phys.* **30**, 3747 (1997).
- [39] G. Gaigalas, S. Fritzsche, and I. P. Grant, *Comput. Phys. Commun.* **139**, 263 (2001).
- [40] I. P. Grant and N. C. Pyper, *J. Phys. B: At. Mol. Phys.* **9**, 761 (1976).
- [41] C. Y. Zhang, K. Wang, M. Godefroid, P. Jönsson, R. Si, and C. Y. Chen, *Phys. Rev. A* **101**, 032509 (2020).
- [42] I. Lindgren and A. Rosén, *Case Stud. At. Phys.* **4**, 93 (1974).
- [43] P. Jönsson, F. Parpia, and C. Froese Fischer, *Comput. Phys. Commun.* **96**, 301 (1996).
- [44] A. Edmonds, *Angular Momentum in Quantum Mechanics* (Princeton University Press, Princeton, New Jersey, 1957).
- [45] A. E. Barzakh, D. Atanasov, A. N. Andreyev, M. Al Monthery, N. A. Althubiti, B. Andel, S. Antalic, K. Blaum, T. E. Cocolios, J. G. Cubiss, P. Van Duppen, T. D. Goodacre, A. de Roubin, Y. A. Demidov, G. J. Farooq-Smith, D. V. Fedorov, V. N. Fedosseev, D. A. Fink, L. P. Gaffney, L. Ghys *et al.*, *Phys. Rev. C* **101**, 034308 (2020).
- [46] P. Pyykkö and M. Seth, *Theor. Chem. Acc.* **96**, 92 (1997).
- [47] C. Froese Fischer, T. Brage, and P. Jönsson, *Computational Atomic Structure. An MCHF Approach* (Institute of Physics Publishing, Bristol, 1997).
- [48] S. Verdebout, P. Rynkun, P. Jönsson, G. Gaigalas, C. Froese Fischer, and M. Godefroid, *J. Phys. B: At., Mol. Opt. Phys.* **46**, 085003 (2013).
- [49] J. Dembczyński and H. Rebel, *Phys. B+C (Amsterdam)* **125**, 341 (1984).
- [50] J. Bieroń, C. Froese Fischer, P. Indelicato, P. Jönsson, and P. Pyykkö, *Phys. Rev. A* **79**, 052502 (2009).
- [51] B. Engels, *Theor. Chim. Acta* **86**, 429 (1993).
- [52] B. Engels, L. A. Eriksson, and S. Lunell, *Adv. Quantum Chem.* **27**, 297 (1996).
- [53] P. Jönsson, A. Ynnerman, C. Froese Fischer, M. R. Godefroid, and J. Olsen, *Phys. Rev. A* **53**, 4021 (1996).
- [54] M. R. Godefroid, G. Van Meulebeke, P. Jönsson, and C. Froese Fischer, *Z. Phys. D-Atoms, Molecules Clusters* **42**, 193 (1997).
- [55] J. Bieroń, C. Froese Fischer, P. Jönsson, and P. Pyykkö, *J. Phys. B: At., Mol. Opt. Phys.* **41**, 115002 (2008).
- [56] J. Bieroń and P. Pyykkö, *Phys. Rev. Lett.* **87**, 133003 (2001).
- [57] J. Bieroń, P. Pyykkö, and P. Jönsson, *Phys. Rev. A* **71**, 012502 (2005).
- [58] J. Bieroń, P. Jönsson, and C. Froese Fischer, *Phys. Rev. A* **60**, 3547 (1999).
- [59] J. Bieroń, P. Jönsson, and C. Froese Fischer, *Phys. Rev. A* **53**, 2181 (1996).
- [60] W. R. Johnson, *Atomic Structure Theory: Lectures on Atomic Physics* (Springer, Berlin, 2007).
- [61] D. Sundholm and J. Olsen, *Phys. Rev. A* **47**, 2672 (1993).
- [62] A. Kramida, Yu. Ralchenko, J. Reader, and NIST ASD Team, NIST Atomic Spectra Database (version 5.7.1) (online), National Institute of Standards and Technology, Gaithersburg, MD. Available at <https://physics.nist.gov/asd>.
- [63] W. Brill, The Arc Spectrum of Tin, Ph.D. thesis, Purdue University, Lafayette, IN, 1964.
- [64] T. Carette, C. Drag, O. Scharf, C. Blondel, C. Delsart, C. Froese Fischer, and M. Godefroid, *Phys. Rev. A* **81**, 042522 (2010).
- [65] J. Li, P. Jönsson, M. Godefroid, C. Dong, and G. Gaigalas, *Phys. Rev. A* **86**, 052523 (2012).
- [66] G. Gaigalas, P. Rynkun, L. Radziūte, D. Kato, M. Tanaka, and P. Jönsson, *Astrophys. J., Suppl. Ser.* **248**, 13 (2020).
- [67] N. Michel, N. S. Oreshkina, and C. H. Keitel, *Phys. Rev. A* **96**, 032510 (2017).
- [68] K. Koch, K. Koepernik, D. Van Neck, H. Rosner, and S. Cottenier, *Phys. Rev. A* **81**, 032507 (2010).
- [69] M. S. Safronova and W. R. Johnson, *Adv. At. Mol. Opt. Phys.* **55**, 191 (2008).
- [70] M. S. Safronova and U. I. Safronova, *Phys. Rev. A* **83**, 052508 (2011).
- [71] H.-K. Chung, B. J. Braams, K. Bartschat, A. G. Császár, G. W. F. Drake, T. Kirchner, V. Kokoouline, and J. Tennyson, *J. Phys. D: Appl. Phys.* **49**, 363002 (2016).
- [72] S. Schiffmann, M. Godefroid, J. Ekman, P. Jönsson, and C. F. Fischer, *Phys. Rev. A* **101**, 062510 (2020).
- [73] F. P. Gustafsson, C. M. Ricketts, M. L. Reitsma, R. F. Garcia Ruiz, S. W. Bai, J. C. Berengut, J. Billowes, C. L. Binnersley, A. Borschevsky, T. E. Cocolios, B. S. Cooper, R. P. de Groote, K. T. Flanagan, A. Koszorus, G. Neyens, H. A. Perrett, A. R. Vernon, Q. Wang, S. G. Wilkins, and X. F. Yang, *Phys. Rev. A* **102**, 052812 (2020).
- [74] J. Eberz, U. Dinger, G. Huber, H. Lochmann, R. Menges, G. Ulm, R. Kirchner, O. Klepper, T. Kühl, and D. Marx, *Z. Phys. A* **326**, 121 (1987).
- [75] G. Barone, R. Mastalerz, M. Reiher, and R. Lindh, *J. Phys. Chem. A* **112**, 1666 (2008).

- [76] M. Tong, P. Jönsson, and C. Froese Fischer, *Phys. Scr.* **48**, 446 (1993).
- [77] Z.-C. Yan, D. K. McKenzie, and G. W. F. Drake, *Phys. Rev. A* **54**, 1322 (1996).
- [78] V. A. Yerokhin, *Phys. Rev. A* **77**, 020501(R) (2008).
- [79] V. A. Yerokhin, *Phys. Rev. A* **78**, 012513 (2008).
- [80] E. Y. Korzinin, N. S. Oreshkina, and V. M. Shabaev, *Phys. Scr.* **71**, 464 (2005).
- [81] N. S. Oreshkina, A. V. Volotka, D. A. Glazov, I. I. Tupitsyn, V. M. Shabaev, and G. Plunien, *Optics Spectro.* **102**, 815 (2007).
- [82] P. Jönsson, C.-G. Wahlström, and C. F. Fischer, *Comput. Phys. Commun.* **74**, 399 (1993).
- [83] J. Bauche and R.-J. Champeau, *Adv. At. Mol. Phys.* **12**, 39 (1976).
- [84] Y. Ishida, H. Iimura, S. Ichikawa, and T. Horiguchi, *J. Phys. B: At., Mol. Opt. Phys.* **30**, 2569 (1997).

## Paper VII



A. Papoulia, B. G. Carlsson, and J. Ekman

Effect of realistic nuclear charge distributions on isotope shifts and progress towards  
the extraction of higher-order nuclear radial moments

*Physical Review A*, 2016, 94(4), 042502

Copyright 2016 American Physical Society





## Effect of realistic nuclear charge distributions on isotope shifts and progress towards the extraction of higher-order nuclear radial moments

A. Papoulia,<sup>1</sup> B. G. Carlsson,<sup>1,\*</sup> and J. Ekman<sup>2</sup>

<sup>1</sup>*Division of Mathematical Physics, LTH, Lund University, Post Office Box 118, S-22100 Lund, Sweden*

<sup>2</sup>*Group for Materials Science and Applied Mathematics, Malmö University, S-20506 Malmö, Sweden*

(Received 13 April 2016; published 3 October 2016)

Atomic spectral lines from different isotopes display a small shift in energy, commonly referred to as the line isotope shift. One of the components of the isotope shift is the field shift, which depends on the extent and the shape of the nuclear charge density distribution. The purpose of this work is to investigate how sensitive field shifts are with respect to variations in the nuclear size and shape and what information of nuclear charge distributions can be extracted from measurements. Nuclear properties are obtained from nuclear density functional theory calculations based on the Skyrme-Hartree-Fock-Bogoliubov approach. These results are combined with multiconfiguration Dirac-Hartree-Fock methods to obtain realistic field shifts and it is seen that phenomena such as nuclear deformation and variations in the diffuseness of nuclear charge distributions give measurable contributions to the isotope shifts. Using a different approach, we demonstrate the possibility to extract information concerning the nuclear charge densities from the observed field shifts. We deduce that combining methods used in atomic and nuclear structure theory gives an improved description of field shifts and that extracting additional nuclear information from measured isotope shifts is possible in the near future with improved experimental methods.

DOI: [10.1103/PhysRevA.94.042502](https://doi.org/10.1103/PhysRevA.94.042502)

### I. INTRODUCTION

Information of nuclear sizes has grown rapidly during the last decades. In the compilation by Angeli and Marinova in 2013 [1], root-mean-square (rms) radii were reported for more than 900 isotopes of which the majority are radioactive systems. This development is a consequence of refined experimental and theoretical methods, and a state-of-the-art example is the frequency comb measurement of the hydrogen-deuterium radius difference by Parthey *et al.* [2]. The plenitude of available data has allowed for detailed investigations of the evolution of nuclear radii for isotope sequences along virtually the entire periodic table. These studies have revealed unexpected trends, especially close to magic numbers, which serve as benchmarks for nuclear structure calculations [3].

However, more detailed and model-independent experimental information of nuclear charge distributions beyond the rms radius is only available for stable or long-lived isotopes from electron scattering experiments. On the theoretical side it has been shown that isotope shifts in heavier systems depend on the nuclear model used [4] and that the contribution from nuclear deformation to the isotope shift in some cases is comparable to the uncertainty in recent dielectronic recombination experiments [5,6].

Experimental techniques such as high-precision laser measurements at the COLLAPS and CRIS experiments at ISOLDE/CERN [7] and dielectronic recombination experiments at the envisaged realization of CRYRING at GSI [8] are constantly evolving. This justifies a more systematic theoretical investigation of what information can be revealed about nuclear charge distributions in exotic systems.

The main objective of this work is to study the effect of realistic charge distributions, taken from nuclear density

functional theory (DFT), on the isotope shift in heavier atoms. In addition, a promising method for the extraction of higher-order radial moments from experimental isotope shifts is also presented and tested.

### II. ISOTOPE SHIFTS

The atomic nucleus is  $\sim 10^4$  smaller than the size of the atom. Even so, the finite mass and extended charge distribution of the nucleus have a measurable effect on atomic spectra. Spectral lines from different isotopes display a small shift in energy referred to as the isotope shift (IS), which can further be decomposed into a mass shift (MS) and a field shift (FS) contribution. The difference in energy between the corresponding atomic level  $i$  of two isotopes  $A$  and  $A'$ , the level isotope shift, can thus be expressed as

$$\delta E_{i,IS}^{A,A'} = \delta E_{i,MS}^{A,A'} + \delta E_{i,FS}^{A,A'} = E_i^{A'} - E_i^A. \quad (1)$$

For a particular atomic transition  $k$  between upper  $u$  and lower  $l$  levels, the difference in energy for a pair of isotopes, namely, the line frequency isotope shift, is consequently given by

$$\begin{aligned} \delta \nu_{k,IS}^{A,A'} &= \delta \nu_{k,MS}^{A,A'} + \delta \nu_{k,FS}^{A,A'} = \nu_k^{A'} - \nu_k^A \\ &= \frac{\delta E_{u,IS}^{A,A'} - \delta E_{l,IS}^{A,A'}}{h}. \end{aligned} \quad (2)$$

The level mass shift contribution can be expressed as

$$\delta E_{i,MS}^{A,A'} = \left( \frac{M' - M}{MM'} \right) K_{MS}^i, \quad (3)$$

where  $M$  and  $M'$  are the atomic masses of the isotopes and  $K_{MS}^i$  is the mass-independent mass shift parameter [9–11]. Although the computation of the mass shift parameters, and hence the mass shift contribution to the isotope shift, represents a challenging task, it is not the main focus of this work. Instead,

\*gillis.carlsson@matfys.lth.se

the focus here is on the extent and shape of nuclear charge distributions which almost exclusively affect the field shift described in detail below.

### A. Field shift

The field shift arises from differences in the nuclear charge density distribution between isotopes caused by the different number of neutrons. Unlike pointlike charge distributions, more realistic charge distributions alter the central field that the atomic electrons experience, and hence the atomic level and transition energies will be affected. Evidently, the field shift effect is more pronounced for electrons moving in  $s_{1/2}$  and  $p_{1/2}$  orbitals due to the nonzero probability of the radial wave functions at the origin. Moreover, the nuclear charge and extent, together with the contraction of the atomic orbitals, increase with the proton number  $Z$  and thus the contribution from the field shift to the isotope shift is found to be dramatically larger in heavier systems.

#### 1. Nonperturbative “exact” method

In atomic structure calculations, where the contribution from the mass shift is neglected, the level field shift can be computed according to Eq. (1) by performing separate calculations for two isotopes  $A$  and  $A'$ , with different parameter sets describing the respective nuclear charge distributions. This method is in general highly model dependent since the description of the nucleus is normally restricted to an approximate model. Moreover, this procedure is cumbersome if calculations are to be performed for many isotope pairs and in addition it may suffer from numerical instabilities since it involves the subtraction of large quantities (atomic binding energies) to obtain a tiny quantity. Nevertheless, this strategy constitutes an “exact” method for estimating the validity of perturbative approaches and the resulting field shifts will be denoted  $\delta v_{k,VA}^{\text{exact}}$  below.

#### 2. Perturbative method

To eliminate the disadvantages of the exact method described above and allow for a more flexible analysis of the field shift, an alternative approach based on perturbation theory may be used. Within the framework of perturbation, the first-order level field shift of level  $i$  can be written

$$\delta E_{i,FS}^{(1)A,A'} = - \int_{R^3} [V_A(\mathbf{r}) - V_{A'}(\mathbf{r})] \rho_i^e(\mathbf{r}) d^3\mathbf{r}, \quad (4)$$

where  $V_A(\mathbf{r})$  and  $V_{A'}(\mathbf{r})$  are the one-electron potentials arising from the different nuclear charge distributions of the two isotopes and  $\rho_i^e(\mathbf{r})$  is the electron density inside the nuclear volume of the reference isotope  $A$ .

Following the work by Seltzer [12], Torbohm *et al.* [13], and Blundell *et al.* [14] and assuming an extended spherical symmetric nuclear charge distribution, it can be shown that the electron density to a very good approximation can be expanded around  $r = 0$  as an even polynomial function keeping only the first few terms:

$$\rho_i^e(\mathbf{r}) \approx b_i(r) = b_{i,1} + b_{i,2}r^2 + b_{i,3}r^4 + b_{i,4}r^6. \quad (5)$$

Inserting the expression above in Eq. (4) and making use of the Laplacian operator in spherical coordinates,

$\nabla^2 r^{2N} = 2N(2N+1)r^{2N-2}$ , Poisson’s equation  $\nabla^2 V_A(\mathbf{r}) = -4\pi\rho_A(\mathbf{r})$ , and finally Eq. (2), the first-order line frequency field shift is given by [14,15]

$$\delta v_{k,FS}^{(1)A,A'} \approx \delta v_{k,RFS}^{A,A'} = \sum_{N=1}^4 F_{k,N} \delta \langle r^{2N} \rangle^{A,A'}, \quad (6)$$

where  $F_{k,N}$  are the so-called line electronic factors expressed as

$$F_{k,N} = \frac{2\pi}{h} \frac{Z \Delta b_{k,N}}{N(2N+1)}, \quad (7)$$

and

$$\delta \langle r^{2N} \rangle^{A,A'} = \langle r^{2N} \rangle^A - \langle r^{2N} \rangle^{A'} \quad (8)$$

are the differences of the nuclear radial moments, of order  $2N$ , of the isotopes  $A$  and  $A'$ . The electronic factors are proportional to the difference of the electronic density inside the nucleus between the upper and lower atomic level, thus,  $\Delta b_{k,N} = b_{u,N} - b_{l,N}$ .

The reformulated field shift (RFS) according to Eq. (6) enables a more versatile analysis of field shifts. This is due to the fact that the radial moments  $\langle r^{2N} \rangle$  used in the expression can be taken from any model, calculation, or experiment. In addition, it is possible to analyze the contributions to the field shift order by order. For example, keeping only the first term in Eq. (6) we obtain

$$\delta v_{i,FS}^{(1)A,A'} \approx \frac{2\pi}{3h} Z \Delta \rho_i^e(\mathbf{0}) \delta \langle r^2 \rangle^{A,A'}, \quad (9)$$

which is a suitable approximation for lighter systems where a constant electron density within the nucleus can be assumed,  $\rho_i^e(\mathbf{r}) \approx b_{i,1} = \rho_i^e(\mathbf{0})$ . For heavier systems, however, the electron density varies inside the nuclear volume and thus the  $N \geq 2$  terms in Eq. (6) must also be considered for an accurate description. Further on, by including these higher-order contributions, the effect on the isotope shift due to details in the nuclear charge distribution can be analyzed. As we shall see, the reversed approach is also possible, namely, to extract higher-order radial moments of the nuclear charge distribution from observed isotope shifts.

### B. Computational procedure

Solutions to the many-body Hamiltonian describing the atom are obtained by performing calculations using the relativistic atomic structure package GRASP2K [16], which is based on the multiconfiguration Dirac-Hartree-Fock (MCDHF) approach. In the MCDHF method, atomic state functions  $\Psi(\gamma P J M_J)$ , which are approximate solutions to the Dirac-Coulomb Hamiltonian, are expanded over configuration state functions (CSFs),  $\Phi(\gamma_i P J M_J)$ , with appropriate total angular momentum ( $J$ ) symmetry and parity  $P$ :

$$\Psi(\gamma P J M_J) = \sum_{i=1}^N c_i \Phi(\gamma_i P J M_J). \quad (10)$$

In the expression above,  $\gamma_i$  represents the configuration, coupling, and other quantum number necessary to uniquely describe the state  $i$ ,  $M_J$  is the projection of  $J$  on the  $z$  axis, and  $c_i$  are mixing coefficients fulfilling the condition  $\sum_{i=1}^N c_i^2 = 1$ .

The CSFs are constructed from one-electron Dirac orbitals that together with the mixing coefficients are obtained in a relativistic self-consistent-field procedure by applying the variational principle [17]. The transverse photon interaction as well as leading quantum electrodynamic (QED) corrections can be accounted for in subsequent relativistic configuration interaction (RCI) calculations [18].

Once a set of ASFs is obtained, the computation of the isotope shift parameters is carried out using the program RIS4 [15], which represents an extension of the predecessor RIS3 [19]. In RIS4 the polynomial expansion  $b_i(r)$  given by Eq. (5) is for each level fitted to the constructed electron density  $\rho_e^i(\mathbf{r})$  using a least-squares method. Finally, by combining the expansion coefficients  $b_{i,N}$  from two or more levels, the line electronic factors are computed for the reference isotope  $A$  according to Eq. (7).

### III. REALISTIC NUCLEAR CHARGE DISTRIBUTIONS

As seen above, the reformulated field shift depends on the radial moments of the nuclear charge distribution. These moments can be calculated from nuclear models that provide accurate charge distributions. In this section, three such models are compared.

#### A. Nuclear charge distribution models

The nuclear charge distribution can be approximated by an analytical expression such as the Fermi distribution

$$\rho(r, \theta) = \frac{\rho_0}{1 + e^{\frac{r-c(\theta)}{a}}}, \quad (11)$$

where, if only axially symmetric quadrupole deformation is considered,  $c(\theta) = c_0[1 + \beta_{20}Y_{20}(\theta)]$ . This modified Fermi distribution has been used previously to investigate the effect of deformation on atomic binding energies in Li-like systems [5,20,21]. In these studies, nuclear deformation parameters extracted from highly accurate muonic atom studies were used [22,23]. The value of  $\rho_0 \approx \rho(r=0)$  is determined by the normalization condition

$$\int \rho(r) dr = 1, \quad (12)$$

and the parameter  $\alpha$  is given by the relation

$$t = 4 \ln(3)\alpha, \quad (13)$$

where  $t$  is the skin thickness of the distribution. The skin thickness is defined as the interval where the density decreases from 90% to 10% of  $\rho(0)$ . The parameter  $c_0$  reflects the size of the nucleus.

In the GRASP2K code [16], the explicit values for these parameters are taken as [4]  $t = 2.3$  fm,  $\beta_{20} = 0$  and the parameter  $c_0$  is chosen so that the rms radius of the nuclear charge distribution becomes

$$\sqrt{\langle r^2 \rangle} = 0.836A^{\frac{1}{3}} + 0.570 \text{ fm } (A > 9), \quad (14)$$

where  $A$  denotes the number of nucleons of the isotope.

Realistic nuclear charge distributions can also be obtained from microscopic nuclear models based on effective interactions. Such models have the advantage that the size, shape, and

diffuseness of the nuclear density is obtained by solving a self-consistent set of Hartree-Fock-Bogoliubov (HFB) equations.

In this work, we adopt the effective Skyrme interaction [24] and consider two different sets of Skyrme parameters called SLY4 and UNEDF1. The parameters in both sets are adjusted to fit experimental data in a broad range of nuclei. The SLY4 set was fitted with an emphasis on describing neutron-rich nuclei [25], whereas the UNEDF1 set constitutes a more recent parametrization fitted to reproduce both ground-state energies as well as radii and single-particle energies [26]. In spherical symmetry, the solutions to the HFB equations are provided by the code HOSPHE (v2.00), which is a new version of the program HOSPHE (v1.02) [27]. In the case of deformed nuclei, we use the code HFBTHO (2.00d) [28], based on a cylindrically deformed harmonic oscillator (HO) basis.

For spherical nuclei, we take into account the finite nature of protons by folding the densities using the convolution formula

$$\varrho_c(\mathbf{r}) = \int d^3r' \rho_p(\mathbf{r}') g(|\mathbf{r} - \mathbf{r}'|), \quad (15)$$

where  $\rho_p(\mathbf{r})$  is the initially calculated proton density and

$$g(r) = (r_0\sqrt{\pi})^{-3} e^{-(r/r_0)^2} \quad (16)$$

the proton form factor, assumed to be a Gaussian with  $r_0 = \sqrt{\frac{2}{3}} r_p^{\text{rms}}$ , where  $r_p^{\text{rms}}$  is the proton rms radius [29]. Experiments to determine the proton radius have resulted in different values of  $r_p^{\text{rms}}$  [30,31], and in this work we adopt the results based on electron scattering measurements assuming  $r_p^{\text{rms}} = 0.88$  fm.

In Fig. 1, the theoretical rms radii are compared to experimental data obtained from elastic electron scattering experiments [32,33]. A total of 16 spherical isotopes of various elements, O, S, Ca, Ni, Sn, and Pb, are used in the comparison. As seen in this figure, both the nuclear models as well as the empirical parametrization [Eq. (14)] are in good agreement with the experimental data.

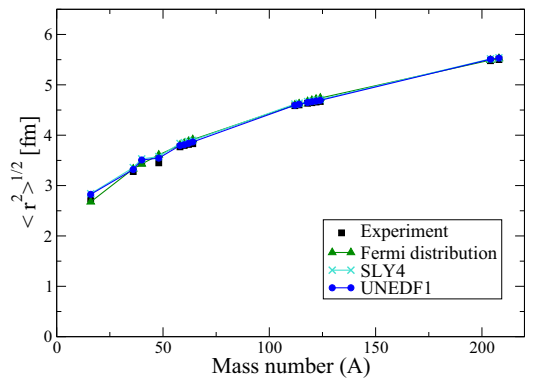


FIG. 1. Rms radii of theoretical charge distributions compared to experimental data. Two different Skyrme parameter sets, SLY4 and UNEDF1, are used with moments calculated after taking into account the finite proton size. The resulting  $\sqrt{\langle r^2 \rangle}$  values from the Fermi distribution used in the GRASP2K code [Eq. (14)] are also included.

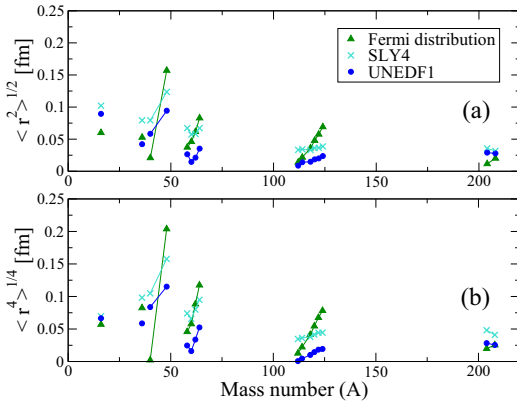


FIG. 2. Discrepancy of (a) the rms radii  $\sqrt{\langle r^2 \rangle}$  and (b) the  $\sqrt[4]{\langle r^4 \rangle}$  moment of the theoretical charge distributions compared to experimental data. Isotopic sequences are connected with lines.

The discrepancy between the theoretical and the experimental  $\sqrt{\langle r^2 \rangle}$  values is shown in Fig. 2(a). As seen in this figure, the more recent Skyrme parameters (UNEDF1) give the best description of the data. The two microscopic models also stand out as they are in general better at capturing the isotopic trends giving flatter curves than the Fermi distribution.

For calculations of field shifts, the higher-order moments may also play an important role and in Fig. 2(b) the discrepancy in the prediction of the  $\sqrt[4]{\langle r^4 \rangle}$  values is shown. This comparison shows the same trend as for the  $\sqrt{\langle r^2 \rangle}$  values, namely, that microscopic models capture the isotopic trends better while the Fermi distribution in general does a good job for the stable nuclei. One might consider using more refined empirical expressions containing a dependence on the difference in proton and neutron numbers, but since such an approach would anyway not capture the important changes caused by deformations, the best approach comes from using state-of-the-art microscopic nuclear models.

In Table I, the standard deviations of the discrepancies for the three models are compared. Considering the average agreement, the Fermi distribution and the Skyrme-SLY4 give similar results while the more recent UNEDF1 is significantly better. In addition, the UNEDF1 set predicts the  $\sqrt{\langle r^2 \rangle}$  and  $\sqrt[4]{\langle r^4 \rangle}$  moments with about the same precision, while the precision deteriorates slightly for the two other models. This agrees with the fact that the full density profiles also tend to be better reproduced by UNEDF1. Higher-order moments are

TABLE I. Standard deviations of discrepancies in  $\sqrt{\langle r^2 \rangle}$  and  $\sqrt[4]{\langle r^4 \rangle}$ , calculated for the three theoretical models.

	$\sqrt{\langle r^2 \rangle}$	$\sqrt[4]{\langle r^4 \rangle}$
Fermi distribution	0.01660	0.01954
Skyrme-SLY4	0.01821	0.01905
Skyrme-UNEDF1	0.01271	0.01260

difficult to compare since more focus is then shifted towards the surface and tail of the density where insufficient precision in the data hampers a qualitative comparison. All in all, the UNEDF1 parametrization describes the nuclear charge distributions more accurately than both the Skyrme-SLY4 and Fermi distributions and therefore realistic nuclear radial moments resulting from this interaction will be used in the following in order to estimate the line field shifts.

## B. Application to line field shifts

In this section, the atomic physics calculations for the electron energies are combined with the use of the microscopic nuclear models for the charge densities. As an example, we consider the resonance transition  $6s^2\ ^1S_0 \rightarrow 6s6p\ ^1P_1^o$  observed in several neutral Ba isotopes. By comparing the line field shift in the isotope series one may be able to draw conclusions on the shape and size of the nuclear density distributions. The most abundant barium isotope on Earth,  $^{138}\text{Ba}$ , is taken as a reference and the shifts in electron energies are thus compared to the values for this isotope. This reference isotope is spherical, while the other isotopes obtained by removing or adding a couple of neutrons are predicted to have more deformed shapes.

Figure 3 shows the calculated line field shifts for the Ba isotope series compared to experimental isotope shifts [34], where theoretical mass shift contributions have been subtracted [35]. The calculations based on the Fermi distribution show a linear dependence on the mass number  $A'$  of the target isotope and fail to capture the general trend. The microscopic nuclear calculations capture both the right trend with neutron number and in addition some of the odd-even staggering.

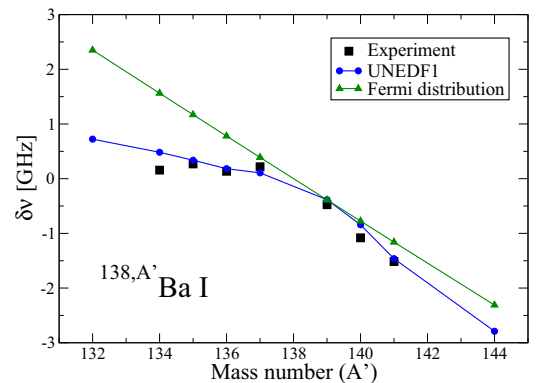


FIG. 3. The absolute line field shift values are compared to the available experimental data [34,35]. Nuclear radial moments resulted from the realistic HFB calculations using the Skyrme-UNEDF1 interaction, as well as from the Fermi distribution, have been used. All plotted values refer to the  $6s^2\ ^1S_0 \rightarrow 6s6p\ ^1P_1^o$  transition.

#### IV. EFFECT OF REALISTIC CHARGE DISTRIBUTIONS ON THE LINE FIELD SHIFTS

In order to investigate the resulting field shifts when replacing the commonly adopted Fermi distribution with more realistic nuclear models, we examine the differences in the predicted field shifts for a variety of isotopes. For such analysis, the Fermi distribution is fitted so that it has the same  $\langle r^2 \rangle$  value as computed from the realistic distributions. Then,

$$\delta v_{\text{Fermi}} = F_{k,1} \delta \langle r^2 \rangle_{\text{realistic}} + \sum_{N=2}^4 F_{k,N} \delta \langle r^{2N} \rangle_{\text{Fermi}}. \quad (17)$$

Thus, the correction when using realistic charge distributions is given by

$$\delta v_{\text{realistic}} - \delta v_{\text{Fermi}} = \sum_{n=2}^4 F_{k,n} [\delta \langle r^{2n} \rangle_{\text{realistic}} - \delta \langle r^{2n} \rangle_{\text{Fermi}}]. \quad (18)$$

In the following two subsections, the size of this correction term will be investigated for lithium-like and neutral systems.

##### A. Li-like systems

Isotope shifts in lithium-like systems have been studied theoretically and experimentally in the past [5,6,36–38] and are thus of particular interest. In Fig. 4, the magnitude of the “correction term”  $\delta v_{\text{realistic}} - \delta v_{\text{Fermi}}$  for one of the resonance transitions has been plotted as a function of the mass number  $A'$  of the target isotope for a wide range of Li-like systems. For the spherical Sn, Pb, Er, and Lv nuclear systems the magnitude

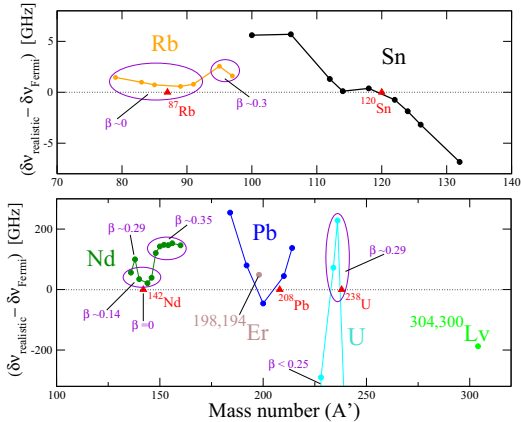


FIG. 4. The corrections  $\delta v_{\text{realistic}} - \delta v_{\text{Fermi}}$  to the line field shift calculations as a function of the mass number  $A'$  of the target isotope for various Li-like systems. For the systems that contain deformed isotopes, the magnitude of the quadrupole deformation parameter  $\beta_{20}$  of the target isotopes  $A'$  is indicatively shown. The isotopes used as reference are marked with triangles and all plotted values refer to the  $1s^2 2s^2 S_{1/2} \rightarrow 1s^2 2p^2 P^o_{1/2}$  resonance transition.

of the corrections increases with  $A'$ . Moreover, the absolute magnitude of the  $\delta v_{\text{realistic}} - \delta v_{\text{Fermi}}$  term increases with the difference between the neutron number  $\Delta N^{A,A'}$  in the isotope sequences of Sn and Pb. When more neutrons are added, they alter the protons distribution, leading to changes in the diffuseness. This effect is not included in the Fermi model where a constant skin thickness  $t \simeq 2.3$  fm is assumed and may be a reason for the observed difference.

In the deformed Rb, Nd, and U systems, the corrections depend on the size of the nuclei as well as the quadrupole deformation parameter  $\beta_{20}$ , which is assumed to be zero in the spherical Fermi model. Hence, for large deformations the corrections for the Rb and Nd isotope pairs are comparable to the ones obtained for the spherical Sn and Pb isotope pairs. For the heavier U isotopes, the corrections become significantly large in spite of the small difference in deformation between the reference and target isotopes.

In Fig. 5, the magnitude of the corrections has been plotted as a function of the calculated deformation parameter  $\beta_{20}$  corresponding to the isotope  $A'$  for some Nd and U isotope pairs. In both plots, the magnitude of the “correction term” increases as the difference between the deformation of reference and target isotope becomes large. The largest corrections are obtained for the uranium isotope pairs  $^{240,238}\text{U}$  and  $^{220,238}\text{U}$ . In this case, the correction amounts to  $\sim 2.3\%$  and  $\sim 2\%$ , respectively.

The two-parameter Fermi model does not take into account the effect of deformation. As a result, the effect of realistic charge distributions on the field shifts is larger in atomic systems with deformed nuclei. The correction term  $\delta v_{\text{realistic}} - \delta v_{\text{Fermi}}$  can, however, be decomposed into two parts and written as

$$\delta v_{\text{realistic}} - \delta v_{\text{Fermi}} = (\delta v_{\text{realistic}} - \delta v_{\text{Fermi}}^{\text{def}}) + (\delta v_{\text{Fermi}}^{\text{def}} - \delta v_{\text{Fermi}}^{\text{sph}}). \quad (19)$$

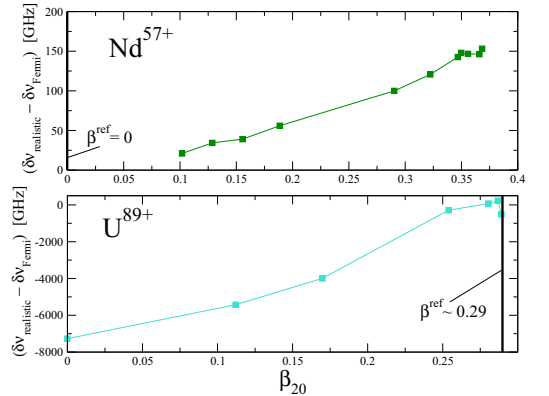


FIG. 5. The corrections  $\delta v_{\text{realistic}} - \delta v_{\text{Fermi}}$  to the line field shift values as a function of the quadrupole deformation parameter  $\beta_{20}$  of the target  $A'$  isotope for various (a)  $\text{Nd}^{57+}$  and (b)  $\text{U}^{89+}$  isotope pairs. In each case, the corresponding deformation of the reference isotope  $A$  is indicated by a vertical line on the plots. All plotted values refer to the same resonance transition as in Fig. 4.

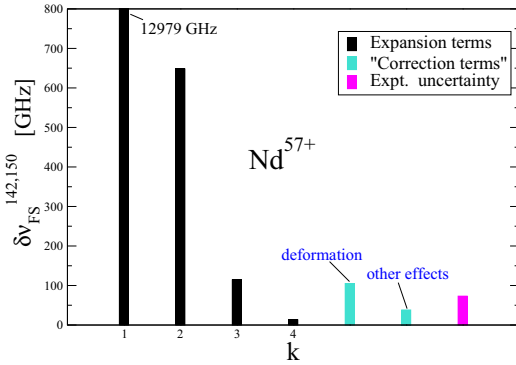


FIG. 6. Decomposition of expansion and correction terms of the  $1s^2 2s^2 S_{1/2} \rightarrow 1s^2 2p^2 P_{1/2}^o$  transition in Li-like  $^{142,150}\text{Nd}$ .

The  $\delta\nu_{\text{Fermi}}^{\text{def}} - \delta\nu_{\text{Fermi}}^{\text{sph}}$  part isolates the effect of deformation, while the remaining  $\delta\nu_{\text{realistic}} - \delta\nu_{\text{Fermi}}^{\text{def}}$  part gives the corrections due to “other effects,” such as density wiggles and differences in diffuseness. In order to separately estimate the effect of deformation in Li-like Nd, the deformed Fermi model was used with  $\beta_{20}$  values obtained from the microscopic nuclear calculations.

Isotope shift (IS) measurements have been performed for the first two resonance transitions of the  $^{142,150}\text{Nd}^{57+}$  pair [37] and the statistical uncertainty of the observed isotope shift for the  $1s^2 2s^2 S_{1/2} \rightarrow 1s^2 2p^2 P_{1/2}^o$  transition is compared to the magnitude of the “correction terms” in Fig. 6. As seen in the figure, the effect of deformation is large enough to be detected by the experiments and the correction due to “other effects” is not negligible.

### B. Neutral atoms

In this section, field shifts in neutral barium are investigated for the three well-known  $6s^2 1S_0 \rightarrow 6s6p 1,3P_1^o$  and  $6s^2 1S_0 \rightarrow 6p^2 3P_1$  transitions. Figure 7 illustrates the dependence of the magnitude of the corrections on the deformation parameter  $\beta_{20}$ . The same trend is seen for the three transitions. As already deduced for  $\text{Nd}^{57+}$  and  $\text{U}^{89+}$  (see Fig. 5) the magnitude of  $\delta\nu_{\text{realistic}} - \delta\nu_{\text{Fermi}}$  increases as the difference between the deformation of reference and target isotope becomes large. However, in neutral barium the magnitude of the correction term  $\delta\nu_{\text{realistic}} - \delta\nu_{\text{Fermi}}$  is a factor  $\sim 10^3$  smaller.

In contrast to the IS measurements in Li-like systems, a greater number of measurements has been performed in neutral atomic systems. Furthermore, in such measurements the accuracy provided is generally much higher. Following the process described in the previous section, the correction term is decomposed for the  $6s^2 1S_0 \rightarrow 6s6p 1P_1^o$  transition of the  $^{138,136}\text{Ba}$  isotope pair. The isotope shift measurements of the corresponding spectral lines [34] carries a statistical error, which is in Fig. 8 compared to the magnitude of the correction terms.

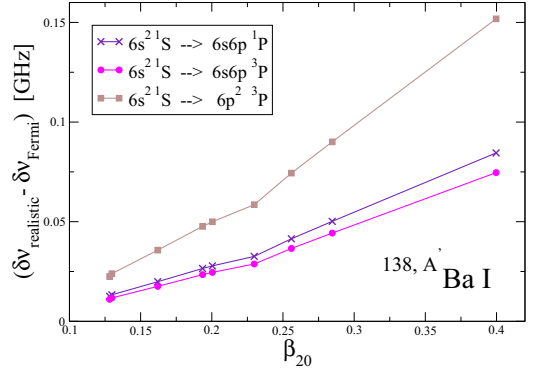


FIG. 7. The corrections  $\delta\nu_{\text{realistic}} - \delta\nu_{\text{Fermi}}$  to the line field shift calculations as a function of the quadrupole deformation parameter  $\beta_{20}$  of the target  $A'$  isotope for the neutral barium isotope pairs.

As seen in Fig. 8, the experimental uncertainty is remarkably small in comparison to the magnitude of the corrections. However, in reality the experimental uncertainty of the field shift is much larger since the theoretical mass shift contribution is in this case associated with large uncertainties, which are not reflected in this figure. The dominating corrections are the “other effects” that arise from the differences between the deformed Fermi distribution and the more realistic charge distributions obtained from the microscopic nuclear calculations.

The major improvement to the line field shift measurements illustrated in Fig. 3 is clearly due to the choice of using realistic rms radii. However, making in addition use of realistic higher-order nuclear moments leads to a non-negligible improvement in the description of the experimental data. According to the current experimental precision in the measurement of the isotope shifts in  $^{136,138}\text{Ba}$  and  $^{150,142}\text{Nd}^{57+}$ , effects like deformation captured by the higher nuclear moments could be detected (see Figs. 6 and 8). As a result, information about such

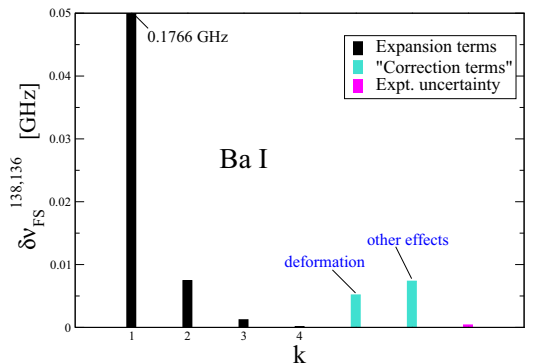


FIG. 8. Decomposition of expansion and correction terms of the  $6s^2 1S_0 \rightarrow 6s6p 1P_1^o$  transition in  $^{138,136}\text{Ba I}$ .



a nuclear property could possibly be deduced from isotope shift observations.

### V. $\delta\langle r^4 \rangle^{A,A'}$ EXTRACTION

The nuclear charge radius is one of the most obvious and fundamental parameters, related to the size of the nucleus. Considering isotope shift measurements, the charge radii of an isotope sequence are typically determined in terms of the differences in the second radial moment  $\delta\langle r^2 \rangle$ , between target isotope  $A'$  and reference isotope  $A$ . In contrast to light nuclei, in heavy nuclear systems the contribution of the higher-order radial moments to the line field shift can be significant and above the observable limit (see Figs. 6 and 8). Moreover, in highly charged heavy systems the contribution of the mass shift effect becomes smaller. This suggests the possibility to extract information about higher nuclear moments.

The reformulation of the field shift, combined with experimental isotope shift measurements, in principle enables the extraction of differences in higher-order radial moments  $\delta\langle r^{2N} \rangle$ ,  $N = 2, 3, 4$ . Consequently, information about the nuclear shapes, deformations, density wiggles, and other nuclear properties can be provided. The extraction of all four radial moments requires four transitions  $k$  to be available. A system of four equations is then solved for

$$\begin{aligned} \delta v_{k,\text{RFS}} = & F_{k,1}\delta\langle r^2 \rangle + F_{k,2}\delta\langle r^4 \rangle \\ & + F_{k,3}\delta\langle r^6 \rangle + F_{k,4}\delta\langle r^8 \rangle, \end{aligned} \quad (20)$$

where  $k = 1, 2, 3, 4$ . However, it is rare that observed isotope shifts are available for four transitions and, in addition, such systems of equations cannot be formed so that they give trustworthy solutions for higher than second-order moments.

### A. RFS expansion using orthogonal moments

As seen in Figs. 6 and 8, all four expansion terms do not equally contribute to the final field shift value. Considering in Fig. 9 the line field shift for the  $^{208,200}\text{Pb}$  pair, the

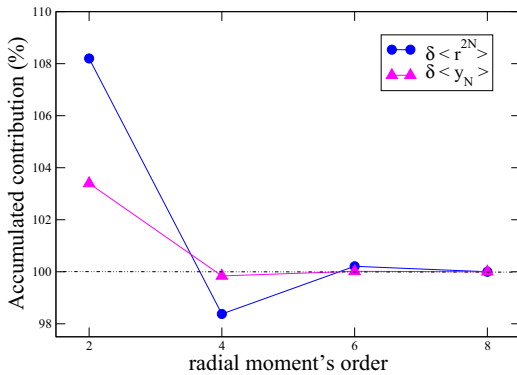


FIG. 9.  $\sum_N F_N \delta\langle r^{2N} \rangle / \delta v$  in percent (circles) compared to the corresponding expression for the rearranged summation (triangles). The plot refers to the  $^{208,200}\text{Pb}$  pair and the  $1s^2 2s^2 S_{1/2} \rightarrow 1s^2 2p^2 P^o_{3/2}$  transition.

fourth-order radial moment adds  $\sim 10\%$  contribution, the sixth moment  $\sim 2\%$ , and the last term, which contains the eighth-order moment, contributes with much less. Thus, it is fair to say that the major correction to the approximation that assumes constant electron density  $\rho_i^e(\mathbf{r}) \approx \rho_i^e(0)$  comes from the second expansion term, i.e.,  $F_{k,2}\delta\langle r^4 \rangle$ , which takes into account the differences between the  $\langle r^4 \rangle$  moments. However, the contribution from higher-order terms is not negligible.

In Eq. (20), the information about the nuclear charge distribution is encoded in a set of nuclear radial moments. These moments are not independent and a faster converging series may be found by instead expanding in a set of orthogonal polynomials (see Appendix). The convergence of this rearranged summation compared with the original summation is shown in Fig. 9. By taking into account only the first term, the line field shift is already much closer to the final value. The second term adds  $\sim 3.5\%$  contribution, the third  $\sim 0.18\%$ , while the last one adds  $\sim 0.016\%$ . Thus, accurate enough field shift predictions can now be provided using only the first two expansion terms containing the differences  $\delta\langle y_1 \rangle$  and  $\delta\langle y_2 \rangle$ , which are in turn given as a function of the  $\delta\langle r^2 \rangle$  and  $\delta\langle r^4 \rangle$  moments (see Appendix). Having only two unknowns means that  $\delta\langle r^2 \rangle$  and  $\delta\langle r^4 \rangle$  can potentially be extracted from knowledge of two observed line field shifts in an isotope pair.

### B. Testing the method

After expanding in the orthonormal basis, for a pair of isotopes  $A, A'$ , the reformulated line field shift can to a very good approximation be expressed as

$$\delta v_{k,\text{RFS}} \approx c_{k,1}\delta\langle y_1 \rangle + c_{k,2}\delta\langle y_2 \rangle, \quad (21)$$

where the  $c_{k,1}$  and  $c_{k,2}$  coefficients are expressed in terms of the  $F_{k,N}$  factors. In order to test the method, theoretical line field shifts  $\delta v_{\text{RFS}}$  were obtained using realistic nuclear radial moments. These line field shifts refer to the  $1s^2 2s^2 S_{1/2} \rightarrow 1s^2 2p^2 P^o_{1/2}$  and  $1s^2 2s^2 S_{1/2} \rightarrow 1s^2 2p^2 P^o_{3/2}$  transitions of the uranium, lead, and neodymium isotope pairs studied in Sec. IV. Using these calculated field shifts as “pseudoexperimental” input data, the equations can be inverted and should yield, if the method is flawless, extracted radial moments which are identical to the realistic nuclear moments used in the computation of the field shifts.

In all cases, the extracted  $\delta\langle r^2 \rangle$  moments are almost identical to the exact  $\delta\langle r^2 \rangle_{\text{realistic}}$  moments. The difference is less than  $0.0002 \text{ fm}^2$  for all lead and uranium isotopes, as well as the neodymium isotopes that are close to spherical. For the highly deformed neodymium isotopes, the difference is slightly larger, of the order of  $\sim 0.001 \text{ fm}^2$ , which still represents a small discrepancy.

In Fig. 10, the extracted  $\delta\langle r^4 \rangle$  values have been plotted and compared to the  $\delta\langle r^4 \rangle_{\text{realistic}}$  representing exact values. The extracted  $\delta\langle r^4 \rangle_{\text{original}}$  values using the first two terms of the original summation  $\delta v_{k,\text{RFS}}^{A,A'} \approx \sum_{N=1}^2 F_{k,N}\delta\langle r^{2N} \rangle$  are in addition illustrated in the same figure. When the rearranged summation is used, the extracted  $\delta\langle r^4 \rangle$  moments are in good agreement with the exact  $\delta\langle r^4 \rangle_{\text{realistic}}$  moments, whereas the  $\delta\langle r^4 \rangle$  moments using the original, but truncated, summation display an observable discrepancy from the exact values. All in all, the expression using the rearranged summation for

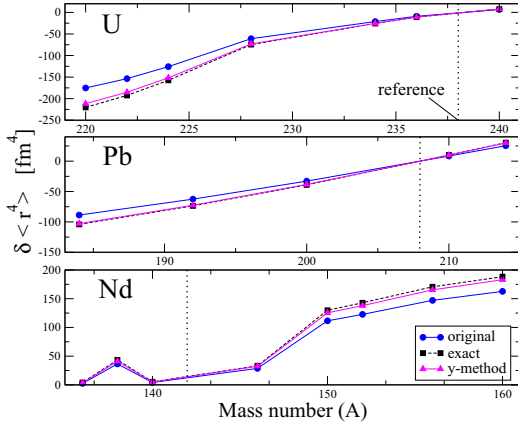


FIG. 10. The extracted  $\delta(r^4)$  values for the uranium, lead, and neodymium isotope pairs, previously studied. The dashed line with squares represents the exact  $\delta(r^4)_{\text{realistic}}$  values, obtained from the HFB and HFBTHO calculations for the spherical lead and the deformed uranium and neodymium isotopes, respectively. The line with triangle symbols represents the extracted  $\delta(r^4)$  when  $\delta v_{k,\text{FS}} \approx c_{k,1}\delta(y_1) + c_{k,2}\delta(y_2)$  is assumed, while the line with circles corresponds to the  $\delta(r^4)_{\text{original}}$  extracted when the original summation in  $\delta v_{k,\text{RFS}}$  has been used.

the reformulated field shift enables the determination of the differences between  $r^2$  and  $r^4$  moments, much more accurately than using the original expression.

### C. Towards the extraction of $\delta(r^2)$ and $\delta(r^4)$ moments using experimental data

In what follows, the major objective is to discuss how  $\delta(r^2)$  and  $\delta(r^4)$  moments can be extracted from experimental data using the method tested above. From observed isotope shifts, experimental field shift values can be obtained by estimating and removing the mass shift contribution and residual effects  $\delta v_{k,\text{RES}}$  from for example QED and nuclear polarization (see, e.g., [6]):

$$\delta v_{k,\text{FS}}^{\text{expt}} = \delta v_{k,\text{IS}}^{\text{expt}} - \delta v_{k,\text{MS}} - \delta v_{k,\text{RES}}. \quad (22)$$

The effect from nuclear polarization is not estimated in this work, but have been studied extensively in the past by Plunien *et al.* [39–42]. For Li-like systems, the contribution is comparable to the effect from deformation and must be taken into account in real situations.

Without making use of RFS, the difference in  $\langle r^2 \rangle$  moments can now be extracted by performing variational calculations where the rms radius of the reference isotope is estimated and  $\delta\langle r^2 \rangle$  is varied until agreement with experimental field shifts is observed (see, for example, [37]):

$$\delta v_{k,\text{FS}}^{\text{expt}} = \delta v_{k,\text{VA}}^{\text{exact}}. \quad (23)$$

The difference in higher moments then follows from the model used to mimic the nuclear charge distribution, for example the Fermi distribution, and hence this method is highly model

TABLE II. The line frequency field shift values, resulting from the variational calculations using GRASP2K and the reformulation of the field shift, are respectively displayed for a few lead and uranium isotope pair combinations. In the last column, the discrepancy between  $\delta v_{k,\text{VA}}^{\text{exact}}$  and  $\delta v_{k,\text{RFS}}$  is computed. “Transition 1” refers to the  $1s^2 2s^2 S_{1/2} \rightarrow 1s^2 2p^2 P^o_{1/2}$  transition.

Transition 1	$\delta v_{k,\text{VA}}^{\text{exact}}$ (GHz)	$\delta v_{k,\text{RFS}}$ (GHz)	$d$ (GHz)
208,192	51 303	50 563	740
208,200	28 938	28 546	392
208,210	−14 186	−14 021	−165
238,234	54 796	53 976	820
238,236	27 412	27 015	397

dependent. However, making use of the reformulation of field shifts using an orthogonal moments basis, we instead use experimental field shift values from two transitions and solve the following equation system in order to extract the  $\delta\langle r^2 \rangle$  and  $\delta\langle r^4 \rangle$  moments virtually model independent:

$$\delta v_{k,\text{FS}}^{\text{expt}} = c_{k,1}\delta\langle y_1 \rangle + c_{k,2}\delta\langle y_2 \rangle + d_k. \quad (24)$$

In the expression above, a term  $d_k$  has been introduced which represents the discrepancy between the “exact” variational solution  $\delta v_{k,\text{VA}}^{\text{exact}}$ , and the RFS solution  $\delta v_{k,\text{RFS}}$ , assuming a spherical Fermi nuclear charge distribution for the reference and the target isotope. To examine the importance of the  $d_k$  term for the extraction of the radial moments, we used GRASP2K and RIS4 to compute  $\delta v_{k,\text{VA}}^{\text{exact}}$  and  $\delta v_{k,\text{RFS}}$  for the resonance transitions in several Li-like lead and uranium isotope pairs. In the calculations, rms radii were taken from the compilation by Angelis and Marinova [1] and the results are presented in Tables II and III. As seen, an expected discrepancy between the  $\delta v_{k,\text{VA}}^{\text{exact}}$  and  $\delta v_{k,\text{RFS}}$  values, i.e., the  $d_k$  term, is observed for both transitions. In our case, this discrepancy is mainly due to QED effects included in the VA calculation that become important in heavy nuclei and which are not included in the perturbative approach. In addition, these QED contributions (vacuum polarization and self-energy) depend on the nuclear size [43] and hence the  $d_k$  terms should be reevaluated when the nuclear parameters of the isotopes are changed. Other assumptions that have been made throughout the formulation of the perturbative approach are expected to play a minor role. Indicatively, for “transition 1” in the uranium isotope pairs the magnitude of the discrepancy is of the order of  $\sim 1.5\%$  of the  $\delta v_{k,\text{VA}}^{\text{exact}}$  value, from which  $\sim 0.1\%$  is due to other than QED effects. It is also seen that the  $d_k$  terms for the two transitions are slightly different, and it turns out that accurately estimating this difference, rather than the magnitude of the

TABLE III. Same as Table II. “Transition 2” refers to the  $1s^2 2s^2 S_{1/2} \rightarrow 1s^2 2p^2 P^o_{3/2}$  transition.

Transition 2	$\delta v_{k,\text{VA}}^{\text{exact}}$ (GHz)	$\delta v_{k,\text{RFS}}$ (GHz)	$d$ (GHz)
208,192	55 459	54 642	817
208,200	31 282	30 848	434
208,210	−15 336	−15 152	−184
238,234	61 189	60 277	912
238,236	30 610	30 169	441



terms, is absolutely crucial in order to extract accurate  $\delta(r^4)$  moments.

We are now ready to show that it is possible to extract  $\delta(r^2)$  and  $\delta(r^4)$  moments if accurate experimental field shifts are available. This is due to the fact that the electronic factors  $c_k$  and the  $d_k$  terms can be accurately estimated also when the rms radii are not known for the reference and/or target isotope. In these cases, we make instead a “qualified guess” for the rms radii. The parametrization, given in Eq. (14), for the rms radius of an isotope  $A$  constitutes an example of such a “qualified guess” and will be used below.

### 1. Root-mean-square radii data available for the reference isotopes

When radial moment differences are deduced from isotope shift measurements, the nuclear parameters are usually known for the reference isotope but not for the target isotope. We will now demonstrate the procedure for how experimental  $\delta(r^2)$  and  $\delta(r^4)$  moments for the  $^{238,234}\text{U}$  isotope can be extracted in such cases by considering the two resonance transitions in Li-like uranium. In what follows,  $^{238}\text{U}$  is the reference isotope,  $r_A^{\text{tab}}$  denote a tabulated rms radius for isotope  $A$  taken from [1],  $r_A^{\text{para}}$  denote a parametrized rms radius for isotope  $A$  using Eq. (14), and spherical Fermi distributions with  $t = 2.30$  fm are used everywhere. Further on it is assumed that accurate  $\delta\nu_{k,\text{RFS}}^{\text{expt}}$  values are available:

- (1) Two separate variational calculations are performed using  $r_{238}^{\text{tab}} = 5.8571$  fm and  $r_{234}^{\text{para}} = 5.7216$  fm, respectively.
- (2)  $\delta\nu_{k,\text{VA}}^{\text{exact}}$  is constructed using the level energies from the  $r_{238}^{\text{tab}}$  and  $r_{234}^{\text{para}}$  calculations in step 1.
- (3)  $\delta\nu_{k,\text{RFS}}$  is computed by using the electronic factors from the  $r_{238}^{\text{tab}}$  calculation and the difference in radial moments as predicted by two spherical Fermi distributions with  $r_{238}^{\text{tab}}$  and  $r_{234}^{\text{para}}$ , respectively.
- (4)  $d_k = \delta\nu_{k,\text{VA}}^{\text{exact}} - \delta\nu_{k,\text{RFS}}$  is computed.
- (5)  $c_k$  factors are computed using the electronic factors in step 3 (see Appendix).
- (6)  $\delta(y_1)$  and  $\delta(y_2)$  are extracted by solving Eq. (24).
- (7)  $\delta(r^2)$  and  $\delta(r^4)$  are computed (see Appendix).

To quantitatively validate the method we replace  $\delta\nu_{k,\text{RFS}}^{\text{expt}}$  with “pseudoexperimental” field shifts constructed from two separate variational calculations using  $r_{238}^{\text{tab}}$  and  $r_{234}^{\text{tab}} = 5.8291$  fm, respectively. In addition, we repeat the procedure for the  $^{238,236}\text{U}$  isotope pair using  $r_{236}^{\text{para}} = 5.7363$  fm and  $r_{236}^{\text{tab}} = 5.8431$  fm. In Table IV, the extracted  $\delta(r^2)$  and  $\delta(r^4)$  moments

TABLE IV. Errors, in  $\text{fm}^2$  and  $\text{fm}^4$ , when extracting the  $\delta(r^2)$  and  $\delta(r^4)$  moments, for the  $^{234,238}\text{U}$  and  $^{236,238}\text{U}$  pairs. It is assumed that the rms radii are unknown for the target isotopes. See text for details.

	238,234	238,236
$\delta(r^2)$	-0.3282	-0.1642
$\delta(r^2)_{\text{expt}}$	-0.3272	-0.1638
Error	0.0010	0.0004
$\delta(r^4)$	-28.9026	-14.3453
$\delta(r^4)_{\text{expt}}$	-27.4419	-13.7693
Error	1.4607	0.5760

are compared to the experimental  $\delta(r^2)_{\text{expt}}$  and  $\delta(r^4)_{\text{expt}}$  moments. As seen, the extracted  $\delta(r^2)$  moments are almost identical to the “experimental” values. In addition, the  $\delta(r^4)$  moments are extracted with an accuracy of 5.3% and 4.2% for the  $^{234,238}\text{U}$  and  $^{236,238}\text{U}$  pairs, respectively. The errors, which are of systematical nature and remarkably small, arise from estimating the  $d$  term using rms radii for the target isotopes which differ by approximately 0.11 fm from the tabulated values used to construct the “pseudoexperimental” field shifts. However, after the extraction one obtains a better estimate for the rms radii of the target isotopes that allows the method to be iteratively improved.

### 2. Root-mean-square radii unknown for both target and reference isotopes

Assuming that the rms radius value of the reference isotope is also unknown, we again try to extract the  $\delta(r^2)$  and  $\delta(r^4)$  moments. A “qualified guess” for the rms radius of  $^{238}\text{U}$  is then needed and we replace  $r_{238}^{\text{tab}}$  with  $r_{238}^{\text{para}} = 5.7508$  fm in the procedure described above.

The results from the extraction of the  $\delta(r^2)$  and  $\delta(r^4)$  moments are presented in Table V. As seen, the  $\delta(r^2)$  moment is extracted almost as accurate as before (see Table IV). Further on, the results from extracting the  $\delta(r^4)$  moments display a discrepancy of  $\sim 10.3\%$  and  $\sim 6.5\%$  from the exact values, for the  $^{234,238}\text{U}$  and  $^{236,238}\text{U}$  pairs, respectively.

The nuclear parameters relevant to the reference isotope have been modified here. Thus, the  $F_k$  factors have also been reevaluated since they are always deduced for the reference isotope. As a result, aside from the new radial moments differences, the  $\delta\nu_{k,\text{RFS}}$  field shifts are computed based on updated sets of  $F_{k,N}$  factors. This explains the larger discrepancy that is observed when extracting the  $\delta(r^2)$  and  $\delta(r^4)$  moments in the latter case (see Table V). However, the results are remarkably good given that the “qualified guess” for the reference isotope is approximately 0.11 fm smaller than the tabulated value used to construct the pseudoexperimental field shifts.

### D. Statistical errors when extracting the $\delta(r^2)$ and $\delta(r^4)$ moments

Above, the  $\delta(r^2)$  and  $\delta(r^4)$  moments were extracted by solving the matrix equation

$$\begin{bmatrix} \delta\nu_{1,\text{RFS}} \\ \delta\nu_{2,\text{RFS}} \end{bmatrix} = C \begin{bmatrix} \delta(y_1) \\ \delta(y_2) \end{bmatrix}. \quad (25)$$

TABLE V. Same as Table IV. Here, it is assumed that rms radii are unknown for both the reference and the target isotopes. See text for details.

	238,234	238,236
$\delta(r^2)$	-0.3287	-0.1640
$\delta(r^2)_{\text{expt}}$	-0.3272	-0.1638
Error	0.0015	0.0002
$\delta(r^4)$	-30.2665	-14.6612
$\delta(r^4)_{\text{expt}}$	-27.4419	-13.7693
Error	2.8246	0.8919

In order to solve for  $y_1$  and  $y_2$ , the matrix  $C$  must be invertible. If the matrix determinant is zero, then the matrix is singular and cannot be inverted. It is not rare that the determinant of such matrix can be close to zero, but still nonzero. In this case, the matrix is close to singular and as a result the values of  $\delta(y_1)$  and  $\delta(y_2)$  will be hugely affected, even by a small change in the field shifts  $\delta v_{1,\text{RFS}}$  and  $\delta v_{2,\text{RFS}}$ . Namely, the extracted  $\delta(y_1)$  and  $\delta(y_2)$  values, and as a consequence the  $\delta(r^2)$  and  $\delta(r^4)$  moments, will to a great degree be affected by the uncertainties in the observed isotope shifts, making the extraction of the radial nuclear moments with high accuracy a difficult task. A  $C$ -matrix determinant equal to zero is obtained if the two equations are linearly dependent. In such case, it is not possible to extract two unknowns. Therefore, the transitions considered should be as independent as possible in terms of electronic factors.

The observed isotope shifts  $\delta v_{k,\text{IS}}^{\text{expt}}$ , and subsequently the observed field shifts  $\delta v_{k,\text{FS}}^{\text{expt}}$ , are associated with uncertainties of a certain magnitude. These uncertainties lead to statistical errors in the extracted nuclear moments. In the next subsections, the propagation of these errors is discussed and how they can be minimized by selecting atomic transitions.

### 1. Statistical errors in relation to the atomic number

In Sec. V B, our method was tested by using  $\delta v_{\text{RFS}}$  line field shifts as pseudoeperimental data. In order to extend this approach to consider uncertainties we assume uncorrelated errors with an uncertainty  $\pm\epsilon$ , where  $\epsilon = \delta v_{k,\text{RFS}} \times 10^{-m}$ , in the  $\delta v_{k,\text{RFS}}$  values that are used for solving the matrix equation [see Eq. (25)]. By varying  $m$ , the magnitude of the field shift uncertainty changes. We can then investigate the effect these uncertainties have on the extracted  $\delta(r^2)$  and  $\delta(r^4)$  values.

The extraction of the  $\delta(r^2)$  and  $\delta(r^4)$  moments was in Sec. V B performed for several uranium, lead, and neodymium isotope pairs (see Fig. 10). By making a reasonable choice of  $m = 3$  for the error  $\epsilon$  in the  $\delta v_{k,\text{RFS}}$  values relevant to these isotope pairs, it is possible to estimate the magnitude of the statistical errors in the extracted  $\delta(r^2)$  and  $\delta(r^4)$  moments. The relative errors of the extracted values for one isotope pair of each of the above elements are indicatively presented in Table VI. The error in  $\delta(r^2)^{142,150}$  is approximately 72% of the magnitude of the resulting value. Besides, the  $\delta(r^4)^{142,150}$  is extracted with significantly greater error. However, the relative error in both  $\delta(r^2)$  and  $\delta(r^4)$  demonstrates a considerable decrease as the atomic number of the isotopes becomes larger.

TABLE VI. The relative error in the extraction of the  $\delta(r^2)$  and  $\delta(r^4)$  moments for the  $^{142,150}\text{Nd}^{57+}$ ,  $^{208,192}\text{Pb}^{79+}$ , and  $^{238,236}\text{U}^{89+}$  pairs. The relative errors are presented as a function of the atomic number of these three elements. The inaccuracy assumed in the  $\delta v_{k,\text{RFS}}$  field shift data is  $\pm\epsilon = \delta v_{k,\text{RFS}} \times 10^{-3}$ .

	$^{142,150}\text{Nd}$	$^{208,192}\text{Pb}$	$^{238,236}\text{U}$
Z	60	82	92
$\frac{\Delta(\delta(r^2))}{ \delta(r^2) }$	0.72	0.39	0.28
$\frac{\Delta(\delta(r^4))}{ \delta(r^4) }$	13.84	5.54	3.65

So far, the extraction of the  $\delta(r^2)$  and  $\delta(r^4)$  moments was performed by making use of  $\delta v_{k,\text{RFS}}$  field shifts and  $F_{k,N}$  line field shift factors that are attributed to the first two resonance transitions, i.e.,  $1s^2 2s^2 S_{1/2} \rightarrow 1s^2 2p^2 P_{3/2}^o$  and  $1s^2 2s^2 S_{1/2} \rightarrow 1s^2 2p^2 P_{3/2}^o$ . For these two transitions in lithium-like systems, the  $F_{k,N}$  factors, as well as the line mass shift parameters  $\Delta K_{k,\text{MS}}$ , can be determined with high accuracy. Therefore, when we in practice attempt to extract the  $\delta(r^2)$  and  $\delta(r^4)$  moments using actual experimental data, the uncertainties in the  $\delta v_{k,\text{FS}}^{\text{expt}}$  values will normally be dominated by the uncertainties in the  $\delta v_{k,\text{IS}}^{\text{expt}}$  measurements.

For the  $^{142,150}\text{Nd}^{57+}$  pair and the previously mentioned transitions such measurements are available [37]. Taking into account the uncertainties in the measured isotope shifts  $\delta v_{k,\text{IS}}^{\text{expt}}$ , the corresponding uncertainties in  $\delta v_{k,\text{FS}}^{\text{expt}}$  appear in the fourth and third digits for each of the above transitions, respectively. In this case, the choice of an error  $\pm\epsilon = \delta v_{k,\text{RFS}} \times 10^{-3}$  in the calculated field shift values seems to be quite realistic. However, according to Table VI the errors in the  $\delta(r^2)$  and  $\delta(r^4)$  values resulting from experimental uncertainties of this magnitude for the neodymium pair are evidently extremely large.

We can therefore draw the conclusion that the extraction of the  $\delta(r^2)^{142,150}$  and  $\delta(r^4)^{142,150}$  moments with satisfactory accuracy is not likely to be a possibility at the moment. Varying  $m$  we deduce that in order for the  $\delta(r^2)^{142,150}$  and  $\delta(r^4)^{142,150}$  to be determined with uncertainties of the order of  $\lesssim 1\%$  and  $\lesssim 14\%$ , respectively, we should assume  $m \geq 5$ . In addition, considering Table VI, a more precise extraction of the  $\delta(r^2)$  and  $\delta(r^4)$  moments should be possible for the lead and in particular for the uranium isotope pairs.

### 2. Independent transitions

Considering the two resonance transitions that were used above for extracting  $\delta(r^2)$  and  $\delta(r^4)$  moments, we note that the same final state takes part in both. Therefore, these two transitions are not entirely independent and the corresponding  $F_{k,N}$  factors do not constitute the best possible set so that we avoid matrix  $C$  being close to singular. As a consequence, the uncertainties in the  $\delta(r^2)$  and  $\delta(r^4)$  values are relatively large. In order to be able to accurately extract both  $\delta(r^2)$  and  $\delta(r^4)$  moments, the precision of the experimental methods must therefore be improved substantially. Alternatively, a larger number of transitions must be available. Using the GRASP2K package, we can easily compute line field shift parameters for more transitions and hence an extended set of  $\delta v_{k,\text{RFS}}$  values can be generated. The matrix equation will then be formed using  $k > 2$  equations, which need to be solved for the same unknowns  $y_1$  and  $y_2$ . Having more equations than number of unknowns leads to a reduction of the statistical errors.

Choosing, for instance, to extract the  $\delta(r^2)$  and  $\delta(r^4)$  moments for the  $^{238,236}\text{U}$  pair, we solve a matrix equation that consists of 16 equations corresponding to 16 different transitions. These transitions involve the following even  $1s^2 2s^2 S_{1/2}$ ,  $1s^2 3s^2 S_{1/2}$ ,  $1s^2 3d^2 D_{3/2,5/2}$  and odd  $1s^2 2p^2 P_{1/2,3/2}^o$ ,  $1s^2 3p^2 P_{1/2,3/2}^o$  states in Li-like uranium. By making the same choice of  $m = 3$  for the error  $\epsilon = \delta v_{k,\text{RFS}} \times 10^{-m}$  in the  $\delta v_{k,\text{RFS}}$  values, we extract the  $\delta(r^2)$  and  $\delta(r^4)$  moments. The extracted  $\delta(r^2)$  moment has exactly the same value

TABLE VII. The relative error in the extraction of the  $\delta(r^2)$  and  $\delta(r^4)$  moments for the  $^{238,236}\text{U}^{89+}$  pair, initially calculated when the first two resonance transitions were studied, when all 16 theoretically available transitions are used and when we finally choose one set of as independent as possible transitions. The uncertainties assumed in the  $\delta\nu_{k,\text{RFS}}$  field shift data are, as in Table VI,  $\pm\epsilon = \delta\nu_{k,\text{RFS}} \times 10^{-3}$ .

$^{238,236}\text{U}$	2 res.	All 16	2 ind.
$\frac{\Delta(\delta(r^2))}{ \delta(r^2) }$	0.28	0.03	0.02
$\frac{\Delta(\delta(r^4))}{ \delta(r^4) }$	3.65	0.38	0.30

as before, whereas the  $\delta(r^4)$  value is also about the same, suffering from approximately the same systematical errors. However, the statistical errors in the extraction of both  $\delta(r^2)$  and  $\delta(r^4)$  have now been decreased significantly (see Table VII).

In practice, such large number of measured transitions is not likely to be available. Trying all different combinations, we realize that the error in the extraction of the  $\delta(r^2)$  and  $\delta(r^4)$  moments, by using a set of only two transitions, varies with the choice of the transitions. For the  $^{238,236}\text{U}$  pair and  $\epsilon = \delta\nu_{k,\text{RFS}} \times 10^{-3}$  we get  $0.0014 \leq \frac{\Delta(\delta(r^2))}{|\delta(r^2)|} \leq 80$  and  $0.0012 \leq \frac{\Delta(\delta(r^4))}{|\delta(r^4)|} \leq 1100$ , for the relative errors in the extraction of the  $\delta(r^2)$  and  $\delta(r^4)$  moments, respectively.

We therefore deduce that in order to limit the magnitude of the statistical errors, it is more important to make a choice of as independent as possible transitions that form the set of equations solved, rather than increasing the number of transitions. Based on this conclusion, instead of extracting the  $\delta(r^2)$  and  $\delta(r^4)$  moments using the first two resonance transitions, a set of two more independent transitions is chosen. Thus, we attempt to extract the  $\delta(r^2)$  and  $\delta(r^4)$  moments for the  $^{238,236}\text{U}$  isotope pair, using the resonance transition  $1s^2 2s^2 S_{1/2} \rightarrow 1s^2 2p^2 P_{1/2}^o$  combined with the  $1s^2 3p^2 P_{1/2}^o \rightarrow 1s^2 3d^2 D_{3/2}$  transition. The resulting relative errors for this combination of transitions are also displayed in Table VII. As seen, the relative errors in the extraction of both  $\delta(r^2)$  and  $\delta(r^4)$  moments are decreased when a more optimal combination of 2 out of the total 16 available transitions is chosen.

TABLE VIII. Same as Table IV. Here, the line field shift factors  $F_{k,N}$  correspond to the  $1s^2 2s^2 S_{1/2} \rightarrow 1s^2 2p^2 P_{1/2}^o$  and  $1s^2 3p^2 P_{1/2}^o \rightarrow 1s^2 3d^2 D_{3/2}$  transitions. Statistical errors are given in the rightmost column assuming uncertainties in the ‘‘pseudoexperimental’’ field shifts according to  $\epsilon = \delta\nu_{k,\text{RFS}} \times 10^{-3}$ .

	$^{238,236}\text{U}$	
$\delta(r^2)$	-0.1646	$\pm 0.0036$
$\delta(r^2)_{\text{exact}}$	-0.1638	
Error	0.0008	
$\delta(r^4)$	-14.7283	$\pm 3.5279$
$\delta(r^4)_{\text{exact}}$	-13.7693	
Error	0.9590	

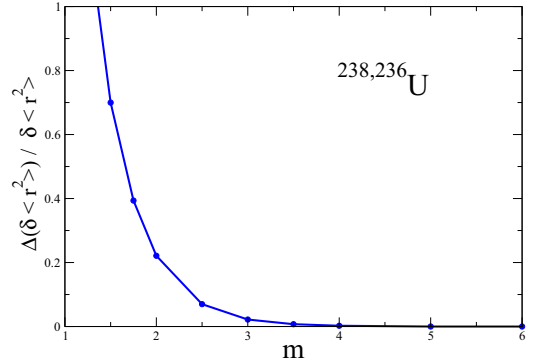


FIG. 11. The relative error in the extraction of the  $\delta(r^2)$  moment as a function of  $m$  number in the assumed uncertainty  $\epsilon = \delta\nu_{k,\text{RFS}} \times 10^{-m}$  of the field shift. For the extraction, the pair of  $1s^2 2s^2 S_{1/2} \rightarrow 1s^2 2p^2 P_{1/2}^o$  and  $1s^2 3p^2 P_{1/2}^o \rightarrow 1s^2 3d^2 D_{3/2}$  transitions in Li-like  $^{238,236}\text{U}$  has been used.

### 3. Errors in the extraction of $\delta(r^4)$ $^{238,236}\text{U}$

Having ascertained that the ‘‘right’’ combination of transitions provides us with reasonably small statistical errors, we can extract the  $\delta(r^2)$  and  $\delta(r^4)$  moments for the  $^{238,236}\text{U}$  isotope pair using pseudoexperimental field shifts, as described in Sec. V C 1, for this ‘‘optimal’’ pair of transitions. The statistical uncertainties are estimated as  $\epsilon = \delta\nu_{k,\text{RFS}} \times 10^{-m}$  with  $m = 3$ , which has been used so far for determining the assumed uncertainty in the  $\delta\nu_{k,\text{RFS}}$  values.

The extracted radial moments together with the resulting errors are displayed in Table VIII. Comparing the respective results of Table IV with the results in Table VIII, we deduce that although in the latter case the systematical errors are larger the statistical errors of the extracted  $\delta(r^2)$  and  $\delta(r^4)$  values are significantly smaller. We see that now the relative statistical errors are  $\frac{\Delta(\delta(r^2))}{|\delta(r^2)|} = 0.022$  and  $\frac{\Delta(\delta(r^4))}{|\delta(r^4)|} = 0.24$ , respectively.

In Figs. 11 and 12, the relative errors in the extraction of the  $\delta(r^2)$  and  $\delta(r^4)$  moments are illustrated as a function of the  $m$  value. As seen, the results are rather sensitive to the  $m$  value and the relative error increases dramatically as the precision of the field shift values decreases. This is even more pronounced for the errors in the extracted  $\delta(r^4)$  moments. Nevertheless, for  $m = 3$  both  $\delta(r^2)$  and  $\delta(r^4)$  moments are extracted with satisfactory accuracy. Thus, we deduce that provided the current experimental precision in the isotope shift measurements, an accurate enough extraction of the  $\delta(r^2)$  and  $\delta(r^4)$  moments could be possible as long as the measured transitions are sufficiently independent in terms of electronic factors.

## VI. SUMMARY AND CONCLUSIONS

Combining nuclear DFT-type models with MCHF calculations for atomic states it is possible to achieve a higher precision in the predictions of atomic line field shifts. Changes in the nuclear charge distribution caused by shell structure, deformations, and variations in the diffuseness of the nuclei

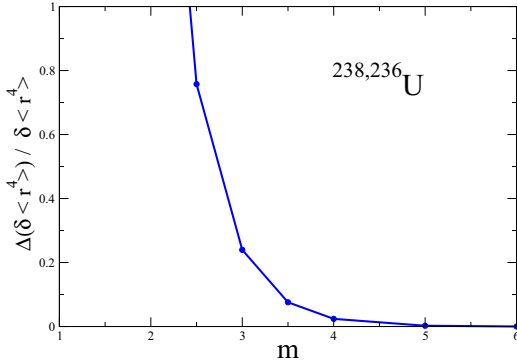


FIG. 12. Same as Fig. 11, but for the relative uncertainty in the extraction of the  $\delta(r^4)$  moment using the same pair of transitions.

are then automatically taken into account. In this work, it is shown that capturing all these effects leads to an improved description of experiments.

With the continuous advancement in experimental methods, one may ask whether the improved precision and access to several atomic transitions makes it possible to obtain more data on the nuclear isotopes than just the  $\delta(r^2)$  values commonly extracted so far. By constructing a set of theoretical field shifts we explore the possibility of extracting information about the nucleus by inverting the first-order perturbation theory equations for the field shifts. In this way, we demonstrate that the electron states are sensitive not only to the  $\delta(r^2)$  values but also to changes in  $\langle r^4 \rangle$  values. This opens the possibility for systematic tabulation of these higher-order nuclear moments. Considering both statistical and systematic errors in the extraction procedure we conclude that an increase in experimental precision by one to two orders of magnitude or access to data for more independent atomic transitions would be essential. As a promising candidate for future experiments, we suggest Li-like uranium where an increase in precision with one order of magnitude along with access to at least two independent transitions would allow accurate  $\delta(r^4)$  values to be extracted.

#### ACKNOWLEDGMENTS

This work was supported by the Swedish Research Council (VR). The authors acknowledge P. Jönsson, Malmö University, and C. Brandau, GSI, for discussions and C. Nazé, J. G. Li, and M. Godefroid for providing the barium MCDHF wave functions.

#### APPENDIX: RFS EXPANSION IN ORTHONORMAL BASIS

The RFS is, for a certain transition, given by the expansion

$$\sum_{N=1}^4 F_N \delta(r^{2N}) = F_1 \delta(r^2) + F_2 \delta(r^4) + F_3 \delta(r^6) + F_4 \delta(r^8),$$

where the line field shift factors  $F_N$  play the role of expansion coefficients. The set of  $r^{2N}$  that forms the basis  $\{r^2, r^4, r^6, r^8\}$  is not orthonormal. It is reasonable to assume that a rearrangement using an orthonormal basis should lead to faster convergence. Here, we orthonormalize the initial basis with respect to the scalar product:

$$\langle u | v \rangle = \int u * v * w r^2 dr,$$

where  $w$  is the weight function that approximates the nucleus. Since the functions  $y_N$ , forming the basis  $\{y_1, y_2, y_3, y_4\}$ , are constructed to be orthogonal they will probe different aspects of the nuclear charge distribution within the nuclear volume. Thus, we expect that the expansion

$$\sum_{N=1}^4 c_N \delta(y_N) = c_1 \delta(y_1) + c_2 \delta(y_2) + c_3 \delta(y_3) + c_4 \delta(y_4)$$

will converge faster than  $\sum_{N=1}^4 F_N \delta(r^{2N})$  does. In the expression above,  $c_N$  are the expansion coefficients. Assuming that the nucleus can be approximated as a hard sphere, one can use  $w = \rho_0 \Theta(R - r)$  with  $R = 1.25A^{1/3}$ . The value of  $\rho_0$  is determined by the normalization condition  $4\pi \int \rho_0 r^2 dr = 1$ . Following the Gram-Schmidt process [44], we obtain

$$\begin{aligned} y_1 &= \frac{3.46556}{\bar{A}^{2/3}} r^2, \\ y_2 &= -\frac{15.2051}{\bar{A}^{2/3}} r^2 + \frac{12.5116}{\bar{A}^{4/3}} r^4, \\ y_3 &= \frac{39.9503}{\bar{A}^{2/3}} r^2 - \frac{80.3573}{\bar{A}^{4/3}} r^4 + \frac{37.1429}{\bar{A}^2} r^6, \\ y_4 &= -\frac{82.4315}{\bar{A}^{2/3}} r^2 + \frac{293.927}{\bar{A}^{4/3}} r^4 - \frac{313.522}{\bar{A}^2} r^6 + \frac{103.367}{\bar{A}^{8/3}} r^8, \end{aligned}$$

where  $\bar{A}$  is taken as the average of the mass numbers of the two isotopes. The sum of the expansion terms has been rearranged but  $\sum_{N=1}^4 F_N \delta(r^{2N}) = \sum_{N=1}^4 c_N \delta(y_N)$  must still hold. The  $c_N$  coefficients can be found by equating same order terms in the above equation. Hence, the new coefficients are

$$\begin{aligned} c_1 &= 0.288554 \bar{A}^{2/3} F_1 + 0.350673 \bar{A}^{4/3} F_1 \\ &\quad + 0.448303 \bar{A}^2 F_3 + 0.592709 \bar{A}^{8/3} F_4, \\ c_2 &= 0.0799258 \bar{A}^{4/3} F_2 + 0.172916 \bar{A}^2 F_3 + 0.2972 \bar{A}^{8/3} F_4, \\ c_3 &= 0.026923 \bar{A}^2 F_3 + 0.08166 \bar{A}^{8/3} F_4, \\ c_4 &= 0.00967424 \bar{A}^{8/3} F_4. \end{aligned}$$

Now, the RFS is given by the summation

$$\sum_{N=1}^4 c_N \delta(y_N)$$

and the matching percentage to the final field shift after each term has been added differs from the one when the original summation is used.

As seen in Fig. 9, the orthogonal expansion converges substantially faster than the original summation. In fact, only the  $\delta(r^2)$  and  $\delta(r^4)$  moments need to be considered as long as the sum is rearranged. Thus, for a pair of isotopes  $A, A'$

and a transition  $k$ , the RFS is to a very good approximation expressed as

$$\delta v_{k,\text{RFS}}^{A,A'} \approx c_{k,1}\delta(y_1) + c_{k,2}\delta(y_2).$$

In case the isotope shifts are known for two transitions, a system of two equations can be formed, and the  $c_{k,1}$  and  $c_{k,2}$  constants can be evaluated using the expressions above. They depend on the line field shift factors  $\bar{F}_{k,N}$  that are different for each transition and which are calculated for the reference isotope  $A$ . Therefore, for two transitions, the problem takes the form of a matrix equation

$$\begin{bmatrix} \delta v_{1,\text{RFS}}^{A,A'} \\ \delta v_{2,\text{RFS}}^{A,A'} \end{bmatrix} \approx \begin{bmatrix} c_{1,1} & c_{1,2} \\ c_{2,1} & c_{2,2} \end{bmatrix} \begin{bmatrix} \delta(y_1) \\ \delta(y_2) \end{bmatrix}.$$

The unknown  $y_1$  and  $y_2$  can thus be solved according to

$$\begin{bmatrix} \delta(y_1) \\ \delta(y_2) \end{bmatrix} \approx C^{-1} \begin{bmatrix} \delta v_{1,\text{RFS}}^{A,A'} \\ \delta v_{2,\text{RFS}}^{A,A'} \end{bmatrix},$$

where  $C^{-1}$  is the inverse matrix of  $\begin{bmatrix} c_{1,1} & c_{1,2} \\ c_{2,1} & c_{2,2} \end{bmatrix}$ . The  $\delta\langle r^2 \rangle$  and  $\delta\langle r^4 \rangle$  moments are finally extracted by solving the equations

$$\begin{bmatrix} \delta(y_1) \\ \delta(y_2) \end{bmatrix} = \begin{bmatrix} 3.46556/\bar{A}^{2/3} & 0 \\ -15.2051/\bar{A}^{2/3} & 12.5116/\bar{A}^{4/3} \end{bmatrix} \begin{bmatrix} \delta\langle r^2 \rangle \\ \delta\langle r^4 \rangle \end{bmatrix}.$$

This can be compared with the original summation, where if the approximate relation

$$\delta v_{k,\text{RFS}}^{A,A'} \approx \bar{F}_{k,1}\delta\langle r^2 \rangle + \bar{F}_{k,2}\delta\langle r^4 \rangle$$

is assumed, the matrix equation to be solved is given by

$$\begin{bmatrix} \delta v_{1,\text{RFS}}^{A,A'} \\ \delta v_{2,\text{RFS}}^{A,A'} \end{bmatrix} \approx \begin{bmatrix} \bar{F}_{1,1} & \bar{F}_{1,2} \\ \bar{F}_{2,1} & \bar{F}_{2,2} \end{bmatrix} \begin{bmatrix} \delta\langle r^2 \rangle \\ \delta\langle r^4 \rangle \end{bmatrix}.$$

- 
- [1] I. Angeli and K. Marinova, Table of experimental nuclear ground state charge radii: An update, *At. Data Nucl. Data Tables* **99**, 69 (2013).
- [2] C. G. Parthey *et al.*, Precision measurement of the hydrogen-deuterium  $1s - 2s$  isotope shift, *Phys. Rev. Lett.* **104**, 233001 (2010).
- [3] S. E. Agbemava, A. V. Afanasjev, D. Ray, and P. Ring, Global performance of covariant energy density functionals: Ground state observables of even-even nuclei and the estimate of theoretical uncertainties, *Phys. Rev. C* **89**, 054320 (2014).
- [4] D. Andrae, Finite nuclear charge density distributions in electronic structure calculations for atoms and molecules, *Phys. Rep.* **336**, 413 (2000).
- [5] Y. S. Kozhedub, O. V. Andreev, V. M. Shabaev, I. I. Tupitsyn, C. Brandau, C. Kozhuharov, G. Plunien, and T. Stöhlker, Nuclear deformation effect on the binding energies in heavy ions, *Phys. Rev. A* **77**, 032501 (2008).
- [6] N. A. Zubova, Y. S. Kozhedub, V. M. Shabaev, I. I. Tupitsyn, A. V. Volotka, G. Plunien, C. Brandau, and Th. Stöhlker, Relativistic calculations of the isotope shifts in highly charged Li-like ions, *Phys. Rev. A* **90**, 062512 (2014).
- [7] M. J. G. Borge, Recent highlights of the isolde facility, *J. Phys.: Conf. Ser.* **580**, 012049 (2015).
- [8] C. Brandau, M. Lestinsky, C. Kozhuharov, A. Müller, S. Schippers, and Th. Stöhlker, High-resolution dielectronic recombination experiments at the upcoming cryring@esr facility, *J. Phys.: Conf. Ser.* **635**, 022084 (2015).
- [9] C. W. P. Palmer, Reformulation of the theory of the mass shift, *J. Phys. B: At. Mol. Phys.* **20**, 5987 (1987).
- [10] V. M. Shabaev, Mass corrections in a strong nuclear field, *Theor. Math. Phys.* **63**, 588 (1985).
- [11] V. Shabaev and A. Artemyev, Relativistic nuclear recoil corrections to the energy levels of multicharged ions, *J. Phys. B: At. Mol. Phys.* **27**, 1307 (1994).
- [12] E. C. Seltzer,  $k$  x-ray isotope shifts, *Phys. Rev.* **188**, 1916 (1969).
- [13] G. Torbohm, B. Fricke, and A. Rosén, State-dependent volume isotope shifts of low-lying states of group-ii  $a$  and  $-ii$   $b$  elements, *Phys. Rev. A* **31**, 2038 (1985).
- [14] S. Blundell, P. Baird, C. Palmer, D. Stacey, and G. Woodgate, A reformulation of the theory of field isotope shift in atoms, *J. Phys. B: At. Mol. Phys.* **20**, 3663 (1987).
- [15] J. Ekman *et al.* [Comp. Phys. Comm. (unpublished)]
- [16] P. Jönsson, G. Gaigalas, J. Bieroń, C. Froese Fischer, and I. Grant, New version: Grasp2k relativistic atomic structure package, *Comput. Phys. Commun.* **184**, 2197 (2013).
- [17] I. P. Grant, *Springer Series on Atomic, Optical and Plasma Physics*, Vol. 40 (Springer, Berlin, 2007).
- [18] B. J. McKenzie, I. P. Grant, and P. H. Norrington, A program to calculate transverse Breit and QED corrections to energy levels in a multiconfiguration Dirac-Fock environment, *Comput. Phys. Commun.* **21**, 233 (1980).
- [19] C. Nazé, E. Gaidamauskas, G. Gaigalas, M. Godefroid, and P. Jönsson, ris3: A program for relativistic isotope shift calculations, *Comput. Phys. Commun.* **184**, 2187 (2013).
- [20] S. A. Blundell, W. R. Johnson, and J. Sapirstein, Improved many-body perturbation theory calculations of the  $n=2$  states of lithiumlike uranium, *Phys. Rev. A* **41**, 1698 (1990).
- [21] W. R. Johnson, J. Sapirstein, and K. T. Cheng, Theory of  $2s_{1/2}-2p_{3/2}$  transitions in highly ionized uranium, *Phys. Rev. A* **51**, 297 (1995).
- [22] J. D. Zumbro, E. B. Shera, Y. Tanaka, C. E. Bemis, R. A. Naumann, M. V. Hoehn, W. Reuter, and R. M. Steffen,  $e2$  and  $e4$  deformations in  $^{233,234,235,238}\text{U}$ , *Phys. Rev. Lett.* **53**, 1888 (1984).
- [23] J. D. Zumbro, R. A. Naumann, M. V. Hoehn, W. Reuter, E. B. Shera, C. E. Bemis, and Y. Tanaka,  $E2$  and  $e4$  deformations in  $^{232}\text{Th}$  and  $^{239,240,242}\text{Pu}$ , *Phys. Lett. B* **167**, 383 (1986).
- [24] P. Ring and P. Schuck, *The Nuclear Many-Body Problem*, 1st ed. (Springer, New York, 1980).
- [25] E. Chabanat, P. Bonche, P. Haensel, J. Meyer, and R. Schaeffer, A Skyrme parametrization from subnuclear to neutron star densities Part ii. Nuclei far from stabilities, *Nucl. Phys. A* **635**, 231 (1998).
- [26] B. A. Brown, New Skyrme interaction for normal and exotic nuclei, *Phys. Rev. C* **58**, 220 (1998).
- [27] B. G. Carlsson, J. Dobaczewski, J. Toivanen, and P. Veselý, Solution of self-consistent equations for the  $N^3\text{LO}$  nuclear

- energy density functional in spherical symmetry. The program hosphé (v1.02), *Comput. Phys. Commun.* **181**, 1641 (2010).
- [28] M. Stoitsov, N. Schunck, M. Kortelainen, N. Michel, H. Nam *et al.*, Axially deformed solution of the Skyrme-Hartree-Fock-Bogoliubov equations using the transformed harmonic oscillator basis (ii) HFBTHO v2.00d: A new version of the program, *Comput. Phys. Commun.* **184**, 1592 (2013).
- [29] A. Bouyssy, J. F. Mathiot, N. Van Giai, and S. Marcos, Relativistic description of nuclear systems in the Hartree-Fock approximation, *Phys. Rev. C* **36**, 380 (1987).
- [30] R. Rosenfelder, Coulomb corrections to elastic electronproton scattering and the proton charge radius, *Phys. Lett. B* **479**, 381 (2000).
- [31] R. Pohl, R. Gilman, G. Miller, and K. Pachucki, Muonic Hydrogen and the Proton Radius Puzzle, *Annu. Rev. Nucl. Part. Sci.* **63**, 175 (2013).
- [32] H. De Vries, C. W. De Jager, and C. De Vries, Nuclear Charge-Density-Distribution Parameters from Electron Scattering, *At. Data Nucl. Data Tables* **36**, 495 (1987).
- [33] G. Fricke, C. Bernhardt, K. Heilig, L. A. Schaller, L. Schellenberg, E. B. Shera, and C. W. Dejager, Nuclear ground state charge radii from electromagnetic interactions, *At. Data Nucl. Data Tables* **60**, 177 (1995).
- [34] W. van Wijngaarden and J. Li, Hyperfine splittings and isotope shifts of  $(6s)21s0-(6s6p)1p1$  transition in barium, *Can. J. Phys.* **73**, 484 (1995).
- [35] C. Nazé, J. G. Li, and M. Godefroid, Theoretical isotope shifts in neutral barium, *Phys. Rev. A* **91**, 032511 (2015).
- [36] J. Li, C. Nazé, M. Godefroid, S. Fritzsche, G. Gaigalas, P. Indelicato, and P. Jönsson, Mass- and field-shift isotope parameters for the  $2s-2p$  resonance doublet of lithiumlike ions, *Phys. Rev. A* **86**, 022518 (2012).
- [37] C. Brandau, C. Kozhuharov, Z. Harman, A. Müller, S. Schippers, Y. S. Kozhedub, D. Bernhardt, S. Böhm, J. Jacobi, E. W. Schmidt, P. H. Mokler, F. Bosch, H.-J. Kluge, Th. Stöhlker, K. Becker, P. Beller, F. Nolden, M. Steck, A. Gumberidge, R. Reuschl, U. Spillmann, F. J. Currell, I. I. Tupitsyn, U. D. Jentschura, V. M. Shabaev, C. H. Keitel, A. Wolf, and Z. Stachura, Isotope Shift in the Dielectronic Recombination of Three-Electron  $^A\text{Nd}^{57+}$ , *Phys. Rev. Lett.* **100**, 073201 (2008).
- [38] S. R. Elliott, P. Beiersdorfer, and M. H. Chen, Trapped-Ion Technique for Measuring the Nuclear Charge radii of Highly Charged Radioactive Isotopes, *Phys. Rev. Lett.* **76**, 1031 (1996).
- [39] G. Plunien, B. Müller, W. Greiner, and G. Soff, Nuclear polarization contribution to the lamb shift in heavy atoms, *Phys. Rev. A* **39**, 5428 (1989).
- [40] G. Plunien, B. Müller, W. Greiner, and G. Soff, Nuclear polarization in heavy atoms and superheavy quasiatoms, *Phys. Rev. A* **43**, 5853 (1991).
- [41] G. Plunien and G. Soff, Nuclear-polarization contribution to the lamb shift in actinide nuclei, *Phys. Rev. A* **51**, 1119 (1995).
- [42] G. Plunien and G. Soff, Erratum: Nuclear-polarization contribution to the lamb shift in actinide nuclei, *Phys. Rev. A* **53**, 4614 (1996).
- [43] T. Beier, P. J. Mohr, H. Persson, and G. Soff, Influence of nuclear size on QED corrections in hydrogenlike heavy ions, *Phys. Rev. A* **58**, 954 (1998).
- [44] E. W. Weisstein, Gram-Schmidt orthonormalization, from MATHWORLD, a Wolfram web resource.



## Atomic Electrons as Sensitive Probes of Nuclear Properties and Astrophysical Plasma Environments

---



This is a thesis about atoms and ions; their structures and the interactions of their electrons with internal and external electromagnetic fields and with the nucleus. I grew up in Athens, Greece, and had my graduate education in Lund. This work was performed at the Department of Materials Science and Applied Mathematics at Malmö University and the Department of Physics at Lund University and was defended on the 7th of May 2021. The picture was taken about a year ago in Cape Town.

